DISSERTATION

INVESTIGATIONS INTO PHOTOCATALYSIS AND ELECTRONIC STRUCTURE FOR TRANSITION METAL AND ACTINIDE COMPLEXES

Submitted by

Robert F. Higgins

Department of Chemistry

In partial fulfillment of the requirements

For the Degree of Doctor of Philosophy

Colorado State University

Fort Collins, Colorado

Fall 2018

Doctoral Committee:

Advisor: Matthew P. Shores

Anthony K. Rappé
James R. Neilson
Andrew McNally
Mingzhong Wu

Copyright by Robert F. Higgins 2018

All Rights Reserved

ABSTRACT

INVESTIGATIONS INTO PHOTOCATALYSIS AND ELECTRONIC STRUCTURE FOR TRANSITION METAL AND ACTINIDE COMPLEXES

Presented herein are investigations into the electronic structure of various metal complexes and how they effect reactivity. The first chapters are centered on how $[Cr(Ph_2phen)_3]^{3+}$ reacts as a photooxidant. The latter part of this work concerns magnetic properties of various first row transition metal and actinide complexes.

In Chapter 1, I provide a background on how understanding electronic structure of transition metal complexes has motivated later work in reactivity. This Chapter also includes a detailed background in photoredox catalysis and different electronic structures of Ru-, Ir- and Cr-containing photosensitizers. It ends with a lead-in to our initial hypotheses and motivations for using Cr as a paramagnetic, Earth-abundant congener to Ru photosensitizers in photoredox manifolds.

Chapters 2-4 illustrate our mechanistic studies into transformations using Cr as a photooxidant to perform [4+2] cycloaddition reactions between (*trans* and *cis*)-anethole and dienes. Chapter 2 focuses on the interactions of oxygen (O_2) in the reaction of *trans*-anethole and isoprene mediated by $[Cr(Ph_2phen)_3]^{3+}$. We determined three separate, yet invaluable roles that oxygen performs in this reaction, which include: (1) protection of the catalyst through excited-state energy-transfer giving $^1O_2$, (2) $^1O_2$ oxidation of the reduced form of the catalyst, regenerating the ground state species and giving $^2O_2^{\bullet-}$ as well as (3) $^2O_2^{\bullet-}$ reduction of the radical cation of the [4+2] product, completing the catalytic cycle. In Chapter 3, I discuss the association that *trans*-anethole and similar dienophiles show with $[Cr(Ph_2phen)_3]^{3+}$ and how this affects the overall reactivity.

Interestingly, diamagnetic analogues do not show the same association. Finally, in Chapter 4, *trans*-anethole is replaced with *cis*-anethole to determine how the overall reactivity changes. These data are supported by reactivity, kinetic and quenching studies to probe the reactivity.

Chapters 5-7 concern similar mechanistic details involving $[Cr(Ph_2phen)_3]^{3+}$ in photocatlytic cycloaddition reactions, except that *trans*-anethole, which is electron-rich, is replaced by 4-methoxychlacone, which is electron-poor. Chapter 5 discusses the synthetic utility of this reaction manifold and initial mechanistic details of the transformation, which reveal an orthogonal mechanism which proceeds through energy transfer when compared to the reactivity of *trans*-anethole with $[Cr(Ph_2phen)_3]^{3+}$. In Chapter 6, the observation of enhanced regioselectivity that is observed when $[Cr(Ph_2phen)_3]^{3+}$ is used is investigated, specifically in comparison to all other Cr- and Ru-photooxidants attempted. This regioselectivity is manifested in the stabilization of a one-bond intermediate, as well as an association between 4-methoxychalcone and $[Cr(Ph_2phen)_3]^{3+}$. To conclude this section, Chapter 7 focuses on the interesting solution-phase equilibria of 4-methoxychalcone and how the association of 4-methoxychlacone with itself and $[Cr(Ph_2phen)_3]^{3+}$ impacts the overall reaction mechanism.

Chapter 8 provides an interesting method of using ferrocenium as an inexpensive and abundant electron-transfer reagent in reactions similar to common photoredox reactions. This uncommon reaction pathway provides an interesting reactivity compared to traditional pericyclic reactions.

The remaining Chapters (9-13) explore the magnetic properties and electronic structures of a variety of first-row and actinide complexes and clusters. Chapter 9 focuses on spin-state switching through oxidation chemistry of both iron and nitrogen atoms in organometallic complexes. The ground states of these complexes can be controllably tuned through sequential oxidation reactions. In Chapter 10, I present the synthesis and magnetic properties of mono- and bis-terpyridine Co(II) complexes. These Co complexes display a variety of coordination

geometries which affect their dynamic magnetic properties. Chapter 11 focuses on the reactivity and magnetic properties of a family of U-acetylide species, where interesting redox chemistry is noted upon addition of redox-inactive crown ether molecules. In Chapter 12, I discuss the magnetic properties of 3 different families of uranium complexes measured in collaboration with Prof. Suzanne Bart's group at Purdue University. Finally, in Chapter 13, I give some broad conclusions about what was learned in the mechanistic studies of Cr-photocatalysis and possible interesting avenues for future work.

ACKNOWLEDGEMENTS

Graduate school has been some of the most interesting years of my life, some of it extremely challenging, but most of it extremely rewarding. First of all, Matt, I couldn't thank you more. You pushed me in ways I didn't think were possible and allowed me to explore every technique I could imagine performing. Your door has always been open for anything and everything I could have needed over these five years. Even though I am leaving Colorado, I know our great friendship will continue for many years and I am thrilled to have worked for you.

Tony, we have really explored some crazy ideas, but have had doing all of this together. I am glad we could keep each other busy over the last 5 years with classes, research and life. I'll surely miss your knowledge and positive attitude as I can continue my career. To Eric, even though you were at CSU for one year of my graduate career, I wouldn't be where I am today without your advice. Your dedication to pure science and interest in all sorts of problems has been a hugely motivating factor in my education. Niels, your attention to detail to ensure everything is as close to correct as we can reasonably manage has been greatly beneficial. I hope you find some sort of likeness for Europeans in your future work, but that's yet to be determined. Jamie, you somehow allowed me into your laboratory for advice and even let me write a paper with you. Even though I only rotated with your group, I always felt like a pseudo member of the Neilson lab, and I appreciate your openness for me. To Joe, while you only overlapped with me at the very end of my graduate career, you gave me plenty of insight into electronic structure of metal complexes that have reason existing. Last but not least, Mike Elliott. I know somewhere you are turning CVs I have printed off in all sorts of directions with a coffee asking why I don't understand why current will always be passing. I think of you often, you were taken too early, and are missed everyday by people here at CSU.

To all of my coworkers and friends, I am glad we got to spend time together and all of the valuable things I have learned from all of you. Christina, while we didn't get along every second, you taught me a lot about persistence and work ethic and I commend you for that. To Steph, Kelsey and David (Daley), thanks for helping me put my foot in the door at Matt's lab when I first got here. To Mike and David, thank you for establishing initial results into C-CLEAR, things would have much more challenging without you two. I wouldn't have any of the little knowledge I have about magnetism without you Indrani; you made learning what is such a difficult topic far easier with your multiple perspectives. To Devon and Andy, our time together was rather brief, but I appreciate the perspectives and attitudes you brought to the lab. Romeo, you are a caring person who has always been there for me in lab and out of it. You have been a great friend throughout grad school and I am excited to continue to see you throughout the rest of my life. Justin, while I don't always understand your music or screensaver choices, you always made me laugh and taught me something new every time we spoke. Brooke, you are always positive and bring smiles to the lab, don't ever let that change. Thank you for your meticulous approach to science, its something every scientist should aspire to have in their results. To Will, Jessica and Nick, you were all fantastic undergrads and I wish you well on your journeys throughout the rest of your (scientific) careers. To my collaborators in C-CLEAR, Steve, Suzie and Sam, thank you for your amazing contributions to this interesting research project.

To Andy, I don't think I will ever have another friend who will join me at Road 34, or a similar establishment, at opening for every Saturday/Sunday for years. Your motivation and constant enthusiasm in all sorts of chemistry were invaluable to my career. Thank you for all of the great memories we made together. Tarik, without you in Matt's group, I don't know where I would be right now. Your background in organic chemistry is basically everything I know and understand about the subject. Why you named your dog Michael, I will never know, but your mysterious and unique perspective to life were always refreshing. To all of my workers and friends

at The Bar and Road 34 (Chad, Efrain, Allie, Vinny, Tony, CJ, Ryan, Nate, Konrad, Kayla, Lorenza, Will, Joe, Schuyler, Ben, Karl, Andrew, Logan, Mitch, Mo…hopefully I am not missing too many people), thank you so much for the constant support and kindness. I will miss all of you very much.

Most importantly, thank you to everyone in my family. Your constant support and motivation have been incredibly helpful to guide me throughout my graduate career. Mom and Dad, you are the best parents I could ask for and I am so happy every time we talk and spend time with each other. To Katie, John and Brodie, thank you for everything. You are the people I normally wake up and falling asleep talking to, and I so happy about that. Aunt Grace, Uncle Jim and Jimmy, I can't wait to move closer to you all and spend as much time together as possible. Grandma Jean and Grace, thank you for your support and guiding me toward my end goals with education. To the rest of the Higgins, Dowe, Mueller, Collins, Oviedo, Crivella, Noyse, Kellman, and all other families who are always so welcoming and supportive, I can't thank you all enough. Well this is probably too long, but I am sure I missed some people. This is for all of you, not me, because without everyone else in my life, I wouldn't have been able to do this.

DEDICATION

For Jean, Neville, Frank and Grace, my guiding lights for instilling the importance of education.

TABLE OF CONTENTS

ACKNOWLEDGEMENTS v
DEDICATION viii
LIST OF TABLES xviii
LIST OF FIGURES xix
Chapter 1: The effect of electronic structure on reactivity: a brief historical background as a lead-in to photoredox catalysis 1
1.1 Werner Complexes in Catalysis 1
1.2 Excited-state properties of Ru 2
1.3 Photoredox reactivity 3
1.4 Cr-photoredox catalysis 7
1.5 Outline of chapters 10
References 11
Chapter 2: Uncovering the Roles of Oxygen in Cr(III) Photoredox Catalysis.* 13
2.1 Introduction 13
2.2 Division of Labor 17
2.3 Experimental 18
2.3.1 Preparation of compounds 18
2.3.2 Preparation of novel metal complexes 18
2.3.3 Electrochemical measurements 19
2.3.4 Catalysis studies 20
2.3.5 Mechanistic measurements and studies 20
2.3.6 Other physical measurements 21
2.3.7 Electronic structure calculations 22

2.4 Results 22
2.4.1 Catalyst syntheses 22
2.4.2 Catalysis studies 23
2.4.3 Electrochemical studies 25
2.4.4 Spectro(electro)chemical studies 31
2.4.5 Photophysical studies 32
2.4.6 Electronic structure calculations 35
2.5 Discussion 39
2.5.1 Excitation of Cr-catalyst 41
2.5.2 Oxidation of dienophile and subsequent cyclization 41
2.5.3 Regeneration of the Cr catalyst 43
2.5.4 Reduction of the cycloadduct radical cation 44
2.5.5 Overall catalytic cycle including oxygen 46
2.5.6 Comparison of Ru- and Cr-based photoredox catalysis 48
2.6 Conclusions and Outlook 49
References 51
Chapter 3: Spin directed, association driven photoredox catalysis 55
3.1 Introduction 55
3.2 Division of labor 56
3.3 Experimental 56
3.3.1 Preparation of known compounds 56
3.3.2 Preparation of novel compounds 57

3.3.3 Kinetics studies 57
3.3.4 Light-flux studies 57
3.3.5 Other physical methods....58
3.4 Results and Discussion 58
3.5 Conclusions....62
References 64
Chapter 4: Effects of *cis/trans*-isomers of anethole into Cr-photoredox reactivity 66
4.1 Introduction....66
4.2 Division of Labor....67
4.3 Experimental 67
4.3.1 Preparation of compounds 67
4.3.2 Reactivity studies 68
4.3.3 Electrochemical studies....68
4.3.4 Kinetic and light flux experiments 68
4.3.5 Quenching experiments 69
4.4 Results and Discussion 70
4.4.1 Catalysis studies 70
4.4.2 Electrochemical studies....73
4.4.3 Photophysical Studies 73
4.4.4 Kinetics Studies 74
4.5 Conclusions....77
References 78
Chapter 5: Detection of an energy transfer pathway in Cr-photocatalysis.* 81

5.1 Introduction....81
5.2 Division of Labor....83
5.3 Experimental....83
5.3.1 Preparation of compounds....83
5.3.2 Preparation of novel metal complexes....84
5.3.3. Mechanistic Measurements and Studies....85
5.3.4. Other Physical Measurements....86
5.3.5. Computational methods....86
5.4 Results and Discussion....87
5.5 Conclusions....96
References....98
Chapter 6: A unique excited state for $[Cr(Ph_2phen)_3]^{3+}$ promotes a selective energy-transfer mechanism....102
6.1 Introduction....102
6.2 Division of Labor....104
6.3 Experimental....105
6.3.1 Preparation of Compounds....105
6.3.2 Mechanistic measurements and studies....105
6.3.3 Electrochemical measurements....106
6.3.4 Other physical measurements....106
6.3.5 Catalysis studies....106
6.4 Results and Discussion....109
6.5 Conclusions and outlook....119

References 121
Chapter 7: Mechanistic studies into substrate-catalyst association in a Cr-photocatalytic system 124
7.1 Introduction.....124
7.2 Division of Labor.....126
7.3 Experimental 126
7.3.1 Preparation of Compounds 126
7.3.2 Mechanistic Measurements and Studies 126
7.3.3 Kinetics Studies 127
7.3.4 Other Physical Measurements 127
7.4 Results and Discussion 127
7.4.1 Catalyst-Substrate Association.....127
7.4.2 Substrate-Substrate Association Studies 129
7.4.3 Kinetic Studies 131
7.4.4 Other quantum yield studies.....134
7.5 Conclusions and Outlook.....136
References 137
Chapter 8: Ferrocenium as a catalytic single electron transfer reagent with excited-state organic substrates. 140
8.1 Introduction.....140
8.2 Division of Labor.....142
8.3 Experimental 142
8.3.1 Preparation of Known Compounds.....142
8.3.2 Preparation of Novel Compounds 143

8.3.3 Reactivity Studies....144
8.3.4 Mechanistic Measurements and Studies....145
8.3.5 Other Physical Measurements....145
8.4 Results and Discussion....146
8.5 Conclusions and Outlook....152
References....153
Chapter 9: A redox tunable ligand which promotes a reversal in superexchange coupling in a trinuclear iron system....156
9.1 Introduction....156
9.2 Division of labor....158
9.3 Experimental....158
9.3.1 Preparation of Compounds....158
9.3.2 Preparation of novel metal complexes....159
9.3.3 Magnetic susceptibility measurements....162
9.3.4 Crystallographic measurements....163
9.3.4 Other physical measurements....163
9.3.5 Computational details....164
9.4 Results and Discussion....165
9.4.1 Syntheses and Characterization....165
9.4.2 Oxidation and Electrochemistry....166
9.4.3 X-Ray Structures....170
9.4.4 Magnetic Properties of Ferric Species....171
9.4.5 Oxidation of Nitrogen Atom....175

9.4.6 Magnetic Properties of **9.7** 177

9.4.7 Computational results 180

9.5 Conclusions....185

References 186

Chapter 10: A family of related Co(II) terpyridine compounds exhibiting field induced single-molecule magnet properties.*....189

10.1 Introduction....189

10.2 Division of Labor....191

10.3 Materials and Methods. 191

10.3.1 General Considerations....191

10.3.2 Preparation of novel metal complexes....192

10.3.3 Magnetic Measurements 193

10.3.4 Crystallographic Measurements 194

10.3.5 Other Physical Measurements 196

10.3.6 Computational Methods 196

10.4 Results and Discussion 197

10.4.1 Syntheses 197

10.4.2 Structural Characterization....199

10.4.3 Magnetic Measurements and Interpretation 201

10.4.4 Computational Studies 206

10.4.5 Conclusions 208

References 210

Chapter 11: Reactivity and magnetic properties for a series of U-acetylide complexes. 214

11.1 Introduction....214

11.2 Division of Labor....215
11.3 Materials and Methods....215
11.3.1 General Considerations....215
11.3.2 Preparation of novel metal complexes....216
11.3.3 Magnetic Measurements....217
11.3.4 Crystallographic Measurements....218
11.3.5 Other Physical Measurements....219
11.4 Results and Discussion....219
11.4.1 Synthesis of **11.1** and **11.2**....219
11.4.2 Crystal structures of **11.1** and **11.2.**....220
11.4.3 Magnetic properties of **11.1** and **11.2**....224
11.4.4 Synthesis and characterization of **11.3**....227
11.5 Conclusion....229
References....230
Chapter 12: Magnetic properties of uranium complexes appended with PDI, alkyl and Tp* ligands.*....233
12.1 Background....233
12.2 Division of Labor....234
12.3 Experimental Details....234
12.4 Results and Discussion....236
12.4.2 U-PDI complexes....240
12.4.3 U-Tp* complexes....244
References....255

Chapter 13: Interesting observations and future implications for small molecule Cr-photocatalysis 258
13.1 Conclusions for Cr-photocatalysis investigations 258
13.2 Association of $[(phenda)_2CrCl_2]Cl$ and *trans*-anethole 258
13.3 Photoreactivity of $[Cr(pic)_3]$ 261
References 264
Appendix 1: Supporting information for chapter 2 265
Appendix 2: Supporting information for chapter 3 269
Appendix 3: Supporting information for chapter 5 272
Appendix 4: Supporting information for chapter 6 276
Appendix 5: Supporting information for chapter 7 284
Appendix 6: Supporting information for chapter 8 290
Appendix 7: Supporting information for chapter 9 297
Appendix 8: Supporting information for chapter 10 302
Appendix 9: Supporting information for chapter 11 306
Appendix 10: Supporting information for chapter 12 311

LIST OF TABLES

Table 2.4.1 Compiled electrochemical data for **2.2**.[a] 28

Table 2.4.2 Compilation of electrochemical data for methoxy-substituted styrenes and cycloproducts. 30

Table 2.4.3 Computed reaction energetics (kcal/mol) 37

Table 4.4.1. Comparative reduction potentials of cis- and trans-anethole 73

Table 4.4.2. Rate constants for several processes cis- and trans-anethole can undergo during reaction conditions. 75

Table 6.4.1. Single wavelength irradiation data for different photosensitizers. 110

Table 9.4.1. Compiled electrochemistry data for **9.1**, **9.3** and **9.5**. 168

Table 9.4.2. Comparison of bend angle in all triarylamine-acetylene bridged metal complexes presently in the literature. 170

Table 9.4.3. Parameters from the magnetic fits performed for **9.2**, **9.4**, **9.6** and **9.7**. 172

Table 9.4.4. Parameters from unsuccessful magnetic fits performed for **9.7**. 178

Table 10.3.1. Crystallographic parameters for **10.1**-**3**.[a] 195

Table 10.4.1. Selected distances (Å) and angles (°) for compounds **10.1-3.** 200

Table 10.4.2. Magnetic parameters for **1**-**3**, obtained via fits and computations.[a] 203

Table 11.4.1 Crystallographic parameters for **11.1** and **11.2.**[a] 222

Table 11.4.2 Selected bond distances (Å) and angles (˚) for **11.1-11.3**. 223

Table 12.4.1. Magnetic susceptibility and magnetization values for [U(p-^{i}PrBn)$_4$], [U(p-^{t}BuBn)$_4$], [U(o-OMeBn)$_4$], [U(p-ClBn)$_4$] and [U(m-OMeBn)$_4$]. 239

Table 12.4.2. Parameters for the magnetic fits for [(Tp*)$_2$U(=N-p-Tol)], [((Tp*)$_2$U)$_2$(p-DIB)], [((Tp*)$_2$U)$_2$(m-DIB)] and [(Tp*)$_2$U]-insertion product using the program PHI.[3] 248

Table 12.4.3 Magnetic susceptibility and magnetization values for [((Tp*)$_2$U)$_2$-p-DEB], [(Tp*)$_2$U(CCPh)], [(Tp*)$_2$U(THF)](BPh$_4$) and [(Tp*)$_2$U(MeCN)$_2$](BPh$_4$). 251

Table 12.4.4 Selected single molecule magnetic values and crystal field parameters acquired from fits using the program PHI[6] for some Tp-containing U(III) complexes. 253

Table A3.1. Computed vertical and adiabatic excitation and ionization energies (eV) for dienes and dienophiles. 274

Table A3.2. Computed vertical and adiabatic total energies for ground state, triplet excited state, cation, and anions (Hartree) for nitrogenous ligands. 275

Table A3.3. Computed vertical and adiabatic excitation, ionization energies, and electron affinities (eV) for nitrogenous ligands where T, IP and EA stand for triplet, ionization potential and electron affinities, respectively. 275

Table A7.1. Magnetic fits for **9.7** where four S = 1/2 spins were used. 301

Table A7.2. Magnetic fits for **9.7** where 2 S=1/2 spins were used. 301

Table A10.1. Comparison of different magnetic and crystallographic properties of U(Tp*) complexes. 332

LIST OF FIGURES

Figure 1.1.1 Isomers of $[(NH_3)_4CoCl_2]Cl$ (a) and representative example of an enantioselective reaction using a Werner complex (b). 1

Figure 1.2.1 Simplified Jablonski diagram for $[Ru(bpy)_3]^{2+}$ 3

Figure 1.3.1 Representative mechanisms for photoredox reactions. 4

Figure 1.3.2 Variable product formation on the basis on the presence of oxygen in a photoredox reaction. 5

Figure 1.3.3 Wavelength switchable photoredox catalysis. 6

Figure 1.3.4 Jablonski diagram for Cr(III) (left) and a Tanabe-Sugano diagram for a d^3 system (right).[33] 7

Figure 1.4.1 Absorption and emission data for $[Cr(acac)_3]$ (left) and a Jablonski diagram for the excited-state dynamics of $[Cr(acac)_3]$ (right).[34] 8

Figure 2.1.1 Initially proposed cycloaddition pathways; the green boxes denote the initial form of the Cr-containing catalyst. Note that isoprene is shown in the form that appears in the cycloadduct; the S-trans form is the major species in solution. 15

Figure 2.1.2 Proposed roles of oxygen in cycloaddition pathways; the green boxes denote the initial form of the Cr-containing catalyst. 16

Figure 2.4.1 Electronic absorption spectra of **1** and **2** in CH_3NO_2. 23

Figure 2.4.2 24

Figure 2.4.4 Cyclic voltammograms (CVs) of **2.1** and **2.2**, collected in 0.1 M Bu_4NPF_6 solutions with a scan rate of 100 mV/s. Solid and dashed lines represent data collected without and with oxygen bubbled through the solution, respectively. The arrows indicate the direction of the scan. The black asterisks indicate the open circuit potentials of the degassed samples. The sharp peak in the CH_3CN data (~-2.2 V) is due to a surface adsorption event that does not affect the reversibility of the system. 26

Figure 2.4.5 CVs of **2.2** obtained under several environmental conditions, collected in 0.1 M Bu_4NPF_6 CH_3NO_2 solutions with a scan rate of 100 mV/s. With the exception of the "dark" trace, the CVs focus on the first reduction event. The arrows indicate the open circuit potential and the direction of the scan. The data for the "dark and O_2" trace (blue) were collected using a glassy carbon working electrode to eliminate surface chemistry. The concentrations of the added diene (isoprene, **2.4**) and alkene (anethole, **2.3**) match those used in the catalytic studies (1:100:1000 **2.2**:**2.3**:**2.4**). 28

Figure 2.4.6 Oxygen dependence of emission quenching of **2.2** by **2.3** in room temperature CH_3NO_2, showing Stern-Volmer behavior (τ_0/τ versus quencher concentration, top) and normalized to initial lifetime ($1/\tau$ versus quencher concentration, bottom). By plotting $1/\tau$, the quenching rate constant (k_q) is equal to the slope: 9.4×10^8 $M^{-1}s^{-1}$ degassed, 9.5×10^8 $M^{-1}s^{-1}$ ambient O_2. The data are fit to a linear function using least-squares methodology. 33

Figure 2.4.7 Electronic absorption difference spectrum after a 40 hour photoreaction in which oxygen was excluded and a simulated spectrum consisting of the growth of **2.1** and loss of **2.2** in a 1:5 ratio. 34

Figure 2.4.8 Computed reaction pathways. The top Figure considers all processes related to Figure 2; the bottom Figure considers energetics associated with superoxide formation as part of catalyst regeneration. Blue entities represent possible routes affected by oxygen-containing species; the red route represents species involved in radical chain events. Free energies (in italics) are provided as kcal/mol relative to the ground state of the photocatalyst **2.2**. 36

Figure 2.5.1 Proposed catalytic cycle. 47

Figure 3.1.1. Selected examples of "catalyst"-substrate interactions prior to reactivity.[6-7, 16] 56

Figure 3.4.1. Representative kinetic data for the Cr-photocatalyzed cycloaddition reaction between trans-anethole and isoprene 59

Figure 3.4.2. The ^{1}H NMR peaks for $[Cr(Ph_2phen)_3]^{3+}$ (0.001 M) in CD_3NO_2 upon titration of trans-anethole. 60

Figure 3.4.3. Representative examples of species that (do not) show association with $[Cr(Ph_2phen)_3]^{3+}$ in CD_3NO_2. 61

Figure 3.4.4. ^{1}H NMR spectra of tris-Ph_2phen metal complexes of Fe(II), Ru(II) and Co(III) in CD_3NO_2 with and without trans-anethole added. 62

Figure 4.4.1 70

Figure 4.4.2 71

Figure 4.4.3 72

Figure 4.4.4. Oxygen dependence of the emission quenching of $[Cr(Ph_2phen)_3]^{3+}$ by trans- (blue trace) and cis-anethole (orange trace) in CH_3NO_2 at 23 °C fit to a linear function using least-squares methodology. 74

Figure 4.4.5. The effect of concentration of light on the production of product. 77

Figure 5.4.1. ^{1}H NMR spectra showing isomeric distribution of VCB intermediates dependent on reaction conditions. Note: VCB **5.5** is drawn as the major isomer for clarity, but is present as a mixture of isomers, as described in ref. 24. 88

Figure 5.4.2. Emission quenching of different sensitizers by **5.1** in $MeNO_2$. 93

Figure 6.4.1. Left: electron absorption spectra for 4-methoxychalcone (**6.3**) and photosensitizers $[Ru(bpz)_3]^{2+}$ (**6.1**), $[Cr(Ph_2phen)_3]^{3+}$ (**6.2**) and $[Cr(dmcbpy)_3]^{3+}$ (**6.8**, dmcbpy = 4,4'-dimethylcarboxylate-2,2'-bipyridine). Data are collected in acetonitrile. Right: results of single wavelength irradiations in nitromethane involving 4-methoxychalcone, three equivalents of isoprene, and various photosensitizers, using 1.0 mol% loadings for $[Ru(bpz)_3]^{2+}$ and 0.5 mol% loadings for $[Cr(Ph_2phen)_3]^{3+}$ and $[Cr(dmcbpy)_3]^{3+}$ (**6.8**). The "blue" irradiation source gives 3×10^{-9} mol einsteins s^{-1} at 340.00(2) nm; the "red" irradiation source gives 5.2×10^{-9} mol einsteins s^{-1} at 450.03(2) nm. 110

Figure 6.4.2. Natural transition orbitals for the lowest energy singlet or quartet excitations ("from" on left, "to" on right) involving outer sphere complexes of 4-methoxychoalcone interacting with $[Ru(bpz)_3]^{2+}$ (top) and $[Cr(Ph_2phen)_3]^{3+}$ (bottom), respectively. The line bond drawing for $[Cr(Ph_2phen)_3]^{3+}$ illustrates the energy transfer pathway, although significant electron transfer is observed in the β-spin NTOs. NTOs for the next transition, 0.1 eV up, also a mixture of energy and electron transfer, are available in the Supporting Information. 113

Figure 6.4.3. The ωb97xd derived spin-density plot of the doublet state for the Heisenberg spin-ladder for excited-states of $[Cr(Ph_2phen)_3]^{3+}$ (a) and the line-bond drawing of this excited-state (b) and a representative molecular orbital diagram showing the electronic structure of one of the

excited-states with the associated notation included below for all permeations of excited-states where d and L indicate states from metal- and ligand-based orbitals, respectively (c).....114

Figure 6.4.4. Left: pictorial representation of the twisted geometry for dienophile **6.2** when associated with complex **6.3**. Right: optimized structure of the catalyst-substrate association complex [**6.2•6.3**], computed with the DLPNO-CCSD(T) functional (left).....116

Figure 6.4.5. Different excited states for **6.2** (left), associated catalyst-substrate species [**6.2•6.3**] (middle) and **6.3** (right), using the DLPNO-CCSD(T) functional; energies in kcal/mol units represent association-induced stabilizations of excited sates; unlabeled energies are in eV units. 117

Figure 7.1.1. Representative electron structures of the lowest-energy excited states for $[Ru(bpz)_3]^{2+}$ (top), $[Cr(bpy)_3]^{3+}$ (middle) and $[Cr(Ph_2phen)_3]^{3+}$ (bottom). Other Ru- and Cr-diimine complexes show the same electronic configurations as $[Ru(bpz)_3]^{2+}$ and $[Cr(bpy)_3]^{3+}$, respectively. 125

Figure 7.4.1. ^1H NMR spectra of $[Cr(Ph_2phen)_3]^{3+}$ (0.0005 M) in CD_3NO_2 with and without the addition of 4-methoxychalcone (50 equiv). 128

Figure 7.4.2. Mass spectra of (a) enone **7.3** (0.010 M) in CH_3NO_2, (b) enone **7.3** (0.010 M) in C_6H_6, (c) enone **7.3** (0.010 M) in $PhCH_3$ and (d) cyclohexyl **7.10** (0.010 M) in CH_3NO_2 in the positive ion mode the highest intensity peaks labeled. Note: The chalcone dimers are drawn arbitrarily as head-to-head even though other arrangements are conceivable.....130

Figure 8.1.1. Energy profiles of 4-methoxychalcone and selected electron transfer reagents..142

Figure 8.4.1. Visible light absorption of the optimized reaction mixture (0.1, 0.3 and 0.005 M **8.4**, **8.6** and $[Fc](BF_4)$, respectively, in $MeNO_2$) before irradiation (blue trace) and after 10 minutes of irradiation (red trace). The gray traces are incremented by 1 minute each. Inset: Photographs of the reaction mixture before (left) and after 10 minutes of irradiation (right). 151

Figure 9.1.1. Chemdraw of trioxyphenylamine compounds (left). Line-bond drawings of MEPA (R = H) and TEPA (R = CCFe(Cp*)(dppe)) subunits where Cp* = pentamethylcyclopentadiene and dppe = 1,2-bis(diphenylphosphino)ethane. 157

Figure 9.4.2. (top) Cyclic voltammograms in CH_3CN for **9.1** and **9.5**, and CH_2Cl_2 for **9.3** collected at 100 mV/s in a 0.1 M Bu_4NPF_6 solution. *Indicates the open circuit potential and the arrow indicates the direction of the scan. (bottom) Square wave voltammograms of **9.5** in a 0.1 M Bu_4NPF_6 CH_3CN solution at a 4 mV step-size collected stepping in the positive direction. 168

Figure 9.4.3. ORTEP representations of the cations of **9.2** (left) and **9.6** (middle) at 40% probabilities where gray, orange, pink, green and blue are C, Fe, P, Cl and N atoms, respectively, with H atoms omitted. **6** sits on a site of higher symmetry as it crystallized in a cubic environment. Line-bond drawing for the bend angle of the traiarylamine ligand (right).....169

Figure 9.4.4. TIP-corrected temperature dependence of the magnetic susceptibility data for **9.2** (blue squares) and **9.4** (orange circles) collected at applied fields of 1000 Oe. The fits were performed using the program Julx.[35] 173

Figure 9.4.5. TIP-corrected temperature dependence of the magnetic susceptibility data for **9.6** and **9.7** at applied fields of 5000 Oe. The fits were performed using the program Julx.[35] 175

Figure 9.4.6. Reduced magnetization data for **9.7**. The best fit lines obtained from ANISOFIT are shown for each field.[36].....180

Figure 9.4.7. MO diagram for the free ligand p-TEPA.....181

Figure 9.4.8. Spin density plot for $[p\text{-TEPA}]^+$. 182

Figure 9.4.9. Spin density plots for **9.6** and **9.7** on the left and right, respectively.....184

Figure 10.4.1. Thermal ellipsoid (40% probability) representations for compounds **10.1** (top) and **10.3** (bottom) and the cation of **10.2b** (middle). All atoms lie on general positions. Co-crystallized solvent, anions (for **10.2b**) and hydrogen atoms are removed for clarity. Orange, blue, grey, red, green, yellow and light green correspond to cobalt, nitrogen, carbon, oxygen, chlorine, sulfur and fluorine atoms, respectively.....199

Figure 10.4.2. Temperature dependence of magnetic susceptibility data for **10.1** (blue diamonds), **10.2b** (green squares), and **10.3** (red circles) collected at an applied field of 1 kOe. The black lines represent best fits using PHI.[24] 202

Figure 10.4.3. Frequency dependence of the out of phase magnetic susceptibility under an applied dc field of 1.5 kOe for **10.1** (left) and 1.25 kOe for **10.3** (right) at the indicated temperature range (1.8 K, 2-8 K in 0.25 K increments). 204

Figure 10.4.4. Frequency dependence of the out of phase magnetic susceptibility with an applied dc field of 1 kOe for **10.2b** at the indicated temperature range (1.8 K, 2-4 K in 0.25 K increments). Inset: Arrhenius plot of relaxation time giving U_{eff} = 6.8 cm^{-1}. 206

Figure 11.4.1 ORTEP representations of **11.1** and **11.2** on the left and right respectively rendered with 40% ellipsoids. Light green, pink, red, yellow and gray represent U, P, O, Li, and C atoms respectively. H atoms are omitted for clarity. These structures are reproduced from Brian S. Newell's Ph.D. dissertation.....220

Figure 11.4.2 Temperature dependence of the magnetic susceptibility data for **11.1** (blue) and **11.2** (red) at applied dc fields of 5000 Oe.....224

Figure 12.4.1. Temperature dependence of magnetic susceptibilities for $[U(p\text{-}^{i}PrBn)_4]$, $[U(p\text{-}^{t}BuBn)_4]$, $[U(o\text{-}OMeBn)_4]$, $[U(p\text{-}ClBn)_4]$ and $[U(m\text{-}OMeBn)_4]$. Data for $[U(p\text{-}^{i}PrBn)_4]$, $[U(o\text{-}OMeBn)_4]$, and $[U(m\text{-}OMeBn)_4]$ were collected at an applied dc field of 5000 Oe, while data for $[U(p\text{-}^{t}BuBn)_4]$ and $[U(p\text{-}ClBn)_4]$ were collected at an applied dc field of 1000 Oe. 237

Figure 12.4.2. Relationship between the 300 K magnetic susceptibility values and Hammett parameter for compounds $[U(p\text{-}^{i}PrBn)_4]$, $[U(p\text{-}^{t}BuBn)_4]$, $[U(p\text{-}ClBn)_4]$ and $[U(m\text{-}OMeBn)_4]$. Note that $[U(o\text{-}OMeBn)_4]$ was not included in the linear fit due to the variation in its inner-coordination sphere**.**.....239

Figure 12.4.3. Top: Temperature dependence of the magnetic susceptibility for compounds $[(^{Mes}PDI^{Me})U(Cp^*)I]$ (gold), $[(^{Mes}PDI^{Me})U(Cp^*)(BCC)]_2$ (black), and $[(^{Mes}PDI^{Me})U(Cp^*)(BCC)]$ (blue) obtained at an applied dc field of 5000 Oe. Bottom: Field dependence of magnetization for compounds $[(^{Mes}PDI^{Me})U(Cp^*)I]$, $[(^{Mes}PDI^{Me})U(Cp^*)(BCC)]_2$, and $[(^{Mes}PDI^{Me})U(Cp^*)(BCC)]$ collected at 1.8 K. 242

Figure 12.4.4. Temperature dependence of the magnetic susceptibility for compounds $[(Tp^*)_2U(=N\text{-}p\text{-}Tol)]$, $[((Tp^*)_2U)_2(p\text{-}DIB)]$**,** $[((Tp^*)_2U)_2(m\text{-}DIB)]$ and $[(Tp^*)_2U]$-insertion product, collected at 1000 ($[((Tp^*)_2U)_2(p\text{-}DIB)]$**,** $[((Tp^*)_2U)_2(m\text{-}DIB)]$ and $[(Tp^*)_2U]$-insertion product) or 5000 Oe ($[(Tp^*)_2U(=N\text{-}p\text{-}Tol)]$).....245

Figure 12.4.5. Temperature dependence of the magnetic susceptibility for $[(Tp^*)_2U(=N\text{-}p\text{-}Tol)]$, $[((Tp^*)_2U)_2(p\text{-}DIB)]$**,** $[((Tp^*)_2U)_2(m\text{-}DIB)]$ and $[(Tp^*)_2U]$-insertion product per U-atom, where the 2-50 K data points are fit (black lines) using the program PHI.[6] Inset: Zoom of the low temperature fits. 247

Figure 12.4.6 Correlation between obtained spin-orbit coupling values and U···B distances...249

Figure 12.4.7 Temperature dependence of the magnetic susceptibility for compounds $[((Tp^*)_2U)_2\text{-}p\text{-}DEB]$, $[((Tp^*)_2U)_2\text{-}m\text{-}DEB]$, $[(Tp^*)_2U(CCPh)]$, $[(Tp^*)_2U(THF)](BPh_4)$ and $[(Tp^*)_2U(MeCN)_2](BPh_4)$

collected at applied field of 1000 ([((Tp*)$_2$U)$_2$-p-DEB] and [(Tp*)$_2$U(MeCN)$_2$](BPh$_4$)) or 5000 Oe ([(Tp*)$_2$U(CCPh)] and [(Tp*)$_2$U(THF)](BPh$_4$)). 250

Figure 12.4.8 Variable temperature in- (top) and out-of-phase (bottom) magnetic susceptibility data for [(Tp*)$_2$U(MeCN)$_2$](BPh$_4$) collected with an applied ac field of 4 Oe and an applied dc field of 1000 Oe. 252

Figure 13.2.1. ^{1}H NMR of [(phenda)$_2$CrCl$_2$]Cl (0.005 M) in (CD$_3$)$_2$SO before and after addition of trans-anethole (0.10 M). 259

Figure 13.2.2. Van't Hoff plot for the association of [(phenda)$_2$CrCl$_2$]Cl and trans-anethole in (CD$_3$)$_2$SO where the slope = ΔH/R and the x-intercept = -ΔS/R (R = gas constant). 260

Figure A1.1. IR spectra of **2.1** (blue trace), **2.2** (orange trace), **2.1** after exposure to O$_2$ (black trace) and **2.1** and **2.2** in degassed CH$_3$NO$_2$ irradiated for 20 minutes and then exposed to air for 30 minutes (green trace). The black trace was gathered after a solution of **2.1** in CH$_3$CN had O$_2$ bubbled through for 10 seconds. The green trace was exposed to air via a needle air outlet and the solvent was removed before the IR was gathered. 265

Figure A1.2. CVs of **2.2** in a 0.1 M dichloromethane solution of Bu$_4$NPF$_6$ referenced to Fc$^+$/Fc. The scans were all started at the rest potential of the cell (-0.1412 V) and swept cathodically. 266

Figure A1.3. Spectro-electrochemical oxidation of 4'-methoxy-2,4-dimethyl-1,2,3,6-tetrahydro-1,1'-biphenyl in CH$_3$CN (0.1 M Bu$_4$NPF$_6$) where all potentials are referenced vs. Fc$^+$/Fc. 266

Figure A1.4. Spectro-electrochemical oxidation of 4'-methoxy-2,4-dimethyl-1,2,3,6-tetrahydro-1,1'-biphenyl in CH$_3$CN (0.1 M Bu$_4$NPF$_6$) after exposure to O$_2$ where all potentials are referenced vs. Fc$^+$/Fc. 267

Figure A1.5. Aromatic region of ^{1}H NMR spectra of experiments where thiophenol spiked into a solution of 3:1 (mol %) **2.1**:**2.2** exposed to air (black trace) and a solution of **2.2** air-free (red trace) after 30 minutes of irradiation (419, 350 and 300 nm sources) and a solution of **2.1**:**2.3** kept air and light free (green trace). The spectra were referenced to CDCl$_3$. The blue protons are represent the peaks of interest for both diphenyl disulfide and thiophenol. The green trace gave integrations showing less than 2% conversion to diphenyl disulfide. 267

Figure A2.1. ^{1}H NMR spectra of [Cr(Ph$_2$phen)$_3$](BF$_4$)$_3$ (0.001 M) in CD$_3$NO$_2$. 269

Figure A2.2. ^{1}H NMR spectra of [Cr(dmcbpy)$_3$](BF$_4$)$_3$ (0.001 M) in CD$_3$NO$_2$ with and without trans-anethole (0.10 M) added. 269

Figure A2.3. ^{1}H NMR spectra of [Ru(bpz)$_3$](PF$_6$)$_2$ (0.001 M) in CD$_3$NO$_2$ with and without trans-anethole (0.10 M) added. The peak present at ~9.9 ppm is a small amount of anisaldehyde impurity from the oxidation of trans-anethole. 270

Figure A2.4. Isoprene concentration dependence on the rate constant under otherwise standard conditions. 270

Figure A2.5. [Cr(Ph$_2$phen)$_3$](BF$_4$)$_3$ concentration dependence on the rate constant under otherwise standard conditions. 271

Figure A3.1. Steady-state emission quenching of [Cr(Ph2phen)3]3+ by 4-methoxychalcone in nitromethane (λex = 450 nm) where a quenching rate constant of kq = 1 × 106 M-1 s-1 is determined, within error of the value determined in the time-resolved experiment. 272

Figure A3.2. Time resolved emission quenching of [Cr(Ph$_2$phen)$_3$]$^{3+}$ by 4-methoxychalcone in nitromethane (λ_{ex} = 450 nm) under inert conditions. A quenching rate constant of $k_q = 2 \times 10^6$ M^{-1} s^{-1} is determined. 273

Figure A3.3. Natural transition orbitals for the lowest quartet excited state for the association complex of $[Cr(Ph_2phen)_3]^{3+}$•4-methoxychalcone. 273

Figure A3.4. Natural transition orbitals for the transition of the alpha orbital to the lowest unoccupied orbital for $[Cr(Ph_2phen)_3]^{3+}$.....274

Figure A4.1. Observed initial rate of formation of **6.6** as a function of photon flux (λ_{ex} = 400 nm). 276

Figure A4.2. Natural transition orbitals for the association complex of $[Cr(dmcbpy)_3]^{3+}$•4-methoxychalcone. Note: These transitions are indicative of electron transfer.....276

Figure A4.3. Natural transition orbitals for the association complex of $[Cr(phen)_3]^{3+}$•4-methoxychalcone. Note: These transitions are indicative of electron transfer.....277

Figure A4.4. α-spin natural transition orbitals for the association complex of $[Cr(Ph_2phen)_3]^{3+}$•4-methoxychalcone. These transitions are the 2nd lowest in energy at 44% occupancy. Note: These transitions are indicative of energy transfer. 277

Figure A4.5. β-spin natural transition orbitals for the association complex of $[Cr(Ph_2phen)_3]^{3+}$•4-methoxychalcone. These transitions are the 2nd lowest in energy at 44% occupancy. Note: These transitions are indicative of electron transfer. 278

Figure A4.6. Spin density plots of the sextet and doublet determinants of the Heisenberg excited state ladder for $[Cr(Ph_2phen)_3]^{3+}$.....278

Figure A4.7. Spin density plots of the sextet and doublet determinants of the Heisenberg excited state ladder for the association complex of $[Cr(Ph_2phen)_3]^{3+}$•4-methoxychalcone. 279

Figure A4.8. ^{1}H NMR spectrum of **6.11**. 279

Figure A4.9. ^{13}C NMR spectrum of **6.11**. 280

Figure A4.10. ^{1}H NMR spectrum of **6.12**. 281

Figure A4.11. ^{13}C NMR spectrum of **6.12**. 281

Figure A4.12. ^{1}H NMR spectrum of **6.13**. 282

Figure A4.13. ^{13}C NMR spectrum of **6.13**. 283

Figure A5.1. Time-dependence of the concentration of 4-methoxychalcone under standard reaction conditions. 284

Figure A5.2. Time-dependence of the concentration of **7.11** under standard reaction conditions. 284

Figure A5.3. Time-dependence of the concentration of **7.6** under standard reaction conditions. 285

Figure A5.4. Time-dependence of the concentration of the respective VCB **7.12** under standard reaction conditions. 285

Figure A5.5. Time-dependence of the concentration of the respective VCB **7.11** and **7.12** following resubjection to $[Cr(Ph_2phen)_3]^{3+}$ in nitromethane (0.10 M). 286

Figure A5.6. Isoprene concentration dependence on the rate constant under otherwise standard conditions where the alkene employed is **7.3** (blue data) or **7.6** (orange data). The open data points correspond to the production of the product for each reaction whereas the filled data points correspond to the production of the VCB.....286

Figure A5.7. Catalyst concentration dependence on the rate constant under otherwise standard conditions where the alkene employed is **7.3** (blue data) or **7.6** (orange data). The open data

points correspond to the production of the product for each reaction whereas the filled data points correspond to the production of the VCB. 287

Figure A5.8. Time-dependence of the concentration of **7.3** and **7.6** under reaction conditions to produce the respective VCB of each alkene. 287

Figure A5.9. Isoprene concentration dependence on the rate constant under reaction conditions to produce the respective VCB of each alkene where the alkene employed is **7.3** (blue data) or **7.6** (orange data). 288

Figure A5.10. Time dependence of concentration of **7.10** under standard reaction conditions. 288

Figure A5.11. Observed initial rate of formation of **7.14** as a function of photon flux (λ_{ex} = 400 nm). 289

Figure A7.1. Field dependence of magnetization for **9.2** collected at 100 K. The data are fit to a linear regression (y = 0.00887x + 4.51E-5) that does not include H = 0 Oe. 297

Figure A7.2. Field dependence of magnetization for **9.4** collected at 100 K. The data are fit to a linear regression (y = 0.0095x + 7.54E-5) that does not include H = 0 Oe. The data point at 1 kOe is omitted due to a centering error. 297

Figure A7.3. Field dependence of magnetization for **9.6** collected at 100 K. The data are fit to a linear regression (y = 0.011x + 1.34E-4) that does not include H = 0 Oe. 298

Figure A7.4. Field dependence of magnetization for **9.7** collected at 100 K. The data are fit to a linear regression (y = 0.012x + 4.81E-3) that does not include H = 0 Oe. The data point at 7 kOe is omitted due to a centering issue. 298

Figure A7.5. Intermolecular contacts in the crystal structure of **9.2**. The distance between C and N atoms is 4.403(4) Å. 299

Figure A7.6. Field dependence of magnetization for **9.2** collected at 1.8 K. The data points at 42.5 and 45 kOe are omitted because of a centering issue. 299

Figure A7.7. EPR spectrum of **9.6** in a 1:1 mixture of CH_2Cl_2:$ClCH_2CH_2Cl$ measured at 100 K. 300

Figure A7.8. ^1H NMR of **9.2** in CD_2Cl_2. 300

Figure A8.1. Field and frequency dependence of the out-of-phase magnetic susceptibility data for **10.1** at 1.8 K. 302

Figure A8.2. Field and frequency dependence of the out-of-phase magnetic susceptibility data for **10.2b** at 1.8 K. 302

Figure A8.3. Field and frequency dependence of the out-of-phase magnetic susceptibility data for **10.3** at 1.8 K. 303

Figure A8.4. Field dependence of magnetization for compound **10.1** collected at 100 K. The data are fit to a linear regression (y = 0.0533x – 6.70E-4) without the 0 kOe data point. 303

Figure A8.5. Field dependence of magnetization for compound **10.2b** collected at 100 K. The data are fit to a linear regression (y = 0.0271x – 2.71E-4) without the 0 kOe data point. 304

Figure A8.6. Field dependence of magnetization for compound **10.3** collected at 100 K. The data are fit to a linear regression (y = 0.0490x – 1.04E-4), without the 0 kOe data point. 304

Figure A8.7. Reduced magnetization collected on **10.1**. The lines represent fits obtained from ANISOFIT 2.0. The values associated with the fit to an anisotropic S = 3/2 ground spin state are as follows: g = 3.39 , D = -105 cm^{-1}, E = 31.6 cm^{-1}. 305

Figure A8.8. Reduced magnetization collected on **10.3**. The lines represent fits obtained from ANISOFIT 2.0. The values associated with the fit to an anisotropic S = 3/2 ground spin state are as follows: g = 2.70, D = 43.6 cm^{-1}, E = 14.5 cm^{-1}. 305

Figure A9.1. UV-vis spectra of **11.1** in Et_2O.....306

Figure A9.2. UV-vis spectra of **11.2** in Et_2O.....306

Figure A9.3. M vs. H data at 100 K for **11.1**. 307

Figure A9.4. M vs. H data at 100 K for **11.2**. 307

Figure A9.5. M vs. H/T at lower temperatures for **11.1** at applied dc fields from 1-5 T at 1 T increments. 308

Figure A9.6. M vs. H/T at lower temperatures for **11.2** at applied dc fields from 1-5 T at 1 T increments. 308

Figure A9.7. In-phase (top) and out-of-phase (bottom) ac magnetic susceptibility data for **11.2** with applied dc fields from 1000 to 5000 Oe at a 4 Oe applied ac field sweeping frequency (1-1500 Hz) at 1.8 K. 309

Figure A10.1. Field dependence of magnetization for $[U(p\text{-}IPrBn)_4]$ collected at 100 K. 311

Figure A10.2. Field dependence of magnetization for $[U(p\text{-}tBuBn)_4]$ collected at 100 K.....311

Figure A10.3. Field dependence of magnetization for $[U(o\text{-}OMeBn)_4]$ collected at 100 K. 312

Figure A10.4. Field dependence of magnetization for $[U(p\text{-}ClBn)_4]$ collected at 100 K. 312

Figure A10.5. Field dependence of magnetization for $[U(m\text{-}OMeBn)_4]$ collected at 100 K. 313

Figure A10.6. Field dependence of magnetization for compound $[(^{Mes}PDI^{Me})U(Cp^*)I]$ collected at 100 K. The data are fit to a linear regression (y = 9.50E-7x – 4.09E-5) that does not include H = 0 Oe. 314

Figure A10.7. Field dependence of magnetization for compound $[(^{Mes}PDI^{Me})U(Cp^*)(BCC)]_2$ collected at 100 K. The data are fit to a linear regression ($y = 2.57E\text{-}6x + 1.90\times10^{-4}$) that does not include H = 0 Oe. 315

Figure A10.8. Field dependence of magnetization for compound $[(^{Mes}PDI^{Me})U(Cp^*)(BCC)]$ collected at 100 K. The data are fit to a linear regression ($y = 1.60E\text{-}6x + 5.15\times10^{-5}$) that does not include H = 0 Oe. 316

Figure A10.9. Field dependence of magnetization for compound $[(Tp^*)_2U(=N\text{-}p\text{-}Tol)]$ collected at 100 K. The data are fit to a linear regression (y = 0.0126x - 1.47E-4) that does not include H = 0 Oe. 316

Figure A10.10. Field dependence of magnetization for compound $[((Tp^*)_2U)_2(m\text{-}DIB)]$ collected at 100 K. The data are fit to a linear regression (y = 0.0289x - 1.73E-4) that does not include H = 0 Oe. 317

Figure A10.11. Field dependence of magnetization for compound $[((Tp^*)_2U)_2(p\text{-}DIB)]$ collected at 100 K. The data are fit to a linear regression (y = 0.0181x – 2.93E-4) that does not include H = 0 Oe. 317

Figure A10.12. Field dependence of magnetization for compound $[(Tp^*)_2U)]$-insertion product collected at 100 K. The data are fit to a linear regression (y = 0.0151x – 8.94E-5) that does not include H = 0 Oe. 318

Figure A10.13. Field dependence of magnetization for compound $[((Tp^*)_2U)_2\text{-}p\text{-}DEB]$ collected at 100 K. The data are fit to a linear regression (y = 0.0268x - 3.89E-5) that does not include H = 0 Oe. 318

Figure A10.14. Field dependence of magnetization for compound [((Tp*)$_2$U)$_2$-m-DEB] collected at 100 K. The data are fit to a linear regression (y = 0.0128x - 3.42E-5) that does not include H = 0 Oe. 319

Figure A10.15. Field dependence of magnetization for compound [(Tp*)$_2$U(CCPh)] collected at 100 K. The data are fit to a linear regression (y = 0.0168x – 5.60E-4) that does not include H = 0 Oe. 319

Figure A10.16. Field dependence of magnetization for compound [(Tp*)$_2$U(THF)](BPh$_4$) collected at 100 K. The data are fit to a linear regression (y = 0.0227x – 5.37E-4) that does not include H = 0 Oe. 320

Figure A10.17. Field dependence of magnetization for compound [(Tp*)$_2$U(MeCN)$_2$](BPh$_4$) collected at 100 K. The data are fit to a linear regression (y = 0.0144x – 1.10E-4) that does not include H = 0 Oe. 320

Figure A10.18. Field dependence of magnetization for [U(p-iPrBn)$_4$] collected at 1.8 K. 321

Figure A10.19. Field dependence of magnetization for [U(p-tBuBn)$_4$] collected at 1.8 K. 322

Figure A10.20. Field dependence of magnetization for [U(o-OMeBn)$_4$] collected at 1.8 K. 323

Figure A10.21. Field dependence of magnetization for [U(p-ClBn)$_4$] collected at 1.8 K. 323

Figure A10.22. Field dependence of magnetization for [U(m-OMeBn)$_4$] collected at 1.8 K. 324

Figure A10.23. Field dependence of magnetization for compound [(Tp*)$_2$U(=N-p-Tol)] collected at 1.8 K. 324

Figure A10.24. Field dependence of magnetization for compound [((Tp*)$_2$U)$_2$(m-DIB)] collected at 1.8 K. 325

Figure A10.25. Field dependence of magnetization for compound [((Tp*)$_2$U)$_2$(p-DIB)] collected at 1.8 K. 325

Figure A10.26. Field dependence of magnetization for compound [(Tp*)$_2$U)]-insertion product collected at 1.8 K. 326

Figure A10.27. Field dependence of magnetization for compounds [((Tp*)$_2$U)$_2$-p-DEB], [(Tp*)$_2$U(CCPh)], [(Tp*)$_2$U(THF)](BPh$_4$) and [(Tp*)$_2$U(MeCN)$_2$](BPh$_4$) collected at 1.8 K. 326

Figure A10.28. Field dependence of magnetization for compound [((Tp*)$_2$U)$_2$-m-DEB] collected at 1.8 K. 327

Figure A10.29. Temperature dependence of the out-of-phase magnetic susceptibility for [(Tp*)$_2$U(CCPh)] collected with an applied ac field of 4 Oe and an applied dc field of 1000 Oe. 327

Figure A10.30. Temperature dependence of the out-of-phase magnetic susceptibility for [(Tp*)$_2$U(THF)](BPh$_4$) collected with an applied ac field of 4 Oe and an applied dc field of 500 Oe. 328

Figure A10.31. Field and frequency dependence of the out-of-phase magnetic susceptibility for compound [((Tp*)$_2$U)$_2$-p-DEB] collected at 2 K (4 Oe ac field). 328

Figure A10.32. Field and frequency dependence of the out-of-phase magnetic susceptibility for compound [((Tp*)$_2$U)$_2$-m-DEB] collected at 2 K (4 Oe ac field). 329

Figure A10.33. Temperature dependent magnetic susceptibility of [(^{Mes}PDI^{Me})U(Cp*)(BCC)]$_2$ and two times the magnetic susceptibility of compound [(^{Mes}PDI^{Me})U(Cp*)I] both collected at 5000 Oe. 330

Figure A10.34. Temperature dependence of the magnetic susceptibility for compounds [((Tp*)$_2$U)$_2$(p-DIB)] and [((Tp*)$_2$U)$_2$(m-DIB)], both collected at 1000 Oe, where the χ_MT data have been subtracted from the data obtained for [(Tp*)$_2$U(=N-p-Tol)]. 331

Figure A10.35. Temperature dependence of the magnetic susceptibility for compound [((Tp*)$_2$U)$_2$-p-DEB] collected at 1000 Oe. The magnetic susceptibility values were subtracted according to the following equation: 331

Chapter 1: The effect of electronic structure on reactivity: a brief historical background as a lead-in to photoredox catalysis

1.1 Werner Complexes in Catalysis

Metal active sites are involved in numerous biological systems for vital transformations. Specifically, this is important to understand function and mechanism of different biologically relevant complexes such as heme,[1] P450[2] and methane monooxygenase[3-4] among many others. Therefore, understanding how these metal-containing species react is intrinsically important to understand how chemical process impact biological sciences. One of the earliest discoveries of how metal complexes show varied properties with subtle differences in structure was made by Alfred Werner in the late 1800s.[5-7] Figure 1.1.1 shows *cis/trans* isomers of an octahedral Co(III) complex which display drastically different optical properties. The *cis* confirmation of $[(NH_3)_4CoCl_2]Cl$ is purple, whereas the *trans* confirmation is green (top of Figure 1.1.1).[8] This was a profoundly impactful find and he was awarded the Nobel prize in 1913 for his efforts in this area.[9]

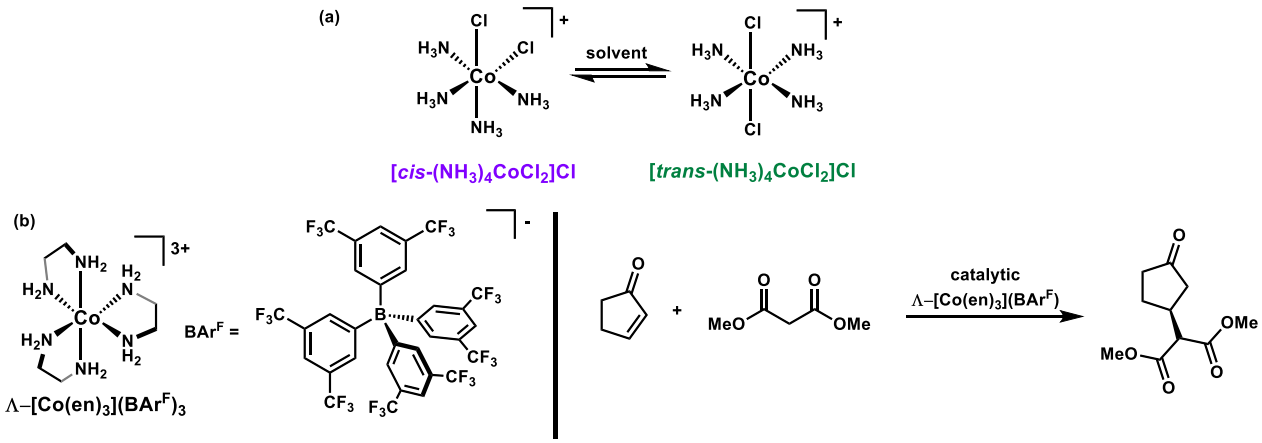


Figure 1.1.1 Isomers of $[(NH_3)_4CoCl_2]Cl$ (a) and representative example of an enantioselective reaction using a Werner complex (b).

While Werner characterized and illustrated some of the most fundamental differences in electronic structure of metal complexes, it took another century before researchers were able to exploit these structures for reactivity. In 2008, John Gladysz reported that Werner complexes could be phase transferred into organic media to perform enantioselective and catalytic Michael additions.[10] This was a profoundly impactful development on the field of synthetic chemistry and shows how nearly 100 years after the initial discovery was made by Werner, Gladysz was able to use these compounds to perform useful organic transformations. This research has made a substantial impact on the field of synthetic chemistry and remains as an unparalleled system that many other chemists are actively researching.[11-13]

1.2 Excited-state properties of Ru

A different way to exploit the electronic structure of metal complexes to perform useful reactivity is through excited-state prcoesses. The most well-known and understood excited-state properties are for Ru-polypyridyl systems including $[Ru(bpy)_3]^{2+}$ (bpy= 2,2'-bipyridine).[14] Figure 1.2.1 shows a Jablonski diagram for the long-lived ^{3}MLCT excited state for $[Ru(bpy)_3]^{2+}$. First, the ground state singlet is excited with light to a ^{1}MLCT state that rapidly intersystem crosses to a longer-lived ^{3}MLCT state, which eventually undergoes thermal relaxation back to the singlet ground state. Notable examples of reactivity exploiting this excited state are water splitting and oxygen reduction catalysis performed in 1970s and 1980s.[15-17]

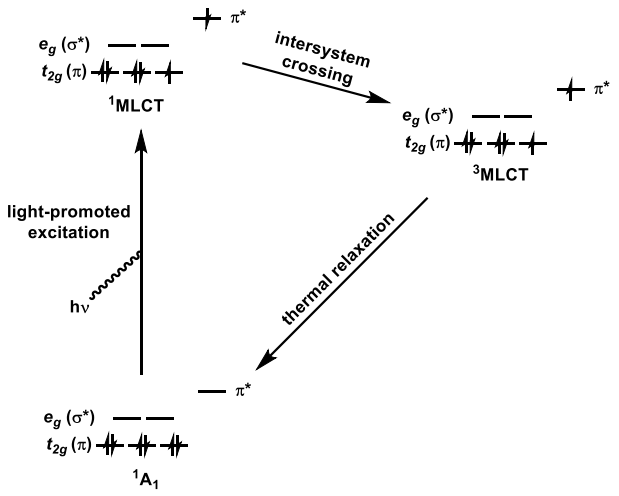


Figure 1.2.1 Simplified Jablonski diagram for $[Ru(bpy)_3]^{2+}$.

1.3 Photoredox reactivity

Recently, the ^{3}MLCT excited state of $[Ru(bpy)_3]^{2+}$ has been heavily studied for use as a photoredox catalyst/initiator with organic substrates.[18-19] Interestingly, $[Ru(bpy)_3]^{2+*}$ can act as an excited-state reductant (electron promoted from Ru to ligand is lost) or excited-state oxidant (electron is added to the Ru center). This bifunctional reactivity has been influential in a variety of fields of chemistry that are not solely centered around organic transformations. The field of photoredox catalysis garnered increasing attention since MacMillan and Yoon's resurgent publications in 2008 and has now expanded into dual-catalytic systems,[20] polymerizations,[21] and a variety of other reactions. The most common photosensitizers for this type of reactivity contain Ru or Ir, where both of their excited-state electronic structures are described in Figure 1.2.1. These are not the only photosensitizers as organic,[22] copper,[23] and cerium[24] among others all use excited-state reactivity to perform challenging and exciting organic transformations. This field has exploded so much that numerous reviews centered around organic transformations,[25-26] dual-catalytic systems,[20] natural product synthesis,[27] earth abundant photosensitizers[28] and the photophysics[29] of these reactions have been published in the last 10 years.

Generalized mechanisms for these transformations specifically suited for an excited-state *photooxidation* are shown in Figure 1.3.1. If the cycle is catalytic, then a photosensitizer occupies some excited state to oxidize a substrate. This radical cation (of the substrate) then performs some other specific transformation, forming the radical cation of the product, which ideally reacts with the reduced form of the photosensitizer, replenishing the initial photosensitizer and completing the catalytic cycle (left side). On the other hand, if the mechanistic cycle begins from a photoinitiated process, the first step remains the same, where the excited-state photosensitizer removes an electron from the substrate. The radical cation of the substrate then undergoes some transformation, forming the radical cation of the product. This radical cation then oxidizes an equivalent of the substrate, forming the product and the radical cation of the substrate, where the initially added photosensitizer is no longer involved in the cycle. Actinometry (photon counting) experiments help determine the differences between these two possible mechanisms.

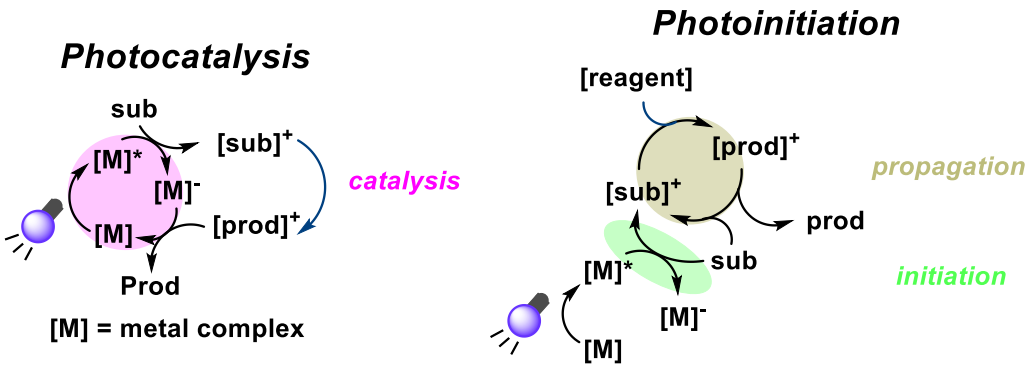


Figure 1.3.1 Representative mechanisms for photoredox reactions.

In the field of photoredox catalysis, there are a few transformations that have been switchable *via* external modulators. One of the more interesting transformations is a report by Curran and Rueping from 2013 (Figure 1.3.2).[30] Under inert conditions, an iridium complex oxidizes an amine by one electron, allowing a radical-mediated insertion into an electron poor

alkene, which then performs a proton-coupled electron-transfer (PCET) reaction to give a straight chain product. Conversely, if the reaction is performed in air, following the initial oxidation of the amine, a [3+2] annulation reaction takes place with subsequent proton abstraction to give the cyclized product. This is an interesting find and shows how these types of reactions can be affected by simple changes, such as exposure to air.

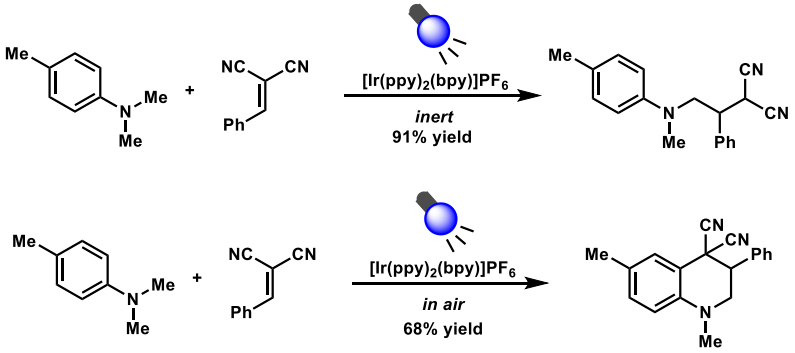


Figure 1.3.2 Variable product formation on the basis on the presence of oxygen in a photoredox reaction.

Another example of switchable reactivity in photoredox reactivity involves a wavelength-dependent study from the König group (Figure 1.3.3) on an arene coupling reaction.[31] This reaction proceeds by reduction of a halogenated arene to form bromide and an arene radical, which is trapped by *N*-methylpyrrole and subsequent PCET leads to a mono-substituted product. When higher energy (lower wavelength) light is used, this monosubstituted product can undergo further reduction with the excited state of the photosensitizer, producing another equivalent of bromide and trapping another equivalent of the pyrrole. Product control by judicious irradiation wavelength is an interesting way to enhance the overall utility of photoredox reactions.

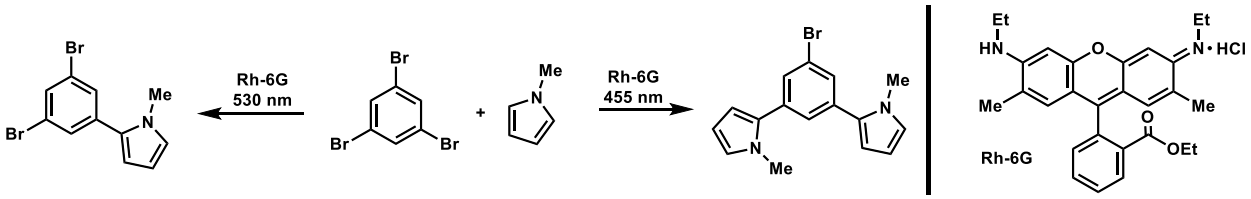


Figure 1.3.3 Wavelength switchable photoredox catalysis.

Something that is underexplored in the literature is reactivity/mechanistic control of a transformation through the choice of a photosensitizer. The main reason that this type of investigation has probably not been explored in-depth is that most of this reactivity is presumed to undergo outer-sphere electron-transfer. If the excited states are all triplet-based for chosen photosensitizers, then the only other variable these photosensitizers have to tune is the excited-state redox potential, potentially limiting the extent of reactivity these species can perform. Therefore, it is an outstanding and interesting possibility to wonder if increased multiplicities of excited states and potentially non-singlet ground state complexes can show long-lived excited states; and if so, how does their photoredox and photocatalysis reactivity change? In 1979, Serpone and Hoffman determined that Cr(III) complexes show microsecond excited-state lifetimes.[32] The initial transient absorption data indicated that this was not a CT event and instead a *d-d* transition. Based on the Tanabe-Sugano diagram, the lowest lying excited state is ^{2}E in character (Figure 1.3.4). This type of system shows paramagnetic behavior in both the ground and excited states.

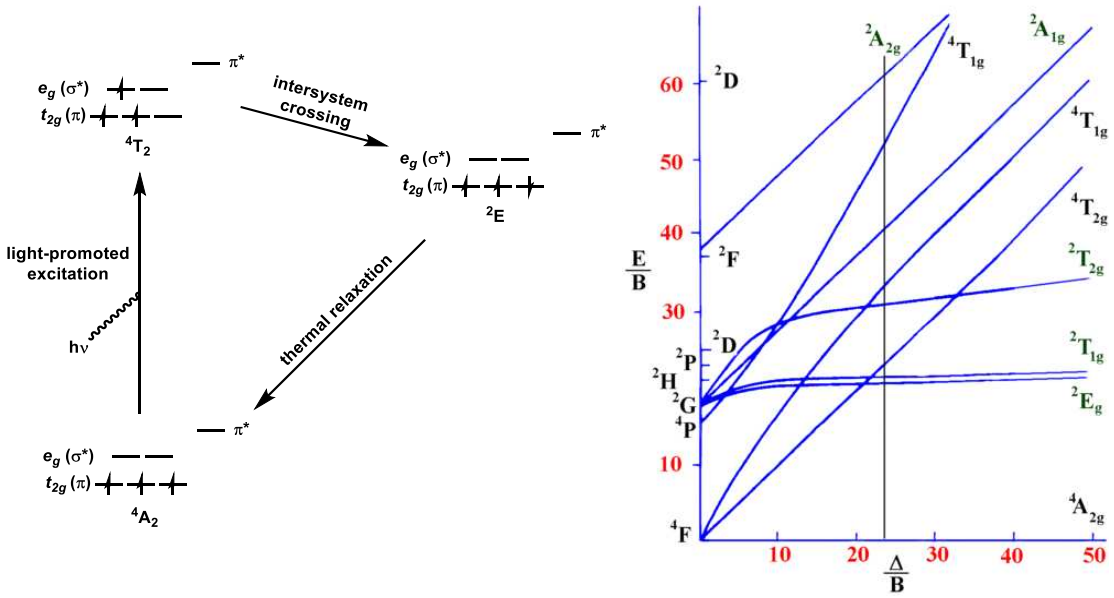


Figure 1.3.4 Jablonski diagram for Cr(III) (left) and a Tanabe-Sugano diagram for a d^3 system (right).[33]

1.4 Cr-photoredox catalysis

To understand the possible transformations these Cr-photosensitizers can perform, the excited-state properties of Cr complexes are examined. To calculate an excited-state redox couple two pieces of information are required: emission energy and reversible electrochemical behavior. For example, $[Cr(acac)_3]$ emits from a ^2E excited-state lifetime of τ = 800 ps.[34] To perform outer-sphere electron transfer, a lifetime of $\tau \geq 2$ ns is required; therefore, $[Cr(acac)_3]$ will likely not be able to promote this type of reactivity. Further, its redox couple for the $[Cr]^{3+/2+}$ couple is at -1.77 V vs. Fc^+/Fc and is irreversible, potentially due to a proton coupled electron transfer mechanism.

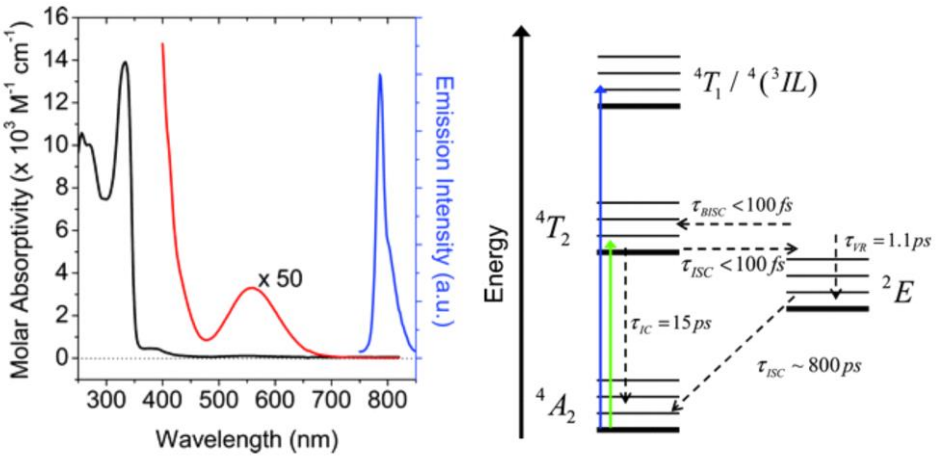


Figure 1.4.1 Absorption and emission data for [Cr(acac)$_3$] (left) and a Jablonski diagram for the excited-state dynamics of [Cr(acac)$_3$] (right).[34]

As mentioned earlier, Cr-polypyridyl complexes show a long lived excited-state lifetime sufficient to perform outer-sphere electron transfer. In addition, these complexes show reversible electrochemistry for their $[Cr]^{3+/2+}$ redox couple, indicating that the reduced form is indefinitely stable. For common Cr-polypyridyl complexes, the excited-state redox potentials range from $[Cr]^{3+*/2+}$ = +0.98-1.42 V vs. Fc^+/Fc, making them potent excited-state oxidants. For reference, the commonly used $[Ru(bpz)_3]^{2+}$ displays an excited-state redox couple of $[Ru(bpz)_3]^{2+*}$ = +1.05 V vs. Fc^+/Fc.

It is now reasonable to hypothesize some reactions that could be performed with these Cr-photosensitizers concerning organic transformations. Classical reactions using radical cations were discovered by Bauld and Steckhan wherein pericyclic reactions were performed.[35] Some of the classic radical-cation pericyclic reactions are shown in Figure 1.4.2. These reactions are initiated by an electron-poor amminium ion which oxidizes 1,3-cyclohexadiene or *trans*-anethole. These reactions are called radical cation Diels-Alder reactions as they give an overall [4+2]-transformation in both cases. The only requirement for these reactions to proceed is that the

oxidation potential of the amminium ion has to be more positive than the organic moiety. Therefore, we set out to try some of these reactions using Cr-photosensitizers.

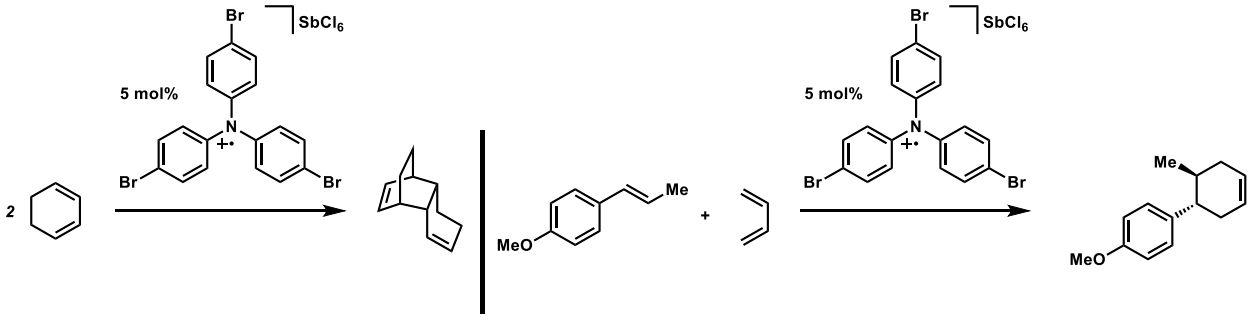


Figure 1.4.2 Representative pericyclic reactions initiated by amminium salts.[35]

Both of the reactions in Figure 1.4.2 were found to work with Cr-photosensitizers in place of triarylamminiums in the initial work published by the Ferreira and Shores groups.[36] This proof-of-concept study not only showed that Cr-based photosensitizers could function in the same reaction arena as Ru and Ir photosensitizers, but also that a few substrates were successful with chromium, that did not react with Ru-based congeners. Interestingly, a few details of the mechanistic implications of this reaction were noted, which remained unanswered in the initial report. First, whilst O_2 was reported to increase yields in the Ru-based reaction, it was found to be necessary in the Cr-based reactions for product formation. Second, the Ru based reaction showed full conversion to product in ~15-30 minutes, whereas the Cr-based reaction did show full conversion for 6-8 hours, even though the products were identical. Therefore as part of my PhD studies, I set out to investigate these discrepancies and to progress the overall reactivity of Cr-photosensitizers in photoredox reactivity. This was performed through the Catalysis Collaboratory of Light-activated Earth Abundant Reagents (C-CLEAR) in collaboration with the groups of Eric M. Ferreira (University of Georgia), Anthony K. Rappé (Colorado State University), Niels H. Damrauer (Colorado University-Boulder) and Tomislav Rovis (Columbia University).

1.5 Outline of chapters

To this end, I present not only the impact of Cr-photocatalysis to understand more generally their electronic structures, but a few different but unique systems involving transition metal and actinide complexes. Chapters 2-4 discuss the impact of chromium catalysts upon the photo-oxidation chemistry of electron-rich alkenes, with particular attention given to *trans*- and *cis*-anethole, where Chapter 2 has been published (*J. Am. Chem. Soc.* **2016**, *138*, 5451-5464). Chapters 5-7 outline how this reactivity changes once electron-poor alkenes, such as 4-methoxychalcone, are used, where part of Chapter 5 has been published (*Chem. Sci.* **2017**, *8*, 654-660). Chapter 8 is focused on using the excited-state redox properties of organic substrates to be oxidized by weak, cheap and abundant ferrocenium salts.

Shifting attention away from photocatalysis, Chapters 9-12 focus on electronic structures of different transition metal and actinide complexes. In Chapter 9, I synthesize novel triarylamino-containing iron complexes and highlight the different magnetic coupling mechanisms (mostly superexchange) before and after oxidation of both the Fe and N atoms. Chapter 10 focuses on the impact of coordination geometry on the dynamic magnetic properties of $[Co(tpy)_{1/2}]^{2+}$ derivatives, which has been published (*Polyhedron*, **2018**, *143*, 193-200). In Chapter 11, I discuss the synthesis, magnetic properties and reactivity on a family of uranium acetylide complexes. Chapter 12 focuses on the impact of magnetic properties on the overall electronic structure of $U^{3+/4+}$ with a variety of redox-active and redox-neutral ligands, where work focusing on U-pyridinediimine and U-alkyl have been published (*Inorg. Chem.* **2016**, *55*, 11854-11866 and *Organometallics*, **2017**, *36*, 3491-3497, respectively). Finally, in Chapter 13, I present some broad conclusions and future directions for interesting findings that require additional attention.

References

1. Liu, J.-G.; Ohta, T.; Yamaguchi, S.; Ogura, T.; Sakamoto, S.; Maeda, Y.; Naruta, Y. *Angew. Chem. Int. Ed.* **2009**, *48*, 9262.
2. Denisov, I. G.; Makris, T. M.; Sligar, S. G.; Schlichting, I. *Chem. Rev.* **2005**, *105*, 2253.
3. Basch, H.; Mogi, K.; Musaev, D. G.; Morokuma, K. *J. Am. Chem. Soc.* **1999**, *121*, 7249.
4. Rosenzweig, A. C.; Frederick, C. A.; Lippard, S. J.; Nordlund, P. *Nature* **1993**, *366*, 537.
5. Werner, A. *Ber. Dtsch. Chem. Ges.* **1911**, *44*, 1887.
6. Werner, A. *Ber. Dtsch. Chem. Ges.* **1913**, *46*, 3674.
7. Werner, A. *Ber. Dtsch. Chem. Ges.* **1914**, *47*, 3087.
8. Jackson, W. G.; McKeon, J. A.; Cortez, S. *Inorg. Chem.* **2004**, *43*, 6249.
9. The Official Web Site of the Nobel Prize. https://www.nobelprize.org/nobel_prizes/chemistry/laureates/1913/ (accessed Apr 11, 2018).
10. Ganzmann, C.; Gladysz, J. A. *Chem. Eur. J.* **2008**, *14*, 5397.
11. Lewis, K. G.; Ghosh, S. K.; Bhuvanesh, N.; Gladysz, J. A. *ACS Cent. Sci.* **2015**, *1*, 50.
12. Ehnbom, A.; Ghosh, S. K.; Lewis, K. G.; Gladysz, J. A. *Chem. Soc. Rev.* **2016**, *45*, 6799.
13. Ghosh, S. K.; Ganzmann, C.; Bhuvanesh, N.; Gladysz, J. A. *Angew. Chem. Int. Ed.* **2016**, *55*, 4356.
14. Caspar, J. V.; Meyer, T. J. *J. Am. Chem. Soc.* **1983**, *105*, 5583.
15. Sutin, N. *J. Photochem.* **1979**, *10*, 19.
16. Sutin, N.; Creutz, C. *Pure Appl. Chem.* **1980**, *52*, 2717.
17. Balzani, V.; Bolleta, F.; Gandolfi, M. T.; Maestri, M. *Top. Curr. Chem.* **1978**, *75*, 1.
18. Nicewicz, D. A.; MacMillan, D. W. C. *Science* **2008**, *322*, 77.
19. Ischay, M. A.; Anzovino, M. E.; Du, J.; Yoon, T. P. *J. Am. Chem. Soc.* **2008**, *130*, 12886.
20. Tellis, J. C.; Primer, D. N.; Molander, G. A. *Science* **2014**, *345*, 433.
21. Theriot, J. C.; Lim, C.-H.; Yang, H.; Ryan, M. D.; Musgrave, C. B.; Miyake, G. M. *Science* **2016**, *352*, 1082.
22. Romero, N. A.; Nicewicz, D. A. *Chem. Rev.* **2016**, *116*, 10075.
23. Paria, S.; Reiser, O. *ChemCatChem* **2014**, *6*, 2477.
24. Yin, H.-L.; Carroll, P. J.; Anna, J. M.; Schelter, E. J. *J. Am. Chem. Soc.* **2015**, *137*, 9234.
25. Shaw, M. H.; Twilton, J.; MacMillan, D. W. C. *J. Org. Chem.* **2016**, *81*, 6898.

26. Prier, C. K.; Rankic, D. A.; MacMillan, D. W. C. *Chem. Rev.* **2013**, *113*, 5322.

27. Staveness, D.; Bosque, I.; Stephenson, C. R. J. *Acc. Chem. Res.* **2016**, *49*, 2295.

28. Larsen, C. B.; Wenger, O. S. *Chem. Eur. J.* **2018**, *24*, 2039.

29. Arias-Rotondo, D. M.; McCusker, J. K. **2016**, *45*, 5803.

30. Zhu, S.-Q.; Das, A.; Bui, L.; Zhou, H.-J.; Curran, D. P.; Rueping, M. *J. Am. Chem. Soc.* **2013**, *135*, 1823.

31. Ghosh, I.; König, B. *Angew. Chem. Int. Ed.* **2016**, *55*, 7676.

32. Serpone, N.; Jamieson, M. A.; Henry, M. S.; Hoffman, M. Z.; Bolletta, F.; Maestri, M. *J. Am. Chem. Soc.* **1979**, *101*, 2907.

33. Tanabe-Sugano Diagrams. http://wwwchem.uwimona.edu.jm/courses/Tanabe-Sugano/TScalcs.html (accessed June 29, 2018).

34. Schrauben, J. N.; Dillman, K. L.; Beck, W. F.; McCusker, J. K. *Chem. Sci.* **2010**, *1*, 405.

35. Bauld, N. L. *Tetrahedron*, **1989**, *45*, 5307.

36. Stevenson, S. M.; Shores, M. P.; Ferreira, E. M. *Angew. Chem. Int. Ed.* **2015**, *54*, 6506.

Chapter 2: Uncovering the Roles of Oxygen in Cr(III) Photoredox Catalysis.*

2.1 Introduction

The resurgence of photoredox catalysis as a field of study reflects the importance of developing new or sustainable coupling reactions, where oxidative and reductive equivalents are selectively required within a mechanism, but may not be introduced at the outset due to chemical incompatibility.[1-5] Most photoredox catalysts participate in one-electron processes, and have been shown to promote a variety of transformations including cyclizations,[6,7] fluorinations[8] and cross-couplings.[9,10] The most widely used catalysts contain Ru(II) and Ir(III) ions. However, there are limitations to the catalysts currently in use: the relative scarcity of Ir and Ru is often cited; in addition, catalysis employing those species can require stoichiometric excited-state trapping agents to increase the lifetime of the reducing or oxidizing agent.[11,12] Photosensitizers sourced from Earth-abundant elements can also be challenged by short excited state lifetimes.[13,14]

In situations where co-reagents and/or promoters are required to exploit for photoredox catalysis, oxygen avails itself as an intriguing candidate, as it is abundant and would simplify reaction setups – it would be ideal to perform reactions in air. Some reports propose oxygen as a replacement for commonly used oxidants such as ferric salts.[6,15] However, oxygen has several drawbacks: it often quenches excited states; it oxidizes metal-containing catalysts and/or photoinitiators; it leads to undesirable products via O_2 incorporation; it is not easy to monitor in reactions.[16-21] Some recent results invoke the importance of oxygen in photoredox catalysis. An

---

*Reproduced with permission from [*J. Am. Chem. Soc.* **2016**, *138*, 5451-5464.] Copyright 2016 American Chemical Society.

exciting report by Yoon and coworkers used a Ru(II)-based system to promote a photoinduced Diels-Alder reaction using electron-rich dienophiles.[6] Oxygen was proposed as the sacrificial oxidant in the mechanism; however, the reaction proceeded without O_2, albeit in lower yield. Oxygen was also proposed as the terminal oxidant in a key step in the scaled-up synthesis of JAK2 Inhibitor LY2784544: oxygen concentration and/or mode of delivery had a significant impact on product yield as well as regioselectivity, but the precise role(s) of oxygen in the reaction pathway is an open question.[22] Another recent finding is the involvement of a trifluoroacetic acid-mediated oxygen oxidative quench of a Cu(I) excited state in the photocatalyzed α-amino C-H bond functionalization.[23] Oxygen is proving to play an important role in photoredox chemistry, but the understanding of its function in these and related systems remains incomplete.

Multi-tool studies are contributing to our understanding of the nuances of reaction mechanisms in photoredox catalysis. Miranda and coworkers combined product studies, transient absorption spectroscopy, and electronic structure theory to probe an imino Diels-Alder reaction.[24] Very recently, Knowles and coworkers reported an in-depth mechanistic study of the oxidation of an indoline to an indole promoted by an Ir(III) photocatalyst, enroute to the natural product Elbasvir.[25] Also, Peters and coworkers recently described the mechanism of a C-S cross-coupling reaction using a Cu photocatalyst.[26] Nevertheless, combined theoretical-experimental studies in this area remain uncommon.

Recently, some of us reported on a family of Cr(III) tris(aromatic diimine) complexes (**[Cr]**$^{3+}$) that could act as photocatalysts for Diels-Alder cycloadditions.[7] Taking advantage of the relatively long excited state lifetimes found in these complexes (up to hundreds of microseconds),[27] we found that stoichiometric organic co-reagents are not required to achieve catalysis. This combined with the employment of an Earth-abundant metal ion provides a prototype for sustainable catalysis. In addition, we found that an intramolecular Diels-Alder reaction proceeded at good yield without byproducts, demonstrating that a chromium based system offers differential reactivity with respect to Ru-based analogues.[6,7]

A preliminary attempt to describe the reaction pathway(s) as applied to the anethole-isoprene Diels-Alder cycloaddition is shown in Figure 2.1.1. This mechanism implies an initial spin-allowed excitation of the Cr(III) complex **[Cr]**$^{3+}$ to a quartet charge transfer excited state, followed by intersystem crossing to a long-lived doublet (^{2}E) excited state. The thus prepared photoactive species **[Cr]**$^{3+*}$ could then oxidize the anethole (dienophile), while being reduced from **[Cr]**$^{3+}$ to **[Cr]**$^{2+}$.[28] The dienophile radical cation would couple with the diene to produce the cyclohexenyl radical cation. The product radical cation could either react with anethole to initiate a radical chain process, or alternatively oxidize **[Cr]**$^{2+}$ to **[Cr]**$^{3+}$ to complete the catalytic cycle. In the radical chain process, the chain is terminated upon regeneration of the **[Cr]**$^{3+}$ species or reaction with another species in solution.

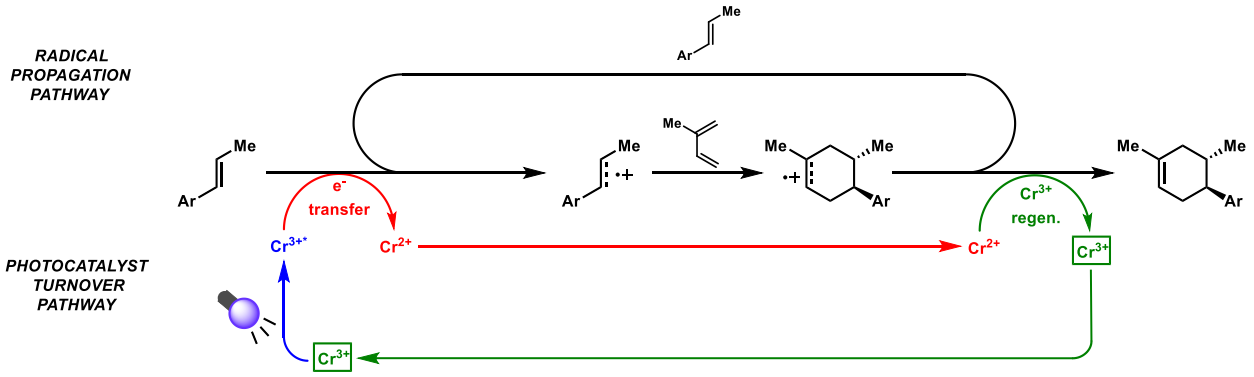


Figure 2.1.1 Initially proposed cycloaddition pathways; the green boxes denote the initial form of the Cr-containing catalyst. Note that isoprene is shown in the form that appears in the cycloadduct; the S-trans form is the major species in solution.

Importantly, this minimalist cycle does not account for our observation that molecular oxygen is required for photocatalytic turnover.[7] In principle, oxygen could oxidize the dienophile or diene to generate an organic radical cation, or perhaps it could oxidize the **[Cr]**$^{2+}$ complex, returning it to its resting state as **[Cr]**$^{3+}$. However, oxygen in aprotic media is not

thermodynamically competent to oxidize any of these species: the O_2/O_2^- couple in acetonitrile is -1.42 V vs Fc^+/Fc,[29,30] while the anethole$^{+/0}$, isoprene$^{+/0}$, and $[Cr(Ph_2phen)_3]^{3+/2+}$ couples occur at +1.0 V, +1.3 V, and -0.64 V vs Fc^+/Fc, respectively.[31-33] If singlet oxygen were somehow generated, its excited state would add approximately +0.98 V of oxidizing potential, which is still electrochemically insufficient to oxidize the organic substrates.

Notwithstanding, we can envision several thermodynamically feasible roles for oxygen in the catalytic cycle (Figure 2.1.2), whether as quencher, redox shuttle or stabilizer of intermediates.

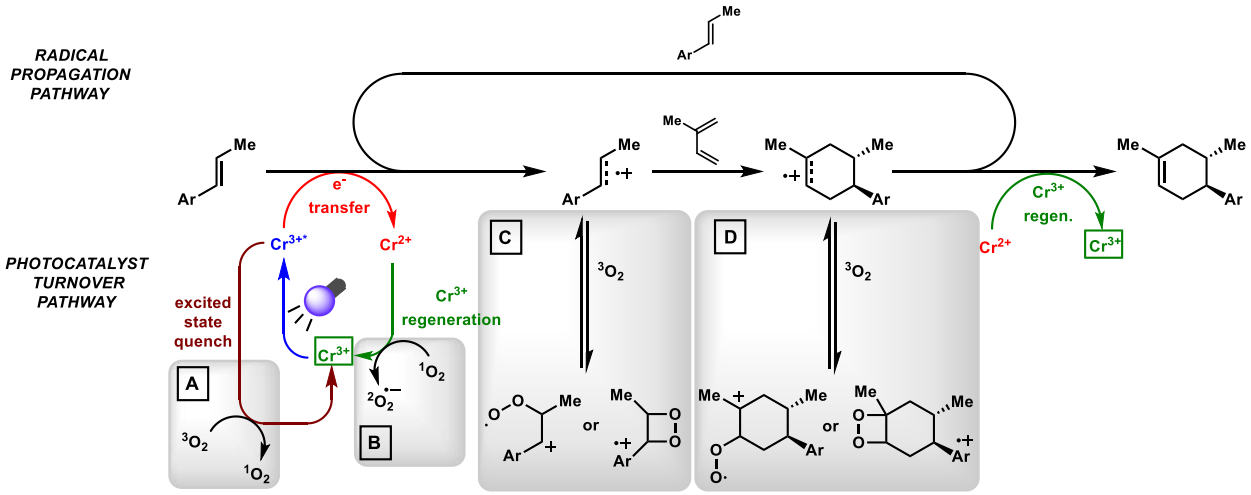


Figure 2.1.2 Proposed roles of oxygen in cycloaddition pathways; the green boxes denote the initial form of the Cr-containing catalyst.

Scenario **A** represents a potential source for singlet oxygen in the reaction mixture. Oxygen is well documented to quench ^{2}**[Cr]**$^{3+}$, forming $^1O_2$.[34] Excited state ^{2}**[Cr]**$^{3+}$ is roughly 1.6 eV above ground state ^{4}**[Cr]**$^{3+}$ and $^1\Delta$ O_2 is 0.98 eV more energetic than ground state $^3\Sigma$ O_2,[35] consistent with facile energy transfer. In acetonitrile, $^1\Delta$ O_2 has a relatively long lifetime of 40 μs.[36] For the proposed catalytic cycle, Cr-excited state quenching by $^3O_2$ may appear somewhat counterproductive but the generation of $^1\Delta$ O_2 could be important elsewhere. For example,

scenario **B** makes use of $^1\Delta$ O_2 as a potential route for catalyst regeneration. For $[Cr(Ph_2phen)_3]^{3+}$, the **[Cr]**$^{3+/2+}$ redox couple is -0.64 V vs Fc^+/Fc[32] and thus $^1\Delta$ O_2 is competent to oxidize **[Cr]**$^{2+}$, whereas ground state O_2 is not. The combination of **A** and **B** represents a closed loop for singlet oxygen but should lead to a build-up of superoxide in the system, which could go on to reduce the product radical cation or another species in solution.

Alternatively or in addition, process **C** shows how molecular oxygen could stabilize the anethole radical cation, driving the oxidation reaction; such behavior has been suggested previously.[37] Related, oxygen could stabilize the product radical cation (scenario **D**), and in turn could regenerate **[Cr]**$^{3+}$ or participate in a radical chain process. In both cases, superoxo species (left structures in **C** and **D**) and dioxetanes (right) represent possible intermediates.

Experiments addressing these and related options are presented and discussed below. We use a combination of synthetic screening, electrochemical and spectroscopic measurements and finally electronic structure computations to determine oxygen's necessary role(s) in redox photocatalysis with a first-row transition-metal catalyst.

2.2 Division of Labor

Unless otherwise noted, all synthesis characterization, analysis and interpretation was performed by Robert F. Higgins. All catalysis studies were performed by Susan M. Stevenson (University of Georgia). Reaction quantum yield data were gathered by David J. Boston. All quenching and ultrafast studies were performed by Samuel M. Shepard and Steven M. Fatur (University of Colorado-Boulder). All computational data were performed by Anthony K. Rappé. Preparation of the manuscript and analysis was performed by Niels H. Damrauer, Eric M. Ferreira, Anthony K. Rappé and Matthew P. Shores. All material in this chapter has been published, see: *J. Am. Chem. Soc.* **2016**, *138*, 5451.

2.3 Experimental

2.3.1 Preparation of compounds

Preparations of all metal complexes were performed inside a dinitrogen-filled glovebox (MBRAUN Labmaster 130). All catalysis screening reactions were performed in air. Acetonitrile (CH_3CN), tetrahydrofuran (THF) and dichloromethane (CH_2Cl_2) were sparged with dinitrogen, passed over alumina, and degassed before use. Nitromethane (CH_3NO_2) was sparged with dinitrogen and subjected to three freeze pump cycles before use. Syringe filters were purchased from VWR international and were fitted with 0.2 µm PTFE membranes. The compounds $[(CH_3CN)_4Cr(BF_4)_2]$ (from $[Cr_2(OAc)_4(H_2O)_2]$),[38] $EtPPh_3Br$,[7] (E)-1-methoxy-2-(prop-1-en-1-yl)benzene,[7] 4'-methoxy-2,4-dimethyl-1,2,3,6-tetrahydro-1,1'-biphenyl,[7] and 2'-methoxy-2,4-dimethyl-1,2,3,6-tetrahydro-1,1'-biphenyl[7] were synthesized according to literature preparations. Tetrabutylammonium hexafluorophosphate (Bu_4NPF_6) was recrystallized twice from ethanol before use. Ferrocene was sublimed before use. Anethole (**2.3**) is the *trans* isomer whenever used in this study. All other compounds and reagents were obtained commercially and were used as received.

2.3.2 Preparation of novel metal complexes

$[Cr(Ph_2phen)_3](BF_4)_2$ (2.1). A solution of Ph_2Phen (250 mg, 0.752 mmol) in 8 mL of a 1:1 dichloromethane/acetonitrile mixture was added to $[(CH_3CN)_4Cr(BF_4)_2]$ (95 mg, 0.243 mmol) in 5 mL of acetonitrile. The solution color turned brown immediately. The reaction mixture was stirred for 1 hour, and then it was filtered through a syringe. The filtrate was dried *in vacuo.* The crude product was recrystallized by diffusion of diethyl ether into a concentrated solution of acetonitrile to afford 232 mg (0.190 mmol, 78 % yield) of brown crystals. UV-vis (CH_3CN) λ_{max}/nm (ε_M/M^{-1} cm^{-1}): 428 (33 100), 490 (19 000), 572 (3060), 874 (16 600). IR (KBr pellet) $\nu_{C=N}$: 1618 cm^{-1}. ESI-MS(+) (CH_3CN): *m/z* 1136.02 $(M - BF_4)^+$. Anal. Calcd. For $C_{72}H_{48}B_2F_8CrN_6$: C, 76.12; H, 4.26; N, 7.40. Found: C, 76.11; H, 4.09; N, 7.58.

$[Cr(Ph_2phen)_3](BF_4)_3$ (2.2). A solution of $AgBF_4$ (62 mg, 0.315 mmol) in 2 mL of acetonitrile was

added to a solution of **2.1** (330 mg, 0.271 mmol) in 10 mL of acetonitrile. Over a period of 8 hours, the color slowly changed from brown to orange and a gray precipitate (Ag metal) formed. The reaction mixture was filtered through Celite to remove the Ag metal and the filtrate was concentrated *in vacuo*. Crystals were grown from a diethyl ether diffusion into a concentrated acetonitrile solution to yield 320 mg (0.245 mmol, 90 % yield) of yellow crystals. IR (KBr pellet) $\nu_{C=N}$: 1624 cm^{-1} ESI-MS(+) (CH_3CN): *m/z* 1222.82 $(M - BF_4)^+$. Anal. Calcd. For $C_{72}H_{48}B_3F_{12}CrN_6$: C, 66.03; H, 3.69; N, 6.42. Found: C, 66.25; H, 3.46; N, 6.68.

2.3.3 Electrochemical measurements

Electrochemical experiments were performed in 0.1 M solutions of Bu_4NPF_6 in CH_3CN, THF, CH_2Cl_2 and CH_3NO_2. Cyclic voltammograms (CVs) and square-wave voltammograms (SWVs) were recorded with a CH Instruments potentiostat (Model 1230A or 660C) using a 0.25 mm Pt disk or 0.25 mm glassy carbon disk working electrode, Ag^+/Ag reference electrode and a Pt wire auxiliary electrode. Scans were collected at rates between 10 mV/s and 2 V/s. Reported potentials are referenced to the $[Cp_2Fe]^+/[Cp_2Fe]$ (Fc^+/Fc), where Cp = cyclopentadiene, redox couple and were determined by adding ferrocene as an internal standard at the conclusion of each electrochemical experiment. Stirred solution experiments were performed using a disk stir bar positioned next to the working electrode. Oxygenated experiments were performed by bubbling O_2 into the experimentation vessel for 10 s prior to data collection. Dark experiments were performed by removing the vessel from all light for 20 minutes before and during scans. To help eliminate electrode interactions with possible superoxide species present, the working electrode was polished before each set of experiments were performed. The surface of the working electrode was also cleaned with a Kimwipe before each scan to help provide a clean surface of the electrode. Spectro-electrochemistry experiments were performed with an Ocean Optics DH-2000-BAL UV-Vis-NIR spectrometer and a Gamry Instruments Reference 600 potentiostat via a Pine Instruments gold honeycomb electrode.

2.3.4 Catalysis studies

In a representative cycloaddition experiment, a flame-dried 2-dram borosilicate vial open to air was charged with anethole (**2.3**, 17.7 mg, 0.120 mmol, 1 equiv), isoprene (**2.4**, 0.120 mL, 1.20 mmol, 10 equiv), $[Cr(Ph_2phen)_3](BF_4)_3$ (1.6 mg, 0.00120 mmol, 1 mol %), and nitromethane (1.20 mL, 0.10 M). The vial was capped and placed in a Rayonet photochemical reactor equipped with 419, 350, and 300 nm light bulbs. The reaction was irradiated with stirring until consumption of **2.3** was complete, as determined by TLC (27 h). The reaction was then diluted with H_2O (1.5 mL) and transferred to a separatory funnel. The layers were separated and the aqueous layer was extracted with Et_2O (3 × 2 mL). The combined organic layers were washed with brine (8 mL), and dried over Na_2SO_4. The volatile materials were removed by rotary evaporation, and the resulting residue was purified by flash chromatography (100 % hexanes → 9:1 hexanes/EtOAc eluent) to afford cycloadduct 4'-methoxy-2,4-dimethyl-1,2,3,6-tetrahydro-1,1'-biphenyl (**2.5**, 22.7 mg, 88 % yield) as a colorless oil. Performing the cycloaddition under more dilute conditions (0.033 M) resulted in a 59 % yield of product **2.5** in 46 h.

2.3.5 Mechanistic measurements and studies

Reaction quantum yields and radical propagation chain lengths were determined by the method reported by Yoon and coworkers.[39] Actinometry experiments were performed using a Newport TLS-300XU tunable light source, which includes a 300 W Xe arc lamp, a Cornerstone 130 Monochromator, and a motorized filter wheel; this instrument provides a wavelength range 250-2400 nm and wavelength selectivity of ± 0.7 nm. Further experimental details are provided in the Supporting Information.

Emission lifetime measurements were conducted in nitromethane solutions of the catalyst at 0.1 absorbance and the indicated concentration of quencher. The solutions were irradiated at 400 nm using the frequency doubled output from a 1kHz repetition rate Ti:Sapphire laser system and emission was measured through a ~15 nm bandpass filter centered at 750 nm using a photomultiplier tube. The resulting decays were fit using a single exponential decay function. Air-

free photochemical measurements were performed on samples prepared in a dinitrogen glovebox and placed in a 1 cm × 1 cm cuvette and sealed with a Teflon valve. Stern-Volmer methodology was employed to determine quenching rate constants from the experimental data. Details of these measurements are available in the Supporting Information.

Superoxide generation under $[Cr]^{3+}/[Cr]^{3+}/O_2$ photo-irradiation conditions was probed by the method recently reported by Ivanović-Burmazović, Moënne-Loccoz, Goldberg and coworkers.[40] A solution of **2.1** (12.72 mg) and **2.2** (4.55 mg, 3:1 mol %) in 2.5 mL of nitromethane was irradiated for 20 minutes (using a combination of 419, 350 and 300 nm sources) before an air outlet was administered and 0.1 mL of thiophenol was added to the reaction mixture. After 30 minutes of stirring, the crude reaction mixture was filtered through a silica plug and concentrated *in vacuo*. The resulting filtrate was analyzed via ^{1}H NMR spectroscopy in $CDCl_3$, indicating a ca. 88 % yield of diphenyl disulfide. Exclusion of light, **2.1**, or oxygen resulted in minimal conversion of thiophenol to diphenyl disulfide (< 5 %). Details of these and related experiments are provided in the Supporting Information.

2.3.6 Other physical measurements

All experiments were conducted at room temperature unless otherwise noted. Absorption spectra were obtained with a Hewlett-Packard 8453 spectrometer in quartz cuvettes with a 1 cm path length. Infrared spectra were measured with a Nicolet 380 FT-IR spectrometer. Mass spectrometric measurements were performed in the positive ion mode on a Thermo LTQ mass spectrometer equipped with an analytical electrospray ion source and a quadrupole ion trap mass analyzer. Electron paramagnetic resonance (EPR) spectra were obtained using a continuous-wave X-band Bruker EMX 200U instrument outfitted with a liquid nitrogen cryostat. Compounds were dissolved in nitromethane and cooled to 120 K to acquire spectra. Elemental analyses were performed by Robertson Microlit Laboratories, Inc. in Madison, NJ.

2.3.7 Electronic structure calculations

The 6-311+g* basis set[41,42] and APFD hybrid density functional[43] were used to obtain the geometries, vibrational frequencies and ideal gas thermodynamic estimates for the molecules computed. The APF hybrid density functional is an explicit linear combination of the B3PW91[44,45] and PBE0 (PBE1PBE)[46-48] hybrid functionals. The 41.1 %:58.9 % combination utilized was selected to minimize long-range artifacts present in standard functionals. The "D" spherical atom model dispersion term has been shown to reproduce large scale CCSD(T) hydrocarbon intermolecular potential curves. The TD-DFT method[49] was used to obtain the excited state energies and oscillator strengths for ^{3}**2.1**$(BF_4)_2$, ^{4}**2.2**$(BF_4)_3$ **2.3**, ^{2}**2.3**$\cdot BF_4$, **2.5**, and ^{2}**2.5**$\cdot BF_4$. Natural transition orbitals (NTOs) were used to assess the character of the electronic transitions. The "from" and "to" NTOs were obtained through diagonalization of the transition density matrix transformed over the occupied and virtual spaces, respectively.[50] Reactions and structures involving isoprene were computed using the *S-trans* form of the molecule, which is the majority species in solution and chemically reactive. Reaction energetics of ionic species were computed including a charge-compensating ion, either BF_4^- or $N(CH_3)_4^+$ (TMA). Further details are provided in the Supporting Information.

2.4 Results

2.4.1 Catalyst syntheses

As a representative example, we have focused our mechanistic studies on $[(Cr(Ph_2phen)_3]^{3+}$ as its photoredox properties are most comparable to Ir- and Ru-containing species, and it promotes the highest cyclization yields in the initial report.[7] The divalent complex, $[Cr(Ph_2phen)_3](BF_4)_2$ (**2.1**), is prepared in a straightforward manner by combining stoichiometric quantities of $[(CH_3CN)_4Cr(BF_4)_2]$ and Ph_2phen in acetonitrile. Compound **2.1** is air-sensitive in acetonitrile solution: the color changes from brown to light yellow over 12 hours when exposed to air, and bubbling O_2 into the solution initiates the color change within 30 seconds. Controlled oxidation of **2.1** with $AgBF_4$ under inert atmosphere successfully produces the trivalent complex

salt **2.2**. This represents the first one-pot method to produce a homoleptic chromium phenanthroline complex without caustic reagents, with a simpler procedure compared to literature reports.[32,51]

The absorption characteristics of **2.1** are quite different from complex **2.2**, as evidenced in Figure 2.4.1. Both complexes feature Cr^{3+} ions: the stronger absorption overall and the near IR bands found in **2.1** are consistent with one of the Ph_2phen ligands acting as a radical anion in **2.1**, while all ligands are neutral in **2.2**.[32] Meanwhile, other salts of **2.2** that have been prepared previously (OTf^- and Cl^-) have nearly identical absorption spectra (Figure 2.4.1), indicating similar solution environments for the trivalent species irrespective of cation-anion interactions.

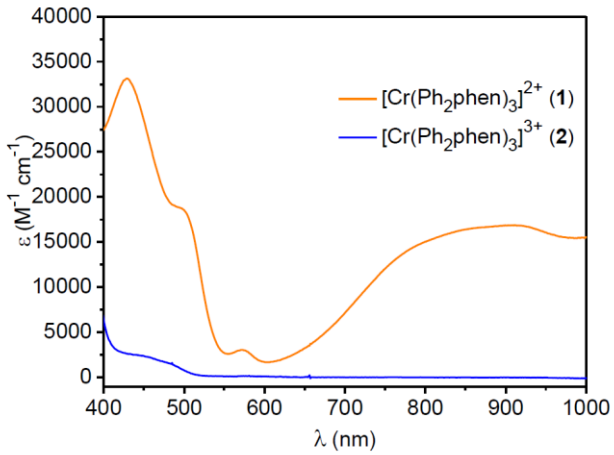
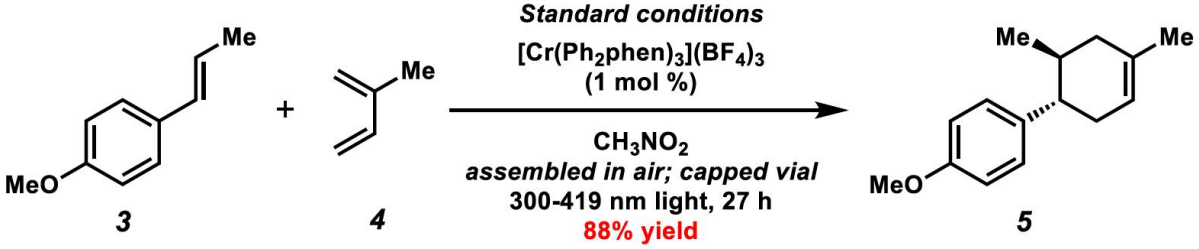


*Figure 2.4.1 Electronic absorption spectra of **1** and **2** in CH_3NO_2.*

2.4.2 Catalysis studies

As a representative reaction, the combination of **2.3** with **2.4** in nitromethane in the presence of catalytic amounts of **2.2**, light and oxygen affords the cycloadduct **2.5** in 88 % yield (Figure 2.4.2). Conveniently, this reaction can be set up open to air, and then just capped. When the reaction is performed in the absence of air (reaction mixture degassed by 3 freeze-pump-thaw cycles prior to irradiation), only trace product is formed. Without an air inlet, the color of the reaction mixture changes from a bright yellow to a darker tannish color over time (Figure 2.4.2).

No product formation occurs when the reaction is performed without light. Further, the addition of dimethylsulfoxide or benzoquinone (the latter is a superoxide scavenger) significantly slows the reaction, and addition of 25 mol % benzoquinone results in only a 2 % yield of product. As noted previously, the cyclization reaction proceeds in acetonitrile with slightly lower yield (70 %). For comparison to the $[Ru(bpz)_3]^{2+}$-photoinitiated system,[6] performing the reaction in dichloromethane affords a comparable but lower yield after 27 hours of irradiation (50 %). We also find that cycloadduct **2.5** can be formed in dimethylformamide (DMF), however this solvent choice relates to spectroscopic studies (*vide infra*) and yields were not obtained.



Modification to standard conditions	*Results*[a]
no air[b]	4% yield
no air[b], 20 mol % cat.	8% yield
10 mol % DMSO	64% yield
10 mol % benzoquinone	34% yield[c]

[a] ^{1}H NMR yields with dodecyl acetate as int. std.
[b] degassed by 3 freeze-pump-thaw cycles
[c] 27% *trans*-anethole remaining



before irradiation



after 24 h irradiation

Figure 2.4.2

Cycloadditions using terminally unsubstituted dienes proceed efficiently. In contrast, when terminally substituted dienes **2.8** and **2.10** are used, the additions occur much more efficiently when the reaction is performed with a needle air outlet compared to a sealed vial (Figure 2.4.3). This observation indicates an important influence of air (O_2) depending on the nature of the reactants, namely if cycloaddition is slowed.

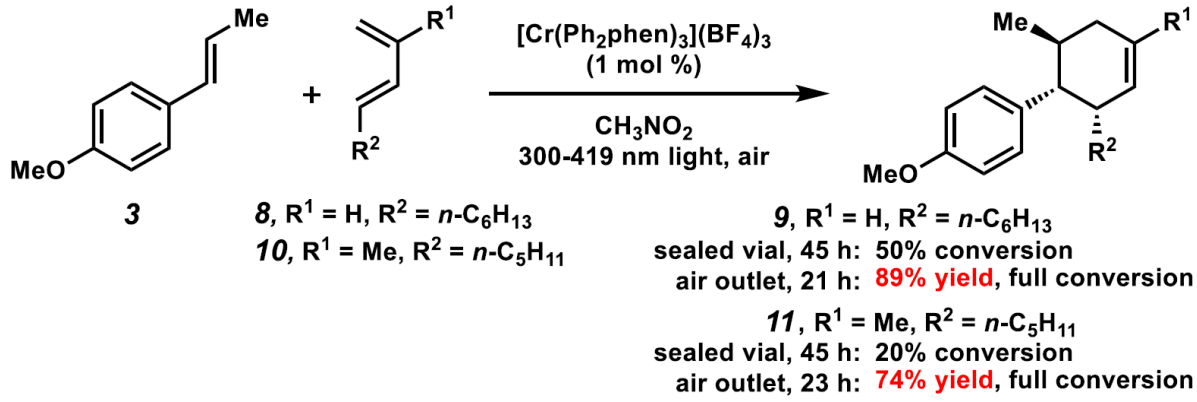


Figure 2.4.3

2.4.3 Electrochemical studies

Cyclic voltammograms of **2.1** and **2.2** in catalytically relevant solvents are shown in Figure 2.4.4, and the electrochemical data are compiled in Table 2.4.1. All of the redox events observed appear to be single electron processes. These assignments are supported by the peak-to-peak potential differences and similarity of currents passed in square wave voltammetry experiments and are consistent with literature precedent.[32]

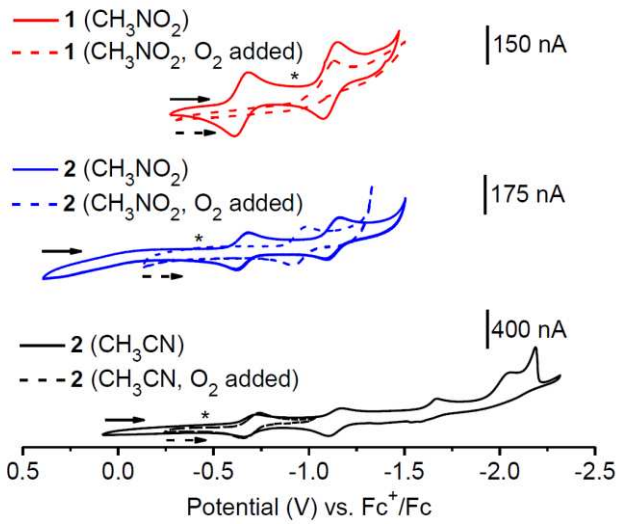


*Figure 2.4.4 Cyclic voltammograms (CVs) of **2.1** and **2.2**, collected in 0.1 M Bu_4NPF_6 solutions with a scan rate of 100 mV/s. Solid and dashed lines represent data collected without and with oxygen bubbled through the solution, respectively. The arrows indicate the direction of the scan. The black asterisks indicate the open circuit potentials of the degassed samples. The sharp peak in the CH_3CN data (~-2.2 V) is due to a surface adsorption event that does not affect the reversibility of the system.*

The CV of divalent **2.1** in CH_3NO_2 (Figure 2.4.2, red trace) is identical to trivalent **2.2** (Figure 2.4.2, blue trace), albeit with a more cathodic open circuit potential. Addition of O_2 via bubbling (10 min) leads to redox irreversibility and eventual disappearance of the original two reduction events. A new and electrochemically irreversible reduction event for the in-situ generated species emerges at -1.14 V vs. Fc^+/Fc. Infrared spectra (Figure A2.1) collected on samples of **2.1** exposed to excess O_2 support the notion that the divalent complex is oxidized by two electrons to form a chromyl species ($[O{=}Cr(Ph_2phen)_2]^{2+}$ (**2.6**)). We note that introduction of excess reducing agent (*e.g.* ferrocene) can regenerate the original electrochemical behavior of **2.1**, indicating possible chemical reversibility.

For polar-aprotic solutions (CH_3NO_2 and CH_3CN) of trivalent **2.2**, the reduction potential of the complex 3+/2+ couple remains isovoltaic. Redox events are significantly less reversible in CH_2Cl_2 compared to the more polar aprotic solvents (Figure A2.2).

Upon addition of O_2 in nitromethane, the reduction potential of **2.2** shifts cathodically by nearly 300 mV, but remains reversible (Figure 2.4.2, blue trace dashed line). We do not observe formation of a chromyl containing species when **2.2** is exposed to O_2 via IR spectroscopy (Figure A2.1). Interestingly, we do not observe a similar shift in acetonitrile under the same conditions (Figure 2, black trace dashed line). We note that the larger electrochemical window for CH_3CN allows us to observe reduction of oxygen to superoxide and subsequent surface chemistry. Collection of square wave voltammograms (SWVs) while stirring alleviates some of the surface chemistry and allows us to confirm reversibility of complex-based reductions in the presence of oxygen in CH_3CN.

To probe the effects of substrates and additives, CVs of **2.2** in CH_3NO_2 obtained under a variety of environmental conditions are presented in Figure 2.4.5. Table 2.4.1 shows the electrochemical data for the first reduction of **2.2** under a variety of conditions. Data from experiments performed in the dark overlap those observed under ambient light (Figures 2.4.4-5), with the proviso that reversibility in the "dark + O_2" experiment requires a glassy carbon electrode in place of a platinum working electrode, otherwise the overall peak shape changes drastically and reversibility decreases, suggestive of surface chemistry. Addition of the dienophile anethole (**2.3**) affords similar redox behavior to the complex alone, with and without added O_2. Addition of diene isoprene (**2.4**) moves the first reduction event anodically, with or without oxygen added, and removes the second reduction event. The diene is present in large excess relative to the Cr-containing complex, and likely perturbs the overall electrochemical environment. Altogether, when the conditions used for the catalytic studies are probed (Table 2.4.1, entry 5) the reversibility of the first reduction of **2.2** in CH_3NO_2 is maintained at a similar potential to **2.2** in inert conditions (-0.64 and -0.68 V respectively).

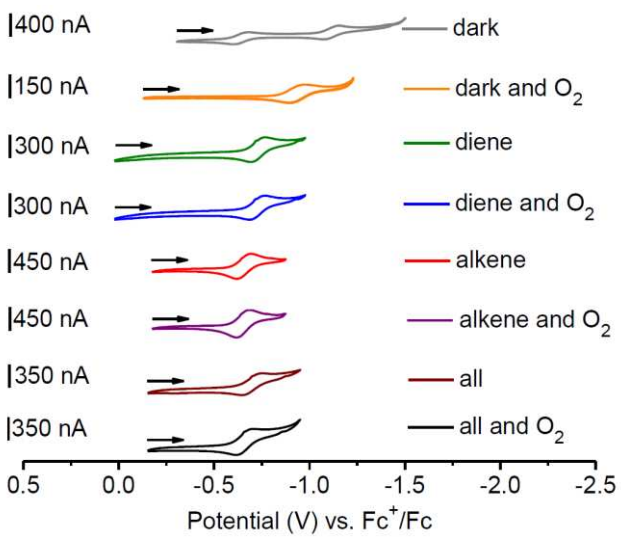


*Figure 2.4.5 CVs of **2.2** obtained under several environmental conditions, collected in 0.1 M Bu_4NPF_6 CH_3NO_2 solutions with a scan rate of 100 mV/s. With the exception of the "dark" trace, the CVs focus on the first reduction event. The arrows indicate the open circuit potential and the direction of the scan. The data for the "dark and O_2" trace (blue) were collected using a glassy carbon working electrode to eliminate surface chemistry. The concentrations of the added diene (isoprene, **2.4**) and alkene (anethole, **2.3**) match those used in the catalytic studies (1:100:1000 **2.2**:**2.3**:**2.4**).*

*Table 2.4.1 Compiled electrochemical data for **2.2**.[a]*

Entry	Solvent (conditions)[b]	E^0_{red} $[Cr]^{3+/2+}$ (V)	$E_{1/2}$ $[Cr]^{3+/2+}$ (V)	ΔE_p (mV) [c]	E^0_{red} $[Cr]^{3+/2+}$ + O_2 (V)	$E_{1/2}$ $[Cr]^{3+/2+}$ + O_2 (V)	ΔE_p (mV)
1	CH_3NO_2	-0.51	-0.66	64	-0.81	-0.97	70
2	CH_3NO_2 (dark)	-0.52	-0.66	64	-0.82	-0.94 [d]	71
3	CH_3NO_2 (+**2.4**)	-0.58	-0.73	72	-0.58	-0.72	72
4	CH_3NO_2 (+**2.3**)	-0.54	-0.66	74	-0.54	-0.65	68
5	CH_3NO_2 (+all)	-0.55	-0.64	65	-0.55	-0.64	65
6	CH_3CN	-0.56	-0.68	69	-0.62	-0.73	167
7	CH_3CN (all)	-0.59	-0.68	76	-0.59	-0.68	88
8	CH_2Cl_2	-0.56	-0.87	irr.	n/a	n/a	n/a
9	CH_2Cl_2 (all)	-0.58	-0.66	127	-0.58	-0.67	147

[a] All $E_{1/2}$ and E^0_{red} values are referenced to Fc^+/Fc, and are determined from CV data collected at 100 mV/s in 0.1 M Bu_4NPF_6 solutions in a dinitrogen atmosphere.

[b] "**+2.3**" indicates addition of anethole (**2.3**); "**+2.4**" indicates addition of isoprene (**2.4**); "+all" indicates the addition of both **2.3** and **2.4**; additives are present at concentrations relevant to catalysis studies.

[c] Values in parentheses represent separation of peak reduction and oxidation currents.

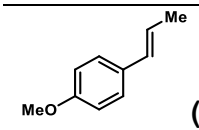
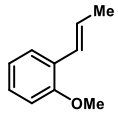
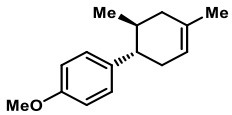
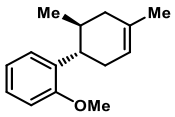
[d] Experiment was performed using a glassy carbon working electrode to avoid surface chemistry.

Analyses of electrochemical behaviors for representative alkenes (substrates and cycloadducts) provide a basis of interaction between catalyst and substrate as well as interactions between substrates and products (Table 2.4.2). In all cases, multiple oxidation events are observed in CVs that probe the oxidizing regime. Square wave voltammetry allows the quasi-reversible nature of these events to be characterized. Stirred and still solutions give different reduction potentials, suggestive of surface chemistry; however, the stirred solution oxidation potentials gathered align well with literature precedent for **2.3**.[52] Based on the oxidation potentials gathered in the presence of oxygen, the only species in solution that can oxidize **2.3** is the excited state of the Cr catalyst **2.2** (+0.98 V vs. Fc^+/Fc in CH_3NO_2). Cationic compounds $\mathbf{2.3^+}$ and $\mathbf{2.5^+}$ are thermodynamically competent to oxidize anything in solution except the solvent (CH_3NO_2 or CH_3CN) or $\mathbf{[Cr]}^{3+}$ catalyst or **2.4**. Furthermore, the corresponding cycloadduct radical cations are more oxidizing than the anetholes, so they are competent to oxidize anything besides solvent, including the reduced Cr catalyst and even diene **2.4**.

We note that in some instances, the redox potentials for the organic substrates and products measured here (Table 2.4.2) can change significantly depending on solvent and/or the presence of oxygen. The most striking changes are observed for the dienophile **2.3**: interestingly, the ~200 mV O_2-induced shift is anodic (more oxidizing) in nitromethane but cathodic (less oxidizing) in acetonitrile. The current data might be interpreted as showing differential interactions

between oxygen and organic molecules; however, further studies are required to explain this behavior, including rigorous control of [O_2] in the reaction. Notwithstanding, the current data show that additives (oxygen, reactants; even solvent choice) can affect the thermodynamics of electron transfer in the cycloaddition reactions studied here.

Table 2.4.2 Compilation of electrochemical data for methoxy-substituted styrenes and cycloproducts.

compound	$E_{1/2}$ $M^{\cdot+/0}$ (V) in CH_3NO_2	+ O_2	$E_{1/2}$ $M^{\cdot+/0}$ (V) in CH_3CN	+ O_2
 **(2.3)**	+0.78	+1.00	+1.07	+0.86
	+1.20	+1.14	+1.23	+1.23
 **(2.5)**	+1.32	+1.24	+1.29	+1.21
	+1.36	+1.38	+1.31	+1.29

All potentials referenced to Fc^+/Fc. All scans were performed at 100 mV/s scan rates in 0.1 M Bu_4NPF_6 solutions. O_2 experiments were performed by bubbling O_2 through the solution for ~15 seconds.

2.4.4 Spectro(electro)chemical studies

Spectroelectrochemical experiments performed on **2.5** aim to determine the absorption characteristics of the species after oxidation (Figure A2.3 and A2.4). When this is performed free of oxygen, the absorption band at 274 nm grows upon electrochemical oxidation whereas the transition at 225 nm remains almost the same. Additionally, the broad band centered at 991 nm decreases as the potential is increased. In the presence of oxygen, the absorption features are quite different, with only two bands of nearly equal intensity centered at 231 and 270 nm. When the potential was made more positive no change is observed in absorption features. We conclude that different reaction pathways are available to the cycloadduct radical cation depending on the availability of oxygen; however, the exact identity of those species is not known.

To probe superoxide formation, an expected side product from $^1O_2$ reduction of **[Cr]**$^{2+}$ to form **[Cr]**$^{3+}$ (Figure 2.1.2, scenario B), several spectroscopic traps have been considered. Direct observation of O_2^- under catalysis conditions is challenging due to low concentrations of the Cr-containing species and high reactivity of the cycloadduct radical cation species: performing the reaction in DMF results in product formation, but the charge transfer band attributed to a $(DMF{\cdot}O_2)^-$ adduct[53] is not observed. Control experiments where only **2.1** and **2.2** are present in nitromethane do show oxidation of the **[Cr]**$^{2+}$ in the presence of oxygen and light irradiation, without formation of a chromyl species (Figure A2.1). Here, whereas addition of superoxide traps such as TEMPOL do not show expected signals in EPR spectra for superoxide spin-trap adducts,[54-56] addition of thiophenol to the aforementioned reaction conditions results in conversion to diphenyl disulfide, indicative of the presence of superoxide (Figure A2.5).[40] While these experimental results do not directly demonstrate superoxide reduction of the cycloadduct radical cation, they do establish the presence of O_2^- under conditions similar to those used for the catalytic studies.

Actinometry experiments allow for the determination of quantum yields and chain lengths for the reaction of **2.3** and **2.4** in the presence of the **[Cr]**$^{3+}$ species **2.1**. Details are provided in

the Supporting Information. The maximum quantum yield (Φ) found is 0.35 from single wavelength excitation at 419 nm. Given a quenching factor (Q) of 0.99, the chain length is also 0.35, consistent with a process that does *not* propagate via a radical chain mechanism.

2.4.5 Photophysical studies

Emission quenching studies performed on **2.2** in room-temperature CH_3NO_2, focusing on the ~750 nm phosphorescence, assist us in further understanding the relationship between the photocatalyst, substrate and oxygen. We observe that the presence of oxygen significantly reduces the observed emission lifetime from 441 to 13 μs upon exposure of the deoxygenated sample to atmospheric oxygen. This is readily attributed to energy-transfer quenching wherein the ^2E excited state of the catalyst is converted to the quartet ground state while triplet oxygen is converted to its excited state singlet.[51] We note that this observation alone might suggest that the presence of oxygen should slow down the reaction by deactivating the catalytically-active ^2E excited state.

However, when dienophile **2.3** is used as the emission quencher for **2.2** in room-temperature CH_3NO_2, Stern-Volmer quenching behavior is observed for the sample in air (with ambient oxygen) as well as for a sample prepared in a dinitrogen glovebox. The results of these studies are displayed in Figure 2.4.6. As seen in both plots, the lifetime of **2.2** decreases upon successive addition of known amounts of **2.3,** suggestive of reduction of the **[Cr]**$^{3+}$ center to **[Cr]**$^{2+}$ with concurrent oxidation of the alkene. The top plot corresponds to a standard Stern-Volmer analysis where the intercept is 1 and where the slope is the lifetime of the molecule τ_0 (inclusive or exclusive of oxygen) multiplied by the quenching rate constant k_q. By dividing out τ_0 (bottom plot), one can remove oxygen dependence from the slope and isolate the measured dependence on anethole concentration. As can be seen from this figure, regardless of the presence of oxygen, the quenching rate constant k_q is nearly identical: 9.4×10^8 $M^{-1}s^{-1}$ for the degassed sample versus 9.5×10^8 $M^{-1}s^{-1}$ in ambient oxygen.

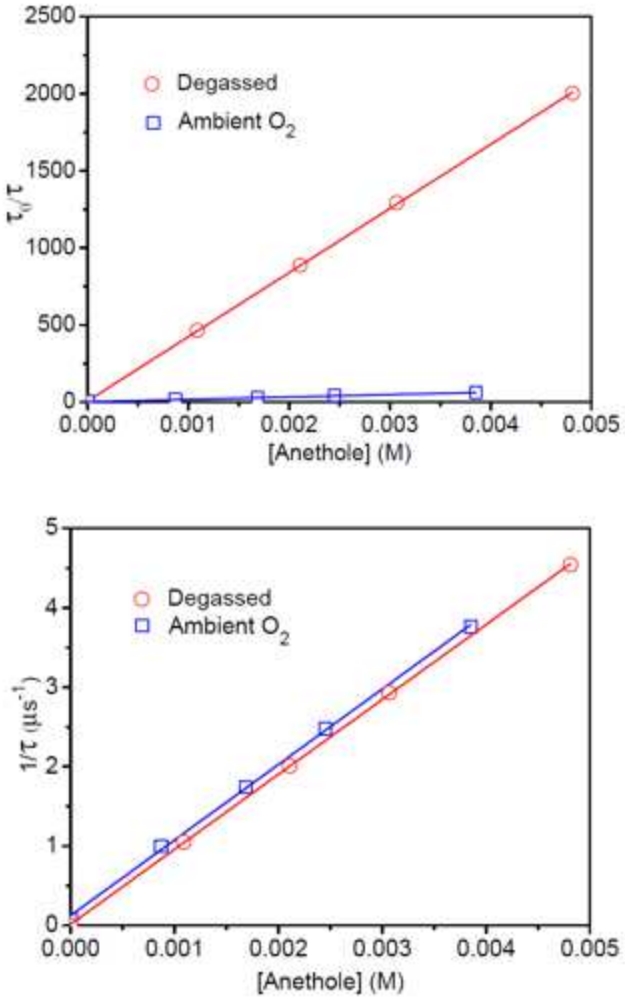


*Figure 2.4.6 Oxygen dependence of emission quenching of **2.2** by **2.3** in room temperature CH_3NO_2, showing Stern-Volmer behavior (τ_0/τ versus quencher concentration, top) and normalized to initial lifetime ($1/\tau$ versus quencher concentration, bottom). By plotting $1/\tau$, the quenching rate constant (k_q) is equal to the slope: 9.4 x 10^8 $M^{-1}s^{-1}$ degassed, 9.5 x 10^8 $M^{-1}s^{-1}$ ambient O_2. The data are fit to a linear function using least-squares methodology.*

The reaction of **2.3** and **2.4** with catalytic **2.2** in nitromethane, monitored by electronic absorption spectroscopy, shows significant differences as a function of oxygen presence. In the oxygen-free experiment, significant spectral changes are observed and plotted as a difference

spectrum in Figure 2.4.7. This spectral shape grows monotonically over time and does not appear to contain unrelated features. We can replicate the salient features as the creation of one equivalent of divalent **2.1** for the loss of every 5 equivalents of trivalent **2.2**. A brown solid precipitates over the course of the experiment, which is likely to be a reduced chromium degradation product due to the enhanced lability of the divalent species relative to the bona fide **[Cr]**$^{3+}$ complex. In contrast, in the presence of oxygen, the loss of **2.2** is observed with no concurrent growth in features attributable to **2.1** nor any appearance of an insoluble brown solid. Changes in relative absorbances (i.e., not just loss of **2.2**) in the visible region are responsible for the darkening of the solution, consistent with some decomposition of Cr-containing catalyst and/or emergence of absorptive radical cations.

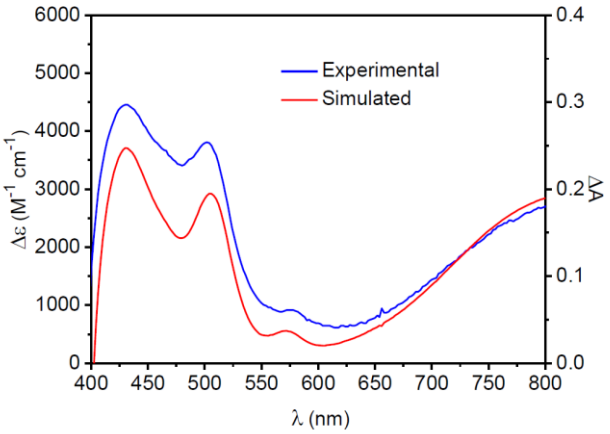


*Figure 2.4.7 Electronic absorption difference spectrum after a 40 hour photoreaction in which oxygen was excluded and a simulated spectrum consisting of the growth of **2.1** and loss of **2.2** in a 1:5 ratio.*

2.4.6 Electronic structure calculations

Density functional electronic structure theory provides energetic corroboration for the various experimental observations. Results are collected in Table 2.4.3 and summarized in Figure 2.4.8.

As with most Diels-Alder reactions, wherein three π bonds are converted into two σ bonds and a π bond, the process is significantly exoergic, computed to be downhill by 28 kcal/mol. The doublet excited state of **2.2**, ^{2}**2.2**, is computed to be thermodynamically competent to oxidize **2.3**, generating a radical cation, ^{2}**2.3**·BF_4, 8 kcal/mol exoergic while for the quartet ground state the reaction is 32 kcal/mol endoergic. Oxidation of the diene, **2.4**, by ^{2}**2.2** is computed to be 7 kcal/mol endoergic. Diene **2.4** is computed to bind to ^{2}**2.3**·BF_4 as a π complex with a binding enthalpy of 10 kcal/mol, but with an endoergic free energy of 3 kcal/mol. The ^{2}**2.3**·BF_4·**2.4** π complex is computed to proceed toward product with an electronic barrier of only 1 kcal/mol, relative to the π complex. The free energy of activation is 4 kcal/mol. The reduced chromium complex ^{3}**2.1**, thermodynamically, can reduce the oxidized cycloadduct product radical cation, ^{2}**2.5**·BF_4. Oxidation of ^{3}**2.1** by $^{3}O_2$ is computed to be endothermic by nearly 6 kcal/mol, while reaction with $^{1}\Delta$ O_2 is exothermic by 15 kcal/mol, with an exoergicity of 12 kcal/mol. Reduction of ^{2}**2.5**·BF_4 by superoxide is computed to be 48 kcal/mol exothermic. Oxidation of **2.3** by $^{1}\Delta$ O_2 is computed to be 21 kcal/mol endoergic.

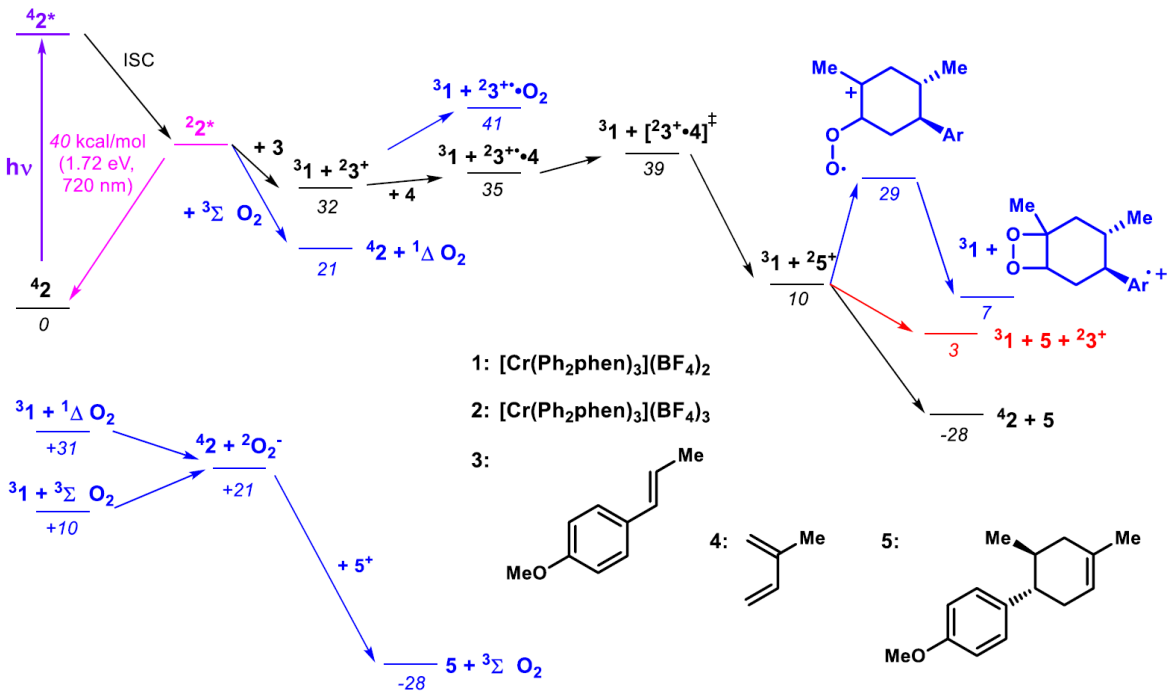


*Figure 2.4.8 Computed reaction pathways. The top Figure considers all processes related to Figure 2; the bottom Figure considers energetics associated with superoxide formation as part of catalyst regeneration. Blue entities represent possible routes affected by oxygen-containing species; the red route represents species involved in radical chain events. Free energies (in italics) are provided as kcal/mol relative to the ground state of the photocatalyst **2.2**.*

Table 2.4.3 Computed reaction energetics (kcal/mol).

Reaction	ΔTE^a	ΔH_r^b	ΔG_r^c
2.3 + **2.4** → **2.5**	-48.0	-44.1	-28.4
^{2}**2.2**$(BF_4)_3$ + **2.3** → ^{3}**2.1**$(BF_4)_2$+ ^{2}**2.3**·BF_4	-4.5	-6.0	-7.8
^{2}**2.2**$(BF_4)_3$ + **2.4** → ^{3}**2.1**$(BF_4)_2$+ ^{2}**2.4**·BF_4	12.6	10.4	7.4
^{4}**2.2**$(BF_4)_3$ + **2.3** → ^{3}**2.1**$(BF_4)_2$+ ^{2}**2.3**·BF_4	35.3	33.8	32.0
2.3 + $^1\Delta$ O_2 + TMA[d]·BF4 → ^{2}**2.3**·BF_4+ $^2O_2$·TMA	20.0	20.6	20.5
^{2}**2.3**·BF_4 + **2.4** → ^{2}**2.3**·BF_4·**2.4**	-9.7	-8.3	2.7
^{2}**2.3**·BF_4·**2.4** → [^{2}**2.3**·BF_4·**2.4**] TS[e]	1.3	1.0	4.3
^{3}**2.1**$(BF_4)_2$ + ^{2}**2.5**·BF_4 → ^{4}**2.2**$(BF_4)_3$ + **2.5**	-42.3	-40.8	-38.5
^{3}**2.1**$(BF_4)_2$ + $^3O_2$ + TMA·BF_4 → ^{4}**2.2**$(BF_4)_3$ + $^2O_2$·TMA	5.7	7.8	9.5
^{3}**2.1**$(BF_4)_2$ + $^1\Delta$ O_2 + TMA·BF_4 → ^{4}**2.2**$(BF_4)_3$ + $^2O_2$·TMA	-15.2	-13.2	-11.5
^{2}**2.5**·BF_4 + $^2O_2$·TMA → **2.5** + $^3O_2$ + TMA·BF4	-48.0	-48.6	-48.0
^{2}**2.3**·BF_4 + $^3O_2$ → ^{2}**2.3**·BF_4·O_2 (superoxo)	-4.9	-2.7	8.7
^{2}**2.3**·BF_4 + $^3O_2$ → ^{2}**2.3**·BF_4·O_2 (dioxetane)	-3.3	-1.2	11.7
2 ^{2}**2.3**·BF_4 → (^{2}**2.3**·BF_4)$_2$	-32.3	-29.0	-12.1
2 ^{2}**2.3**·BF_4 + $^3O_2$ → (**2.3**·BF_4)$_2O_2$	-44.6	-39.6	-13.5
^{2}**2.5**·BF_4 + $^3O_2$ → ^{2}product·BF_4·O_2 (superoxo)	6.9	7.3	19.4
^{2}**2.5**·BF_4 + $^3O_2$ → ^{2}product·BF_4·O_2 (superoxo) TS	10.4	9.9	21.7
^{2}**2.5**·BF_4 + $^3O_2$ → ^{2}product·BF_4·O_2 (dioxetane)	-18.1	-15.7	-2.6
2.5 + $^3O_2$ → product·O_2 (dioxetane)	-19.3	-16.8	-4.1
^{2}**2.5**·BF_4+ **2.3** →product + ^{2}**2.3**·BF_4	-7.0	-7.0	-6.5
^{2}**2.5**·BF_4+ **2.4** →^{2}**2.5**·BF_4·**2.4**	-10.8	-9.3	2.5
^{2}**2.5**·BF_4·**2.4**+ **2.3** →**2.5**·**2.4**+ ^{2}**2.3**·BF_4	-2.3	-2.4	-4.4

[a] ΔTE is the difference in total energies

[b] ΔH_r adds zero point and heat capacity effects

[c] ΔG_r adds the entropic contribution

[d] TMA is tetramethylammonium ion

[e] TS is transition state

The dienophile anethole, **2.3**, is observed to quench ^{2}**2.2**. The triplet excited state of **2.3** is computed to be 74 kcal/mol (vertical, 60 kcal/mol adiabatic) above the ground state while ^{2}**2.2** is at 39 kcal/mol. Oxidation of **2.3** by ^{2}**2.2** is 4 kcal/mol exothermic while reduction of ^{2}**2.3**·BF_4 by ^{3}**2.1**$(BF_4)_2$ is 35 kcal/mol exothermic.

To investigate whether $^3O_2$ is thermodynamically competent to stabilize ^{2}**2.3**·BF_4 or the resultant ^{2}**2.5**·BF_4, superoxo and dioxetane radical cation structures were computed. Both superoxo and dioxetane isomers are computed to be slightly exothermic but significantly endoergic for ^{2}**2.3**·BF_4, 9 and 12 kcal/mol, respectively. For ^{2}**2.5**·BF_4 superoxide formation is endoergic by 19 kcal/mol while radical cation dioxetane formation is 3 kcal/mol exoergic. The saddlepoint for ^{2}**2.5**·BF_4 superoxide formation is 22 kcal/mol endoergic (3 kcal/mol above the intermediate).

To contribute to our understanding of the electrochemistry, the radical cation dimer of **2.3** was studied along with the analogous dimer peroxide: these species were found by Bard and coworkers to be formed electrochemically.[31] Both dimeric complexes were computed to be exoergic, by 12 and 14 kcal/mol, respectively.

Finally, to investigate whether a radical chain process is viable, reduction of **2.3** by ^{2}**2.5**·BF_4 was considered. The process was computed to be 7 kcal/mol exoergic.

2.5 Discussion

As outlined in the introduction, the observed photocatalytic coupling of anethole (**2.3**) with isoprene (**2.4**), mediated by $[Cr(Ph_2phen)_3](BF_4)_3$ (**2.2**), requires the presence of oxygen. Data relevant to the catalytic cycle and several potential roles for O_2 have been considered and are discussed in light of the results presented above.

Before proceeding, a comment on measured electrochemical potentials is warranted by their importance in designing (photo)redox catalytic Figures and choosing "viable" reactants. From a strictly thermodynamic standpoint, the feasibility of an electron transfer event depends on the electrochemical onset potential ($E^0_{red/ox}$). This quantity is also directly related to the results of electronic structure computations. However, in a complex catalytic system, especially photoredox systems, the *rate* of electron transfer also matters, as it affects the concentrations of key intermediates that may be involved in (non-redox) processes downstream. Practically, $E_{1/2}$ reduction potentials are considered to be more applicable because they are related to the peak currents produced in the redox event, and thus generally indicate fast-enough kinetics. Notwithstanding, slow kinetics may prevent a key intermediate from being produced in an otherwise thermodynamically competent reaction; conversely, an irreversible process subsequent to electron transfer may allow a reaction to proceed where the $E_{1/2}$ values might suggest thermodynamic incompetence.

Both thermodynamics and kinetics of electron transfer are affected by changes in local environment. Unfortunately, we find several examples of recent photocatalysis literature that report reduction potentials without reference to solvent and other environmental conditions. It is well known that reduction potentials can vary greatly depending on solvent: for instance, Ag^+/Ag reduction is +40 mV in acetonitrile but +650 mV in dichloromethane (both vs. Fc^+/Fc).[57,58] Related, several photoredox catalysis reactions afford good yields only in uncommon solvents such as 1,3-dimethyl-2,4,5,6-tetrahydro-2(1H)-pyrimidinone (DMPU) or trifluoroethanol.[59,60]

Given this context, we investigated the reduction potential of **2.2** under several conditions to quantify the relative impacts on a key step in the catalytic process. Our original goal was to measure these potentials in environments matching as closely as possible the catalysis conditions *in operando*. Depending on the additives (substrates and/or O_2), we observe that the $E_{1/2}$ value for **2.2** changes by up to 330 mV, and that reversibility is not always maintained. When substrates and/or oxygen are present, we find that the shifts in reduction potentials (Figure 3) appear to be dominated by the diene (**2.4**), which is present in 1000-fold excess relative to the catalyst **2.2**. Here, the electrolyte is an important perturbation, because the concentration of O_2 is salt-dependent: for example [O_2] is decreased by a factor of ~2 when salt is present in acetonitrile.[29] Unfortunately, these electrochemical experiments are not possible without a salt present. Besides $E_{1/2}$ values, the difference in peak oxidation and reduction currents (ΔE_p) provides some indication of how electron transfer rates are modulated by the additives. For instance, under dinitrogen the ΔE_p values for **2.2** and **2.2** + **2.3** are 64 and 74 mV, respectively (Table 1), indicating slower kinetics for the latter even though the thermodynamics remain constant ($E_{1/2}$ = -0.66 V).

Key findings from this exploration are as follows. First, the catalyst shows varied reduction potentials in nitromethane with and without oxygen added, but once substrates **2.3** and **2.4** are included, the reduction potential is quite similar to that measured under oxygen-free conditions. Second, the catalyst reduction potentials are similar in different solvents when both substrates and oxygen are present, but the decrease in peak potential difference suggest that the kinetics of electron transfer are a little faster in nitromethane than acetonitrile. Finally, while measurement of electrochemical properties *in operando* is a good target, here [O_2] is difficult to control experimentally, and intractable to follow computationally; in these cases it is better to use the potentials generated from pristine conditions where all additives (especially O_2 here) can be controlled.

2.5.1 Excitation of Cr-catalyst

The reaction is initiated by visible or NUV light excitation of the Cr catalyst to what is thought to be a charge transfer transition (^{4}CT $\leftarrow$ ^{4}A), followed by non-radiative decay including intersystem crossing into a lower energy, long-lived ^{2}E state. From this state, the photochemistry can occur since it persists on a microsecond time scale, well beyond the time required to diffuse in solution and interact with a substrate. From this excited state, the catalyst can phosphoresce with a maximum intensity at 750 nm, well outside of the absorbing region. This provides a suitable signal for investigating the excited state behavior of the catalyst in the present system, which has been studied previously.[32,61] Oxygen is observed to quench this doublet excited state through an energy transfer pathway, reducing the amount of photoexcited catalyst and slowing down the overall reaction but not inhibiting it. This quenching event also results in the formation of singlet oxygen.[51]

2.5.2 Oxidation of dienophile and subsequent cyclization

The ^{2}E excited state of the chromium catalyst **2.2** is energetically competent to oxidize the dienophile **2.3**, computed to be 8 kcal/mol exoergic, while electrochemical ($E_{1/2}$) potentials suggest thermoneutrality. Electrochemical data (Figures 2.4.2 and 2.4.3) collected on reactants **2.3** and **2.4** and catalyst **2.2** further validate the computations. The observed quenching behavior in Figure 2.4.4 supports the kinetic viability of the process. Given the energetic inaccessibility of the dienophile triplet excited state, quenching likely occurs via electron transfer from the dienophile to the chromium complex, followed by either back electron transfer from chromium to the dienophile radical cation or dissociation of the radical cation. Here, the catalytically productive process (dissociation) can be favored by cation-cation repulsion, as the photo-reduced chromium complex is still divalent. The rate of the excited state quenching event involving **2.2*** and **2.3** is almost identical in and out of the presence of oxygen, confirming that oxygen does not play a significant role in dienophile oxidation. Further, as demonstrated in Figure 5, under photolysis conditions but without oxygen, the catalyst **2.2** is reduced to **2.1**.

Experimentally we find that final product formation is not observed in the absence of chromium, confirming that oxygen alone is not able to perform this reaction. Oxidation of the dienophile **2.3** by $^1\Delta$ O_2 is computed to be 21 kcal/mol endoergic; this reaction is even more unfavorable if ground state $^3O_2$ is used. Furthermore, singlet oxygen has an oxidation potential of -0.44 V vs. Fc^+/Fc which makes it unable to oxidize **2.3** in nitromethane with O_2 present ($E_{1/2}$ = +1.00 V vs. Fc^+/Fc corresponds to a free energy difference of 33 kcal/mol). Oxidation of the diene is also not observed in any reactions since this is not thermodynamically accessible by **2.2**, whether in ground or excited states. Oxidation of isoprene is computed to be 7 kcal/mol endoergic. $E_{1/2}$ data also suggest a 7 kcal/mol endoergicity.

We note that mono-oxidized *para*-trans anethole **2.3**$^+$ is reported to electrochemically dimerize,[31] but we do not observe this reaction under the standard reaction conditions used for the catalysis studies. Even though the reaction involves two cations combining to form a dication, we compute the radical cation dimerization reaction of ^{2}**2.3**$\cdot BF_4$ to be 12 kcal/mol exoergic in acetonitrile, consistent with what was observed previously by Demaille and Bard.[31] Reaction of two equivalents of ^{2}**2.3**$\cdot BF_4$ with $^3O_2$ is computed to be 13 kcal/mol exoergic. Despite favorable thermodynamics, dimerization is not observed within reasonable limits of detection under our photocatalytic conditions, likely due to a concentration effect. Electrochemically, the concentration of anethole radical cation builds up near the electrode to promote dimerization, while under chemical oxidation or photocatalytic oxidation conditions the radical cation is dispersed throughout the solution, in low concentration. Dating to the 1970s, such anodic chemistry has proven challenging for dienes and dienophiles.[33,62-64]

An alternative role for oxygen in the mechanism is to stabilize the dienophile radical cation **2.3**$^+$ so that it has sufficient lifetime to find a diene in solution. However, we compute the formation of end- or side-on (dioxetane) oxygen complexes with **2.3**$^+$ to be endergonic (Table 3) and we do

not observe these species spectroscopically. In addition, the similar initial rate constants observed in the quenching of **2.2*** by **2.3** with and without oxygen present do not support formation of an intermediate species.

Radical cyclization involving **2.3**$^{+}$ and **2.4** to form **2.5**$^{+}$ should be – and is computed to be – nearly barrierless. The 10-fold excess of diene utilized in catalysis conditions favors anethole radical cation reaction with a diene rather than with another dienophile. Thus, we conclude that oxygen does not play a significant role in the oxidation of the dienophile and subsequent cyclizations with alkenes.

2.5.3 Regeneration of the Cr catalyst

Under catalytic conditions but absent O_2, the loss of ~80 % of the trivalent Cr complex **2.2** signal suggests that the excited state complex is prone to decomposition, most likely from ligand loss and/or solvent incorporation, as described previously.[27] Related, build-up of the divalent Cr species **2.1** (Figure 2.4.9) indicates that the radical cyclo-intermediate, ^{2}**2.5**$^{+}$, does not succeed overall as an oxidant, returning the catalyst to the bona fide 3+ oxidation state, even though it is thermodynamically competent to do so. The computed exoergicity of that reaction is 39 kcal/mol, and the electrochemistry of the two species suggest favorable reactivity ($E_{1/2}$ data suggest a 43 kcal/mol exoergicity), but no product is formed without oxygen, so the kinetics of the air-free route must be relatively slow. Possible explanations for this non-event are as follows: first, the diffusion rates of large ionic species are expected to be dramatically slower than those of oxygen and redox congeners (*e.g.* superoxide); separately or in conjunction, cation-cation repulsion may prevent radical cation approach to the photoreduced Cr^{2+} complex.[65,66]

Related, we do not believe that a chromyl species (formed when divalent **2.1** is exposed to excess oxygen bubbled through solution) is actively involved in the regeneration of the catalyst. We observe spectroscopic evidence for this species only when the divalent complex **2.1** is exposed to oxygen, not when the trivalent complex **2.2** is used. In addition, we do not observe a chromyl species under conditions when diene and dienophiles are present in the reaction mixture.

The oxidized species has no significant absorptions in the visible spectrum where the highest overall reaction yields are obtained. Finally, any mechanism in which chromyl participation is invoked requires a two-electron oxidation and diimine ligand (here, Ph_2phen) dissociation to form the species, followed by one electron reduction and ligand re-association. While not impossible,[67] given the dilute nature of the Cr-containing complexes in solution, the polar solvents used, and the overall slow kinetics, we would expect the required ligand binding events are unlikely to occur in this catalytic cycle.

Based on the combined experimental and computational studies, we hypothesize that regeneration of **2.2** comes in two forms. First, ground state oxygen ($^3\Sigma$ O_2) can quench the excited state **2.2***: this produces singlet oxygen ($^1\Delta$ O_2) and likely prevents ligand loss in the Cr-containing complex. Second, $^1\Delta$ O_2, formed from the observed quenching of the photoexcited ^{2}**2.2** species, returns the catalyst to its 3+ oxidation state, and forms superoxide in the process.

2.5.4 Reduction of the cycloadduct radical cation

Considering species in solution that could reduce the radical cation cycloadduct to the final product **2.5**, the photo-reduced Cr catalyst **2.1** is competent to reduce **2.5**$^+$ directly. In addition, the dienophile **2.3** is both computationally and electrochemically capable of reducing **2.5**$^+$, and thus could participate in a radical chain pathway. However, we observe minimal product (**2.5**) formation when oxygen is excluded from the reaction mixtures, consistent with the idea that neither the reduced catalysts nor dienophiles are efficient electron shuttles in this system, even though the former are easily phototogenerated and the latter are present in large concentration relative to cycloadduct cations formed.

The principal role of an oxygen-containing species is difficult to observe directly. Whereas the radical cation **2.5**$^+$ is not sufficiently stable to interrogate directly, spectroelectrochemistry experiments performed on **2.5** show different radical cation species depending on the availability

of oxygen. In related systems, cyclic alkylperoxides have been proposed and isolated previously after oxidation of oxidatively reactive substrates.[68,69]

However, despite favorable thermodynamics and literature precedent, neither dioxetanes nor the products of transient dioxetane formation are observed under photocatalytic conditions. Once formed, dioxetanes are known to fragment, forming aldehyde or ketone cleavage products.[68] For the cycloaddtion product **2.5**, the radical cation dioxetane is computed to be 3 kcal/mol exoergic relative to the radical cation. Further, the subsequently reduced dioxetane is 3 kcal/mol exoergic relative to the observed product and $^3O_2$. Plausible formation of the dioxetane radical cation involves the intermediacy of a superoxo complex. For the cycloaddition product the spin density is completely localized on the aromatic ring. The superoxide intermediate is 19 kcal/mol endoergic, relative to the radical product and $^3O_2$, and the saddlepoint another 3 kcal/mol above the intermediate.

Given the considerations listed above, and the fact that oxygen is necessary for the reaction to proceed, we hypothesize that an oxygen-containing species acts as the electron transfer agent for the last step of the catalytic cycle. Superoxide is thermodynamically competent to reduce the product cyclohexenyl radical cation: the O_2/O_2^- couple in acetonitrile is -1.42 V vs Fc^+/Fc,[29,30] while the **2.5**$^+$/**2.5** couple is centered at +1.3 V (suggesting a 63 kcal/mol exoergicity); the computed exoergicity of the reaction is 48 kcal/mol. In contrast to the reaction of reduced catalyst **2.1** with **2.5**$^+$, where charge-charge interactions are repulsive, here there is an electrostatic attraction between the negatively charged superoxide and **2.5**$^+$, and approach of radicals is likely near barrier-free.

Amassing direct evidence of cycloadduct radical cation reduction by superoxide *in operando* is challenging due to the low concentrations and high reactivities of the two species. One piece of indirect evidence is the significantly lower product yield for reactions performed in the presence of benzoquinone, a known superoxide scavenger,[70] consistent with inhibition of superoxide. In addition, the reaction quantum yield determinations are not consistent with radical

chain propagation, suggesting that a species other than the dienophile **2.3** is responsible for generating new radical cations.

More directly, photoirradiation of oxygenated solutions of **2.1** and **2.2** (without other organic reactants) results in the oxidation of all **[Cr]$^{2+}$** to **[Cr]$^{3+}$** without formation of chromyl species, consistent with $^1O_2$ consumption. The superoxide presumably formed by concomitant reduction of singlet oxygen is not detected spectroscopically using either TEMPOL (a spin-trap) or DMF (a charge-transfer trap) presumably due to slow kinetics of formation in nonaqueous media in the former case and weak binding interactions in the latter. However, addition of thiophenol to the photoirradiated mixture results in the rapid formation of diphenyl disulfide, as observed via ^{1}H NMR spectroscopy; this has been employed recently as a reporter reaction for the detection of superoxide.[40] Thus, although the reaction of superoxide with **2.5$^+$** is not directly observed, there is strong evidence for presence of superoxide in the catalytic system and its potential to interact with an organic substrate.

2.5.5 Overall catalytic cycle including oxygen

Our current understanding of the Cr-mediated cycloaddition catalytic cycle is provided in Figure 2.5.1. Oxygen appears to protect the Cr catalyst by quenching the excited state when substrate (dienophile) is not immediately available; it also oxidizes the **[Cr]**$^{2+}$ species to regenerate the catalyst; finally, it shuttles electrons to the cycloadduct cation (as superoxide) to produce the final product.

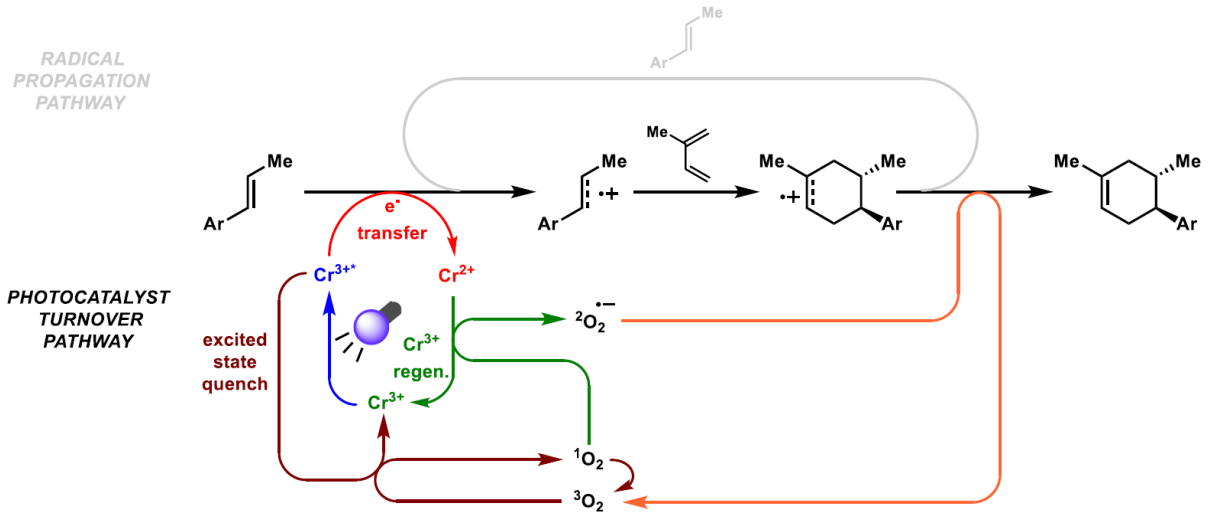


Figure 2.5.1 Proposed catalytic cycle.

In principle, oxygen's roles in this Cr-catalyzed system form closed cycles in which there is no net change in oxygen concentration and/or buildup of oxygen-containing (photo)redox side products. In practice, the efficiency of intermediate formation – for example, superoxide, which appears to be the key player in final product formation – should depend heavily on the relative concentrations of singlet oxygen, Cr catalyst and light, and also the stability of the oxidized dienophile. Imbalance in any of these concentrations could overexpress superoxide, leading to incorporation into cyclized products; alternatively, insufficient superoxide should slow product formation and/or activate a radical chain pathway, both of which could lead to lower yields and/or loss of stereochemical control. As shown in Figure 4, yields for different substrates may be affected by relative concentrations of O_2, reflective of this delicate balance; further studies probing concentration effects are in progress. We note that all of the relevant species are present in solution in comparable (mM) concentrations.[71] In addition, Cr excited state quenching by oxygen and substrate are competitive;[72] and excited state lifetimes for the catalyst and $^1\Delta$ O_2 (13 μs and 40 μs, respectively) are also comparable. It is rather amazing that this catalytic cycle works!

Notwithstanding, this seemingly fortuitous catalytic cycle presents an efficient means to perform photocatalytic reactions.

2.5.6 Comparison of Ru- and Cr-based photoredox catalysis

At this juncture it is reasonable to compare the present Cr-catalyzed system **2.2** to the literature $[Ru(bpz)_3]^{2+}$ photoredox system.[73,74] In acetonitrile, the excited state reduction potentials for $[Ru(bpz)_3]^{2+*/1+}$ and $[Cr(Ph_2phen)_3]^{3+*/2+}$ are nearly identical (~1 V vs. Fc^+/Fc). The excited state lifetime is significantly shorter for the Ru complex than the Cr species, even if the quenching effects of oxygen are included (< 0.9 μs and 13 μs, respectively). The ground state reduction potentials for both $[Ru(bpz)_3]^{2+/1+}$ and $[Cr(Ph_2phen)_3]^{3+/2+}$ in CH_3CN are such that neither of the reduced forms of these catalysts should be oxidized by $^3O_2$ (the Ru complex is much closer), but both are competent to reduce the cycloaddition product radical cation. Interestingly, however, neither appears to do so. Absent O_2, a 48 % yield of **2.5** is reported for the $[Ru(bpz)_3]^{2+}$-containing system; whereas for **2.2**, only trace amounts of **2.5** are observed. This difference is consistent with minimal photocatalyst turnover for each, but with Ru serving as an initiator for a radical chain (with a radical chain length of roughly 50), while Cr only produces approximately stoichiometric product.[39] Reported $^3O_2$ quenching rates for excited states in the related complexes $[Ru(bpy)_3]^{2+}$ and $[Cr(bpy)_3]^{3+}$ are 6.8×10^8 $M^{-1}s^{-1}$ and 2.5×10^7 $M^{-1}s^{-1}$, respectively, in acetonitrile.[75,76] Wrighton and Markham have reported competitive oxygen and aryl alkene quenching in Ru-based systems,[77,78] comparable to our observation of competitive quenching by dienophile and oxygen in a Cr-based system. In general, for each photophysical process Ru is faster and/or has a shorter lifetime than the Cr complex studied here.

We note that one additional point of divergence is solvent choice. Optimal product yields are obtained in nitromethane for the Cr-based system, and dichloromethane for the Ru-initiated process. Performing the reaction of interest in dichloromethane leads to an overall lower yield compared to nitromethane (50 vs 88 % respectively), and we observe no significant change in overall reaction rates. At this time, we cannot rule out differential interactions between solvent

and reactants or intermediates, but the data collected thus far suggest that solvent choice does not switch the dominant mechanistic pathway observed.

Regarding oxygen's influence, Yoon and coworkers observed endoperoxide product formation in the $[Ru(bpz)_3]^{2+}$-mediated oxidative cyclization of bis(styrenyl) substrates under standard photocatalytic conditions.[79] The formation of this product is predominant when increasing the oxygen concentration (via headspace pressure) from 1 atm to 4 atm. The authors proposed that the initially formed radical cation was intercepted by triplet oxygen, forming an endoperoxide radical cation.[79] From this result it is clear that oxygen can be involved directly in the reaction sequence, and relatively small changes in experimental conditions can alter final product distributions.

Based on these observations and assembled data, we suggest that $[Ru(bpz)_3]^{2+}$ and $[Cr(Ph_2phen)_3]^{3+}$ (**2.2**) likely follow a common catalytic cycle, comparable to what is shown in Figure 6, where relatively small deviations in rates and lifetimes favor the radical chain mechanism for the Ru complex, but oxygen-mediated photocatalysis for the Cr complex. Because the excited states of Ru-containing complexes react more quickly with organic substrates (by approximately a factor of 10), this arguably increases the concentration of cycloadduct radical cation in the reaction mixture, which in turn favors the radical chain pathway. Meanwhile, the longer excited state lifetime of the Cr complex offers more opportunities for energy transfer to $^3O_2$ to produce $^1O_2$. Here, a larger build-up of $^1O_2$ ultimately leads to a higher concentration of superoxide, which in turn reduces the concentration of cycloadduct radical cation by reduction. This lower concentration of cycloadduct radical cation deactivates the radical chain pathway. Kinetic models that test these ideas are being constructed and will be reported at a later date.

2.6 Conclusions and Outlook

The Cr-photocatalyzed Diels-Alder reaction between anethole and isoprene has been investigated with a range of tools with the goal of refining the reaction mechanism, specifically defining the critical role(s) that oxygen plays in this catalytic cycle and perhaps others. We observe

a direct interaction between the long-lived (^{2}E) Cr(III) excited state and dienophile, supporting the previously reported mechanistic hypothesis that the Cr excited state directly participates in anethole oxidation. Further, from the build-up of **2.1** under catalytic conditions, absent O_2 (Figure 5), we conclude that even though thermodynamically competent, the cycloaddition product radical cation is not kinetically competent to directly oxidize the reduced Cr catalyst. We observe that ^{2}E Cr(III) excited state quenching by oxygen and anethole are competitive processes but follow orthogonal paths. Oxygen quenching does not shut down the catalytic cycle, in fact it appears to be critical for catalyst stability and therefore catalytic turnover. We support the previous observation that oxygen does not play the deleterious role of oxidizing the organic substrates or product, rather we suggest that it serves as an electron shuttle, through the intermediacy of superoxide, between the reduced Cr catalyst and the oxidized cycloaddition product.

The results presented herein provide insight to oxygen's participation as a sustainable reagent in photoredox catalysis. The results also support the proposition that long-lived excited states in Cr(III) complexes can make available mechanistically distinct pathways from processes initiated by heavier congeners (e.g. Ru and Ir). These alternative reaction pathways could be exploited to achieve orthogonal reactivity. At the same time, the divergent reaction sequences are likely accessible to both heavy and light transition metal complexes, and small changes in environmental conditions may allow switching between radical chain and photocatalytic pathways. Our current and future efforts aim to parameterize the kinetic and thermodynamic quantities involved in this oxygen-mediated mechanism, so as to optimize reaction scope and control product structure.

References

1. Prier, C. K.; Rankic, D. A.; MacMillan, D. W. C. *Chem. Rev.* **2013**, *113*, 5322.

2. Xuan, J.; Xiao, W. J. *Angew. Chem. Int. Ed.* **2012**, *51*, 6828.

3. Narayanam, J. M. R.; Stephenson, C. R. J. *Chem. Soc. Rev.* **2011**, *40*, 102.

4. Yoon, T. P.; Ischay, M. A.; Du, J. N. *Nat. Chem.* **2010**, *2*, 527.

5. Beatty, J. W.; Stephenson, C. R. J. *Acc. Chem. Res.* **2015**, *48*, 1474.

6. Lin, S. S.; Ischay, M. A.; Fry, C. G.; Yoon, T. P. *J. Am. Chem. Soc.* **2011**, *133*, 19350.

7. Stevenson, S. M.; Shores, M. P.; Ferreira, E. M. *Angew. Chem. Int. Ed.* **2015**, *54*, 6506.

8. Ventre, S.; Petronijevic, F. R.; MacMillan, D. W. C. *J. Am. Chem. Soc.* **2015**, *137*, 5654.

9. Zuo, Z. W.; Ahneman, D. T.; Chu, L. L.; Terrett, J. A.; Doyle, A. G.; MacMillan, D. W. C. *Science* **2014**, *345*, 437.

10. Noble, A.; McCarver, S. J.; MacMillan, D. W. C. *J. Am. Chem. Soc.* **2015**, *137*, 624.

11. Bock, C. R.; Meyer, T. J.; Whitten, D. G. *J. Am. Chem. Soc.* **1974**, *96*, 4710.

12. Meyer, T. J. *Acc. Chem. Res.* **1989**, *22*, 163.

13. Gualandi, A.; Marchini, M.; Mengozzi, L.; Natali, M.; Lucarini, M.; Ceroni, P.; Cozzi, P. G. *ACS Catal.* **2015**, *5*, 5927.

14. Shepard, S. G.; Fatur, S. M.; Rappe, A. K.; Damrauer, N. H. *J. Am. Chem. Soc.* **2016**, *138*, 2949.

15. Ledwith, A. *Acc. Chem. Res.* **1972**, *5*, 133.

16. Valentin, J. S. *Chem. Rev.* **1973**, *73*, 235.

17. Wilke, G.; Schott, H.; Heimbach, P. *Angew. Chem. Int. Ed.* **1967**, *6*, 92.

18. Holland, P. L. *Dalton Trans.* **2010**, *39*, 5415.

19. Boisvert, L.; Goldberg, K. I. *Acc. Chem. Res.* **2012**, *45*, 899.

20. Fogler, E.; Efremenko, I.; Gargir, M.; Leitus, G.; Diskin-Posner, Y.; Ben-David, Y.; Martin, J. M. L.; Milstein, D. *Inorg. Chem.* **2015**, *54*, 2253.

21. Anson, C. W.; Ghosh, S.; Hammes-Schiffer, S.; Stahl, S. S. *J. Am. Chem. Soc.* **2016**, DOI: 10.1021/jacs.6b00254.

22. Douglas, J. J.; Cole, K. P.; Stephenson, C. R. J. *J. Org. Chem.* **2014**, *79*, 11631.

23. Nicholls, T. P.; Constable, G. E.; Robertson, J. C.; Gardiner, M. G.; Bissember, A. C. *ACS Catal.* **2016**, *6*, 451.

24. Perez-Ruiz, R.; Domingo, L. R.; Consuelo-Jimenez, M.; Miranda, M. A. *Org. Lett.* **2013**, *13*, 5116.

25. Yayla, H. G.; Peng, F.; Mangion, I. K.; McLaughlin, M.; Campeau, L.-C.; Davies, I. W.; DiRocco, D. A.; Knowles, R. R. *Chem. Sci.* **2015**, *7*, 2066.

26. Johnson, M.; Hannoun, K. I.; Tan, Y.; Fu, G.; Peters, J. C. *Chem. Sci.* **2016**, DOI: 10.1039/C5SC04709A.

27. Serpone, N.; Jamieson, M. A.; Henry, M. S.; Hoffman, M. Z.; Bolletta, F.; Maestri, M. *J. Am. Chem. Soc.* **1979**, *101*, 2907.

28. Here the use of **[**Cr**]**$^{n+}$ indicates the charge for the entire complex. In places where the formal oxidation state of the metal ion is specified, we use Stock nomenclature.

29. Li, Q.; Batchelor-McAuley, C.; Lawrence, N. S.; Hartshorne, R. S.; Compton, R. G. *J. Electroanal. Chem.* **2013**, *688*, 328.

30. Pavlishchuk, V. V.; Addison, A. W. *Inorg. Chim. Acta* **2000**, *298*, 97.

31. Demaille, C.; Bard, A. J. *Acta Chem. Scand.* **1999**, *53*, 842.

32. McDaniel, A. M.; Tseng, H. W.; Damrauer, N. H.; Shores, M. P. *Inorg. Chem.* **2010**, *49*, 7981.

33. Shono, T.; Ikeda, A. *Chem. Lett.* **1976**, *5*, 311.

34. Pfeil, A. *J. Am. Chem. Soc.* **1971**, *93*, 5395.

35. Huber, K. P.; Herzberg, G. *Molecular Spectra and Molecular Structure IV. Constants of Diatomic Molecules*; van Nostrand Reinhold: New York, NY, 1979.

36. Wilkinson, F.; Brummer, J. G. *J. Phys. Chem. Ref. Data* **1981**, *10*, 809.

37. Chen, C. C.; Fox, M. A. *J. Comput. Chem.* **1983**, *4*, 488.

38. Henriques, R. T.; Herdtweck, E.; Kuhn, F. E.; Lopes, A. D.; Mink, J.; Romao, C. C. *J. Chem. Soc. Dalton Trans.* **1998**, 1293.

39. Cismesia, M. A.; Yoon, T. P. *Chem. Sci.* **2015**, *6*, 5426.

40. McQuiken, A. C.; Matsumura, H.; Durr, M.; Confer, A. M.; Sheckelton, J. P.; Siegler, M. A.; McQueen, T. M.; Ivanovic-Burmazovic, I.; Moenne-Loccoz, P.; Goldberg, D. P. *J. Am. Chem. Soc.* **2016**, DOI: 10.1021/jacs.5b12741.

41. Krishnan, R.; Binkley, J. S.; Seeger, R.; Pople, J. A. *J. Chem. Phys.* **1980**, *72*, 650.

42. Hay, P. J. *J. Chem. Phys.* **1977**, *66*, 4377.

43. Austin, A.; Petersson, G. A.; Frisch, M. J.; Dobek, F. J.; Scalmani, G.; Throssell, K. *J. Chem. Theory Comput.* **2012**, *8*, 4989.

44. Perdew, J. P.; Chevary, J. A.; Vosko, S. H.; Jackson, K. A.; Pederson, M. R.; Singh, D. J.; Fiolhais, C. *Phys. Rev. B* **1992**, *46*, 6671.

45. Perdew, J. P.; Chevary, J. A.; Vosko, S. H.; Jackson, K. A.; Pederson, M. R.; Singh, D. J.; Fiolhais, C. *Phys. Rev. B* **1993**, *48*, 4978.

46. Adamo, C.; Barone, V. *J. Chem. Phys.* **1999**, *110*, 6158.

47. Perdew, J. P.; Burke, K.; Ernzerhof, M. *Phys. Rev. Lett.* **1996**, *77*, 3865.

48. Perdew, J. P.; Burke, K.; Ernzerhof, M. *Phys. Rev. Lett.* **1997**, *78*, 1396.

49. Scalmani, G.; Frisch, M. J.; Mennucci, B.; Tomasi, J.; Cammi, R.; Barone, V. *J. Chem. Phys.* **2006**, *124*.

50. Martin, R. L. *J. Chem. Phys.* **2003**, *118*, 4775.

51. Serpone, N.; Hofmann, M. Z.; Jamieson, M. A. *Inorg. Chim. Acta* **1978**, *31*, L447.

52. Bauld, N. L. *Tetrahedron* **1985**, *45*, 5307.

53. Slough, W. *Chem. Commun.* **1965**, 184.

54. Krishna, M. C.; Grahame, D. A.; Samuni, A.; Mitchell, J. B.; Russo, A. *P. Natl. Acad. Sci. USA* **1992**, *89*, 5537.

55. Samuni, A.; Krishna, C. M.; Mitchell, J. B.; Collins, C. R.; Russo, A. *Free Rad. Res. Commun.* **1990**, *9*, 241.

56. Reddan, J. R.; Sevilla, M. D.; Giblin, F. J.; Padgaonkar, V.; Dziedzic, D. C.; Leverenz, V.; Misra, I. C.; Peters, J. L. *Exp. Eye Res.* **1993**, *56*, 543.

57. Song, L.; Trogler, W. C. *Angew. Chem. Int. Ed.* **1992**, *31*, 770.

58. Connelly, N. G.; Geiger, W. E. *Chem. Rev.* **1996**, *96*, 877.

59. Petronijevic, F. R.; Nappi, M.; MacMillan, D. W. C. *J. Am. Chem. Soc.* **2013**, *135*, 18323.

60. Griffin, J. D.; Zeller, M. A.; Nicewicz, D. A. *J. Am. Chem. Soc.* **2015**, *137*, 11340.

61. Forster, L. S. *Chem. Rev.* **1990**, *90*, 331.

62. Baltes, H.; Steckhan, E.; Schafer, H. J. *Chem. Ber.* **1978**, *111*, 1294.

63. Cerrai, P.; Guerra, G.; Tricoli, M.; Nucci, L. *Euro. Polymer J.* **1980**, *16*, 867.

64. Nigenda, S. E.; Schleich, D. M.; Narang, S. C.; Kuemi, T. *J. Electrochem. Soc.* **1987**, *134*, 2465.

65. Weber, J. M.; Rawls, M. T.; MacKenzie, V. J.; Limoges, B. R.; Elliott, C. M. *J. Am. Chem. Soc.* **2007**, *129*, 313.

66. Beccia, M. R.; Biver, T.; Garcia, B.; Leal, J. M.; Secco, F.; Venturini, M. *Inorg. Chem.* **2011**, *50*, 10152.

67. We note that the chromyl species appears to re-form the divalent compound **1** when reducing agents are added to chromyl-containing solutions.

68. Story, P. R.; Whited, E. A.; Alford, J. A. *J. Am. Chem. Soc.* **1972**, *94*, 2143.

69. Lu, Z.; Parrish, J. D.; Yoon, T. P. *Tetrahedron* **2014**, *70*, 4270.

70. Samoilova, R. I.; Crofts, A. R.; Dikanov, S. A. *J. Phys. Chem. A* **2011**, *115*, 11589.

71. Initial concentrations of the dienophile and diene are 0.12 mM and 1.2 mM, respectively; the catalyst is present at 0.0012 mM concentration. Estimates of O_2 concentration in anhydrous CH_3CN range from 1.26 mM (with 0.1 M Bu_4NClO_4)[31] to 2.42 mM in (salt-free).[64] Under saturated O_2 conditions these concentrations jump to 6.3 mM and 12.1 mM, respectively.

72. The literature quantum yield for $^1O_2$ production by $[(Cr(bpy)_3]^{3+}$ is 0.86, with a quenching rate constant of 2.5×10^7 $M^{-1}s^{-1}$.[65] Our para-anethole quenching rate constant is 9.5×10^8 $M^{-1}s^{-1}$.

73. Crutchley, R. J.; Lever, A. B. P. *Inorg. Chem.* **1982**, *21*, 2276.

74. Gonzales-Velasco, J.; Rubinstein, I.; Crutchley, R. J.; Lever, A. B. P.; Bard, A. J. *Inorg. Chem.* **1983**, *22*, 822.

75. Hoffman, M. Z.; Bolletta, F.; Moggi, L.; Hug, G. L. *J. Phys. Chem. Ref. Data* **1989**, *18*, 219.

76. Tiyabhorn, A.; Zahir, K. O. *Can. J. Chem.* **1996**, *74*, 336.

77. Wrighton, M.; Markham, J. *J. Phys. Chem.* **1973**, *77*, 3042.

78. Representative quenching rates for $[Ru(bpy)_3]^{2+}$ include: 1,4-dinitrobenzene, 6.6×10^9 $M^{-1}s^{-1}$; 4-Methoxy-N,N-dimethylaniline 5.0×10^9 $M^{-1}s^{-1}$; both in 0.1 M Et_4NClO_4 in CH_3CN.

79. Parrish, J. D.; Ischay, M. A.; Lu, Z.; Guo, S.; Peters, N. R.; Yoon, T. P. *Org. Lett.* **2012**, *14*, 1640.

Chapter 3: Spin directed, association driven photoredox catalysis

3.1 Introduction

Photoredox catalysis continues to advance and reshape synthetic methods in organic chemistry.[1-3] With very few exceptions, these light-induced transformations rely upon Marcus theory (*i.e.*, collisional based reactivity) through electron transfer to proceed.[4-5] Notable examples where traditional outer-sphere electron transfer is subverted include Meggers' work on inner-sphere electron transfer using chiral iridium complexes[6] and Bach's templates/catalysts that direct electron/energy transfer for cyclization reactions (see Figure 3.1.1).[7-8] While these two groups have shown robust control of their systems, little other work has been performed to attenuate radical propagation in photoredox systems. Recently, the Yoon group eloquently showed that H-bond accepting substrates can interact with ligands on an Ir-photosensitizer, giving excellent enantioselectivity.[9] This is inherently important to all electron/energy transfer reactions and thus additional research is required to obviate high concentrations of radicals in these reactions.[10-11]

In this vein, we noticed some peculiar results in our system of Diels-Alder reactions with electron rich alkenes, such as *trans*-anethole, and dienes photocatalyzed by $[Cr(Ph_2phen)_3]^{3+*}$.[14-15] Our proposed mechanism requires two photons to go from starting material to product, which is quite uncommon. We showed that $[Cr(Ph_2phen)_3]^{3+}$ and $[Ru(bpz)_3]^{2+}$ display different mechanisms but didn't determine why these mechanisms are orthogonal. Very recently, we reported the mechanistic differences that $[Cr(Ph_2phen)_3]^{3+}$ and $[Ru(bpz)_3]^{2+}$ display in the cycloaddition reaction of electron-poor alkenes, such as 4-methoxychalcone and dienes. Therefore, we set out to re-investigate the *trans*-anethole and isoprene cycloaddition reaction to further understand these mechanistic pathways.

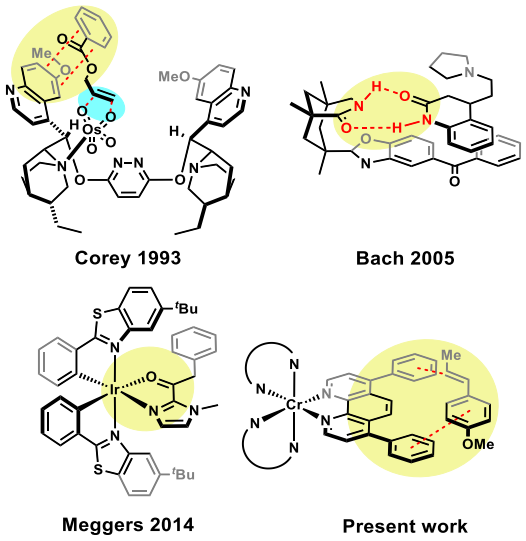


Figure 3.1.1. Selected examples of "catalyst"-substrate interactions prior to reactivity.[6-7, 16]

3.2 Division of labor

All experimental data and their analyses and interpretations were performed by Robert F. Higgins. All computations were performed by Anthony K. Rappé. Analysis and interpretation of the results was performed by Eric M. Ferreira, Anthony K. Rappé and Matthew P. Shores.

3.3 Experimental

3.3.1 Preparation of known compounds

The metal complexes $[Cr(bpy)_3](BF_4)_3$, $[Cr(phen)_3](BF_4)_3$, $[Cr(dmcbpy)_3](BF_4)_3$, $[Cr(Ph_2phen)_3](BF_4)_3$[1] and $[Ru(Ph2phen)_3](Cl)_2$[2] were prepared according to literature procedures. The organic molecules (*E*)-*tert*-Butyldimethyl(4-(prop-1-en-1-yl)phenoxy)silane[3] and 4'-methoxy-2,4-dimethyl-1,2,3,6-tetrahydro-1,1'-biphenyl[3]. *Trans*-anethole was passed through a flash column (silica gel) prior to use. 4-methoxychalcone was recrystallized twice from EtOH prior to use. Irradiation was performed with a Kessil® A160WE TUNA BLUE (blue light) source or an ecosmart$_{TM}$ 23 W CFL bulb. Flash chromatography was performed using Silicycle silica gel (230-400 mesh). All other compounds and reagents were used as received from chemical suppliers.

3.3.2 Preparation of novel compounds

$[Co(Ph_2phen)_3](BF_4)_3$. To a mixture of Ph_2phen (100 mg, 0.301 mmol) in 6 mL of 2:1 CH_3CN:CH_2Cl_2 was added $[Co(H_2O)_6](BF_4)_2$ (33 mg, 0.097 mmol) in 3 mL CH_3CN. The solution immediately turned dark orange and was allowed to stir for 1 hour. Afterwards, $NOBF_4$ (12 mg, 0.10 mmol) in 2 mL of CH_3CN was added. Over the period of 2 hours, the color of the reaction mixture changed from dark orange to yellow. After an additional hour of stirring, Et_2O (30 mL) was added until a yellow precipitate formed, which was collected *via* filtration and washed with Et_2O (2 × 5 mL). The collected precipitate was dried under vacuum for 2 hours, giving $[Co(Ph_2phen)_3](BF_4)_3$ (124 mg, 0.094 mmol) as a light-yellow powder at a 97 % yield. Electronic absorption data is in agreement with a previously reported synthesis of the Cl^- salt of the complex.[7] ESI-MS(+) (CH_3CN): *m/z* 1229.33 $(M - BF_4)^+$.

$[Fe(Ph_2phen)_3](BF_4)_2$ was prepared according to the literature using $[Fe(H_2O)_6](BF_4)_2$ in place of $[Fe(NH_3)_4SO_4]\cdot 6(H_2O)$.[8] ESI-MS(+) ($CH_3CN$): *m/z* 1139.33 $(M - BF_4)^+$.

3.3.3 Kinetics studies

Kinetic parameters were determined by monitoring the course of the reaction through ^1H NMR analysis until the reaction reached at least 80% completion. Standard reaction conditions were employed for these analyses with 0.1 molar equivalents of mesitylene added as an internal standard.[5] An NMR tube charged with all reagents was removed at discrete time intervals, the stir bar was removed and the tube was wrapped in felt and transported to the spectrometer. The NMR spectra were collected with a longer-than-normal relaxation delay (t_1 = 5 seconds) to ensure that paramagnetic signals from the Cr-catalyst did not interfere with the acquisition of the spectra.

3.3.4 Light-flux studies

These experiments were performed using a Newport TLS-300XU tunable light source, which includes a 300 W Xe arc lamp, a Cornerstone 130 monochromator and a motorized filter. Variable wattages (100-300 W from lamp) were used and the sample was irradiated for 16 hours for each experiment. The specific wattages used for these experiments were 200, 250, 270, 285

and 300 W. NOTE: Photon flux and wattage of these lasers do not provide a linear relationship, so multiple wattages are necessary even if they are concentrated in one regime, to obtain photon fluxes across a useful range. The flux of the laser at each wattage was determined using standard actinometry studies with $K_3[Fe(ox)_3]$.[6]

3.3.5 Other physical methods

All experiments were conducted at room temperature unless otherwise noted. Absorption spectra were obtained with a Hewlett-Packard 8453 spectrometer in quartz cuvettes with a 1 cm path length. NMR studies were performed on either a Varian 400 MHz spectrometer. Mass spectrometric measurements were performed in the positive ion mode on a Thermo LTQ mass spectrometer equipped with an analytical electrospray ion source and a quadrupole ion trap mass analyzer. Each measurement, unless otherwise noted, was performed with the capillary temperature = 175 °C, spray voltage = 5 kV, and spray current = 91 μamps.

3.4 Results and Discussion

To begin, we gathered kinetic data for the reaction of *trans*-anethole and isoprene to determine the rate-determining step. The determined rate constant when *trans*-anethole and isoprene are reacted using our optimized Cr-photoredox conditions is 4.07×10^{-6} M s^{-1} (Figure 3.4.1). When the concentrations of isoprene and $[Cr(Ph_2phen)_3]^{3+}$ were varied individually and the concentration of *trans*-anethole remained constant, no change in rate constant is observed (Figures A3.4-A3.5). Therefore, the most appropriate rate law is zeroth-order overall. This zeroth-order determined rate limiting step is unexpected. Considering that classical zeroth order reactions derive from competitive inhibition dubbed Michaelis-Menten kinetics, we were motivated to investigate whether a substrate-catalyst interaction occurs in this system.[17]

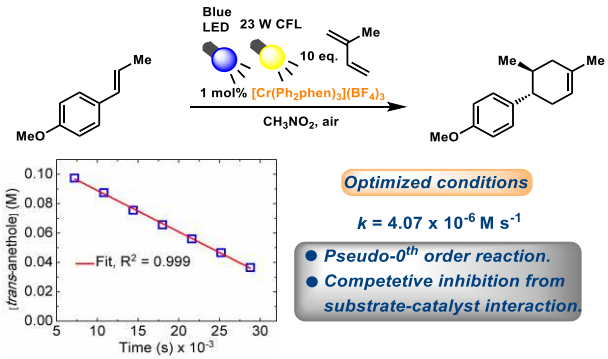


Figure 3.4.1. Representative kinetic data for the Cr-photocatalyzed cycloaddition reaction between trans-anethole and isoprene

While many techniques could potentially be used to investigate the potential interactions of *trans*-anethole and $[Cr(Ph_2phen)_3]^{3+}$, the paramagnetic nature of the chromium species complicates many of these techniques. Interestingly, the ^1H NMR spectrum of $[Cr(Ph_2phen)_3]^{3+}$ shows good resolution and all peaks are within the normal range when a paramagnetic sequence is performed (Figure A3.1). This is a curious result, as paramagnetic substances normally show peak broadening and large peak shifts up- or downfield depending on the (pseudo)-contact shift of the respective protons.[18] Since intrinsic spin-orbit coupling of the metal center and further, the electronic anisotropy of paramagnetic species dictates the degree of peak shifts in the resultant spectrum, it might not be surprising that this Cr^{3+} ion shows a relatively standard ^1H NMR response. This is because pseudo-octahedral Cr^{3+} (d^3 electronic configuration) is electronically isotropic and has a small spin-orbit coupling value for the free ion (275 cm^{-1}).[19-20] Some ^1H NMR spectra of Cr^{3+} complexes have shown traditional paramagnetic responses, but a survey of the literature and further experiments (see supporting information) show that this is a combination of differential ligand-fields/symmetries for the Cr^{3+} compounds and the identity of the solvent.[21-22] For $[Cr(Ph_2phen)_3]^{3+}$, spectra that are obtained in CD_3NO_2 and CD_3CN show good resolution, which give us a handle to study the solution phase properties more in-depth. Adding *trans*-anethole to a solution of $[Cr(Ph_2phen)_3]^{3+}$ shows peak changes in the protons associated with the

ligand, which are observed *via* an ^{1}H NMR titration (Figure 3.4.2), giving an association constant of K_{assoc} = 342(4) M^{-1}.[23]

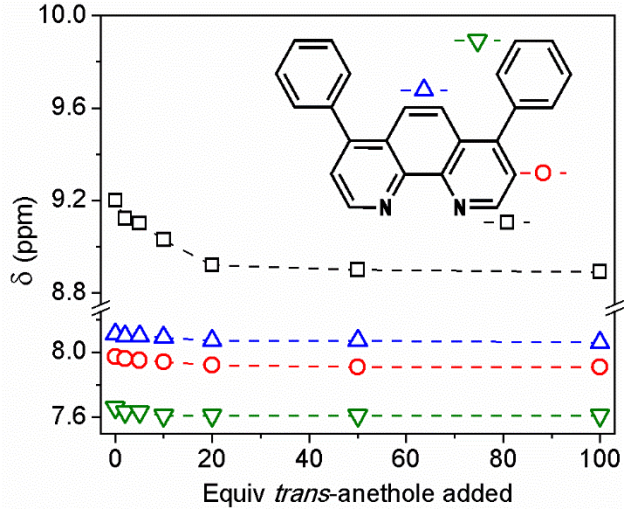


Figure 3.4.2. The ^{1}H NMR peaks for $[Cr(Ph_2phen)_3]^{3+}$ (0.001 M) in CD_3NO_2 upon titration of trans-anethole.

We also investigated substrates and reagents other than *trans*-anethole that could potentially associate with $[Cr(Ph_2phen)_3]^{3+}$. Figure 3.4.3 shows some molecules that are tested for association with $[Cr(Ph_2phen)_3]^{3+}$ in CD_3NO_2, probed through ^{1}H NMR experiments. Organic species that include an extended π-system show association with $[Cr(Ph_2phen)_3]^{3+}$. Smaller species that do not contain at least one phenyl ring do not show association, at least with a large enough K_{assoc} value to determine through NMR experiments. Of interest, O_2 does not appear to show association, contrary to a previously reported computational report by Yu and Dang.[24] Notwithstanding, we are not implicating that no intermolecular interactions occur between $[Cr(Ph_2phen)_3]^{3+}$ and these other species, we are just stating that whatever interactions may be occurring are not energetically favorable enough for us to observe by these methods.

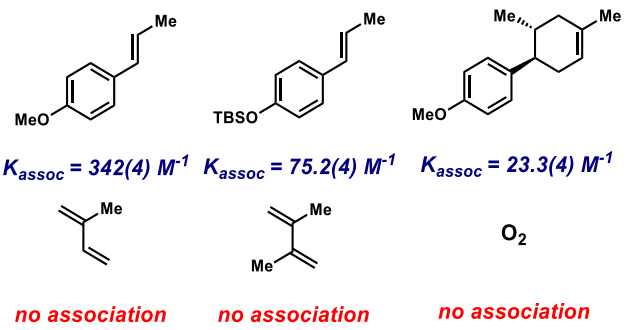


Figure 3.4.3. Representative examples of species that (do not) show association with $[Cr(Ph_2phen)_3]^{3+}$ in CD_3NO_2.

While these results are interesting, we wanted to determine how prevalent this association is to our Cr-photocatalysts and other more generalized photocatalysts: this type of interaction leading to efficacious photo-reactivity has been invoked previously by Zhang and others in a pyrene-sensitized defluorination reaction of arenes.[25] The metal complexes $[Cr(bpy)_3]^{3+}$, $[Cr(phen)_3]^{3+}$ and $[Cr(dmcbpy)_3]^{3+}$ (all charged species are BF_4^- salts, bpy = 2,2'-bipyridine, phen = 1,10-phenanthroline and dmcbpy = 4,4'-dimethylcarboxylate-2,2'-bipyridine) do not show association with *trans*-anethole through ^1H NMR analyses in CD_3NO_2 (Figure A3.2).[26] Unsurprisingly, $[Ru(bpz)_3](PF_6)_2$ also does not show association to *trans*-anethole through the same NMR analysis (Figure A3.3). These results indicate that the extended π-system is likely facilitating this substrate-catalyst association. Thus, an alternative hypothesis can be postulated that the identity of the metal-center is unimportant, outside of scaffolding the Ph_2phen ligand, for this association event to occur.

Therefore, we synthesized a family of known homoleptic metal complexes that contain Ph_2phen ligands. To our surprise $[Ru(Ph_2phen)_3]Cl_2$,[27] $[Fe(Ph_2phen)_3](BF_4)_2$[28] and $[Co(Ph_2phen)_3](BF_4)_3$[29] fail to show any behavior consistent with association of *trans*-anethole *via* ^1H NMR experiments (Figure 3.4.4). Also, none of these M-Ph_2phen complexes show conversion to the cyclohexenyl product in the presence of *trans*-anethole and isoprene. These three metal

ions are all low-spin (diamagnetic, $S = 0$) d^6 and reside either in a divalent or trivalent cationic state. This is important, because it implies that the charge of the Cr-complex is not directing this association event, but rather the paramagnetic nature of this ion appears to be the more important factor. The exact phenomena that cause the prerequisite of nonzero electronic spin for this association event is still under investigation, but its ramifications are broad reaching and likely unsurprising as paramagnetic species are often more reactive than diamagnetic congeners.[30-32]

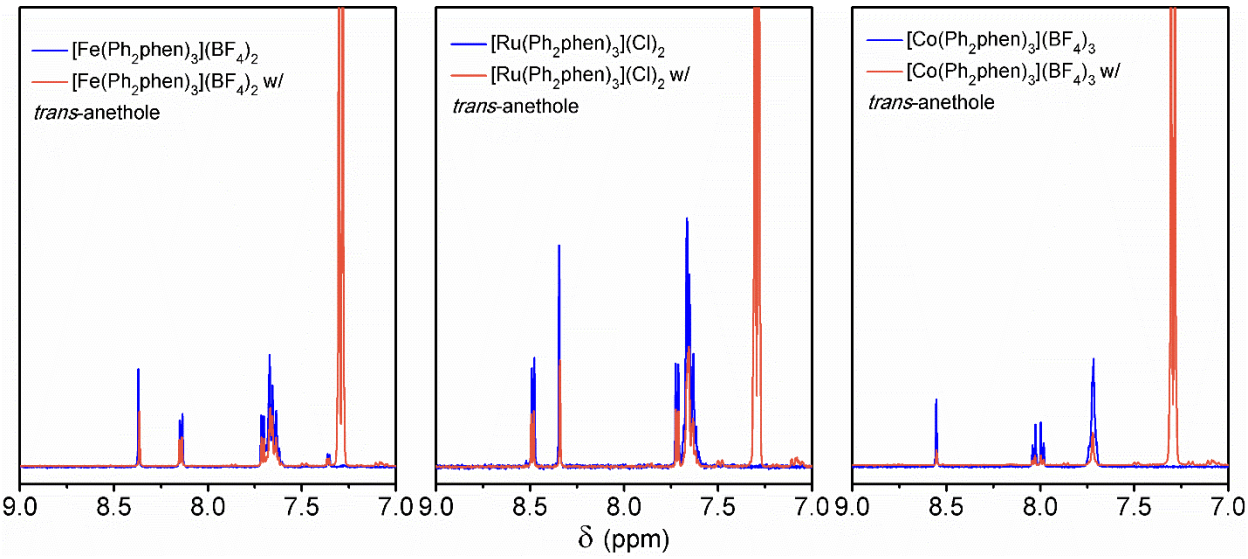


Figure 3.4.4. ^{1}H NMR spectra of tris-Ph$_2$phen metal complexes of Fe(II), Ru(II) and Co(III) in CD$_3$NO$_2$ with and without trans-anethole added.

3.5 Conclusions

These results build upon our growing findings on the differences in reaction pathway(s) when $[Cr(Ph_2phen)_3]^{3+}$ is used for photoredox cycloaddition reactions. We hypothesize that this association could be enhanced by altering the structure of the substrate or by modification of a 4,7-substituted phen ligand with a more extended π-system. Further, this association event gives a possibility for more selective reactions than traditional outer-sphere electron transfer reactions.

Our current aim is to investigate smaller/simpler Cr-species that show this same phenomenon in hopes of performing more efficacious characterization and computational methods on this association event.

In conclusion, we present an in-depth investigation into the association of substrates and $[Cr(Ph_2phen)_3]^{3+}$ in photoredox reactions. This association can be turned-off by steric modification of the substrates and importantly, this association is not observed for other Cr-photosensitizers. The two main takeaways from this study are: (1) $[Cr(Ph_2phen)_3]^{3+}$ gives an alternative photoredox pathway compared to other commonly used photosensitizers (*i.e.*, $[Ru(bpz)_3]^{2+}$) through an association-enabled pathway and (2) the paramagnetic nature of Cr^{3+} is important to the observed association. We are currently investigating the origins behind the requirement of a paramagnetic ion for this association event and will report on these results in due course.

References

1. Shaw, M. H.; Twilton, J.; MacMillan, D. W. C. *J. Org. Chem.* **2016**, *81*, 6898.

2. Prier, C. K.; Rankic, D. A.; MacMillan, D. W. C. *Chem. Rev.* **2013**, *113*, 5322.

3. Skubi, K. L.; Yoon, T. P. *Nature* **2014**, *515*, 45.

4. Marcus, R. A. *J. Chem. Phys.* **1956**, *24*, 966.

5. Marcus, R. A. *Annu. Rev. Phys. Chem.* **1964**, *15*, 155.

6. Huo, H.-H.; Shen, X.-D.; Wang, C.-Y.; Zhang, L.-L.; Röse, P.; Chen, L.-A.; Harms, K.; Marsch, M.; Hilt, G.; Meggers, E. *Nature* **2014**, *515*, 100.

7. Bauer, A.; Westkamper, F.; Grimme, S.; Bach, T. *Nature* **2005**, *436*, 1139.

8. Coote, S. C.; Bach, T. *J. Am. Chem. Soc.* **2013**, *135*, 14948.

9. Skubi, K. L.; Kidd, J. B.; Jung, H.; Guzei, I. A.; Baik, M.-H.; Yoon, T. P. *J. Am. Chem. Soc.* **2017**, *139*, 17186.

10. Cismesia, M. A.; Yoon, T. P. *Chem. Sci.* **2015**, *6*, 5426.

11. Studer, A.; Curran, D. P. *Angew. Chem. Int. Ed.* **2016**, *55*, 58.

12. Johnson, M. W.; Hannoun, K. I.; Tan, Y. C.; Fu, G. C.; Peters, J. C. *Chem. Sci.* **2016**, *7*, 4091.

13. Yayla, H. G.; Peng, F.; Mangion, I. K.; McLaughlin, M.; Campeau, L.-C.; Davies, I. W.; DiRocco, D. A.; Knowles, R. R. *Chem. Sci.* **2016**, *7*, 2066.

14. Higgins, R. F.; Fatur, S. M.; Shepard, S. G.; Stevenson, S. M.; Boston, D. J.; Ferreira, E. M.; Damrauer, N. H.; Rappé, A. K.; Shores, M. P. *J. Am. Chem. Soc.* **2016**, *138*, 5451.

15. Stevenson, S. M.; Shores, M. P.; Ferreira, E. M. *Angew. Chem. Int. Ed.* **2015**, *54*, 6506.

16. Corey, E. J.; Noe, M. C.; Sarshar, S. *J. Am. Chem. Soc.* **1993**, *115*, 3828.

17. Johnson, K. A.; Goody, R. S. *Biochemistry* **2011**, *50*, 8264.

18. Drago, R. S. *Physical methods for chemists.* 2nd edition; Saunders College publishing: Fort Worth, 1992.

19. La Mar, G. N.; Horrocks, W. D.; Holm, R. H. *NMR of paramagnetic molecules; principles and applications.* Academic Press: New York, 1973.

20. Cole, G. M.; Garrett, B. B. *Inorg. Chem.* **1970**, *9*, 1898.

21. Freitas, A. R.; Silva, M.; Ramos, M. L.; Justino, L. L. G.; Fonseca, S. M.; Barsan, M. M.; Brett, C. M. A.; Silva, M. R.; Burrows, H. D. *Dalton Trans.* **2015**, *44*, 11491.

22. Cantuel, M.; Bernardinelli, G.; Imbert, D.; Bünzli, J.-C. G.; Hopfgartner, G.; Piguet C. *J. Chem. Soc., Dalton Trans.* **2002**, 1929.

23. The equation used for the calculation of the association constant (K_{assoc}) is $K_{assoc} = \frac{[Cr\cdots substrate]}{[Cr][substrate]}$

24. Yang, Y.-M.; Liu, Q.; Zhang, L.; Yu, H.-Z.; Dang, Z.-M. *Organometallics* **2017**, *36*, 687.

25. Lu, J.-Z.; Khetrapal, N. S.; Johnson, J. A.; Zeng, X. C.; Zhang, J. *J. Am. Chem. Soc.* **2016**, *138*, 15805.

26. McDaniel, A. M.; Tseng, H.-W.; Damrauer, N. H.; Shores, M. P. *Inorg. Chem.* **2010**, *49*, 7981.

27. Babu, E.; Mareeswaran, P. M.; Singravadivel, S.; Bhuvaneswari, J.; Rajagopal, S. *Spectrochim. Acta A* **2014**, *130*, 553.

28. Mudasir A.; Yoshioka, N.; Inoue, H. *J. Coord. Chem.* **2001**, *52*, 333.

29. Shah, D. M.; Davies, K. M.; Hussam, A. *Langmuir* **1997**, *13*, 4729.

30. Holland, P. L. *Acc. Chem. Res.* **2015**, *48*, 1696.

31. Studer, A.; Curran, D. P. *Nat. Chem.* **2014**, *6*, 765.

32. Chirik, P. J. *Angew. Chem. Int. Ed.* **2017**, *56*, 5170.

33. Le, C.; Wismer, M. K.; Shi, Z.-C.; Zhang, R.; Conway, D. V.; Li, G.; Vachal, P. Davies, I. W.; MacMillan, D. W. C. *ACS Central Sci.* **2017**, *3*, 647.

34. This number is reported as pseudo zeroth-order so that it can be easily compared to the rate constant of the overall reaction between *trans*-anethole and isoprene.

35. Lin, S. S.; Ischay, M. A.; Fry, C. G.; Yoon, T. P. *J. Am. Chem. Soc.* **2011**, *133*, 19350.

36. Yoon, T. P. *ACS Catal.* **2013**, *3*, 895.

Chapter 4: Effects of *cis/trans*-isomers of anethole into Cr-photoredox reactivity

4.1 Introduction

The field of homogeneous photocatalysis continues to expand with reports of novel transformations occurring at a rapid rate.[1-4] Unfortunately, mechanistic exploration of these photocatalytic reactions remains an underexplored facet of this rich area of research. A main focus of examples of such studies has been to probe the nature of radical propagation pathways or catalyst-centric property based studies;[5-8] as of yet, however, few reports have focused on understanding the intrinsic roles of organic substrates in these reactions. Further, while product mixtures can sometimes contain stereoisomeric mixtures, the origin of stereodivergence of these processes has not been comprehensively investigated.[9-12] While mechanistic rationale for the formation of diverse product mixtures has been thoroughly explored within the context of electron transfer catalysis,[13-18] stereoconvergent (or divergent) mechanisms could potentially change upon inclusion of light, which can induce bond rotation and/or rearrangement. Photon energy has been applied as a dial that chemists tune regularly, imparting reactivity that can be modified using a specific wavelength of light.[19-22] For instance, Wiest and Lewis have used both DFT methods and quenching studies toward determine stereoconvergent effects with regard to organic photosensitizers,[23-25] and while these studies have provided excellent insight into these types of reactions, additional studies to help determine intrinsic reaction characteristics including electrochemistry, kinetics and synthetic studies are useful to advance our overall understanding of these processes.[6, 26]

One variable in photochemical reactions that has been overlooked in recent years is light flux. While wavelength tuning is fairly straightforward in practice, the modulation of light flux has not been exploited in the same way with the exception of some actinometry experiments.[5-7, 27] For the most part actinometry experiments are only used to probe the existence of a radical chain in the reaction, but not other aspects of the mechanism. This is of importance because nominally,

photocatalytic reactions are often reported with unknown concentrations of the fundamental reactant, light. Analyses of this type would offer great insight into reaction pathways that rely on catalyst regeneration and re-excitation as opposed to radical propagation.

With these motivations, we aimed at investigating both light flux and stereoconvergence within our previously reported Cr-photocatalyzed Diels-Alder manifold. Specifically, the use of conjugated alkenes including styrenes, gives a straightforward platform with which to investigate the effect of light flux in photocatalytic reactions.[28-31] Additionally, *E* and *Z* alkene isomers can be synthesized independently, which allows stereoconvergence to be studied simultaneously with light flux. Thus, presented herein are the combined synthetic, computational and photophysical characterization of the stereoconvergence in the [4+2] reaction between anethole and competent dienes.

4.2 Division of Labor

All kinetic and spectroscopic studies were performed by Robert F. Higgins. All catalysis studies were performed by Susan M. Stevenson (University of Georgia). All quenching and ultrafast studies were performed by Steven M. Fatur (University of Colorado-Boulder). Interpretation and analysis of the experimental data was performed by Robert F. Higgins, Susan M. Stevenson, Steven M. Fatur, Niels H. Damrauer, Eric M. Ferreira, Anthony K. Rappé and Matthew P. Shores.

4.3 Experimental

4.3.1 Preparation of compounds

The compounds $[Cr(Ph_2phen)_3](BF_4)_3$[5] and *cis*-anethole[33] were synthesized according to known literature preparations. All other compounds and reagents were obtained commercially and used as received.

4.3.2 Reactivity studies

Reactions were performed in $MeNO_2$ with the dienophile (0.10 M), diene (3 equiv) and 1 mol% Cr-salt added with irradiation from a Kessil® A160WE TUNA BLUE LED source at the highest intensity and most blue (highest energy) setting ~3 inches from the vials. The measured temperature of the vials ranged from 30-32 °C over the course of the reaction. Dodecyl acetate (0.010 M) was added as an internal standard for all optimization and substrate scope experiments to acquire conversion percentages or NMR yields. NMR studies were performed on a Varian 400 MHz spectrometer.

4.3.3 Electrochemical studies

Electrochemical experiments were performed in 0.1 M solutions of Bu_4NPF_6 in $MeNO_2$ or MeCN in air. A blank was collected and then the analyte was added to the electrochemical cell, which was then sparged for a minimum of 10 minutes before any further data were collected. Cyclic voltammograms (CVs) and square-wave voltammograms (SWVs) were obtained with a CH Instruments potentiostat (Model 1230A or 660C) using a 0.25 mm glassy carbon disk working electrode, Ag^+/Ag reference electrode and a Pt wire counter electrode. Scans were collected at rates between 0.10 V s^{-1} and 10 V s^{-1} for CVs. Reported potentials are referenced to the $[Cp_2Fe]^+/[Cp_2Fe]$ (Fc^+/Fc, where Cp = cyclopentadienyl) redox couple, and were determined by adding ferrocene as an internal standard at the conclusion of each electrochemical experiment.

4.3.4 Kinetic and light flux experiments

Kinetic parameters were determined by monitoring the course of the reaction through ^1H NMR analysis until the reaction reached at least 80% completion. Standard reaction conditions were employed for these analyses with 0.1 molar equivalents of mesitylene added as an internal standard.[31] An NMR tube charged with all reagents was removed at discrete time intervals, the stir bar was removed and the tube was wrapped in felt to reduce ambient light irradiation and transported to the spectrometer. The NMR spectra were collected with a longer-than-normal relaxation delay (t_1 = 5 seconds) to ensure that paramagnetic signals from the Cr-catalyst did not

interfere with the acquisition of the spectra. The experiments controlling light flux were performed using a Newport TLS-300XU tunable light source, which includes a 300 W Xe arc lamp, a Cornerstone 130 monochromator and a motorized filter. Variable wattages (100-300 W) were used and the sample was irradiated for 16 hours for each experiment. The specific wattages used for these experiments were 200, 250, 270, 285 and 300 W. NOTE: Photon flux and wattage of these lasers do not provide a linear relationship, so multiple wattages are necessary even if they are concentrated in one regime, to obtain photon fluxes across a useful range. The flux of the laser at each wattage was determined using standard actinometry studies with $K_3[Fe(ox)_3]$.[32]

4.3.5 Quenching experiments

Samples of the photocatalyst dissolved in 3.0 mL of nitromethane were prepared in 1 cm × 1 cm quartz cuvettes with an absorbance of ~0.1 at the excitation wavelength, 450 nm. For oxygen-free conditions, samples were prepared in a dinitrogen-filled glovebox and sealed in a cuvette equipped with a Kontes HI-VAC valve. Addition of a known volume of a stock solution of the quencher dissolved in nitromethane was used to achieve the desired concentration. For time-resolved photoluminescence experiments, a pulsed Nd:YAG laser (Continuum Surelite II) with a 10 Hz repetition rate, ~5 ns pulse width, and centered at 355 nm was used to pump a Continuum Surelite optical parametric oscillator to obtain other excitation colors and the power was attenuated as needed using neutral density filters. Following excitation with the unfocused 450 nm beam, emission was collected at a right angle and measured through a ~15 nm bandpass filter centered at 750 nm (chromium complexes) or 600 nm (ruthenium complexes) using a Hamamatsu H9305-02 photomultiplier tube (PMT) operating at – 900 Vdc. The PMT response was recorded using a LeCroy 9384L Oscilloscope and averaged over 1000 scans. We confirmed that the measured signal was linear in the power range of our experiments. The resulting data were fit using Igor Pro 6.37 (WaveMetrics) and a single exponential decay function. For static emission experiments, a xenon arc lamp was used in conjunction with an Olis SLM 8000C

spectrofluorometer. Quenching rate constants were obtained from the measured emission intensity or τ values using the Stern-Volmer equation.

4.4 Results and Discussion

4.4.1 Catalysis studies

We have previously shown that electron-rich alkenes such as *trans*-anethole can participate in [4+2] cycloadditions with dienes when promoted by $[Cr(Ph_2phen)_3]^{3+}$.[5, 31] These reactions resulted in the *anti*-product in all cases; however, when *Z*-alkenes such as *cis*-anethole are used, once again only the *anti*-product is obtained with no evidence of the *syn*-product (Figure 4.4.1). Additionally, the reaction appears to slow over time (50, 66 and 75% conversion over 24, 46 and 120 hours respectively) while isomerization continues at a constant rate. While the *cis* adduct does isomerize to the *trans*-species (Figure 4.4.2), albeit slower than the rate of formation of product, this reaction is much slower when subjecting *cis*-anethole to the reaction conditions. Because isomerization could occur before photo-oxidation (of anethole) or during the cycloaddition steps, we studied the isomerization effects.

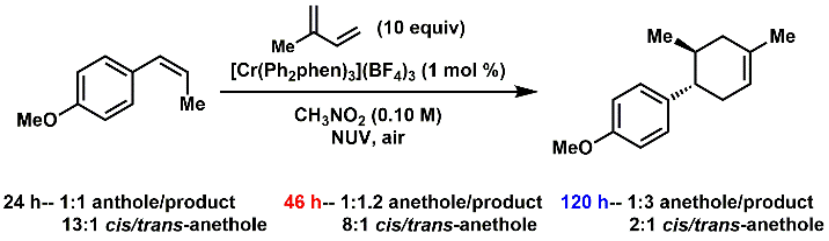
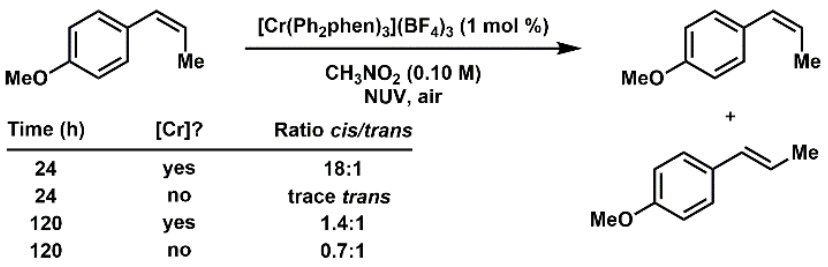


Figure 4.4.1

To quantify the catalyst effect on the isomerization of *cis*-anethole, reaction conditions are mimicked excluding the diene coupling partner (Figure 4.4.2). At first, it appears that *cis* to *trans* isomerization is slow with almost no isomerization observed in the first 24 h. After 120 hours, however, $[Cr(Ph_2phen)_3]^{3+}$ has isomerized *cis*-anethole to a lesser extent (1.4:1 *cis*:*trans*)

compared to catalyst-free isomerization (0.7:1 *cis*:*trans*), indicating that the catalyst inhibits the isomerization of *cis*-anethole. This can be rationalized by considering that a reasonable fraction of higher energy light is absorbed by the catalyst, thus decreasing the rate of photoisomerization. Notably, when *trans*-anethole is subjected to the same irradiation conditions, no isomerization to the *cis* isomer is observed. The present results indicate that *cis*-anethole does not react under irradiation with $[Cr(Ph_2phen)_3]^{3+}$ but can isomerize to the *trans*-isomer and proceed to react.



Time (h)	[Cr]?	Ratio *cis/trans*
24	yes	18:1
24	no	trace *trans*
120	yes	1.4:1
120	no	0.7:1

Figure 4.4.2

Yoon and others observed only *anti*-products whether *cis*- or *trans*-anethole was used as a cyclization partner in a [3+2] reaction with oxidized phenols.[33] Further, previous reports by Bauld concerning alkene isomerization facilitated by triarylamminiums, which do not require light to proceed, offer alternative hypotheses since *syn*-products have been observed in [4+2] cycloadditions.[17, 34-35] For the sake of comparison, we subjected our substrates to Bauld's catalyst system (Figure 4.4.3). C*is*-anethole shows a 17% isomerization from *cis*- to *trans*-anethole (5:1 ratio) after 5 minutes; this increased isomerization rate is unsurprising given that Bauld reports that reactions with electron-rich alkenes and the triarylamminium initiators show full consumption of starting material in under 5 minutes at decreased temperature. While Bauld has shown reactivity with several different alkenes,[36-37] a [4+2] reaction between *cis*-anethole and isoprene was never been reported with triarylamminiums, so we attempted the reaction using only this isomer, according to his standard reaction conditions. As with $[Cr(Ph_2phen)_3]^{3+}$, we observe only

the *anti*-product, with 10% *cis*-anethole (and no *trans*-anethole) remaining after 5 minutes. These results indicate that the cyclization step and subsequent transformations, which are too fast to characterize, remain consistent when $[Cr(Ph_2phen)_3]^{3+}$ or triarylamminiums are used as electron-transfer reagents.

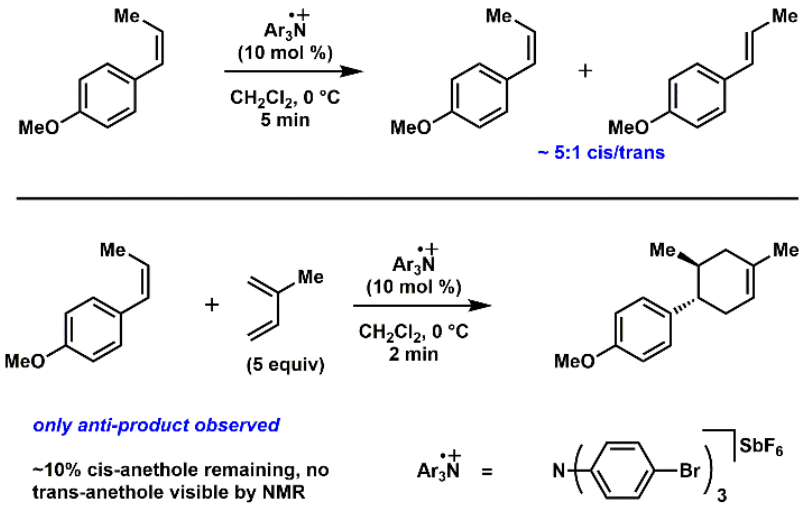


Figure 4.4.3

Overall, these preliminary studies indicate that while alkene isomerization occurs prior to oxidation of the electron-rich alkene when $[Cr(Ph_2phen)_3]^{3+}$ is utilized, isomerization alone is not fast enough to give the *anti*-product as a singly formed isomer, leaving three main scenarios giving rise to the observed stereoconvergence: (1) C*is*-anethole is not thermodynamically oxidizable by the catalyst, which could be probed *via* electrochemistry. (2) If *cis*-anethole is able to be oxidized by the catalyst, this process is not kinetically viable, which could be investigated through quenching studies. (3) The isomerization rate accounts for only a part of the observed stereoconvergence and subsequent cycloaddition steps also contribute to the observed stereoconvergence.

4.4.2 Electrochemical studies

Many studies concerning the redox properties of alkene isomers have mainly focused on synthetic utility[38] and reactivity after oxidation.[39-40] There has also been a direct study relating the electrochemical potential ($E_{1/2}$) differences between alkene isomers and their reactivity in catalysis, specifically epoxidation.[41] Electrochemical data which concern the catalyst $[Cr(Ph_2phen)_3]^{3+}$ and its interaction with substrates have been collected previously,[5] so attention was focused toward the properties of the substrates (Table 4.4.1). The data collected show nearly identical values for the oxidation of either *cis/trans*-anethole (entries 1 and 5). Once again, the inclusion of oxygen in the experiment gives rise to a cathodic shift of 200 mV in onset potential for *cis*-anethole in nitromethane (entry 2). Importantly, $[Cr(Ph_2phen)_3]^{3+}$ ($E^{3+*/2+}$ = +0.98 V vs. Fc^+/Fc) used in these studies is able to oxidize both of these compounds, indicating that *cis* to *trans* isomerization is not required for the reaction to proceed forward thermodynamically. Finally, with consideration of reaction conditions, the *trans* isomer is actually slightly easier to oxidize by 20 mV (entries 2 and 6).

Table 4.4.1. Comparative reduction potentials of cis- and trans-anethole.

entry	anethole (conditions)	$E_{1/2}$ (V)	$M^{\bullet+/0}$	E^o_{ox} (V)	$M^{\bullet+/0}$
1	*trans* (CH_3NO_2)[a]	+0.78		+0.48	
2	*trans* (CH_3NO_2, O_2)	+1.00		+0.57	
3	*trans* (CH_3CN)	+1.07		+0.75	
4	*trans* (CH_3CN, O_2)	+0.86		+0.77	
5	*cis* (CH_3NO_2)	+0.89		+0.79	
6	*cis* (CH_3NO_2, O_2)	+0.97		+0.59	
7	*cis* (CH_3CN)	+0.89		+0.68	
8	*cis* (CH_3CN, O_2)	+0.92		+0.74	

All potentials are reported vs. Fc^+/Fc in 0.1 M Bu_4NPF_6 solutions of the designated solvent. All experiments were performed at 100 mV/s scan rates for CVs or 4 mV increments for SWVs. [a]Potentials for *trans*-anethole are reported from ref 5.

4.4.3 Photophysical Studies

The quenching of the ^2E excited state emission (~750 nm) of $[Cr(Ph_2phen)_3]^{3+}$ by *cis*- and *trans*-anethole is also explored (Figure 4.4.4). While *cis*-anethole is not as effective at quenching

the excited state of $[Cr(Ph_2phen)_3]^{3+}$ as the *trans* isomer, it still quenches at a sufficient rate to efficiently perform electron transfer. The calculated quenching rate constants (k_q) are 9.5 and 2.6 × 10^8 M^{-1} s^{-1} for *trans*- and *cis*-anethole, respectively. These values are measured in air as the presence of oxygen is required for the reaction to proceed. Notably, quenching studies with isoprene show no change in the excited-state lifetime of $[Cr(Ph_2phen)_3]^{3+}$, suggesting that there is no interaction between the diene and the excited state of the catalyst. The nearly fourfold increase in quenching ability of *trans*-anethole compared to the *cis* isomer suggests that an interaction between *trans*-anethole and the catalyst provides a more kinetically favorable reaction pathway. Therefore, the small concentration of *trans*-anethole present in solution would react faster with $[Cr(Ph_2phen)_3]^{3+}$ than the *cis* analog.

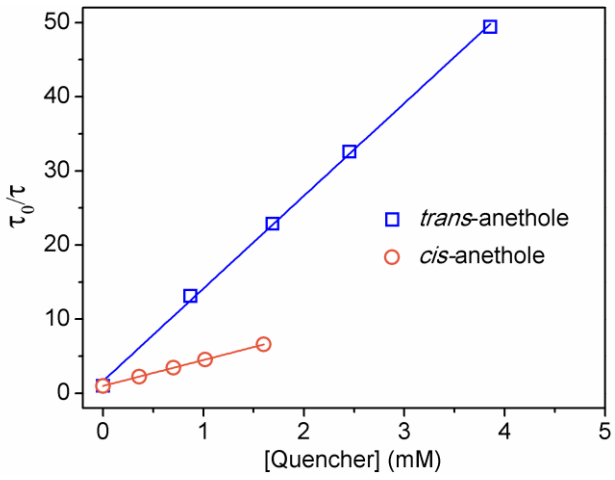


Figure 4.4.4. Oxygen dependence of the emission quenching of $[Cr(Ph_2phen)_3]^{3+}$ by trans- (blue trace) and cis-anethole (orange trace) in CH_3NO_2 at 23 °C fit to a linear function using least-squares methodology.

4.4.4 Kinetics Studies

To help glean further mechanistic information, initial rate kinetic dara are gathered for the photochemical reaction of isoprene with *cis*-anethole (Table 4.4.2). To establish a grasp on easily

tunable components, the concentrations of anethole, isoprene and catalyst are altered. Surprisingly, each of these reactants are found to be zeroth order overall (entries 1 and 3), which is an uncommon result. These results are uncommon especially considering other kinetic analyses of electron-transfer reactions.[14-15] To elucidate subtle effects, more advanced kinetic studies such as Blackmond kinetic analyses would have to be employed,[42] which is outside the scope of this study. Further, the rate constants for the cycloaddition reaction between *trans*- or *cis*-anethole and isoprene are nearly identical, which was unexpected (Table 4.4.2, entry 1). This was difficult at first to rationalize considering the longer reaction times required when *cis*-anethole are employed in catalysis studies with $[Cr(Ph_2phen)_3]^{3+}$.

To help explain this, a rate constant for the isomerization of *cis*-anethole to the *trans* isomer under identical conditions is collected. These data imply that a first order approximation is appropriate, which is expected for alkene isomerization. We observe that the isomerization had a rate constant comparable to the rate constant of the reaction, after correcting for concentration (Table 4.4.2, entries 1 and 2), indicating that the rate limiting step in the reaction of *cis*-anethole with isoprene is most likely isomerization to the *trans*-species.

Table 4.4.2. Rate constants for several processes cis- and trans-anethole can undergo during reaction conditions.

entry	conditions	*trans*-anethole	*cis*-anethole
1	isoprene	4.07×10^{-6} M s^{-1}	4.74×10^{-6} M s^{-1}
2	isomerization	N/A	4.02×10^{-5} s^{-1}
3	decomposition	5.75×10^{-7} M s^{-1}	N/A
4	light	3.85×10^{-6} s^{-1}	3.48×10^{-6} s^{-1}

The decomposition of *trans*-anethole was also monitored both in the presence of the catalyst and absence of $[Cr(Ph_2phen)_3]^{3+}$. No quantifiable amount of *trans*-anethole decomposes within eight hours of irradiation without $[Cr(Ph_2phen)_3]^{3+}$ present, which is the amount of time needed for the cycloaddition reaction with isoprene to go to ~80% completion considering our our

other kinetic results (Table 4.4.2, entry 1). When $[Cr(Ph_2phen)_3]^{3+}$ is present, appreciable decomposition of *trans*-anethole is observed, which we present as a zeroth order approximation to give a direct comparison to the cycloaddition reaction (Table 4.4.2, entry 3). As this is a fairly fast decomposition pathway, it gives a reasonable explanation of the lower yields obtained from this reactivity compared to a similar system published by Yoon and others.[30] In that study, the reaction times are much shorter and therefore the forward reaction should proceed with less decomposition of the substrate(s).[30]

Since we observe that rates are dependent on the light sources used to irradiate the reaction; therefore, it is likely that photon flux has a dramatic effect on this reactivity. While this phenomenon has been observed in productive heterogeneous photocatalytic reactions,[43-47] to the best of our knowledge, light involvement in a rate law has not been observed for a homogeneous photoredox catalytic reaction. This is likely due to the difficult nature of quantifying a concentration of light as well as the variable emission and reaction quantum yields, which all complicate mechanistic implications.[27] With these concepts in mind, kinetic data are collected with consideration of the concentration of light for the cyclization of isoprene with both *trans*- and *cis*-anethole (Figure 4.4.5). We found that light exhibits a first order dependence on the rate in our system for both *cis*- and *trans*-anethole. Interestingly, the rate constants indicate determined here indicate that *trans*-anethole reacts *slower* than *cis*-anethole when a known photon flux is applied. These data are quite complicated and their full scope and implications are still being investigated in our laboratories. Synthesis of a faster reacting (more electron-rich) alkene, such as *cis*-3,4-dimethoxy-*β*-methylstyrene, to these reaction conditions and determine the *syn/anti*-ratio of the products. This could help indicate the rate to which isomerization occurs at the different elementary steps of this reaction sequence.

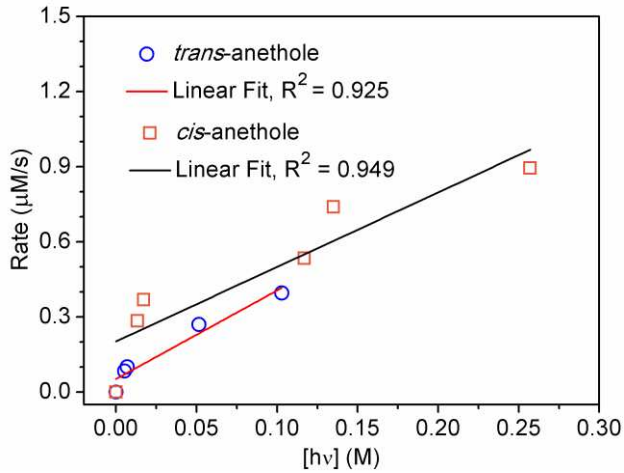


Figure 4.4.5. The effect of concentration of light on the production of product.

4.5 Conclusions

In all, we report investigations of stereoconvergence for a Cr-photocatalyzed Diels-Alder reaction. Our findings include catalysis studies which indicate the formation of the *anti*-product whether an *E* or *Z* isomer are subjected to reaction conditions. Electrochemical and photophysical studies corroborate that both substrates are thermodynamically oxidizable and quench the excited state of the catalyst, respectively. Kinetic studies indicate the inclusion of light into the rate law, which is not a commonly observed phenomenon in homogenous photocatalysis. The present work may allow for broad generalization of uncommon stereochemical findings in photocatalysis while also expanding on kinetic models of photocatalytic reactions.

References

1. Prier, C. K.; Rankic, D. A.; MacMillan, D. W. C. *Chem. Rev.* **2013**, *113*, 5322.

2. Poplata, S.; Tröster, A.; Zou, Y.-Q.; Bach, T. *Chem. Rev.* **2016**, *116*, 9748.

3. Skubi, K. L.; Blum, T. R.; Yoon, T. P. *Chem. Rev.* **2016**, *116*, 10035.

4. Kärkäs, M. D.; Porco, J. A.; Stephenson, C. R. J. *Chem. Rev.* **2016**, *116*, 9638.

5. Higgins, R. F.; Fatur, S. M.; Shepard, S. G.; Stevenson, S. M.; Boston, D. J.; Ferreira, E. M.; Damrauer, N. H.; Rappé, A. K.; Shores, M. P. *J. Am. Chem. Soc.* **2016**, *138*, 5451.

6. Yayla, H. G.; Peng, F.; Mangio, I. K.; McLaughlin, M. M.; Campeau, L.-C.; Davies, I. W.; DiRocco, D. A.; Knowles, R. R. *Chem. Sci.* **2016**, *7*, 2066.

7. Johnson, M. W.; Hannoun, K. I.; Tan, Y.; Fu, G. C.; Peters, J. C. *Chem. Sci.* **2016**, *7*, 4091.

8. Kärkäs, M. D.; Matsuura, B. S.; Stephenson, C. R. J. *Science* **2015**, *349*, 1285.

9. Amador, A. G.; Sherbrook, E. M.; Yoon, T. P. *J. Am. Chem. Soc.* **2016**, *138*, 4722.

10. Cavanaugh, C. L.; Nicewicz, D. A. *Org. Lett.* **2015**, *17*, 6082.

11. Grandjean, J. M. M.; Nicewicz, D. A. *Angew. Chem. Int. Ed.* **2013** *52*, 3967.

12. Yoshioka, E.; Kohtani, S.; Tanaka, E.; Hata, Y.; Miyabe, H. *Tetrahedron* **2015**, *71*, 773.

13. Reynolds, D. W.; Lorenz, K. T.; Chiou, H. S.; Bellville, D. J.; Pabon, R. A.; Bauld, N. L. *J. Am. Chem. Soc.* **1987**, *109*, 4960.

14. Lorenz, K. T.; Bauld, N. L. *J. Am. Chem. Soc.* **1987**, *109*, 1157.

15. Kim, T.; Pye, R. J.; Bauld, N. L. *J. Am. Chem. Soc.* **1990**, *112*, 6285.

16. Haberl, U.; Wiest, O.; Steckhan, E. *J. Am. Chem. Soc.* **1999**, *121*, 6730.

17. Bauld, N. L.; Gao, D. X. *J. Chem. Soc. Perkin Trans. 2* **2000**, *5*, 931.

18. Rehbein, J.; Carpenter, B. K. *Phys. Chem. Chem. Phys.* **2011**, *13*, 20906.

19. Schuster, D. I.; Lem, G.; Kaprinidis, N. A. *Chem. Rev.* **1993**, *93*, 3.

20. Muller, F.; Mattay, J. *Chem. Rev.* **1993**, *93*, 99.

21. Schultz, D. M.; Yoon, T. P. *Science* **2014**, *343*, 985.

22. Hoffmann, N. *Chem. Rev.* **2008**, *108*, 1052.

23. Sevov, C. S.; Wiest, O. *J. Org. Chem.* **2008**, *73*, 7909.

24. Saettel, N. J.; Wiest, O.; Singleton, D. A.; Meyer, M. P. *J. Am. Chem. Soc.* **2002**, *124*, 11552.

25. Lewis, F. D.; Kojima, M. *J. Am. Chem. Soc.* **1988**, *110*, 8664.

26. Devery, J. J.; Douglas, J. J.; Nguyen, J. D.; Cole, K. P.; Flowers, R. A.; Stephenson, C. R. J. *Chem. Sci.* **2015**, *6*, 537.

27. Cismesia, M. A.; Yoon, T. P. *Chem. Sci.* **2015**, *6*, 5426.

28. Riener, M.; Nicewicz, D. A. *Chem. Sci.* **2013**, *4*, 2625.

29. Ischay, M. A.; Ament, M. S.; Yoon, T. P. *Chem. Sci.* **2012**, *3*, 2807.

30. Lin, S.-S.; Ischay, M. A.; Fry, C. G.; Yoon, T. P. *J. Am. Chem. Soc.* **2011**, *133*, 19350.

31. Stevenson, S. M.; Shores, M. P.; Ferreira, E. M. *Angew. Chem. Int. Ed.* **2015**, *54*, 6506.

32. Montalti, M.; Murov, S. L. *Handbook of photochemistry*. 3rd ed.; CRC/Taylor & Francis: Boca Raton, **2006**.

33. Blum, T. R.; Zhu, Y.; Nordeen, S. A.; Yoon, T. P. *Angew. Chem. Int. Ed.* **2014**, *53*, 11056.

34. Bauld, N. L.; Pabon, R. *J. Am. Chem. Soc.* **1983**, *105*, 633.

35. Pabon, R. A.; Bauld, N. L. *J. Am. Chem. Soc.* **1984**, *106*, 1145.

36. Bauld, N. L.; Bellville, D. J.; Harirchian, B.; Lorenz, K. T.; Pabon, R. A.; Reynolds, D. W.; Wirth, D.; Chiou, H. S.; Marsh, B. K. *Acc. Chem. Res.* **1987**, *20*, 371.

37. Bauld, N. L. *Tetrahedron* **1989**, *45*, 5307.

38. Arata, M.; Miura, T.; Chiba, K. *Org. Lett.* **2007**, *9*, 4347.

39. Doherty, A. P.; Scott, K. *J. Electroanal. Chem.* **2004**, *442*, 35.

40. Kraiya, C.; Singh, P.; Todres, A. V.; Evans, D. H. *J. Electroanal. Chem.* **2004**, *563*, 171.

41. He, G. X.; Mei, H. Y.; Bruice, T. C. *J. Am. Chem. Soc.* **1991**, *113*, 5644.

42. Blackmond, D. G. *Angew. Chem. Int. Ed.* **2005**, *44*, 4302.

43. Inel, Y.; Okte, A. N. *J. Photochem. Photobio. A* **1996**, *96*, 175.

44. Okte, A. N.; Resat, M. S.; Inel, Y. *J. Photochem. Photobio. A* **2000**, *134*, 59.

45. Villarreal, T. L.; Gomez, R.; Gonzalez, M.; Salvador, P. *J. Phys. Chem. B* **2004**, *108*, 20278.

46. Montoya, J. F.; Velasquez, J. A.; Salvador, P. *Appl. Catal. B-Environ.* **2009**, *88*, 50.

47. Montoya, J. F.; Atitar, M. F.; Bahnemann, D. W.; Peral, J.; Salvador, P. *J. Phys. Chem. C* **2014**, *118*, 14276.

Chapter 5: Detection of an energy transfer pathway in Cr-photocatalysis.*

5.1 Introduction

Radical cation pericyclic reactions offer dramatic rate accelerations relative to thermal Diels-Alder reactions, and have been exploited in a variety of transformations.[1-3] Notwithstanding, the incredibly fast reaction rates obligate the use of lower temperatures where yields can suffer, potentially limiting synthetic utility for more structurally complex substrates. Recent developments in photoredox catalysis have reinvigorated pericyclic reactions as well as other radical-mediated processes.[4-5] A key feature of photoredox reactivity is increased control in the generation of reactive (radical) intermediates, allowing detailed characterization of variable mechanisms for pericyclic and related reactions.[6-12]

Classically, pericyclic reactions have been described as concerted processes; however, electron transfer processes, such as radical cation Diels-Alder (RCDA) cycloadditions and vinylcyclobutane (VCB) rearrangements, represent a well-known class of reactivity. Conversely, the energy transfer process of triplet sensitization has been used to prepare cyclobutanes.[13] For example, the excited-state of 4-methoxychalcone (**5.1**) is quenched by isoprene (**5.2**), $k_q = 1.5 \times 10^8$ $M^{-1}s^{-1}$, to produce a VCB species.[14] Photoredox catalysis often proceeds *via* electron transfer; however, excited-state energy transfer has recently been implicated in select examples.[15-17]

To the extent that regioselectivity manifests in pericyclic reactions, it is thought to derive from preferential stabilization of particular one-bond intermediates, either from inductive cation (tertiary compared to secondary) or resonance radical (allylic/benzylic) stabilization.[18] All three of

---

*Reproduced with permission from *ACS Catalysis*, submitted for publication. Unpublished work copyright 2018 American Chemical Society. This chapter is up to date as of 7/6/18.

these pathways – RCDA, VCB rearrangement and energy transfer – likely share a critical one-bond intermediate. Computational studies on small model systems include all three general pathways,[19-23] where electron transfer pathways have been more heavily studied.

Relevant to this regioselectivity discussion, some of us recently reported that the cycloaddition of **5.1** and **5.2** produces cyclohexene products (**5.3**, Figure 5.4.1) with *>10:1* regioselectivity when the chromium photosensitizer, $[Cr(Ph_2phen)_3]^{3+}$ (**5.4**, Ph_2phen = 4,7-diphenyl-1,10-phenanthroline) is employed.[24] This reaction, mediated by **5.4**, produces a different major isomer of the [4+2] product compared to thermal processes[25] or Lewis acid catalysis[26] performed on quite similar enones, which give isomer ratios of *2:3* and *1:99*, respectively. In our previous work, we identified several pathways by which the observed product could form, in alignment with prior efforts by Bauld and co-workers on all-organic non-light activated systems.[18, 27] Here, we show that in the photoredox realm, catalyst choice is critical in regioselectivity of these reactions, with significant mechanistic implications for enhanced structural control using a Cr-containing photocatalyst.

Considering that electrochemical data for *trans*-anethole indicates thermodynamic competence for a one electron oxidation by all Ru- and Cr-photosensitizers implicated in this study and 4-methoxychalcone is ***not*** thermodynamically oxidizable (*via* electrochemical experiments)[27] by any of these light-absorbing species, the mechanisms of these transformations might be different. Further, when $[Ru(bpz)_3]^{2+}$ is used for the [4+2] reaction between *trans*-anethole and isoprene, no *trans*-anethole remains after only 15 minutes,[12, 30] whereas starting material remains after 6 hours when using 4-methoxychalcone in place of *trans*-anethole.[27] Finally, there are no literature examples of oxidation reactions using 4-methoxychalone as a one-electron donor, giving increased motivation to determine how this electron-deficient substrate interacts with traditional electron-transfer reagents. Specifically, we hypothesize that these observations indicate that established electron-transfer (radical cation) reactivity observed when *trans*-anethole and photosensitizers are reacted is likely different (*e.g.*, energy transfer, triplet reactivity) when 4-

methoxychalcone is used. Finally, radical-cation reactivity with trans-anethole produces only one regioisomer of the product, whereas using 4-methoxychalcone gives mixtures of regioisomers. This further indicates a possible mechanistic divergence between these two reaction manifolds. Therefore, we present a mechanistic investigation on the mechanistic distinctions when electron-rich alkenes such as *trans*-anethole and electron-poor alkenes such as 4-methoxychalcone are used in photo(redox) reactions.

5.2 Division of Labor

All synthesis, in-situ monitoring of reactions, electrochemistry, spectroscopy and reaction quantum yields were performed by Robert F. Higgins. All time resolved spectroscopy was performed by Steven M. Fatur (Colorado University-Boulder). All computational methods were performed by Anthony K. Rappé. Analysis and interpretation of experimental and computational details was performed by Niels H. Damrauer, Eric M. Ferreira, Anthony K. Rappé and Matthew P. Shores.

5.3 Experimental

5.3.1 Preparation of compounds

The compounds $[Cr(Ph_2phen)_3](BF_4)_3$,[28] $[Cr(dmcbpy)_3](BF_4)_3$,[29] $[(CH_3CN)_4Cr(BF_4)_2]$[30] and (2-(4-methoxyphenyl)-3-methyl-3-vinylcyclobutyl)(phenyl)methanone[24] 1-methoxy-4-(2-nitrovinyl)benzene[31] and 4'-methoxy-4-methyl-2-nitro-1,2,3,6-tetrahydro-1,1'-biphenyl[24] were synthesized according to known literature preparations. All chromium compounds were prepared under inert conditions in a glovebox (MBRAUN Labmaster 130). 4-methoxychalcone was recrystallized twice from EtOH before use. All other compounds and reagents were obtained commercially and used as received. Irradiation of reactions was performed in an aluminum-foil lined box with a stirring plate with a 23 W compact fluorescent light (CFL) bulb (EcoSmart 23 W bright white CFL spiral light bulb, 1600 lumens). Ratios of the Diels-Alder isomers were determined through analyses of crude ^1H NMR spectra. All experiments were performed at room

temperature. Reactions performed under N_2 had a stream of N_2 bubbling through the solution for at least 15 minutes before sealing.

5.3.2 Preparation of novel metal complexes

General Procedure.

A solution of diimine ligand (3.1 equiv) in a 1:1 dichloromethane/acetonitrile mixture was added to $[(CH_3CN)_4Cr(BF_4)_2]$ (1 equiv) in acetonitrile. The reaction mixture was stirred for 1 hour, and then a solution of $AgBF_4$ (1 equiv) in acetonitrile was added. Over a period of 8 hours, the color slowly changed to orange and a gray precipitate (Ag metal) formed. The reaction mixture was filtered through Celite, to remove the Ag metal, and the filtrate was concentrated *in vacuo*. This filtrate was then taken up in a minimal amount of acetonitrile and diethyl ether (1:5 MeCN:Et_2O) was slowly added until a yellow suspension was observed. The yellow powder was then isolated by vacuum filtration and the precipitate was washed with Et_2O (3 × 5 mL).

$[Cr(bpy)_3](BF_4)_3$.

Prepared according to the General Procedure using bpy (2,2'-bipyridine) (126 mg, 0.807 mmol), $[(CH_3CN)_4Cr(BF_4)_2]$ (105 mg, 0.260 mmol) and $AgBF_4$ (52.5 mg, 0.260 mmol). The "*divalent*" Cr compound was maroon in color. The product was isolated as a yellow powder giving 104 mg (51% yield). UV-vis matches literature values for the OTf^- salt.[29] IR (ATR) $\nu_{C=N}$: 1605 cm^{-1}. ESI-MS(+) (CH_3CN): *m/z* 694.15 $(M - BF_4)^+$. Anal. Calcd. For $C_{30}H_{24}B_3F_{12}CrN_6$: C, 46.14; H, 3.10; N, 10.76. Found: C, 46.65; H, 2.83; N, 10.38.

$[Cr(phen)_3](BF_4)_3$.

Prepared according to the General Procedure using phen (1,10-phenanthroline) (49 mg, 0.269 mmol), $[(CH_3CN)_4Cr(BF_4)_2]$ (35 mg, 0.0898 mmol) and $AgBF_4$ (17.5 mg, 0.0898 mmol). The "*divalent*" Cr compound was green/brown in color. The product was isolated as a yellow powder giving 56 mg (72% yield). UV-vis matches literature values for the OTf^- salt.[29] IR (ATR) $\nu_{C=N}$: 1606 cm^{-1}. ESI-MS(+) (CH_3CN): *m/z* 772.20 $(M - BF_4)^+$. Anal. Calcd. For $C_{36}H_{30}B_3F_{12}CrN_6$: C, 50.33; H, 3.52; N, 9.78. Found: C, 50.50; H, 3.89; N, 9.41.

5.3.3. Mechanistic Measurements and Studies

Reaction quantum yields were determined by the method reported by Yoon and Cismesia.[12] Actinometry experiments were performed using a Newport TLS-300XU tunable light source, which includes a 300 W Xe arc lamp, a Cornerstone 130 monochromator and a motorized filter.

Samples of the photocatalyst dissolved in 3.0 mL of nitromethane were prepared in 1 cm × 1 cm quartz cuvettes with an absorbance of ~0.1 at the excitation wavelength, 450 nm. For oxygen-free conditions, samples were prepared in a dinitrogen-filled glovebox and sealed in a cuvette equipped with a Kontes HI-VAC valve. Addition of a known volume of a stock solution of the quencher dissolved in nitromethane was used to achieve the desired concentration. For time-resolved photoluminescence experiments, a pulsed Nd:YAG laser (Continuum Surelite II) with a 10 Hz repetition rate, ~5 ns pulse width, and centered at 355 nm was used to pump a Continuum Surelite optical parametric oscillator to obtain other excitation colors and the power was attenuated as needed using neutral density filters. Following excitation with the unfocused 450 nm beam, emission was collected at a right angle and measured through a ~15 nm bandpass filter centered at 750 nm (chromium complexes) or 600 nm (ruthenium complexes) using a Hamamatsu H9305-02 photomultiplier tube (PMT) operating at – 900 Vdc. The PMT response was recorded using a LeCroy 9384L Oscilloscope and averaged over 1000 scans. We confirmed that the measured signal was linear in the power range of our experiments. The resulting data were fit using Igor Pro 6.37 (WaveMetrics) and a single exponential decay function. For static emission experiments, a xenon arc lamp was used in conjunction with an Olis SLM 8000C spectrofluorometer. Quenching rate constants were obtained from the measured emission intensity or τ values using the Stern-Volmer equation.

5.3.4. Other Physical Measurements

Infrared spectra were measured with a Bruker Tensor II spectrometer with an ATR attachment using a diamond crystal. NMR studies were performed on a Varian 400 MHz spectrometer. Elemental analyses were performed by Robertson Microlit Laboratories, Inc. in Madison, NJ or Midwest Microlit in Indianapolis, IN. Absorption spectra were obtained with a Hewlett-Packard 8453 spectrometer in quartz cuvettes with a 1 cm path length. Electrochemical experiments were performed in 0.1 M solutions of Bu_4NPF_6 in CH_3NO_2. Cyclic voltammograms (CVs) were recorded with a CH Instruments potentiostat (Model 1230A or 660C) using a 0.25 mm Pt disk or 0.25 mm glassy carbon disk working electrode, Ag^+/Ag reference electrode and a Pt wire auxiliary electrode. Scans were collected at a rate of 100 mV/s. Reported potentials are referenced to the $[Cp_2Fe]^+/[Cp_2Fe]$ (Fc^+/Fc), where Cp = cyclopentadienyl, redox couple and were determined by adding ferrocene (which was sublimed before use) as an internal standard at the conclusion of each electrochemical experiment. Oxygenated experiments were performed by bubbling O_2 into the experimentation vessel for 10 seconds prior to data collection. To help eliminate electrode interactions with possible superoxide species present, the working electrode was polished before each set of experiments were performed. The surface of the working electrode was also cleaned with a Kimwipe before each scan to help provide a clean surface of the electrode.

5.3.5. Computational methods

Geometries, vibrational frequencies, ideal gas thermodynamic estimates, and total energies for the molecules included in Figure 5.4.2 were computed using the ωB97xd density functional,[32] a 6-311+g* basis,[33-34] a PCM continuum solvent,[35] and the g16 electronic structure package.[36] Single point DLPNO-CCSD(T)[37-40] computations utilized the cc-pvtz basis set,[41] a PCM continuum solvent[42] and the ORCA 4.01 electronic structure package.[43] Geometries and total energies for the molecules included in Figure 5.4.3 were computed using the APFD density

functional,[44] a 6-311+g* basis,[33] a PCM continuum solvent[35] and the g16 electronic structure package.[36]

5.4 Results and Discussion

For the reaction in Figure 5.4.1, **5.4** promotes significantly higher regioselectivity compared to several Ru- or Cr-containing photosensitizers with similar photooxidative properties, such as $[Ru(bpz)_3]^{2+}$ (bpz = 2,2'-bipyrazine) and $[Cr(dmcbpy)_3]^{3+}$ (dmcbpy = 4,4'-dimethylcarboxylate-2,2'-bipyridine). This interesting result challenges the standard understanding that the photosensitizers participate in collisional based (outer sphere) reactivity, which might be expected to yield similar product distributions. Note that long-lived excited-states of $[Cr(Ph_2phen)_3]^{3+}$ and $[Ru(bpz)_3]^{2+}$ are not thermodynamically capable of single electron transfer (SET) reactions with **5.1** under the reaction conditions,[24, 28-29, 45-47] suggesting other pathways are operative.

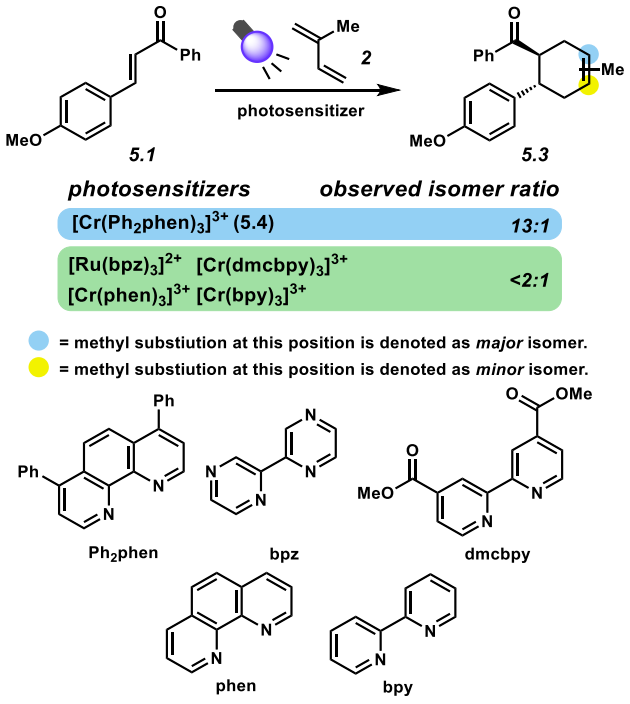


Figure 5.4.1. Regioselectivity of Diels Alder cycloaddition product formation with select Cr- and Ru-containing photosensitizers

In addition to the Diels-Alder product, a mixture of VCB species (**5.5**) are formed and consumed over the course of the reaction. Using ^{1}H NMR spectroscopy, we find that VCBs are formed slowly by direct irradiation in the absence of a photosensitizer, with low conversion, affording a mixture of VCB isomers (Figure 5.4.1). The addition of a metal photosensitizer influences the regioselectivity of the VCBs formed: as with the final product, we observe enhanced selectivity for **5.4** relative to other photosensitizers; notwithstanding, a stereochemical resolution pathway cannot be discounted. These results do not necessarily refute previously proposed routes to the final product **5.5**,[24] but do indicate the predominance of a single pathway for reactions with **5.4**, one that presumably differs from the other photosensitizers in a significant way.

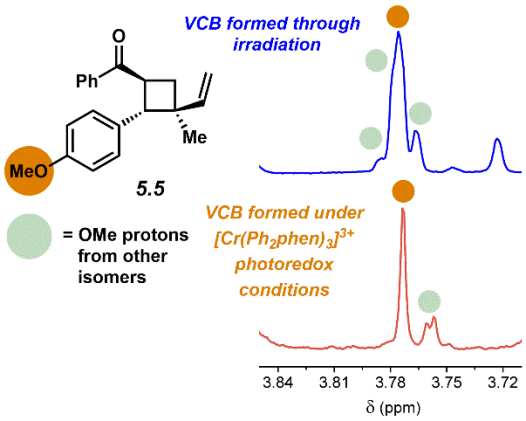


*Figure 5.4.1. ^{1}H NMR spectra showing isomeric distribution of VCB intermediates dependent on reaction conditions. Note: VCB **5.5** is drawn as the major isomer for clarity, but is present as a mixture of isomers, as described in ref. 24.*

Computational studies can expedite investigation of potential pathways in our reaction manifold. To account for possible catalyst-substrate interactions, we chose the ωB97xd functional because it incorporates range-separation needed for potential charge transfer character and an empirical dispersion term to describe van der Waals interactions found in π-interacting complexes. To show that it was appropriate for the **5.1** + **5.2** system, we first performed a

comparative ωB97xd/DLPNO-CCSD(T) study of a smaller ethylene + isoprene system, examining both radical cation and triplet excited state pathways (Figure A5.1). All methodological, energetic and structural results are collected in the supplementary material. Good agreement between the reaction surfaces, along with small impacts of ideal gas thermodynamic corrections, suggest that ωB97xd total energy differences offer an adequate representation of the energetics of the Diels Alder cycloadditions.

The reaction between **5.1** and **5.2** was modelled according to several pathways.[48] For the electron transfer pathway (top of Figure 5.4.2), [**5.5**]$^{+\bullet}$ is nearly degenerate with the one-bond intermediate radical cation [Int]$^{+\bullet}$, while formation of [**5.3**]$^{+\bullet}$ is exothermic. For the triplet pathway (middle of Figure 5.4.2), formation of either ^{3}[**5.5**] and ^{3}[**5.3**] is significantly endothermic, and entropic constriction would amplify this. As suggested previously,[21-23] intersystem crossing from ^{3}[Int] to ^{1}[Int] would lead to the formation of **5.3** and **5.5** (blue species in Figure 5.4.2). For ^{1}[Int], the broken symmetry $M_S = 0$ configuration is ~1 kcal mol^{-1} lower in energy than the triplet state. On the $M_S = 0$ surface (blue pathway, bottom of Figure 2), the barrier to closure for ^{1}[**5.5**] is 3.5 kcal mol^{-1}, while closure to ^{1}[**5.3**] has a barrier of 1.0 kcal mol^{-1}. Finally, the computed barrier for the thermal Diels-Alder of 23.3 kcal mol^{-1} relative to the singlet π-complex (bottom of Figure 5.4.2), is consistent with these reactions proceeding thermally only at quite elevated temperatures.

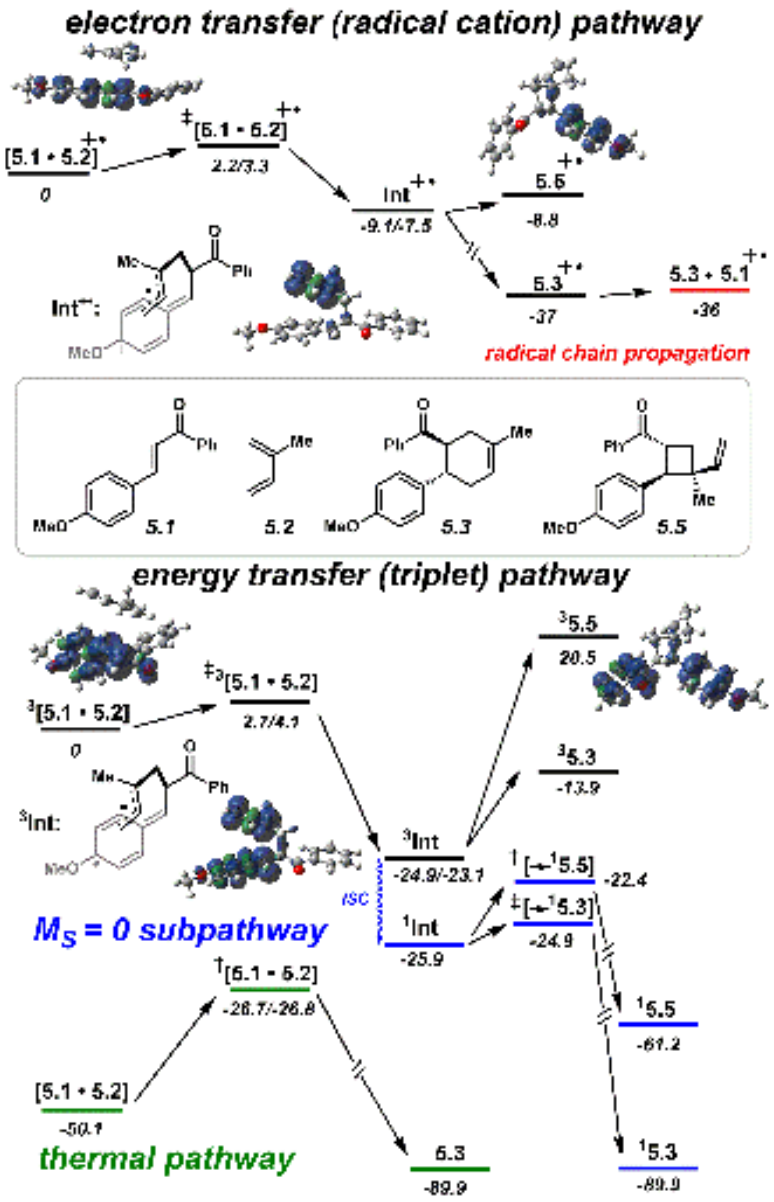


Figure 5.4.2. Computed reaction pathways for radical cation (top) and triplet-sensitized (middle) pathways for either [2+2] or [4+2] coupling reactions between 4-methoxychalcone and isoprene. The singlet (M_s = 0, blue) and thermal (bottom green) pathways are both on the same energy surface as the triplet pathway. Energies (in italics) are provided in kcal mol^{-1} relative to the ground state π complex for each pathway. States with two numbers correspond to the major/minor isomer energies as defined in Figure 5.4.1. Hash line breaks denote compression of the energy scale to fit on in the Figure. Spin-density plots are provided for select species:

*blue and green lobes indicate α and β spins, respectively. The thermal pathway is set to -50.1 kcal mol^{-1} which is the excitation energy for triplet enone **5.1**. (‡) denotes transition state.*

Several intriguing observations can be gleaned from the computations. First, if the electron transfer pathway involving **5.1** occurs and generates [**5.5**]$^{\bullet+}$, its cycloreversion to [Int]$^{\bullet+}$ is exothermic. Spin density in [**5.5**]$^{\bullet+}$ is mostly localized on the anisole moiety with only minor delocalization onto the adjacent C-C bond of the cyclobutane, consistent with dominant cleavage of this C-C bond during ring opening. Second, based on the computed energies, an energy transfer pathway is highly exothermic and therefore likely to proceed. Finally, the energy barriers to form either isomer of the product are quite similar, indicating that these energies alone do not explain the experimentally observed highly regioselective process. Unfortunately, the functional ωB97xd does not indicate an energetic preference for either of the isomers of the product. This indicates that for this reactivity sequence is likely divergent from previously studied cycloaddition reactions such as ethylene + isoprene (*vide supra*).

To address the differences in observed regioselectivity, computations using the benchmark DLPNO-CCSD(T) functional are performed. Interestingly, when ^{3}[**5.1**] is flat, the energy difference in the respective transition states for the major and minor products is only 0.7 kcal mol^{-1}, indicating little preference in product selectivity (Figure 5.4.3); however, when ^{3}[**5.1**] is twisted, a difference of 4.5 kcal mol^{-1} in the transition states is observed, with the transition state on the path to the major product lower in energy (Figure 5.4.3). Since little to no regioselectivity is expected if the transition state involves a flat configuration for enone **5.1**, a twisted configuration is expected when **5.4** is used. The minimal energy difference also helps explain why all other Cr- and Ru-photosensitizers provide small regioselectivities. The origin of the twisted transition state for enone **5.1** when **5.4** is used is explained in more detail in a following section (*vide infra*).

If the energy difference between the two twisted one-bond transition states, discussed above, is used to assess discrimination of product formation for enone **5.1**, then a nearly 2000:1 differentiation is expected.[36] Since selectivities this large are not observed *in vitro*, there are a couple of reasonable explanations: (1) photocatalyst **5.4** proceeds to initiate reactivity through both electron and energy transfer pathways where energy transfer imparts a significant role; (2) that there is geometric relaxation in the transition states when coordinated to the metal complex (*vide infra*) that reduces the energy differences in the transition states.[37] Notwithstanding, the energy difference points to why **5.4** potentially governs a selective reaction between enone **5.1** and diene **5.2**. We are currently investigating these effects further; however, these initial findings indicate that an energy-transfer mechanism is likely preferred when 4-methoxychalcone reacts with isoprene.

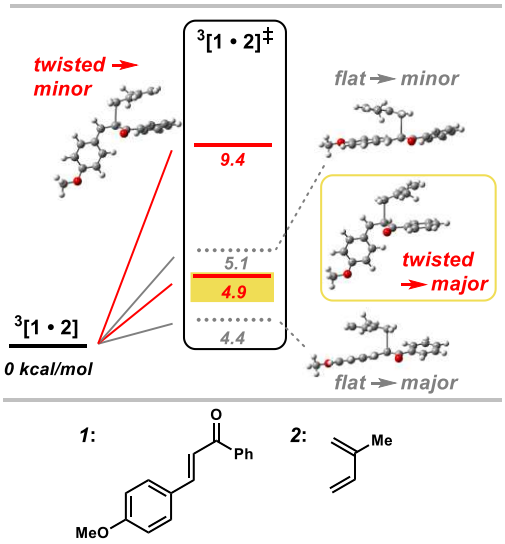


*Figure 5.4.3. Differences in the transition state energies for isoprene reacting with 4-methoxychlacone in a triplet manifold probed using the DLPNO-CCSD(T) functional. Major indicates insertion of diene **5.2** into enone **5.1** to form the isomer of the major product and minor indicates the same but for the minor isomer of the product.*[38]

To further discriminate between these mechanistic pathways, Stern-Volmer analysis are performed. Successive addition of **5.1** to a solution of **5.4** quenches the ^{2}E excited state of $[Cr(Ph_2phen)_3]^{3+}$, with a bimolecular quenching rate constant $k_q = 2 \times 10^6\ M^{-1}s^{-1}$ in both ambient and inert conditions (Figures 5.4.2, A5.1-2). This value is ~500× smaller than what was previously observed when using the more electron rich substrate *trans*-anethole.[28] On the other hand, enone **5.1** quenches the ^{2}E excited state of $[Cr(dmcbpy)_3]^{3+}$ with a much larger (~300×), $k_q = 6.0 \times 10^8\ M^{-1}s^{-1}$. As we have previously shown, this complex is 440 mV more potent as a photooxidant than $Cr(Ph_2phen)_3]^{3+}$,[29] and these results are consistent with collisional electron transfer from **5.1** to $[Cr(dmcbpy)_3]^{3+}$, likely beginning a radical cation sequence. Interestingly, $[Ru(bpz)_3]^{2+*}$ is also quenched by enone **5.1** with a large rate constant $k_q = 1.4 \times 10^8\ M^{-1}\ s^{-1}$. We highlight the observation that those metal complexes exhibiting a large k_q in the presence of **5.1** (*i.e.*, $[Cr(dmcbpy)_3]^{3+}$ and $[Ru(bpz)_3]^{2+}$) are also species exhibiting diminished regioselectivity compared to **5.4**.

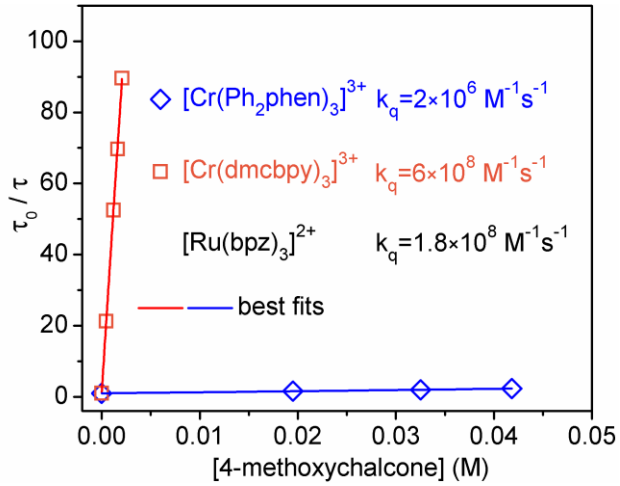


*Figure 5.4.2. Emission quenching of different sensitizers by **5.1** in $MeNO_2$.*

Whereas quantum of yield of reaction data are helpful in determining mechanisms in photoredox reactions,[12] obtaining such information for **5.1** + **5.2** is complicated by the fact that

excited-state enone **5.1** also reacts. Since VCB **5.5** shows higher energy absorption than enone **5.1** and no long-lived excited-state, it provides a reasonable handle for characterizing catalytic/initiated processes in this reaction Figure. When **5.4** is combined with VCB **5.5** and subjected to monochromatic 400 nm irradiation in CD_3NO_2, a quantum yield of reaction of Φ = 0.93 is observed.[24] The same reaction substituting $[Ru(bpz)_3]^{2+}$ for **5.4** gives a quantum yield of reaction of Φ = 7.8(8). The low quantum yield of emission value for $[Cr(dmcbpy)_3]^{3+}$ precludes its inclusion in analogous studies.[29] Related, quantum yield of reaction values for a VCB isolated in the combination of 1-methoxy-4-(2-nitrovinyl)benzene and isoprene,[49] are Φ = 0.10(2) and 1.96(16) using $[Cr(Ph_2phen)_3]^{3+}$ and $[Ru(bpz)_3]^{2+}$, respectively.[50] Although these data only represent the transformation of a VCB to a cyclohexene and not the overall reaction, they indicate divergent reactivity dependent solely on photosensitizer choice, and this result strongly suggests that $[Ru(bpz)_3]^{2+}$ promotes radical chain propagation, an electron transfer event, to some extent in this reaction manifold.[51]

To investigate the impact of a metal center on this reaction pathway, TD-DFT calculations of excited state energies for **5.4** are performed. Interestingly, the lowest energy quartet excited state of **5.4** is not metal-centered, but rather is best described as a ligand-centered triplet ($^3[Ph_2phen]$) antiferromagnetically coupled to a quartet metal center ($^4[Cr]^{3+}$) as part of a Heisenberg doublet/quartet/sextet spin ladder (Figure A5.3). Furthermore, when **5.1** is associated with $[Cr(Ph_2phen)_3]^{3+}$, the lowest energy TD-DFT-computed quartet excited state again consists of a triplet coupled to the quartet metal center (Figure A5.4), but now the triplet is localized mainly on the substrate (^{3}[**5.1**]) rather than the Ph_2phen ligand. This controlled organization of the triplet through association may allow the two unpaired electrons on ^{3}[**5.1**] to couple with the three electrons on the $^4[Cr]^{3+}$ center; this may impact both the rate of intersystem crossing and the cycloaddition regioselectivity, including the trajectory of **5.2** approaching **5.1**.

To compare these results to other substrates used in similar reactivity, computed vertical and adiabatic triplet excitation energies and ionization potentials for a series of dienes and dienophiles are computed and collected in Table A5.1. As expected, the ionization potentials for dienophiles that are not thermodynamically competent to undergo oxidative electron transfer, such as **5.1**, are computed to be substantially larger (~0.5 eV) than dienophiles, such as *trans*-anethole, that can be oxidized by **5.4*** (Figure 5.4.4, top).[28] On the other hand, dienophiles such as 4-methyoxychalcone have significantly smaller vertical triplet excitation energies than *trans*-anethole, making them more susceptible to triplet state reactivity, in agreement with the computational data shown in Figure 5.4.2.

Further, the computed vertical and adiabatic triplet excitation energies, ionization potentials and electron affinities for a series of nitrogenous base ligands allow for comparison of triplet state energies between the dienophiles and ligands such as Ph_2phen (Tables A5.2-3). The triplet state of Ph_2phen is significantly lower in energy than bpz and dmcbpy, consistent with a ligand triplet excited-state being favored for **5.4** when associated to **5.1** (Figure A5.3). Of note, since the quantum yield of the VCB rearrangement is $\Phi > 1$, electron transfer and radical cascade must be feasible when $[Ru(bpz)_3]^{2+}$ is used. Finally, when $[Cr(dmcbpy)_3]^{3+}$ is used, electron transfer is thermodynamically feasible, where the initiated radical cascade allows **5.2** to cyclize unrestrictedly, once again limiting regioselectivity.

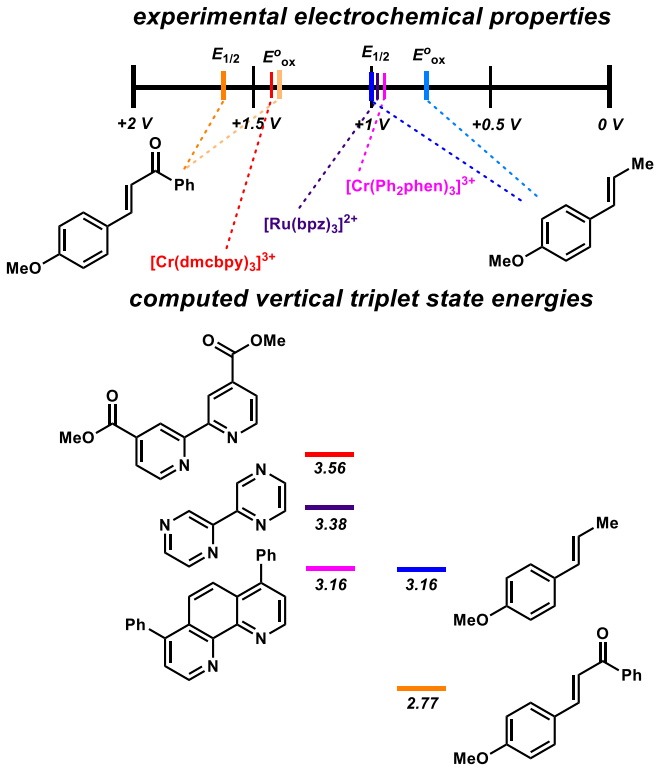


Figure 5.4.4. Top: electrochemical data for several dienophiles and photosensitizers (excited state redox potentials), all referenced to the Fc^{+}/Fc redox couple.[24, 28] The two values for the dienophiles indicate the half-wave ($E_{1/2}$, darker trace) and onset (E°_{ox}, lighter trace) potentials for each species. Bottom: triplet state energies (eV) for some dienophiles and ligands.

5.5 Conclusions

In conclusion, we present initial findings that implicate $[Cr(Ph_2phen)_3]^{3+}$ as a structural selectivity differentiator in the Diels-Alder reactivity of electron-poor alkenes and dienes. The combined results of reactivity, excited-state quenching and computational studies suggest that **5.4** singularly promotes a regioselective energy transfer pathway. Other related Cr- and Ru-photosensitizers apparently do not participate in this pathway, due to the accessibility of lower-energy electron transfer pathways, or possibly an inability to create appropriate photosensitizer-substrate assemblies. These results build upon our growing knowledge about orthogonal mechanistic pathways for photoredox reactions promoted by Ru and Cr photosensitizers.[12, 28]

Although experimental and computational efforts to understand details concerning the regioselectivity of these reactions are in progress, initial calculations suggest that **5.4** participates in an energy transfer pathway that proceeds through a substrate-catalyst [**5.1•5.4**] assembly, which would offer a new way to preferentially stabilize reactive intermediates in the assembly of structurally controlled C-C bond formation reactions.

References

1. Bell, F.A.; Crellin, R. A.; Fujii, H.; Ledwith, A. *J. Chem. Soc., Chem. Commun.* **1969**, 251-252.

2. Bell, F. A.; Ledwith, A.; Sherrington, D. C. *J. Chem. Soc., Chem. Commun.* 1969, 2719-2720.

3. Schutte, R.; Freeman, G. R. *J. Am. Chem. Soc.* **1969**, *91*, 3715-3720.

4. Nicewicz, D. A.; MacMillan, D. W. C. *Science* **2008**, *322*, 77-80.

5. Ischay, M. A.; Anzovino, M. E.; Du, J.; Yoon, T. P. *J. Am. Chem. Soc.* **2008**, *130*, 12886-12887.

6. Skubi, K. L.; Blum, T. R.; Yoon, T. P. *Chem. Rev.* **2016**, *116*, 10035-10074.

7. Romero, N.A.; Nicewicz, D. A. *Chem. Rev.* **2016**, *116*, 10075-10166.

8. Staveness, D.; Bosque, I.; Stephenson, C. R. J. *Acc. Chem. Res.* **2016**, *49*, 2295-2306.

9. Poplata, S.; Tröster, A.; Zou, Y.-Q.; Bach, T. *Chem. Rev.* **2016**, *116*, 9748-9815.

10. Shaw, M. H.; Twilton, J.; MacMillan, D. W. C. *J. Org. Chem.* **2016**, *81*, 6898-6926.

11. Studer, A.; Curran, D. P. *Angew. Chem.* **2016**, *128*, 58-102.; *Angew. Chem. Int. Ed.* **2016**, *55*, 58-102.

12. Cismesia, M. A.; Yoon, T. P. *Chem. Sci.* **2015**, *6*, 5426-5434.

13. Lewis, F. D.; Hirsch, R. H. *J. Am. Chem. Soc.* **1976**, *98*, 5914-5924.

14. Caldwell, R. A.; Singh, M. *J. Am. Chem. Soc.* **1983**, *105*, 5139-5140.

15. Welin, E. R.; Le, C.; Arias-Rotondo, D. M.; McCusker, J. K.; MacMillan, D. W. C. *Science* **2017**, *355*, 380-384.

16. Blum, T. R.; Miller, Z. D.; Bates, D. M.; Guzei, I. A.; Yoon, T. P. *Science* **2016**, *354*, 1391-1395.

17. Skubi, K. L.; Kidd, J. B.; Jung, H.; Guzei, I. A.; Baik, M.-H.; Yoon, T. P. *J. Am. Chem. Soc.* **2017**, *139*, 17186-17192.

18. Bauld, N. L. *Tetrahedron* **1989**, *45*, 5307-5363.

19. Hofmann, M.; Schaefer, H. F. *J. Am. Chem. Soc.* **1999**, *121*, 6719-6729.

20. Valley, N. A.; Wiest, O. *J. Org. Chem.* **2007**, *72*, 559-566.

21. Domingo, L. R.; Pérez-Prieto, J. *ChemPhysChem* **2006**, *7*, 614-618.

22. González-Béjar, M.; Stiriba, S.-E.; Domingo, L. R.; Pérez-Prieto, J.; Miranda, M. A. *J. Org. Chem.* **2006**, *71*, 6932-6941.

23. Ess, D. H.; Hayden, A. E.; Klärner, F.-G.; Houk, K. N. *J. Org. Chem.* **2008**, *73*, 7586-7592.

24. Stevenson, S. M.; Higgins, R. F.; Shores, M. P.; Ferreira, E. M. *Chem. Sci.* **2017**, *8*, 654-660.

25. Chee, C. F.; Abdullah, I.; Buckle, M. J. C.; Abd Rahman, N. *Tetrahedron Lett.* **2010**, *51*, 495-498.

26. Liu, Z.; Ganguly, R.; Vidović, D. *Dalton Trans.* **2017**, *46*, 753-759.

27. Reynolds, D. W.; Harirchian, B.; Chiou, H.-S.; Marsh, B. K.; Bauld, N. L. *J. Phys. Org. Chem.* **1989**, *2*, 57-88.

28. Higgins, R. F.; Fatur, S. M.; Shepard, S. G.; Stevenson, S. M.; Boston, D. J.; Ferreira, E. M.; Damrauer, N. H.; Rappé, A. K.; Shores, M. P. *J. Am. Chem. Soc.* **2016**, *138*, 5451-5464.

29. McDaniel, A. M.; Tseng, H.-W.; Damrauer, N. H.; Shores, M. P. *Inorg. Chem.* **2010**, *49*, 7981-7991.

30. Henriques, R. T.; Herdtweck, E.; Kühn, F. E.; Lopes, A. D.; Mink, J.; Romão, C. C. *J. Chem. Soc., Dalton Trans.* **1998**, 1293-1297.

31. Yang, H.; Fu, L.; Wei, L.; Liang, J.; Binks, B. P. *J. Am. Chem. Soc.* **2015**, *137*, 1362-1371.

32. Chai, J.-D.; Head-Gordon, M. *Phys. Chem. Chem. Phys.* **2008**, *10*, 6615-6620.

33. Krishnan, R.; Binkley, J. S.; Seeger, R.; Pople, J. A. *J. Chem. Phys.* **1980**, *72*, 650-654.

34. Hay, P. J. *J. Chem. Phys.* **1977**, *66*, 4377-4384.

35. Tomasi, J.; Mennucci, B.; Cammi, R. *Chem. Rev.* **2005**, *105*, 2999-3094.

36. Frisch, M.J.; Trucks, G. W.; Schlegel, H. B.; Scuseria, G. E.; Robb, M. A.; Cheeseman, J. R.; Scalmani, G.; Barone, V.; Petersson, G. A.; Nakatsuji, H.; Li, X.; Caricato, M.; Marenich, A. V.; Bloino, J.; Janesko, B. G.; Gomperts, R.; Mennucci, B.; Hratchian, H. P.; Ortiz, J. V.; Izmaylov, A. F.; Sonnenberg, J. L.; Williams-Young, D; Ding, F.; Lipparini, F.; Egidi, F.; Goings, J.; Peng, B.; Petrone, A.; Henderson, T.; Ranasinghe, D.; Zakrzewski, V. G.; Gao, J.; Rega, N.; Zheng, G.; Liang, W.; Hada, M.; Ehara, M.; Toyota, K.; Fukuda, R.; Hasegawa, J.; Ishida, M.; Nakajima, T.; Honda, Y.; Kitao, O.; Nakai, H.; Vreven, T.; Throssell, K.; Montgomery Jr., J. A.; Peralta, J. E.;

Ogliaro, F.; Bearpark, M. J.; Heyd, J. J.; Brothers, E. N.; Kudin, K. N.; Staroverov, V. N.; Keith, T. A.; Kobayashi, R.; Normand, J.; Raghavachari, K.; Rendell, A. P.; Burant, J. C.; Iyengar, S. S.; Tomasi, J.; Cossi, M.; Millam, J. M.; Klene, M.; Adamo, C.; Cammi, R.; Ochterski, J. W.; Martin, R. L.; Morokuma, K.; Farkas, O.; Foresman, J. B.; Fox, D. J. Gaussian 16, Revision A.03, Gaussian, Inc., Wallingford CT, 2016.

37. Pinski, P.; Riplinger, C.; Valeev, E. F. *J. Chem. Phys.* **2015**, *143*, 034108.

38. Riplinger, C.; Pinski, P.; Becker, U.; Valeev, E. F.; Neese, F. *J. Chem. Phys.* **2016**, *144*, 024109.

39. Guo, Y.; Sivalingam, K.; Valeev, E. F.; Neese, F. *J. Chem. Phys.* **2016**, *144*, 094111.

40. Neese, F.; Valeev, E. F. *J. Chem. Phys.* **2016**, *144*, 144109.

41. Dunning, T. H. *J. Chem. Phys.* **1989**, *90*, 1007-1023.

42. Neese, F. *J. Chem. Phys.* **2003**, *119*, 9428-9443.

43. Neese, F. The ORCA program system. *WIRES Comput. Mol. Sci.* **2012**, *2*, 73-78.

44. Austin, A.; Petersson, G. A.; Frisch, M. J.; Dobek, F. J.; Scalmani, G.; Throssell, K. *J. Chem. Theory Comput.* **2012**, *8*, 4989-5007.

45. Gonzales-Velasco, J.; Rubinstein, I.; Crutchley, R. J.; Lever, A. B. P.; Bard, A. J. *Inorg. Chem.* **1983**, *22*, 822-825.

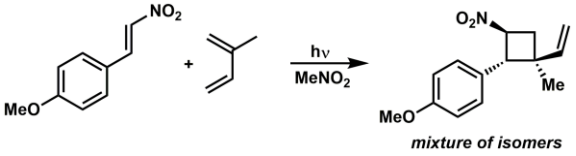
46. Lin, S.-S.; Ischay, M. A.; Fry, C. G.; Yoon, T. P. *J. Am. Chem. Soc.* **2011**, *133*, 19350-19353.

47. Stevenson, S. M.; Shores, M. P.; Ferreira, E. M. *Angew. Chem.* **2015**, *127*, 6606-6610.; *Angew. Chem. Int. Ed.* **2015**, *54*, 6506-6510.

48. To highlight differences in the respective reaction pathways, energies are taken as relative to an initial π-complexes: for the electron transfer pathway this involves [**5.1**]$^{\bullet+}$ and is referred to as [**5.1•5.2**]$^{\bullet+}$, whereas for the energy transfer pathway it involves the twisted ^{3}[**5.1**] and is referred to as ^{3}[**5.1•5.2**]. Barriers to the one-bond intermediate Int$^{\bullet+}$ or ^{3}Int are comparable for either pathway; however, for the energy transfer pathway, both unpaired electrons are resonance-stabilized in the **^{3}**[Int], a property that is absent in the simpler ethylene model.

49. $[Ru(bpz)_3]^{2+}$ has been observed to photo-initiate other [4+2] processes: see reference 12.

50. This reaction described is shown below:



Where these coupling partners were found to be successful to form the cyclohexene product in ref. 24.

51. Reaction quantum yields performed with the VCB derived from the nitroalkene starting materials used 450 nm irradiation to avoid as much competitive absorption by the nitro-VCB species as possible. See Figure S6 for the absorption spectrum of this species.

Chapter 6: A unique excited state for $[Cr(Ph_2phen)_3]^{3+}$ promotes a selective energy-transfer mechanism

6.1 Introduction

Photoredox catalysis is intrinsically important as an alternative and environmental friendly way to prepare organic molecules.[1-5] Recently, interesting and unexpected reaction mechanisms have been elucidated in organic photocatalysis.[6-10] Knowledge of mechanistic pathways allows for the advance of synthesis through judicious choice of reactivity partners. As a representative example, a Diels-Alder cycloaddition between *trans*-anethole and isoprene proceeds *via* photoinitiation through radical chain when using $[Ru(bpz)_3]^{2+}$ (**6.1**, bpz = 2,2'-bipyrazine), as reported by the Yoon group;[11-12] whereas, for the same starting materials, photocatalysis is observed when using $[Cr(Ph_2phen)_3]^{3+}$ (**6.2**), as reported by some of us.[13-14] These results are peculiar since the excited-state redox potentials for **6.1** and **6.2** are nearly identical, so the reactivity is expected to be the same for a strictly outer-sphere process (Figure 6.1.1).[15-18]

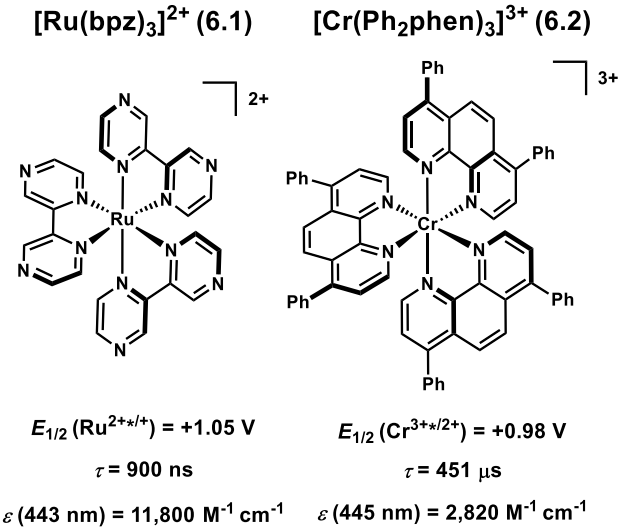


*Figure 6.1.1. Selected (photo)physical properties of **6.1** and **6.2**.*

Related, we also reported the [4+2] cycloaddition of electron-deficient ethereal chalcones and dienes, mediated by **6.2**.[19] This process is likely mechanistically distinct from the dienophile oxidation-based cycloadditions (*e.g.*, *trans*-anethole plus isoprene) also mediated by **6.2***,[13-14] due to the insufficiently oxidizing excited-state redox potential for **6.2** relative to the chalcone substrates. We also very recently reported that in this reaction **6.2** provides greater regioselectivity than all other Ru- and Cr-photosensitizers and hypothesized that a substrate-catalyst pre-association provided unique access to energy-transfer processes that avoided electron-transfer-dominated pathways. This is significant since it indicates that the different mechanistic pathways promoted by **6.1** and **6.2** generate a *more* selective reaction for **6.2**, giving greater support for its synthetic utility in photocatalysis. These results raise the intriguing possibility that the computationally hypothesized substrate-catalyst association has the potential to give a different way to selectively control (excited) bond-forming intermediates that is not strictly based on classical organic structure control via steric hindrance and/or electronics.[20]

Maybe most intriguingly, we posited that the reactivity between **6.2** and enone **6.3** did not derive from ^{2}E character[21-22] but instead from higher-energy (Frank-Condon) excited states that are not solely metal-based.[20] Therefore, the complexity of this reaction garners meaningful motivation for further investigations; in addition to forming the Diels-Alder cycloadduct, homodimerization of enone **6.3** to cyclobutane **6.5** is observed, as well as formation of a chalcone-isoprene vinylcyclobutane (VCB) product **6.4**, neither of which involve an external photosensitizer (Figure 6.1.2). Excited-state reactivity of enone **6.3*** complicates further understanding of the distinct roles that different phosensitizers have in this reaction manifold. To further probe this interesting reaction, we asked the question, can enone **6.3**, react with excited-state photosensitizers while remaining in a ground state (green pathway, Figure 6.1.2)?

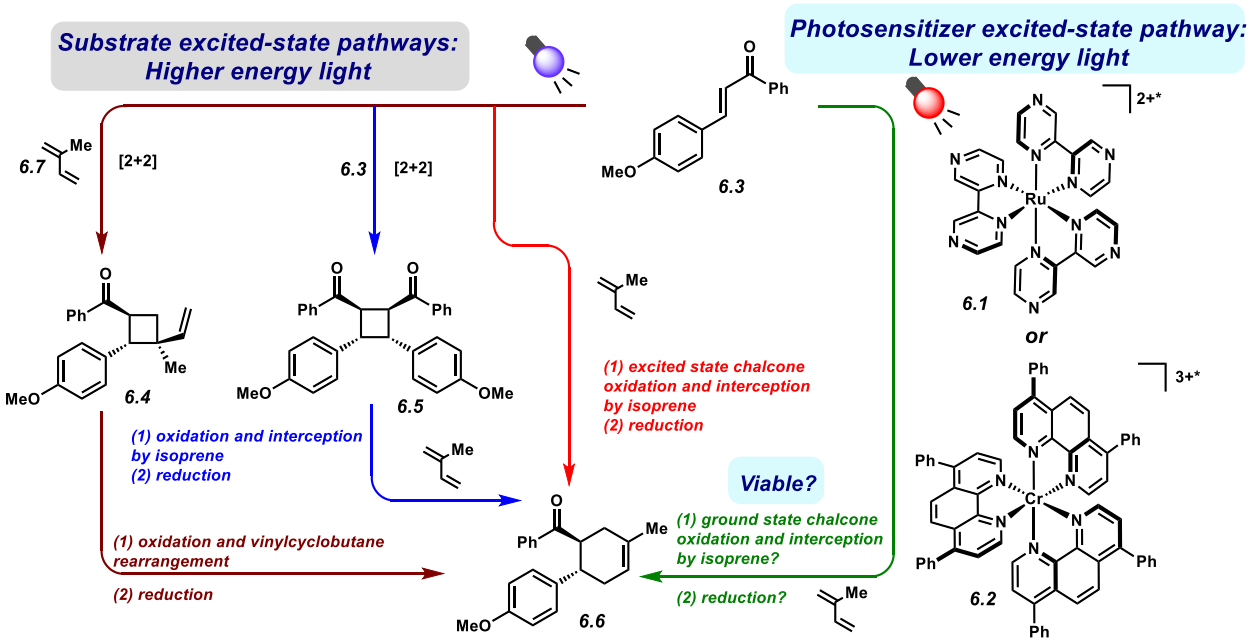


Figure 6.1.2. Outline of different reaction pathways for the reaction of 4-methoxychalcone, ***6.3*** *and isoprene,* ***6.7****.*

Photon-energy controlled reaction pathways have been investigated by Ghosh and König, where at a particular wavelength an arene is mono-activated, but upon increasing the energy of light (lower wavelength), the reaction selectively switches to a bis-activation of the arene.[23] Here, we aim to understand if the differential excited-state reactivity of **6.2** compared to other photosensitizers can be exploited to react with ground-state enone **6.3**. Therefore, we present this study in which selective irradiation of **6.2** and other photosensitizers is used to determine primary mechanisms in the reaction manifold of [4+2] cycloadditions between electron-deficient 4-methoxychalcone and isoprene.

6.2 Division of Labor

All synthesis, characterization and interpretation was performed by Robert Higgins. All computational work was performed and interpreted by Anthony Rappé. Analysis and

interpretation of the experimental details was performed by Eric M. Ferreira, Anthony K. Rappé and Matthew P. Shores.

6.3 Experimental

6.3.1 Preparation of Compounds

Acetonitrile (CH_3CN) was sparged with dinitrogen, passed over alumina, and degassed before use. Nitromethane (CH_3NO_2) was sparged with dinitrogen and subjected to three freeze-pump-thaw cycles before use. Benzene was distilled over CaH_2 and subjected to three freeze-pump-thaw cycles before use. The compounds $[Cr(Ph_2phen)_3](BF_4)_3$ (**6.2(BF$_4$)$_3$**),[14] $[Cr(dmcbpy)_3](BF_4)_3$ (**6.8(BF$_4$)$_3$**),[15] $[Cr(phen)_3](BF_4)_3$ (**6.9(BF$_4$)$_3$**),[20] (*E*)-3-(4-methoxyphenyl)-1-phenylprop-2-en-1-one (**6.3**),[24] (*E*)-1-(4-(*tert*-butyl)phenyl)-3-(4-methoxyphenyl)prop-2-en-1-one (**6.10**),[25] (2-(4-methoxyphenyl)-3-methyl-3-vinylcyclobutyl)(phenyl)methanone (**6.4**)[19] and ((1*R*,2*S*,3*R*,4*S*)-3,4-bis(4-methoxyphenyl)cyclobutane-1,2-diyl)bis(phenylmethanone) (**6.5**)[19] were synthesized according to known literature preparations. Qualitative thin layer chromatography (TLC) analysis was performed on 250 mm thick, 60 Å, glass backed, F254 silica (Silicycle, Quebec City, Canada); samples were visualized with UV light. Flash chromatography was performed using Silicycle silica gel (230-400 mesh). Ferrocene was sublimed before use. All other compounds and reagents were obtained commercially and used as received.

6.3.2 Mechanistic measurements and studies

Single-wavelength experiments were performed using a Newport TLS-300XU tunable light source, which includes a 300 W Xe arc lamp, a Cornerstone 130 monochromator and a motorized filter. These experiments were performed in an NMR tube at a specified time for consistency among experiments. Once the sample was irradiated for the allotted time, the stir bar was removed, and the NMR tube was wrapped in felt and carried to the NMR spectrometer. An ^1H NMR spectrum was then collected where conversion percentages were determined through relative integrations using mesitylene (normally 0.010 M) as an internal standard. Oxygen was

excluded from the reaction mixtures by bubbling N_2 gas through the solution for at least 15 minutes.

6.3.3 Electrochemical measurements

Electrochemical experiments were performed in 0.1 M solutions of Bu_4NPF_6 in $MeNO_2$ in air. The Bu_4NPF_6 was purified by recrystallization from anhydrous EtOH twice. A blank was collected and then the analyte was added to the electrochemical cell, which was then degassed for a minimum of 10 minutes before any further data were collected. Cyclic voltammograms (CVs) and square-wave voltammograms (SWVs) were obtained with a CH Instruments potentiostat (Model 1230A or 660C) using a 0.25 mm glassy carbon disk working electrode, Ag^+/Ag reference electrode and a Pt wire counter electrode. Scans were collected at rates between 0.10 V s^{-1} and 10 V s^{-1} for CVs and at a step-size of 0.004 V and a frequency of 15 Hz for SWVs. Reported potentials are referenced to the $[Cp_2Fe]^+/[Cp_2Fe]$ (Fc^+/Fc, where Cp = cyclopentadienyl) redox couple, and were determined by adding ferrocene as an internal standard at the conclusion of each electrochemical experiment.

6.3.4 Other physical measurements

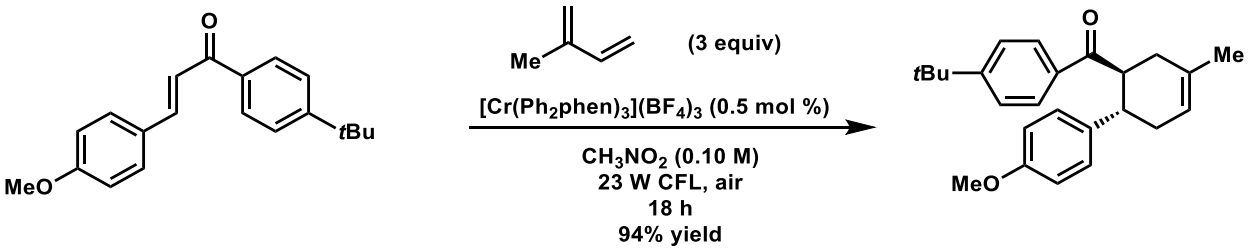
All experiments were conducted at room temperature unless otherwise noted. Absorption spectra were obtained with a Hewlett-Packard 8453 spectrometer in quartz cuvettes with a 1 cm path length. Infrared spectra were measured with a Nicolet 380 FT-IR spectrometer. NMR studies were performed on a Varian 400 MHz spectrometer. High resolution mass spectrometry was performed on an Agilent 6220 TOF LC/MS interfaced to an Agilent 1200 HPLC with an ESI source.

6.3.5 Catalysis studies

General procedure

To a flame dried 3.5 mL shell vial open to air was added alkene (1 equiv), diene (3 equiv), $[Cr(Ph_2phen)_3](BF_4)_3$ (0.5 mol %) and nitromethane (0.10 M). The vial was then capped and equipped with an air outlet (needle place through the cap) and irradiated with a bright white 23 W compact fluorescent light bulb in an enclosed housing (cardboard box) lined with aluminum foil.

Illumination was continued until consumption of the alkene was observed (TLC). The reaction mixture was subjected to rotary evaporation and the resulting residue was purified via flash chromatography.



Cyclohexene 6.12.

Prepared according to the General Procedure using alkene **6.10** (29.4 mg, 0.100 mmol), diene **6.7** (30.1 mL, 0.300 mmol), [(Cr(Ph_2phen)$_3$](BF_4)$_3$ (0.7 mg, 0.000500 mmol) and nitromethane (1.00 mL). The reaction mixture was irradiated for 18 h. The crude product was purified by flash chromatography (9:1 hexanes/EtOAc eluent) to afford cyclohexene **6.12** (33.9 mg, 94% yield, 4:1 isomeric ratio) as a colorless oil.

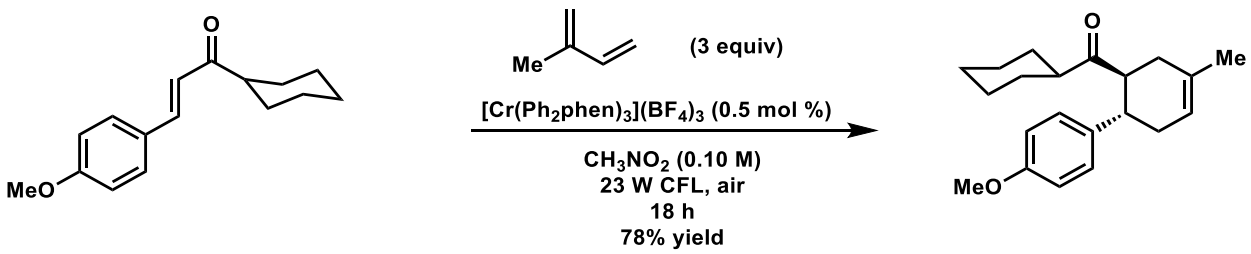
TLC: R_f = 0.41 in 9:1 hexanes/EtOAc, visualized by UV.

^{1}H NMR (400 MHz; $CDCl_3$): δ 7.78 (d, *J* = 8.2 Hz, 2H), 7.40 (d, *J* = 8.2 Hz, 2H), 7.13 (d, *J* = 8.6 Hz, 2H), 6.71 (d, *J* = 8.6 Hz, 2H), 5.55 (br s, 1H), 4.01-3.95 (m, 1H), 3.70 (s, 3H), 3.22 (td, *J* = 11.0, 5.9 Hz, 1H), 2.40-2.21 (comp. m, 4 H), 1.73 (s, 3H), 1.32 (s, 9H).

^{13}C NMR (100 MHz; $CDCl_3$): δ 203.1, 157.7, 156.4, 136.8, 134.6, 132.5, 128.4, 128.0, 125.4, 120.9, 113.7, 55.1, 47.1, 41.3, 35.3, 35.0, 34.3, 31.0, 23.2.

IR (ATR, neat): 2960, 2835, 1674, 1604, 1512, 1245, 1178, 1035, 826, 543 cm^{-1}.

HRMS (ESI+): *m/z* calc'd for $(M+H)^+$ $[C_{25}H_{31}O_2]^+$: 363.2324, found 363.2309.



Cyclohexene 6.13.

Prepared according to the General Procedure using alkene **6.11** (24.4 mg, 0.100 mmol), diene **6.7** (30.1 mL, 0.300 mmol), [(Cr(Ph_2phen)$_3$](BF_4)$_3$ (0.7 mg, 0.000500 mmol) and nitromethane (1.00 mL). The reaction mixture was irradiated for 18 h. The crude product was purified by flash chromatography (9:1 hexanes/EtOAc eluent) to afford cyclohexene **6.13** (24.3 mg, 78% yield, 8:1 isomeric ratio) as a colorless oil.

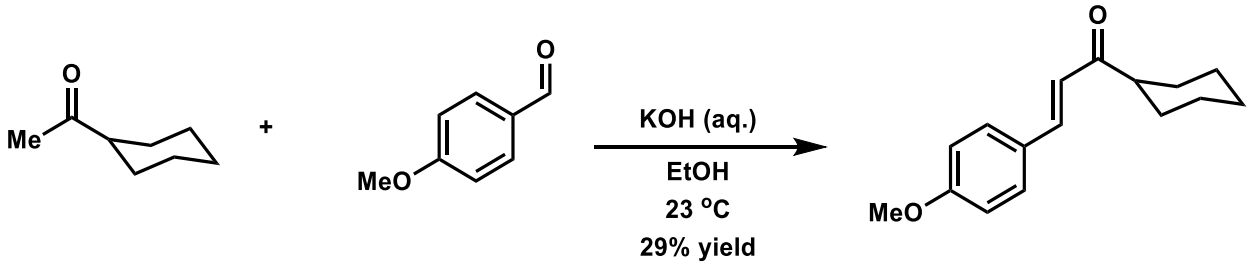
TLC: R_f = 0.55 in 9:1 hexanes/EtOAc, visualized by UV.

^{1}H NMR (400 MHz; $CDCl_3$): δ 7.10 (d, *J* = 8.6 Hz, 2H), 6.80 (d, *J* = 8.6 Hz, 2H), 5.48 (br s, 1H), 3.77 (s, 3H), 3.11 (td, *J* = 11.1, 5.5 Hz, 1H), 2.94-2.87 (m, 1H), 2.28-2.17 (comp. m, 4H), 2.05-1.93 (comp. m, 2H), 1.71 (s, 3H), 1.67-1.54 (comp. m, 3H), 1.26-0.94 (comp. m, 5H).

^{13}C NMR (100 MHz; $CDCl_3$): δ 217.1, 158.1, 136.1, 132.4, 128.7, 120.6, 113.7, 55.2, 51.9, 42.0, 34.4, 33.5, 28.2, 27.2, 25.8, 25.3, 23.2.

IR (ATR, neat): 2922, 2852, 1697, 1512, 1243, 1181, 1034, 889, 817, 543 cm^{-1}.

HRMS (ESI+): *m/z* calc'd for $(M+H)^+$ $[C_{21}H_{29}O_2]^+$: 313.2168, found 313.2157.



Enone 11.

To anisaldehyde (1.08 g, 7.92 mmol) in EtOH (75.0 mL) and aq. (KOH 3.20 g in 6 mL H_2O) at 23 ˚C was added methylcyclohexylketone (1.00 g, 7.92 mmol). The reaction mixture was capped and

stirred at ambient temperature for 16 h. Then, EtOH was removed by rotary evaporation and the crude mixture was extracted into EtOAc (50 mL) and washed with H_2O (50 mL). The aqueous layer was extracted with EtOAc (3 x 50 mL) and the organic layers were combined and washed with brine (75 mL) and dried over $MgSO_4$. After filtration, the solvent was removed by *in vacuo* where the crude residue was purified by flash chromatography (8:1 hexanes/EtOAc eluent) to afford enone **6.11** (0.560 g, 29% yield) as a white powder.

TLC: R_f = 0.40 in 4:1 hexanes/EtOAc, visualized by UV.

^{1}H NMR (400 MHz; CD_3NO_2): δ 7.61 (d, *J* = 9.0 Hz, 2H), 7.54 (d, *J* = 16.1 Hz, 1H), 6.98 (d, *J* = 9.0 Hz, 2H), 6.78 (d, *J* = 16.1 Hz, 1H), 3.85 (s, 3H), 2.77-2.70 (m, 1H), 1.89-1.84 (comp. m, 2H), 1.82-1.77 (comp. m, 2H), 1.71-1.66 (m, 1 H), 1.40-1.32 (comp. m, 4H), 1.29-1.21 (m, 1H).

^{13}C NMR (100 MHz; CD_3NO_2): δ 199.1, 157.5, 137.3, 125.8, 123.5, 118.6, 110.2, 50.7, 44.7, 25.5, 21.7, 21.4.

IR (ATR, neat): 2928, 1676, 1593, 1506, 1303, 1256, 1024, 992, 621, 536 cm^{-1}.

HRMS (ESI+): *m/z* calc'd for $(M+H)^+$ $[C_{16}H_{21}O_2]^+$: 245.1542, found 245.1533.

6.4 Results and Discussion

The electronic absorption properties of reactants and photosensitizers are sufficiently separable to allow selective excitation of species and exploration of viable reaction pathways. Enone **6.3** (green trace in Figure 6.4.1) absorbs most strongly at 340 nm, but fails to show any absorption at longer wavelengths (lower energy).[26] The Ru- and Cr-containing complexes used in this study also absorb in the 300-350 nm region, but enone **6.3** is present in at least 100-fold excess under irradiation conditions. In the 400-500 nm region, all the metal complexes show significant absorption. Therefore, performing single wavelength irradiations at wavelengths >400 nm allows the photosensitizer to be selectively excited while enone **6.3** dominantly remains as a ground state singlet.

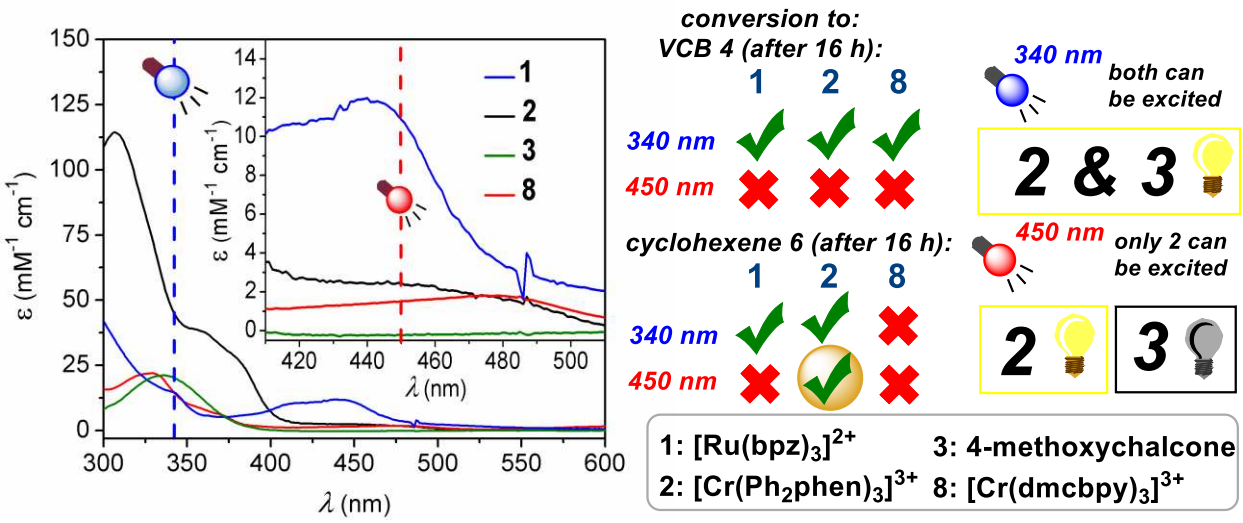


*Figure 6.4.1. Left: electron absorption spectra for 4-methoxychalcone (**6.3**) and photosensitizers $[Ru(bpz)_3]^{2+}$ (**6.1**), $[Cr(Ph_2phen)_3]^{3+}$ (**6.2**) and $[Cr(dmcbpy)_3]^{3+}$ (**6.8**, dmcbpy = 4,4'-dimethylcarboxylate-2,2'-bipyridine). Data are collected in acetonitrile. Right: results of single wavelength irradiations in nitromethane involving 4-methoxychalcone, three equivalents of isoprene, and various photosensitizers, using 1.0 mol% loadings for $[Ru(bpz)_3]^{2+}$ and 0.5 mol% loadings for $[Cr(Ph_2phen)_3]^{3+}$ and $[Cr(dmcbpy)_3]^{3+}$ (**6.8**). The "blue" irradiation source gives 3 × 10^{-9} mol einsteins s^{-1} at 340.00(2) nm; the "red" irradiation source gives 5.2 × 10^{-9} mol einsteins s^{-1} at 450.03(2) nm.*

Table 6.4.1. Single wavelength irradiation data for different photosensitizers.

irradiation wavelength (nm)	photosensitizer	conversion to VCB **6.4**	conversion to cyclohexene **6.6**
340	$[Ru(bpz)_3]^{2+}$	24.1	1.4
340	$[Cr(dmcbpy)_3]^{3+}$	26.2	0
340	$[Cr(phen)_3]^{3+}$	16.8	1.0
340	$[Cr(Ph_2phen)_3]^{3+}$	22.2	2.4
340[a]	$[Cr(Ph_2phen)_3]^{3+}$	19.5	0.8
450	$[Ru(bpz)_3]^{2+}$	0	0
450	$[Cr(dmcbpy)_3]^{3+}$	0	0
450	$[Cr(phen)_3]^{3+}$	0	trace
450	$[Cr(Ph_2phen)_3]^{3+}$	0	*8*
450[a]	$[Cr(Ph_2phen)_3]^{3+}$	0	*7.4*

Enone **3** comprised most of the remaining material for these experiments, indicating a lack of significant decomposition. [a] reaction was performed without O_2 present.

To provide some preliminary information about single wavelength irradiation for this system, experiments are performed using monochromatic 340 nm irradiation, which is where enone **6.3** most strongly absorbs. Most of the observed conversion produces VCB **6.4** with a small conversion to cyclohexene **6.6** for **6.1**, **6.2** and $[Cr(phen)_3]^{3+}$ (**6.9**) after 16 hours. In assessing conversion efficiency, it is important to note that the photon flux for this type of monochromatic light source is much lower than the photon flux for a CFL bulb used in bulk irradiations. The decreased photon flux will diminish conversions if these reactions are photon limited, which appears to be the case for these systems (*vide infra*, Figure A6.1). Further, exclusion of O_2 from the reaction mixture containing $[Cr(Ph_2phen)_3]^{3+}$ shows similar conversion from enone **6.3** to VCB **6.4**, but lower conversion to cyclohexene **6.6** over the period of 16 hours, implicating the presence of O_2 for pathways involving excitation of enone **6.3**.[27]

In alignment with our expectations, at 450 nm irradiation, no conversion of **6.3** to VCB **6.4** is observed, owing to the inability of enone **6.3** to absorb at that energy. Cyclohexene **6.6** is not observed using either $[Ru(bpz)_3]^{2+}$ or $[Cr(dmcbpy)_3]^{3+}$. Peculiarly, when selectively exciting $[Cr(Ph_2phen)_3]^{3+}$ at 450 nm, significant and selective conversion from enone **6.3** to cyclohexene **6.6** is observed after 16 hours (Figure 6.4.1 and Table 6.4.1). No conversion to VCB **6.4** is observed under the same conditions. This is the most direct evidence available showing Cr chromophore excitation leading directly to final Diels Alder cycloadduct product, and further, VCB is not an intermediate in the lower-energy photochemical process.

While these results are quite intriguing, several outstanding questions remain. First, even though only photosensitizer **6.2** reacts when excited and enone **6.3** remains in a ground state, why is this energy transfer process selective compared to electron transfer processes for **6.1** and **6.8**? Second, **6.1** absorbs almost an order of magnitude more light at 450 nm than **6.2**, in addition **6.8** is more photooxidizing than **6.2** by 440 mV, which motivates, why does **6.2** show efficient reactivity in comparison to **6.1** and **6.8**?

In our previous report, the potential surface for energy and electron transfer pathways between enone **6.3** and diene **6.7** was investigated using the ωb97xd functional[28] with a 6-311+g* basis set, indicating that an electronic structure of three unpaired electrons on the Cr ion that are coupled to two unpaired electrons on the ligand is reasonable for a reactive excited state.[29] Accompanying TD-DFT computations indicated that the triplet state for the ligand, Ph_2phen, was lower in energy than other commonly used polypyridyl ligands

However, we did not know the extent to which this electronic structure pervaded in the overall reactivity. To assess the impact of transition metal complex on reaction pathway, APFD[30] TD-DFT excited states were computed for enone **6.3** coordinated to a range of metal complexes including, **6.1**, **6.2**, **6.8** and **6.9**. APFD was selected, rather than ωb97xd, due to better agreement between computed and measured excitation energies. For example, the lowest singlet excitation energy computed for **6.1** with ωb97xd appears at 375 nm, whereas APFD gives the lowest quartet excited state at 440 nm (Figure 6.4.1, left side); the latter compares favorably to the electronic absorption spectrum of **6.1**, which has a low-energy feature around 450 nm. The natural transition orbitals (NTOs)[31] for the lowest excited states for **6.1** and **6.2** are provided in Figure 6.4.2. Other low-lying transitions for **6.2** and transitions for **6.8** and **6.9** are presented in the supplemental information (Figures A6.2-A6.5).

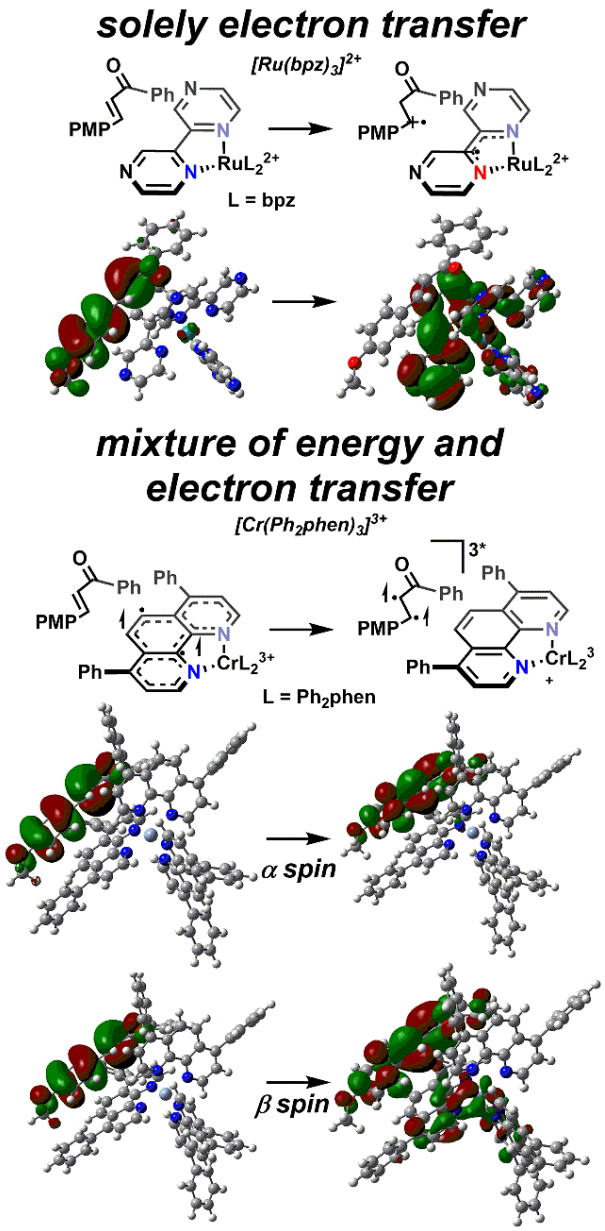


Figure 6.4.2. Natural transition orbitals for the lowest energy singlet or quartet excitations ("from" on left, "to" on right) involving outer sphere complexes of 4-methoxychoalcone interacting with $[Ru(bpz)_3]^{2+}$ (top) and $[Cr(Ph_2phen)_3]^{3+}$ (bottom), respectively. The line bond drawing for $[Cr(Ph_2phen)_3]^{3+}$ illustrates the energy transfer pathway, although significant electron transfer is observed in the β-spin NTOs. NTOs for the next transition, 0.1 eV up, also a mixture of energy and electron transfer, are available in the Supporting Information.

For the complexes that show lower selectivity of product distribution (**6.1**, **6.8** and **6.9**), the lowest energy excited states, singlet for **6.1** and quartet for **6.8** and **6.9**, are consistent with excited-state *electron-transfer* from **6.3** to the polypyridyl ligand of the respective metal complex. In contrast, for **6.2**, the lowest two excited states are mixtures of electron transfer from enone **6.3** to a Ph_2phen ligand of **6.2** and *energy-transfer*, that is available through association of coupled ^{3}[**6.3**] and $^4[Cr]^{3+}$ (Figure 6.4.2, bottom). The spin-density plots for the doublet and sextet members of a doublet, quartet, and sextet Heisenberg ladder are provided in Figures 6.4.3 and A6.6. Therefore, this excited state consists of a quartet state on the Cr-center and a triplet state on the Ph_2phen ligand, resulting in a Heisenberg spin-ladder, which has been previously hypothesized for **6.2**.[32] This excited state is quite interesting as it presents a triplet-state on the ligand, stabilized by the unpaired spins on the chromium center, that is ideally situated for an energy-transfer process with another species that can occupy a triplet excited state, such as enone **6.3**. We think that this is a synthetically useful discovery since it shows that **6.2*** can act not only as potent oxidative photoredox catalyst through electron-transfer,[13-14] but also as a uniquely situated photocatalytic energy-transfer reagent in different cycloaddition reactions, providing dual-reactivity applications.[20]

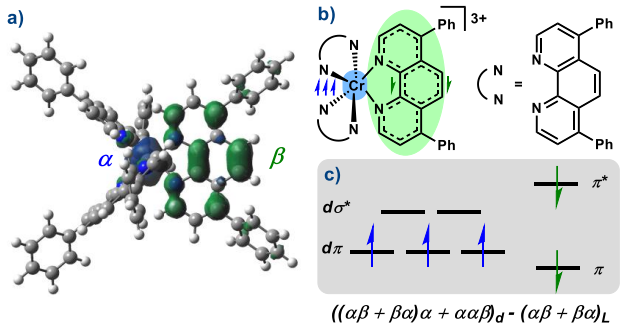


Figure 6.4.3. The ωb97xd derived spin-density plot of the doublet state for the Heisenberg spin-ladder for excited-states of $[Cr(Ph_2phen)_3]^{3+}$ (a) and the line-bond drawing of this excited-state (b) and a representative molecular orbital diagram showing the electronic structure of one of the

excited-states with the associated notation included below for all permeations of excited-states where d and L indicate states from metal- and ligand-based orbitals, respectively (c).

This excited state helps support the unique reactivity of **6.2** in this reaction manifold. Further data are necessary to experimentally the electronic structure of this excited state, which are currently underway in our laboratories. This type of excited state is also present once **6.2** and **6.3** are associated after energy transfer from the Ph_2phen ligand to enone **6.3** (Figure A6.7). In the sextet state, the unpaired spins that are localized on **6.3** are now alpha (blue). This suggests that in this spin manifold, ^{3}[**6.3**] is magnetically coupled to $^4[Cr]^{3+}$, similarly to the Ph_2phen ligand and $^4[Cr]^{3+}$ for the Frank Condon states in the Heisenberg spin-ladder (Figures 6.4.3 and A6.7). Geometry optimization of the sextet state results in a complex wherein **6.3** distorts to a conformation where the dienophile C-C double bond has twisted and is in a triplet conformation.

This is an interesting result as we previously found that the lowest energy transition states of the first bond-forming step for both the major and minor products between enone **6.3** and diene **6.7** showed enone **6.3** as nearly flat. To further probe these results, the DLPNO-CCSD(T) method[33-36] was used in combination with a cc-pVQZ basis set,[37] where the geometries from our previous results using the ωb97xd functional were employed (Figures 6.4.4 and 6.4.5). CCSD(T) has long served as the benchmark standard electron correlation method for largely single reference systems. Reassuringly, similar energies were obtained when the DLPNO-CCSD(T) method was used in comparison to our previous results.[20] Interestingly, we find that the optimized structure of the association complex, [**6.2•6.3**], shows **6.3** in a twisted configuration (Figure 6.4.4).

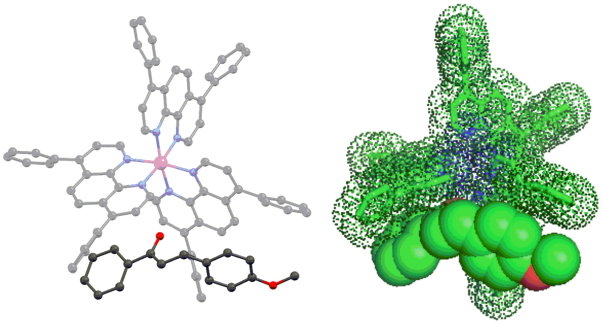


*Figure 6.4.4. Left: pictorial representation of the twisted geometry for dienophile **6.2** when associated with complex **6.3**. Right: optimized structure of the catalyst-substrate association complex [**6.2•6.3**], computed with the DLPNO-CCSD(T) functional (left).*

Having established experimental and computational agreement with this system, we now investigate the excited-state properties and thermodynamic potentials for electron-transfer for enone **6.3**. Figures 6.4.5 and A6.7 show the energy of ^{3}**6.3** plotted in red, triplet ligand energies in green, and the electron transfer energies from **6.3** to both **6.1** and **6.2** in black. This is important because neither **6.1** nor **6.2** can perform electron transfer with enone **6.3** thermodynamically from their lowest lying ^{3}MLCT or ^{2}E excited states when enone **6.3** remains in a ground state. Specifically, the ^{2}E of **6.2** at 1.64 eV for **6.2** *does not* have the driving force for electron-transfer. Coordination of **6.3** lowers the energy of electron transfer, by 7 to 3 kcal mol^{-1} for **6.1** and **6.2**, respectively. Accordingly, coordination of **6.3** also lowers the ^{3}**6.3** excited-state energies, by 10 to 5 kcal mol^{-1} for **6.1** and **62**, respectively. The ^{3}**6.2** computed excited state at 455 nm *does* have the driving force for energy transfer.

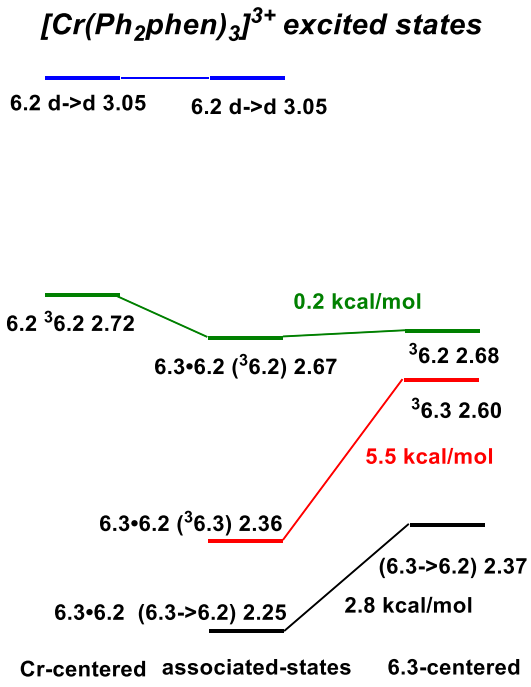


*Figure 6.4.5. Different excited states for **6.2** (left), associated catalyst-substrate species [**6.2•6.3**] (middle) and **6.3** (right), using the DLPNO-CCSD(T) functional; energies in kcal/mol units represent association-induced stabilizations of excited sates; unlabeled energies are in eV units.*

Since **6.1** and **6.3** do not show any productive reactivity at 450 nm irradiation, where excited states of **6.1** will be populated, this indicates it is likely **6.1** and **6.3** do not engage in an association event. Conversely, **6.2** and **6.3** do show productive reactivity at 450 nm irradiation, indicating that an association complex is far more likely. Therefore, we suggest that ^{1}MLCT excited state for **6.1** undergoes rapid intersystem crossing to the ^{3}MCLT state and performs electron transfer with enone **6.3**, forming the radical cation of **6.3**. Conversely, for **6.2**, the triplet ligand excited state is not perturbed by coordination to **6.3**, where internal conversion (energy transfer) to the lower energy [^{3}**6.3**•^{4}**6.2**] state should be rapid, which is followed by subsequent cycloaddition with isoprene forming cyclohexene **6.6**. Not only is this an extremely rare phenomenon in photocatalysis reactivity, a triplet ligand excited state to perform energy-transfer

to an organic molecule is an uncommon excited-state manifold for reactivity. This has the potential for broad implications outside of this reactivity scope.

These computational findings indicate that triplet energy manifold of both **6.3** and the ligands of these photosensitizers is intrinsically important. In a related system, Zhang and others found that fluorinated aromatic substrates and pyrenyl photosensitizers displayed π-hole π-complex interactions, which led to the defluorohydrogenation of these substrates when exposed to light.[40] In this vein, we investigated whether similar interactions are apparent for the reactivity between **6.2** and **6.3**. When enone **6.3** and **6.2** are irradiated in the presence of isoprene by using benzene, a solvent capable of strong π-interaction, in place of nitromethane, under the optimized reaction conditions (16 h CFL irradiation) conversions of 45 and 48% to VCB **6.4** and cyclohexene **6.6**, respectively, are observed. When benzene is applied as the solvent for single wavelength 450 nm irradiation, no detectable amount of VCB **6.4** or cyclohexene **6.6** is observed after 16 hours. This result highlights the subtle changes in this system that can have profound impact on the reactivity.[41]

Further, substrates that have sterically hindering groups (**6.10**) and/or saturation (**6.11**) in one of the two phenyl rings in enone **6.3** are used as dienophiles for this reaction to probe their potential reactivity. Figure 6.4.1 shows that these compounds are both quite proficient in standard reaction conditions with **6.2** as the photosensitizer, where *tert*-butyl derivative **6.10** gives a 94% yield and cyclohexyl derivative **6.11** gives a 78% yield. Of note, neither of these species are thermodynamically oxidizable as determined by electrochemical experiments (Figure 6.4.1). Interestingly, the isomer ratio for cyclohexenes **6.12** and **6.13** obtained from CFL irradiation are 8:1 and 4:1, respectively. These ratios indicate that the selective energy-transfer pathway is likely not as preferred for enones **6.10** and **6.11** as it is for enone **6.3** when **6.2** is employed as the photosensitizer. Therefore, it is reasonable that the resulting product ratios are more similar to electron-transfer reactions when photosensitizers **6.1**, **6.8** or **6.9** are used. When **6.3** is replaced by derivatives **6.10** or **6.11** for these 450 nm single wavelength experiments, no product formation

is observed in the presence of **6.2**, bolstering a hypothesis which proposes that the possible intermolecular interactions between **6.2** and **6.3** are π in nature. These results highlight the dichotomy in this reaction sequence that is dependent not only photosensitizer choice, but also substrate choice as well.

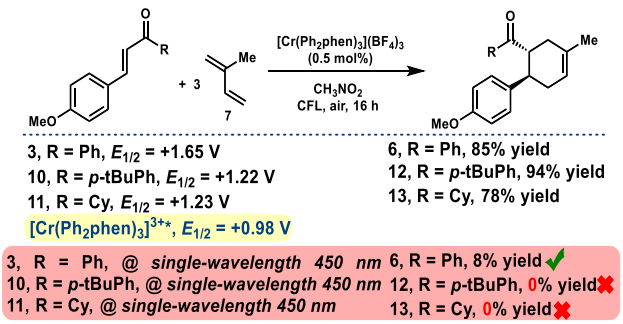


Figure 6.4.1. Reactivity of novel substrates in our standard conditions. Electrochemical measurements are performed in 0.10 M Bu_4NPF_6 nitromethane solution.

6.5 Conclusions and outlook

In conclusion, we present findings that support association-directed excited-state energy transfer as a viable reaction pathway for cycloaddition reactions involving $[Cr(Ph_2phen)_3]^{3+*}$. Dual-mode reactivity of $[Cr(Ph_2phen)_3]^{3+*}$ is dictated by substrate selection: electron-deficient dienophiles, such as 4-methoxychalcone, operate through a photocatalytic energy-transfer process, whereas electron-rich dienophiles such as *trans*-anethole undergo a photo-oxidative electron-transfer pathway. Computational data indicate that the energy-transfer-active excited state (three unpaired electrons on Cr magnetically coupled to two unpaired electrons on the ligand) is uniquely accessed by $[Cr(Ph_2phen)_3]^{3+*}$. Other Cr- and Ru-containing photosensitizers occupy this excited state at much higher energies and therefore proceed through only electron transfer mechanisms through well-studied and reactivity-established excited states. Importantly, detailed calculations indicate that the regioselectivity of the cycloaddition reaction between 4-

methoxychalcone and isoprene arises from preferential orientation of 4-methoxychalcone through a substrate-catalyst interaction. In turn, judicious modification of the chemical make-up of dienophile substrates can withdraw access to the selective energy-transfer pathway of $[Cr(Ph_2phen)_3]^{3+*}$. These results highlight the exceptional properties of $[Cr(Ph_2phen)_3]^{3+}$ as a unique reagent for cycloaddition reactions and suggest ways in which suitably modified polypyridyl-type complexes with different metals may toggle between electron- and energy-transfer excited-state reaction manifolds.

References

1. Skubi, K. L.; Blum, T. R.; Yoon, T. P. *Chem. Rev.* **2016**, *116*, 10035.

2. Romero, N. A.; Nicewicz, D. A. *Chem. Rev.* **2016**, *116*, 10075.

3. Staveness, D.; Bosque, I.; Stephenson, C. R. J. *Acc. Chem. Res.* **2016**, *49*, 2295.

4. Poplata, S.; Tröster, A.; Zou, Y.-Q.; Bach, T. *Chem. Rev.* **2016**, *116*, 9748.

5. Shaw, M. H.; Twilton, J.; MacMillan, D. W. C. *J. Org. Chem.* **2016**, *81*, 6898.

6. Johnson, M. W.; Hannoun, K. I.; Tan, Y. C.; Fu, G. C.; Peters, J. C. *Chem. Sci.* **2016**, *7*, 4091.

7. Yayla, H. G.; Peng, F.; Mangion, I. K.; McLaughlin, M.; Campeau, L.-C.; Davies, I. W.; DiRocco, D. A.; Knowles, R. R. *Chem. Sci.* **2016**, *7*, 2066.

8. Pitre, S. P.; Yoon, T. P.; Scaiano, J. C. *Chem. Commun.* **2017**, *53*, 4335.

9. Pitre, S. P.; Scaiano, J. C.; Yoon, T. P. *ACS Catal.* **2017**, *7*, 6440.

10. Bartling, H.; Eisenofer, A.; König, B.; Gschwind, R. M. *J. Am. Chem. Soc.* **2016**, *138*, 11860.

11. Cismesia, M. A.; Yoon, T. P. *Chem. Sci.* **2015**, *6*, 5426.

12. Lin, S.-S.; Ischay, M. A.; Fry, C. G.; Yoon, T. P. *J. Am. Chem. Soc.* **2011**, *133*, 19350.

13. Stevenson, S. M.; Shores, M. P.; Ferreira, E. M. *Angew. Chem. Int. Ed.* **2015**, *54*, 6506.

14. Higgins, R. F.; Fatur, S. M.; Shepard, S. G.; Stevenson, S. M.; Boston, D. J.; Ferreira, E. M.; Damrauer, N. H.; Rappé, A. K.; Shores, M. P. *J. Am. Chem. Soc.* **2016**, *138*, 5451.

15. McDaniel, A. M.; Tseng, H.-W.; Damrauer, N. H.; Shores, M. P. *Inorg. Chem.* **2010**, *49*, 7981.

16. Prier, C. K.; Rankic, D. A.; MacMillan, D. W. C. *Chem. Rev.* **2013**, *113*, 5322.

17. Crutchley, R. J.; Lever, A. B. P. *Inorg. Chem.* **1982**, *21*, 2276.

18. Gonzales-Velasco, J.; Rubinstein, I.; Crutchley, R. J.; Lever, A. B. P.; Bard, A. J. *Inorg. Chem.* **1983**, *22*, 822.

19. Stevenson, S. M.; Higgins, R. F.; Shores, M. P.; Ferreira, E. M. *Chem. Sci.* **2017**, *8*, 654.

20. Higgins, R. F.; Fatur, S. M.; Damrauer, N. H.; Ferreira, E. M.; Rappé, A. K.; Shores, M. P. *In submission.*

21. Serpone, N.; Jamieson, M. A.; Henry, M. S.; Hoffman, M. Z.; Bolletta, F.; Maestri, M. *J. Am. Chem. Soc.* **1979**, *101*, 2907.

22. Forster, L. S. *Chem. Rev.* **1990**, *90*, 331.

23. Ghosh, I.; König, B. *Angew. Chem. Int. Ed.* **2016**, *55*, 7676.

24. Chang, M.-Y.; Tsai, C.-Y.; Wu, M.-H. *Tetrahedron* **2013,** *69*, 6364.

25. Matthias, C.; Cartoni, A.; Kuck, D. *Int. J. Mass Spectrom.* **2006,** *255*, 195.

26. These results agree with the impacts O_2 had upon the Cr-mediated reaction in ref. 14.

27. We note that a single-wavelength experiment centered at 480 nm, the λ_{max} of emission for enone **6.3**, shows no conversion to VCB **6.4** or cyclohexene **6.6**, when enone **6.3** and diene **6.7** are reacted. When the same reaction is performed with 0.5 mol% **6.2**, no conversion to VCB **6.4** is observed, but 3.1% conversion is observed to cyclohexene 6 after 16 hours. The irradiation source gives a wavelength width of 480.03(2) nm.

28. Chai, J.-D.; Head-Gordon, M. *Phys. Chem. Chem. Phys.* **2008**, *10*, 6615.

29. Krishnan, R.; Binkley, J. S.; Seeger, R.; Pople, J. A. *J. Chem. Phys.* **1980**, *72*, 650.

30. Austin, A.; Petersson, G. A.; Frisch, M. J.; Dobek, F. J.; Scalmani, G.; Throssell, K. *J. Chem. Theory Comput.* **2012**, *8*, 4989.

31. Martin, R. L. *J. Chem. Phys.* **2003**, *118*, 4775.

32. Ohno, T.; Kato, S.; Kaizaki, S.; Hanazki, I. *Inorg. Chem.* **1986**, *25*, 3853.

33. Pinski, P.; Riplinger, C.; Valeev, E. F. *J. Chem. Phys.* **2015**, *143*, 034108.

34. Pavošević, F.; Pinski, P.; Riplinger, C.; Neese, F.; Valeev, E. F. *J. Chem. Phys.* **2016**, *144*, 144109.

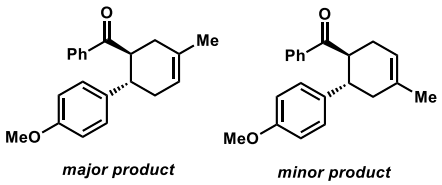
35. Guo, Y.; Sivalingam, K.; Valeev, E. F.; Neese, F. *J. Chem. Phys.* **2016**, *144*, 094111.

36. Riplinger, C.; Pinski, P.; Becker, U.; Valeev, E. F.; Neese, F. *J. Chem. Phys.* **2016**, *144*, 024109.

37. Dunning, T. H. *J. Chem. Phys.* **1989**, *90*, 1007-1023.

38. The expected differentiation is calculated according to the relationship between energy and equilibria in solution.

39. The major and minor products are shown below:



40. Lu, J. Z.; Khetrapal, N. S.; Johnson, J. A.; Zheng, X. C.; Zhang, J. *J. Am. Chem. Soc.* **2016**, *138*, 15805.

41. An alternative reason for the lower conversion in benzene is the relative insolubility of $[Cr(Ph_2phen)_3]^{3+}$ in that solvent.

Chapter 7: Mechanistic studies into substrate-catalyst association in a Cr-photocatalytic system

7.1 Introduction

Pericyclic reactions (*e.g.*, [2+2] and [4+2] cycloadditions) proceed through a variety of pathways including concerted, radical cation and Lewis acid-mediated.[1-3] Recently, photoredox reactivity has opened new ways of performing these reactions, which have been proposed to proceed through both electron and energy transfer pathways.[4-8] Determining the differences between these two pathways is important to provide unique routes to synthesize novel organic molecules. For example, the Yoon group has investigated a Diels-Alder cycloaddition reaction between *trans*-anethole and isoprene where $[Ru(bpz)_3]^{2+}$ (bpz = 2,2'-bipyrazine) (**7.1**) acts as a photoinitiator through a chain propagation mechanism.[9-10] Conversely, we found that using the same starting materials with $[Cr(Ph_2phen)_3]^{3+}$ (Ph_2phen = 4,7-diphenyl-1,10-phenanthroline) (**7.2**) as the photocatalyst required oxygen and that the catalyst was regenerated in the reaction.[11-12] These results are peculiar since the excited-state redox potentials for both of these photosensitizers are nearly identical, so the reactivity may be initially expected to be the same for both species.[13-16] Interestingly, both of these pathways involved electron transfer as the major transformation involving both $[Ru(bpz)_3]^{2+}$ and $[Cr(Ph_2phen)_3]^{3+}$.

Similar to these results, we very recently reported that $[Cr(Ph_2phen)_3]^{3+}$ gives a more regioselective than all other photosensitizers for the cycloaddition reaction between 4-methoxychalcone (**7.3**) and isoprene (**7.4**), which was hypothesized to occur through a substrate-catalyst pair through an energy transfer pathway elucidated through computational data.[17-18] The results in this report not only further supported the mechanistic differences between $[Ru(bpz)_3]^{2+}$ and $[Cr(Ph_2phen)_3]^{3+}$, but also implicated all other Cr-photosensitizers as operating under the same conditions as $[Ru(bpz)_3]^{2+}$. Therefore, $[Cr(Ph_2phen)_3]^{3+}$ performs unique reactivity that other photosensitizers are not able to perform. We followed this work up with a selective excitation

study, where we show that only $[Cr(Ph_2phen)_3]^{3+}$ reacts when in an excited-state and that all other "*photosensitizers*" employed require the substrate to be in an excited state.[19] These data further support a substrate-catalyst pair that likely engage in an energy transfer mechanism for efficacious reactivity. Importantly, this distinction is likely due to $[Cr(Ph_2phen)_3]^{3+}$ presiding in a different excited-state than other photosensitizers (Figure 7.1.1).

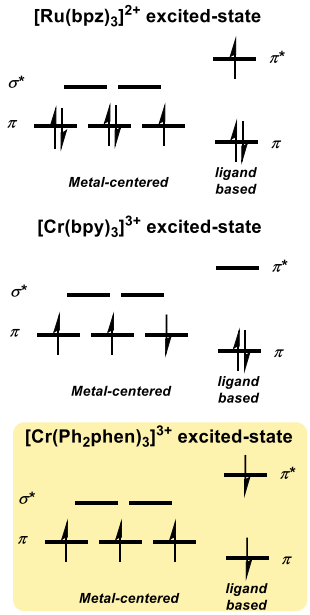


Figure 7.1.1. Representative electron structures of the lowest-energy excited states for $[Ru(bpz)_3]^{2+}$ (top), $[Cr(bpy)_3]^{3+}$ (middle) and $[Cr(Ph_2phen)_3]^{3+}$ (bottom). Other Ru- and Cr-diimine complexes show the same electronic configurations as $[Ru(bpz)_3]^{2+}$ and $[Cr(bpy)_3]^{3+}$, respectively.

These different excited-states wherein a singlet ligand-based excited-state for $[Cr(bpy)_3]^{3+}$ and doublet ligand-based excited-state for $[Ru(bpz)_3]^{2+}$ make electron transfer reactivity viable; however, the triplet ligand-based excited-state for $[Cr(Ph_2phen)_3]^{3+}$ is oriented well for energy transfer reactivity. To provide further details of how these variable electronic structures effect reactivity, we describe a multi-tool approach to provide evidence on the role of substrate and

photocatalyst toward reaction pathway(s) in electron-poor photo(redox/catalysis) cycloaddition reactions.[17] We combine reactivity, spectroscopic, speciation, kinetic and computational methods to progress toward a more complete mechanistic overview of this reaction landscape.

7.2 Division of Labor

All synthesis, characterization, analysis and interpretation was performed by Robert F. Higgins. Interpretation and analysis of experimental details was performed by Eric M. Ferreira, Anthony K. Rappé and Matthew P. Shores.

7.3 Experimental

7.3.1 Preparation of Compounds

Acetonitrile (CH_3CN) was sparged with dinitrogen, passed over alumina, and degassed before use. Nitromethane (CH_3NO_2) was sparged with dinitrogen and subjected to three freeze-pump-thaw cycles before use. The compounds $[Cr(Ph_2phen)_3](BF_4)_3$,[12] $[Cr(dmcbpy)_3](BF_4)_3$ (**7.5**),[13] $[Cr(bpy)_3](BF_4)_3$,[18] (*E*)-3-(4-methoxyphenyl)-1-phenylprop-2-en-1-one,[20] (*E*)-1-methoxy-4-(2-nitrovinyl)benzene (**7.6**),[21] (*E*)-1-(4-(tert-butyl)phenyl)-3-(4-methoxyphenyl)prop-2-en-1-one (**7.7**),[22] ethyl (*E*)-3-(4-methoxyphenyl)acrylate (**7.8**),[23] (*E*)-3-(4-methoxyphenyl)acrylic acid (**7.9**),[24] (E)-1-cyclohexyl-3-(4-methoxyphenyl)prop-2-en-1-one[19] and (2-(4-methoxyphenyl)-3-methyl-3-vinylcyclobutyl)(phenyl)methanone[17] (**7.10**) were synthesized according to known literature preparations. All other compounds and reagents were obtained commercially and used as received.

7.3.2 Mechanistic Measurements and Studies

Reaction quantum yields were determined by the method reported by Yoon and Cismesia.[9] Actinometry experiments were performed using a Newport TLS-300XU tunable light source, which includes a 300 W Xe arc lamp, a Cornerstone 130 monochromator and a motorized filter.

7.3.3 Kinetics Studies

All kinetic parameters (excluding quenching rate constants) were determined by monitoring the course of the reaction *via* ^{1}H NMR until the reaction reached at least 80% completion in each case. Standard reaction conditions were employed for these analyses with 0.1 molar equivalents of mesitylene added as an internal standard. To monitor the reaction, the NMR tube charged with all reagents was removed at discrete time intervals, the stir bar was removed, and the tube was wrapped in felt and transported to the spectrometer. Care was taken to ensure no extraneous light reached the sample. The NMR spectra were collected with a longer-than-normal relaxation delay (t_1 = 5 seconds) to ensure that paramagnetic signals from the Cr-catalyst did not interfere with the acquisition of the spectra.

7.3.4 Other Physical Measurements

All experiments were conducted at room temperature unless otherwise noted. Absorption spectra were obtained with a Hewlett-Packard 8453 spectrometer in quartz cuvettes with a 1 cm path length. Infrared spectra were measured with a Nicolet 380 FT-IR spectrometer. NMR studies were performed on either a Varian 400 MHz spectrometer (paramagnetic spectrum acquisition) or a Varian Inova 500 MHz spectrometer (2D experiments). Mass spectrometric measurements were performed in the positive ion mode on a Thermo LTQ mass spectrometer equipped with an analytical electrospray ion source and a quadrupole ion trap mass analyzer. Each measurement, unless otherwise noted, was performed with the capillary temperature = 175 °C, spray voltage = 5 kV, and spray current = 91 μamps.

7.4 Results and Discussion

7.4.1 Catalyst-Substrate Association

To further validate intermolecular interactions between 4-methoxychalcone and $[Cr(Ph_2phen)_3]^{3+}$ in solution, ^{1}H NMR studies are conducted. When a ^{1}H NMR spectrum is acquired for $[Cr(Ph_2phen)_3](BF_4)_3$ with a standard sequence, no peaks other than solvents are observed, which is expected for the paramagnetic species. Interestingly, performing a

paramagnetic ^{1}H NMR sequence (fast relaxation delays and wider spectral range) to acquire spectroscopic data for $[Cr(Ph_2phen)_3](BF_4)_3$ gives a surprisingly clean spectrum, despite what is normally expected for paramagnetic species, with all peaks within the normal window.[25-26] This is likely due to the isotropic nature of the unpaired electrons in the pseudo-octahedral d^3 electronic geometry as well as the net ionic factor, since $[Cr(Ph_2phen)_3]^{3+}$ is formally a tri-cationic salt.

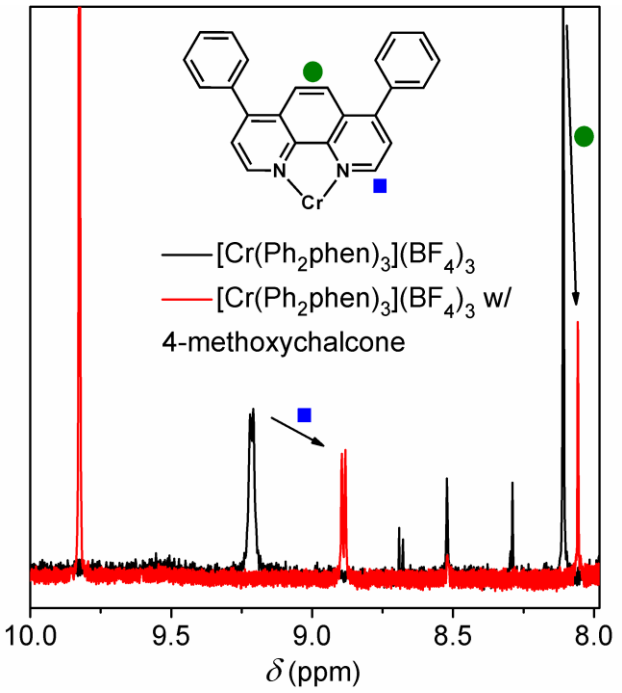


Figure 7.4.1. ^{1}H NMR spectra of $[Cr(Ph_2phen)_3]^{3+}$ (0.0005 M) in CD_3NO_2 with and without the addition of 4-methoxychalcone (50 equiv).

When 4-methoxychalcone is added to a CD_3NO_2 solution of $[Cr(Ph_2phen)_3]^{3+}$, some peaks associated with the bound Ph_2phen ligands to the Cr-center shift (Figure 7.4.1). These peak shifts all occur in the upfield direction (*i.e.*, increased shielding of these protons), which is expected for a π-interaction.[27] Even though a large excess of 4-methoxychalcone is added to see the peak shifts in the ^{1}H NMR spectrum, the optimized reaction conditions deliver a 200:1 ratio of 4-methoxychalcone:$[Cr(Ph_2phen)_3]^{3+}$, and thus this interaction is expected to be pervasive in the

reaction mixture. In addition, this interaction is expected to be critically important to the inherent reaction mechanism(s). Even though the observed peaks that shift are farthest spatially from the phenyl rings, where a π-association is likely to occur, these peaks are not as obscured by the peaks inherent to 4-methoxychalcone, making them easier to track. Further, based on contact shifts with the paramagnetic Cr^{3+} center (d^3, S = 3/2), it is not surprising that these peaks would shift more relative to peaks farther separated from the metal ion. Addition of isoprene (600:1), vinylcyclobutane (VCB) (**7.11**) of **7.3** and **7.4** (200:1), *tert*-butyl enone **7.9** (200:1), cyclohexyl enone **7.10** (200:1) or complete exclusion of O_2 does not cause any peak shifts in the paramagnetic ^{1}H NMR spectrum of $[Cr(Ph_2phen)_3]^{3+}$.

To further understand the extent of these intermolecular interactions, other photosensitizers are investigated. The ^{1}H NMR data collected for $[Cr(bpy)_3](BF_4)_3$ and $[Cr(dmcbpy)_3](BF_4)_3$ show no peak shifts upon addition of enone **7.3** in CD_3NO_2. These results invoke that $[Cr(Ph_2phen)_3]^{3+}$ shows differences when compared to other Cr-photosensitizers.[28]

7.4.2 Substrate-Substrate Association Studies

Unfortunately, we were not able to calculate a quantitative association constant for the interaction of $[Cr(Ph_2phen)_3]^{3+}$ and 4-methoxychalcone. While this is a puzzling discovery, upon further examination, it is likely due to complications in the solution properties of 4-methoxychalcone. Mass spectrometry offers sensitivity to low concentrations and can be used in the identification of strong intermolecular interactions.[29-30] The mass spectrum of 4-methoxychalcone shows evidence of dimerization and tetramerization in solution likely due to aggregation in solution (Figure 7.4.2, left side: a figure); interestingly, the *dimer* peaks are higher in intensity than the monomer peak, indicative that the equilibrium in solution may be pushed to the *dimer*. In contrast, cyclohexyl-based substrate **7.10** does not show any higher order mass peaks, indicating that any interactions are most likely not occurring as strongly here for cyclohexyl-based substrate **7.10** as for 4-methoxychalcone. Further, these data indicate that this aggregation is likely from π-interactions, which we hypothesized in our previous work.[19] Interestingly, when an

aromatic solvent is used (benzene or toluene), only the parent ion is observed as the protonated mono-cation.

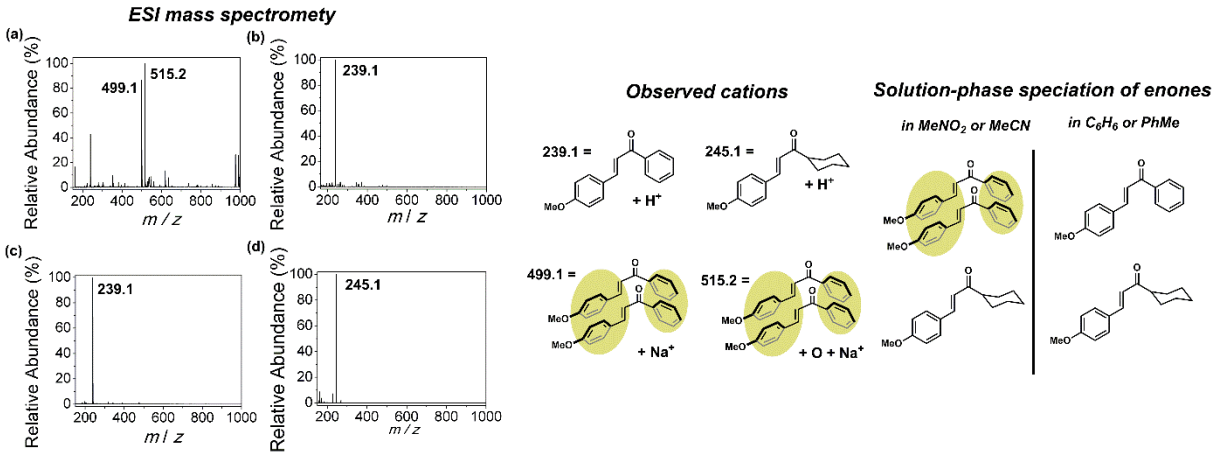


*Figure 7.4.2. Mass spectra of (a) enone **7.3** (0.010 M) in CH_3NO_2, (b) enone **7.3** (0.010 M) in C_6H_6, (c) enone **7.3** (0.010 M) in $PhCH_3$ and (d) cyclohexyl **7.10** (0.010 M) in CH_3NO_2 in the positive ion mode the highest intensity peaks labeled. Note: The chalcone dimers are drawn arbitrarily as head-to-head even though other arrangements are conceivable.*

These results indicate not only that π-interactions are likely present in solution for enone **7.3**, but also that these interactions can be “turned off” by dearomatizing one of the two phenyl rings present in the molecule. Multiple other control experiments indicate that these interactions are not a manifestation of the mass spectrometer and do give qualitative insight into the solution dynamics of enone **7.3** and related species. In support of these findings, other studies have shown the presence of intermolecular interactions through ESI-MS experiments.[29-31] The equilibria of these chalcones can apparently be perturbed though by solubilizing enone **7.3** in aromatic solvents. When toluene or benzene are used as solvent, only the parent ion of 4-methoxychalcone in its protonated form is observed in the mass spectra. These experiments indicate that when solvents π-interact with 4-methoxychalcone, the self-association of 4-methoxychalcone is

disturbed and the equilibria are shifted more towards the monomer.[32] These findings are in agreement with an electronic absorption study on the parent complex, chalcone, in cyclohexane.[33]

7.4.3 Kinetic Studies

To further understand this system and attempt to provide rate determining steps for these reactions, kinetic data tracking the time-course of the reaction are collected and presented for substrates enone **7.3**, nitroalkene **7.6** and cyclohexane **7.10**. To accomplish this, isolable reactive intermediates are resubjected to ascertain their potential kinetic competency in the reaction manifold as well. Three separate reactions are analyzed using initial rate kinetic data to determine rate orders and constants of all characterizable species present (Figure 7.4.1). These reactions are as follows: (1) the light-induced [2+2] cycloaddition between the selected dienophile and isoprene without any $[Cr(Ph_2phen)_3]^{3+}$ added, (2) the vinylcyclobutane rearrangement of isolated VCBs to the cyclohexene products in the presence of $[Cr(Ph_2phen)_3]^{3+}$, and (3) the optimized reaction conditions. All individual plots for each of these experiments are available in the appendix (Figures A7.1-A7.10).

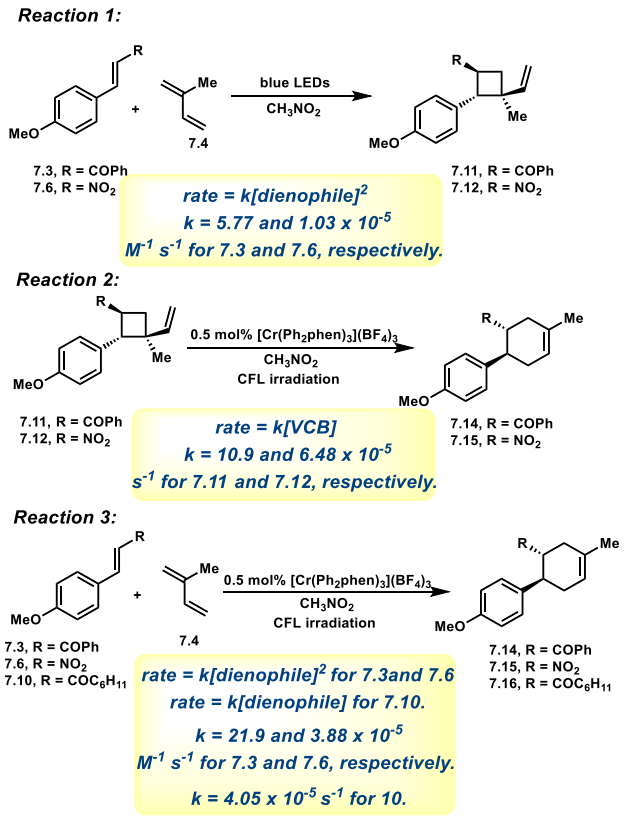


Figure 7.4.1. Different reactions monitored for kinetic data.[a]

[a]reaction 1 used a higher energy irradiation source because it failed to progress at a reasonable rate with CFL irradiation.

For the [2+2] cycloaddition in the absence of catalyst, (reaction 1), the reaction shows pseudo-second order behavior with respect to enone **7.3** and pseudo-zeroth order behavior with respect to the diene, with a rate constant of $k_{[2+2]} = 5.77 \times 10^{-5}$ M^{-1} s^{-1}. When nitroalkene **7.6** is used in place of 4-methoxychalcone, the same rate orders are observed with a rate constant of $k_{[2+2]} = 1.03 \times 10^{-5}$ M^{-1} s^{-1}. These reactions are remarkably slow; however, the rates are reasonable considering a light-promoted [2+2] cycloaddition between an electron-poor alkene and a relatively unreactive diene is expected to be slow.[34] Also, these rates are likely slower than what occurs in the optimized reaction, since this measurement only gives the rates for the light-promoted [2+2] reaction between these electron deficient alkenes and isoprene, whereas $[Cr(Ph_2phen)_3]^{3+*}$ is

potentially able to perform an oxidatively-promoted [2+2] reaction between these two species via the aforementioned substrate excited state pathway.

When the isolated [2+2] product, VCB **7.11**, is subjected to reaction conditions (reaction 2), the kinetic data appears pseudo-first order in the process. In addition, the catalyst ($[Cr(Ph_2phen)_3]^{3+}$) is found to be pseudo-zeroth order. The rate constant for this transformation is $k_{VCB} = 1.09 \times 10^{-4}$ s^{-1} which is quite fast considering the other elementary step(s) studied. When nitro-VCB **7.12** is subjected to the same conditions as described above, the rate orders of individual components are identical, and the rate constant for the reaction is $k_{VCB} = 6.48 \times 10^{-5}$ s^{-1}. The overall rates are reasonable when compared to other sigmatropic rearrangements of vinylcyclobutanes.[35-37] Given the pseudo-first order kinetics with respect to VCB **7.11,** the rate determining step involves oxidation of this species, prior to the vinylcyclobutane rearrangement. Although the diene is not present in any rate law, it is worth noting that yields still decrease precipitously when fewer than three equivalents of isoprene are added. Finally, the catalyst also does not appear in any rate law determined, which has been observed in photocatalytic reactions previously,[38] and which is expected for photon-limited transformations. Variable photon flux experiments are performed where a strong dependence on reaction rate is observed, indicating that this reaction is photon-limited (Figure A7.11).

Finally, the optimized reaction (reaction 3), displays a rate dependence on enone **3** (pseudo-second order), while no rate dependence for either isoprene or $[Cr(Ph_2phen)_3]^{3+}$ is observed. The rate constant for the overall reaction was found to be $k_{[4+2]} = 2.19 \times 10^{-4}$ M^{-1} s^{-1} when considering the rate dependencies of enone **7.3**. Meanwhile, when enone **7.3** is replaced by nitroalkene **7.6**, the same rate law is observed and the rate constant is $k_{[4+2]} = 3.88 \times 10^{-5}$ M^{-1} s^{-1}. On the other hand, when cyclohexane **7.10** is monitored, pseudo-first order behavior is observed for cyclohexane **7.10** and no rate dependence for diene **7.4** or $[Cr(Ph_2phen)_3]^{3+}$, where the determined rate constant is $k_{[4+2]} = 4.05 \times 10^{-5}$ s^{-1}. These results indicate that the overall structure of the substrate dictates the rate law of the reaction but does not impede reactivity under

the optimized conditions. Further, these results suggest that energy transfer from $[Cr(Ph_2phen)_3]^{3+}$ to the dienophile is likely the rate-determining step, which is also photon-limited.

The peculiar second-order kinetics require a reaction or pre-equilibria prior to the presumed photocatalytic cycle (*e.g.*, [2+2] coupling). Previously, some of us investigated the reactivity of the homo-[2+2] product **7.13**, which consists of two molecules of enone **7.3**, towards isoprene in our photocatalytic reaction manifold.[17] We found that cyclobutane **7.13** shows a yield of 20% (**7.13** → **7.14**) and a 16% yield of cycloreversion to enone **7.3** under the optimized reaction conditions, suggesting it is likely not involved in the predominant pathway in this reaction. This indicates production/formation of cyclobutane **7.13** is likely not a viable explanation for pseudo-second order kinetics (with respect to enone **7.3**) that we observe herein, implicating the involvement of an association between 4-methoxychalcone molecules, in agreement with the mass spectrometric results. The results for cyclohexane **7.13** indicate it is *not* a requirement of the reaction for two equivalents of dienophile to be present for efficacious reactivity and instead appears to be a feature of the structural makeup of the specific dienophile. Notwithstanding, it is possible that a more complex mechanism is present, but we have not gathered any additional data to indicate a reasonable alternative at this time.

7.4.4 Other quantum yield studies

Thus far, it appears that $[Cr(Ph_2phen)_3]^{3+}$ is discriminate to the substrate for this reactivity. Based on our previous results and the present results the substrates *tert*-butyl derivative **7.9** and cyclohexane **7.10** do not associate with the catalyst, $[Cr(Ph_2phen)_3]^{3+}$. Without association, the substrates should be free to migrate in solution and be susceptible to radical chain propagation. To investigate this hypothesis, a few different experiments are performed.

As previously stated, when $[Cr(Ph_2phen)_3]^{3+}$, *tert*-butyl derivative **7.9** and isoprene are subjected to monochromatic 450 nm irradiation, no product is formed (Figure 2, section a). Since radical chain propagation relies upon thermodynamic redox potentials, doping experiments could probe this phenomenon. Specifically, VCB **7.11** is doped into a solution of *tert*-butyl derivative **7.9**

and monitored to see if ^{t}Bu-cyclohexene **7.17** is formed through enone entry into the radical cascade at 450 nm (section b in Figure 2). Indeed, ^{t}Bu-cyclohexene **7.17** is formed when $[Ru(bpz)_3]^{2+}$ is irradiated at single wavelength 450 nm light in the presence of *tert*-butyl derivative **7.9**, isoprene and VCB **7.11**. Since compound **7.9** does not show association with $[Cr(Ph_2phen)_3]^{3+}$ *via* our NMR experiments, an analogous experiment is performed with $[Cr(Ph_2phen)_3]^{3+}$ in place of $[Ru(bpz)_3]^{2+}$. Once again, ^{t}Bu-cyclohexene **7.17** forms; the detection of small amounts of radical chain propagation is revealed when a substrate-catalyst association is not viable when $[Cr(Ph_2phen)_3]^{3+}$ is used. To further support this observation of radical chain propagation with *tert*-butyl derivative **7.9**, reaction quantum yields are gathered. When $[Ru(bpz)_3]^{2+}$ is used, Φ = 5.1(5) and with $[Cr(Ph_2phen)_3]^{3+}$, Φ = 1.8(3) (sections c and d of Figure 10, respectively). These results indicate that the association event suppresses the formation of long radical chains in solution, therefore, giving similar reactivity profiles for $[Ru(bpz)_3]^{2+}$ and $[Cr(Ph_2phen)_3]^{3+}$.

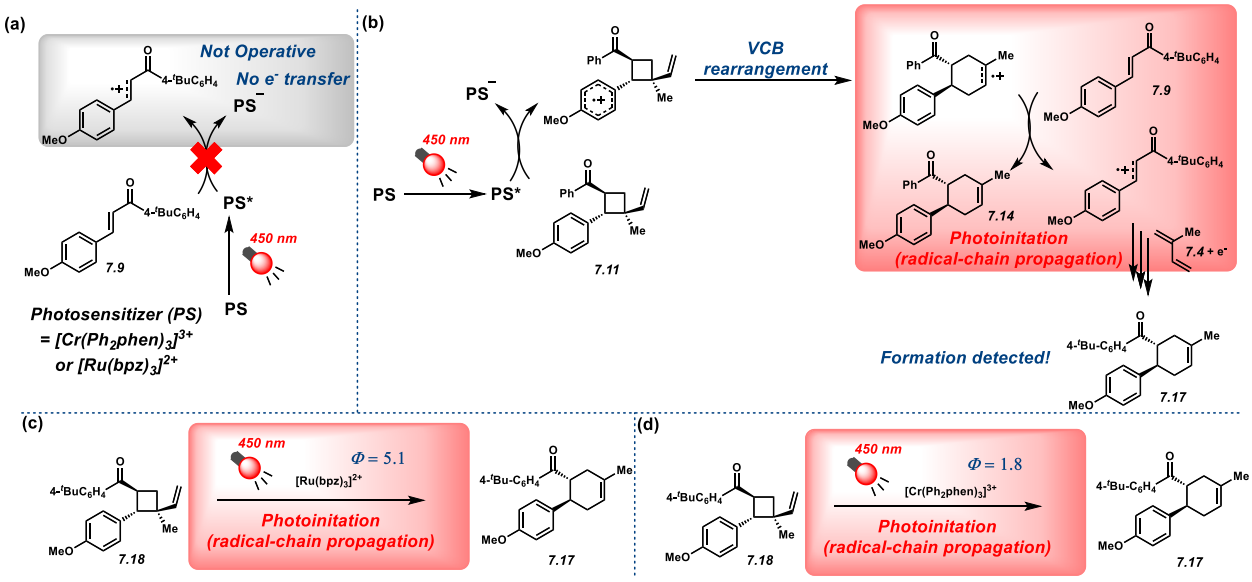


Figure 7.4.2. Outline of different reaction pathways for $[Ru(bpz)_3]^{2+}$ and $[Cr(Ph_2phen)_3]^{3+}$ with bulky dienophiles.

7.5 Conclusions and Outlook

In conclusion, these results indicate that the catalyst, $[Cr(Ph_2phen)_3]^{3+}$, acts as a photocatalyst toward 4-methoxychalcone through a pre-association event between substrate and catalyst through an energy transfer mechanism. An especially important distinction of this reactivity is that all other photosensitizers tested are not able to perform this pathway. In addition, we present novel methods to investigate mechanistic subtitles of photoredox reactions for straightforward analysis about intermolecular interactions and the presence of radical chains in solution.

References

1. Houk, K. N.; González, J.; Li, Y. *Acc. Chem. Res.* **1995**, *28*, 81.

2. Bauld, N. L.; Bellville, D. J.; Harirchian, B.; Lorenz, K. T.; Pabon, R. A.; Reynolds, D. W.; Wirth, D. D.; Chiou, H.-S.; Marsh, B. K. *Acc. Chem. Res.* **1987**, *20*, 371.

3. Birney, D. M.; Houk, K. N. *J. Am. Chem. Soc.* **1990**, *112*, 4127.

4. Shaw, M. H.; Twilton, J.; MacMillan, D. W. C. *J. Org. Chem.* **2016**, *81*, 6898.

5. Studer, A.; Curran, D. P. *Angew. Chem., Int. Ed.* **2016**, *55*, 58.

6. Blum, T. R.; Miller, Z. D.; Bates, D. M.; Guzei, I. A.; Yoon, T. P. *Science* **2016**, *354*, 1391.

7. Welin, E. R.; Le, C.; Arias-Rotondo, D. M.; McCusker, J. K.; MacMillan, D. W. C. *Science* **2017**, *355*, 380.

8. Skubi, K. L.; Kidd, J. B.; Jung, H.; Guzei, I. A.; Baik, M.-H.; Yoon, T. P. *J. Am. Chem. Soc.* **2017**, *139*, 17186.

9. Cismesia, M. A.; Yoon, T. P. *Chem. Sci.* **2015**, *6*, 5426.

10. Lin, S.-S.; Ischay, M. A.; Fry, C. G.; Yoon, T. P. *J. Am. Chem. Soc.* **2011**, *133*, 19350.

11. Stevenson, S. M.; Shores, M. P.; Ferreira, E. M. *Angew. Chem. Int. Ed.* **2015**, *54*, 6506.

12. Higgins, R. F.; Fatur, S. M.; Shepard, S. G.; Stevenson, S. M.; Boston, D. J.; Ferreira, E. M.; Damrauer, N. H.; Rappé, A. K.; Shores, M. P. *J. Am. Chem. Soc.* **2016**, *138*, 5451.

13. McDaniel, A. M.; Tseng, H.-W.; Damrauer, N. H.; Shores, M. P. *Inorg. Chem.* **2010**, *49*, 7981.

14. Prier, C. K.; Rankic, D. A.; MacMillan, D. W. C. *Chem. Rev.* **2013**, *113*, 5322.

15. Crutchley, R. J.; Lever, A. B. P. *Inorg. Chem.* **1982**, *21*, 2276.

16. Gonzales-Velasco, J.; Rubinstein, I.; Crutchley, R. J.; Lever, A. B. P.; Bard, A. J. *Inorg. Chem.* **1983**, *22*, 822.

17. Stevenson, S. M.; Higgins, R. F.; Shores, M. P.; Ferreira, E. M. *Chem. Sci.* **2017**, *8*, 654.

18. Higgins, R. F.; Fatur, S. M.; Damrauer, N. H.; Ferreira, E. M.; Rappé, A. K.; Shores, M. P. *In submission.*

19. Higgins, R. F.; Damrauer, N. H.; Ferreira, E. M.; Rappé, A. K.; Shores, M. P. *In submission.*

20. Chang, M.-Y.; Tsai, C.-Y.; Wu, M.-H. *Tetrahedron* **2013**, *69*, 6364.

21. Yang, H. Q.; Fu, L. M.; Wei, L. J.; Liang, J. F.; Binks, B. P. *J. Am. Chem. Soc.* **2015**, *137*, 1362.

22. Matthias, C.; Cartoni, A.; Kuck, D. *Int. J. Mass Spectrom.* **2006**, *255*, 195.

23. Kelly, C. B.; Ovian, J. M.; Cywar, R. M.; Gosselin, T. R.; Wiles, R. J.; Leadbeater, N. E.; *Org. Biomol. Chem.* **2015**, *13*, 4255.

24. Salabert, J.; Sebastián, R. M.; Vallribera, A.; Cívicos, J. F.; Nájera, C. *Tetrahedron* **2013**, *69*, 2655.

25. Drago, R. S. *Physical methods for chemists.* 2nd ed.; Saunders College Pub.: Ft. Worth, 1992.

26. La Mar, G. N.; Horrocks, W. D.; Holm, R. H. *NMR of paramagnetic molecules; principles and applications.* Academic Press: New York, 1973.

27. Shetty, A. S.; Zhang, J. S.; Moore, J. S. *J. Am. Chem. Soc.* **1996**, *118*, 1019.

28. To address some other possibilities, it does not appear that any of this reactivity proceeds through Cr(0)-arene intermediates, which are possible if this was an intermolecular interaction. Exposure of $Cr(CO)_6$ (5 mol%) to the optimized reaction conditions gives no product after 16 hours of CFL irradiation. Further, subjection of VCB **7.10** (0.10 M) to $Cr(CO)_6$ gives no product after the same irradiation conditions. Of final note, both of these experiments were stirred in the dark for ~3 hours prior to any irradiation in hope of forming the tricarbonyl-chromium arene complex prior to any possible electron transfer. As mentioned above, Zhang and others reported on a pyrenyl photosensitizer that experiences π-interactions with fluorinated substrates prior to electron transfer (reference 21). While it might be more surprising that ligated Ph_2phen units display π-interactions with substrates compared to substituted pyrenes, this ligand still contains a large conjugated π-system. In a related system, $[Cr(Ph_2phen)_3]^{3+}$ was found to show divergent emission behavior when embedded in poly-electric materials containing cyclohexyl microdomains (increased ^2E emission signal) when compared to naphthyl microdomains (decreased ^2E emission signal), reference: Canete, P.; Rios, H. E.; Vargas, V.; Ronco, S.; Isaacs, M.; Urzua, M. D., *J. Colloid. Interface Sci.* **2008,** *318*, 183-187. These results collectively implicate this novel, associative reaction pathway that it appears selective to the $[Cr(Ph_2phen)_3]^{3+}$ catalyst.

29. Frański, R.; Gierczyk, B. *J. Am. Soc. Mass Spectr.* **2010**, *21*, 545.

30. Qin, Z.; Qiu, B.; Sun, J. M.; Zhao, W. B.; Luo, H. *J. Mass Spectrom.* **2014**, *49*, 266.

31. Banerjee, S.; Yang, Y.-F.; Jenkins, I. D.; Liang, Y.; Toutov, A. A.; Liu, W.-B.; Schuman, D. P.; Grubbs, R. H.; Stoltz, B. M.; Krenske, E. H.; Houk, K. N.; Zare, R. N. *J. Am. Chem. Soc.* **2017**, *139*, 6880.

32. One final note about this technique, that is of the utmost importance, is the ionization source of the mass spectrometry performed. All mass spectrometry (outside of characterizing novel organic molecules) that is performed herein uses an electrospray ionization (ESI) source, specifically with a linear-trap quadrupole (LTQ). This instrument gives relatively soft ionization, and a harder ionization method would probably dismantle the molecular framework of enone **7.3** and thus its intermolecular interactions. Further, soft ionization probably indicates what occurs in solution to a more accurate degree than hard ionization methods. Even though cyclohexyl

substrate **7.10** does not show π-interactions in the ESI-MS experiments, it still reacts efficiently in our overall [4+2] chemistry. Therefore, these substrate-substrate interactions are not a requirement for the reactivity but instead a feature of some of these species. A multitude of different techniques and control experiments are performed to detect any possible substrate-substrate interaction.

33. Blanco, S. E.; Ferretti, F. H. *Talanta* **1998**, *45*, 1103.

34. Schuster, D. I.; Lem, G.; Kaprinidis, N. A. *Chem. Rev.* **1993**, *93*, 3.

35. Bauld, N. L. *Tetrahedron* **1989**, *45*, 5307.

36. Reynolds, D. W.; Harirchian, B.; Chiou, H.-S.; Marsh, B. K.; Bauld, N. L. *J. Phys. Org. Chem.* **1989**, *2*, 57.

37. Kim, T.; Pye, R. J.; Bauld, N. L. *J. Am. Chem. Soc.* **1990**, *112*, 6285.

38. Yayla, H. G.; Peng, F.; Mangion, I. K.; McLaughlin, M.; Campeau, L.-C.; Davies, I. W.; DiRocco, D. A.; Knowles, R. R. *Chem. Sci.* **2016**, *7*, 2066.

Chapter 8: Ferrocenium as a catalytic single electron transfer reagent with excited-state organic substrates.

8.1 Introduction

The ferrocenium/ferrocene redox couple is arguably the most studied electrochemical phenomenon in organometallic chemistry.[1] This redox couple is fully reversible and is used as an internal standard by many organometallic/coordination chemists at the conclusion of electrochemical experiments.[2] One of the most common uses for ferrocenium, or electronically modified ferrocenium analogues, has been as a stoichiometric one electron oxidant for coordination and organometallic complexes.[1] Some other uses for ferrocene derivatives in synthetic methods include incorporation into ligand backbones for selective reactivity,[3-5] while others have recently prepared metallo-polymers or self-capped chains for increased electrochemical control.[6-7]

Even with its rich history and fully reversible electrochemistry, it is uncommonly used sub-stoichiometrically in organic chemistry.[8] Some of the common uses for sub-stoichiometric ferrocenium have been in redox relays[9-13] and polymerizations in electrochemical methods.[14-16] A unique example reported by the Jahn group involves low loadings (5 mol%) of ferrocene to a TEMPO salt to perform a *catalytic* tandem aza-Michael/radical cyclization reaction.[17] Other catalytic uses of ferrocenium involve its Lewis acidic nature to perform Diels-Alder reactions.[18-19] Of particular interest to this study, the Ross group has reported a sub-stoichiometric Lewis-acidic Diels-Alder coupling of electron-poor alkenes and dienes.[20] Interestingly, we are not aware of a catalytic use of ferrocenium as an electron transfer reagent without a redox relay (*i.e.*, electrochemical reactivity) system present. This reveals an exciting and untapped use of ferrocenium for various radical-based organic transformations.

From a classical perspective, studies by Bauld,[21-22] Steckhan[23-24] and others[25] used potent ground-state single electron transfer (SET) reagents to initiate reactions (mainly cycloadditions)

that propagate *via* radicals. Conversely, a report by Caldwell and Singh in 1983, some substituted chalcone molecules have shown excited-state lifetimes at quite large energies to perform energy-transfer.[26] For example, the aromatic olefin, 4-methoxychalcone (**8.1**), has an emission energy of λ_{em} = 480 nm (2.58 eV, 60 kcal mol^{-1}) and a lifetime of τ = 23 ns.[26] From a synthetic perspective, this is a highly tempting pathway to exploit for new reaction development because of the extremely large energies.

Figure 8.1.1 shows an energy diagram which describes the ground-state and excited-state energies for this enone. Interestingly, when 4-methoxychalcone is an excited-state,[26-27] ferrocenium has 0.93 eV (21 kcal mol^{-1}) of thermodynamic force for an electron transfer event.[1] After electron transfer, the radical cation of 4-methoxychalcone can be quenched by a diene to form a cycloaddition product. This cyclohexenyl radical cation shows a redox potential of +1.33 V vs Fc^{+}/Fc,[28] which means that its one-electron oxidized radical cation is thermodynamically reducible by ferrocene (1.33 eV of driving force, 31 kcal mol^{-1}), giving the potential for a catalytic system. This idea has similarities to recent work by the Melchiorre group;[29] however, the electron transfer reagent in this work always remains in the ground-state and the photosensitizer is the substrate. The proposed reactivity also allows us to study the prevalence of a solely excited-state pathway by an organic substrate, which we proposed is potentially viable in an analogous photoredox reaction promoted by a Cr-photocatalyst.[27] Therefore, we set out to determine the synthetic utility of ferrocenium as a catalytic electron transfer reagent.

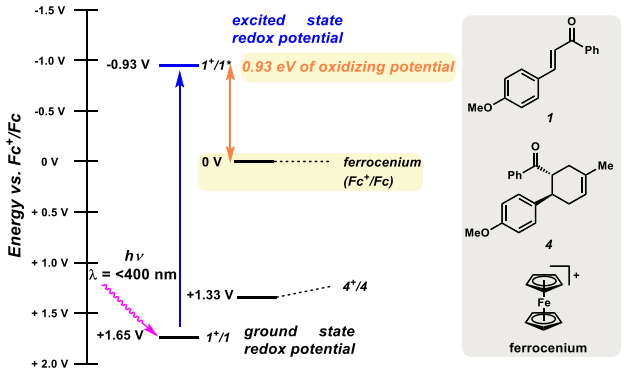


Figure 8.1.1. Energy profiles of 4-methoxychalcone and selected electron transfer reagents.

8.2 Division of Labor

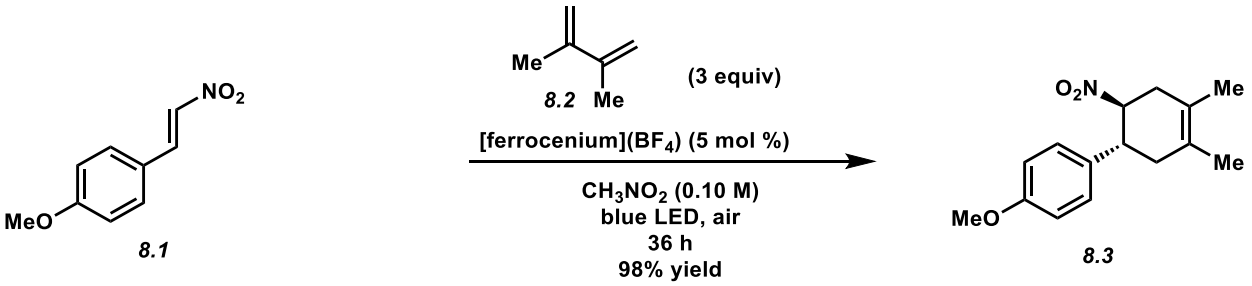
Unless otherwise noted, all synthesis, characterization, analysis and interpretation was performed by Robert F. Higgins. All interpretation and analysis o experimental details was performed by Eric M. Ferreira and Matthew P. Shores.

8.3 Experimental

8.3.1 Preparation of Known Compounds

The compounds [Fc](BF_4) (Fc = bis(cyclopentadienyl)iron),[30] [Fc](Bar^F) (Bar^F = tetrakis(3,5-bis(trifluoromethyl)phenyl)borate),[31] [Me_8Fc](BF_4),[32-33] [Me_{10}Fc](PF_6),[34] (*E*)-3-(4-methoxyphenyl)-1-phenylprop-2-en-1-one,[35] (*E*)-1-methoxy-4-(2-nitrovinyl)benzene,[36] (*E*)-1-(4-(tert-butyl)phenyl)-3-(4-methoxyphenyl)prop-2-en-1-one,[37] ethyl (*E*)-3-(4-methoxyphenyl)acrylate,[38] (*E*)-3-(4-methoxyphenyl)acrylic acid,[39] (2-(4-methoxyphenyl)-3-methyl-3-vinylcyclobutyl)(phenyl)methanone were synthesized according to known literature preparations. Ferrocene was sublimed before use. All other compounds and reagents were obtained commercially and used as received.

8.3.2 Preparation of Novel Compounds



Cyclohexene 8.3.

Prepared according to the General Procedure using alkene **8.1** (16.2 mg, 0.0904 mmol), diene **8.2** (30.8 µL, 0.282 mmol), [Fc](BF_4) (1.23 mg, 0.00452 mmol) and nitromethane (0.900 mL). The reaction mixture was irradiated for 36 h. The crude product was purified by flash chromatography (9:1 hexanes/EtOAc eluent) to afford cyclohexene **8.3** (23.2 mg, 98% yield) as an off-white solid.

TLC: R_f = 0.70 in 3:1 hexanes/EtOAc, visualized by UV.

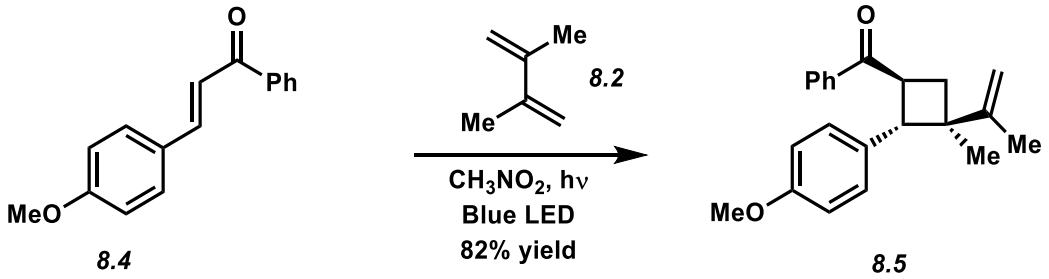
^{1}H NMR (400 MHz; $CDCl_3$): δ 7.14 (d, *J* = 9.0 Hz, 2H), 6.85 (d, *J* = 8.6 Hz, 2H), 4.89 (td, *J* = 11.0, 5.5 Hz, 1H), 3.78 (s, 3H), 3.36 (ddd, *J* = 17.6, 10.2, 7.4 Hz, 1H), 2.83-2.77 (m, 1H), 2.61-2.56 (m, 1H), 2.35-2.28 (m, 2H), 1.71 (s, 3H), 1.66 (s, 3H).

^{13}C NMR (100 MHz; $CDCl_3$): δ 158.9, 132.1, 128.3, 125.7, 122.0, 114.2, 88.2, 55.2, 44.1, 39.5, 37.1, 18.5, 18.4.

IR (ATR, neat): 2916, 2841, 1614, 1547, 1515, 1372, 1247, 1035, 833, 557 cm^{-1}.

HRMS (ESI+): *m/z* calc'd for $(M+NH_4)^+$ $[C_{15}H_{23}N_2O_3]^+$: 279.1709, found 279.1703.

This molecule has been characterized previously,[40] although some of the spectroscopic data do not perfectly match, which is why we present these data.



VCB 8.5.

To enone **8.4** (375 mg, 1.57 mmol) in CH_3NO_2 (786 µL) was added diene **8.2** (3.57 mL, 31.4 mmol, 20 equiv). The reaction mixture was capped, stirred and irradiated with blue LEDs for 24 h when full consumption of the enone starting material was observed. Then, CH_3NO_2 was removed by rotary evaporation and the crude mixture was purified by flash chromatography (15:1 hexanes/EtOAc eluent) to afford VCB **8.5** (0.431 g, 82% yield) as a white powder.

TLC: R_f = 0.64 in 3:1 hexanes/EtOAc, visualized by UV.

^{1}H NMR (400 MHz; $CDCl_3$): δ 7.92 (d, *J* = 7.4 Hz, 2H), 7.54 (t, *J* = 7.0 Hz, 1H), 7.43 (t, *J* = 7.8 Hz, 2H), 7.17 (d, *J* = 8.6 Hz, 2H), 6.84 (d, *J* = 8.6 Hz, 2H), 4.93 (dd, *J* = 16.8, 10.2 Hz, 1H), 4.83 (d, *J* = 24.3 Hz, 1H), 4.17 (q, *J* = 9.4 Hz, 1H), 4.17 (d, *J* = 9.8 Hz, 1H), 3.79 (s, 3H), 2.38 (t, *J* = 10.2 Hz, 1H), 2.17 (t, *J* = 10.2 Hz, 1H), 1.79 (s, 3H), 1.17 (s, 3H).

^{13}C NMR (100 MHz; $CDCl_3$): δ 200.4, 158.2, 152.6, 136.2, 132.9, 132.0, 129.2, 128.5, 128.4, 113.5, 108.6, 55.2, 47.7, 45.1, 41.3, 36.0, 22.0, 18.8.

IR (ATR, neat): 3070, 2921, 1677, 1515, 1449, 1252, 1183, 1040, 828, 692 cm^{-1}.

HRMS (ESI+): *m/z* calc'd for $(M+H)^+$ $[C_{22}H_{25}O_2]^+$: 321.1855, found 321.1847.

8.3.3 Reactivity Studies

Reactions were performed in $MeNO_2$ with the dienophile (0.10 M), diene (3 equiv) and 5 mol% ferrocenium salt added with irradiation from a Kessil® A160WE TUNA BLUE LED source at the highest intensity and most blue (lowest energy) setting ~3 inches from the vials. The measured temperature of the vials ranged from 30-32 °C over the course of the reaction. Mesitylene (0.010 M) was added as an internal standard for all optimization and substrate scope experiments to

acquire conversion percentages or NMR yields. After irradiation was schecomplete for an experiment, the solvent was removed under vacuum and the crude mixture was passed through a silica plug (~2 inches of silica gel with a 0.5 cm diameter pipette, Silicycle silica gel (230-400 mesh)) in CH_2Cl_2. After 25 mL of CH_2Cl_2 was eluted, the collected solution was evaporated to dryness and a ^1H NMR spectrum was obtained. The ferrocenium complexes were kept in a glovebox (MBraun Labmaster 130 or Vigor SciLab SG2400) to ensure their stability.

8.3.4 Mechanistic Measurements and Studies

Reaction quantum yields were determined by the method reported by Yoon and Cismesia.[41] Actinometry experiments were performed using a Newport TLS-300XU tunable light source, which includes a 300 W Xe arc lamp, a Cornerstone 130 monochromator and a motorized filter.

Samples of the photocatalyst dissolved in 3.0 mL of nitromethane were prepared in 1 cm × 1 cm quartz cuvettes with an absorbance of ~0.1 at the excitation wavelength, 450 nm. Addition of a known volume of a stock solution of the quencher dissolved in nitromethane was used to achieve the desired concentration.

Single-wavelength experiments were performed using the same instrumentation as the actinometry studies. These experiments were performed in an NMR tube at a specified time for consistency among experiments. Once the sample was irradiated for the allotted time, the stir bar was removed, and the NMR tube was wrapped in felt and carried to the NMR spectrometer. An ^1H NMR spectrum was then collected where conversion percentages were determined through relative integrations using mesitylene (normally 0.010 M) as an internal standard.

8.3.5 Other Physical Measurements

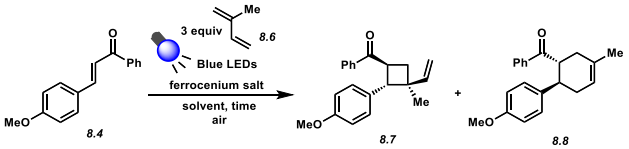
Infrared spectra were measured with a Bruker Tensor II spectrometer with an ATR attachment using a diamond crystal. Electronic absorption spectra were measured with a Hewlett-Packard 8453 spectrometer in quartz cuvette with a 1 cm path length. NMR studies were performed on a Varian 400 MHz spectrometer (paramagnetic spectrum acquisition). Fluorometry

experiments were performed on a Horiba Jobin-Yvon FluoroLog-3 Spectrofluorometer with a 450W Xenon lamp. Samples were dissolved in MeCN until the absorption where excitation will be performed reaches a value of ~0.1 abs. Excitation wavelengths for different substrates ranged from λ_{ex} = 320-380 nm, in 20 nm increments, with no observable changes. The excitation wavelengths used for VCB **8.7** ranged from λ_{ex} = 260-280 nm, in 5 nm increments. Mass spectrometric measurements were performed in the positive ion mode on a Thermo LTQ mass spectrometer equipped with an analytical electrospray ion source and a quadrupole ion trap mass analyzer. Each measurement, unless otherwise noted, was performed with the capillary temperature = 175 °C, spray voltage = 5 kV, and spray current = 91 μamps. High resolution mass spectrometry was performed on an Agilent 6220 TOF LC/MS interfaced to an Agilent 1200 HPLC with an ESI source.

8.4 Results and Discussion

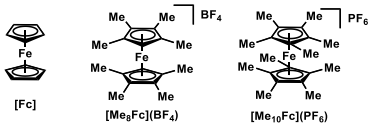
To begin, stoichiometric ferrocenium is added to a reaction mixture of **8.4** and isoprene (**8.6**) to determine if this reactivity is viable. After 6 hours of irradiation, conversion to vinylcyclobutane (VCB, **8.7**) and cyclohexenyl products is observed (Figure 8.4.1). Interestingly, *decreased* mole loadings of ferrocenium species display *increased* reactivity. The low conversions observed with stoichiometric ferrocenium are likely caused by competitive absorption by the ferrocenium species which results in less enone **8.4** species in excited states. The choice of ferrocenium salt does not have a large impact on the overall conversion to either product (*e.g.*, [2+2] or [4+2]). Using methyl-decorated ferrocenium species gives diminished reactivity, which is likely due to the more cathodic reduction potentials of the salts (see Figure 8.4.1).[1] Reactions that are performed under inert conditions or in the dark show decreased reactivity. Isolation/resubjection of VCB **8.7** to reaction conditions does not show conversion to compound **8.8**, indicating that electron transfer from [**8.4**]* to ferrocenium is likely the operative and potentially only pathway (*vide infra*). This is important as it indicates this reaction is likely *not* a cascade sequence and indicates that direct reactivity with enone **8.4** and ferrocenium is more likely the

operative mechanism. The lack of oxidation of VCB **8.7** under these reaction conditions is expected since the redox potential of **8.7** ($E°_{ox}$ = + 0.77 V vs. Fc^+/Fc in $MeNO_2$)[42] and lack of a long-lived excited state.[43]



entry	ferrocenium salt	mol% loading	solvent	time (h)	conversion to 8.7 (%)	conversion to 8.8 (%)
1	$[Fc](BF_4)$	100	$MeNO_2$	6	12	9
2[e]	$[Fc](BF_4)$	100	$MeNO_2$	6	9	4
3[f]	$[Fc](BF_4)$	100	$MeNO_2$	6	0	0
4	$[Fc](BF_4)$	100	$MeNO_2$	24	39	43
5	$[Fc](BF_4)$	20	$MeNO_2$	24	33	46
6[c]	$[Fc](BF_4)$	5	$MeNO_2$	24	16	69
7	$[Fc](BF_4)$	1	$MeNO_2$	24	21	27
8	$[Me_8Fc](BF_4)$	5	$MeNO_2$	24	30	61
9	$[Me_{10}Fc](PF_6)$	5	$MeNO_2$	24	26	59

[c] reaction goes to full conversion after 36 h. [e] reaction was sparged with N_2 before irradiation.
[f] reaction was performed in the dark. No starting material was consumed for this entry.



$E_{1/2}$ in MeCN vs. Fc^+/Fc (V) = 0 -0.35 -0.59

Figure 8.4.1. Optimization of reaction conditions.

Polar aprotic solvents such as $MeNO_2$ give the most efficient reactivity, although a few different solvents (MeCN and CH_2Cl_2) show reasonable support for the reaction conditions (Figures A8.1-A8.6). The results from the solvent screen are in agreement with previous results in Yoon's and our laboratories for similar reactions using photoredox methods.[44-46]

Nitroalkenes appear to work the best under the optimized reaction conditions, but a variety of functional groups are compatible with the reaction conditions. A couple of notable products are **8.14 and 8.15**, since these species contain electron donating functional groups which include phenol and tolyl. These are important as previous photoredox reactions similar to ones performed in this report only proceed with ethereal functional groups appended to the aryl ring.[27] This not only shows the scope of this reactivity, but highlights its differences compared to other photoredox

processes. A few different mono and di-substituted dienes (at the 2 and 3 positions) work with under the reaction conditions. Use of an asymmetric diene, such as **8.6**, gives decent yields and regioselectivity values up to *3:1* (Figure 8.4.2). Unfortunately, deviation from para-methoxyphenyl functionalities give mixtures of [2+2] and [4+2] products that are difficult to separate from each other. We are currently investigating the cause of this lack of selectivity upon change in substituents or substitution patterns.

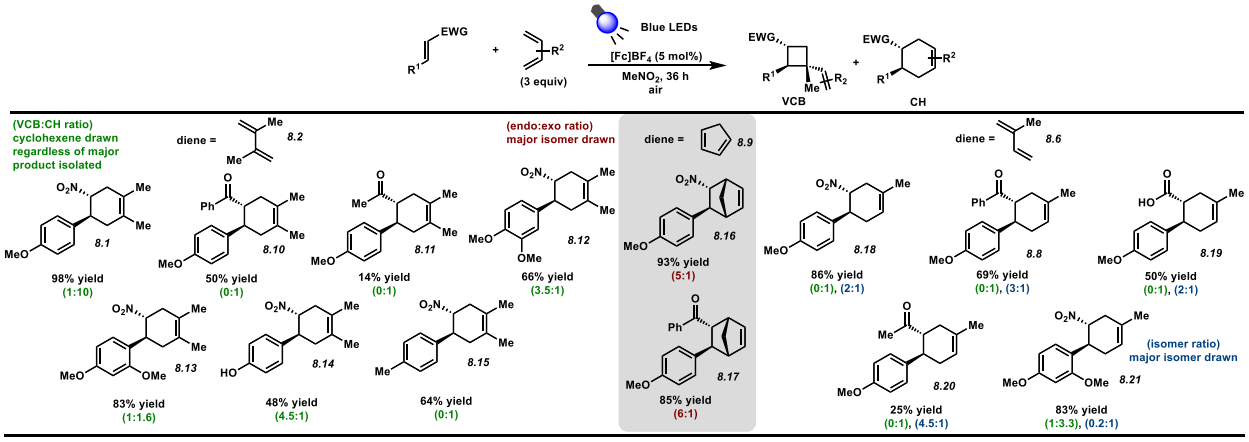


Figure 8.4.2. Substrate scope for the reaction conditions.

Nevertheless, irradiation of any of these 1,2-disubstituted alkenes and dienes without any ferrocenium results in only [2+2] products. Therefore, the ferrocenium is performing reactivity that is photoactivated and beneficial for cycloaddition product. In an effort to determine how much of this reactivity is radical cation (electron transfer) based, some time stamped reactions are performed (Figure 8.4.3). Interestingly, the addition of ferrocenium increases the rate of cycloadduct formation significantly when irradiated, whereas solely Lewis-acid based reactivity results in rather slow reactivity (Figure A8.3 and entries 6-7 in Figure A8.6). Theses results suggest that the ferrocenium performs beneficial electron-transfer reactivity, but further data are needed to further solidify this hypothesis.

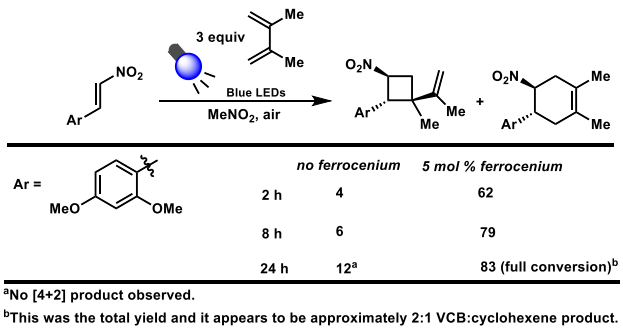


Figure 8.4.3. Time-stamped reactions of background and ferrocenium-mediated cycloadditions.

Since ferrocene itself is a far more common laboratory reagent, indefinitely bench stable and trivial to purify, we have vested interested in using it in place of ferrocenium starting materials. Substitution of ferrocene for ferrocenium in the optimized reaction conditions does not show any conversion to product; however, addition of 5 mol% $AgBF_4$ (relative to **8.4**) as an external oxidant toward ferrocene (also 5 mol%) immediately gives a blue suspension, where after 30 hours of irradiation full conversion from enone **8.4** to cyclohexene **8.8** (Figure 8.4.4) is observed. While the formation of ferrocenium in these reaction conditions is not surprising, eliminating isolation/purification steps of the ferrocenium material makes this reactivity more practical. We think this result is quite important as it not only shows the robust nature of the reaction, but also that these reaction conditions are amenable to nearly all synthetic laboratories.

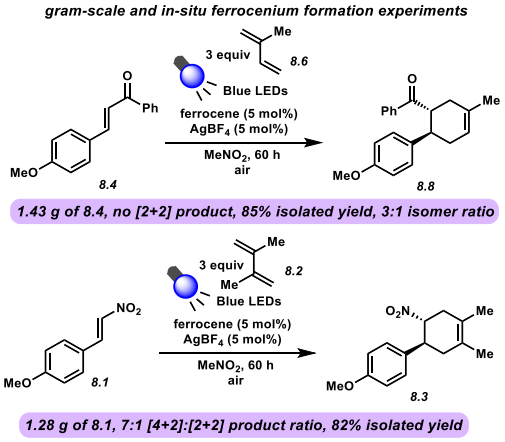


*Figure 8.4.4. In-situ formation of ferrocenium yields conversion to cyclohexene **8.8**.*

To probe different aspects of the mechanism, we perform some further experiments. *In-situ* electronic absorption spectroscopy of a nitromethane solution of **8.4** (0.1 M), **8.6** (3 equiv) and $[Fc]BF_4$ (5 mol%) shows that within 10 minutes of irradiation, conversion of ferrocenium to ferrocene is observed (Figure 8.4.1). The charge transfer (CT) of ferrocenium centered at 618 nm[47] decreases quickly upon irradiation concomitant with an increase in absorption ~460 nm, indicating conversion to ferrocene.[48] The isosbestic point at 516 nm indicates a direct electron transfer conversion of ferrocenium to ferrocene.

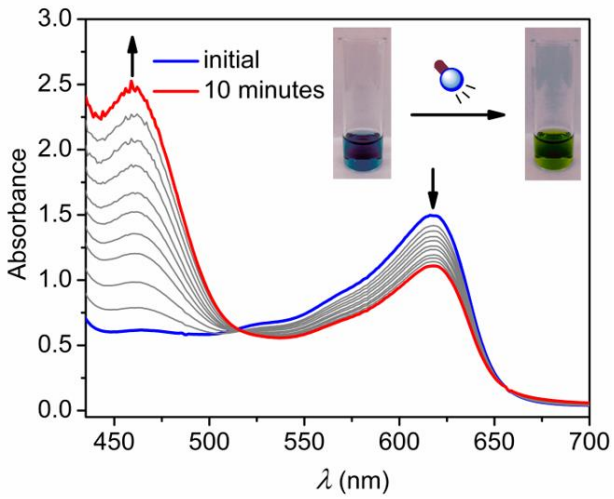


*Figure 8.4.1. Visible light absorption of the optimized reaction mixture (0.1, 0.3 and 0.005 M **8.4**, **8.6** and [Fc](BF$_4$), respectively, in MeNO$_2$) before irradiation (blue trace) and after 10 minutes of irradiation (red trace). The gray traces are incremented by 1 minute each. Inset: Photographs of the reaction mixture before (left) and after 10 minutes of irradiation (right).*

To determine whether the primary mechanism for this reaction consists of catalytic turnover of ferrocene to ferrocenium or radical chain propagation, reaction quantum yield data are gathered. A reaction quantum yield of Φ = 0.088(10) was determined for the reaction between **8.4** and **8.6** using [Fc]BF$_4$.[41, 49-50] This result helps support the lack of radical chain propagation as a major mechanistic pathway in these reaction conditions.

With these results, we propose a working mechanism, shown in Figure 8.4.5. Enone **8.4** is excited by near-UV light to allow a thermodynamically favorable single electron transfer from [**8.4**]* to ferrocenium, forming the radical cation of 4-methoxychalcone and ferrocene, respectively. This radical cation then cyclizes with isoprene (either [2+1 or [4+1], overall) forming the radical cation of the product ($E_{1/2}$ = +1.33 V vs. Fc$^+$/Fc),[28] which then oxidizes ferrocene back to ferrocenium completing the reaction cycle and giving **8.8**.

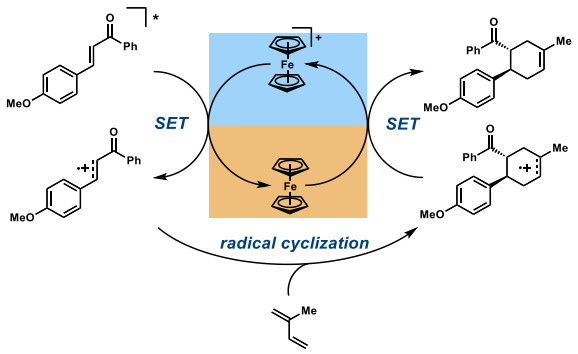


Figure 8.4.5. Proposed mechanism for a [4+2] process

8.5 Conclusions and Outlook

These results indicate that using excited-state reactivity of organic molecules can lead to straightforward and catalytic electron transfer reactions with common reagents, such as ferrocenium. Importantly, these results indicate that electron-poor alkenes can perform excited state electron transfer, which is an extremely rare use in organic synthesis. Using ferrocenium catalytically is likely to have substantial impact on numerous electron transfer reactions. We particularly think that the *in-situ* formation of ferrocenium by addition of catalytic ferrocene and $AgBF_4$ casts a broad net across the field of electron transfer reactivity. In conclusion we present the novel method of using ferrocenium as a catalytic electron transfer reagent in a photoredox manifold, by exploiting the excited state properties of electron-poor alkenes.

References

1. Connelly, N. G.; Geiger, W. E. *Chem. Rev.* **1996,** *96*, 877-910.

2. Elgrishi, N.; Rountree, K. J.; McCarthy, B. D.; Rountree, E. S.; Eisenhart, T. T.; Dempsey, J. L. *J. Chem. Educ.* **2018,** *95*, 197-206.

3. Broderick, E. M.; Guo, N.; Vogel, C. S.; Xu, C. L.; Sutter, J.; Miller, J. T.; Meyer, K.; Mehrkhodavandi, P.; Diaconescu, P. L. *J. Am. Chem. Soc.* **2011,** *133*, 9278-9281.

4. Wang, X. K.; Thevenon, A.; Brosmer, J. L.; Yu, I. S.; Khan, S. I.; Mehrkhodavandi, P.; Diaconescu, P. L. *J. Am. Chem. Soc.* **2014,** *136*, 11264-11267.

5. Blaser, H.-U.; Brieden, W.; Pugin, B.; Spindler, F.; Studer, M.; Togni, A. *Top Catal.* **2002,** *19*, 3-16.

6. Inkpen, M. S.; Scheerer, S.; Linseis, M.; White, A. J. P.; Winter, R. F.; Albrecht, T.; Long, N. J. *Nat. Chem.* **2016,** *8*, 825-830.

7. Musgrave, R. A.; Russell, A. D.; Manners, I. *Organometallics* **2013,** *32*, 5654-5667.

8. Toma, S.; Šebesta, R. *Synthesis-Stuttgart* **2015,** *47*, 1683-1695.

9. Wu, Z. J.; Xu, H. C. *Angew. Chem. Int. Edit.* **2017,** *56*, 4734-4738.

10. Zhu, L.; Xiong, P.; Mao, Z. Y.; Wang, Y. H.; Yan, X. M.; Lu, X.; Xu, H. C. *Angew. Chem. Int. Edit.* **2016,** *55*, 2226-2229.

11. Hou, Z. W.; Mao, Z. Y.; Song, J.; Xu, H. C., *ACS Catal.* **2017,** *7*, 5810-5813.

12. Lennox, A. J. J.; Nutting, J. E.; Stahl, S. S. *Chem. Sci.* **2018,** *9*, 356-361.

13. Torriero, A. A. J.; Shiddiky, M. J. A.; Burgar, I.; Bond, A. M. *Organometallics* **2013,** *32*, 128-136.

14. Bultz, E.; Ouchi, M.; Fujimura, K.; Sawamoto, M.; Cunningham, M. F. *Polymer* **2016,** *106*, 313-319.

15. Fujimura, K.; Ouchi, M.; Sawamoto, M. *Macromolecules* **2015,** *48*, 4294-4300.

16. Fujimura, K.; Ouchi, M.; Sawamoto, M. *ACS Macro. Lett.* **2012,** *1*, 321-323.

17. Kafka, F.; Holan, M.; Hidasova, D.; Pohl, R.; Cisarova, I.; Klepetarova, B.; Jahn, U. *Angew. Chem. Int. Edit.* **2014,** *53*, 9944-9948.

18. Gibis, K. L.; Helmchen, G.; Huttner, G.; Zsolnai, L. *J. Organomet. Chem.* **1993,** *445*, 181-186.

19. Locke, A. J.; Richards, C. J. *Organometallics* **1999,** *18*, 3750-3759.

20. Kelly, T. R.; Maity, S. K.; Meghani, P.; Chandrakumar, N. S. *Tetrahedron Lett.* **1989,** *30*, 1357-1360.

21. Bellville, D. J.; Wirth, D. D.; Bauld, N. L. *J. Am. Chem. Soc.* **1981,** *103*, 718-720.

22. Bauld, N. L. *Tetrahedron*, **1989**, *45*, 5307-5363.

23. Dapperheld, S.; Steckhan, E.; Brinkhaus, K. H. G.; Esch, T. *Chem. Beritche* **1991,** *124*, 2557-2567.

24. Steckhan, E. in *Topics in Current Chemistry – Electrochemistry I, Vol. 142* (eds.: E. Steckhan). Spinger, Berlin, Heidelberg, **1987**. pp. 1-69.

25. Balzani, V. in *Electron Transfer in Chemistry*. Wiley-VCH, Weiheim, New York, **2001**.

26. Caldwell, R. A.; Singh, M. *J. Am. Chem. Soc.* **1983,** *105*, 5139-5140.

27. Stevenson, S. M.; Higgins, R. F.; Shores, M. P.; Ferreira, E. M. *Chem. Sci.* **2017,** *8*, 654-660.

28. This value can be found in the supporting information of reference ***27*** (Table S3, entry 12 or Figure S1, red trace).

29. Arceo, E.; Jurberg, I. D.; Alvarez-Fernandez, A.; Melchiorre, P. *Nat. Chem.* **2013,** *5*, 750-756.

30. Scholz, S.; Scheibitz, M.; Schodel, F.; Bolte, M.; Wagner, M.; Lerner, H. W. *Inorg. Chim. Acta* **2007,** *360*, 3323-3329.

31. Chavez, I.; Alvarez-Carena, A.; Molins, E.; Roig, A.; Maniukiewicz, W.; Arancibia, A.; Arancibia, V.; Brand, H.; Manriquez, J. M. *J. Organomet. Chem.* **2000,** *601*, 126-132.

32. Hendrick, D. N.; Sohn, Y. S.; Gray, H. B. *Inorg. Chem.* **1971,** *10*, 1550-1555.

33. Grimm, R. L.; Bierman, M. J.; O'Leary, L. E.; Strandwitz, N. C.; Brunschwig, B. S.; Lewis, N. S. *J. Phys. Chem. C* **2012,** *116*, 23569-23576.

34. Perucha, A. S.; Bolte, M. *Acta Crystallogr. E* **2007,** *63*, M1703-U1120.

35. Chang, M.-Y.; Tsai, C.-Y.; Wu, M.-H. *Tetrahedron* **2013,** *69*, 6364-6370.

36. Yang, H. Q.; Fu, L. M.; Wei, L. J.; Liang, J. F.; Binks, B. P. *J. Am. Chem. Soc.* **2015,** *137*, 1362-1371.

37. Matthias, C.; Cartoni, A.; Kuck, D. *Int. J. Mass. Spectrom.* **2006,** *255*, 195-212.

38. Kelly, C. B.; Ovian, J. M.; Cywar, R. M.; Gosselin, T. R.; Wiles, R. J.; Leadbeater, N. E. *Org. Biomol. Chem.* **2015,** *13*, 4255-4259.

39. Salabert, J.; Sebastian, R. M.; Vallribera, A.; Civicos, J. F.; Najera, C. *Tetrahedron* **2013,** *69*, 2655-2659.

40. Ayerbe, M.; Cossio, F. P. *Tetrahedron Lett.* **1995,** *36*, 4447-4450.

41. Cismesia, M. A.; Yoon, T. P. *Chem. Sci.* **2015,** *6*, 5426-5434.

42. This value was obtained in the presence of 2 equiv of isoprene and can be found in the supporting information of reference ***27*** (Table S3, entry 6 or Figure S1, blue trace).

43. This compound did not show any emission at λ_{ex} >300 nm in $MeNO_2$ or MeCN.

44. Stevenson, S. M.; Shores, M. P.; Ferreira, E. M. *Angew. Chem. Int. Edit.* **2015,** *54*, 6506-6510.

45. Higgins, R. F.; Fatur, S. M.; Shepard, S. G.; Stevenson, S. M.; Boston, D. J.; Ferreira, E. M.; Damrauer, N. H.; Rappe, A. K.; Shores, M. P. *J. Am. Chem. Soc.* **2016,** *138*, 5451-5464.

46. Lin, S. S.; Ischay, M. A.; Fry, C. G.; Yoon, T. P. *J. Am. Chem. Soc.* **2011,** *133*, 19350-19353.

47. Singh, A.; Chowdhury, D. R.; Paul, A. *Analyst* **2014,** *139*, 5747-5754.

48. Vorotyntsev, M. A.; Zinovyeva, V. A.; Konev, D. V.; Picquet, M.; Gaillon, L.; Rizzi, C. *J. Phys. Chem. B* **2009,** *113*, 1085-1099.

49. This experiment was performed in CH_3NO_2 with an excitation wavelength of λ_{ex} = 350 nm.

50. As a cautionary note, the reaction quantum yield value obtained probably gives an improper view on the efficiency of the overall reaction. Since the emission quantum yield of 4-methoxychalcone is far less efficient than species such as $[Cr(Ph_2phen)_3]^{3+}$ or $[Ru(bpz)_3]^{2+}$, this value is likely larger; however, even if the value increases by an order of magnitude, the value is still within the photocatalysis regime, giving support toward ferrocenium being catalytic in this reaction manifold.

Chapter 9: A redox tunable ligand which promotes a reversal in superexchange coupling in a trinuclear iron system.

9.1 Introduction

Extended molecular systems that encompass metal-alkyne bonds and conjugated ligands display promise for optics and electronics.[1-3] These applications rely on exceptional and cooperative orbital overlap leading to strong magnetic (superexchange) or electronic coupling. Many iron- and ruthenium-acetylide species have been studied and characterized; interestingly, these two metals exhibit rather different properties.[4-7] Generally, iron species show redox tunability with concomitant spin-state control, whereas ruthenium complexes promote increased coupling due to the increased covalency considering the stronger metal-ligand bond as well as larger spin-orbit coupling.[4-7] Coupling mechanisms (ferro- or antiferromagnetic) as well as the magnitude of these interactions are variable in these systems, but are necessary considerations for practical applications for these complexes. While a variety of systems have been studied for these materials, an increased necessity to control switching properties has arisen since using switches as a modular property could allow for versatile materials that encompass two or more states with varied properties.

One straightforward way to alter these properties is the introduction of a redox active unit into the ligand framework. This could allow for a variable electronic structure of the complex upon a redox event, which could alter electronic/magnetic communication pathways. Recent examples from the Harris and Layfield groups showed that upon reduction/oxidation of a bridging ligand in multinuclear metal complexes, single molecule magnet (SMM) properties could be switched on/off.[8-11] Alternatively, a triarylamine-containing compound (Figure 9.1.1, left) showed switching from a doublet to triplet ground state upon oxidation.[12] The triradical species used in this study displayed strong antiferromagnetic coupling (J = -285 cm^{-1}) between unpaired spins; however, the oxidized product behaved as a ferromagnetically coupled diradical species (J = 209 cm^{-1}).[12]

The observed properties indicated an increase in the ground state of the motif (S = ½ to S = 1) and also showed that the superexchange coupling within triarylamines could be reversed upon oxidation. This makes triarylamines viable and attractive targets for eventual materials in applied fields of optics or electronics. Furthermore, reported reduction potentials of triarylamines sit far anodic to many organometallic-iron species, thus selective oxidation of both redox active moieties (Fe and N atoms) is plausible.[13-14]

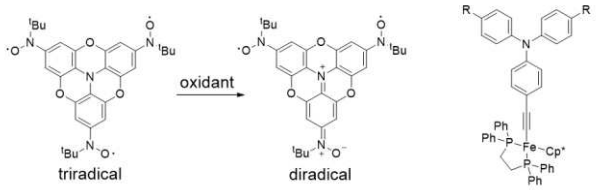


Figure 9.1.1. Chemdraw of trioxyphenylamine compounds (left). Line-bond drawings of MEPA (R = H) and TEPA (R = CCFe(Cp)(dppe)) subunits where Cp* = pentamethylcyclopentadiene and dppe = 1,2-bis(diphenylphosphino)ethane.*

In addition, triarylamines have been employed in classes of materials such as dye-sensitized solar cells[15-18] and metal-organic frameworks.[19-22] Notwithstanding, magnetic studies of triarylamine-containing molecules are sparse with only a few observations made.[12-13] Interestingly, the planarity of a triarylamine system increases conjugation allowing for increased superexchange coupling compared to analogous tetrahedral-triarylphosphine systems.[23-24] Unlike all carbon-based systems, triarylamines cause a spin-repolarization at the nitrogen center.[13] This imparts a reversal in the expected superexchange pathway in other studied conjugated systems.[12-13] The physical basis of this phenomenon is derived from the unfilled *p*-orbital on the nitrogen atom that retains the spin-orientation instead of propagating a spin-flip. It is still unclear whether this spin-polarization occurs upon oxidation of the nitrogen in a metal containing system.

Furthermore, a comparison of the nature of magnetic coupling in triarylamine-systems prior to and after oxidation of the N-atom has not been explored in metal-containing species.[12]

A previous study reported the magnetic properties of both mononuclear [(η^2-dppe)(η^5-C_5Me_5)Fe[C≡C(1,4-$C_6H_4NPh_2$)]](PF_6) and trinuclear ([{(η^2-dppe)(η^5-C_5Me_5)FeC≡C(1,4-C_6H_4)}$_3$N](PF_6)$_3$) complexes (Figure 9.1.1, right). This study indicated that antiferromagnetic coupling is observed in the trinuclear species and is purely of intramolecular origin caused by spin-repolarization at the nitrogen; however, the nature of the coupling after oxidation of the nitrogen atom was not investigated. Additionally, no crystallographic data of the trinuclear complex were collected making a complete magnetostructural correlation difficult.[13] Thereby we set out to investigate an analogous system collecting both magnetic and crystallographic data of the trinuclear species to help determine if subtle structural changes have profound magnetic impacts. In this report we synthesized mono-, di- and triferrous complexes which were oxidized to their ferric counterparts. In addition, we also oxidized the N-atom of the triarylamine to determine what affects this redox change has on the magnetic properties of the system.

9.2 Division of labor

All syntheses, characterization, analyses and interpretations of the experimental data were performed by Robert F. Higgins. The computational work was performed by Justin P. Joyce. Robert F. Higgins, Justin P. Joyce, Anthony K. Rappé and Matthew P. Shores also analyzed and interpreted the data.

9.3 Experimental

9.3.1 Preparation of Compounds

Preparations and Manipulations of all metal complexes were performed inside a dinitrogen-filled glovebox (MBRAUN Labmaster 130). Pentane was distilled over sodium metal and subjected to three freeze pump thaw cycles prior to use. Other solvents were sparged with dinitrogen, passed over alumina, and degassed prior to use. The compounds (dmpe)$_2$$FeCl_2$,[25] *p*-MEPA,[26] *p*-DEPA,[27] *p*-TEPA[6] and thianthrenium tetrafluoroborate[28] ($ThBF_4$) were synthesized

according to their literature preparations. Tetrabutylammonium hexfluorophosphate (Bu_4NPF_6) was recrystallized twice from ethanol before use and checked electrochemically for purity. Triethylamine (Et_3N) was distilled over CaH_2 before use. Ferrocene was sublimed before use. All other reagents were purchased commercially and used without further purification.

9.3.2 Preparation of novel metal complexes

[(dmpe)$_2$FeCl(*μ-p*-MEPA)] (9.1)

Solid $(dmpe)_2FeCl_2$ (111 mg, 0.260 mmol) was added to a stirring solution of H-MEPA (70 mg, 0.260 mmol) in 5 mL methanol at room temperature. Upon dissolution of the Fe-containing compound, 0.2 mL Et_3N was added to the green solution causing an immediate color change to orange and the formation of a precipitate. The reaction mixture was stirred for an additional 30 minutes, then filtered. The solid precipitate was washed with 2 mL cold methanol and dried under dinitrogen, affording 125 mg (0.189 mmol, 73% yield) of a light orange solid. IR (KBr) $\nu_{C\equiv C}$: 2046 cm^{-1}. ^1H NMR (C_6D_6): δ 7.07 (d, 4H, aryl), 7.02-6.95 (m, 8H, aryl), 6.79 (t, 2H, aryl), 1.61 (m, 8H, CH_2), 1.36 ppm (d, 24H, CH_3). ^{31}P NMR (C_6D_6): δ 65.15 ppm. ESI MS(+) (CH_3CN): 660.2 (**M** + H)$^+$ (calcd 660.2) *m/z* . UV-vis (CH_3CN) λ_{max} (ε_M): 202 (79800), 303 (18100), 382 (20400) nm ($L \cdot mol^{-1} \cdot cm^{-1}$). Anal. calcd For $C_{32}H_{46}ClFeNP_4$: C, 58.24; H, 7.03; N, 2.12. Found: C, 57.85; H, 6.63; N, 2.06.

[(dmpe)$_2$FeCl(*μ-p*-MEPA)](PF$_6$) (9.2). A solution of $AgPF_6$ (20 mg, 0.0791 mmol) in 1 mL acetonitrile was added to a solution of **9.2** (50 mg, 0.0759 mmol) in 3 mL acetonitrile. A color change from orange to dark green was observed over the course of two minutes. After an additional 30 minutes of stirring, the reaction mixture was filtered through Celite and the filtrate was concentrated *in vacuo*. The green solid was then dissolved in dichloromethane and upon evaporation of this solution, x-ray quality crystals were obtained after collection and washing with Et_2O (5 mL) giving 51 mg (0.0638 mmol, 84% yield) of a dark green crystals. IR (KBr) $\nu_{C\equiv C}$: 1983 (br) cm^{-1}. ESI MS(+) (CH_3CN): 659.2 (**M** – PF_6)$^+$ (calcd. 659.2) *m/z*. UV-vis (CH_3CN) λ_{max} (ε_M): 204

(57100), 306 (25500), 398 (4710), 885 (9910) nm ($L \cdot mol^{-1} \cdot cm^{-1}$). Anal. calcd For $C_{32}H_{46}ClF_6FeNP_5$: C, 47.75; H, 5.76; N, 1.74. Found: C, 47.80; H, 5.40; N, 1.81.

[(dmpe)$_4$Fe$_2$Cl$_2$(μ_2-*p*-DEPA)] (9.3). Solid $(dmpe)_2FeCl_2$ (126 mg, 0.294 mmol) was added to a stirring solution of H_2DEPA (43 mg, 0.147 mmol) in 5 mL methanol at room temperature. Upon dissolution of the Fe-containing compound, 0.2 mL Et_3N was added to the green solution causing an immediate color change to orange and the formation of a precipitate. The reaction mixture was stirred for an additional 30 minutes, then filtered. The solid precipitate was washed with 2 mL cold methanol and dried under dinitrogen, affording 131 mg (0.114 mmol, 78% yield) of a light orange solid. IR (KBr) $\nu_{C\equiv C}$: 2041 cm^{-1}. ^{1}H NMR (C_6D_6): δ 7.09-6.83 (m, 13H, aryl), 1.62 (m, 16H, CH_2), 1.36-1.34 ppm (s, 48H, CH_3). ^{31}P NMR (C_6D_6): δ 65.19 ppm. ESI MS(+) (CH_3CN): 1074.2 (**M** + H)$^+$ (calcd 1074.2) *m/z* . UV-vis (CH_3CN) λ_{max} (ε_M): 204 (52800), 358 (15320), 384 (16060) nm ($L \cdot mol^{-1} \cdot cm^{-1}$). Anal. calcd For $C_{46}H_{77}Cl_2Fe_2NP_8$: C, 51.42; H, 7.22; N, 1.30. Found: C, 51.20; H, 7.25; N, 1.73.

[(dmpe)$_4$Fe$_2$Cl$_2$(μ_2-*p*-DEPA)](NO$_3$)$_2$ (9.4). A solution of $AgNO_3$ (15 mg, 0.0879 mmol) in 1 mL acetonitrile was added to a solution of **9.3** (45 mg, 0.0419 mmol) in 3 mL acetonitrile. A color change from orange to dark green was observed over the course of two minutes. After 30 minutes of stirring, the reaction mixture was filtered through Celite and the filtrate was concentrated *in vacuo*. The green solid was then dissolved in a sparing amount of methanol, where slow evaporation of diethyl ether gave dark green crystals. These crystals were collected *via* filtration and washed with diethyl ether (5 mL) giving 45 mg (0.0379 mmol, 91% yield) of a dark green crystals. IR (KBr) $\nu_{C\equiv C}$: 1992 (br) cm^{-1}. ESI MS(+) (CH_3CN): 1135.2 (**M** – NO_3)$^+$ (calcd 1135.2) *m/z*. Absorption sprectrum (CH_3CN) λ_{max} (ε_M): 206 (103900), 321 (32900), 898 (11800) nm ($L \cdot mol^{-1} \cdot cm^{-1}$). Anal. calcd For $C_{46}H_{77}Cl_2Fe_2N_3O_6P_8$: C, 46.10; H, 6.48; N, 3.51. Found: C, 45.84; H, 6.25; N, 3.24.

[(dmpe)$_6$Fe$_3$Cl$_3$(μ_3-*p*-TEPA)] (9.5). Solid $(dmpe)_2FeCl_2$ (80 mg, 0.236 mmol) was added to a stirring solution of H_3TEPA (21 mg, 0.0788 mmol) in 5 mL methanol at room temperature. Upon

dissolution of the Fe-containing compound, 0.1 mL Et_3N was added to the green solution causing an immediate color change to orange and the formation of a precipitate. The reaction mixture was stirred for an additional 30 minutes, then filtered. The precipitate was washed with 2 mL cold methanol and dried under dinitrogen, affording 99 mg (0.0785 mmol, 99% yield) of an orange solid. IR (KBr) $\nu_{C\equiv C}$: 2047 cm^{-1}. ^1H NMR (C_6D_6): δ 6.92 (d, 6H, aryl), 6.88 (d, 6H, aryl), 1.62 (m, 24H, CH_2), 1.37 ppm (s, 72H, CH_3). ^{31}P NMR (C_6D_6): δ 65.24 ppm. ESI MS(+) (CH_3CN): 1488.2 (**M** + H)$^+$ (cald. 1488.2), 1099.2 (**M** – (dmpe)$_2$FeCl) + 2H)$^+$ (calcd. 1099.2) *m/z*. UV-vis (THF) λ_{max} (ε_M): 294 (25100), 398 (8280) nm ($L \cdot mol^{-1} \cdot cm^{-1}$). Anal. calcd For $C_{60}H_{108}Cl_3Fe_3NP_{12}$: C, 48.40; H, 7.31; N, 0.94. Found: C, 48.44; H, 7.06; N, 0.86.

[(dmpe)$_6$Fe$_3$Cl$_3$(μ_3-*p*-TEPA)](OTf)$_3$ (9.6). A solution of AgOTf (28 mg, 0.118 mmol) in 1 mL acetonitrile was added to a solution of **9.5** (50 mg, 0.0393 mmol) in 5 mL acetonitrile. An immediate color change was observed from orange to dark green. After 30 minutes of stirring, the reaction mixture was filtered through Celite and the filtrate was concentrated *in vacuo*. The green solid was dissolved in a sparing amount of acetonitrile and upon slow diffusion of diethyl ether into this solution, x-ray quality crystals were formed. These crystals were collected *via* filtration where the collected crystals were washed with diethyl ether, giving 62 mg (0.0320 mmol, 81% yield) of dark green crystals. IR (KBr) $\nu_{C\equiv C}$: 1995 (br) cm^{-1}. ESI MS(+) (CH_3CN): 1785.1 (**M** – OTf)$^+$ (calcd. 1785.1), 818.1 (**M** – 2OTf)$^{2+}$ (calcd. 818.1) *m/z*. UV-vis (CH_3CN) λ_{max} (ε_M): 203 (84260), 294 (36180), 342 (44480), 599 (4130), 897 (17030) nm ($L \cdot mol^{-1} \cdot cm^{-1}$) . Anal. calcd For $C_{63}H_{108}Cl_3F_9Fe_3NO_9P_{12}S_3$: C, 39.08; H, 5.62; N, 0.72. Found: C, 38.63; H, 5.43; N, 1.08.

[(dmpe)$_6$Fe$_3$Cl$_3$(μ_3-*p*-TEPA)](BF$_4$)$_4$ (9.7). A solution of **9.6** (80 mg, 0.0458 mmol) in 15 mL acetonitrile was cooled to -78ºC. In a syringe, $ThBF_4$ (6 mg, 0.0458 mmol) in 3 mL acetonitrile was added dropwise to the reaction vessel. After warming to room temperature over two hours, the reaction mixture was concentrated *in vacuo*. The residue was then washed with pentane (3 x 5 mL) and the resulting green-blue solid was dissolved in benzonitrile and upon slow diffusion of tetrahydrofuran into the solution (~7 days), green-blue crystals were formed. These crystals were

collected *via* filtration and the crystals were washed with THF (5 mL), giving 56 mg (0.0306 mmol, 67% yield) of green-blue crystals. IR (KBr) $\nu_{C\equiv C}$: 2000 (br), $\nu_{C=C=C}$: 1936 (br) cm^{-1}. ESI MS(+) (CH_3CN): *m/z* 1488.3 (**M** – $(dmpe)_2FeCl$ + 2H + $CH_3CN)^+$ (calcd 1488.3). UV-vis (CH_3CN) λ_{max} (ε_M): 204 (96600), 340 (36710), 605 (2120), 858 (8000) nm ($L{\cdot}mol^{-1}{\cdot}cm^{-1}$). Anal. calcd For $C_{60}H_{108}Cl_3F_{16}Fe_3NP_{12}B_4$: C, 39.24; H, 5.93; N, 0.76. Found: C, 39.48; H, 5.79; N, 0.88.

9.3.3 Magnetic susceptibility measurements

Magnetic susceptibility data were collected with a Quantum Design MPMS XL SQUID magnetometer or a Quantum Design PPMS dynacool system. In the glovebox, finely ground crystalline samples were loaded into polyethylene bags and sealed. For measurements on the MPMS the bags containing the samples were inserted into straws. When samples were measured on the PPMS, bags were either inserted into a straw or wedged between two quartz rods and taped to ensure the placement of the sample. Ferromagnetic impurity checks were performed for each sample at 100 K by sweeping the field (0 – 10 or 20 kOe, Figures A9.1-4). Curvature in the *M* versus *H* plot between 0 and ~2000 Oe indicates the presence of ferromagnetic impurities. When this behavior is observed, susceptibility data were collected at magnetic fields where the field dependence is linear (5000 Oe for compound **9.7**). Magnetization measurements were collected at 1.8 K at applied fields ranging from 0 to 50 kOe. Reduced magnetization data were collected on integral fields of 10, 20, 30, 40 and 50 kOe with temperatures ranging from 1.8 to 20 K. Compound **9.4** was fit using the Hamiltonian with the form shown in equation 9.1. Reduced magnetization data were fit using ANISOFIT 2.0[29] using the Hamiltonian shown in equation 9.2. Data were corrected for the magnetization of the sample holder by subtracting the susceptibility of an empty container, and for diamagnetic contributions of the sample by using Pascal's constants.[30]

$$\hat{H} = -2J\widehat{S_1} \cdot \widehat{S_2} \qquad (9.1)$$

$$\hat{H} = D\widehat{S_z^2} + E\left(\widehat{S_z^2} + \widehat{S_y^2}\right) + g_{iso}\mu_B S \cdot H \qquad (9.2)$$

9.3.4 Crystallographic measurements

[Fe-MEPA](PF_6) and [Fe_3TEPA]($OTf)_3$ were characterized by single-crystal X-ray analysis. Crystals were coated in Paratone oil prior to removal from the glovebox, supported on Cryoloops, and mounted on a Bruker Kappa Apex 2 CCD diffractometer under a stream of cold nitrogen. All data collections were performed with Mo Kα radiation and a graphite monochromator. Initial lattice parameters were determined from a minimum of 112 reflections harvested from 36 frames; these parameters were later refined against all data. Data sets were collected targeting full coverage and fourfold redundancy. Data were integrated and corrected for absorption effects with the Apex 2 software package. Structures were solved by direct methods and refined with the SHELXTL software package. Displacement parameters for all non-hydrogen atoms were refined anisotropically with the exception of disordered atoms. Hydrogen atoms were added at the ideal positions and refined using a riding model in which the isotropic displacement parameters were set at 1.2 times those of the attached carbon atom (1.5 for methyl carbons). Disorder was modeled in [Fe-MEPA](PF_6) for half of a dmpe ligand (atoms C29-32) where each carbon was modeled over two positions at 49.1 and 50.9% occupancy. C29B was modelled isotropically as the atom went NPD if modelled anisotropically. An EDAP command was used for C29A, using the anisotropic thermal parameters from atom C23.

9.3.4 Other physical measurements

Electronic absorption spectra were obtained in air-free quartz cuvettes with a Hewlett-Packard 8453 spectrophotometer. IR spectra were measured with a Nicolet 380 FT-IR spectrophotometer using KBr pellets. Mass spectrometric measurements were performed in the positive ion mode on a Thermo LTQ mass spectrometer equipped with an analytical electrospray ion source and a quadrupole ion trap mass analyzer. Each measurement, unless otherwise noted, was performed with the capillary temperature = 175 °C, spray voltage = 5 kV, and spray current = 91 μamps.^{1}H and ^{31}P NMR spectra were recorded on an Agilent (Varian) 400MR (400 MHz). All NMR spectra were collected in either d^6-benzene or d^2-dichloromethane and referenced to

tetramethylsilane (TMS, δ = 0.00 ppm). Electron paramagnetic resonance (EPR) spectra were obtained using a continuous-wave X-band Bruker EMX 200U instrument outfitted with a liquid nitrogen cryostat. Compounds were dissolved in a 1:1 mixture of dichloromethane and 1,2-dichloroethane to form a glass at low temperature. Electrochemical experiments were performed in 0.1 M solutions of Bu_4NPF_6 in dichloromethane, benzonitrile or acetonitrile. Cyclic voltammograms (CVs), differential pulse voltammograms (DPVs) and square-wave voltammograms (SWVs) were recorded with a CH Instruments potentiostat (Model 1230A or 660C) using a 0.25 mm Pt disk working electrode, Ag/Ag^+ pseudo-reference electrode, and Pt wire auxiliary electrode. Scan rates were collected from 10 mV/s up to 2 V/s. Reported potentials are referenced to the $[Cp_2Fe]^+/[Cp_2Fe]$ (Fc^+/Fc), where Cp = cyclopentadiene, redox couple and were determined by adding ferrocene as an internal standard at the conclusion of each electrochemical experiment. Elemental analyses were performed by Robertson Microlit Laboratories (Madison, NJ).

9.3.5 Computational details

Calculations were performed using crystal structure coordinates in which C-H distances were adjusted to RC-H sp^3 = 1.09 Å and RC-H sp^2 = 1.07 Å. Disorder was treated through the docking of an analogous crystal structure fragment while maintaining bond distances, angles, and torsion which largely impact magnetic exchange. Only the cation was considered and the triflate counter anion was removed prior to calculations. The Gaussian 09 electronic structure software package was applied, using an APFD functional with the 6-311+g(d) basis set. An unrestricted formalism of the wavefunction was used for all open-shell species. An extra quadratically convergent SCF procedure was included to aid in the convergence given the presence of low-lying excited states. Single point energy calculations were conducted on the quintet, quartet, triplet, doublet, and singlet to investigate the possible states and overall exchange interactions for compounds **9.6** and **9.7**. The net spin density plots were generated with an isovalue of 0.003. A

geometry optimization was performed at the same level of theory for the neutral and oxidized ligand set, *p*-TEPA.

9.4 Results and Discussion

9.4.1 Syntheses and Characterization

The syntheses of mono-, di-, and trinuclear Fe complexes proceed from the requisite alkynyl triphenylamine (Figure 9.4.1). The metalation of each ligand is carried out in an identical manner and has been previously reported with a slight variation to improve yields.[14] Analogous complexes of **9.1** and **9.5** replacing $(dmpe)_2FeCl$ units with $(dppe)(\eta^5\text{-}C_5Me_5)Fe$ subgroups were prepared via stabilization of the vinylidene intermediate using KPF_6 and subsequently deprotonation of the vinylidene via ^{t}BuOK.[13] Nevertheless, the proposed mechanism remains the same, which is initiated by $(dmpe)_2FeCl_2$ undergoing solvolysis in the presence of CH_3OH then forming a vinylidene whereupon the vinylic proton is extracted by a base (Et_3N) and the ferrous-acetylide species precipitates from CH_3OH.[31] The complexes **9.1**, **9.3** and **9.5** are characterized by elemental analysis (EA), IR, ^{1}H and ^{31}P NMR and mass spectrometry (MS) to ensure bulk purity. Since peak broadening and no signals outside of the normal window are observed in NMR experiments, the iron center(s) present in **9.1**, **9.3** and **9.5** were all assigned as low-spin ($S = 0$) species. A single peak was observed in each ^{31}P spectrum consistent with a single average environment for all P atoms. Ionization in MS did not readily occur and fragmentation was commonly observed; however, no obvious impurities are observed in **9.1**, **9.3** or **9.5**. IR spectroscopy confirmed a complete reaction by the disappearance of the acetylinic proton(s) and a shift to lower energy of the alkyne stretch (C≡C) for **9.1**, **9.3** and **9.5** when compared to their respective free ligands.

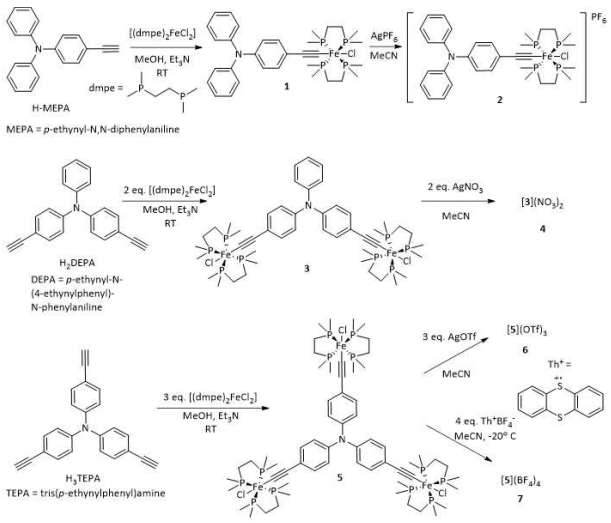


*Figure 9.4.1. Synthetic routes to **9.1**-**9.7**.*

9.4.2 Oxidation and Electrochemistry

In order to generate paramagnetic species, suitable oxidizing agents for $Fe^{II} \rightarrow F^{III}$ and $N^0 \rightarrow N^{\bullet+}$ transformations are determined *via* electrochemical experiments. Previous reports by Field indicated that the electrochemical behavior for the ferrous and ferric compounds containing iron-acetylide subunits are identical except for the open circuit potential. Therefore, electrochemical measurements are performed only on **9.1**, **9.3** and **9.5** (Table 9.4.1 and Figure 9.4.2).[32] The reduction potential of the Fe^{III}/Fe^{II} couples range from -0.59 to -0.65 V (versus Fc^+/Fc) and are in good agreement with literature precedent for iron-acetylides tethered by phosphines.[13-14] If coupled events, or multiple peaks are observed for multimetallic species (**9.3** and **9.5**) concerning the $Fe^{III/II}$ event, then electronic/magnetic communication should be large in magnitude. Compounds **9.3** and **9.5** did not exhibit coupled redox events for the Fe^{III}/Fe^{II} event, an early indication that electronic communication between/among the metal centers might be smaller in magnitude than previously studied systems.[13-14] In the cyclic voltammograms of **9.1**, **9.3** and **9.5** multiple redox events are observed at more potentials anodic of the $Fe^{III/II}$ event, making the assignment of a possible $N^{\bullet+/0}$ event difficult to discern. These other events are hypothesized to

be Fe^{IV}/Fe^{III} or $P^{\bullet+/0}$ events; however, these products could not be isolated to allow further characterization. Therefore, stirred solution experiments are performed to elucidate which event is the $N^{\bullet+/0}$ couple for **9.5**. Indeed, the peaks more anodic than the first two events (scanning positive) are not observed in the stirred solution experiment. This indicates the most cathodic of the events in the oxidizing regime for **9.5** is likely the $N^{\bullet+/0}$ couple, which is present at +0.40 V vs. Fc^{+}/Fc (Figure 2). This value is in good agreement with previously reported metal acetylide appended triarylamines.[33] Further, the current passed for the Fe^{III}/Fe^{II} couple is ~3 times more than the $N^{\bullet+/0}$ couple, giving justification for these electron transfer assignments.

The cyclic voltammogram of compound **9.3** shows large ΔE_p (peak to peak difference) values for both the Fe^{III}/Fe^{II} and $N^{\bullet+/0}$ couples (Figure 9.4.2, blue trace). This is likely due to the electrochemical data being gathered in CH_2Cl_2, due to insolubility of **9.3** in CH_3CN; however, complexes **9.1** and **9.5** show much smaller ΔE_p values in CH_2Cl_2 when compared to **9.3** (Table 9.4.1). Therefore, there must be exceedingly slow kinetics for the observed electron transfer events for **9.3** when compared to **9.1** and **9.5**. The other ΔE_p values collected for **9.1**, **9.3** and **9.5** are in reasonable agreement with 1-electron processes in moderately to poorly conducting solvents.

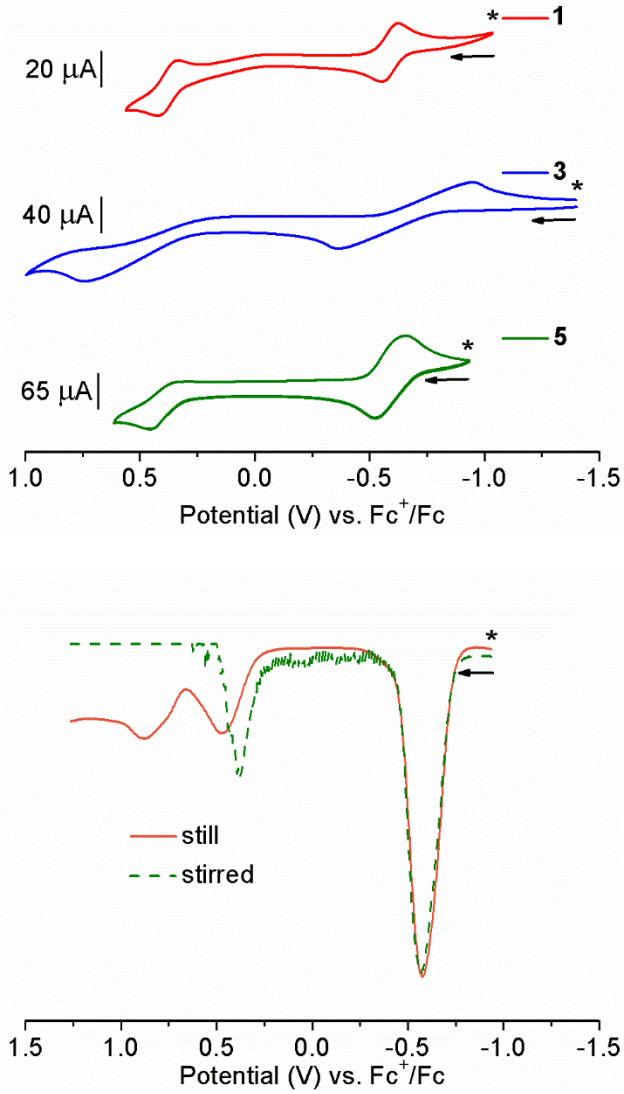


*Figure 9.4.2. (top) Cyclic voltammograms in CH_3CN for **9.1** and **9.5**, and CH_2Cl_2 for **9.3** collected at 100 mV/s in a 0.1 M Bu_4NPF_6 solution. *Indicates the open circuit potential and the arrow indicates the direction of the scan. (bottom) Square wave voltammograms of **9.5** in a 0.1 M Bu_4NPF_6 CH_3CN solution at a 4 mV step-size collected stepping in the positive direction.*

*Table 9.4.1. Compiled electrochemistry data for **9.1**, **9.3** and **9.5**.*

Complex (Solvent)	$N^{\bullet+/0}$ $E_{1/2}$ (V)	$N^{\bullet+/0}$ ΔE_p (mV)	$Fe^{III/II}$ $E^{ox}_{1/2}$ (V)	$Fe^{III/II}$ ΔE_p (mV)
9.1 (CH_2Cl_2)	+0.38	110	-0.60	100
9.1 (CH_3CN)	+0.37	88	-0.60	77
9.3 (CH_3CN)	+0.42	85	-0.59	85

9.3 (CH_2Cl_2)	+0.34	570	-0.64	570
9.5 (CH_2Cl_2)	+0.37	180	-0.65	180
9.5 (CH_3CN)	+0.40	140	-0.60	140
9.5 (PhCN)	+0.37	140	-0.59	140

All potentials are referenced to Fc^+/Fc and each experiment is performed at 100 mV/s in a 0.1 M Bu_4NPF_6 solution.

The electrochemical data indicate that Ag^I salts can be used to selectively generate the ferric salts **9.2**, **9.4** and **9.6** without also oxidizing the N atom. Treatment of **9.1**, **9.3** and **9.5** with $AgPF_6$, $-NO_3$ and -OTf salts, respectively, gives clean reactions that immediately turn from orange to dark green. The choice of silver salt is based on the purity of the corresponding Fe^{III} salts. Using IR as a preliminary characterization method, the acetylide stretches decrease in energy from 2046 to 1983 cm^{-1}, 2041 to 1992 cm^{-1} and 2047 to 1995 cm^{-1} for **9.2**, **9.4** and **9.6**, respectively, upon oxidation, consistent with previously reported oxidation reactions of iron-alkynyl complexes.[14]

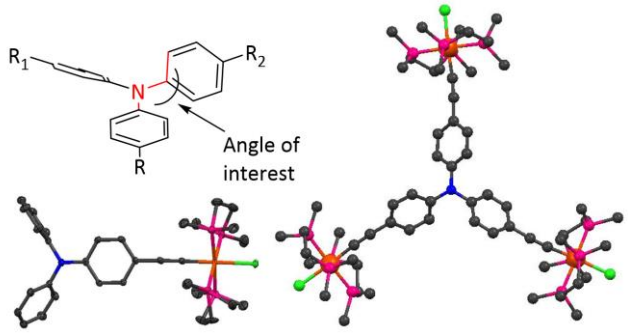


*Figure 9.4.3. ORTEP representations of the cations of **9.2** (left) and **9.6** (middle) at 40% probabilities where gray, orange, pink, green and blue are C, Fe, P, Cl and N atoms, respectively, with H atoms omitted. **6** sits on a site of higher symmetry as it crystallized in a cubic environment. Line-bond drawing for the bend angle of the traiarylamine ligand (right).*

9.4.3 X-Ray Structures

Crystal structures of **9.2** and **9.6** were collected to verify molecular structure (Figure 9.4.3). The Fe-C bond distances are 1.85(1) and 1.88(1) Å (average) for **9.2** and **9.6**, respectively, which are in good agreement with literature precedent.[14] Concerning the Fe-Cl bonds, the distances are 2.299(1) and 2.33(3) Å for **9.2** and **9.6**, respectively. The average Fe-P bond distances are 2.272(1) and 2.27(1) Å for **9.2** and **9.6**, respectively. Also of interest are the N-C bond distances which were 1.385(5) and 1.45(2) Å for the carbons α-to the Fe center(s) for **9.2** and **9.6**, respectively; however the α-carbons of the unsubstituted phenyl rings in **9.2** have an average bond distance of 1.438(5) Å. Interestingly, an opposite trend is observed in ((dppe)(η^5-C_5Me_5)Fe[C≡C(1,4-$C_6H_4NPh_2$)]) (Figure 1 right, R = H) where the substituted α-carbon had a C-N bond distance of 1.437(4) Å whereas the unsubstituted α-carbons had an average C-N bond distance of 1.413(4) Å.[13] We attribute this to π-π stacking interactions, where neighboring Fe-complexes are 4.403(4) Å apart, which also helps explain the differences in planarity of these complexes (Figure A9.5). Since the collected data did not agree with published trends, we were interested to analyze the N-C-C angle about the nitrogen atom to the α-carbon to the β-carbon of the substituted phenyl rings (Figure 9.4.3, upper left). In addition to the structures that were collected for this study, structures from previous studies are also included for comparison purposes (Table 9.4.2).[34]

Table 9.4.2. Comparison of bend angle in all triarylamine-acetylene bridged metal complexes presently in the literature.

Compound	# of substituents	Bend angle (º)	Reference
9.2	1	111.26	this work
((dppe)(η^5-C_5Me_5)Fe[C≡C(1,4-$C_6H_4NPh_2$)])	1	111.17	10
[(dmetpa)$_2$(PEt_3)$_2$Pt]	1	118.71	8a
[(dmetpa)$_2$(PPh_3)$_2$Pt]	1	120.28	8b
[$(CO)_3$(bpy)Re(TEPA)]	1	122.23	14
[$(CO)_3$(Me_2bpy)Re(TEPA)]	1	117.62	14

$[(CO)_3(^tBu_2bpy)Re(TEPA)]$	1	124.33	14
9.6	3	113.77	this work

From all crystallographic data available, it is difficult to identify a consistent trend since only mononuclear complexes and one trinuclear complex have been reported; however, packing affects such as π-π stacking increase the overall bend angle in all cases. Metal charge also has an effect, as the Re(I) complexes have the largest angles, Pt(II) has smaller angles and the Fe(III) compounds have the smallest. This could be caused by an increase in electron withdrawing ability as charge increases, delocalizing electron density from the lone pair of the amine over the rest of the molecule. Additionally, it also appears that the size of the metal has an effect, which could be related to packing effects or strength of the metal-ligand bond.

On a related note, we have previously reported that the magnetic coupling is expected to increase depending on the rotation of the $(dmpe)_2FeCl$ about the alkyne. In $[(dmpe)_6Fe_3Cl_3(\mu_3\text{-}TEB)]^{3+}$ (where TEB = 1,3,5-triethynylbenzene), the three $(dmpe)_2FeCl$ subunits had rotation angles of 36.9, 83.2 and 83.2º where 0º gives the optimal overlap. In the crystal structure of **9.6**, the rotation angle is 0.8º for all the $(dmpe)_2FeCl$ because of the symmetry equivalence of the space group. This would mean that that **9.6** would have close to the optimal value for magnetic coupling among the iron centers. With this information, we collected the magnetic properties of all paramagnetic species synthesized.

9.4.4 Magnetic Properties of Ferric Species.

The room temperature $\chi_M T$ value for **9.2** is 0.43 cm^3Kmol^{-1}, which is in good agreement with a non-interacting $S = ½$ ion (0.375 cm^3Kmol^{-1} assuming $g = 2.00$) (Figure 9.4.4). Upon cooling, a near linear decrease in the $\chi_M T$ product is observed until ~10 K where a slightly more substantial decrease is observed where at 4 K the $\chi_M T$ value is 0.32 cm^3Kmol^{-1}. The linear decrease in $\chi_M T$ values as the temperature is reduced is a hallmark of temperature independent paramagnetism (TIP), while the drop-off at low temperatures (<20K) is likely antiferromagnetic coupling or

magnetic anisotropy. Axial zero field splitting is not permitted for an $S = ½$ ground state, therefore we ascribe this decrease in the susceptibility product to intermolecular antiferromagnetic coupling. Indeed, π-π stacking interactions are present in the solid-state structure (4.403(4) Å) between cations, which permit a reasonable magnetic exchange pathway (Figure A9.5). To quantify this exchange coupling as well as the presumed TIP, JulX is used as the magnetic fitting software (Figure 9.4.4).[35] The parameters for all magnetic fits that are discussed in this report are listed in Table 9.4.3.

*Table 9.4.3. Parameters from the magnetic fits performed for **9.2**, **9.4**, **9.6** and **9.7**.*

compound	g_1	g_2	g_3	J_{12} (cm^{-1})	Θ (cm^{-1})	TIP (cm^3mol^{-1}) x 10^{-6}	f_{sum}
9.2	1.91	-	-	-	-0.33	273	0.0036
9.4[a]	2.15	2.15	-	-14.45	-	1258	0.0016
9.6[b]	2.00*	2.00*	2.00*	-10.28	-1.41	864	0.033
9.7[c]	2.10*	-	-	-	-2.64	366	0.041

*indicates a parameter that was held constant. [a]An $S = 5/2$ impurity at 2.2% is included in this fit. [b]For **9.6**, $J_{12} = J_{13} = J_{23}$. [c]The ANISOFIT data for **7** gave values of $D = 11.89$ cm^{-1} and $E = 0.001$ cm^{-1} when g is held constant at 2.10.[36]

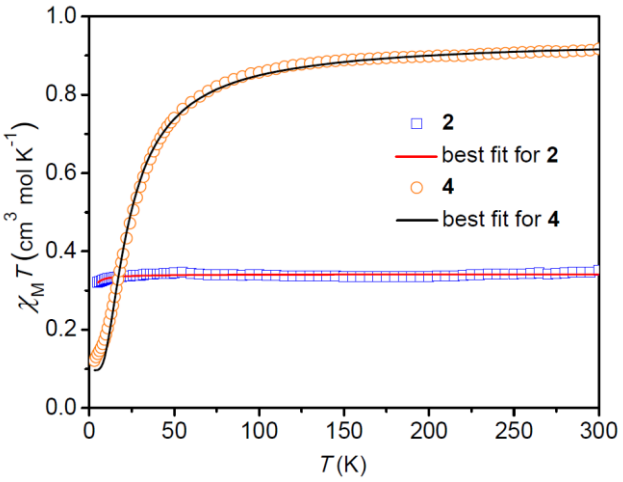


*Figure 9.4.4. TIP-corrected temperature dependence of the magnetic susceptibility data for **9.2** (blue squares) and **9.4** (orange circles) collected at applied fields of 1000 Oe. The fits were performed using the program Julx.*[35]

The parameters for the magnetic fit for **9.2** are in good agreement with literature precedent for an S = ½ mononuclear iron-acetylide complex.[14] A saturation of magnetization experiment collected at 1.8 K displays a magnetization value of 0.81 μ_B at 50 kOe that almost reaches saturation (Figure A9.6). These data are consistent with an S = ½ system with a g value lower than 2 and the presence of antiferromagnetic interactions (intermolecular in this case).

The magnetic susceptibility data for **9.4** show a room temperature $\chi_M T$ value of 1.30 cm^3Kmol^{-1}, which is higher than expected for two non-interacting S = ½ spins (0.75 cm^3Kmol^{-1}, g = 2.00) (Figure 5). Upon decreasing temperature, the $\chi_M T$ product decreases linearly until around 50 K whereupon the decrease becomes more drastic until 2 K where $\chi_M T$ = 0.10 cm^3Kmol^{-1}. This large decrease in $\chi_M T$ value is likely either antiferromagnetic coupling or magnetic anisotropy. Once again, S = ½ ions cannot display magnetic anisotropy, so this decrease in susceptibility value is likely antiferromagnetic coupling. Applying the Bleany-Bowers equation (experimental section) to **9.4** gives a reasonable fit for the data, indicative of the presence of intramolecular

antiferromagnetic coupling for **9.4**. When an intermolecular value is applied in the fit for **9.4**, no changes are observed in the values of the parameters or the quality of the fit, so this is not applied in the fit for **9.4**. Even though the *g* values are slightly higher than what is observed for **9.2**, the values are in excellent agreement with literature precedent.[14] An impurity (which is included in the fit) is not able separable from the sample although no ferromagnetic impurities are detected at 100 K (Figure A9.2) and all other bulk purity measurements indicate that **9.4** is pure. Further, a saturation of magnetization experiment for **9.4** at 1.8 K, indicates a magnetization value of 0.27 μ_B at 50 kOe, suggestive of some excited state involvement or the presence of a paramagnetic (or ferromagnetic) impurity. The intramolecular antiferromagnetic interactions observed for **9.4** indicate that indeed, antiferromagnetic interactions occur with the inclusion of the N-atom. To further investigate these interesting properties, magnetic susceptibility experiments are performed on **9.6**.

The trinuclear system (**9.6**) displays a room temperature $\chi_M T$ value of 1.34 cm^3Kmol^{-1}, slightly higher than the expected value for three non-interacting $S = ½$ ions (1.125 cm^3Kmol^{-1}, $g = 2.00$) (Figure 9.4.5). Upon decreasing the temperature, a near linear decrease is observed until around 100 K, where the decrease becomes slightly steeper until 2 K, where the $\chi_M T$ value reaches 0.34 cm^3Kmol^{-1}. The fit employed for **9.6** is based upon the Hamiltonian and the Van-Vleck equations shown in equations 9.3 and 9.4.

$$\hat{H} = -2J(S_a \cdot S_b + S_a \cdot S_c + S_b \cdot S_c) \qquad (9.3)$$

$$\chi_M T = \frac{Ng^2\beta^2}{4k} \frac{1+5\exp(\frac{3J}{kT})}{1+\exp(\frac{3J}{kT})} \qquad (9.4)$$

Due to the close packing and close Fe-Fe distances (8.29(4) Å) in the solid state structure of **9.6**, a Weiss constant (θ) is included in the fit. The parameters from this fit are in agreement the fits for **9.2** and **9.4** and show (similarly to **9.4**) that the N atom causes antiferromagnetic

interactions for **9.6**. The similar intramolecular superexchange coupling values (*J*) that are observed in the fits of **9.4** and **9.6** indicate a nearly identical superexchange mechanism, as expected. At 1.8 K with an applied field of 50 kOe, the magnetization value for **9.6** is 0.81 μ_B, providing evidence for a magnetic ground state of $S = ½$ for **9.6**. This is typical of a triangular system that promotes antiferromagnetic interactions.[37-42] The magnetic properties of **9.2**, **9.4** and **9.6** indicate that the nitrogen atom is intimately involved in the superexchange coupling of these systems. In an effort to probe what effects redox chemistry has upon the magnetic ground state and coupling pathways of these triangular complexes, we attempted oxidation reactions of the N atom for compounds **9.2**, **9.4** and **9.6**.

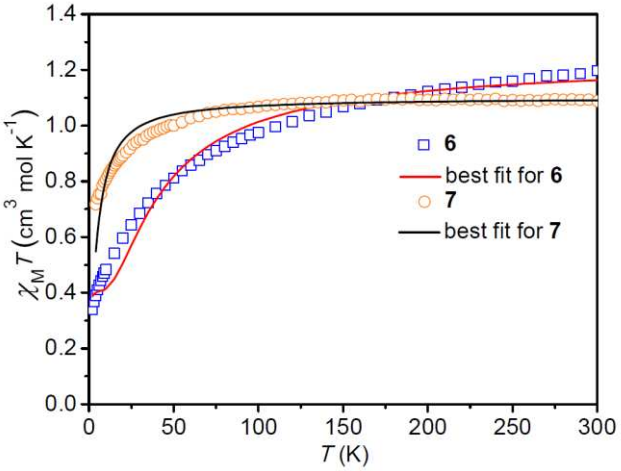


*Figure 9.4.5. TIP-corrected temperature dependence of the magnetic susceptibility data for **9.6** and **9.7** at applied fields of 5000 Oe. The fits were performed using the program Julx.*[35]

9.4.5 Oxidation of Nitrogen Atom

We set out to oxidize the central nitrogen of **9.2**, **9.4** and **9.6** using thianthrenium tetrafluoroborate ($ThBF_4$) to determine the differences in the magnetic properties upon oxidation. The overall air and temperature stability of **9.2** and **9.4** once the nitrogen atom is oxidized is quite

poor. In fact, **9.4** is so unstable once the N-atom is oxidized, that it could not be characterized at room temperature and only persisted at liquid nitrogen temperatures for a matter of seconds before decomposition. The stability of **9.2** upon N-atom oxidation is slightly better and the time before decomposition is determined to be 20 minutes at room temperature *via* UV-Vis spectroscopy (Figure A9.7). Fortunately, the oxidation product of **9.2** is stable at liquid nitrogen temperatures, so *in-situ* EPR and ^{1}H NMR were used to characterize the electronic structure of this transient product. No signal is observed in the EPR spectrum at 100 K, indicative of an integer spin ground state. Interestingly, the ^{1}H NMR of **9.2** shows peak broadening and peaks upfield to -30 ppm (Figure A9.8), indicative of the presence of a paramagnetic species. We attribute the lack of an EPR response to strong antiferromagnetic coupling between the nitrogen and iron center, and that upon warming, a paramagnetic response persists. If the nitrogen and iron atoms are strongly antiferromagnetically coupled, then the same coupling mechanism is presumably no longer apparent, which should promote ferromagnetic coupling in **9.7**.

The stability of **9.6** when oxidized is much greater than that of the oxidized products of **9.2** or **9.4**. Multiple reaction pathways are attempted to oxidize **9.6** to **9.7**; however, most that are performed above -20 ºC gave only decomposition products that are not easily characterized. To obtain a pure sample of **9.7**, compound **9.6** is oxidized by $ThBF_4$ at -78 ºC in a frozen slurry of acetonitrile. We also note that $NOBF_4$ could be used in place of $ThBF_4$; however, it gives a much lower yield (12%) presumably because the release of NO gas causes too much heat in the reaction vessel. Also, the reaction could be performed at room temperature using $AgBF_4$ in CH_2Cl_2, but these conditions gave only a 3% yield likely due to temperature insensitivity of the product.

To determine the formal oxidation state(s) of the iron atoms present in **9.7** as well as to locate the radical, EPR spectroscopy was performed, giving results comparable to **9.6** but with a much more pronounced resonance centered around 3440 Gauss (g = 2.02) (Figure A9.9). This type of resonance is indicative of a ligand radical or triplet ground state (*vide infra*). Further, UV-

Vis data indicate a new peak upon oxidation of **9.6** located at 605 nm, which is attributed to the radical π→π* orbital on the nitrogen center. While this is a higher energy transition than other previously reported organic amminium radicals,[43] it agrees well with amminium radicals within metal complexes.[44-45]

*9.4.6 Magnetic Properties of **9.7***

The room temperature $\chi_M T$ value for **9.7** is 1.20 cm^3Kmol^{-1}, which is lower than what is expected for four non-interacting S = 1/2 ions (1.50 cm^3Kmol^{-1}, g = 2.00) (Figure 9.4.5). Upon cooling, the $\chi_M T$ product remains relatively constant until ~75 K where a more noticeable decrease is observed until 4 K where a $\chi_M T$ value of 0.72 cm^3Kmol^{-1} is observed. These data indicate a probable triplet ground state, but more data are required to justify this observation further. The magnetization data, which do not saturate, reach 1.52 μ_B at 1.8 K with an applied field of 50 kOe (Figure 9.4.6), indicative of a ground state of S = 1 with large axial anisotropy (D) (Table 9.4.3), g values lower than 2 and/or the presence of antiferromagnetic interactions. To help support an S = 1 ground state, we present reduced magnetization data (M vs. H/T) where the isofield lines do not overlay, indicative of magnetic anisotropy (Figure 9.4.6). Using ANISOFIT to fit these data, the best fit came from an S = 1 ground state, supporting this assignment as an appropriate magnetic ground state (Table 9.4.3).[36] With these analyses, the $\chi_M T$ data for **9.7** are fit to a variety of equations. At first, a known Hamiltonian (equation 9.5) for the construction shown in Figure 9.4.1 is employed.[46]

$$\hat{H} = -2J(S_{A1}\cdot S_B + S_{A2}\cdot S_B + S_{A3}\cdot S_B) + \beta H[g_A(S_{A1} + S_{A2} + S_{A3}) + g_B S_B] \quad (9.5)$$

$$\chi_M T = \frac{N g^2 \beta^2}{4k} \frac{6\exp(\frac{-7J}{4kT}) + 30\exp(\frac{3J}{4kT})}{1 + 3\exp(\frac{-7J}{4kT}) + 5\exp(\frac{3J}{4kT})} \quad (9.6)$$

$$\text{where } g = (\frac{g_A^2 + g_A^2 + g_A^2}{3}) + g_B^2$$

Figure 9.4.1. Representation of coupling pathways via the Hamiltonian presented in Equation 9.3.

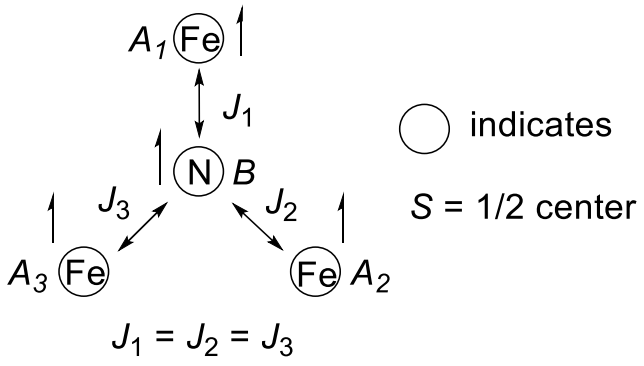


*Table 9.4.4. Parameters from unsuccessful magnetic fits performed for **9.7**.*

fit (ions involved)	g_{A1}	g_{A2}	g_{A3}	g_B	J_{12}, J_{13} (cm^{-1})	J_{34} (cm^{-1})	Θ (cm^{-1})	TIP (cm^3 mol^{-1}) x 10^{-6}	f_{sum}
4 S = ½	2.00*	2.00*	2.00*	2.00*	+279.5	-1728.9	-	796	0.096
2 S = ½, S = 1	1.54	1.54	1.54	-	-0.005	-	-2.54	674	0.025
2 S = ½	2.10*	2.10*	-	-	+581.8	-	-3.48	392	0.032

*indicates a parameter that was held constant. J_{13} was only applied for the second fit.

No fit using the Van-Vleck equation shown in Equation 9.4 provides a reasonable fit for the solid-state magnetic data. The addition of other parameters such as TIP and zero-field splitting did not provide a fit that confidently represent the data (Tables A9.1-2). This indicates that a system with completely localized spins is likely not an appropriate representation of the data. This is suggestive that a different superexchange pathway is present which is unsurprising given the previous systems that equation 9.4 has been applied to all contain oxo- or hydroxyl-bridged species.[46-50] Not surprisingly, these systems have much shorter spin-spin distances and weaker ligand fields, which could give rise to a different magnetic coupling pathway. Also, this is the first

example of a mixed metal-ligand radical system with such a geometry (Figure 9.4.1), which could also affect the observed properties.

Numerous scenarios are used to attempt to fit the magnetic susceptibility data, including the use of four $S = 1/2$ ions, two $S = ½$ and one $S = 1$ ion, two $S = ½$ ions and one $S = 1$ ion to accommodate the different possible ground states (Table 9.4.4). The coupling constant values for the first scenario were unreasonably large and the overall fit does not represent an appropriate model for the system. The second possibility does not fit well because of the large expected $\chi_M T$ value at room temperature for non-interacting spins (1.75 cm^3Kmol^{-1} when g = 2.00), so small and unreasonable g values are required for this fit to be an appropriate model. The scenario that included two $S = ½$ ions is more reasonable, except that the coupling constant (J) is quite large. Comparing this fit to the situation with $S = 1$, there are quite a few similarities. The TIP and θ values are nearly the same. Therefore, the appropriate model for this system involves two strongly coupled $S = ½$ ions. Since these spins couple so strongly, we are using the model of $S = 1$ as a more appropriate model. Each of the parameters in this fit are consistent with literature precedent.[14, 51-52] Through these different analyses and fits, it is difficult to approximate the magnitude of apparent superexchange coupling between the iron centers and nitrogen (antiferromagnetic) and among the irons (ferromagnetic); although due to the small $\chi_M T$ values it is predicted that these two interactions are of similar and large magnitude.

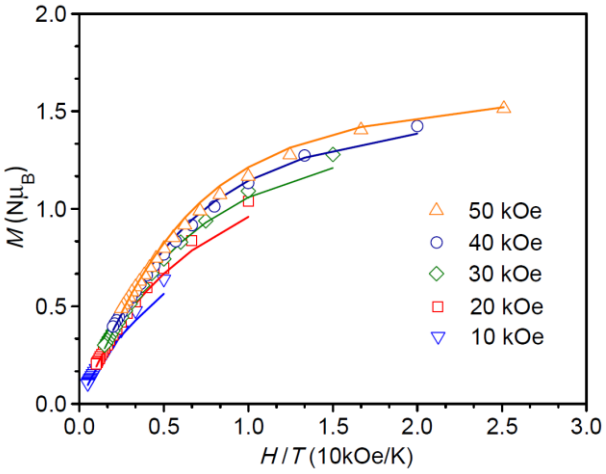


*Figure 9.4.6. Reduced magnetization data for **9.7**. The best fit lines obtained from ANISOFIT are shown for each field.*[36]

These magnetic results indicate that upon oxidation of the N atom, the Fe atoms antiferromagnetically couple strongly to the N while ferromagnetically coupling to each other. The same coupling mechanism that is observed for complexes **4** and **6** is no longer apparent upon oxidation as evidenced by the magnetic properties of **7**. The *in-situ* generation of the oxidized product of **2** shows a similar electronic structure to the observed results for **7**, albeit from a smaller amount of data. To justify these observed magnetic results, calculations are reported for some of the complexes measured herein.

9.4.7 Computational results

To further characterize the effects of the sp^2-hybridized nitrogen center played in the magnetic properties of the complex, calculations are performed. The spin polarization model has been largely successful in the control of magnetic interactions through organic design principles, even in the presence of N-heteroatoms. As such, it is peculiar that the antiferromagnetic interactions of **9.6** and similar known compounds do not follow this established trend.

An MO diagram was generated for the ligand, *p*-TEPA, and arranged according to the 'A' and 'E' symmetry labels of the C_{3v} point group of the molecule (Figure 9.4.7). We have previously demonstrated that the magnetic orbitals of the metal centers are delocalized through the LUMO of analogous organic linkers. The nitrogen center is not involved in the LUMO, 2e*, and the orbitals are delocalized through the sp^2-hybridized carbon at the 4-position of the adjacent phenyl ring. The absence of the nitrogen center from the exchange pathway explains the antiferromagnetic interactions between metal centers while the large distance between delocalized carbon atoms (2.44 Å) clarifies the small magnitude of the exchange. Rather than antiferromagnetic exchange occurring through spin repolarization at the nitrogen center, the sp^2 hybridized nitrogen is not symmetry compatible with the orbital for magnetic exchange.

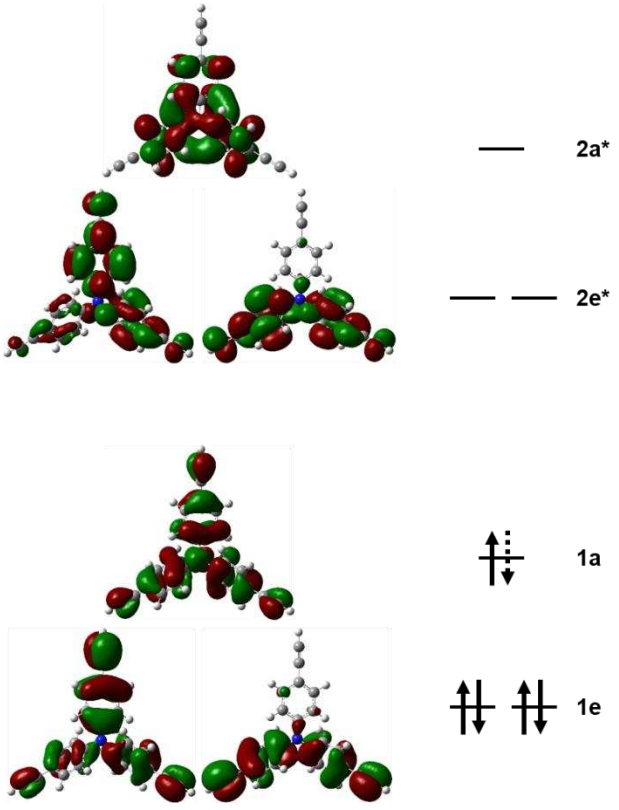


Figure 9.4.7. MO diagram for the free ligand p-TEPA.

The oxidation of *p*-TEPA moves the exchange pathway to the SOMO, 1a. The nitrogen center is delocalized with this orbital which reestablishes the ferromagnetic exchange predicted from considerations of spin polarization (Figure 9.4.8). The spin density plot of the triplet was generated and shows strong delocalization of the unpaired electron throughout the ligand set. This is indicative of providing strong magnetic exchange interactions between bridged metal centers through orbital overlap.

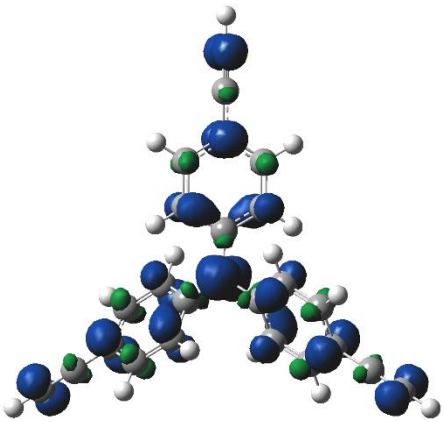
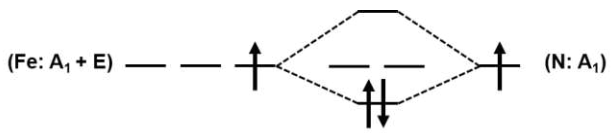
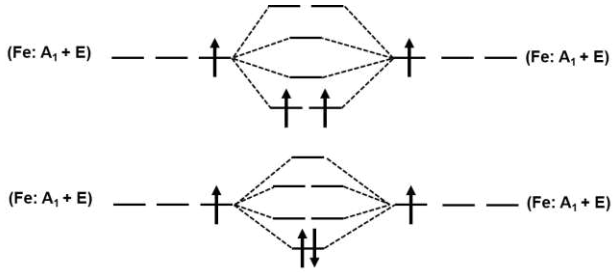


Figure 9.4.8. Spin density plot for [p-TEPA]$^{+}$.

The nature of the exchange interactions was also considered according to fragment analysis. The Fe^{III}-centers are each defined through an irreducible representation of A_1 + E while the nitrogen center possesses A_1 symmetry. The overlap between these magnetic fragments yield a bonding and antibonding arrangement and a set of doubly degenerate non-bonding orbitals. The stabilization of the bonding orbital provides stabilization to pair spins between the Fe^{III}-centers and the organic radical.



The nature of the exchange interaction between Fe^{III}-centers is more ambiguous due to the unstated ordering of the bonding orbitals through symmetry considerations alone. This is exhibited in the experimental through the tunable nature of their interaction *via* oxidation of the organic linker. If the doubly degenerate orbital is stabilized with respect to the single bonding orbital it is anticipated that a ferromagnetic interaction will result by proxy of Hund's rule. Since the Fe^{III}-centers must be anti-aligned with respect to the nitrogen radical it is reasonable to assume that the e-orbital will be oriented to maintain this interaction for **9.7**.



The energy of the accessible states of **9.6** and **9.7** differ in the number of exchange interactions ($K_{i,j}$) between electrons of parallel spin, modeled through virtue of the Pauli Exclusion Principle. However, the current single-determinant methodology fails to capture the total number of configurations that are possible for any antiferromagnetic interactions. A multi-determinant approach is currently in development to isolate the energy and spin orientation of the distinct states. The currently utilized broken-symmetry approach provides valuable qualitative information which readily reproduces the sign and magnitude of exchange interactions.

The spin density plots for the quartet and doublet states of **9.6** display ferromagnetic and antiferromagnetic interactions, respectively, between the Fe^{III}-centers. While spin is shown delocalized on the alkyne moieties there is minimal character located across the phenyl rings and central nitrogen. This is indicative of the weak magnetic interactions exhibited by the multi-nuclear

system. The doublet is lower in energy than the quartet and predicts a $J_{Fe\text{-}Fe}$ = -6.5 cm^{-1} which is multiplied by a factor of (3/2) to account for the spin-flip of a three-electron system, as derived from the Heisenberg Spin model. The theoretical value of -9.8 cm^{-1} is in close agreement with the experimental fit of -10.3 cm^{-1}.

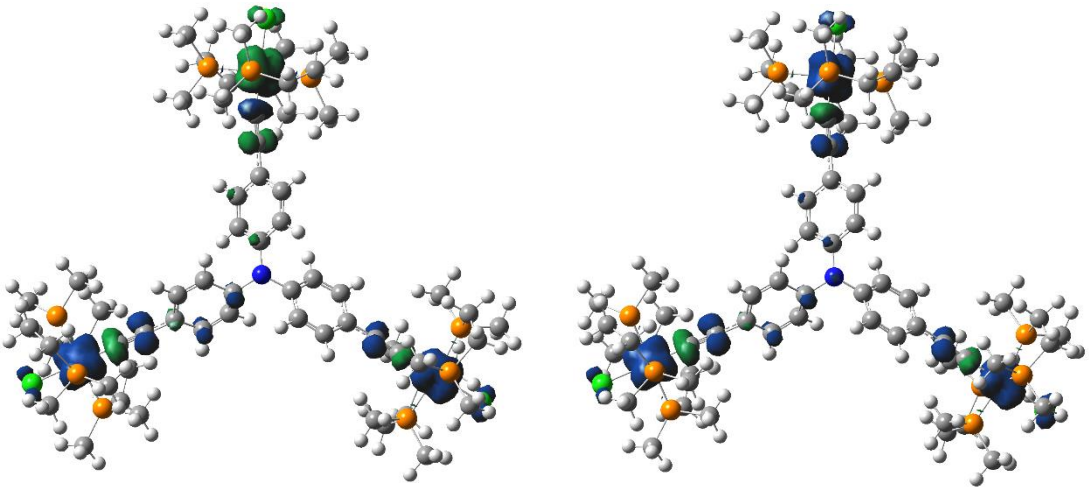


*Figure 9.4.9. Spin density plots for **9.6** and **9.7** on the left and right, respectively.*

The oxidation of the nitrogen center allows for a distinct exchange pathway between the Fe^{III}-centers and the organic radical. The spin density plot of the triplet state displays a ferromagnetic interaction between the Fe^{III}-centers and an antiferromagnetic arrangement with the central nitrogen. This is calculated as the energetic ground state and predicts a $J_{Fe\text{-}N}$ of -40.6 cm^{-1}. The quintet and the singlet states are degenerate in energy and both exhibit an equal number of $K_{Fe,N}$ and $K_{Fe,Fe}$ in their spin density plots. This suggests that the exchange between Fe^{III}-centers is of opposite sign but of equal magnitude as it calculates $J_{Fe\text{-}Fe}$ of 40.6 cm^{-1}.

9.5 Conclusions

In this report, we present the syntheses and characterization of iron-triarylamine complexes tethered by alkynes. Each complex is characterized by both local structure and bulk purity methods. Electrochemical data collected indicate that oxidation(s) could be executed on the Fe and N centers, selectively. In addition, we collected magnetic susceptibility data on all paramagnetic species. We find that a spin-repolarization is observed for **9.4** and **9.6**, consistent with literature precedent. However, upon oxidation significant antiferromagnetic coupling occurs between iron and nitrogen atoms as well as significant ferromagnetic coupling among iron atoms. This oxidation event increases the magnetic ground states from $S = ½$ to $S = 1$ for **9.6** and **9.7**, respectively. These experimental results are supported by computational findings on various aspects of the system studied. Overall, this study demonstrates that ligand oxidation causes large changes in superexchange interactions and has implications for future work with SMMs.

References

1. Long, N. J.; Williams, C. K. *Angew. Chem. Int. Ed.* **2003**, *42*, 2586.

2. Sugawara, T.; Komatsu, H.; Suzuki, K. *Chem. Soc. Rev.* **2011**, *40*, 3105.

3. Zhou, G.-J.; Wong, W.-Y. *Chem. Soc. Rev.* **2011**, *40*, 2541.

4. Cao, Z.; Xi, B.; Jodin, D. S.; Zhang, L.; Cummings, S. P.; Gao, Y.; Tyler, S. F.; Fanwick, P. E.; Crutchley, R. J.; Ren, T. *J. Am. Chem. Soc.* **2014**, *136*, 12174.

5. Halet, J.-F.; Lapinte, C. *Coord. Chem. Rev.* **2013**, *257*, 1584.

6. Onitsuka, K.; Ohara, N.; Takei, F.; Takahashi, S. *Dalton Trans.* **2006**, 3693.

7. Paul, F.; Lapinte, C. *Coord. Chem. Rev.* **1998**, *178-180*, 431.

8. Jeon, I.-R.; Park, J. G.; Xiao, D. J.; Harris, T. D. *J. Am. Chem. Soc.* **2013**, *135*, 16845.

9. Degayner, J. A.; Jeon, I.-R.; Harris, T. D. *Chem. Sci.* **2015**, *6*, 6639.

10. Gaudette, A. I.; Jeon, I.-R.; Anderson, J. S.; Grandjean, F.; Long, G. J.; Harris, T. D. *J. Am. Chem. Soc.* **2015**, *137*, 12617.

11. Moilanen, J. O.; Chilton, N. F.; Day, B. M.; Pugh, T.; Layfield, R. A. *Angew. Chem. Int. Ed.* **2016**, *55*, 5521.

12. Suzuki, S.; Nagata, A.; Kuratsu, M.; Kozaki, M.; Tanaka, R.; Shiomi, D.; Sugisaki, K.; Toyota, K.; Sato, K.; Takui, T.; Okada, K. *Angew. Chem. Int. Ed.* **2012**, *51*, 3193.

13. Grelaud, G.; Cador, O.; Roisnel, T.; Argouarch, G.; Cifuentes, M. P.; Humphrey, M. G.; Paul, F. *Organometallics* **2012**, *31*, 1635.

14. Hoffert, W. A.; Rappé, A. K.; Shores, M. P. *J. Am. Chem. Soc.* **2011**, *133*, 20823.

15. Robson, K. C. D.; Bomben, P. G.; Berlinguette, C. P. *Dalton Trans.* **2012**, *41*, 7814.

16. Robson, K. C. D.; Hu, K.; Meyer, G. J.; Berlinguette, C. P. *J. Am. Chem. Soc.* **2013**, *135*, 1961.

17. Robson, K. C. D.; Koivisto, B. D.; Yella, A.; Sporinova, B.; Nazeeruddin, M. K.; Baumgartner, T.; Grätzel, M.; Berlinguette, C. P. *Inorg. Chem.* **2011**, *50*, 5494.

18. Robson, K. C. D.; Koivisto, B. D.; Berlinguette, C. P. *Inorg. Chem.* **2012**, *51*, 1501.

19. Hua, C.; D'Alessandro, D. M. *CrystEngComm* **2014**, *16*, 6331.

20. Hua, C.; Turner, P.; D'Alessandro, D. M. *Dalton Trans.* **2013**, *42*, 6310.

21. Wu, P.; He, C.; Wang, J.; Peng, X.; Li, X.; An, Y.; Duan, C. *J. Am. Chem. Soc.* **2012**, *134*, 14991.

22. Wu, P.; Wang, J.; Li, Y.; He, C.; Xie, Z.; Duan, C. *Adv. Funct. Mater.* **2011**, *21*, 2788.

23. Grelaud, G.; Tohme, A.; Argouarch, G.; Roisnel, T.; Paul, F. *New J. Chem.* **2011**, *35*, 2740.

24. Tohme, A.; Grelaud, G.; Argouarch, G.; Roisnel, T.; Bondon, A.; Paul, F. *Inorg. Chem.* **2013**, *52*, 8993.

25. Girolami, G. S.; Wilkinson, G.; Galas, A. M. R.; Thornton-Pett, M.; Hursthouse, M. B. *J. Chem. Soc. Dalton Trans.* **1985**, 1339.

26. Xu, F.; Peng, L.; Orita, A.; Otera, J. *Org. Lett.* **2012**, *14*, 3970.

27. Shi, L.; He, C.; Zhu, D.; He, Q.; Li, Y.; Chen, Y.; Sun, Y.; Fu, Y.; Wen, D.; Cao, H.; Cheng, J. *J. Mater. Chem.* **2012**, *22*, 11629.

28. Boduszek, B.; Shine, H. J. *J. Org. Chem.* **1988**, *53*, 5142.

29. Shores, M. P.; Sokol, J. J.; Long, J. R. *J. Am. Chem. Soc.* **2002**, *124*, 2279.

30. Bain, G. A.; Berry, J. F. *J. Chem. Educ.* **2008**, *85*, 532.

31. Le Narvor, N.; Lapinte, C. *Organometallics* **1995**, *14*, 634.

32. Field, L. D.; George, A. V.; Laschi, F.; Malouf, E. Y.; Zanello, P. *J. Organomet. Chem.* **1992**, *435*, 347.

33. Grelaud, G.; Cador, O.; Roisnel, T.; Argouarch, G.; Cifuentes, M. P.; Humphrey, M. G.; Paul, F. *Organometallics* **2012**, *31*, 1635.

34. Chung, W. K.; Wong, K. M.-C.; Lam, W.-H.; Zhu, L.; Zhu, N.; Kwok, H.-S.; Yam, V. W.-W. *New J. Chem.* **2013**, *37*, 1753.

35. Bill, E.; Max Planck Institute for Bioinorganic Chemistry: Mulheim an der Ruhr, Germany, **2008**.

36. Shores, M. P.; Sokol, J. J.; Long, J. R. *J. Am. Chem. Soc.* **2002**, *124*, 2279.

37. Beckett, R.; Colton, R.; Hoskins, B. F.; Martin, R. L.; Vince, D. G. *Aust. J. Chem.* **1969**, *22*, 2527.

38. Chaudhuri, P.; Karpenstein, I.; Winter, M.; Butzlaff, C.; Bill, E.; Trautwein, A. X.; Florke, U.; Haupt, H. J. *J. Chem. Soc. Chem. Commun.* **1992**, 321.

39. Pinero, D.; Baran, P.; Boca, R.; Herchel, R.; Klein, M.; Raptis, R. G.; Renz, F.; Sanakis, Y. *Inorg. Chem.* **2007**, *46*, 10981.

40. Butcher, R. J.; Oconnor, C. J.; Sinn, E. *Inorg. Chem.* **1981**, *20*, 537.

41. Angaridis, P. A.; Baran, P.; Boca, R.; Cervantes-Lee, F.; Haase, W.; Mezei, G.; Raptis, R. G.; Werner, R. *Inorg. Chem.* **2002**, *41*, 2219.

42. Angaroni, M.; Ardizzoia, G. A.; Beringhelli, T.; Lamonica, G.; Gatteschi, D.; Masciocchi, N.; Moret, M. *J. Chem. Soc. Dalton Trans.* **1990**, 3305.

43. Bell, F. A.; Ledwith, A.; Sherrington, D. C. *J. Chem. Soc. C* **1969**, 2719.

44. Jones, S. C.; Coropceanu, V.; Barlow, S.; Kinniburgh, T.; Timofeeva, T.; Bredas, J.-L.; Marder, S. R. *J. Am. Chem. Soc.* **2004**, *126*, 11782.

45. Vincent, K. B.; Parthey, M.; Yufit, D. S.; Kaupp, M.; Low, P. J. *Polyhedron* **2015**, *86*, 31.

46. Lloret, F.; Journaux, Y.; Julve, M. *Inorg. Chem.* **1990**, *29*, 3967.

47. Pavlishchuk, V.; Birkelbach, F.; Weyhermuller, T.; Wieghardt, K.; Chaudhuri, P. *Inorg. Chem.* **2002**, *41*, 4405.

48. Khanra, S.; Kuepper, K.; Weyhermuller, T.; Prinz, M.; Raekers, M.; Voget, S.; Postnikov, A. V.; de Groot, F. M. F.; George, S. J.; Coldea, M.; Neumann, M.; Chaudhuri, P. *Inorg. Chem.* **2008**, *47*, 4605.

49. Gudel, H. U.; Hauser, U. *Inorg. Chem.* **1980**, *19*, 1325.

50. Tian, H.; Qiao, X.; Xie, C. Z.; Ouyang, Y.; Xu, J. Y. *J. Coord. Chem.* **2017**, *70*, 1207.

51. Halet, J.-F. L., C. *Coord. Chem. Rev.* **2013**, *257*, 1584.

52. Paul, F. L., C. *Coord. Chem. Rev.* **1998**, *178-180*, 431.

Chapter 10: A family of related Co(II) terpyridine compounds exhibiting field induced single-molecule magnet properties.*

10.1 Introduction

Single-molecule magnets (SMMs) show promise for potential applications such as high-density data storage, quantum computation and spintronic devices.[1] For data storage, a key focus is optimizing magnetic anisotropy parameters toward large and negative axial (*D*) values with minimal rhombic (*E*) terms. Initial studies on mononuclear systems focused largely on lanthanoid complexes;[2-3] however, mononuclear first row transition metal complexes have also displayed interesting SMM properties. Mononuclear SMMs have been sourced from V(IV),[4] Cr(II),[5] Mn(III/IV),[6-7] Fe(I/II/III),[8-10] Co(I),[11] Ni(I/II)[12-13] and Cu(II) ions.[14] Notwithstanding, Co(II) is the most studied ion for mononuclear first row SMMs.[15]

Interest in high-spin Co(II) compounds derives from the large inherent large spin-orbit coupling of this ion, leading to systems with large anisotropy. Magnetic anisotropy can be tuned through modification of the coordination geometry about the Co(II) center. Geometric distortions which decrease symmetry often lead to novel orientations of the magnetic axes as well as increased access to low-lying excited states, resulting in increased magnetic anisotropy.[16-17] Prudent selection of multi-dentate ligands that provide steric strain can result in distorted geometries about the metal center. This strategy has been employed in the preparation of square pyramidal Co(II) compounds with tridentate ligands. Traditional pincer ligands (NNN) combined with Co(II) ions lead to complexes with intriguing dynamic magnetic properties. The pentacoordinate pyridinediimine-based Co complexes displayed slow magnetic relaxation upon application of a dc field with modest barriers (U_{eff} = 11-17 cm^{-1}).[18]

---

*Reproduced with permission from [*Polyhedron* **2018**, *143*, 193-200.] Copyright 2018 ScienceDirect.

Other pincer-like ligands, such as 2,2':6',2"-terpyridine (tpy) (Figure 10.1.1), have been utilized for synthesis of Co(II) complexes which also show magnetic relaxation in the presence of an applied dc field.[19] In principle, the magnetic properties of Co(II) tpy complexes may be modulated in a straightforward manner with judicious selection of substituent, as the 4' position of tpy is easily diversifiable and some derivatized analogs are commercially available. Slattery and coworkers have studied inductive effects arising from 4'-substituent identity on the room temperature spin state of Co(II) tpy complexes in solution: high spin states were observed in most cases, except when 4' = H or *p*-tolyl.[20] This study found a linear free energy relationship between the $E_{1/2}$ value of the Co(III/II) redox couple and the electronics of the substituent on the tpy ligand, but the same relationship was not observed for the magnetic moment of the Co(II) compounds.

Since Co(II)-tpy complexes have shown a structure-property relationship for magnetic properties,[19] we are motivated to further study these properties, controlling electronic factors on the tpy ligand(s). Specifically, we sought to investigate the influence of the electronic nature of the 4' substituent of tpy on variable temperature magnetic properties of the Co(II) complexes in the solid state, focusing on dynamic properties. As a preliminary evaluation of these effects, we chose to install easily-prepared tpy ligands with relative extremes in electronic character. Therefore, pyrrolidinyl and trifluoromethansulfonyl substituents were chosen as representative electron-donating and -withdrawing groups, respectively, with comparable steric bulk. Herein, we present the syntheses, crystallographic and magnetic properties for [(OTftpy)$CoCl_2$] (**10.1**), [Co(pyrtpy)$_2$](BPh_4)$_2$ (**10.2b**) and [(OTftpy)Co(κ_2-O_2NO)$_2$] (**10.3**).

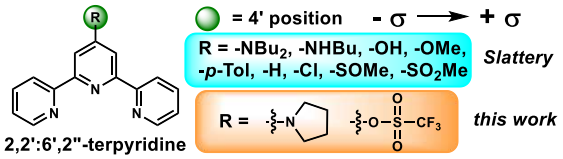


Figure 10.1.1. Molecular structure of 2,2':6',2"-terpyridine and use as pincer-like ligand in Co(II) complexes.

10.2 Division of Labor

Unless otherwise noted, all synthesis, characterization, analysis and interpretation was performed by Robert F. Higgins. The synthesis of the ligands was assisted by Tarik J. Ozumerzifon. All computational work was performed by Justin P. Joyce. The preparation of this manuscript for publication was assisted by Brooke N. Livesay. All interpretation and analysis was performed by Robert F. Higgins, Justin P. Joyce, Anthony K. Rappé and Matthew P. Shores. All work in this chapter has been published, see: *Polyhedron* **2018**, *143*, 193.

10.3 Materials and Methods.

10.3.1 General Considerations

Preparations of all metal complexes were performed in air and at ambient conditions on the benchtop, unless otherwise noted. The ligands 4'-trifluoromethylsulfonate-2,2':6',2"-terpyridine (OTftpy)[21] and 4'-pyrrolidine-2,2':6',2"-terpyridine (pyrtpy)[22] were prepared according to known literature procedures. Water was purified from a Millipore Milli-Q® Water System with a four-filter system attachment. Syringe filters (VWR international) were fitted with 0.2 μm PTFE membranes. All other reagents were purchased commercially and used without further purification.

10.3.2 Preparation of novel metal complexes

[(OTftpy)$CoCl_2$] (10.1)

A solution of $[Co(H_2O)_6]Cl_2$ (46 mg, 0.193 mmol) in 1:1 v:v CH_3OH:H_2O (5 mL total) was added to a mixture of OTftpy (74 mg, 0.194 mmol) in 1:1 v:v CH_3OH:H_2O (7 mL total), and the resulting orange mixture was stirred for 30 minutes. The reaction mixture was passed through a syringe filter and the solvent was removed *in vacuo*, giving **10.1** as a green powder. Diffraction quality single crystals were obtained from slow diffusion of diethyl ether into a concentrated methanolic solution of **10.1** (39.5 mg, 40% yield). UV/Vis (MeCN) λ_{max}/nm (ε_M/$M^{-1}cm^{-1}$): 195 (52400), 274 (16000), 282 (15800), 322 (14000), 337 (7030), 401 (545). ESI-MS(+) (MeCN): *m/z* 475.00 $(M - Cl)^+$. Anal. Calcd. For $[C_{16}H_{10}N_3O_3F_3SCl_2Co]$: C, 37.60; H, 1.97; N, 8.22. Found: C, 37.69; H, 1.98; N, 8.15.

[$Co(pyrtpy)_2$](BPh_4)$_2$ (10.2b)

A solution of $[Co(H_2O)_6](NO_3)_2$ (29 mg, 0.099 mmol) in 1:1 v:v CH_3OH:H_2O (5 mL total) was added to a suspension of pyrtpy (60 mg, 0.198 mmol) in 1:1 v:v CH_3OH:H_2O (7 mL total), and the resulting orange mixture was stirred for 30 minutes. The reaction was then passed through a syringe filter and the solvent was removed *in vacuo.* The residue was then washed with Et_2O (2 × 5 mL), giving a dark orange powder (65 mg, 84% yield) which was assigned as $[Co(pyrtpy)_2](NO_3)_2$ (**10.2a**). ESI-MS(+) (MeCN): *m/z* 725.20 ($[Co(pyrtpy)_2](NO_3) - NO_3)^+$. The compound was used in the next step without further characterization or purification. A concentrated solution of **10.2a** (52 mg) in MeOH (2 mL) was added dropwise to a stirring solution of $NaBPh_4$ (500 mg, 1.46 mmol) in MeOH (10 mL), resulting in the immediate formation of a light orange precipitate. The resulting suspension was stirred for 15 minutes, collected by filtration, and washed successively with MeOH (2 × 5 mL) and Et_2O (1 × 5 mL), giving **10.2b** as an orange solid. Diffraction quality single crystals were grown from diffusion of diisopropyl ether into a concentrated solution of **10.2b** in dichloroethane (6.2 mg, 7% yield for anion exchange, 6% total yield over two steps). UV/Vis (MeCN) λ_{max}/nm (ε_M/$M^{-1}cm^{-1}$): 234 (76400), 268 (29300), 275

(31500), 367 (7360). ESI-MS(+) (MeCN): *m/z* 331.75 (M - 2 BPh_4)$^{2+}$. Anal. Calcd. For [$C_{86}H_{76}N_8B_2Co$]: C, 79.33; H, 5.88; N, 8.61. Found: C, 79.63; H, 6.05; N, 8.22.

[(OTftpy)Co(κ_2-$O_2NO)_2$] (10.3)

A solution of [$Co(H_2O)_6$]($NO_3)_2$ (32 mg, 0.131 mmol) in 1:1 v:v CH_3OH:H_2O (8 mL total) was added to a mixture of OTftpy (50 mg, 0.13 mmol) in 1:1 v:v CH_3OH:H_2O (7 mL total) and the resulting orange solution was stirred for 30 minutes. The reaction mixture was then passed through a syringe filter and the solvent was removed *in vacuo*, giving **10.3** as an orange powder. Diffraction quality single crystals were obtained from diffusion of diethyl ether into a concentrated solution of **10.3** in acetonitrile (32.8 mg, 45% yield). UV/Vis (MeCN) λ_{max}/nm (ε_M/$M^{-1}cm^{-1}$): 221 (59100), 281 (24800), 314 (12000), 380 (2570).ESI-MS(+) (MeCN): *m/z* 502.00 (M - NO_3)$^+$. Anal. Calcd. For [$C_{16}H_{12}CoF_3N_5O_{10}S$]: C, 33.00; H, 2.08; N, 12.03. Found: C, 33.19; H, 2.25; N, 12.39.

10.3.3 Magnetic Measurements

Magnetic susceptibility data were collected with a Quantum Design MPMS-XL SQUID magnetometer. Finely ground crystalline samples were loaded into polyethylene bags and sealed on the benchtop, and then the bags were inserted into drinking straws. Ferromagnetic impurity checks were performed for each sample at 100 K by sweeping the field (0 – 10 kOe): linearity in plots indicated lack of significant ferromagnetic impurities (Figures A10.4-A10.6). Static (dc) magnetic susceptibility data were collected at temperatures ranging from 2 K to 300 K at an applied field of 1 kOe. Dynamic (ac) susceptibility data were collected with an oscillating field of 4 Oe in the frequency range of 1.0-1500 Hz. Data were corrected for the magnetization of the sample holder by subtracting the susceptibility of an empty container, and for diamagnetic contributions of the sample by using Pascal's constants.[23] The magnetic susceptibility data were fit to the spin Hamiltonian described in equation 1, using the program PHI.[24] The reduced magnetization data were fit to equation 2, using the program ANISOFIT 2.0 (Figures A107-A10-8).[25]

$$\widehat{H} = \sum D_i\left[S_{z,i}^2 - 1/3S_i(S_i+1) + E_i/D_i\left(S_{x,i}^2 - S_{y,i}^2\right)\right] + \sum g_{xx,i}\beta\check{S}_{x,i}\cdot\overbrace{B_x} + g_{yy,i}\beta\check{S}_{y,i}\cdot\overbrace{B_y} + g_{zz,i}\beta\check{S}_{z,i}\cdot\overbrace{B_z} \quad (1)$$

$$\widehat{H} = D\widehat{S_z^2} + E\left(\widehat{S_x^2} + \widehat{S_y^2}\right) + g_{iso}\mu_B S\cdot H \quad (2)$$

10.3.4 Crystallographic Measurements

Key structural data for compounds **10.1**-**3** are provided in Table 10.3.1. Crystals were coated in Paratone oil, supported on Cryoloops, and mounted on a Bruker Kappa Apex 2 CCD diffractometer under a stream of cold nitrogen. All data collections were performed with Mo Kα radiation and a graphite monochromator. Initial lattice parameters were determined from a minimum of 310 reflections harvested from 36 frames; these parameters were later refined against all data. Data sets were collected targeting full coverage and fourfold redundancy. Data were integrated and corrected for absorption effects with the Apex 2 (**10.2b** and **10.3**) or Apex 3 (**10.1**) software packages.[26-27] Structures were solved by direct methods and refined with the SHELXTL software package.[28] Displacement parameters for all non-hydrogen atoms were refined anisotropically. All hydrogens were assigned to ideal positions and refined using a riding model with an isotropic thermal parameter 1.2 times that of the attached carbon atom. The large R_{int} value for **10.2b** is likely due to the fairly weak diffraction of the chosen crystal since it was rather thin. Unfortunately, all other crystals of **10.2b** that were measured gave poorer diffraction data. The water molecule in compound **10.3** was refined without H atoms on the O atom since the O atom went NPD when refined with H atoms. The compounds have been uploaded to the CCDC and have the following identifiers: 1559155 (**10.1**), 1559156 (**10.2b**) and 1559157 (**10.3**).

*Table 10.3.1. Crystallographic parameters for **10.1**-**3**.*[a]

	10.1	**10.2b**	**10.3**
Formula	$C_{16}H_{10}N_3O_3F_3SCl_2Co$	$C_{86}H_{76}N_8B_2Co$	$C_{16}H_{12}N_5O_{10}F_3SCo$
Formula wt	511.16	1302.09	580.28
Space Group	$P\,2_1/c$	$C\,2/c$	$P\,\bar{1}$
a, Å	8.0310(16)	28.311(4)	8.3939(3)
b, Å	11.449(2)	17.290(4)	9.6552(4)
c, Å	20.220(4)	27.830(5)	13.8310(5)
α, deg	90	90	82.307(1)
β, deg	96.16(3)	90.928(9)	78.170(1)
γ, deg	90	90	79.277(1)
V, Å^3	1848.4(6)	13621(5)	1072.48(7)
Z	4	8	2
T, K	100(2)	100(2)	120(2)
Radiation, λ (Å)	0.71073	0.71073	0.71073
d_{calc}, g/cm^3	1.837	1.270	1.797
μ (mm^{-1})	1.385	0.306	0.990
F (0 0 0)	1020.0	5480.0	582.0
Crystal size (mm)	0.339 × 0.118 × 0.116	0.930 × 0.188 × 0.153	1.091 × 0.259 × 0.161
Θ range (°)	2.0 – 26.5	1.4 – 23.3	1.5 – 24.7
Reflections measured	37992	141765	21211
Unique reflections	3731	9796	3633
R_{int}	0.0430	0.2076	0.0419

Reflections with $F^2 > 4\sigma$ (F^2)	3112	5436	2986
Number of parameters	262	874	325
GOF	1.061	0.975	1.012
R_1[b], %	2.97	5.43	2.68
wR_2, %	7.04	14.17	6.79
$\Delta\rho_{max}$ $\Delta\rho_{min}$ (e Å^{-3})	-0.456 – 0.592	-0.562 – 0.885	-0.319 – 0.541
Refine_ls_shift/su_max	0.001	0.000	0.001
Refine_ls_shift/su_mean	0.000	0.000	0.000

[a]Obtained with graphite-monochromated Mo Kα (λ = 0.71073 Å) radiation. [b]$R_1 = \Sigma ||F_o| - |F_c||/\Sigma|F_o|$, w$R_2 = \{\Sigma[w(F_o^2 - F_c^2)^2]/\Sigma[w(F_o^2)^2]\}1/2$ for $F_o > 4\sigma(F_o)$.

10.3.5 Other Physical Measurements

All experiments were conducted at room temperature unless otherwise noted. Electronic absorption spectra were obtained with a Hewlett-Packard 8453 spectrophotometer using quartz cuvettes with a 1 cm path length. IR spectra were measured with a Nicolet 380 FT-IR spectrophotometer using a Smart Performer ZnSe attenuated total reflectance (ATR) accessory. Mass spectrometry experiments were performed in the positive ion mode on a Finnigan LTQ mass spectrometer, equipped with an analytic electrospray ion source and a quadrupole ion trap mass analyzer. Each measurement was performed with the capillary temperature = 175 °C, spray voltage = 5 kV, and spray current = 91 μA. Elemental analyses were performed by Robertson Microlit Laboratories (Ledgewood, NJ).

10.3.6 Computational Methods

Calculations were performed using crystal coordinates with C-H distances adjusted to RC-H sp^3 = 1.09 Å and RC-H sp^2 = 1.07 Å. For **10.2b**, only the cation was investigated and thus the

tetraphenylborate anions were removed prior to performing the calculation. A CASSCF/NEVPT2[29-32] *ab initio* treatment with a def2-SVP basis set[33-34] was performed with the ORCA 3.03 software package,[35] utilizing an RI approximation. An active space of seven electrons in five orbitals (5, 7), with a state averaging of six quartets and seven doublets was selected to generate the magnetic properties.[36]

10.4 Results and Discussion

10.4.1 Syntheses

The ligands OTftpy and pyrtpy are prepared following known literature preparations.[21-22] The relatively strongly electron-donating and -withdrawing properties of a trifluoromethanesulfonyl and pyrrolidinyl group, respectively, make them suitable candidates to probe ligand donor effects on the magnetic properties of Co complexes. Reports of various Co(II) tpy compounds show a preference for mono or bis ligation of tpy ligands to the Co(II) center based on solvent choice.[37-38] Overall, $[Co(4'\text{-R-tpy})_2]^{2+}$ (R = Cl, OMe, H) compounds exhibit greater stability in aqueous rather than organic solutions. In an effort to synthesize only bis-coordinated species, all reactions ligating tpy to Co(II) are performed in a 1:1 MeOH:H_2O solutions, as described previously by Slattery and others.[20] Compounds **10.1** and **10.3**, which bind only one tpy ligand, are prepared by addition of OTftpy to MeOH:H_2O solutions of $[Co(H_2O)_6]Cl_2$ and $[Co(H_2O)_6](NO_3)_2$, respectively. The bis-tpy species compound **10.2b** is prepared by addition of pyrtpy to $[Co(H_2O)_6](NO_3)_2]$ and subsequent anion exchange using excess $NaBPh_4$ in methanol. The nitrate-containing intermediate is likely $[Co(pyrtpy)_2](NO_3)_2$ (**10.2a**) based on mass spectrometry characterization. Prior to any other characterization, the compounds **10.1**-**3** are recrystallized and characterized by elemental analysis and mass spectrometry to ensure bulk purity.

It has previously been reported that the reaction of tpy ligands with Co(II) ions gives mono- or bis-ligated species solely on the choice of solvents and their associated polarities.[20, 39-40] Even in the presence of two equivalents of OTftpy, only the monoligated product is observed, therefore it appears that more complex equilibria are operative that rely on the Co(II) salt choice and/or

ligand choice. Interestingly, we use $[Co(H_2O)_6](NO_3)_2$ as a starting material for **10.2b** and **10.3** and observe differently substituted products (bis tpy for **10.2b** and mono tpy for **10.3**), therefore we suspect that the choice of ligand affects the equilibria to a greater extent than the Co(II) starting material. We attribute the observed synthetic differences to the electronic nature of the ligands OTftpy and pyrtpy. The ligand OTftpy generates a weak ligand field given the large electron withdrawing nature of the trifluoromethylsulfonyl group (σ_p = 0.53), whereas a pyrrolidine group is strongly electron-donating (σ_p = -0.83 for -NMe_2).[41] Therefore, we hypothesize that the competing equilibria of ligation of solvent, or more likely anions, when OTftpy is employed drives forward mono ligation whereas the equilibria are pushed toward the bis ligated species when a stronger field ligand (pyrtpy) is used. Since the solvents remain the same in all cases, a direct comparison of competing ligation events directly on the nature of the tpy ligand is appropriate. Notwithstanding, Slattery and others have reported that direct syntheses in H_2O give bis(terpyridine) compounds when electron withdrawing groups are present. [38] These results increase the understanding of solvent and anion effects probed previously when 4'-methoxy-2,2':6',2"-terpyridine is used.[38]

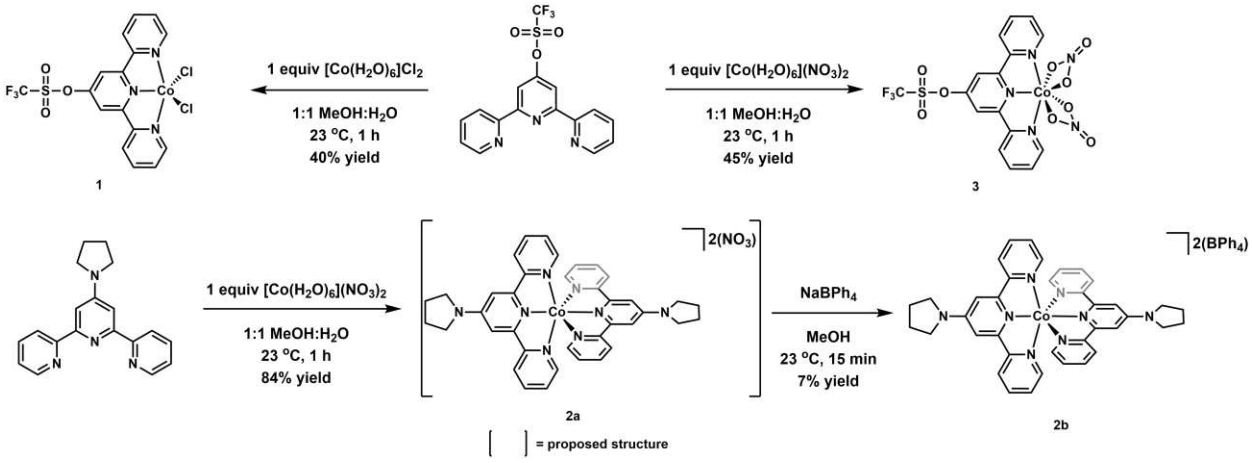


*Figure 10.4.1. Syntheses of compounds **1**-**3**.*

10.4.2 Structural Characterization

Single crystal x-ray diffraction analysis of **10.1** and **10.2b** is carried out at 100 K and at 120 K for **3** (Figure 10.4.1). Compounds **10.1** and **10.2b** crystallize in the monoclinic space groups $P2_1/c$ and $C2/c$, respectively, whereas compound **10.3** crystallizes in the triclinic space group $P\bar{1}$.

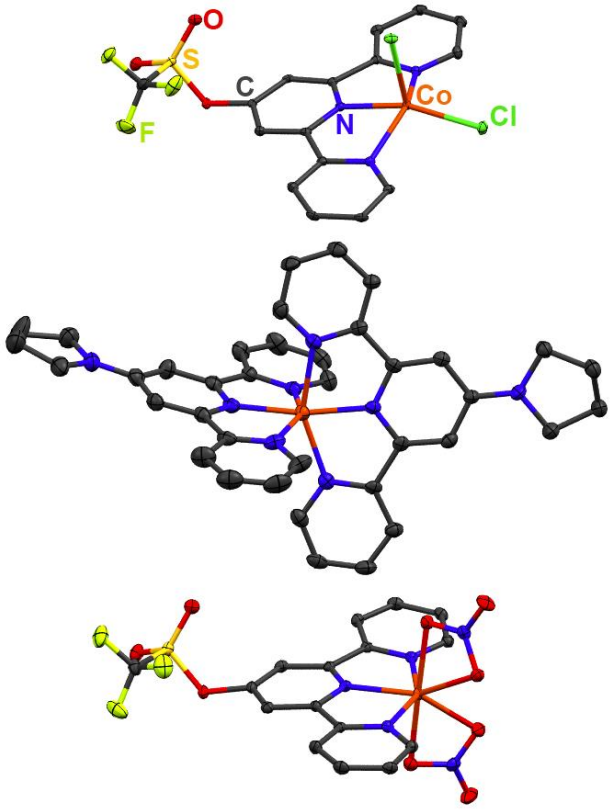


*Figure 10.4.1. Thermal ellipsoid (40% probability) representations for compounds **10.1** (top) and **10.3** (bottom) and the cation of **10.2b** (middle). All atoms lie on general positions. Co-crystallized solvent, anions (for **10.2b**) and hydrogen atoms are removed for clarity. Orange, blue, grey, red, green, yellow and light green correspond to cobalt, nitrogen, carbon, oxygen, chlorine, sulfur and fluorine atoms, respectively.*

The crystal structure of **10.1** shows a single OTftpy ligand and two chloride anions bound to the Co(II) center in a five-coordinate geometry, in agreement with the bulk purity analyses of

the compound. The geometric parameter (τ_5) is calculated to determine how the geometry deviates from ideal square pyramidal ($\tau_5 = 0$) or trigonal bipyramidal ($\tau_5 = 1$) geometries, where $\tau_5 = 0.234$ for **10.1**, suggestive of a slightly distorted square pyramidal geometry as the Co(II) center puckers out of the basal plane.[42-43] This coordination environment about the cobalt ion has been observed for a similar tpy system reported by Murugesu and others.[19] Average Co-$N_{central}$ and Co-N_{distal} distances in **10.1** are consistent with previously published high spin Co(II) compounds (Table 10.4.1).[19, 44-45]

*Table 10.4.1. Selected distances (Å) and angles (°) for compounds **10.1-3.***

Crystallographic parameter	**10.1**	**10.2b**	**10.3**
Average Co-$N_{central}$ (Å)	2.079(2)	2.022(4)	2.088(2)
Average Co-N_{distal} (Å)	2.130(3)	2.147(4)	2.155(2)
N_{distal}-Co-N_{distal} angle (°)	143.28(9)	151.9(1)	151.31(7)
Co-X distance (Å)	2.304(9)	--	2.216(2)
Closest intermolecular distance= (Å)	3.479(4)[a]	3.388(8)[b]	3.419(4)[c]

[a]Pyridine rings of neighboring molecules using the two closest atoms. [b]A pyridine ring of the cation and a phenyl ring of a tetraphenylborate counter anion using the two closest atoms. [c]Pyridine rings of neighboring molecules using the two closest atoms.

The crystal structure for compound **10.2b** indicates that two pyrtpy ligands coordinate to the Co(II) center, leading to a six-coordinate geometry. The structural distortion parameter Σ[46] (124.8°) indicates a large distortion away from perfect octahedral geometry (Σ = 0°). Notably, the nitrogen of the pyrrolidine ring is trigonal planar (176.4(5) and 177.2(4)°); this has also been observed when this ligand is bound to a manganese ion.[47] All other structural parameters are in

agreement with compound **10.1** with exception of the Co-$N_{central}$ bond length, which is shorter in **10.2b**. Previous Co(R-tpy)$_{2-n}$ (n = 0, 1) compounds have exhibited a range of Co-$N_{central}$ bond distances irrespective of 4'-substituent identity and there does not appear to be a generalizable trend.[38] Interestingly, compound **10.3** exhibits heptacoordinate geometry about the Co center with both nitrate ions bound in κ_2 fashion. This observation is extremely uncommon and is usually only seen when less sterically demanding ligands are employed.[38, 48-49] Similar to **10.1** and **10.2b**, compound **10.3** displays structural parameters in agreement with previously published high spin Co(II) compounds.

10.4.3 Magnetic Measurements and Interpretation

The temperature dependencies of magnetic susceptibility for **10.1-3** are presented in Figure 10.4.2. All three compounds exhibit similar behavior across all temperatures. As a representative example, for **10.2b** , the $\chi_M T$ value at 300 K is 2.98 cm^3 K mol^{-1}, higher than expected for the spin-only value for high-spin Co(II) (1.875 cm^3 K mol^{-1} when g = 2.0), but reasonable considering that the Co(II) ion features large spin-orbit coupling.[50] Upon decreasing the temperature, the $\chi_M T$ product decreases monotonically until ~75 K, where the decrease becomes more pronounced; at 3 K, the $\chi_M T$ value is 2.43 cm^3 K mol^{-1}. The downturn in magnetic susceptibility value at low temperature is indicative of magnetic anisotropy and/or weak intermolecular antiferromagnetic coupling. The closest intermolecular Co-Co distances are 8.031(2), 13.917(3) and 11.5546(5) for **10.1**, **10.2b** and **10.3**, respectively, precluding any significant through-space antiferromagnetic interactions. In the crystal packing of **10.1**-**3**, however, hydrogen bonding and π stacking interactions are both plausible. To probe the extent to which these interactions are operative, the magnetic susceptibility data for all three complexes were fit using PHI (Figure 10.4.2 and Table 10.4.2).[24] These fits indicate large D values, suggestive of significant magnetic anisotropy present for **10.1**-**3** and the addition of a mean field approximation (θ) did not greatly improve the fit, indicating minimal intermolecular interactions for

10.1-**3**. Further, the *g* values obtained from these fits are in agreement with other high spin Co(II) compounds.[19, 50] The larger $\chi_M T$ product for **10.3** across all temperatures when compared to **10.1** and **10.2b** is rationalized as being due to a lowered excited state energy (near degeneracy) due to the seven coordinate geometry of **10.3**.[51] We do note that this type of geometry is uncommon and that orbital near degeneracy is likely only one of many contributing factors.

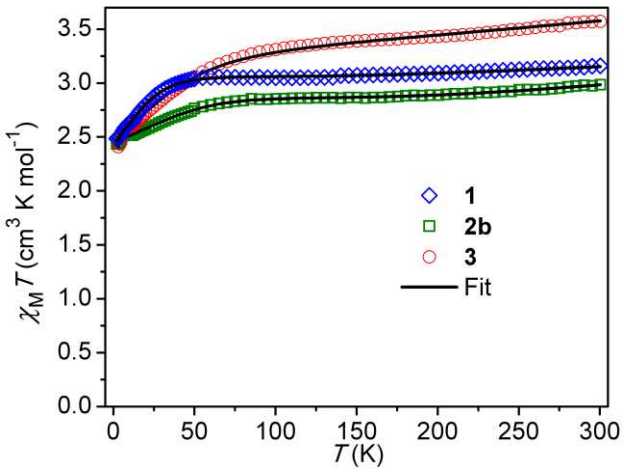


*Figure 10.4.2. Temperature dependence of magnetic susceptibility data for **10.1** (blue diamonds), **10.2b** (green squares), and **10.3** (red circles) collected at an applied field of 1 kOe. The black lines represent best fits using PHI.[24]*

To further analyze the magnetic properties of these species, reduced magnetization data are gathered. These data are fit using the program ANISOFIT 2.0,[25] where the magnitudes of *D, E* and *g* are consistent with the fits of the magnetic susceptibility data performed with PHI (Figures A10.7-A10.8). We note that the signs of anisotropy parameters cannot be reliably determined from fits to magnetization data.

*Table 10.4.2. Magnetic parameters for **10.1**-**3**, obtained via fits and computations.*[a]

	$g_{\parallel}$	$g_{\perp}$	D (cm^{-1})	E (cm^{-1})	R^2 (PHI)	TIP ($cm^3\ mol^{-1}$)	U_{eff} (cm^{-1})	τ_o (1×10^{-5} s)
10.1	2.26 (2.22)	2.98 (2.73)	-22.2 (-25.2)	3.53 (7.02)	0.9948	0.000900	--	--
10.2b	0.754 (2.11)	2.97 (2.90)	-53.6 (-48.2)	5.53 (7.37)	0.9950	0.00200	6.8	3.1
10.3	2.50 (2.15)	3.00 (2.28)	-41.4 (-7.23)	4.50 (1.32)	0.9850	0.00156	--	--

[a]Data in parentheses are computed values.

Under zero applied dc field, no out-of-phase ac susceptibility (χ'') responses are observed for **10.1**-**3** at 1.8 K. This not surprising, as six-coordinate Co(II) species rarely display slow relaxation of magnetization without an applied dc field and no examples of five- or seven-coordinate Co(II) species have been reported in the absence of applied dc fields.[50] Under a dc magnetic field, χ'' responses are observed for all three compounds. For compound **10.1**, as the dc field is increased from 0 Oe (at 1.8 K), a relaxation event appears at ~120 Hz and reaches a maximum χ'' value at 2 kOe. A second event at lower frequencies (~3 Hz) is observed below applied fields of 1.5 kOe. Therefore, the temperature dependent ac magnetic susceptibility measurements for **10.1** are measured at 1.5 kOe in an attempt to isolate a single relaxation event (Figure A10.1). Upon increasing the temperature from 1.8 K, the lower frequency signal decreases in intensity quickly until 3.5 K, where it is no longer present. The second relaxation event that is observed at higher frequencies shifts to even higher frequencies as the temperature increases from 1.8 K until the peak can no longer be observed at 5 K. These results are similar to those determined by the Murugesu group in the parent analog, [Co(tpy)Cl_2].[19] It is interesting that the two relaxation events that are observed for **10.1** occur at similar frequencies and are not easily separable, whereas variance in the dc field applied for [Co(tpy)Cl_2] allowed for separation of the two events. This could be attributed to the over 2 Å difference in the Co-Co distances of [Co(tpy)Cl_2] and compound **10.1**. Recently, the Murugesu group studied the effect of intermolecular interactions on the two relaxation events of a Co(II) SMM.[51] As the Co-Co distance increased, the lower frequency event was shifted to higher frequencies. In [Co(tpy)Cl_2], the Co-

Co distance of 5.8763(9) Å results in the lower frequency relaxation event not overlapping with the second relaxation event. In contrast, the increase in Co-Co distance (8.031(2) Å) in compound **10.1** results in two overlapping relaxation events.

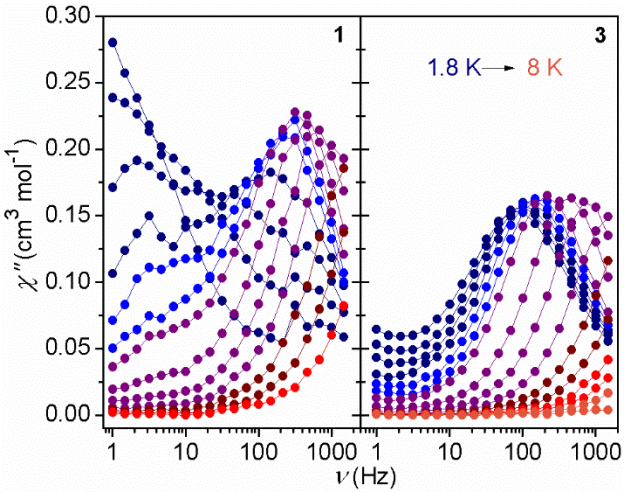


*Figure 10.4.3. Frequency dependence of the out of phase magnetic susceptibility under an applied dc field of 1.5 kOe for **10.1** (left) and 1.25 kOe for **10.3** (right) at the indicated temperature range (1.8 K, 2-8 K in 0.25 K increments).*

The field-dependent out of phase ac magnetic susceptibility for **10.2b** (at 1.8 K) shows a single relaxation event near 100 Hz that reaches a maximum χ'' value at 1 kOe (Figure A10.2). There is likely no quantum tunneling occurring in compound **10.2b**, as the relaxation frequency shifts to higher values as temperature is increased (Figure 10.4.4). These data can be fit to an Arrhenius equation, giving a relaxation barrier of U_{eff} = 6.8 cm^{-1} with a pre-exponential constant (τ_0) of 3.1 x 10^{-5} s.

For compound **10.3**, as the dc field is increased while temperature is held at 1.8 K, a relaxation peak is also observed near 100 Hz, reaching a maximum χ'' value at 1.25 kOe. A

second relaxation event begins to appear near 1 Hz in applied fields above 0.5 kOe (Figure A10.3). The temperature-dependent ac magnetic susceptibility measurements for **10.3** are therefore measured at 1.25 kOe to maximize the χ'' response and minimize the contribution from the second relaxation peak. Upon increasing temperature from 1.8 K, the lower frequency event decreases in magnitude until 3.0 K, where it is no longer observed. The primary χ'' response shifts to higher frequency as the temperature is increased from 1.8 K, until the peak is no longer observed at 4.5 K (Figure 10.4.3). The differences in ac data for **10.1**-**3** are attributed to the difference in the coordination environments around the Co(II) center. Compounds **10.1** and **10.3** each exhibit two relaxation events, similar to other five- and seven-coordinate Co(II) SMMs.[52-54] Meanwhile, compound **10.2b** only has one relaxation process, as is seen in other six-coordinate Co(II) compounds.[55-57] Compared to Co(II) SMMs with similar coordination environments, **10.2b** has a thermal barrier (U_{eff}) that is in good agreement with literature precedent. While, the U_{eff} is smaller in magnitude, the lifetime of **10.2b** is comparable to previously published [Co(tpy)X_2] and six-coordinate Co(II) compounds that behave as field-induced SMMs.[19, 50, 58] The lower U_{eff} could be attributed to the shorter range of the χ'' value maxima of the relaxation event compared to those previously reported.

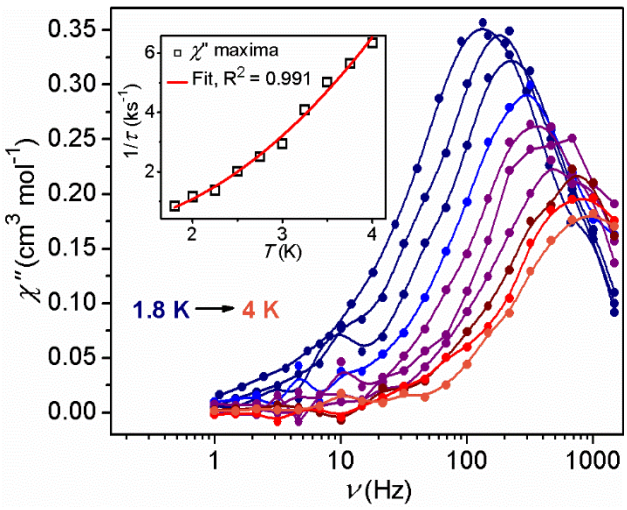


Figure 10.4.4. Frequency dependence of the out of phase magnetic susceptibility with an applied dc field of 1 kOe for ***10.2b*** *at the indicated temperature range (1.8 K, 2-4 K in 0.25 K increments). Inset: Arrhenius plot of relaxation time giving* U_{eff} *= 6.8* cm^{-1}.

10.4.4 Computational Studies

In an effort to understand the variable dynamic magnetic properties for **10.1**-**3**, we performed NEVPT2 computations using def2-SVP as the basis set. Recent efforts to compute exact *D* values for mononuclear complexes have mostly satisfied only sign and relative magnitude values of *D*.[59-66] Comparing experimentally and computationally-determined anisotropy parameters for the compounds presented here, the trends observed from magnetic measurements are largely mirrored by the computational results.

For complex **10.1**, the three lowest lying orbitals most closely correspond to the canonical "t_{2g}" set (d_{xy}, d_{xz} and d_{yz} orbitals) and are therefore labelled as δ_1, δ_2, and δ_3. We note that δ_2 and δ_3 are not strictly degenerate due to symmetry considerations (and this is the case for all three compounds presented here), but are nearly equal in energy. The remaining two d orbitals, most like the "e_g" set (d_{x2-y2} and d_{z2}), comprise the dσ* antibonding orbitals. As shown in Figure 10.4.2, the ground state configuration is $\delta_1^2\delta_2^2\delta_3^1\sigma^*_1{}^1\sigma^*_2{}^1$, and all relevant excited states maintain single

occupation of the dσ* orbitals. The two lowest lying accessible excited states for **10.1** are 1180 ($\delta_1^2\delta_2^2\delta_3^1$ to $\delta_1^2\delta_2^1\delta_3^2$) and 3180 ($\delta_1^2\delta_2^2\delta_3^1$ to $\delta_1^1\delta_2^2\delta_3^2$) cm^{-1} above the described ground state.

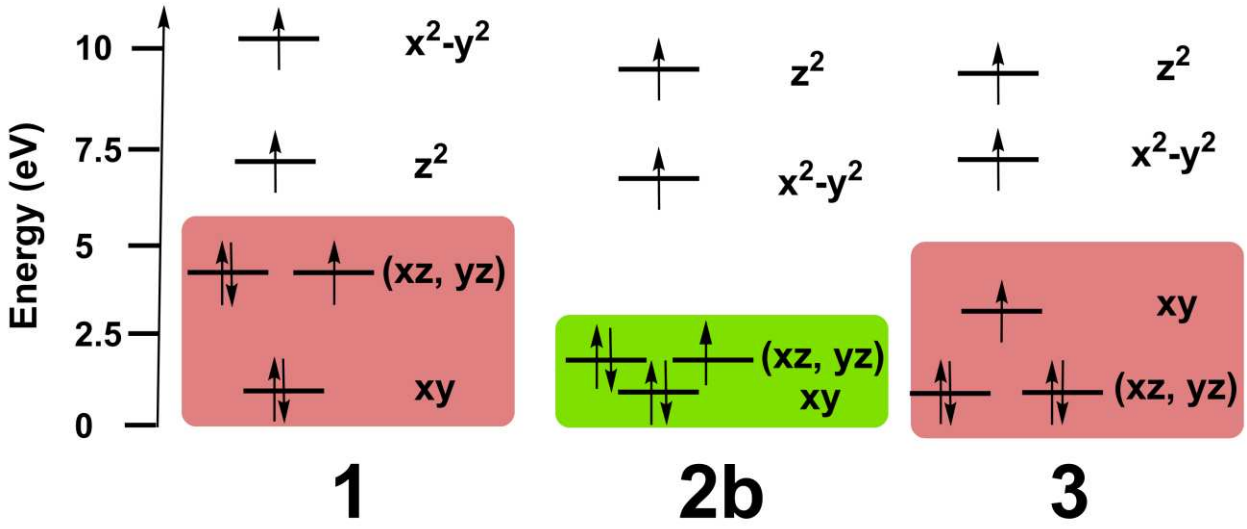


Figure 10.4.2. Orbital splitting diagrams of compounds obtained from computational results.

Complex **10.3** displays similar computational results to **10.1**, albeit with reversed order of the dπ orbitals. The d orbital splitting description for **10.3** consists of two nearly degenerate lowest d_{xz} and d_{yz} orbitals (non-bonding) and the next highest orbital possesses d_{xy} character (4440 cm^{-1} higher in energy): antibonding interactions with the O atoms increases its energy relative to the other two dπ orbitals. Finally, the other two d orbitals (d_{x2-y2} and d_{z2}) are of explicitly dσ* antibonding character (1370 cm^{-1} above the lowest). The first accessible excited state for **10.3** is 3310 cm^{-1} above the ground state ($\delta_1^2\delta_2^2\delta_3^1$ to $\delta_1^2\delta_2^1\delta_3^2$). The origin of the orbital energy differences, which also display more antibonding character, is rationalized through an analysis of the spectrochemical series. Because nitrate and chloride are both π-donor ligands, the π orbitals of the ligands are lower in energy when compared to the δ_1, δ_2, and δ_3 orbitals, rendering this set more antibonding in character. Therefore, the energy splitting of the orbitals increase as the

electronic geometry is no longer octahedral in nature, which has been discussed previously for Co(II) complexes.[67]

Conversely, the orbitals in complex **10.2b** split in a pseudo octahedral geometry, perturbed by a Jahn-Teller distortion that results in axial compression, with d_{z2} slightly higher in energy than d_{x2-y2} by 2900 cm^{-1}. In contrast to **10.1** and **10.3**, all three orbitals of the dπ set are nearly degenerate, with large consequences for anisotropy properties. The first two accessible excited states are only 661 ($\delta_1^2\delta_2^2\delta_3^1$ to $\delta_1^2\delta_2^1\delta_3^2$) and 2190 ($\delta_1^2\delta_2^2\delta_3^1$ to $\delta_1^2\delta_2^1\delta_3^2$) cm^{-1} higher in energy than the ground state. Contributions of excited states to magnetic properties are inversely proportional the excitation energy. This decreased excitation energy leads to a higher degree of spin-orbit coupling to manifest in this system, causing the *D* value to be larger, in agreement with experimental results (Table 10.4.2). The computational results help support the observed dynamic magnetic properties considering that only one relaxation event is observed for **10.2b** and shows the most anisotropy manifesting from the orbital splitting. Conversely, the computed impact of spin-orbit coupling is less for **10.1** and **10.3**, which both show multiple relaxation pathways. These results contribute to the growing literature combining experimental and computational results aimed at enhancing the delicate magnetic properties of Co(II) SMMs.

10.4.5 Conclusions

The results presented here show how varied magnetic properties can arise from differing molecular geometries about Co(II) centers and also how the ligand field affects the relative energies of d orbitals, leading to enhanced (or suppressed) axial anisotropies. In compounds **10.1** and **10.3**, the Co center ligates one OTftpy ligand and two anions (*via* either κ_1 or κ_2 coordination), whereas in pseudo-octahedral **10.2b**, two pyrtpy ligands are bound. This results in three distinct coordination environments, where compound **10.1** is pseudo square pyramidal, **10.2b** is pseudo octahedral and **10.3** as pseudo pentagonal bipyramidal. Magnetic measurements indicate these complexes are high spin at all temperatures probed and possess significant magnetic

anisotropies. These data are combined with computational work to elucidate *g*, *E* and *D* values. Slow relaxation of magnetization is observed for each complex under applied dc fields. Compounds **10.1** and **10.3** exhibit two non-isolable relaxation events, preventing the calculation of a relaxation barrier; however, **10.2b** exhibits one event with a small barrier to relaxation, which is not uncommon for tpy based ligand sets about Co(II) centers. These results are explained by the lower lying excited states contributing to a larger *D* value for **10.2b** than in **10.1** and **10.3**. The differences in axial anisotropy in these systems manifests in the dynamic magnetic properties, giving rise to different relaxation behavior. The results presented here suggest that efforts to maximize $|D|$ in Co(II) tpy-based systems should focus on 6-coordinate complexes; efforts are underway to find conditions under which binding of two tpy-type ligands with electron withdrawing substituents can be achieved.

References

1. Bogani, L.; Wernsdorfer, W. *Nat. Mater.* **2008**, *7*, 179.

2. Rinehart, J. D.; Long, J. R. *Chem. Sci.* **2011**, *2*, 2078-2085.

3. Woodruff, D. N.; Winpenny, R. E. P.; Layfield, R. A. *Chem. Rev.* **2013**, *113*, 5110.

4. Tesi, L.; Lucaccini, E.; Cimatti, I.; Perfetti, M.; Mannini, M.; Atzori, M.; Morra, E.; Chiesa, M.; Caneschi, A.; Sorace, L.; Sessoli, R. *Chem. Sci.* **2016**, *7*, 2074.

5. Deng, Y.-F.; Han, T.; Wang, Z. X.; Ouyang, Z. W.; Yin, B.; Zheng, Z. P.; Krzystek, J.; Zheng, Y.-Z. *Chem. Commun.* **2015**, *51*, 17688.

6. Vallejo, J.; Pascual-Álvarez, A.; Cano, J.; Castro, I.; Julve, M.; Lloret, F.; Krzystek, J.; De Munno, G.; Armentano, D.; Wernsdorfer, W.; Ruiz-García, R.; Pardo, E. *Angew. Chem. Int. Ed.* **2013**, *52*, 14075.

7. Ding, M.; Cutsail, G. E.; Aravena, D.; Amoza, M.; Rouzières, M.; Dechambenoit, P.; Losovyj, Y.; Pink, M.; Ruiz, E.; Clérac, R.; Smith, J. M. *Chem. Sci.* **2016**, *7*, 6132.

8. Zadrozny, J. M.; Xiao, D. J.; Atanasov, M.; Long, G. J.; Grandjean, F.; Neese, F.; Long, J. R. *Nat. Chem.* **2013**, *5*, 577.

9. Freedman, D. E.; Harman, W. H.; Harris, T. D.; Long, G. J.; Chang, C. J.; Long, J. R. *J. Am. Chem. Soc.* **2010**, *132*, 1224.

10. Mossin, S.; Tran, B.L.; Adhikari, D.; Pink, M.; Heinemann, F.W.; Sutter, J.; Szilagyi, R. K.; Meyer, K.; Mindiola, D. J. *J. Am. Chem. Soc.* **2012**, *134*, 13651.

11. Meng, Y.-S.; Mo, Z. B.; Wang, B.-W.; Zhang, Y.-Q.; Deng, L.; Gao, S. *Chem. Sci.* **2015**, *6*, 7156.

12. Poulten, R. C.; Page, M. J.; Algarra, A. G.; Le Roy, J. J.; López, I.; Carter, E.; Llobet, A.; Macgregor, S. A.; Mahon, M. F.; Murphy, D. M.; Murugesu, M.; Whittlesey, M. K. *J. Am. Chem. Soc.* **2013**, *135*, 13640.

13. Miklovič, J.; Valigura, D.; Boča, R.; Titiš, J. *Dalton Trans*. **2015**, *44*, 12484.

14. Boča, R.; Rajnák, C.; Titiš, J.; Valigura, D. *Inorg. Chem.* **2017**, *56*, 1478.

15. Karasawa, S.; Zhou, G. Y.; Morikawa, H.; Koga, N. *J. Am. Chem. Soc.* **2003**, *125*, 13676.

16. Rechkemmer, Y.; Breitgoff, F. D.; van der Meer, M.; Atanasov, M.; Hakl, M.; Orlita, M.; Neugebauer, P.; Neese, F.; Sarkar, B.; van Slageren, J. *Nat. Commun.* **2016**, 7.

17. Cahier, B.; Perfetti, M.; Zakhia, G.; Naoufal, D.; El-Khatib, F.; Guillot, R.; Rivière, E.; Sessoli, R.; Barra, A. L.; Guihéry, N.; Mallah, T. *Chem. Eur. J.* **2017**, *23*, 3648.

18. Jurca, T.; Farghal, A.; Lin, P. H.; Korobkov, I.; Murugesu, M.; Richeson, D. S. *J. Am. Chem. Soc.* **2011**, *133*, 15814.

19. Habib, F.; Luca, O. R.; Vieru, V.; Shiddiq, M.; Korobkov, I.; Gorelsky, S. I.; Takase, M. K.; Chibotaru, L. F.; Hill, S.; Crabtree, R. H.; Murugesu, M. *Angew. Chem. Int. Ed.* **2013**, *52*, 11290.

20 Chambers, J.; Eaves, B.; Parker, D.; Claxton, R.; Ray, P. S.; Slattery, S. J. *Inorg. Chim. Acta* **2006**, *359*, 2400.

21. Holbrey, J. D.; Tiddy, G. J. T.; Bruce, D. W. *J. Chem. Soc. Dalton Trans.* **1995**, 1769.

22. Johansson, O. *Synthesis-Stuttgart* **2006**, 2585.

23. Bain, G. A.; Berry, J. F. *J. Chem. Educ.* **2008**, *85*, 532.

24. Chilton, N. F.; Anderson, R. P.; Turner, L. D.; Soncini, A.; Murray, K. S. *J. Comput. Chem.* **2013**, *34*, 1164.

25. Shores, M. P.; Sokol, J. J.; Long, J. R. *J. Am. Chem. Soc.* **2002**, *124*, 2279.

26. *APEX2* **2012**, Bruker AXS Inc. Madison, WI.

27. *APEX3* **2015**, Bruker AXS Inc. Madison, WI.

28. Sheldrick, G. M. *Acta Cryst. A* **2008**, *64*, 112.

29. Angeli, C.; Cimiraglia, R.; Evangelisti, S.; Leininger, T.; Malrieu, J. P. *J. Chem. Phys.* **2001**, *114*, 10252.

30. Angeli, C.; Cimiraglia, R.; Malrieu, J. P. *Chem. Phys. Lett.* **2001**, *350*, 297.

31. Angeli, C.; Cimiraglia, R.; Malrieu, J.. P. *J. Chem. Phys*. **2002**, *117*, 9138.

32. Angeli, C.; Borini, S.; Cestari, M.; Cimiraglia, R. *J. Chem. Phys.* **2004**, *121*, 4043.

33. Schafer, A.; Horn, H.; Ahlrichs, R. *J. Chem. Phys.* **1992**, *97*, 2571.

34. Schafer, A.; Huber, C.; Ahlrichs, R. *J. Chem. Phys.* **1994**, *100*, 5829.

35. Neese, F. *WIRES Comput. Mol. Sci.* **2012**, *2*, 73.

36. Ganyushin, D.; Neese, F. *J. Chem. Phys.* **2008**, *128*, 114117.

37. Henderson, I. M.; Hayward, R. C. *J. Mater. Chem.* **2012**, *22*, 21366.

38. Constable, E. C.; Harris, K.; Housecroft, C. E.; Neuburger, M.; Zampese, J. A. *Dalton Trans.* **2011**, *40*, 11441.

39. Cook, L. J. K.; Tuna, F.; Halcrow, M. A. *Dalton Trans.* **2013**, *42*, 2254.

40. Elgrishi, N.; Chambers, M. B.; Fontecave, M. *Chem. Sci.* **2015**, *6*, 2522.

41. Hansch, C.; Leo, A.; Taft, R. W. *Chem. Rev.* **1991**, *91*, 165.

42. Shaffer, D. W.; Bhowmick, I.; Rheingold, A. L.; Tsay, C.; Livesay, B. N.; Shores, M. P.; Yang, J. Y. *Dalton Trans.* **2016**, *45*, 17910.

43. Addison, A. W.; Rao, T. N.; Reedijk, J.; Vanrijn, J.; Verschoor, G. C. *J. Chem. Soc. Dalton Trans.* **1984**, 1349.

44. Rajnák, C.; Titiš, J.; Fuhr, O.; Ruben, M.; Boča, R. *Inorg. Chem.* **2014**, *53*, 8200.

45. Palion-Gazda, J.; Świtlicka-Olszewska, A.; Machura, B.; Grancha, T.; Pardo, E.; Lloret, F.; Julve, M. *Inorg. Chem.* **2014**, *53*, 10009.

46. Halcrow, M. A. *Chem. Soc. Rev.* **2011**, *40*, 4119.

47. Sjödin, M.; Gätjens, J.; Tabares, L. C.; Thuéry, P.; Pecoraro, V. L.; Un, S. *Inorg. Chem.* **2008**, *47*, 2897.

48. Su, S.-Q.; Kamachi, T.; Yao, Z. S.; Huang, Y.-G.; Shiota, Y.; Yoshizawa, K.; Azuma, N.; Miyazaki, Y.; Nakano, M.; Maruta, G.; Takeda, S.; Kang, S.; Kanegawa, S.; Sato, O. *Nat. Commun.* **2015**, 6.

49. Juhász, G.; Matsuda, R.; Kanegawa, S.; Inoue, K.; Sato, O.; Yoshizawa, K. *J. Am. Chem. Soc.* **2009**, *131*, 4560.

50. Frost, J. M.; Harriman, K. L. M.; Murugesu, M. *Chem. Sci.* **2016***, 7*, 2470.

51. Palii, A.; Tsukerblat, B.; Klokishner, S.; Dunbar, K. R.; Clemente-Juan, J. M.; Coronado, E. *Chem. Soc. Rev.* **2011**, *40*, 3130.

52. Habib, F.; Korobkov, I.; Murugesu, M. *Dalton Trans.* **2015**, *44*, 6368.

53. Chen, L.; Chen, S.-Y.; Sun, Y.-C.; Guo, Y.-M.; Yu, L.; Chen, X.-T.; Wang, Z.; Ouyang, Z. W.; Song, Y.; Xue, Z.-L. *Dalton Trans.* **2015**, *44*, 11482.

54. Rajnák, C.; Titiš, J.; Miklovič, J.; Kostakis, G.E.; Fuhr, O.; Ruben, M.; Boča, R. *Polyhedron*, **2017**, *126*, 174.

55. Zhang, Y.-Z.; Gómez-Coca, S.; Brown, A. J.; Saber, M. R.; Zhang, X.; Dunbar, K. R. *Chem. Sci.* **2016**, *7*, 6519.

56. Novikov, V. V.; Pavlov, A. A.; Nelyubina, Y. V.; Boulon, M.-E.; Varzatskii, O. A.; Voloshin, Y. Z.; Winpenny, R. E. *J. Am. Chem. Soc.* **2015**, *137*, 9792.

57. Pavlov, A. A.; Nelyubina, Y. V.; Kats, S. V.; Penkova, L. V.; Efimov, N. N.; Dmitrienko, A. O.; Vologzhanina, A. V.; Belov, A. S.; Voloshin, Y. Z.; Novikov, V. V. *J. Phys. Chem. Lett.* **2016**, 4111.

58. Craig, G. A.; Murrie, M. *Chem. Soc. Rev.* **2015**, *44*, 2135.

59. Gómez-Coca, S.; Urtizberea, A.; Cremades, E.; Alonso, P. J.; Camón, A.; Ruiz, E.; Luis, F. *Nat. Commun.* **2014**, 5.
60. Korchagin, D. V.; Shilov, G. V.; Aldoshin, S. M.; Morgunov, R. B.; Talantsev, A. D.; Yureva, E. A. *Polyhedron* **2015**, *102*, 147.

61. Herchel, R.; Váhovská, L.; Potočňák, I.; Trávnáček, Z. *Inorg. Chem.* **2014**, *53*, 5896.

62. Gómez-Coca, S.; Aravena, D.; Morales, R.; Ruiz, E. *Coord. Chem. Rev.* **2015**, *289*, 379.

63. Nemec, I.; Liu, H.; Herchel, R.; Zhang, X. Q.; Trávníček, Z. *Synthetic Met.* **2016**, *215*, 158.

64. Zhang, Y.-Z.; Gómez-Coca, S.; Brown, A. J.; Saber, M. R.; Zhang, X.; Dunbar, K. R. *Chem. Sci.* **2016**, *7*, 6519.

65. Woods, T. J.; Ballesteros-Rivas, M. F.; Gómez-Coca, S.; Ruiz, E.; Dunbar, K. R. *J. Am. Chem. Soc.* **2016**, *138*, 16407.

66. Ozumerzifon, T. J.; Bhowmick, I.; Spaller, W. C.; Rappé, A. K.; Shores, M. P. *Chem. Commun.* **2017**, *53*, 4211.

67. Gomez-Coca, S.; Cremades, E.; Aliaga-Alcalde, N.; Ruiz, E. *J. Am. Chem. Soc.* **2013**, *135*, 7010.

Chapter 11: Reactivity and magnetic properties for a series of U-acetylide complexes.

11.1 Introduction

Single molecule magnets (SMMs) which incorporate lanthanides use large intrinsic single-ion anisotropies to enhance properties.[1-4] Similar to lanthanides, actinides maintain large single-ion anisotropy potent for SMM behavior; however, actinides that show SMM properties are far less common than lanthanide complexes.[5-9] Therefore, new methods must be administered to extend SMM properties to more actinide containing species. Ligand design and scaffolds are the most straightforward way to harness large amounts of anisotropy. To date the only mononuclear uranium complexes to show magnetic relaxation are U^{III} and U^{V} ions.[5-10] Therefore we set out to explore the magnetic properties of U^{IV} ions and the effect of ligand-coordination upon them in an attempt to synthesize U^{IV} SMMs.

U^{IV} compounds have mostly exhibited comparable magnetic properties, where upon cooling the paramagnetic complex, with spin $S = 1$, gradually relaxes to a diamagnetic ground state having spin of $S = 0$.[11-13] If distortions are present in the bonding environments, low-lying states similar in energy to the ground state can be occupied, which cause spin-pairing for U^{IV} ions as temperature is decreased. Examples of non-"classical" U^{IV} magnetism have been reported, mainly stemming from spin-orbit coupling interactions between uranium and a transition metal.[14-23] Some U^{IV} complexes have exhibited non-traditional magnetic behavior, mostly multimetallic species, by incorporating magnetic coupling strategies and some occupation of magnetic ground states at low temperatures.[24-30]

All mononuclear U^{IV} compounds that have shown non-classical magnetic behavior all contain a U-alkyl bond.[26, 31] This behavior appears as a constant $\chi_M T$ value until about 50-100 K where a more precipitous drop-off occurs. In fact, when more U-alkyl bonds are present the drop-off occurs at lower temperatures compared to a higher temperature drop-off with less U-alkyl

bonds.[26, 31] Also other considerations such as other ligands present in the first-coordination sphere have shown little effect to date. As of now all U^{IV} complexes with U-alkynyl motifs have shown classical U^{IV} magnetic behavior.[24] In this vein, we sought out to investigate whether an increased number of U-alkynyl linkages in a complex could cause magnetic behavior similar to U-alkyl complexes. Herein, we present the synthesis and magnetic characterization of $[(dmpe)_2U(CCPh)_4]$ (**11.1**) and $[(dmpe)_2U(CCPh)_5(Li{\cdot}Et_2O)]$ (**11.2**). Furthermore, in attempts to explore the potential reactivity of **2**, we isolated a reduced product $[(dmpe)_2U(CCPh)_4(Li{\cdot}(CH_2Cl_2)_2)]$ (**11.3**).

11.2 Division of Labor

The initial synthesis and characterization of the U(IV)-acetylide complexes was performed by Brian S. Newell. All of the magnetic characterization was performed by Robert F. Higgins. All of the reactivity studies of $[(dmpe)_2U(CCPh)_5(Li{\cdot}Et_2O)]$ (**11.2**) was performed by Robert F. Higgins. Crystal structures were solved by Brian S. Newell (**11.1** and **11.2**) and Robert F. Higgins (**11.3**). Interpretation and analysis was performed by Brian S. Newell, Robert F. Higgins and Matthew P. Shores.

11.3 Materials and Methods

11.3.1 General Considerations

All manipulations were carried out either standard Schlenk techniques on a N_2 manifold or inside a N_2-filled glovebox (MBRAUN Labmaster 130). Pentane was distilled over sodium metal, degassed (freeze-pump-thaw 3 x 30 min) and stored under an atmosphere of dinitrogen. Diethylether was degassed and stored under an atmosphere of dinitrogen. UCl_4,[1] $(dmpe)_2UCl_4$,[2] and $(dmpe)_2UMe_4$[3] (dmpe = 1,2-bis(dimethylphosphino)-ethane) were prepared according to the literature. Methyllithium (MeLi) and *n*-butyllithium (*n*-BuLi) was titrated prior to use with accurately weighed amounts of menthol and 2,2'-bipyridyl. Phenylacetylene was distilled under vacuum before use. Lithium phenylacetylide was synthesized by reacting the appropriate stoichiometric

amount of *n*-BuLi in pentane with phenylacetylene fresh for each reaction. All other reagents were obtained from commercial vendors and used without further purification.

Caution! *Depleted uranium (primary isotope ^{238}U) is a weak α emitter (4.197 MeV) with a half-life of 4.47 x 10^9 years; manipulations and reactions should be carried out in monitored fume hoods or in an inert atmosphere glovebox in a radiation laboratory equipped with α- and β-particle counting equipment*.

11.3.2 Preparation of novel metal complexes

[(dmpe)$_2$U(CCPh)$_4$] (11.1) Phenylacetylene (145 µL, 1.32 mmol) was added dropwise to a stirred solution of [(dmpe)$_2$UMe$_4$] (175 mg, 0.292 mmol) in 15 mL of pentane at -40 ˚C. The resulting solution changed from brown to purple quickly and after 30 min the reaction was stopped. All volatiles were removed in vacuo to afford a purple solid (225 mg, 82 % yield based on [(dmpe)$_2$UMe$_4$]). Single crystals suitable for X-ray analysis were grown from a concentrated pentane solution maintained at -40 ˚C overnight. Absorption spectrum (Et_2O) λ_{max} (ε_M): 486 (233), 534 (217), 559 (245), 668 (83), 739 (359), 907 (53), 954 (83), 1007 nm ($L \cdot mol^{-1} \cdot cm^{-1}$). IR (mineral oil) 643 (w), 691 (m), 723 (m), 754 (w), 773 (w), 830 (w), 864 (m), 890 (m), 929 (m), 944 (m), 996 (w), 1023 (w), 1067 (w), 1085 (w), 1155 (w), 1170 (w), 1194 (w), 1275 (m), 1292 (m), 1304 (m), 1377 (s) 1461 (s), 1591 (m), 2047 (m), 2671 (w), 2724 (w), 2840 (s) 2924 (s) cm^{-1}. ^{1}H NMR (293 K, C_6D_6): δ 15.87 (s, 8 H, Ar-*H*), 11.98 (s, 4 H, Ar-*H*), 9.19 (s, 8 H, Ar-*H*), 1.85 (s, 24 H, P*CH$_3$*), -28.13 ppm (s, 8 H, P*CH$_2$*). Anal. Calcd. For $C_{44}H_{52}P_4U$: C 56.05; H, 5.56; Found C, 53.55; H, 5.81.

[(dmpe)$_2$U(CCPh)$_5$(Li·Et$_2$O)] (11.2) [(dmpe)$_2$UCl$_4$] (280 mg, 0.412 mmol) and LiCCPh (230 mg, 2.13 mmol) were added to a vial and cooled to -40 ˚C for 1 hr. Cold Et_2O (15 mL, -40 ˚C) was added subsequently and over 30 seconds, the mixture changed from colorless to maroon and was stirred for an additional 30 min. The mixture was filtered and concentrated down to 3 mL under reduced pressure and cooled to -40 ˚C overnight. A red-brown precipitate was collected by filtration and dried in vacuo to give red-brown crystals (380 mg, 82 % yield based on [(dmpe)$_2$UCl$_4$]). Single crystals suitable for X-ray analysis were grown from a concentrated Et_2O

solution maintained at -40 ˚C overnight. Absorption spectrum (Et_2O) λ_{max} (ε_M): 721 nm (138 $L \cdot mol^{-1} \cdot cm^{-1}$). IR (mineral oil) 642 (w), 691 (m), 727 (m), 755 (w), 772 (w), 831 (w), 865 (m), 890 (m), 929 (m), 943 (m), 975 (m), (997 (w), 1024 (w), 1066 (w), 1091 (w), 1153 (w), 1173 (w), 1194 (w), 1270 (m), 1286 (m), 1304 (m), 1377 (s) 1461 (s), 1566 (m), 2042 (m), 2671 (w), 2724 (w), 2840 (s) 2924 (s) cm^{-1}. Anal. Calcd. For $C_{44}H_{52}P_4U$: C 59.79; H, 6.00; Found C, 59.90; H, 6.20.

$[(dmpe)_2U(CCPh)_4(Li \cdot (CH_2Cl_2)_2)]$ (11.3) $[(dmpe)_2U(CCPh)_5(Li \cdot Et_2O)]$ (369 mg, 0.328 mmol) was added to a vial and dissolved in Et_2O (5 mL) and placed in the freezer for 30 min. After 30 min, the vial was charged with 12-crown-4 (0.058 mL, 0.361 mmol) whereupon an orange precipitate formed immediately. The reaction mixture was stirred for 30 min at ambient temperature and then was filtered *in vacuo* and the precipitate was washed with cold Et_2O (2 × 5 mL). The isolated precipitate was then dissolved in CH_2Cl_2 (3 mL) and placed in the freezer overnight. After 16 hours, light orange crystals had formed which were isolated by vacuum filtration giving the title compound (158 mg, 0.141 mmol) at a 43% yield. Absorption spectrum (Et_2O) λ_{max} (ε_M): 486, 745 nm. ^7Li NMR (194 MHz; CD_2Cl_2): δ 0.16.

11.3.3 Magnetic Measurements

Magnetic susceptibility measurements were collected using a Quantum Design MPMS XL SQUID magnetometer. Powdered microcrystalline samples were loaded in polyethylene bags and sealed in the glovebox, inserted into a straw and transported to the SQUID magnetometer under dintrogen. For **11.2**, it was transported over a bed of liquid N_2. Ferromagnetic impurities were checked through a variable field analysis using fields from 0 to 10000 Oe at 100 K. DC magnetic susceptibility data were collected at temperatures ranging from 2 to 300 K at applied fields of 1000 and 5000 Oe. Susceptibility data reproducibility were confirmed by performing full scans on samples made from different batches. Magnetization measurements were collected at temperatures from 2 to 35 K at applied fields of 10, 20, 30, 40 and 50 kOe. AC magnetic susceptibility data were collected for **11.2**, at temperatures from 1.8 to 10 K at an AC applied field of 4 Oe and a DC applied field of 1000 Oe with switching frequencies of 200 and 1000 Hz.

Contributions to the magnetization from the polyethylene bag and straw were measured independently and subtracted from the total measured signal. Data were corrected for diamagnetic contributions using Pascal's constants.[32]

11.3.4 Crystallographic Measurements

Structures were determined for the new compounds listed. Single crystals were coated with Paratone-N-oil in the glovebox and mounted under a cold stream of dinitrogen gas. **11.2** was kept chilled via liquid N_2 before mounting due to its solubility in Paratone-N-oil. Single crystal X-ray diffraction data were acquired on a Bruker Kappa APEX II CCD diffractometer with Mo Kα radiation (λ = 0.71073 Å) and a graphite monochromator. Initial lattice parameters were obtained from a least-squares analysis of more than 100 reflections; these parameters were later refined against all data. None of the crystals showed significant decay during data collection. Data were integrated and corrected for Lorentz and polarization effects using Bruker APEX2 software, and semi-empirical absorption corrections were applied using SCALE with the aid of numerical face indexing.[4] Space group assignments were based on systematic absences, *E* statistics, and unsuccessful refinement of the structures. Structures were solved using the Patterson method and were refined with the aid of successive Fourier difference maps against all data using the SHELXTL 6.14 software package.[5] Thermal parameters for all atoms with $Z \geq 3$ were refined anisotropically. All hydrogen atoms were assigned to ideal positions and refined using a riding model with an isotropic thermal parameter 1.2 times that of the attached carbon atom (1.5 times for methyl hydrogens). All metric parameters can be found in the CIF files included. In the structure of **11.2**, there are several disordered components. Both dmpe ligands, two phenylacetylide ligands and the coordinated Et_2O solvent are disordered over two sites. The dmpe ligands bound to the uranium center have a site occupancy ratio refining to 80:20. The two disordered phenylacetylide ligands involve C14-C20 and C31-C36 with site occupancy ratios refining to 46:54 and 49:51 respectively. For the coordinated Et_2O solvent, C53-C56 are disordered with a site occupancy ratio refining to 45:55.

11.3.5 Other Physical Measurements

Electronic absorption spectra were obtained in solution in an air-free quartz cell of path length 1 cm on an Agilent 8453 spectrophotometer. ^{1}H NMR spectra were recorded using a Varian INOVA 500 MHz instrument, and the spectra were referenced internally using residual protio solvent resonances relative to tetramethylsilane (δ = 0 ppm). Infrared spectra were collected on a Thermo Nicolet 380 FTIR spectrometer as mineral oil mulls pressed between sodium chloride (salt) plates. Elemental analyses were performed by the Micro-Mass facility at the University of California, Berkeley.

11.4 Results and Discussion

*11.4.1 Synthesis of **11.1** and **11.2***

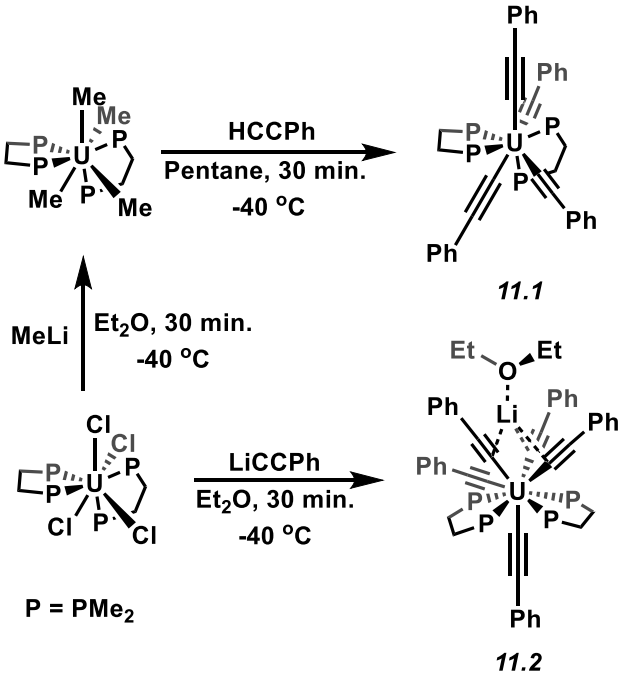


*Figure 11.4.1 Synthesis of **11.1** and **11.2**.*

Upon addition of $(dmpe)_2UCl_4$ to LiCCPh in Et_2O, the reaction mixture turned maroon and produced $(dmpe)_2U(CCPh)_5(Li{\cdot}Et_2O)$ (**11.2**). However, if $(dmpe)_2UCl_4$ is first converted to $(dmpe)_2UMe_4$ and added to HCCPh in Et_2O, a purple mixture arises and yields the product $(dmpe)_2U(CCPh)_4$ (**11.1**). When NaCCPh is used in place of LiCCPh when reacted with $(dmpe)_2UCl_4$, **11.1** is formed; if HCCPh is used however, starting materials are recovered. Lithium encapsulation in a uranium complex has been observed,[24, 33-35] along with heteroleptic nona-coordination.[36-38] UV-vis, IR, and ^{1}H NMR spectroscopy were used to characterize **11.1** and **11.2** as well as elemental analysis and SC-XRD. The structures of **11.1** and **11.2** are presented in Figure 11.4.1 illustrates the inner coordination sphere of **11.1** and **11.2** with the bond distances shown in Table 11.4.2 and pertinent crystallographic parameters are presented in Table 11.4.1.

*11.4.2 Crystal structures of **11.1** and **11.2.***

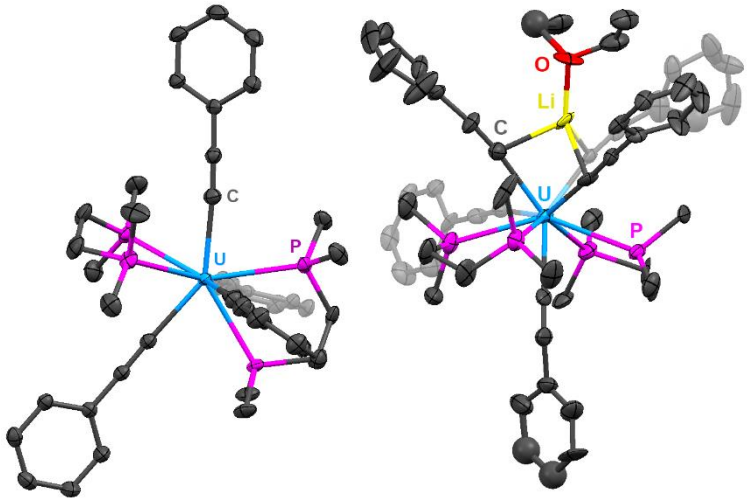


*Figure 11.4.1 ORTEP representations of **11.1** and **11.2** on the left and right respectively rendered with 40% ellipsoids. Light green, pink, red, yellow and gray represent U, P, O, Li, and C atoms respectively. H atoms are omitted for clarity. These structures are reproduced from Brian S. Newell's Ph.D. dissertation.*

In the crystal structure of **11.1**, the U-center is directly bonded to four carbon and four phosphorous atoms. The coordination environment around the uranium is a distorted square antiprismatic geometry. The two dmpe ligands are *trans* to one another and rotated by ~90°. The packing motif indicates that little to no π stacking is involved among the phenyl rings of the phenylacetylide ligands. Additionally, no solvent is present within the crystal lattice of **11.1**. Unlike the bonding environment of **11.1**, **11.2** is directly bonded to five carbon and four phosphorous atoms. Complex **11.2** encompasses a heavily distorted monocapped square antiprismatic coordination geometry around the uranium atom. The two dmpe ligands are *trans* to each other; conversely, they are not rotated by 90º as was observed in **11.1**. Also, the dmpe ligands are bent slightly out of plane in the same direction. Three of the phenylacetylide ligands form an enclosure to trap the lithium ion within the π-system of three acetylide moieties. The crystal-packing environment of **11.2** shows intermolecular π stacking within the unit and among neighboring unit cells as well.

The structure of **11.1** indicates a U^{IV} ion due to four anionic acetylide ligands with no other cations or anions present. Even though **11.2** is directly bonded to five anionic acetylides, the crystal structure indicates that it is also an U^{IV} ion due to the presence of a lithium cation. Also, the presence of peaks in the UV-vis spectrum of **11.2** supports the assigned oxidation state (Figure A11.2). Bond lengths and angles can be compared to previous reports with the oxidation states of the Uranium atoms known.

Bond distances for **11.1** and **11.2** are comparable to published uranium compounds bonded to aryl-acetylide and phosphine ligands.[14, 24, 39-43] The increased uranium-carbon/phosphorous bond lengths in **11.2** are most likely due to steric bulk due to increased ligand coordination. The steric bulk also had an effect on the bond angles of **11.2**.

*Table 11.4.1 Crystallographic parameters for **11.1** and **11.2**.*[a]

	11.1	**11.2**	**11.3**
Formula	$C_{44}H_{52}P_4U$	$C_{56}H_{57}LiOP_4U$	$C_{45}H_{54}LiP_4Cl_2U$
Formula wt	942.77	1124.95	
Color, habit	purple block	maroon block	orange block
T, K	120(2)	120(2)	120(2)
Space group	$P2_1/c$	$P\bar{1}$	$P2_1$
Z	4	2	2
a, Å	21.7865(6)	11.5046(3)	12.1459(13)
b, Å	13.5803(4)	13.8617(3)	28.008(3)
c, Å	14.8702(4)	20.6359(5)	14.6396(16)
α, deg	90	70.407(1)	90
β, deg	99.865(2)	86.074(1)	111.768(2)
γ, deg	90	69.160(1)	90
V, Å^3	4334.6(2)	2892.67(12)	4625.0(9)
d_{calc}, g/cm^3	1.445	1.292	1.482
GOF	1.04	1.16	1.04
$R_1(wR_2)$[b], %	3.21(5.68)	4.87(15.97)	4.42(10.28)

[a]Obtained with graphite-monochromated Mo Kα (λ = 0.71073 Å) radiation.

[b] $R_1 = \Sigma ||F_o| - |F_c||/\Sigma|F_o|$, $wR_2 = \{\Sigma[w(F_o^2 - F_c^2)^2]/\Sigma[w(F_o^2)^2]\}1/2$ for $F_o > 4\sigma(F_o)$.

*Table 11.4.2 Selected bond distances (Å) and angles (°) for **11.1-11.3**.*

	11.1	**11.2**	**11.3**
U-P (Å)	2.9773(6)	3.0105(6)	2.991(2)
U-CC (Å)	2.472(2)	2.5296(4)	2.485(2)

An interesting feature pertaining to the structure of **11.2** that include a short U-Li distance of 3.15(4) Å. The proximity of the lithium adduct to the uranium center forces the phosphine ligands to bend out of plane and become symmetric by a mirror-image. This structural distortion caused breaking of the symmetric environment around the U center, and thus possibly influencing the anisotropy of the metal center in **11.2**. Stability of the Li atom arises from π-electron donation from three of the acetylide ligands in **11.2**, along with electron donation from the lone pairs of the oxygen of the diethyl ether. To date, this is the closest U-Li distance reported in the literature.

From this crystallographic data it is evident that the ligand field environments are different when comparing **11.1** and **11.2**. The near mirror-image orientation of the dmpe ligands in **11.2** should alter the magnetic properties of **11.2**. Short U-U distances are known to cause magnetic coupling if small enough or if electronic exchange can occur.[7, 10, 39-43] In the structures of **11.1** and **11.2**, the closest U-U distances are 9.84(4) and 10.99(7) Å respectively, therefore magnetic exchange is not plausible. Due to this comparatively large separation, we ignore the possibility of spatial interactions between the metal centers.

*11.4.3 Magnetic properties of **11.1** and **11.2***

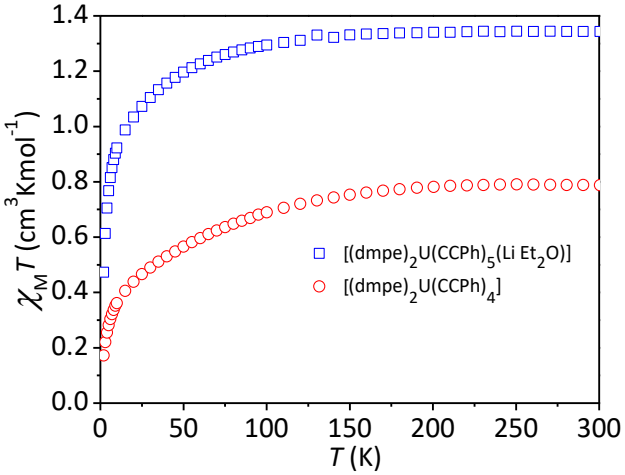


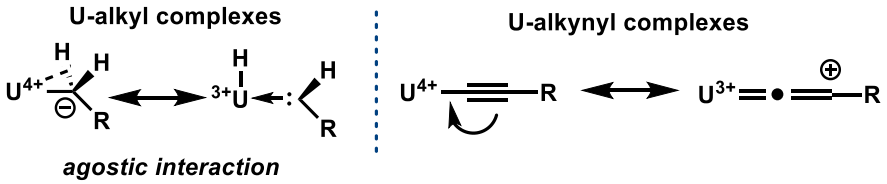
*Figure 11.4.2 Temperature dependence of the magnetic susceptibility data for **11.1** (blue) and **11.2** (red) at applied dc fields of 5000 Oe.*

With this in mind, we set out to investigate the magneto-structural differences between **11.1** and **11.2**. The temperature dependence of magnetic susceptibility data for **11.1** and **11.2** is shown in Figure 11.4.2, which was measured at an applied dc field of 5000 Oe. At 300 K, the $\chi_M T$ value for **11.1** is 0.79 cm^{3}Kmol^{-1} which remains relatively constant until 150 K where $\chi_M T$ falls faster to 0.17 cm^{3}Kmol^{-1} at 2 K. The 300 K value is slightly lower than expected for an $S = 1$ system where either a spin-only approximation (1.00 cm^{3}Kmol^{-1}) or spin-orbit coupling approximation (1.63 cm^{3}Kmol^{-1}) are used; however, the value at room temperature is in good agreement with literature precedent for U^{IV} ions.[11-13] The magnetic data for **11.2** resemble **11.1** qualitatively but not quantitatively. At 300 K, the $\chi_M T$ value for **11.2** is 1.34 cm^{3}Kmol^{-1} which remains almost constant until around 50 K where it begins to decrease more quickly until 10 K where the data falls sharply to 0.47 cm^{3}Kmol^{-1} at 2 K.

To probe the magnetic ground states of **11.1** and **11.2**, we examined the low temperature $1/\chi_M$ values of both complexes. The same ground state is occupied when the low-temperature data overlaps among different U^{IV}-complexes.[36] At 2 K, the $1/\chi_M$ values for **11.1** and **11.2** are 11.6 and 4.21 molcm^{-3} respectively, see supporting information. These data indicate that the ground state of **11.2** at low-temperatures encompasses residual spin based on a different ground state being occupied as compared to **11.1**. To further elucidate the magnetic ground states, low temperature *M* vs. *T* provides additional evidence into this claim (Figures A11.5-.6). At 5 T, the *M* values for **11.1** and **11.2** are 0.281 and 0.453 μ_B respectively. This further supports the hypothesis that a non-magnetic ground state is occupied by **11.1** since this *M* value is one of the highest for a U^{IV} ion. While this type of behavior has been previously observed with U^{IV} complexes, it has been attributed to high-symmetry structures.[26-30] To our knowledge, **11.2** is the first well-studied mononuclear U^{IV} system with a magnetic ground state caused by the ligand environment with low symmetry. Since a small amount of residual spin remained for **11.2** at low temperatures, ac magnetic susceptibility data was collected for **11.2** (Figure A11.7). A very weak out-of-phase response was found under applied dc fields above 1000 Oe. However, we do not attribute any slow relaxation of magnetization due to the intensity of the response and lack of a well-defined peak.

The nature of the non-traditional magnetic properties from U-alkyl and alkynyl subunits has a few possible explanations. The first, which only applies to U-alkyl complexes, is through an agostic interaction. If the U atom can remove electron density from a C-H bond, then it could populate other orbitals and act as a pseudo-U^{III} ion with a carbene in place of an alkyl ligand (see below). However, as of now, no U^{IV}-alkyl-containing crystal structure has indicated agostic interactions either because U-H distances are too long or disorder has not permitted placement of H atoms.[31] A second explanation for these properties is through resonance stabilizing a pseudo-dianionic ligand. This can be explained through a phenylacetylide ligand where two

electrons from the acetylide are isolated on the terminal carbon (see below). This could stabilize more electrons on the metal center and thus again allowing a pseudo-U^{III} ion. These results indicate that ligand choice is much more influential on the magnetic properties of mononuclear uranium complexes than coordination environment.



While we attribute the interesting magnetic properties of **11.2** to unquenched relaxation of the spin from $S = 1$ to $S = 0$, there is a possibility of anisotropic effects on the system as well. However, distinguishing the decrease in $\chi_M T$ between the spin state change from $S = 1$ to $S = 0$ and increased anisotropy would be an extremely difficult task. Additionally, we do not expect anisotropy in a system with an $S = 0$ state. However, if similar systems that are nine-coordinate around a U^{IV} center are synthesized, it can be expected that an $S = 1$ ground state can be achieved, possibly by modifying the capping ligand on the lithium ion (Et_2O in this case) or modification of the auxillary ligands (dmpe in this case). Anisotropic effects would become quite strong in the aforementioned case due to the inherent single-ion anisotropy associated with U-ions that paramagnetism could be maintained at low temperatures. Based on the crystallographic and magnetic data, we believe that the steric bulk and ligand-field present in **11.2** do not allow complete relaxation to a diamagnetic ground state at low temperatures, which is an interesting find for an actinide species.

*11.4.4 Synthesis and characterization of **11.3***

To stabilize the capping ligand of **11.2** which is hypothesized to improve the temperature stability of **11.2**, further synthetic modifications are performed. Addition of 12-crown-4 to a solution of **11.2** in Et_2O immediately results in an orange precipitate. Interestingly, this precipitate was found to be insoluble in all solvents except for CH_2Cl_2 (it was even insoluble in $ClCH_2CH_2Cl$!). Upon cooling the orange precipitate solution in CH_2Cl_2, orange block crystals were obtained which gave $[(dmpe)_2U(CCPh)_4(Li\cdot(CH_2Cl_2)_2)]$ (**11.3**). Peculiarly, addition of a completely redox innocent species, 12-crown-4, resulted in a reduction of the uranium center by one electron. This reaction proceeds with as little as 10 mol % of 12-crown-4 added with respect to **11.2**. To further investigate this complex, some control reactions are performed.

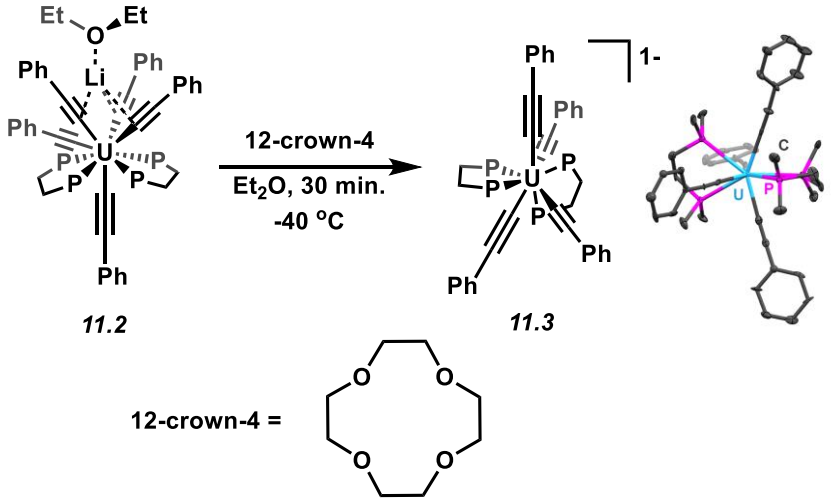


*Figure 11.4.2 Synthesis of **11.1** and **11.3**.*

Addition of other alkali chelating agents such as TMEDA, 15-crown-5 or 18-crown-6 to a solution of **11.2** in Et_2O does not result in any reactivity. On the other hand, addition of benzo-12-crown-4 to a solution of **11.2** in Et_2O gives **11.3**, but dibenzo-12-crown-4 does not react. This

indicates that some amount of steric hindrance must be present for the reaction to proceed. This is presumably caused by a tight-ion pair formed by the lithium cation and the anionic uranium complex. Further, *in-situ* IR spectroscopy indicates the formation of diphenylbutadiyne is formed under the reaction conditions (Figure A11.8). This molecule could be formed from "radical" coupling of two phenylacetylide radicals, or reductive elimination from a uranium center. To probe these two possible processes, a solution of **11.2** (1 equiv) in Et_2O with BHT (1 equiv) is stirred and then 12-crown-4 (10 mol % to **11.2**) is added, which does not result in **11.3**. This indicates that this process likely involves one-electron chemistry. As a final control experiment, complex **11.1** is added to Li metal and 12-crown-4 in Et_2O, which does not result in **11.3**. Therefore, **11.1** is likely not involved in the conversion of **11.2** → **11.3**. With these results we propose the mechanism (shown in Figure 11.4.3) as a means of production for **11.3**. To begin, complex **11.2** and 12-crown-4 perform a ligand exchange reaction, presumably with 1 equivalent of 12-crown-4 and 2 equivalents of **11.2** to form a reactive adduct. The initiation of metal catalysis *via* crown ethers has been previously reported.[44-45] This initial step is then followed by a biradical bond-forming reaction between two phenylacetylene-radical species, forming diphenylbutadiyne and two electron equivalents reducing each uranium ion by one electron. After dissociation of the 12-crown-4, the catalytic cycle is completed, forming **11.3**. Further studies investigating this mechanism are currently underway in our laboratory.

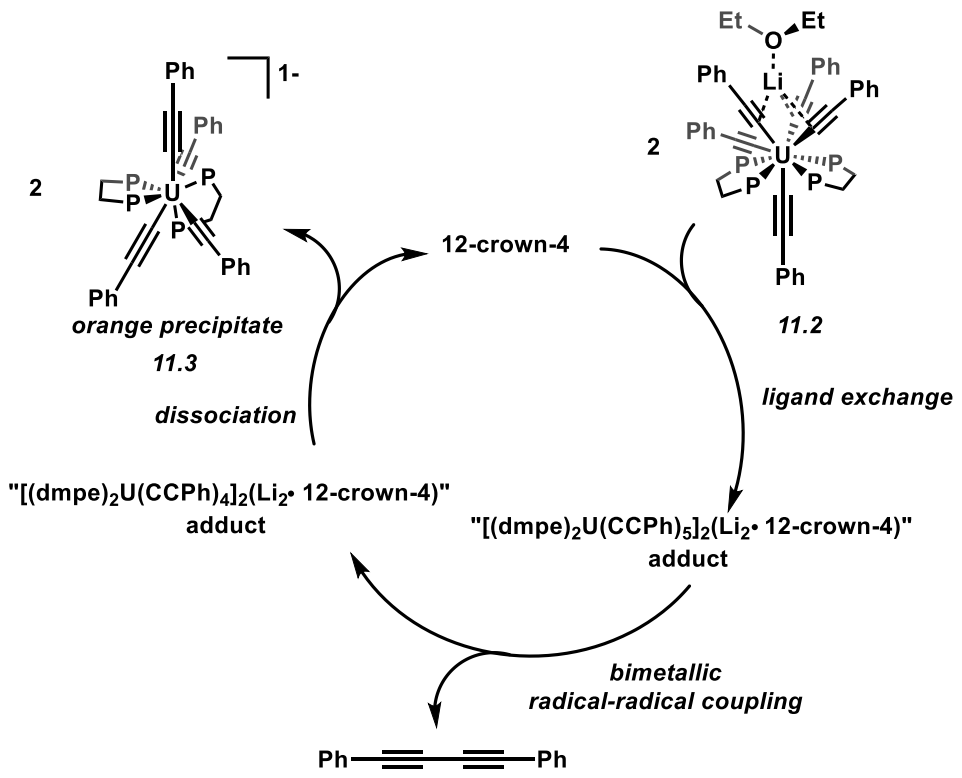


*Figure 11.4.3 Proposed mechanism for the formation of **11.3**.*

11.5 Conclusion

In conclusion, two U^{IV} complexes and one new U^{III} complex containing acetylide ligands are reported. Compound **11.1** is eight-coordinate with four phenylacetylide and two bidentate dmpe ligands, where **11.2** is nona-coordinate with fives phenylacetylide and two bidentate dmpe ligands with an encapsulated lithium within three of acetylide groups. The temperature dependent magnetic susceptibility data for **11.2** is higher than expected at 300 K where $\chi_M T = 1.34$ cm^3Kmol^{-1}. The coordination environment of **11.2** is strained, specifically the two pseudo mirror-image dmpe moieties experience much strain both in bond distance and angle. We attribute these differences in magnetic results to the ligand environment of **11.2** allowing some occupation of a magnetic ground state at low temperatures. In an effort to stabilize the coordination geometry, Li-abstraction reagents were used, which resulted in a surprising reduction of the U ion.

References

1. Rinehart, J. D.; Long, J. R. *Chem. Sci.* **2011**, *2*, 2078.

2. Habib, F.; Murugesu, M. *Chem. Soc. Rev.* **2013**, *42*, 3278.

3. Woodruff, D. N.; Winpenny, R. E. P.; Layfield, R. A. *Chem. Rev.* **2013**, *113*, 5110.

4. Layfield, R. A. *Organometallics* **2014**, *33*, 1084.

5. Rinehart, J. D.; Long, J. R. *J. Am. Chem. Soc.* **2009**, *131*, 12558.

6. Antunes, M. A.; Pereira, L. C. J.; Santos, I. C.; Mazzanti, M.; Marçalo, J.; Almeida, M. *Inorg. Chem.* **2011**, *50*, 9915.

7. Mills, D. P.; Moro, F.; McMaster, J.; van Slageren, J.; Lewis, W.; Blake, A. J.; Liddle, S. T. *Nat. Chem.* **2011**, *3*, 454.

8. Mougel, V.; Chatelain, L.; Pécaut, J.; Caciuffo, R.; Colineau, E.; Griveau, J. C.; Mazzanti, M. *Nat. Chem.* **2013**, *5*, 482.

9. King, D. M.; Tuna, F.; McInnes, E. J. L.; McMaster, J.; Lewis, W.; Blake, A. J.; Liddle, S. T. *Nat. Chem.* **2013**, *5*, 482.

10. King, D. M.; Tuna, F.; McMaster, J.; Lewis, W.; Blake, A. J.; McInnes, E. J. L.; Liddle, S. T. *Angew. Chem. Int. Ed.* **2013**, *52*, 4921.

11. Castro-Rodriguez, I.; Olsen, K.; Gantzel, P.; Meyer, K. *J. Am. Chem. Soc.* **2003**, *125*, 4565.

12. Lewis, A. J.; Williams, U. J.; Kikkawa, J. M.; Carroll, P. J.; Schelter, E. J. *Inorg. Chem.* **2012**, *51*, 37.

13. Lewis, A. J.; Williams, U. J.; Carroll, P. J.; Schelter, E. J. *Inorg. Chem.* **2013**, *52*, 7326.

14. Rinehart, J. D.; Harris, T. D.; Kozimor, S. A.; Bartlett, B. M.; Long, J. R. *Inorg. Chem.* **2009**, *48*, 3382.

15. Monreal, M. J.; Diaconescu, P. L. *Organometallics* **2008**, *27*, 1702.

16. Diaconescu, P. L.; Arnold, P. L.; Baker, T. A.; Mindiola, D. J.; Cummins, C. C. *J. Am. Chem. Soc.* **2000**, *122*, 6108.

17. Kozimor, S. A.; Bartlett, B. M.; Rinehart, J. D.; Long, J. R. *J. Am. Chem. Soc.* **2007**, *129*, 10672.

18. Rinehart, J. D.; Bartlett, B. M.; Kozimor, S. A.; Long, J. R. *Inorg. Chim. Acta* **2008**, *361*, 3534.

19. Salmon, L.; Thuéry, P.; Rivière, E.; Ephritikhine, M. *Inorg. Chem.* **2006**, *45*, 83.

20. Graves, C. R.; Yang, P.; Kozimor, S. A.; Vaughn, A. E.; Clark, D. L.; Conradson, S. D.; Schelter, E. J.; Scott, B. L.; Thompson, J. D.; Hay, P. J.; Morris, D. E.; Kiplinger, J. L. *J. Am. Chem. Soc.* **2008**, *130*, 5272.

21. Schelter, E. J.; Wu, R. L.; Scott, B. L.; Thompson, J. D.; Morris, D. E.; Kiplinger, J. L. *Angew. Chem. Int. Ed.* **2008**, *47*, 2993.

22. Kiplinger, J. L.; Scott, B. L.; Schelter, E. J.; Tournear, J. A. P. D. *J. Alloys Comp.* **2007**, *444*, 477.

23. Gardner, B. M.; Lewis, W.; Blake, A. J.; Liddle, S. T. *Inorg. Chem.* **2011**, *50*, 9631.

24. Newell, B. S.; Rappé, A. K.; Shores, M. P. *Inorg. Chem.* **2010**, *49*, 1595.

25. Karraker, D. G.; Stone, J. A.; Jones, E. R.; Edelstein, N. *J. Am. Chem. Soc.* **1970**, *92*, 4841.

26. Fortier, S.; Melot, B. C.; Wu, G.; Hayton, T. W. *J. Am. Chem. Soc.* **2009**, *131*, 15512.

27. Patel, D.; Moro, F.; McMaster, J.; Lewis, W.; Blake, A. J.; Liddle, S. T. *Angew. Chem. Int. Ed.* **2011**, *50*, 10388.

28. Brown, J. L.; Fortier, S.; Lewis, R. A.; Wu, G.; Hayton, T. W. *J. Am. Chem. Soc.* **2012**, *134*, 15468.

29. Patel, D.; Tuna, F.; McInnes, E. J. L.; Lewis, W.; Blake, A. J.; Liddle, S. T. *Angew. Chem. Int. Ed.* **2013**, *52*, 13334.

30. King, D. M.; McMaster, J.; Tuna, F.; McInnes, E. J. L.; Lewis, W.; Blake, A. J.; Liddle, S. T. *J. Am. Chem. Soc.* **2014,** *136*, 5619.

31. Fortier, S.; Walensky, J. R.; Wu, G.; Hayton, T. W. *J. Am. Chem. Soc.* **2011**, *133,* 11732.

32. Bain, G. A.; Berry, J. F. *J. Chem. Educ.* **2008**, *85*, 532.

33. Arney, D. S. J.; Burns, C. J. *J. Am. Chem. Soc.* **1995**, *117*, 9448.

34. Korobkov, I.; Gorelsky, S.; Gambarotta, S. *J. Am. Chem. Soc.* **2009**, *131*, 10406.

35. Fortier, S.; Wu, G.; Hayton, T. W. *Inorg. Chem.* **2008**, *47*, 4752.

36. Berhet, J. C.; Thuéry, P.; Ephritikhine, M. *Inorg. Chem.* **2005**, *44*, 1142.

37. Gaunt, A. J.; Scott, B. L.; Neu, M. P. *Inorg. Chem.* **2006**, *45*, 7401.

38. Haddad, S. F.; Al-Far, R. H.; Ahmed, F. R. *Acta Cryst. C* **1987**, *43*, 453.

39. Graves, C. R.; Scott, B. L.; Morris, D. E.; Kiplinger, J. L. *Organometallics* **2008**, *27*, 3335.

40. Edwards, P. G.; Andersen, R. A.; Zalkin, A. *Organometallics* **1984**, *3*, 293.

41. Edwards, P. G.; Parry, J. S.; Read, P. W. *Organometallics* **1995**, *14*, 3649.

42. Spencer, L. P.; Gdula, R. L.; Hayton, T. W. *Chem. Commun.* **2008**, 4986.

43. Lewis, A. J.; Carrol; P. J.; Schelter, E. J. *J. Am. Chem. Soc.* **2013**, *135*, 13185.

44. Smith, A. B.; Boldi, A. M. *J. Am. Chem. Soc.* **1997**, *119*, 6925.

45. Tietze, L. F.; Geissler, H.; Gewert, J. A.; Jakobi, U. *Synlett* **1994**, 511.

Chapter 12: Magnetic properties of uranium complexes appended with PDI, alkyl and Tp* ligands.*

12.1 Background

This chapter concerns the magnetic properties of three families of uranium complexes. The magnetic properties of molecular uranium species are of interest to many broader fields of chemistry including single molecule magnets[1] and spintronics[2] among others. Compared to transition metals, whose oxidation states are sometimes vague due to ligand radicals or lanthanides, which are almost entirely trivalent, uranium and other transactinide species show extremely oxidation state dependent magnetic properties and can encompass many paramagnetic oxidation states.[3] These properties are further complicated by large spin-orbit coupling values and a fundamental lack of understanding of potential exchange coupling among these ions.[4-5] Therefore, it is important to analyze uranium species of different oxidation states and ligand field strengths to develop a physical understanding of these species.

Herein, I discuss the magnetic properties of a series of tetraalkyl uranium complexes, U-pyridinediimine (PDI) complexes with a variety of reduced PDI ligands, and a larger series of bulky tris-pyrazolylborate (Tp*) ligated U-complexes. The tetraalkyl species were investigated as a fundamental understanding of ligand electronic effects on U(IV) magnetic properties. The PDI complexes were investigated to understand the extent to which ligand radicals interact with U(IV) ions concomitantly with electronic structure determinations. Finally, the Tp* complexes were measured as analogous species to transition metal complexes, which show differential exchange coupling and to understand the extent to which excited states affect the dynamic magnetic

---

*Reproduced in part with permission from [*Inorg. Chem.* **2016**, *55*, 11854-11866. and *Organometallics* **2017**, *36*, 3491-3497.] Copyright 2016 and 2017 American Chemical Society.

properties of these species. Since each family has it's own background and motivation for synthesis and magnetic characterization, much of the background for these complexes will be presented together with the results and discussion.

12.2 Division of Labor

All dc and ac magnetic properties were collected, analyzed and interpreted by Robert F. Higgins. Synthesis and all other characterization was performed by John J. Kiernicki (Purdue University, PDI complexes), Sara A. Johnson (Purdue University, alkyl complexes) and Caleb J. Tatebe (Purdue University, Tp* complexes) in Suzanne C. Bart's research group. Analysis and assistance in interpretation was performed by Joseph M. Zadrozny and Matthew P. Shores. The data concerning the tetraalkyl compounds have been published, see: *Organometallics* **2017**, *36*, 3491. The data concerning the PDI compounds have been published, see: *Inorg. Chem.* **2016**, *55*, 11854.

12.3 Experimental Details

Magnetic susceptibility data were collected using a Quantum Design MPMS XL SQUID magnetometer. All sample preparations were performed inside a dinitrogen-filled glovebox (MBRAUN Labmaster 130). Powdered microcrystalline samples were loaded into polyethylene bags and sealed in the glovebox. The bags that contained compounds [((Tp*)$_2$U)$_2$-*p*-DEB], [((Tp*)$_2$U)$_2$-*m*-DEB], [(Tp*)$_2$U(CCPh)], [(Tp*)$_2$U(THF)](BPh$_4$) and [(Tp*)$_2$U(MeCN)$_2$](BPh$_4$) were subsequently sealed in an additional polyethylene bag to ensure inert conditions as these complexes showed heightened air-sensitivity. After sealing in the bags, the samples were inserted into a straw and transported to the magnetometer under dinitrogen. Ferromagnetic impurities were checked through a variable field analysis (0 to 10 kOe) of the magnetization at 100 K (Figures A12.1-17), which showed that for [(Tp*)$_2$U(MeCN)$_2$](BPh$_4$), [((Tp*)$_2$U)$_2$-*p*-DEB], [((Tp*)$_2$U)$_2$(*p*-DIB)], [((Tp*)$_2$U)$_2$(*m*-DIB)] and [(Tp*)$_2$U]-insertion product major ferromagnetic impurities were likely not present. As a precaution, the variable temperature magnetic susceptibility data for [(Tp*)$_2$U(=N-*p*-Tol)], [(Tp*)$_2$U(THF)](BPh$_4$), [(Tp*)$_2$U(CCPh)] and [((Tp*)$_2$U)$_2$-

m-DEB] were collected at 5000 Oe due to non-linearity in the magnetization data collected at 100 K. Magnetic susceptibility data were collected at temperatures ranging from 2 to 300 K (Figures 12.4.1, 12.4.3, 12.4.4 and 12.4.7). Magnetic susceptibility data were collected at temperatures ranging from 2 to 300 K. Magnetization measurements were collected at 1.8 K while varying the applied field up to 50 kOe (Figures 12.4.3, A12.18-28). Dynamic magnetic measurements were performed with a 4 Oe applied ac field (Figure 12.4.8, A12.29-32). Fits acquired with the program PHI[6] to determine a potential coupling constant for [((Tp*)$_2$U)$_2$-*p*-DEB], [((Tp*)$_2$U)$_2$-*m*-DEB] used the following equation: $\widehat{H} = -2J\widehat{S_1} \cdot \widehat{S_2}$. Fits that include crystal field and magnetic anisotropic parameters used the following equation:

$$\hat{H} = \sum D_i\left[S_{z,i}^2 - 1/3S_i(S_i+1) + E_i/D_i\left(S_{x,i}^2 - S_{y,i}^2\right)\right] + \sum g_{xx,i}\beta\check{S}_{x,i} \cdot \widecheck{B_x} + g_{yy,i}\beta\check{S}_{y,i} \cdot \widecheck{B_y} + g_{zz,i}\beta\check{S}_{z,i} \cdot \widecheck{B_z} + \sum_{k=2,4,6}\sum_{q=-k}^{k} B_k^q \hat{O}_k^q + \mu_B g_J \hat{J} \cdot \vec{B}$$

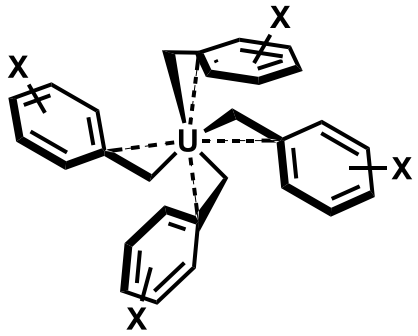
Fits that include only crystal field parameters used the following equation:

$$\hat{H} = \sum_{k=2,4,6}\sum_{q=-k}^{k} B_k^q \hat{O}_k^q + \mu_B g_J \hat{J} \cdot \vec{B}$$

Data were corrected for the diamagnetic contributions of the sample holder and bag by subtracting empty containers; corrections for the sample were calculated from Pascal's constants.[7]

12.4 Results and Discussion

12.4.1 Tetraalkylcompounds



X = *p*-^{i}Pr, *p*-^{t}Bu, *o*-OMe, *p*-Cl and *m*-OMe

Figure 12.4.1 Molecular representation of U-tetraalkyl species.

With a family of homoleptic uranium tetrabenzyl compounds that differ in their electronic properties in hand, variable temperature magnetic susceptibility measurements were performed for [U(*p*-^{i}PrBn)$_4$], [U(*p*-^{t}BuBn)$_4$], [U(*o*-OMeBn)$_4$], [U(*p*-ClBn)$_4$] and [U(*m*-OMeBn)$_4$] to determine if the electron donating nature of the benzyl substituent influences the magnetic properties. Unfortunately, the parent compound U(CH$_2$Ph)$_4$ proved too unstable to include in this study. The measured temperature dependencies of the $\chi_M T$ products for [U(*p*-^{i}PrBn)$_4$], [U(*p*-^{t}BuBn)$_4$], [U(*o*-OMeBn)$_4$], [U(*p*-ClBn)$_4$] and [U(*m*-OMeBn)$_4$] are shown in Figure 12.4.1, and the tabulated magnetic data for all complexes are presented in Table 12.4.1.

At 300 K, the $\chi_M T$ values for [U(*p*-^{i}PrBn)$_4$], [U(*p*-^{t}BuBn)$_4$], [U(*o*-OMeBn)$_4$], [U(*p*-ClBn)$_4$] and [U(*m*-OMeBn)$_4$] range from 0.95 to 1.10 cm^{3}Kmol^{-1} (μ_{eff} = 2.76-2.96), and these values slowly decrease upon cooling until approximately 50 K; below this temperature, $\chi_M T$ values decrease sharply to 0.11-0.26 cm^{3}Kmol^{-1} (μ_{eff} = 0.95-1.23) at 2 K. These magnetic susceptibility ranges match well with those for tetrahedral U(N(SiMe$_3$)$_2$)$_4$ (μ_{eff} = 1.32-2.94),[8] and are on par for those reported for tetravalent [U(CH$_2$^{t}Bu)$_5$]$^-$ (μ_{eff} = 2.36-3.09)[9] and UI(N(SiMe$_3$)$_2$)$_3$ (μ_{eff} = 2.16-3.35).[10] The

observed temperature dependencies align with literature precedent for mononuclear tetravalent uranium complexes, where non-interacting U(IV) f^2 ions that are ground state singlets typically show paramagnetic responses at higher temperatures due to population of magnetic excited states. As observed here and previously,[11] complexes containing U-alkyl fragments show distinctive temperature dependent behavior in that the onset of a sharper downturn in $\chi_M T$ (or μ_{eff}) values occurs at a lower temperature as compared to other U(IV) complexes.

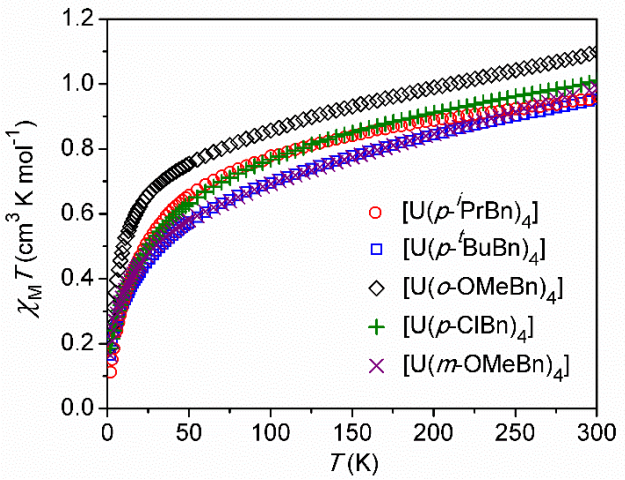


Figure 12.4.1. Temperature dependence of magnetic susceptibilities for [U(p-^{i}PrBn)$_4$], [U(p-^{t}BuBn)$_4$], [U(o-OMeBn)$_4$], [U(p-ClBn)$_4$] and [U(m-OMeBn)$_4$]. Data for [U(p-^{i}PrBn)$_4$], [U(o-OMeBn)$_4$], and [U(m-OMeBn)$_4$] were collected at an applied dc field of 5000 Oe, while data for [U(p-^{t}BuBn)$_4$] and [U(p-ClBn)$_4$] were collected at an applied dc field of 1000 Oe.

In order to fully understand the magnetic behavior of these derivatives, experiments to study the field dependencies of magnetization were also performed (Figures A12.18-22). Although none of the complexes display saturation at 50 kOe, the small magnetization values of 0.10-0.49 μ_B at low temperature (1.8 K) and high field are consistent with ground state singlets

mixed with paramagnetic excited states expected for U(IV) ions, as these values typically approach 0 μ_B.

Seeking evidence of synthetic tunability of electronic properties, we explored potential trends in magnetization, magnetic susceptibility and temperature independent paramagnetism (TIP)[5, 12-14] as a function of substituent donation. The magnetic data obtained for [U(*o*-OMeBn)$_4$], which was previously established as an 8-coordinate species arising from ligation to the O atoms, show the largest susceptibility and magnetization values at all temperatures. This can be attributed to the change in coordination geometry, and thus precludes further comparison with the rest of the family of compounds. For the remaining compounds, plots of representative magnetic quantities versus $\sigma_{p/m}$ are presented in Figures 12.4.2. Interestingly, we observe a subtle but clear correlation between room temperature magnetic susceptibility ($\chi_M T$) values and electron withdrawing ability of benzyl substituents. Magnetic property dependence on ligand substituent properties has been studied in Fe(II) spin-crossover systems, albeit over smaller σ ranges.[15-16] A possible explanation for these observations is that as the electron-withdrawing nature of the ligand increases, the magnetic ground state of uranium is destabilized, thus populating more excited states. This is unlikely to be the only consideration, as we note that TIP dependence on $\sigma_{p/m}$ is weak, but generally electron-withdrawing substituents give larger TIP values. Notwithstanding, the clear trend observed may offer a magnetic handle for tracking reactivity.

Table 12.4.1. Magnetic susceptibility and magnetization values for [U(p-^{i}PrBn)$_4$], [U(p-^{t}BuBn)$_4$], [U(o-OMeBn)$_4$], [U(p-ClBn)$_4$] and [U(m-OMeBn)$_4$].

	$\chi_M T$ 300 K (cm^3Kmol^{-1})	$\chi_M T$ 2 K (cm^3Kmol^{-1})	μ_{eff} 300 K	μ_{eff} 2 K	M 1.8 K 50 kOe (μ_B)
[U(*p*-^{i}PrBn)$_4$]	0.96	0.11	2.77	0.95	0.10
[U(*p*-^{t}BuBn)$_4$]	0.95	0.16	2.76	1.15	0.25
[U(*p*-ClBn)$_4$]	1.01	0.18	2.84	1.22	0.36
[U(*m*-OMeBn)$_4$]	0.99	0.16	2.81	1.15	0.31
[U(*o*-OMeBn)$_4$]	1.09	0.19	2.96	1.23	0.49

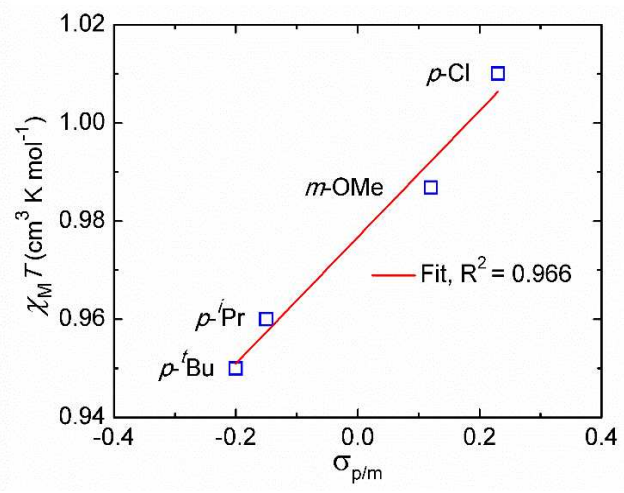
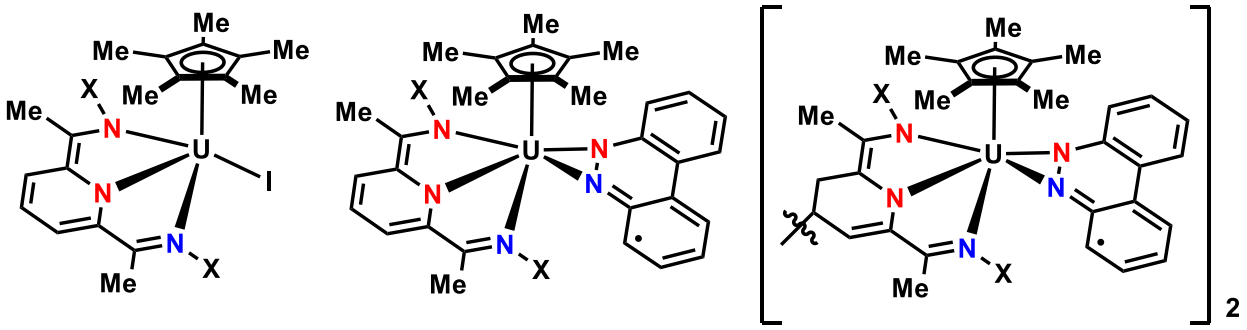


Figure 12.4.2. Relationship between the 300 K magnetic susceptibility values and Hammett parameter for compounds [U(p-^{i}PrBn)$_4$], [U(p-^{t}BuBn)$_4$], [U(p-ClBn)$_4$] and [U(m-OMeBn)$_4$]. Note that [U(o-OMeBn)$_4$] was not included in the linear fit due to the variation in its inner-coordination sphere.

12.4.2 U-PDI complexes



X =2,4,6-trimethylphenyl, N = neutral, N = monoanionic

Figure 12.4.2 Molecular representation of U-PDI complexes.

The magnetic susceptibilities of the pyridine(diimine) uranium species [(^{Mes}PDI^{Me})U(Cp*)I], [(^{Mes}PDI^{Me})U(Cp*)(BCC)] and [(^{Mes}PDI^{Me})U(Cp*)(BCC)]$_2$ were measured in the solid state at variable temperatures using SQUID magnetometry at 5000 Oe. Compound [(^{Mes}PDI^{Me})U(Cp*)I] was used as a reference, since this species is established to be a closed shell, uranium(IV) compound with no ligand radical(s) present.[17] The magnetic susceptibility for [(^{Mes}PDI^{Me})U(Cp*)I] ranges from 1.20 cm^{3}Kmol^{-1} (μ_{eff} = 3.15) at 300 K to 0.03 cm^{3}Kmol^{-1} (μ_{eff} = 0.46) at 2 K; such values are typically encountered for non-interacting U(IV) ions where ground state singlets show paramagnetic responses at higher temperatures due to population of magnetic excited states (Figure 13.4.3).[3, 18-20] In contrast, compound [(^{Mes}PDI^{Me})U(Cp*)(BCC)], which is formulated as a monomeric uranium(IV) species with a benzo[*c*]cinnoline radical shows a higher low temperature magnetic susceptibility of 0.67 cm^{3}Kmol^{-1} (μ_{eff} = 2.32, 4 K) as compared to [(^{Mes}PDI^{Me})U(Cp*)I], which is expected for the presence of an unpaired electron at this temperature. The high temperature magnetic susceptibility for [(^{Mes}PDI^{Me})U(Cp*)(BCC)] of 1.29 cm^{3}Kmol^{-1} (μ_{eff} = 3.21) is indistinguishable from [(^{Mes}PDI^{Me})U(Cp*)I]. Compound [(^{Mes}PDI^{Me})U(Cp*)(BCC)]$_2$ is dimeric and proposed to be composed of two units each with an unpaired electron on the benzo[*c*]cinnoline

radical. This is reflected in the magnetic susceptibility measurements, which shows a $\chi_M T$ value that is twice as high for [(^{Mes}PDI^{Me})U(Cp*)(BCC)]$_2$ as compared to [(^{Mes}PDI^{Me})U(Cp*)(BCC)]. At 300 K, the $\chi_M T$ value of 2.48 cm^{3}Kmol^{-1} (μ_{eff} = 4.46) is consistent with the presence of two uranium(IV) centers, as half of that value (1.24 cm^{3}Kmol^{-1}) is very close to the 1.20 and 1.29 cm^{3}Kmol^{-1} obtained for [(^{Mes}PDI^{Me})U(Cp*)I] and [(^{Mes}PDI^{Me})U(Cp*)(BCC)], respectively. The 2 K total susceptibility value of 0.82 cm^{3}Kmol^{-1} (μ_{eff} = 2.55) is as expected for an S = 1 ground state species that displays significant magnetic anisotropy.

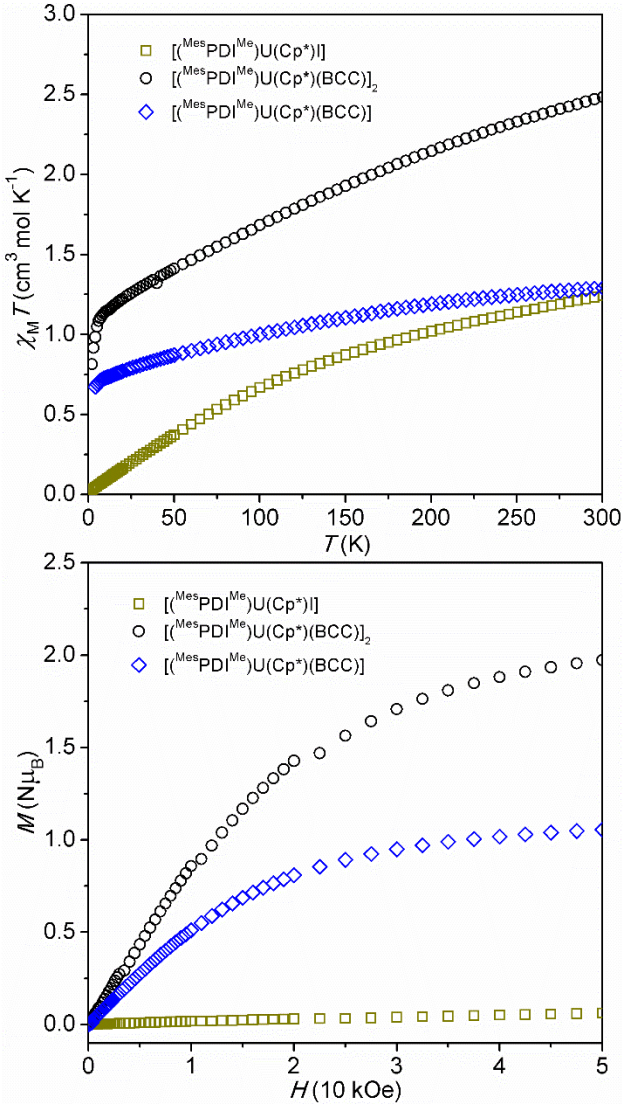


Figure 12.4.3. Top: Temperature dependence of the magnetic susceptibility for compounds [(Mes PDIMe)U(Cp)I] (gold), [(Mes PDIMe)U(Cp*)(BCC)]2 (black), and [(Mes PDIMe)U(Cp*)(BCC)] (blue) obtained at an applied dc field of 5000 Oe. Bottom: Field dependence of magnetization for compounds [(Mes PDIMe)U(Cp*)I], [(Mes PDIMe)U(Cp*)(BCC)]2, and [(Mes PDIMe)U(Cp*)(BCC)] collected at 1.8 K.*

Magnetization experiments were executed up to a field of 50 kOe to further understand the magnetic behavior of [(MesPDIMe)U(Cp*)I], [(MesPDIMe)U(Cp*)(BCC)]2, and

[(^{Mes}PDI^{Me})U(Cp*)(BCC)] at low temperature (1.8 K) (Figure 12.4.3). At this temperature, a closed shell uranium(IV) molecule, which would be a ground state singlet, would have a saturation value that approaches 0 μ_B. The value of 0.07 μ_B obtained for [(^{Mes}PDI^{Me})U(Cp*)I] is very close to 0, in agreement with the structural and spectroscopic data that supports a U(IV)-[^{Mes}PDI^{Me}]$^{2-}$ motif free of ligand radicals. By comparison, compound [(^{Mes}PDI^{Me})U(Cp*)(BCC)] displays a value of 1.06 μ_B at 1.8 K, consistent with the theoretical value of 1.00 μ_B (g = 2.0) and indicative of the presence of a ligand radical.[21-23] The spectroscopic and structural data obtained for [(^{Mes}PDI^{Me})U(Cp*)(BCC)] point towards localization of this ligand radical on the benzo[*c*]cinnoline ligand, rather than the [^{Mes}PDI^{Me}] ligand. Thus, the electronic structure assignment for [(^{Mes}PDI^{Me})U(Cp*)(BCC)] is as a 5f^2, U(IV) ion and a radical benzo[*c*]cinnoline ligand, supported by a closed shell [^{Mes}PDI^{Me}]$^{2-}$ ligand. Saturation experiments for dimeric [(^{Mes}PDI^{Me})U(Cp*)(BCC)]$_2$ produced a value of 1.9 μ_B at 1.8 K, roughly twice that of [(^{Mes}PDI^{Me})U(Cp*)(BCC)], again consistent with a ground state triplet with negligible communication between electrons. Taken together with the spectroscopic and crystallographic data, these data for [(^{Mes}PDI^{Me})U(Cp*)(BCC)]$_2$ are consistent with two U(IV)-[BCC]$^{1-}$ fragments supported by closed shell [^{Mes}PDI^{Me}]$^{2-}$ ligands. Of final note, the magnetic properties of compound [(^{Mes}PDI^{Me})U(Cp*)(BCC)] are not consistent with typical U(IV) magnetic properties when one ligand radical is present;[24] however, large magnetic susceptibility values at low temperature for U(IV) ions are known in the literature.[10, 25-26] Therefore, it is likely a more intimate spin-system is present in the case of [(^{Mes}PDI^{Me})U(Cp*)(BCC)]. Considering the magnetic properties of compound [(^{Mes}PDI^{Me})U(Cp*)(BCC)], the data for compound [(^{Mes}PDI^{Me})U(Cp*)(BCC)]$_2$ are not unexpected. If two spin-systems (one radical and one U(IV) ion for each) weakly ferromagnetically couple in [(^{Mes}PDI^{Me})U(Cp*)(BCC)]$_2$, then the S = 1 ground state has potential to show magnetic anisotropy, which was observed (Figure A12.33). Accordingly, an example of a ligated pyridine which undergoes a homo-molecular dimerization where two spin-systems ferromagnetically

couple is known in the literature.[27] Furthermore, there is another example where four spin centers are present in a molecule where the magnetic behavior was best modelled as two spin systems interacting.[28] Therefore, the most reasonable representation of the magnetic data for compound $[(^{Mes}PDI^{Me})U(Cp^*)(BCC)]_2$ is two spin-systems, each having one ligand radical and one U(IV) ion, weakly ferromagnetically coupling resulting in a ground state of $S = 1$.

12.4.3 U-Tp complexes*

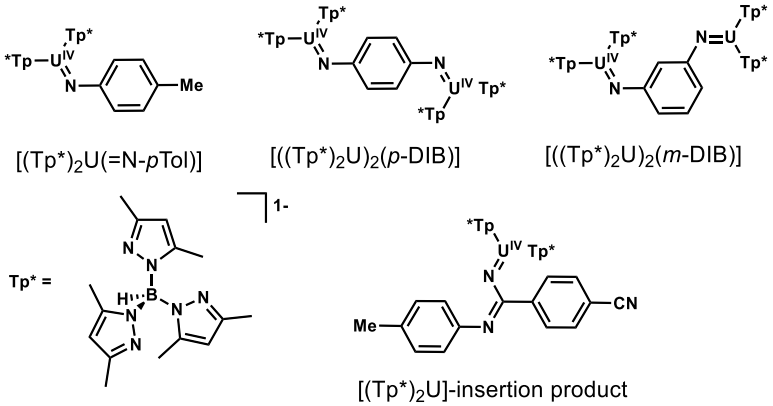


Figure 12.4.3 Molecular representation of U(IV)-imido complexes.

Magnetic susceptibility data are gathered for compounds for $[(Tp^*)_2U(=N\text{-}p\text{-}Tol)]$, $[((Tp^*)_2U)_2(p\text{-}DIB)]$, $[((Tp^*)_2U)_2(m\text{-}DIB)]$ and $[(Tp^*)_2U]$-insertion product (Figure 12.4.4). Compound $[(Tp^*)_2U(=N\text{-}p\text{-}Tol)]$ displays a room temperature magnetic susceptibility value of 0.98 cm^3Kmol^{-1} (μ_{eff} = 2.84), which slowly decreases until around 100 K where the decrease becomes more pronounced until reaching a value of 0.08 cm^3Kmol^{-1} (μ_{eff} = 0.64) at 2 K. These data are typical of mononuclear U(IV) complexes,[3] which show the well-precendented triplet-to-singlet relaxation over the entire temperature regime. For further assessment of this ground state, magnetization data show no indication of saturation at 50 kOe reaching a value of 0.24 μ_B, suggestive of a mononuclear U(IV) species.

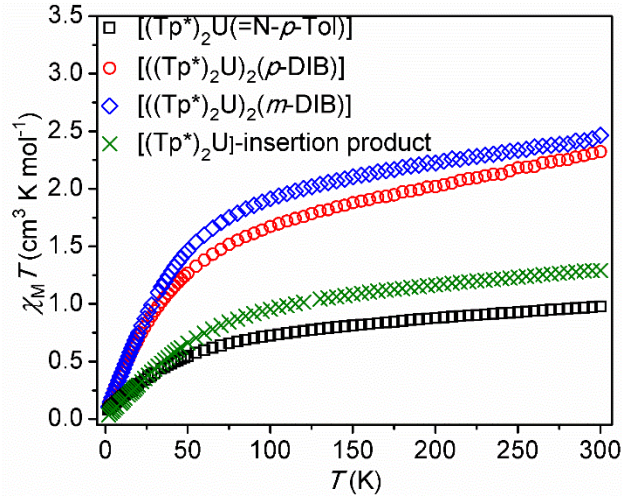


Figure 12.4.4. Temperature dependence of the magnetic susceptibility for compounds [(Tp)$_2$U(=N-p-Tol)], [((Tp*)$_2$U)$_2$(p-DIB)], [((Tp*)$_2$U)$_2$(m-DIB)] and [(Tp*)$_2$U]-insertion product, collected at 1000 ([((Tp*)$_2$U)$_2$(p-DIB)], [((Tp*)$_2$U)$_2$(m-DIB)] and [(Tp*)$_2$U]-insertion product) or 5000 Oe ([(Tp*)$_2$U(=N-p-Tol)]).*

The two dinuclear compounds, [((Tp*)$_2$U)$_2$(*p*-DIB)] and [((Tp*)$_2$U)$_2$(*m*-DIB)], exhibit similar behavior, considering two U(IV) ions, where at room temperature, the susceptibility products give values of 2.32 and 2.46 cm^{3}Kmol^{-1} (μ_{eff} = 4.31 and 4.44), respectively. Upon cooling, these susceptibility values decrease gradually until around 100 K where the downturn becomes more pronounced, eventually reaching values of 0.12 and 0.11 cm^{3}Kmol^{-1} (μ_{eff} = 0.98 and 0.94) at 2 K for [((Tp*)$_2$U)$_2$(*p*-DIB)] and [((Tp*)$_2$U)$_2$(*m*-DIB)], respectively. These data are similar to dimeric U(IV) complexes with ligands typically described as relatively covalent.[3, 5] To further confirm the U(IV) ground states for both complexes, magnetization data collected at 1.8 K up to an applied field of 50 kOe are small in magnitude (0.35 and 0.33 μ_B for [((Tp*)$_2$U)$_2$(*p*-DIB)] and [((Tp*)$_2$U)$_2$(*m*-DIB)], respectively) and do not saturate; typical of U(IV) compounds that occupy some magnetic excited states even at low temperatures. Having established the oxidation states of these complexes through magnetometry, we investigate other potentially interesting magnetic

properties. Andersen and coworkers described bridging U(V) imido-dimers where the *para* substituted species displayed a Néel temperature of ~20 K, unlike the *meta* analog, which showed behavior consistent with two non-interacting U(V) centers.[29] Alternatively, Liddle and Chilton discussed crystal field effects in chalcogenide tethered U(IV) dimers.[30] Therefore, these U(IV)-imido analogs, have potential for differential magnetic properties.

To address possible magnetic exchange for [((Tp*)$_2$U)$_2$(*p*-DIB)] and [((Tp*)$_2$U)$_2$(*m*-DIB)] we performed a subtraction method first reported by Rinehart *et al.*[4] using [(Tp*)$_2$U(=N-*p*-Tol)] as a mononuclear surrogate (Figure A12.44). Fitting these data with PHI,[6] no reasonable fit could be obtained using a *J* tensor in the applied Hamiltonian. Further, no obvious inflection point is observed in the χ_M vs *T* data (Figure 12.4.5), indicative of no long range magnetic interactions. These results indicate that neither [((Tp*)$_2$U)$_2$(*p*-DIB)] and [((Tp*)$_2$U)$_2$(*m*-DIB)] show data consistent with magnetic exchange coupling (ferromagnetic or antiferromagnetic) after a subtraction method is performed.

Since magnetic exchange coupling is likely not operative, we now investigate the possibility of crystal field effects in these complexes.[31] Even though typical paramagnetic behavior is not observed in their χ_M vs *T* data (subtle inflection point at lower temperatures, ~20-30 K), magnetic exchange is not invoked. Instead single-ion crystal field effects are hypothesized as the major contributing cause for this phenomenon. Analysis of the χ_M vs *T* data for [(Tp*)$_2$U(=N-*p*-Tol)], [((Tp*)$_2$U)$_2$(*p*-DIB)] and [((Tp*)$_2$U)$_2$(*m*-DIB)] (Figure 12.4.5) shows that the same phenomenon is observed for [((Tp*)$_2$U)$_2$(*m*-DIB)]. The collected magnetic data are fit in a similar fashion to Chilton and Liddle's method, where the results of these fits are shown in Figure 12.4.5 and Table 12.4.2. When the entire temperature range is fit, the resultant parameters are unreasonable: when an $S = 1$ impurity is included in the fits for compounds [(Tp*)$_2$U(=N-*p*-Tol)], [((Tp*)$_2$U)$_2$(*p*-DIB)] and [((Tp*)$_2$U)$_2$(*m*-DIB)], the quality of the fit did not greatly improve and the impurity was consistently below 0.01%, indicative that these compounds are relatively impurity-free. Further, if these fits were performed using two separate U ions for [((Tp*)$_2$U)$_2$(*p*-DIB)] and

[((Tp*)$_2$U)$_2$(*m*-DIB)], no reasonable fits are obtained. These fits are consistent with other U(IV) complexes with regard to the orbital reduction (*k*) and g_J parameters.[31-32] Not surprisingly, all three of these complexes show smaller *k* values when compared to the bridging chalcogenide species, since the inclusion of metal-imido bonds should display more covalent behavior than chalcogenide bridges.[31]

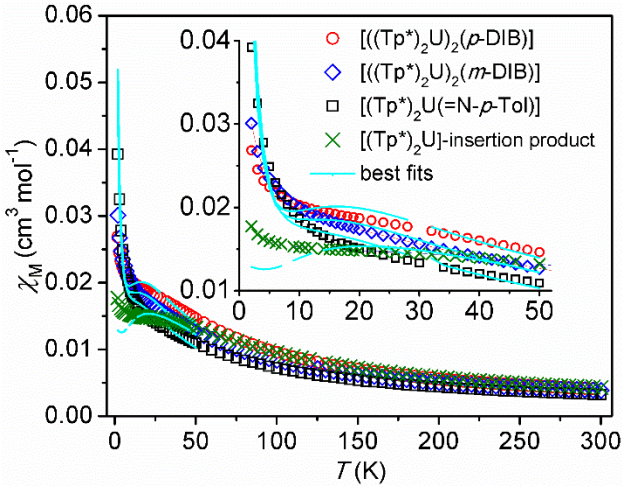


Figure 12.4.5. Temperature dependence of the magnetic susceptibility for [(Tp)$_2$U(=N-p-Tol)], [((Tp*)$_2$U)$_2$(p-DIB)], [((Tp*)$_2$U)$_2$(m-DIB)] and [(Tp*)$_2$U]-insertion product per U-atom, where the 2-50 K data points are fit (black lines) using the program PHI.[6] Inset: Zoom of the low temperature fits.*

Interestingly, the spin-orbit coupling parameter (B^0_2) differs greatly among [((Tp*)$_2$U)$_2$(*p*-DIB)] when compared to [((Tp*)$_2$U)$_2$(*m*-DIB)] and [(Tp*)$_2$U(=N-*p*-Tol)]. These results are interesting in the context of the ligand field splittings of these complexes, which are expected to be similar given the geometries about the individual U atoms. Compound [((Tp*)$_2$U)$_2$(*m*-DIB)] has an average U···B distance of 3.66(1) Å whereas compounds [((Tp*)$_2$U)$_2$(*p*-DIB)] and [(Tp*)$_2$U(=N-*p*-Tol)] display U···B distances of 3.70(1) and 3.69(1) Å, respectively. While this change is small, the difference in spin-orbit coupling value is only 12 cm^{-1}, so a difference in bonding is expected

to be small. The shorter U···B distances for [((Tp*)$_2$U)$_2$(*m*-DIB)] compresses the Tp* ligands closer to the U center. These shorter distances are expected to increase the frontier LUMO orbitals in energy, which is what is observed (B^0_2 value). To further validate these excited state energies for [((Tp*)$_2$U)$_2$(*p*-DIB)] and [((Tp*)$_2$U)$_2$(*m*-DIB)], we measure and analyze another complex, [(Tp*)$_2$U]-insertion product. The crystal structure data for this species indicates a U···B distance of 3.63(1) allows for a larger range of U···B distances in this family of U-imidos to be characterized. Interestingly, fitting the magnetic susceptibility data for [(Tp*)$_2$U]-insertion product gives the largest B^0_2 value of the family. Providing a relationship between these spin-orbit coupling values and the U···B distance (Figure 12.4.6) gives a linear correlation, further strengthening this argument. Therefore, to increase the spin-orbit coupling values of U(Tp*)$_2$ complexes, the most straightforward manner appears to be decreasing the U···B distance.

Table 12.4.2. Parameters for the magnetic fits for [(Tp)$_2$U(=N-p-Tol)], [((Tp*)$_2$U)$_2$(p-DIB)], [((Tp*)$_2$U)$_2$(m-DIB)] and [(Tp*)$_2$U]-insertion product using the program PHI.*[3]

Complex	B^0_2 (cm^{-1})	*k*	g_J	R^2	U···B distance (Å)
[(Tp*)$_2$U(=N-*p*-Tol)]	1.22	0.760	1.00	99.992	3.70(1)
[((Tp*)$_2$U)$_2$(*p*-DIB)]	1.38	0.798	1.18	99.993	3.69(1)
[((Tp*)$_2$U)$_2$(*m*-DIB)]	13.2	0.831	1.33	99.990	3.67(1)
[(Tp*)$_2$U]-insertion product	31.1	0.805	1.37	99.985	3.63(1)

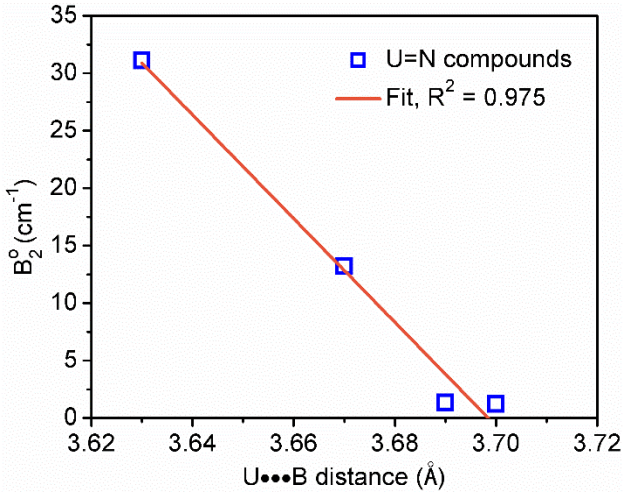


Figure 12.4.6 Correlation between obtained spin-orbit coupling values and U···B distances.

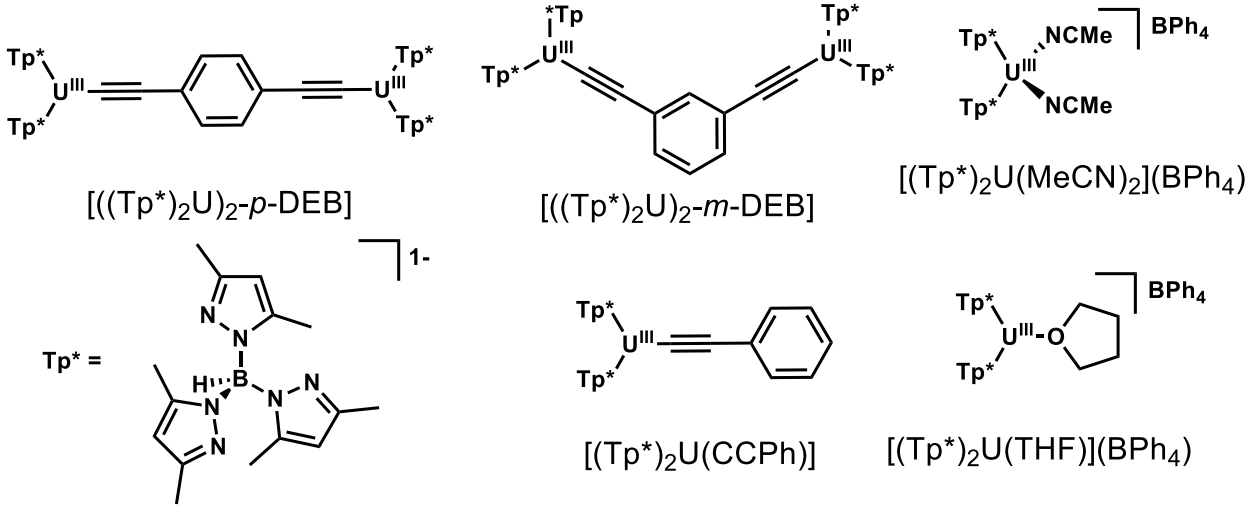


Figure 12.4.4 Molecular representation of U(III) bis-Tp complexes.*

To test how these hypotheses hold up in the context of similar complexes, we measure the magnetic properties of a series of $U(Tp^*)_2$ complexes where the U atom is in the 3+ oxidation state. Magnetic properties are collected for $[((Tp^*)_2U)_2$-*p*-DEB], $[((Tp^*)_2U)_2$-*m*-DEB], $[(Tp^*)_2U(CCPh)]$, $[(Tp^*)_2U(THF)](BPh_4)$ and $[(Tp^*)_2U(MeCN)_2](BPh_4)$ where the variable temperature magnetic susceptibility are presented in Figure 12.4.7. Each of the mononuclear

species displays quite similar data, so only the data for [(Tp*)$_2$U(CCPh)] are described, but pertinent values for all compounds are given in Table 12.4.3. Compound [(Tp*)$_2$U(CCPh)] displays a $\chi_M T$ value of 1.42 cm^{3}Kmol^{-1} (μ_{eff} = 3.37) at 300 K, which decreases monotonically across all temperatures until 10 K, where a more pronounced decrease occurs until 2 K, where the susceptibility product reaches a value of 0.62 cm^{3}Kmol^{-1} (μ_{eff} = 2.23). Magnetization data collected at 1.8 K up to 50 kOe shows near saturation at 0.79 μ_B for [(Tp*)$_2$U(CCPh)] (Figure A12.27). These data are typical of mononuclear U(III) species (ground state term symbol $^4I_{9/2}$), supporting the assignment of a U(III) oxidation state for [(Tp*)$_2$U(CCPh)], [(Tp*)$_2$U(THF)](BPh$_4$) and [(Tp*)$_2$U(MeCN)$_2$](BPh$_4$).[3, 33]

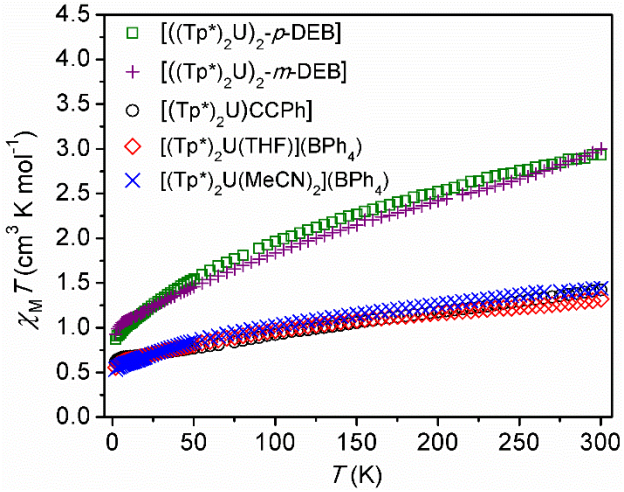


Figure 12.4.7 Temperature dependence of the magnetic susceptibility for compounds [((Tp)$_2$U)$_2$-p-DEB], [((Tp*)$_2$U)$_2$-m-DEB], [(Tp*)$_2$U(CCPh)], [(Tp*)$_2$U(THF)](BPh$_4$) and [(Tp*)$_2$U(MeCN)$_2$](BPh$_4$) collected at applied field of 1000 ([((Tp*)$_2$U)$_2$-p-DEB] and [(Tp*)$_2$U(MeCN)$_2$](BPh$_4$)) or 5000 Oe ([(Tp*)$_2$U(CCPh)] and [(Tp*)$_2$U(THF)](BPh$_4$)).*

Table 12.4.3 Magnetic susceptibility and magnetization values for [((Tp)$_2$U)$_2$-p-DEB], [(Tp*)$_2$U(CCPh)], [(Tp*)$_2$U(THF)](BPh$_4$) and [(Tp*)$_2$U(MeCN)$_2$](BPh$_4$).*

Complex	$\chi_M T$ (cm^{3}Kmol^{-1}) 300 K, (μ_{eff})	$\chi_M T$ (cm^{3}Kmol^{-1}) 2 K, (μ_{eff})	M (μ_B) 50 kOe, 1.8 K
[((Tp*)$_2$U)$_2$-*p*-DEB]	2.93 (4.84)	0.87 (2.64)	1.61
[((Tp*)$_2$U)$_2$-*m*-DEB]	3.00 (4.90)	0.93 (2.73)	1.73
[(Tp*)$_2$U(CCPh)]	1.42 (3.37)	0.62 (2.23)	0.79
[(Tp*)$_2$U(THF)](BPh$_4$)	1.32 (3.25)	0.56 (2.12)	0.72
[(Tp*)$_2$U(MeCN)$_2$](BPh$_4$)	1.44 (3.39)	0.53 (2.06)	0.94

The dinuclear compound [((Tp*)$_2$U)$_2$-*p*-DEB] displays a room temperature $\chi_M T$ value of 2.93 cm^{3}Kmol^{-1} (μ_{eff} = 4.84), which decreases monotonically across all temperatures until 2 K, where the $\chi_M T$ value reaches 0.87 cm^{3}Kmol^{-1} (μ_{eff} = 2.64) (Figure 12.4.7). These data are consistent with the presence of two U(III) ions, as the expected room temperature $\chi_M T$ value for two non-interacting $^4I_{9/2}$ ground states is 3.29 cm^{3}Kmol^{-1} (μ_{eff} = 5.13).[3] A magnetic saturation experiment performed at 1.8 K shows near-saturation at 1.61 μ_B with an applied field of 50 kOe (Figure A12.27), further suggesting the presence of two U(III) ions in compound [((Tp*)$_2$U)$_2$-*p*-DEB].[34] Based on the susceptibility data across all temperatures, it appears that the U(III) ions are non-interacting; however, we applied a literature precedented subtraction method to further investigate the presence of exchange coupling.[4] After subtraction, the susceptibility data do not indicate significant interactions between the U(III) ions in compound [((Tp*)$_2$U)$_2$-*p*-DEB] (Figure A13.35)**.** In addition, no reasonable fits are obtained when using PHI[6] to fit the subtracted data to extract a coupling constant (*J*) value. Further, the closest intermolecular U···U distance is 9.064(4) Å and no H-bonding or π-stacking pathways are obvious in the crystal structure, suggesting a lack of intermolecular interactions for compound [((Tp*)$_2$U)$_2$-*p*-DEB].

To further investigate the electronic structure and magnetic properties of these complexes, ac data are collected. Dynamic magnetic data indicate that [((Tp*)$_2$U)$_2$-*p*-DEB] likely displays slow magnetic relaxation; however, due to the limits of our instrument, a relaxation barrier and lifetime

are not quantifiable. Interestingly, all three mononuclear complexes [(Tp*)$_2$U(CCPh)], [(Tp*)$_2$U(THF)](BPh$_4$) and [(Tp*)$_2$U(MeCN)$_2$](BPh$_4$) display magnetic relaxation that is slow enough to be measured. While none of these complexes shows zero field relaxation at the frequency range measured, each shows field-induced magnetic relaxation that is optimized at applied dc fields of either 500 ([(Tp*)$_2$U(THF)](BPh$_4$)) or 1000 Oe ([(Tp*)$_2$U(CCPh)] and [(Tp*)$_2$U(MeCN)$_2$](BPh$_4$), Figures 12.4.8, A12.29-30). Fitting these data to the Arrhenius equation ($\tau = \tau_0 \exp(U_{eff} k_B^{-1} T^{-1})$) gives lifetimes and barriers that compare well to literature precedent for mononuclear U(III) complexes (Table 12.4.4).[33, 35-38] As a first approximation, it is expected that [(Tp*)$_2$U(THF)](BPh$_4$) and [(Tp*)$_2$U(MeCN)$_2$](BPh$_4$) show similar properties that are different than [(Tp*)$_2$U(CCPh)] based on the varied ligand fields. The ligands THF and MeCN are both weak-field and π-accepting whereas phenylacetylide is a strong-field, σ-donating ligand. While differences are observed, comparison to other (Tp*)$_2$U complexes suggests that a simple ligand field argument is not appropriate to describe the variable dynamic magnetic properties of these complexes (Table 12.4.4).[36-37]

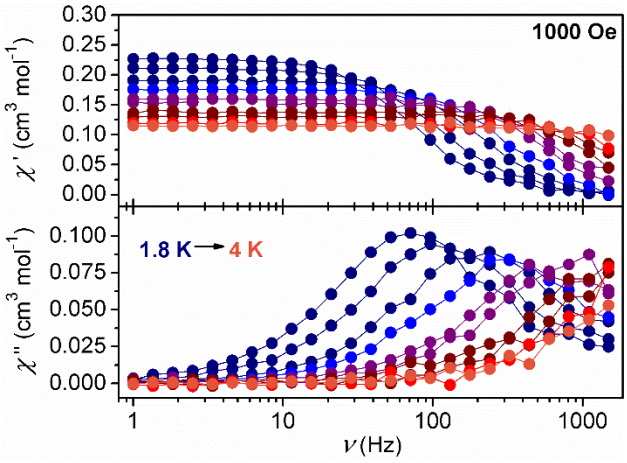


Figure 12.4.8 Variable temperature in- (top) and out-of-phase (bottom) magnetic susceptibility data for [(Tp)$_2$U(MeCN)$_2$](BPh$_4$) collected with an applied ac field of 4 Oe and an applied dc field of 1000 Oe.*

Table 12.4.4 Selected single molecule magnetic values and crystal field parameters acquired from fits using the program PHI[6] for some Tp-containing U(III) complexes.

Complex	τ_0 (1×10^{-6} s)	U_{eff} (cm^{-1})	g_J	B^0_2 (cm^{-1})	k	D (cm^{-1})	R^2	ref
$[(Tp^*)_2U(I)]$	0.18	21.0	0.539	17.1	0.811	-16.9	99.90	36,38
$[(Tp^*)_2U(bpy)](I)$	0.14	18.2	0.337	14.7	0.850	-22.4	99.65	35
$[U(BPz_2H_2)_3]$	1.2	8	0.426	5.5	0.731	-24.1	99.99	38
$[((Tp^*)_2U)_2$-*p*-DEB]	--	--	0.575	***19.7***	0.816	-20.7	99.24	this work
$[((Tp^*)_2U)_2$-*m*-DEB]	--	--	0.690	***28.7***	0.862	-14.4	99.31	this work
$[(Tp^*)_2U(CCPh)]$	2.08	6.81	0.507	15.7	0.756	-15.6	99.83	this work
$[(Tp^*)_2U(THF)](BPh_4)$	4.28	9.00	0.516	16.1	0.869	-9.8	99.70	this work
$[(Tp^*)_2U(MeCN)_2](BPh_4)$	4.00	8.36	0.624	9.7	0.896	-16.9	99.61	this work

Many different phenomena and/or interactions are possible to explain the different ac magnetic properties that are observed for these Tp*-containing U(III) complexes. Dipolar interactions are likely not affecting the relaxation times in any of these complexes based on closest contact U···U intermolecular distances and the lack of H-bonding and π-stacking pathways (Table A12.1).[37, 39] Further, no clear trend is apparent for average U···B distances of these complexes (Table A12.1). Charge density also doesn't appear to be a major factor as no obvious trend is observable when comparing salts and neutral complexes. These species seem relatively unperturbed by coordination number since ligation to one or two ancillary groups does not show an obvious trend for these $(Tp^*)_2U$ fragments. Crystal field effects are possible, but a simple analysis of the nephelauxetic series suggests that $[(Tp^*)_2U(I)]$ and $[(Tp^*)_2U(CCPh)]$ should show similar properties, which is not experimentally observed.[40] Further, it is likely difficult to extract accurate Racah parameter (β) values from electronic absorption data for these species, making this analysis ambiguous. An alternative approach to determine crystal field parameters is fitting magnetic susceptibility data, which was recently introduced by Chilton and Liddle.[30] These fits indicate no clear trend between the dynamic magnetic properties of these U(III) complexes and the parameters g_J, orbital reduction (k) or axial anisotropy tensor (D); however, the spin-orbit coupling (B^0_2) term indicates that $[((Tp^*)_2U)_2$-*p*-DEB] experiences the largest energy gap between the ground and first excited state when compared to all other complexes in this study. In fact,

when these fits are applied to other literature pyrazolylborate-U(III) species, the trend remains. Maybe more importantly, the B^0_2 values acquired from these fits for [$(Tp^*)_2U(I)$], [$(Tp^*)_2U(bpy)$](I) and [$U(BPz_2H_2)_3$] are in qualitative agreement with computations performed using the SO-CASPT2 method, justifying the validity of these fits.[37]

These results indicate that excited state contributions, specifically the energy gap between the ground and first excited state dictate dynamic magnetic properties in U(III) complexes. There is also a decent correlation that increased excited state mixing (smaller B^0_2 values) extends the relaxation lifetimes (τ_0) as well. A decrease in the excited state mixing for [$((Tp^*)_2U)_2$-*p*-DEB] increases quantum tunneling of magnetization and decreases the relaxation lifetime. Little to no apparent dipolar quenching of the slow magnetic relaxation is observed. These results give an alternative option for maximizing dynamic magnetic properties in U(III) complexes.[41] Of note, this trend is the opposite for lanthanide counterparts, as isolation of a pure ground state enhances dynamic magnetic properties.[42] However, excited state mixing is a preferable property for transition metal SMMs,[43] suggestive that future design of actinide SMMs should align more with *d* electron analogues.

References

1. Rinehart, J. D.; Long, J. R. *Chem. Sci.* **2011**, *2*, 2078.

2. Bogani, L.; Wernsdorfer, W. *Nat. Mater.* **2008**, *7*, 179.

3. Kindra, D. R.; Evans, W. J. *Chem. Rev.* **2014**, *114*, 8865.

4. Rinehart, J. D.; Harris, T. D.; Kozimor, S. A.; Bartlett, B. M.; Long, J. R. *Inorg. Chem.* **2009**, *48*, 3382.

5. Newell, B. S.; Rappé, A. K.; Shores, M. P. *Inorg. Chem.* **2010**, *49*, 1595.

6. Chilton, N. F.; Anderson, R. P.; Turner, L. D.; Soncini, A.; Murray, K. S. *J. Comput. Chem.* **2013**, *34*, 1164.

7. Bain, G. A.; Berry, J. F. *J. Chem. Educ.* **2008**, *85*, 532.

8. Lewis, A. J.; Williams, U. J.; Carroll, P. J.; Schelter, E. J. *Inorg. Chem.* **2013**, *52*, 7326.

9. Fortier, S.; Melot, B. C.; Wu, G.; Hayton, T. W. *J. Am. Chem. Soc.* **2009**, *131*, 15512.

10. Fortier, S.; Brown, J. L.; Kalsoyannis, N.; Wu, G.; Hayton, T. W. *Inorg. Chem.* **2012**, *51*, 1625.

11. Fortier, S.; Melot, B. C.; Wu, G.; Hayton, T. W. *J. Am. Chem. Soc.* **2009**, *131*, 15512.

12. Almond, P. M.; Deakin, L.; Porter, M. J.; Mar, A.; Albrecht-Schmitt, T. E. *Chem. Mater.* **2000**, *12*, 3208.

13. Kiplinger, J. L.; Pool, J. A.; Schelter, E. J.; Thompson, J. D.; Scott, B. L.; Morris, D. E. *Angew. Chem. Int. Ed.* **2006**, *45*, 2036.

14. Schelter, E. J.; Morris, D. E.; Scott, B. L.; Thompson, J. D.; Kiplinger, J. L. *Inorg. Chem.* **2007**, *46*, 5528.

15. Lin, H.-J.; Siretanu, D.; Dickie, D. A.; Subedi, D.; Scepaniak, J. J.; Mitcov, D.; Clérac, R.; Smith, J. M. *J. Am. Chem. Soc.* **2014**, *136*, 13326-13332.

16. Cook, L. J. K.; Kulmaczewski, R.; Mohammed, R.; Dudley, S.; Barrett, S. A.; Little, M. A.; Deeth, R. J.; Halcrow, M. A. *Angew. Chem. Int. Ed.* **2016**, *55*, 4327-4331.

17. Kiernicki, J. J.; Newell, B. S.; Matson, E. M.; Anderson, N. H.; Fanwick, P. E.; Shores, M. P.; Bart, S. *Inorg. Chem.* **2014**, *53*, 3730.

18. Castro-Rodriguez, I.; Meyer, K. *Chem. Commun.* **2006**, 1353.

19. Schelter, E. J.; Veauthier, J. M.; Graves, C. R.; John, K. D.; Scott, B. L.; Thompson, J. D.; Pool-Davis-Tournear, J. A.; Morris, D. E.; Kiplinger, J. L. *Chem. Eur. J.* **2008**, *14*, 7782.

20. Jilke, R. E.; Spencer, L. P.; Kuiper, D. L.; Scott, B. L.; Williams, U. J.; Kikkawa, J. M.; Schelter, E. J.; Boncella, J. M. *Inorg. Chem.* **2011**, *50*, 4235.

21. Lam, O. P.; Feng, P. L.; Heinemann, F. W.; O'Connor, J. M.; Meyer, K. *J. Am. Chem. Soc.* **2008**, *130*, 2806.

22. Lam, O. P.; Anthon, C.; Heinemann, F. W.; O'Connor, J. M.; Meyer, K. *J. Am. Chem. Soc.* **2008**, *130*, 6567.

23. Castro-Rodriguez, I.; Nakai, H.; Zakharov, L. N.; Rheingold, A. L.; Meyer, K. *Science* **2004**, *305*, 1757.

24. Anderson, N. H.; Odoh, S. O.; Yao, Y. Y.; Williams, U. J.; Schaefer, B. A.; Kiernicki, J. J.; Lewis, A. J.; Goshert, M. D.; Fanwick, P. E.; Schelter, E. J.; Walensky, J. R.; Gagliardi, L.; Bart, S. C. *Nat. Chem.* **2014**, *6*, 919.

25. Fortier, S.; Walensky, J. R.; Wu, G.; Hayton, T. W. *J. Am. Chem. Soc.* **2011**, *133*, 11732.

26. Seaman, L. A.; Fortier, S.; Wu, G.; Hayton, T. W. *Inorg. Chem.* **2011**, *50*, 636.

27. Dugan, T. R.; Bill, E.; MacLeod, K. C.; Christian, G. J.; Cowley, R. E.; Brennessel, W. W.; Ye, S. F.; Neese, F.; Holland, P. L. *J. Am. Chem. Soc.* **2012**, *134*, 636.

28. Wong, J. L.; Higgins, R. F.; Bhowmick, I.; Cao, D. X.; Szigethy, G.; Ziller, J. W.; Shores, M. P.; Heyduk, A. F. *Chem. Sci.* **2016**, *7*, 1594.

29. Rosen, R. K.; Andersen, R. A.; Edelstein, N. M. *J. Am. Chem. Soc.* **1990**, *112*, 4588.

30. Gardner, B. M.; King, D. M.; Tuna, F.; Wooles, A. J.; Chilton, N. F.; Liddle, S. T. *Chem. Sci.* **2017**, *8*, 6207.

31. Gardner, B. M.; King, D. M.; Tuna, F.; Wooles, A. J.; Chilton, N. F.; Liddle, S. T. *Chem. Sci.* **2017**, *8*, 6207.

32. King, D. M.; Cleaves, P. A.; Wooles, A. J.; Gardner, B. M.; Chilton, N. F.; Tuna, F.; Lewis, W.; McInnes, E. J. L.; Liddle, S. T. *Nat. Commun.* **2016**, 7.

33. Moro, F.; Mills, D. P.; Liddle, S. T.; van Slageren, J. *Angew. Chem. Int. Ed.* **2013**, *52*, 3430.

34. Milles, D. P.; Moro, F.; McMaster, J.; van Slageren, J.; Lewis, W.; Blake, A. J.; Liddle, S. T. *Nat. Chem.* **2011**, *3*, 454.

35. Rinehart, J. D.; Long, J. R. *J. Am. Chem. Soc.* **2009**, *131*, 12558.

36. Antunes, M. A.; Pereira, L. C. J.; Santos, I. C.; Mazzanti, M.; Marçalo, J.; Almeida, M. *Inorg. Chem.* **2011**, *50*, 9915.

37. Coutinho, J. T.; Antunes, M. A.; Pereira, L. C. J.; Bolvin, H.; Marçalo, J.; Mazzanti, M.; Almeida, M. *Dalton Trans.* **2012**, *41*, 13568.

38. Rinehart, J. D.; Meihaus, K. R.; Long, J. R. *J. Am. Chem. Soc.* **2010**, *132*, 7572.

39. Sun, Y. M.; McDonald, R.; Takats, J.; Day, V. W.; Eberspacher, T. A. *Inorg. Chem.* **1994**, *33*, 4433.

40. Figgis, B. N.; Hitchman, M. A., *Ligand field theory and its applications*. Wiley-VCH: New York, **2000**.

41. Meihaus, K. R.; Long, J. R. *Dalton Trans.* **2015**, *44*, 2517.

42. Layfield, R. A. *Organometallics* **2014**, *33*, 1084.

43. Frost, J. M.; Harriman, K. L. M.; Murugesu, M. *Chem. Sci.* **2016**, *7*, 2470.

Chapter 13: Interesting observations and future implications for small molecule Cr-photocatalysis

13.1 Conclusions for Cr-photocatalysis investigations

The results presented in Chapters 2-8 bear great significance for a few different reasons. Firstly, the difference in reactivity of *trans*-anethole and 4-methoxychalcone under Cr-photocatalysis conditions (electron vs. energy transfer) is of interest to the field of organic chemistry. Such a small structural change that causes such a large change in the mechanistic landscape of the reactivity is quite uncommon and bears great significance. Further, the association of substrates to $[Cr(Ph_2phen)_3]^{3+}$, which affects reactivity (photocatalysis *vs.* photoinitiation) opens new questions for perceived outer-sphere electron-transfer reactions in general. Finally, the unique dual reactivity of $[Cr(Ph_2phen)_3]^{3+}$ (electron and energy transfer) based on substrate identity is a unique way to control organic reactivity. Even with the multitude of useful chemistry that $[Cr(Ph_2phen)_3]^{3+}$ can perform, there are remaining and outstanding questions about some of its reactivity in general. As an example, it is quite large for a single molecule and makes computational data acquisition slower and more expensive. To successfully screen large amounts of potentially interesting Cr^{3+} complexes, it is important to find a smaller complex that shows similar properties. This is also important so that we can validate the calculations are giving us accurate data.

13.2 Association of $[(phenda)_2CrCl_2]Cl$ and *trans*-anethole

Performed with Cassandra Mason, Ellery Rourke and Anthony K. Rappé at CSU.

To investigate whether smaller Cr^{3+} species show a similar association as $[Cr(Ph_2phen)_3]^{3+}$ does to *trans*-anethole and 4-methoxychalcone, we screened numerous complexes. $[Cr(acac)_3]$ (acac = acetylacetonate) and $[Cr(pic)_3]$ (pic = picolinate) fail to show any data consistent with association to either *trans*-anethole or 4-methoxychalcone. Interestingly, the complex $[(phenda)_2CrCl_2]Cl$[1] (phenda = *o*-phenylenediamine) shows data consistent with association when

trans-anethole is added to solution (Figure 13.2.1). These data show peak shifts in the upfield (more shielded) direction, which is consistent with π-interactions.[2] We hypothesize that this species preferably associates with *trans*-anethole because the chromium species is cationic and has the most extended π-system compared to the other small Cr-complexes we investigated.

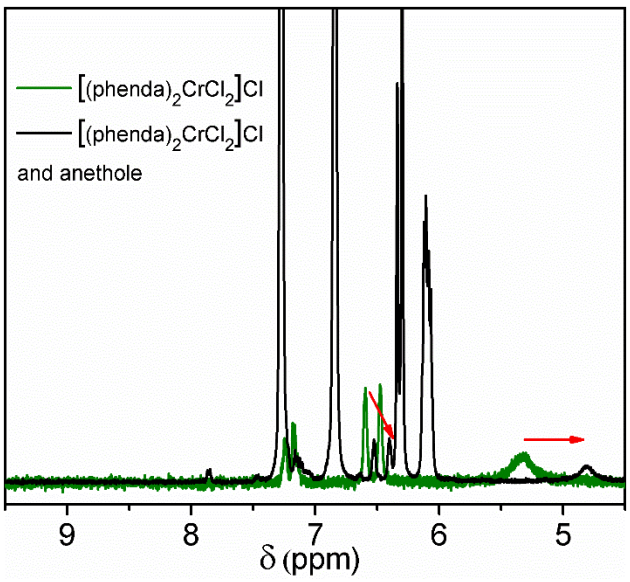


Figure 13.2.1. ^{1}H NMR of [(phenda)$_2$CrCl$_2$]Cl (0.005 M) in (CD$_3$)$_2$SO before and after addition of trans-anethole (0.10 M).

From this initial positive result, we performed a titration study at 25 °C to obtain an association constant (K_{assoc}), which gave a value of K_{assoc} = 244(4) M^{-1} considering a bimolecular process. This value is comparable to a previous report by Corey and others performing dihydroxylations of alkenes using a templated osmium catalyst.[3] More importantly, variable temperature studies of this complex allow us to obtain other thermodynamic values including entropies and enthalpies. These are important as computational methods cannot accurately model entropy values; in addition, entropy values vary drastically and are rarely discussed when describing intermolecular interactions. Performing a temperature dependent study and applying

a Van't Hoff analysis, these thermodynamic parameters were gathered for the association of $[(phenda)_2CrCl_2]Cl$ and *trans*-anethole: ΔH = -12.2(9) kcal mol^{-1} and ΔS = -30.6(21) cal mol^{-1} K^{-1} (Figure 13.2.2).

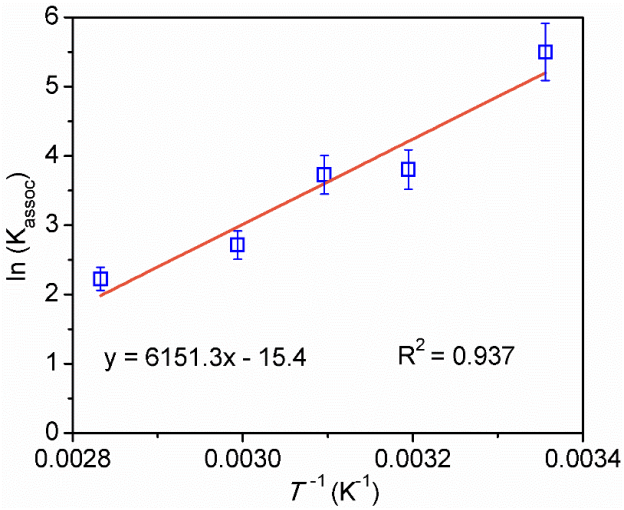


Figure 13.2.2. Van't Hoff plot for the association of $[(phenda)_2CrCl_2]Cl$ and trans-anethole in $(CD_3)_2SO$ where the slope = $\Delta H/R$ and the x-intercept = $-\Delta S/R$ (R = gas constant).

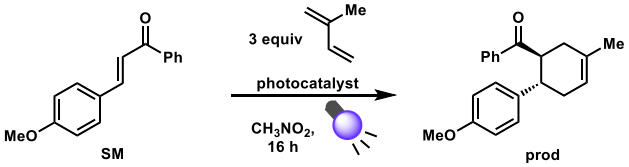
These values compare favorably to a previous study by the Moore group for the self-association of macrocyclic alkynyl-tethered ring systems (ΔH < -5.6(3) kcal mol^{-1} and ΔS < -13.6(10) cal mol^{-1} K^{-1}).[2] More importantly, the experimental thermodynamic values show great agreement to the computational values (ΔH = -11.8 kcal mol^{-1} and ΔS = -40.2 cal mol^{-1} K^{-1}), which were determined through an APFD functional and a 6-311+g* basis set in an acetonitrile solvent. This is enormously important as experimental and computational agreement is necessary for continued progress in this field, as there are only two reported studies with similar computational and experimental agreement.[4-5]

While these results are interesting and add to our growing knowledge about the roles of Cr^{3+} in photocatalytic systems, there are a few additional details that are required before publication is reasonable for these results. Firstly, the NMR data were collected in DMSO, but the calculations were performed in an acetonitrile solvent. Unfortunately, $[(phenda)_2CrCl_2]Cl$ is insoluble in acetonitrile, so it is reasonable for the calculations to also be performed in a DMSO solvent. This is also important since the DMSO molecules could be displacing the chloride anions, giving a different Cr-species. We prepared $[(phenda)_2Cr(OTf)_2]OTf$ in an effort to increase the solubility of the Cr-species; however, this species did not display data consistent with association when it was in solution (both DMSO and acetonitrile) when *trans*-anethole is added. In addition, performing a Van't Hoff analysis of the association between $[Cr(Ph2phen)_3]^{3+}$ and *trans*-anethole would be beneficial to support these analyses as being accurate, instead of just self-consistent for one system.

13.3 Photoreactivity of $[Cr(pic)_3]$

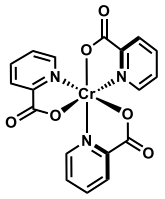
Even though $[Cr(pic)_3]$ does not show association with *trans*-anethole or 4-methoxychalcone, we are still motivated to test its photoreactivity. The complex, $[Cr(pic)_3]$, is an additive found in vitamin tablets that can be purchased over-the-counter.[6] Performing photocatalysis with a vitamin purchased at a pharmacy is not only an inherently valuable teaching tool, but it also is important as it highlights the expansive nature of this reactivity. The electrochemical data indicate that $[Cr(pic)_3]$ should be unable to perform almost any photoredox chemsitry.[7-8] Indeed, for a well-studied oxidative process of a [4+2] cycloaddition between *trans*-anethole and isoprene, no reactivity is observed when $[Cr(pic)_3]$ is added. Conversely, when $[Cr(pic)_3]$ is added to 4-methoxychalcone and isoprene, [2+2] and [4+2] reactivity is observed (Figure 13.3.1). Since this is likely not proceeding through an oxidative electron-transfer process from an excited-state of $[Cr(pic)_3]$ (Figure 13.3.1, entry 6), it is more likely that the reaction proceeds through excited-state 4-methoxychalcone performing electron-transfer or through a different energy-transfer process.

Nevertheless, productive reactivity is observed with [$Cr(pic)_3$] that is greater than background photoreactivity between 4-methoxychalcone and isoprene. Future work detailing this reaction that would be beneficial involves distinguishing between the two most likely aforementioned mechanistic pathways to obtain the [4+2] product. Some different aims to probe this outstanding and unanswered question could be using substituted picolinate ligands. The redox couple that is likely involved if an electron-transfer is present is the $Cr^{3+/2+}$ reduction (although it is likely the chromium ion stays as Cr^{3+} and one of the ligand is mono-reduced). This redox couple could be shifted more anodic (oxidizing) with additional electron-withdrawing groups being substituted onto the ligand. The opposite trend could occur to shift the redox couple more cathodic (reducing), with substituents that are electron-donating in character. The goal here would be to see the possible differences in reactivity which could in turn indicate whether the redox-potential for [$Cr(pic)_3$] is involved in this reactivity. If it does, it is likely through excited-state 4-methoxychalcone being oxidized as opposed to energy-transfer reactivity.

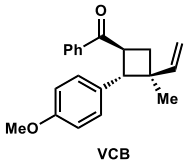


entry	catalyst loading	light source	VCB conversion (%)	prod conversion (%)
1	5 mol%	NUV + 23 W CFL	16	79
2	1 mol%	23 W CFL	68	14
3	1 mol%	NUV + 23 W CFL	69	23
4	0.5 mol%	23 W CFL	77	15
5	0.5 mol%	NUV + 23 W CFL	37	11
6	5 mol%	530 nm[a]	0	0
7	2 mol%	NUV + 23 W CFL	47	53
8[b]	5 mol%	NUV + 23 W CFL	60	0

[a]performed as a single wavelength experiment. [b]The reaction mixture was sparged for 15 minutes with N_2 before the reaction mixture was irradiated.



photocatalyst



VCB

Figure 13.3.1 Optimization and control experiments for the [2+2]/[4+2] reaction sequence of 4-methoxychalcone and isoprene using [Cr(pic)$_3$].

References

1. Redshaw, C.; Wilkinson, G.; Hussainbates, B.; Hursthouse, M. B. *J. Chem. Soc., Dalton Trans.* **1992**, 1803-1811.

2. Shetty, A. S.; Zhang, J. S.; Moore, J. S. *J. Am. Chem. Soc.* **1996,** *118*, 1019-1027.

3. Corey, E. J.; Noe, M. C. *J. Am. Chem. Soc.* **1996,** *118*, 319-329.

4. Mammen, M.; Shakhnovich, E. I.; Deutch, J. M.; Whitesides, G. M. *J. Org. Chem.* **1998,** *63*, 3821-3830.

5. Plata, R. E.; Singleton, D. A. *J. Am. Chem. Soc.* **2015,** *137*, 3811-3826.

6. Barton, D.; Nakanishi, K. j.; Meth-Cohn, O., *Comprehensive natural products chemistry*. 1st ed.; Elsevier: Amsterdam; New York, 1999.

7. Stearns, D. M.; Armstrong, W. H. *Inorg. Chem.* **1992,** *31*, 5178-5184.

8. Liu, B.; Liu, Y. F.; Chai, J.; Hu, X. Q.; Wu, D. M.; Yang, B. S. *J. Inorg. Biochem.* **2016,** *164*, 110-118.

Appendix 1: Supporting information for chapter 2

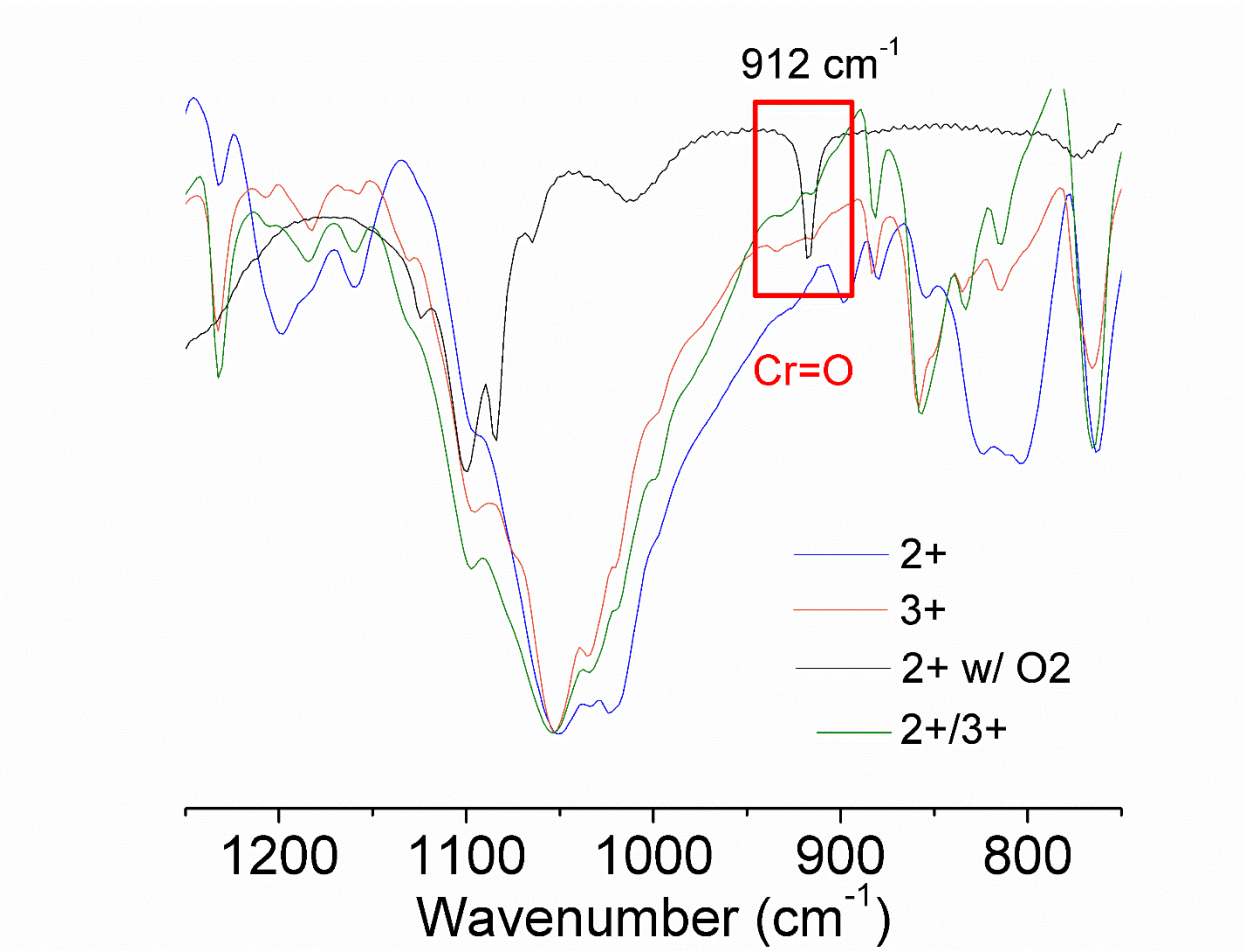


*Figure A1.1. IR spectra of **2.1** (blue trace), **2.2** (orange trace), **2.1** after exposure to O_2 (black trace) and **2.1** and **2.2** in degassed CH_3NO_2 irradiated for 20 minutes and then exposed to air for 30 minutes (green trace). The black trace was gathered after a solution of **2.1** in CH_3CN had O_2 bubbled through for 10 seconds. The green trace was exposed to air via a needle air outlet and the solvent was removed before the IR was gathered.*

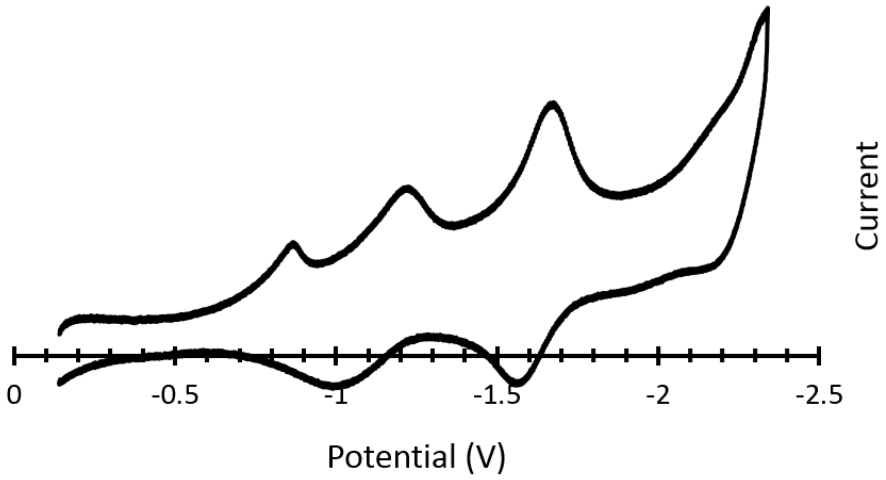


*Figure A1.2. CVs of **2.2** in a 0.1 M dichloromethane solution of Bu_4NPF_6 referenced to Fc^+/Fc. The scans were all started at the rest potential of the cell (-0.1412 V) and swept cathodically.*

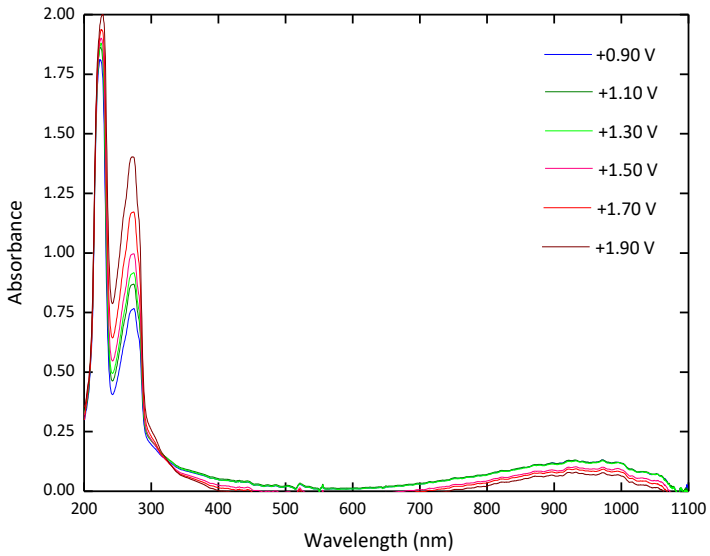


Figure A1.3. Spectro-electrochemical oxidation of 4'-methoxy-2,4-dimethyl-1,2,3,6-tetrahydro-1,1'-biphenyl in CH_3CN (0.1 M Bu_4NPF_6) where all potentials are referenced vs. Fc^+/Fc.

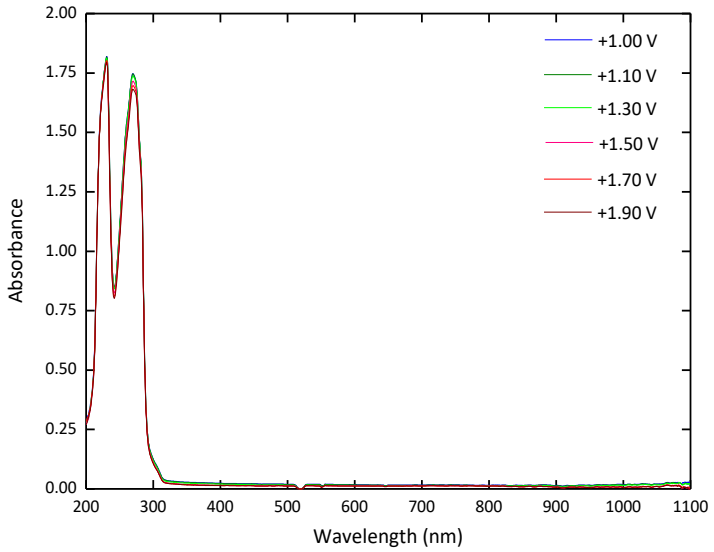


Figure A1.4. Spectro-electrochemical oxidation of 4'-methoxy-2,4-dimethyl-1,2,3,6-tetrahydro-1,1'-biphenyl in CH_3CN (0.1 M Bu_4NPF_6) after exposure to O_2 where all potentials are referenced vs. Fc^+/Fc.

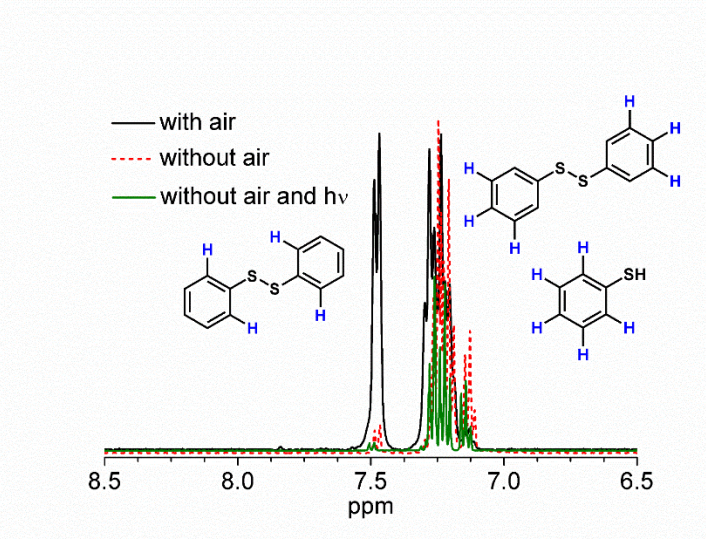


*Figure A1.5. Aromatic region of ^1H NMR spectra of experiments where thiophenol spiked into a solution of 3:1 (mol %) **2.1**:**2.2** exposed to air (black trace) and a solution of **2.2** air-free (red trace) after 30 minutes of irradiation (419, 350 and 300 nm sources) and a solution of **2.1**:**2.3***

kept air and light free (green trace). The spectra were referenced to $CDCl_3$. The blue protons are represent the peaks of interest for both diphenyl disulfide and thiophenol. The green trace gave integrations showing less than 2% conversion to diphenyl disulfide.

Appendix 2: Supporting information for chapter 3

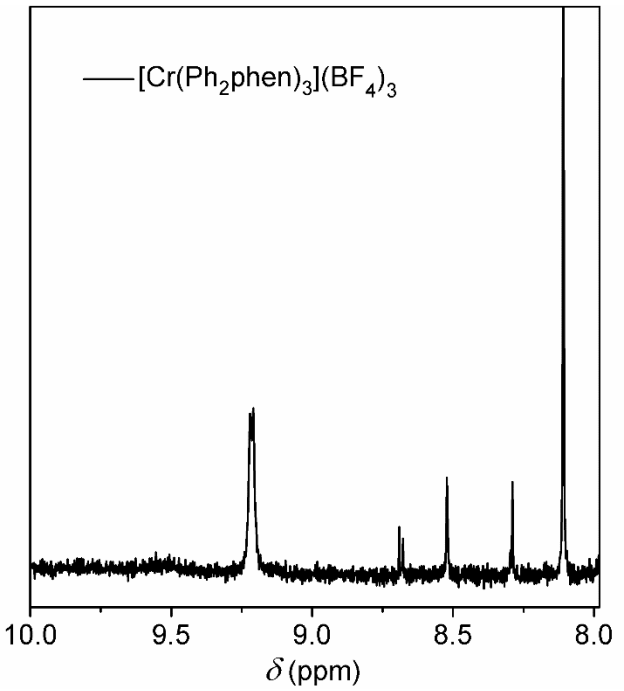


Figure A2.1. ^{1}H NMR spectra of $[Cr(Ph_2phen)_3](BF_4)_3$ (0.001 M) in CD_3NO_2.

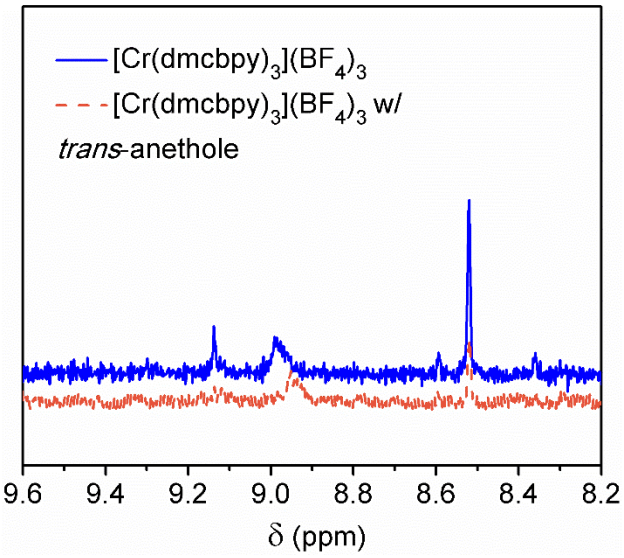


Figure A2.2. ^{1}H NMR spectra of $[Cr(dmcbpy)_3](BF_4)_3$ (0.001 M) in CD_3NO_2 with and without trans-anethole (0.10 M) added.

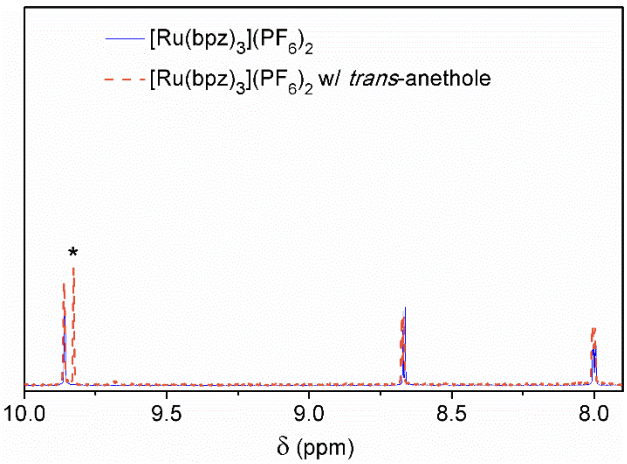


Figure A2.3. ^{1}H NMR spectra of $[Ru(bpz)_3](PF_6)_2$ (0.001 M) in CD_3NO_2 with and without trans-anethole (0.10 M) added. The peak present at ~9.9 ppm is a small amount of anisaldehyde impurity from the oxidation of trans-anethole.

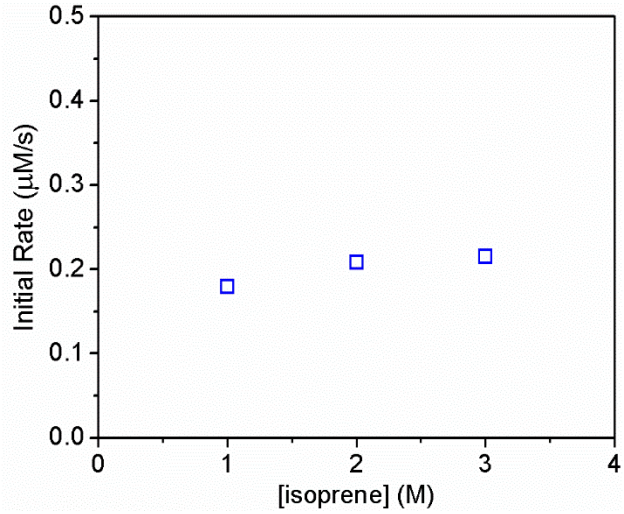


Figure A2.4. Isoprene concentration dependence on the rate constant under otherwise standard conditions.

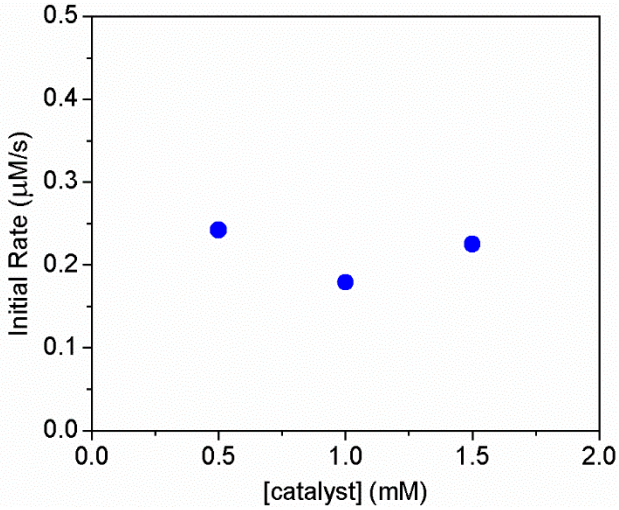


Figure A2.5. $[Cr(Ph_2phen)_3](BF_4)_3$ concentration dependence on the rate constant under otherwise standard conditions.

Appendix 3: Supporting information for chapter 5

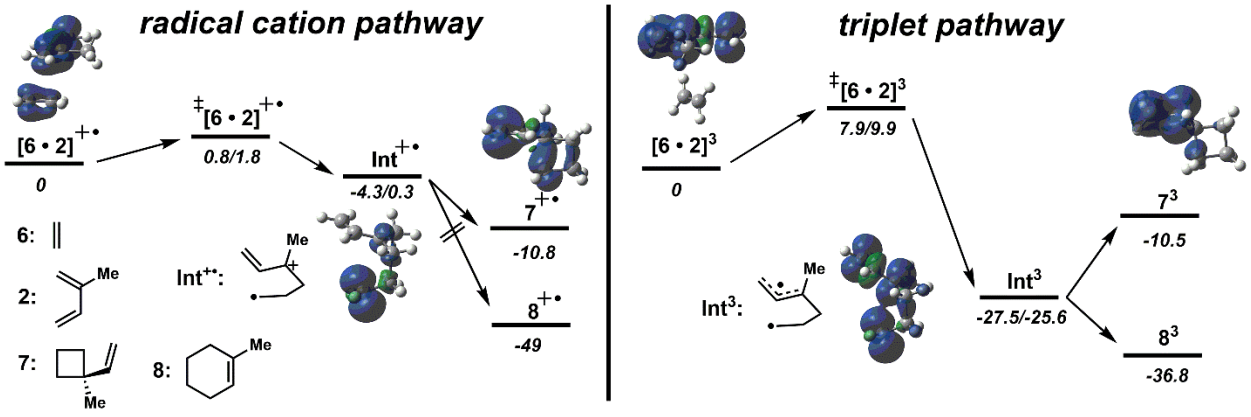


Figure A3.1. Computed reaction pathways for [2+2] and [4+2] reactions between ethylene and isoprene for radical cation (left) and triplet (right) pathways. The images are spin density plots.

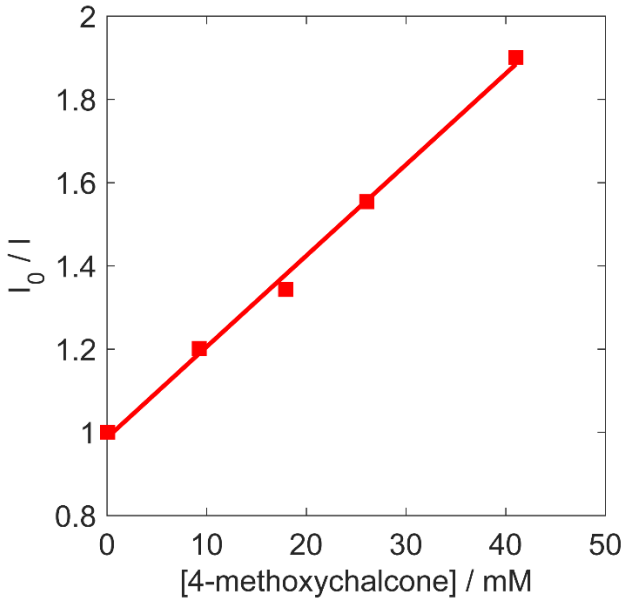


Figure A3.1. Steady-state emission quenching of [Cr(Ph2phen)3]3+ by 4-methoxychalcone in nitromethane (λex = 450 nm) where a quenching rate constant of kq = 1 × 106 M-1 s-1 is determined, within error of the value determined in the time-resolved experiment.

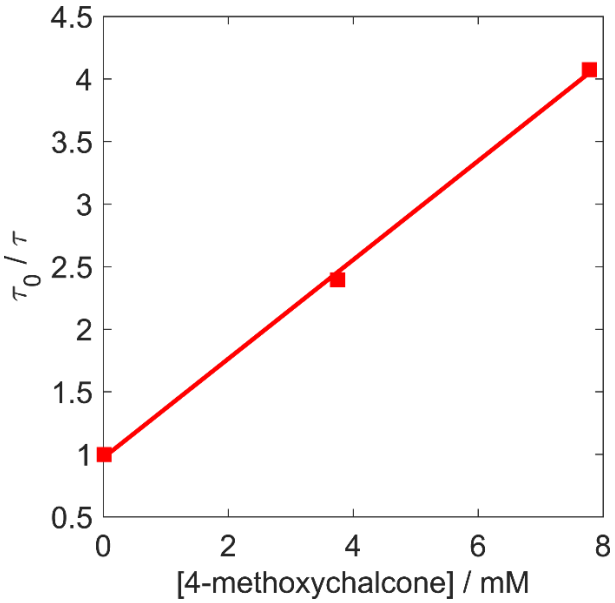


Figure A3.2. Time resolved emission quenching of $[Cr(Ph_2phen)_3]^{3+}$ by 4-methoxychalcone in nitromethane (λ_{ex} = 450 nm) under inert conditions. A quenching rate constant of $k_q = 2 \times 10^6$ M^{-1} s^{-1} is determined.

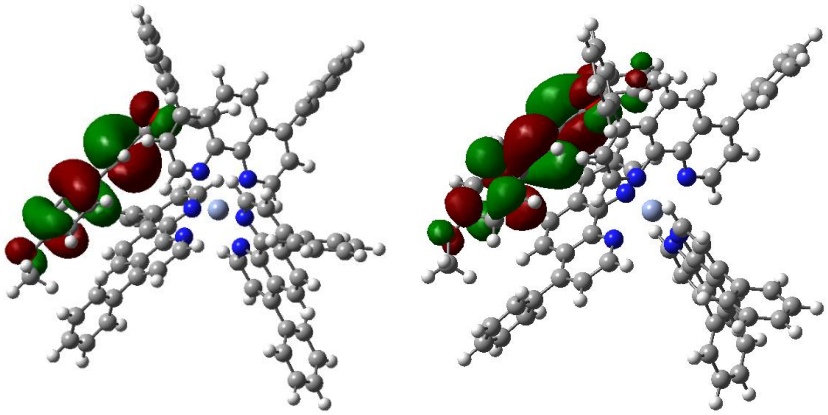


Figure A3.3. Natural transition orbitals for the lowest quartet excited state for the association complex of $[Cr(Ph_2phen)_3]^{3+}$•4-methoxychalcone.

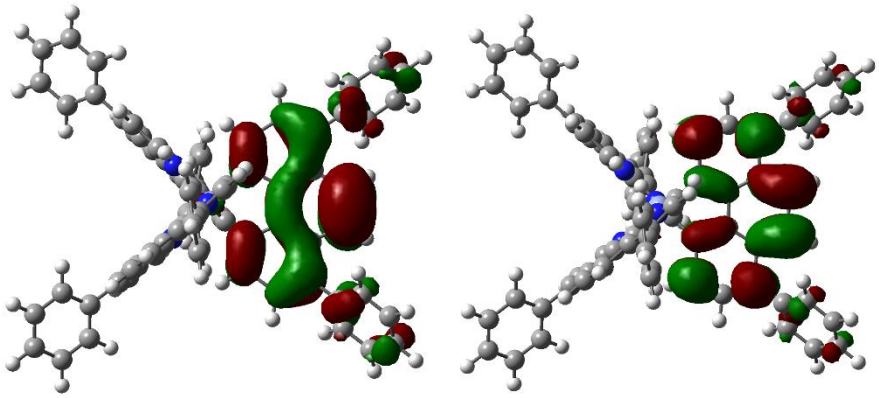


Figure A3.4. Natural transition orbitals for the transition of the alpha orbital to the lowest unoccupied orbital for $[Cr(Ph_2phen)_3]^{3+}$.

Table A3.1. Computed vertical and adiabatic excitation and ionization energies (eV) for dienes and dienophiles.

	T virt	T adia	relax	IP virt	IP adia	relax
ethylene	4.336	2.686	1.650	7.79	7.62	0.17
isoprene trans	3.240	2.289	0.951	6.53	6.37	0.16
isoprene cis	3.475	2.207	1.268	6.60	6.30	0.30
dimethylbutadiene	3.283	2.558	0.725	6.48	6.33	0.15
cyclopentadiene	3.147	2.418	0.729	6.22	6.04	0.18
cyclohexadiene	2.869	2.122	0.748	6.01	5.77	0.23
n-pent-isoprene	3.131	2.274	0.856	6.19	6.00	0.19
trans-anethole	3.163	2.278	0.885	5.77	5.57	0.20
cis-anethole	3.456	2.198	1.258	5.90	5.66	0.24
ortho-trans-anethole	3.272	2.241	1.031	5.95	5.71	0.24
trans-anethole-Ome	3.220	2.607	0.613	6.18	6.02	0.17
Nitro-anethole	2.335	2.058	0.277	6.46	6.32	0.15
Acetyl-anethole	2.584	2.194	0.390	6.18	6.01	0.17
4MeO-chalcone	2.601	2.096	0.505	6.22	6.03	0.19
tbutyl-chalcone	2.620	2.096	0.524	6.20	6.01	0.19
chex-"chalcone"	2.634	2.039	0.595	6.18	6.02	0.17
chalcone-Ome	2.770	2.060	0.710	6.73	6.53	0.20
anethole ethyl ester	2.757	2.208	0.549	6.19	6.02	0.17

Table A3.2. Computed vertical and adiabatic total energies for ground state, triplet excited state, cation, and anions (Hartree) for nitrogenous ligands.

	neutral	T virt	T adia	Cation Virt	Cation Adiabatic	Anion virt	Anion adia
cis_flat_bipy	-495.0773446	-494.9485516	-494.9685634	-494.8261559	-494.8308469	-495.1532401	-495.1603639
cis_flat_dime_bipy	-573.6667793	-573.5359089	-573.5561224	-573.4188333	-573.423482	-573.7369886	-573.7446862
cis_flat_dimeester_bipy	-950.6129122	-950.4910635	-950.5073355	-950.3523695	-950.3574338	-950.712399	-950.7178308
phenanthroline	-571.2682536	-571.1480254	-571.1660076	-571.0238407	-571.0288825	-571.3430954	-571.3484786
tetrame_phen	-728.4413797	-728.3253523	-728.3423733	-728.2052905	-728.2103797	-728.5151719	-728.5199934
batho_phen	-1033.094412	-1032.978936	-1032.997342	-1032.85719	-1032.863747	-1033.174102	-1033.179751
bpz	-537.13329	-527.00912	-527.020922	-526.86501	-526.87385	-527.23081	-527.23704

Table A3.3. Computed vertical and adiabatic excitation, ionization energies, and electron affinities (eV) for nitrogenous ligands where T, IP and EA stand for triplet, ionization potential and electron affinities, respectively.

cis_flat_bipy	virt T	T adia	relax	IP virt	IP adia	relax	ea virt	ea adia	relax
cis_flat_dime_bipy	3.50	2.96	0.54	6.84	6.71	0.13	2.07	2.26	0.19
cis_flat_dimeester_bipy	3.56	3.01	0.55	6.75	6.62	0.13	1.91	2.12	0.21
phenanthroline	3.32	2.87	0.44	7.09	6.95	0.14	2.71	2.85	0.15
tetrame_phen	3.27	2.78	0.49	6.65	6.51	0.14	2.04	2.18	0.15
batho_phen	3.16	2.69	0.46	6.42	6.29	0.14	2.01	2.14	0.13
bpz	3.38	2.83	0.55	7.30	7.06	0.24	2.65	2.82	0.17

Appendix 4: Supporting information for chapter 6

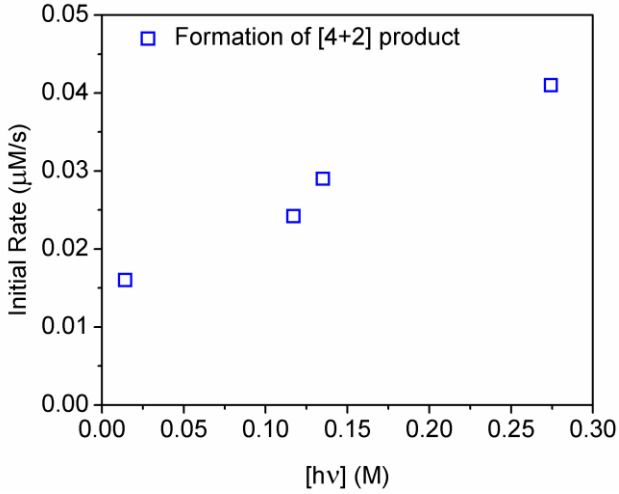


*Figure A4.1. Observed initial rate of formation of **6.6** as a function of photon flux (λ_{ex} = 400 nm).*

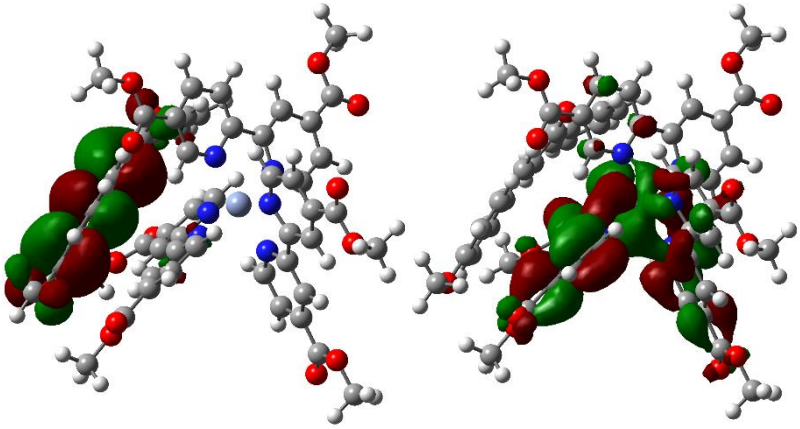


Figure A4.2. Natural transition orbitals for the association complex of $[Cr(dmcbpy)_3]^{3+}$•4-methoxychalcone. Note: These transitions are indicative of electron transfer.

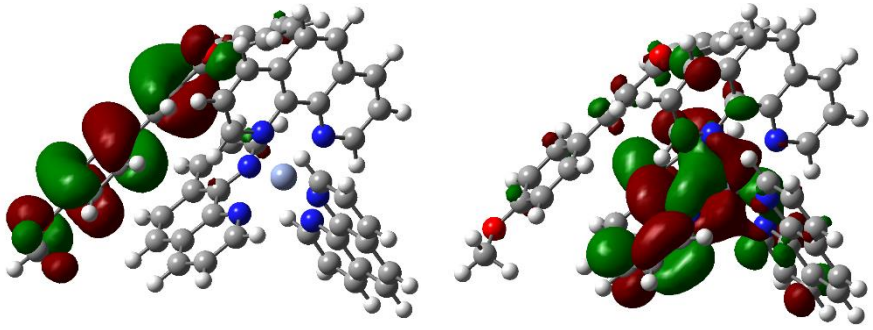


Figure A4.3. Natural transition orbitals for the association complex of $[Cr(phen)_3]^{3+}$•4-methoxychalcone. Note: These transitions are indicative of electron transfer.

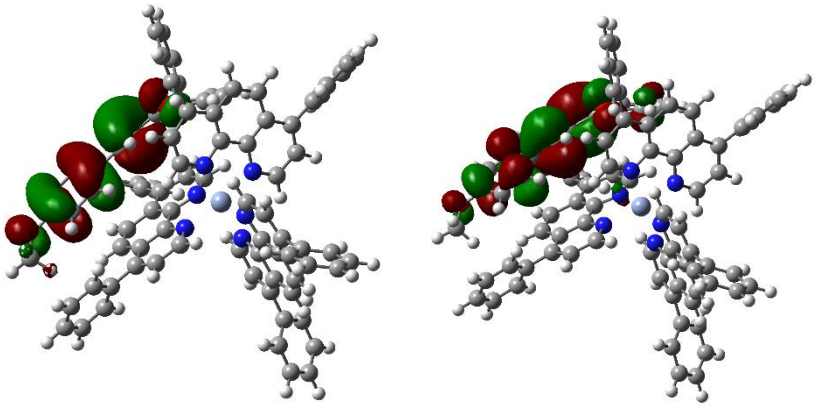


Figure A4.4. α-spin natural transition orbitals for the association complex of $[Cr(Ph_2phen)_3]^{3+}$•4-methoxychalcone. These transitions are the 2nd lowest in energy at 44% occupancy. Note: These transitions are indicative of energy transfer.

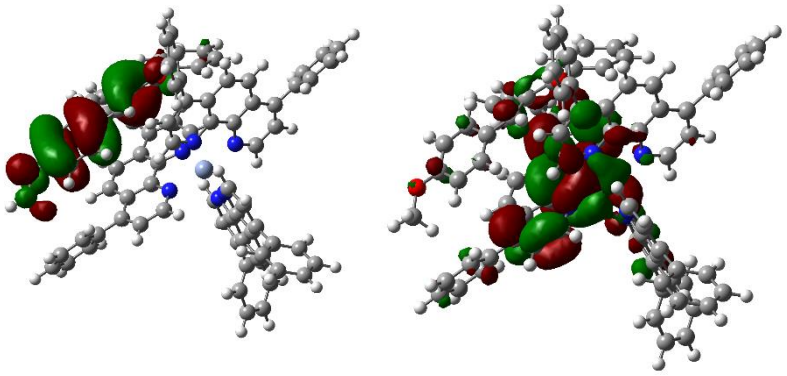


Figure A4.5. β-spin natural transition orbitals for the association complex of $[Cr(Ph_2phen)_3]^{3+}$•4-methoxychalcone. These transitions are the 2nd lowest in energy at 44% occupancy. Note: These transitions are indicative of electron transfer.

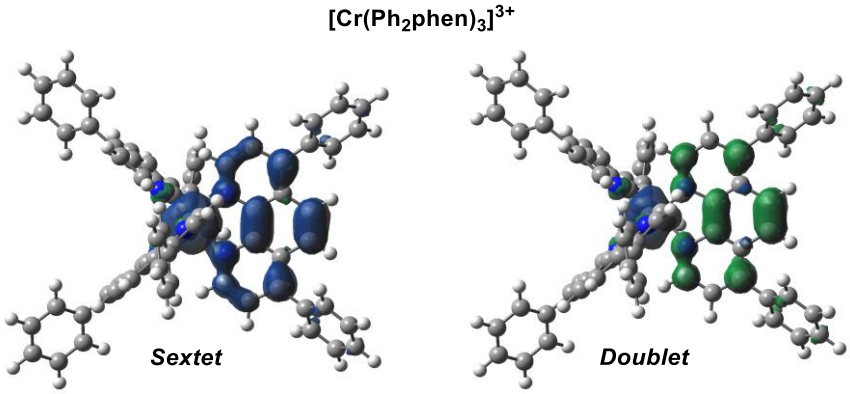


Figure A4.6. Spin density plots of the sextet and doublet determinants of the Heisenberg excited state ladder for $[Cr(Ph_2phen)_3]^{3+}$.

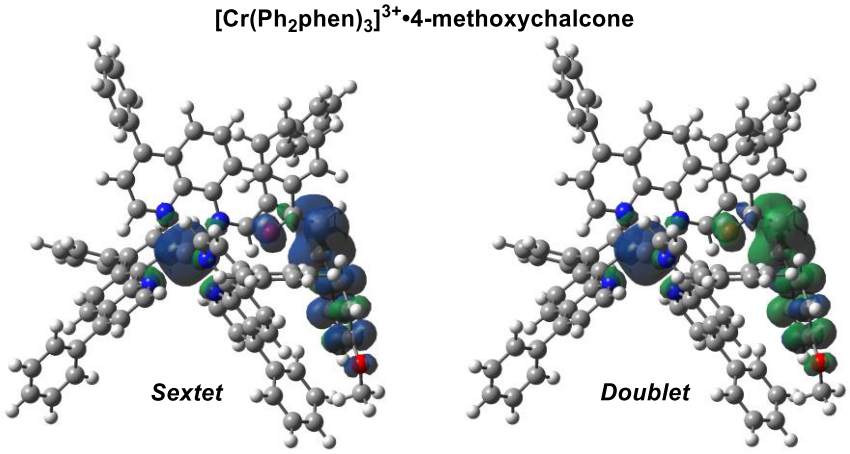


Figure A4.7. Spin density plots of the sextet and doublet determinants of the Heisenberg excited state ladder for the association complex of $[Cr(Ph_2phen)_3]^{3+}$•4-methoxychalcone.

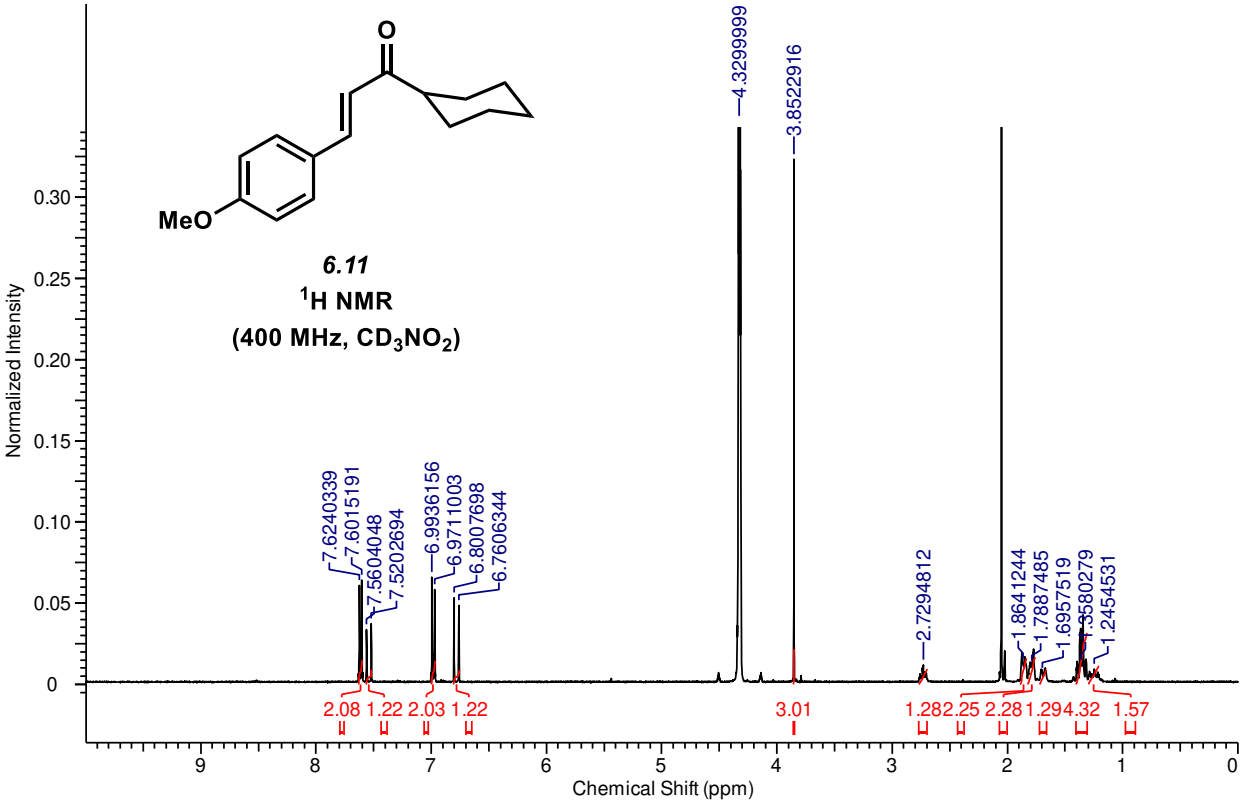


*Figure A4.8. ^1H NMR spectrum of **6.11**.*

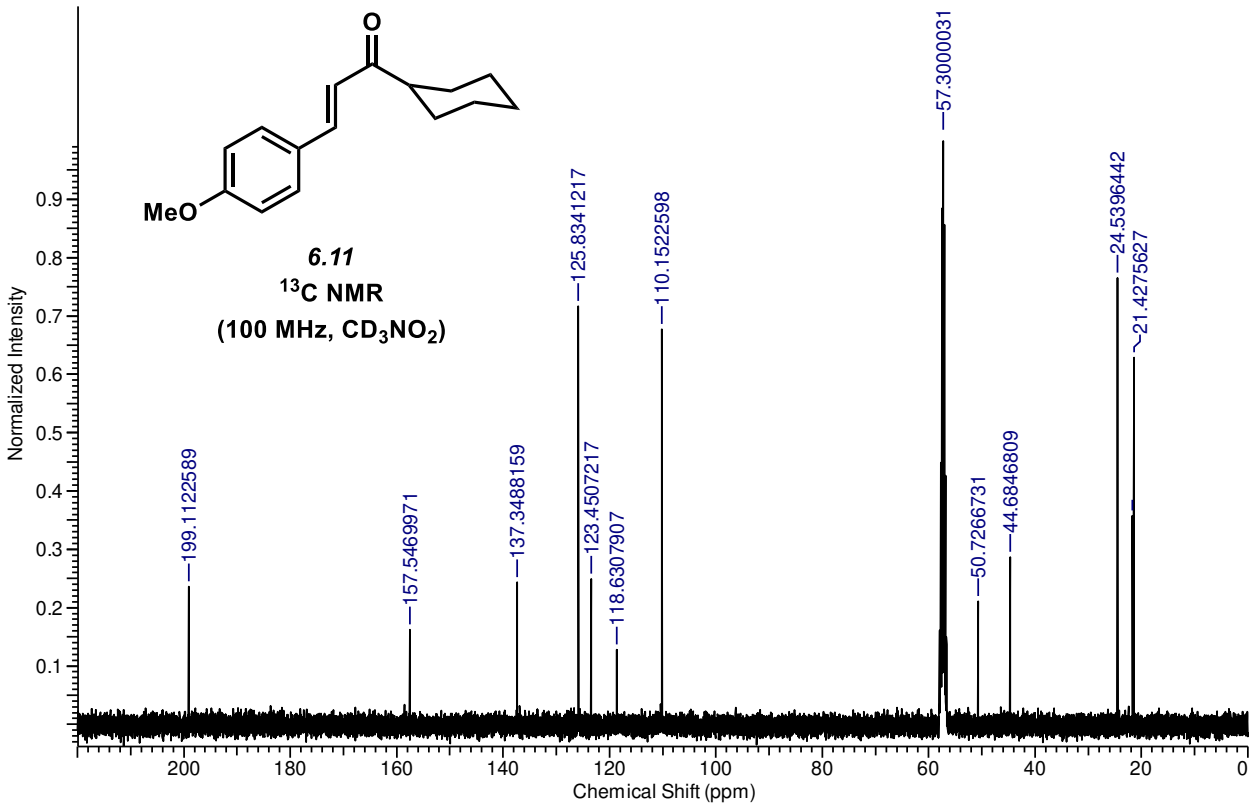


*Figure A4.9. ^{13}C NMR spectrum of **6.11**.*

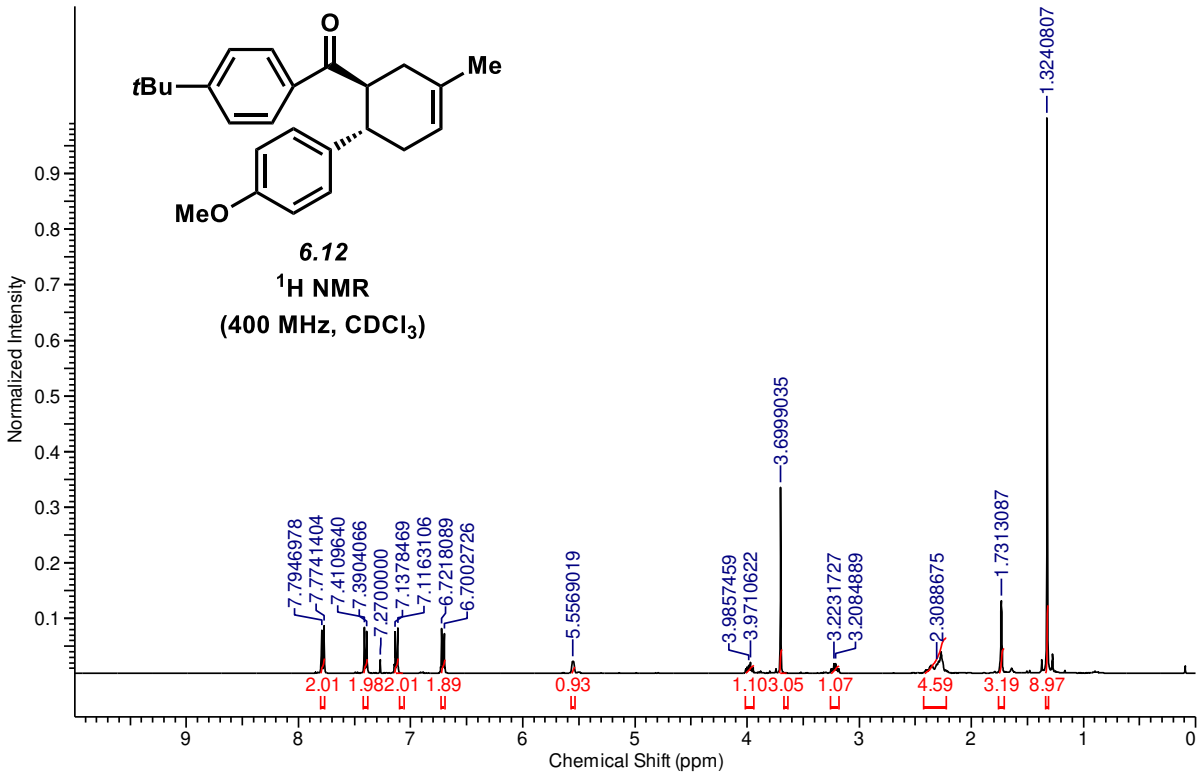


*Figure A4.10. ^{1}H NMR spectrum of **6.12**.*

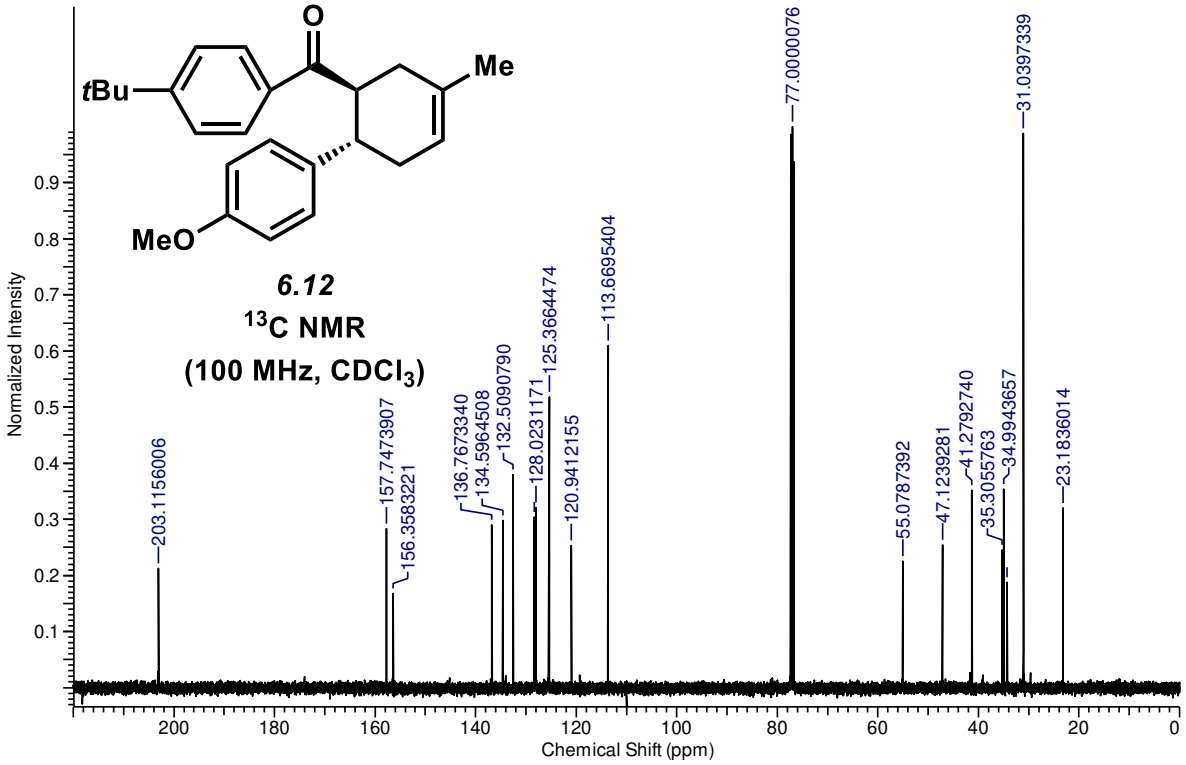


*Figure A4.11. ^{13}C NMR spectrum of **6.12**.*

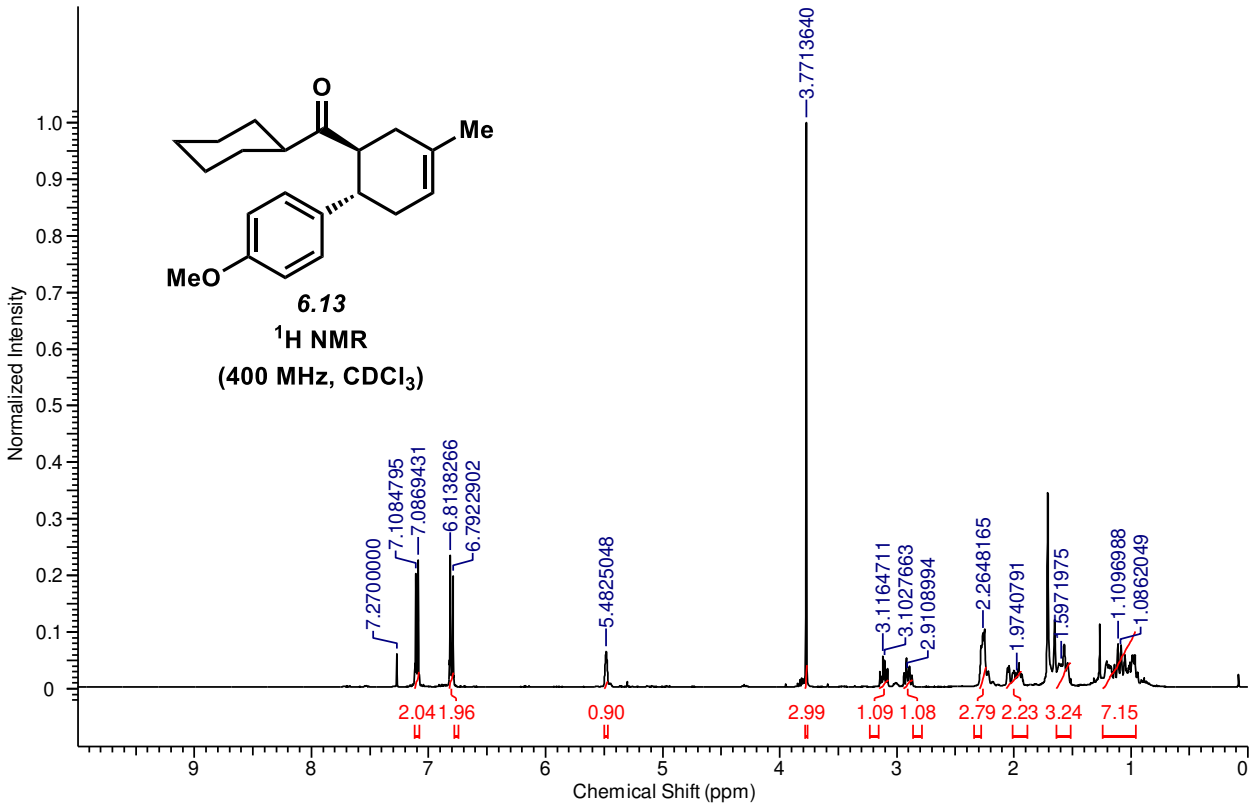


*Figure A4.12. ^{1}H NMR spectrum of **6.13**.*

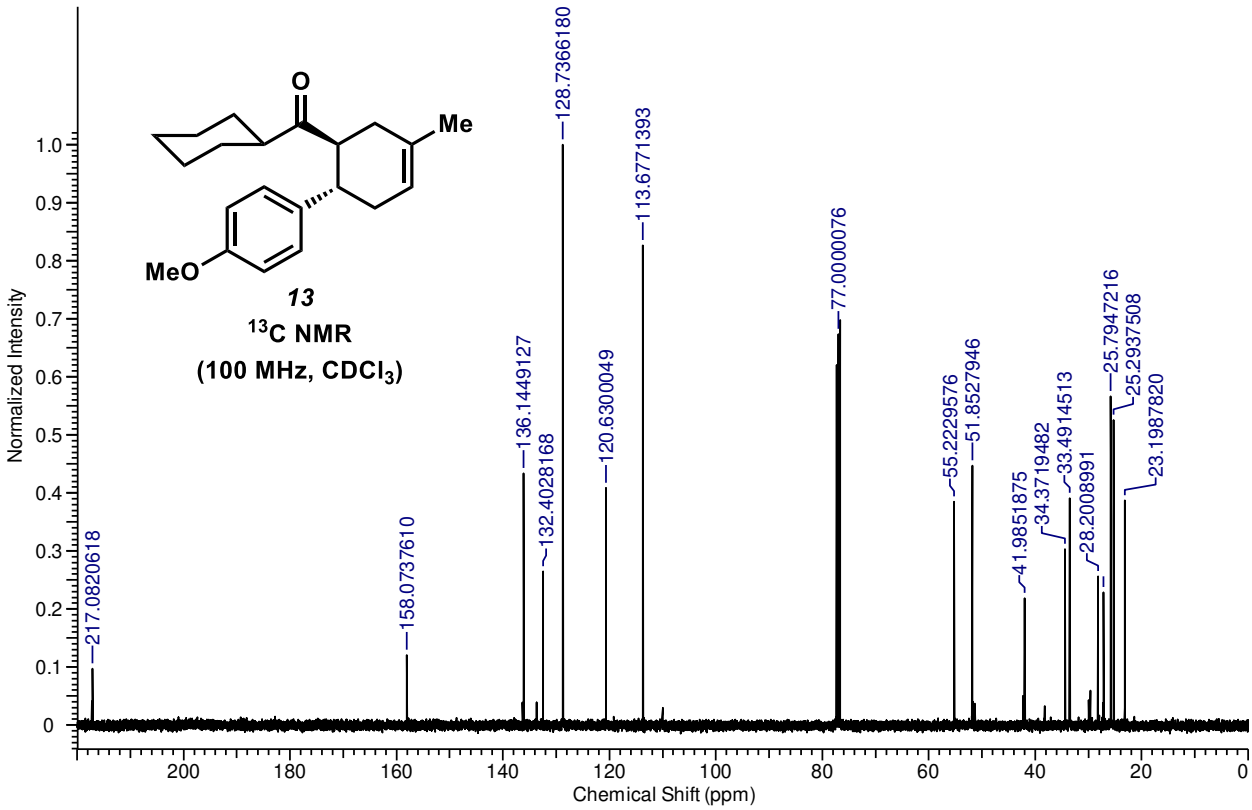


*Figure A4.13. ^{13}C NMR spectrum of **6.13**.*

Appendix 5: Supporting information for chapter 7

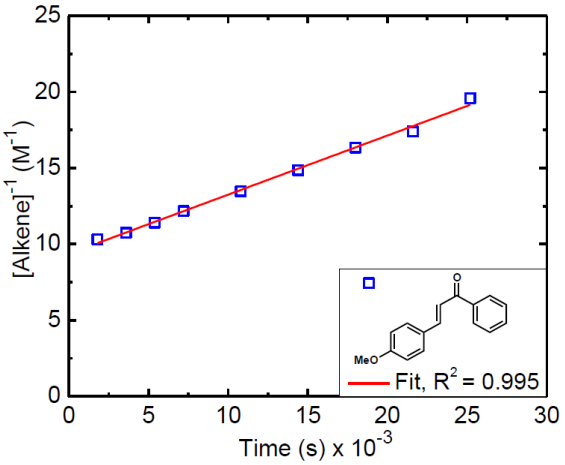


Figure A5.1. Time-dependence of the concentration of 4-methoxychalcone under standard reaction conditions.

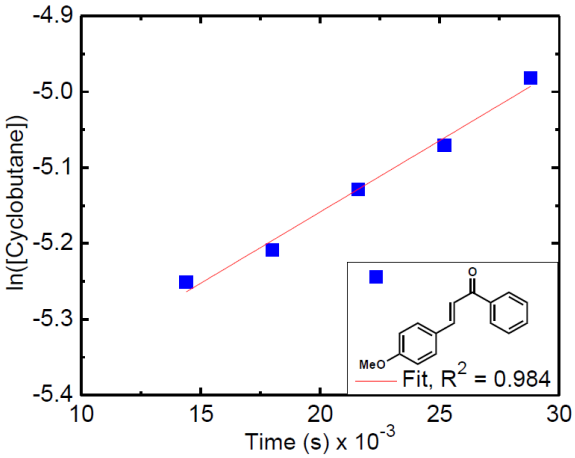


*Figure A5.2. Time-dependence of the concentration of **7.11** under standard reaction conditions.*

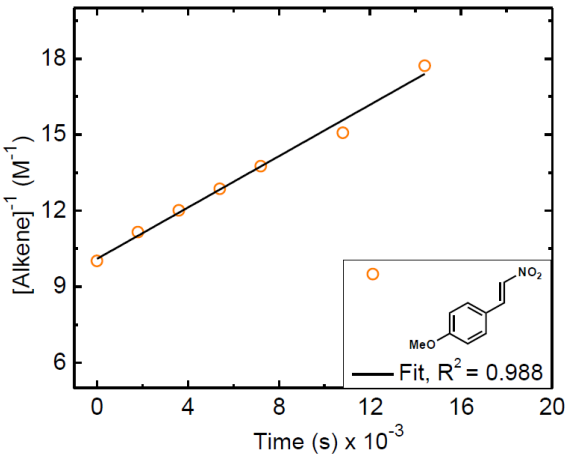


*Figure A5.3. Time-dependence of the concentration of **7.6** under standard reaction conditions.*

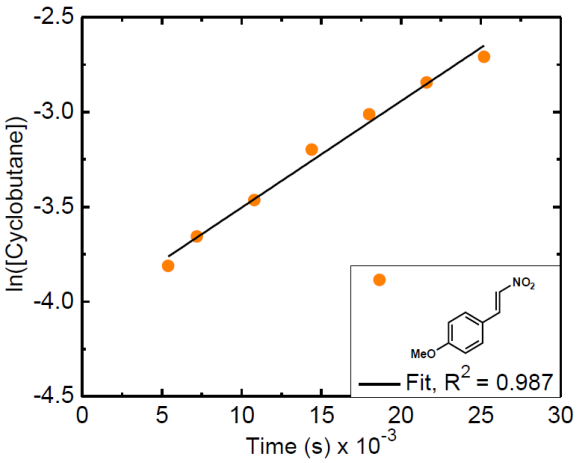


*Figure A5.4. Time-dependence of the concentration of the respective VCB **7.12** under standard reaction conditions.*

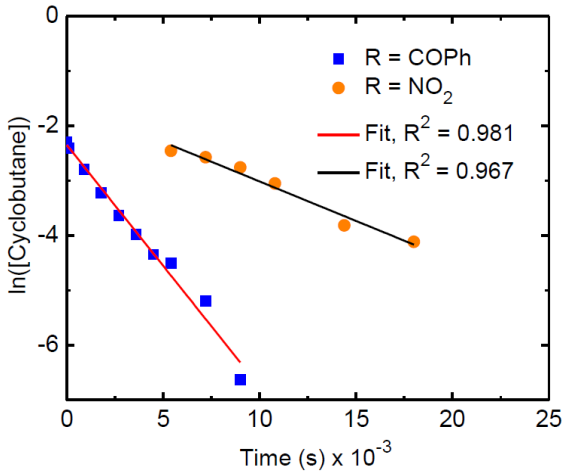


*Figure A5.5. Time-dependence of the concentration of the respective VCB **7.11** and **7.12** following resubjection to $[Cr(Ph_2phen)_3]^{3+}$ in nitromethane (0.10 M).*

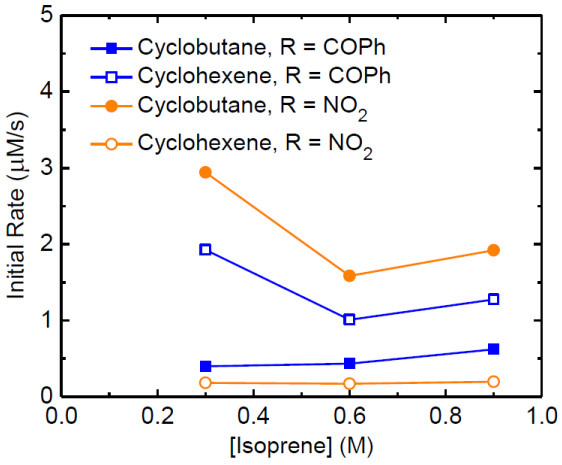


*Figure A5.6. Isoprene concentration dependence on the rate constant under otherwise standard conditions where the alkene employed is **7.3** (blue data) or **7.6** (orange data). The open data points correspond to the production of the product for each reaction whereas the filled data points correspond to the production of the VCB.*

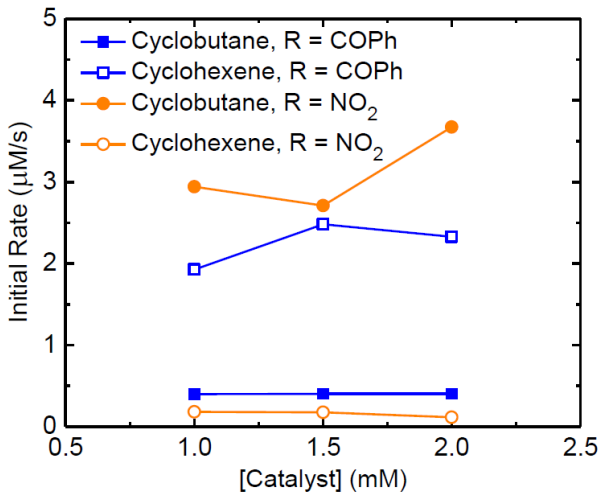


*Figure A5.7. Catalyst concentration dependence on the rate constant under otherwise standard conditions where the alkene employed is **7.3** (blue data) or **7.6** (orange data). The open data points correspond to the production of the product for each reaction whereas the filled data points correspond to the production of the VCB.*

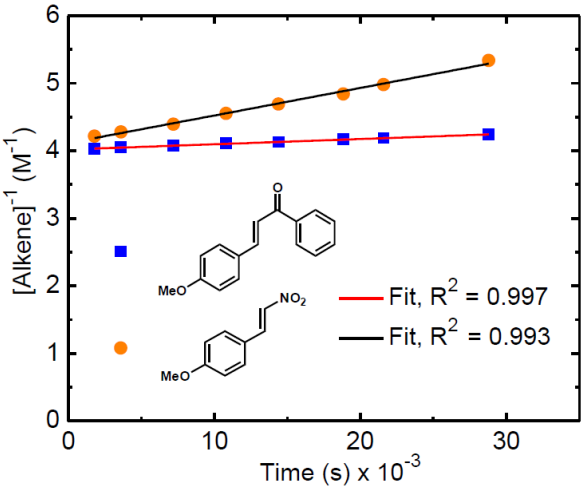


*Figure A5.8. Time-dependence of the concentration of **7.3** and **7.6** under reaction conditions to produce the respective VCB of each alkene.*

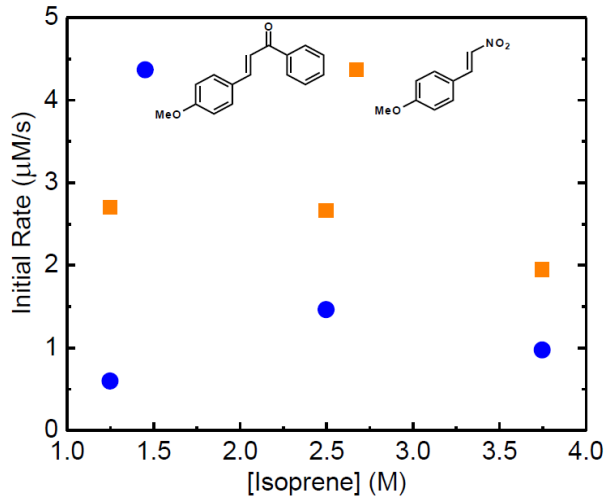


*Figure A5.9. Isoprene concentration dependence on the rate constant under reaction conditions to produce the respective VCB of each alkene where the alkene employed is **7.3** (blue data) or **7.6** (orange data).*

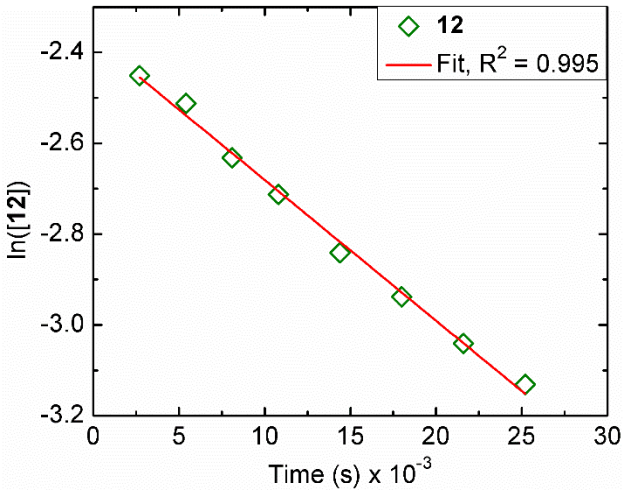


*Figure A5.10. Time dependence of concentration of **7.10** under standard reaction conditions.*

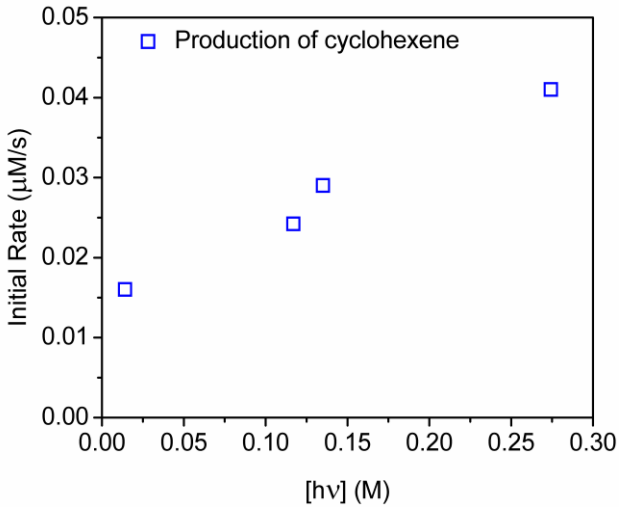
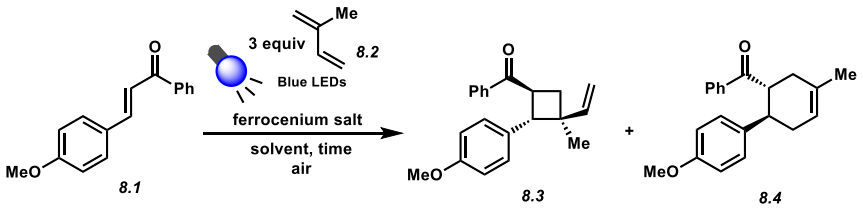


*Figure A5.11. Observed initial rate of formation of **7.14** as a function of photon flux (λ_{ex} = 400 nm).*

These data indicate that as the concentration of photons is increased, the initial rate of the reaction increases and therefore the reaction can be described as photon limited. A perfectly linear correlation would indicate a one photon process, whereas a perfectly exponential correlation would indicate a two-photon process. Unfortunately, neither of these fits accurately describe the data in Figure A7.11. This is not overly surprising because of the large number of competing pathways, some of which are one-photon processes and other processes which are two-photon in nature.

Appendix 6: Supporting information for chapter 8



entry	ferrocenium salt	mol% loading	solvent	time (h)	conversion to 3 (%)	conversion to 8.4 (%)
1	$[Fc](PF_6)$	5	$MeNO_2$	24	44	8. 54
2	$[Fc](BAr^F)$	5	$MeNO_2$	24	32	51
3	$[Me_8Fc](BF_4)$	5	$MeNO_2$	24	30	61
4	$[Me_{10}Fc](PF_6)$	5	$MeNO_2$	24	26	59

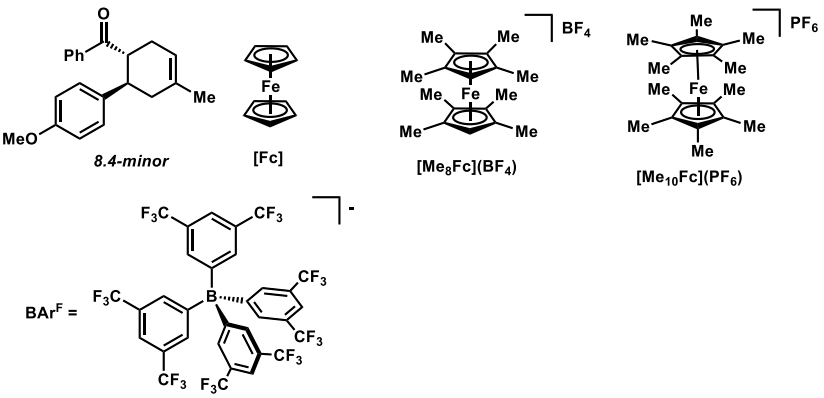
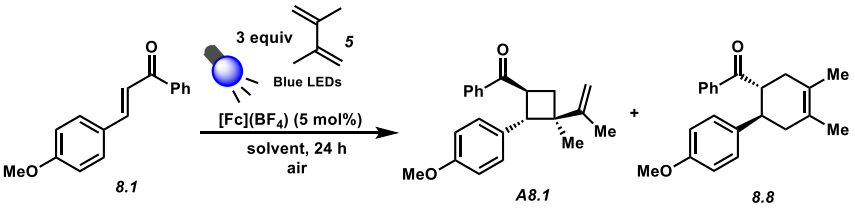


Figure A7.1. Additional control/optimization experiments using various ferrocenium starting materials.

The ground state redox potentials for $[Me_8Fc]^+$ and $[Me_{10}Fc]^+$ are -0.35 and -0.59 V in MeCN vs Fc^+/Fc, respectively.



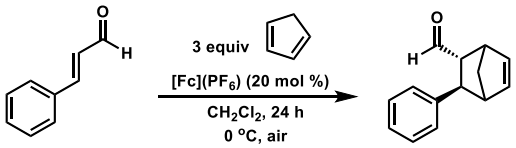
entry	solvent	conversion to A8.1 (%)[a]	conversion to 8.8 (%)[a]	8.1 remaining (%)
1	$MeNO_2$	21	46	0
2	MeCN	39	49	4
3	MeOH	21	9	0
4	^{i}PrOH	23	8	4
5	CH_2Cl_2	27	42	0
6	EtOAc	55	16	2
7	PhMe	12	5	0
8	DMF	64	4	12
9	DMSO	48	8	0
10	THF	65	12	3



[Fc]

[a]conversion indicates the NMR yield obtained for the experiment.

Figure A6.2. Solvent scope for the differences in [2+2] and [4+2] products using 4-methoxychalcone and 2,3-dimethylbutadiene.



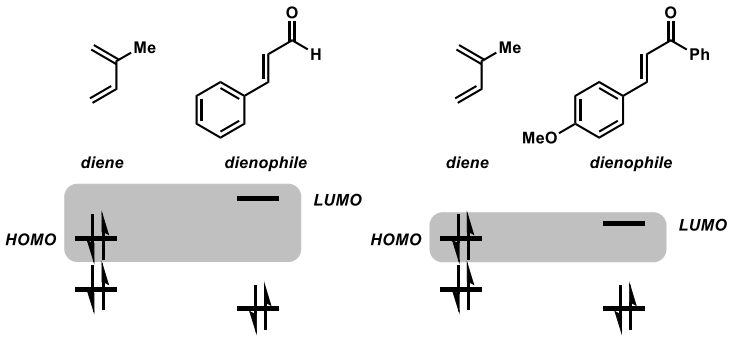
entry	NMR yield of prod (%)	cinamaldehyde remaining (%)	endo:exo ratio
1[a]	59	N/A	88:12
2[b]	55	0	85:15
3[c]	52	0	76:24



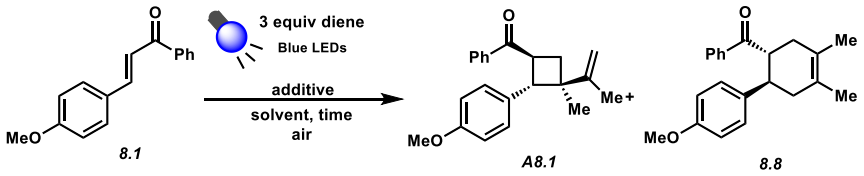
[Fc]

[a]reported from *Tetrahedron Lett.* 1989, *30*, 1357. [b]irradiation from blue LEDs. [c]reaction was performed in the dark.

Figure A6.3. Comparison of previously reported Lewis-acid catalyzed Diels-Alder reactivity with and without irradiation.



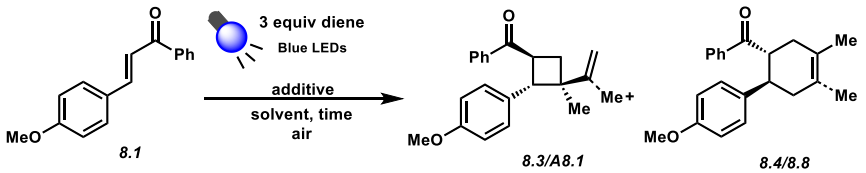
The results obtained in Figure A6.3 compared to the results determined are explained in the above molecular orbital drawing. The example on the left is represents typical demand for Diels-Alder reactions. While the phenyl ketone for 4-methoxychlacone on the left is an electron withdrawing group, the *para*-substituted methoxy group is electron donating making the α-carbon of the alkene (relative to the anisole moiety) not quite electron-poor enough for normal demand for a Diels-Alder reaction. This will increase the barrier to form the [4+2] product making a photo-initiated pathway feasible for 4-methoxychalcone.



entry	additive	mol% loading	solvent	time (h)	conversion to A8.1 (%)[a]	conversion to 8.8 (%)[a]	8.1 remaining (%)	diene
1	none	N/A	$MeNO_2$	24	15	0	71	2,3-dimethylbutadiene
2	none	N/A	MeCN	24	34	0	35	2,3-dimethylbutadiene
3	none	N/A	MeOH	24	11	0	39	2,3-dimethylbutadiene
4	none	N/A	^{i}PrOH	24	13	0	42	2,3-dimethylbutadiene
5	none	N/A	CH_2Cl_2	24	14	0	65	2,3-dimethylbutadiene
6	none	N/A	EtOAc	24	31	0	54	2,3-dimethylbutadiene
7	none	N/A	PhMe	24	trace	0	93	2,3-dimethylbutadiene
8	none	N/A	DMF	24	18	0	63	2,3-dimethylbutadiene
9	none	N/A	DMSO	24	17	0	64	2,3-dimethylbutadiene
10	none	N/A	THF	24	8	0	73	2,3-dimethylbutadiene

[a] conversion indicates the NMR yield obtained for the experiment.

Figure A6.4. Comparison of [2+2] reactivity of 4-methoxychalcone and isoprene in different solvents.



entry	additive	mol% loading	solvent	time (h)	conversion to 8.3/A8.1 (%)[a]	conversion to 8.4/8.8 (%)[a]	8.1 remaining (%)	diene
1	[Fc]	5	$MeNO_2$	36	32	0	46	isoprene
2	[Fc]	100	$MeNO_2$	36	9	0	86	isoprene
3	$AgBF_4$	5	$MeNO_2$	36	31	16	31	isoprene
4	$AgBF_4$	100	$MeNO_2$	36	45	15	31	isoprene
5	[Fc]	5	$MeNO_2$	24	89	0	trace	2,3-dimethylbutadiene
6	[Fc]	100	$MeNO_2$	24	64	0	6	2,3-dimethylbutadiene
7[b]	$[Fc]BF_4$	5	$MeNO_2$	48	29	34	trace	isoprene



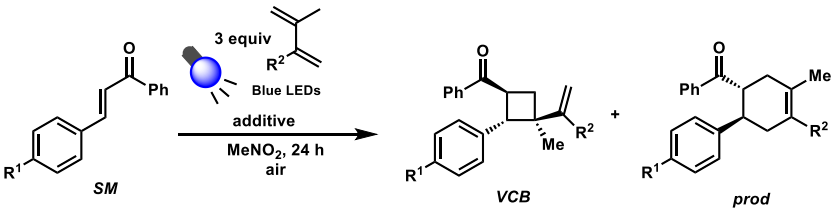
[Fc]

[a] conversion indicates the NMR yield obtained for the experiment. [b] reaction was performed with anhydrous and degassed solvent and diene.

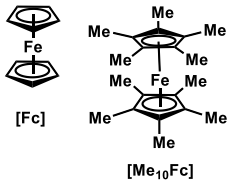
Figure A6.5. Comparison of [2+2] reactivity of 4-methoxychalcone and isoprene in different solvents.

Because of the slow reactivity and the fairly weak oxidation potential of ferrocenium, we were hoping to understand the background [2+2] reactivity in this reaction manifold. The light mediated [2+2] between 4-methoxychalcone and 2,3-dimethylbutadiene shows some solvent dependence solvent dependence (Figure A6.4). While investigating the prevalence of radical cation [2+2] between these two species and between 4-methoxychlacone and isoprene, we observed some peculiar results when ferrocene was used in place of the ferrocenium. Specifically, we observed drastically increased rates of formation of vinylcyclobutane (VCB) species (Figure A8.5, entries 1 and 5). This is quite a puzzling result and occurs even with decamethylferrocene (Figure A8.6, entry 5), indicating that a Lewis-acid mediated transformation is likely not the source of this increased production of VCB species. Interestingly, it is well precedented that a triplet-sensitized [2+2] pathway is viable with ferrocene. This has been postulated to occur through energy transfer of alkenes to the Cp ligand. We find this reactivity extremely odd, but it occurs

nonetheless. We hesitate to comment further about this reactivity and think that anymore discussion is beyond the scope of this report.



entry	R^1	R^2	additive	mol %	conversion to VCB (%)[a]	conversion to prod (%)[a]	SM remaining (%)
1	H	H	[Fc]	5	78	0	14
2	H	H	[Fc]	100	24	0	66
3	H	Me	[Fc]	5	79	0	16
4	H	Me	[Fc]	100	29	0	54
5	OMe	Me	[Me_{10}Fc]	5	87	0	8
6[b]	OMe	Me	[Fc]	5	0	0	95
7[b]	OMe	Me	[Fc](BF_4)	5	3	8	81



[a] conversion indicates the NMR yield obtained for the experiment.
[b] reaction was performed in the dark.

Figure A6.6. Control reactions with ferrocene.

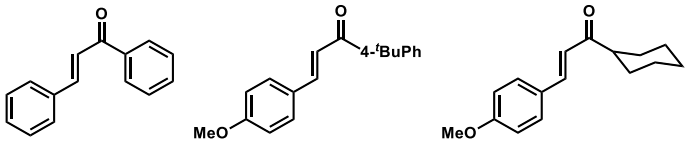
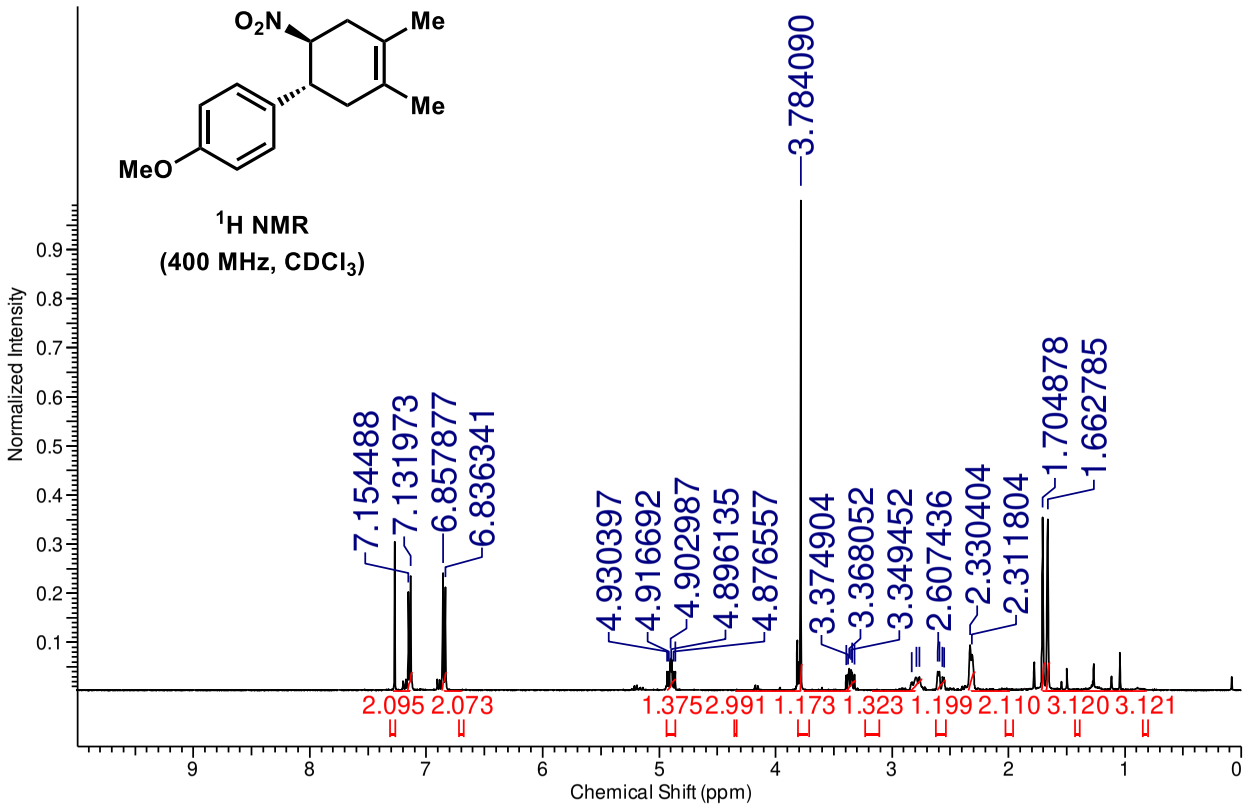
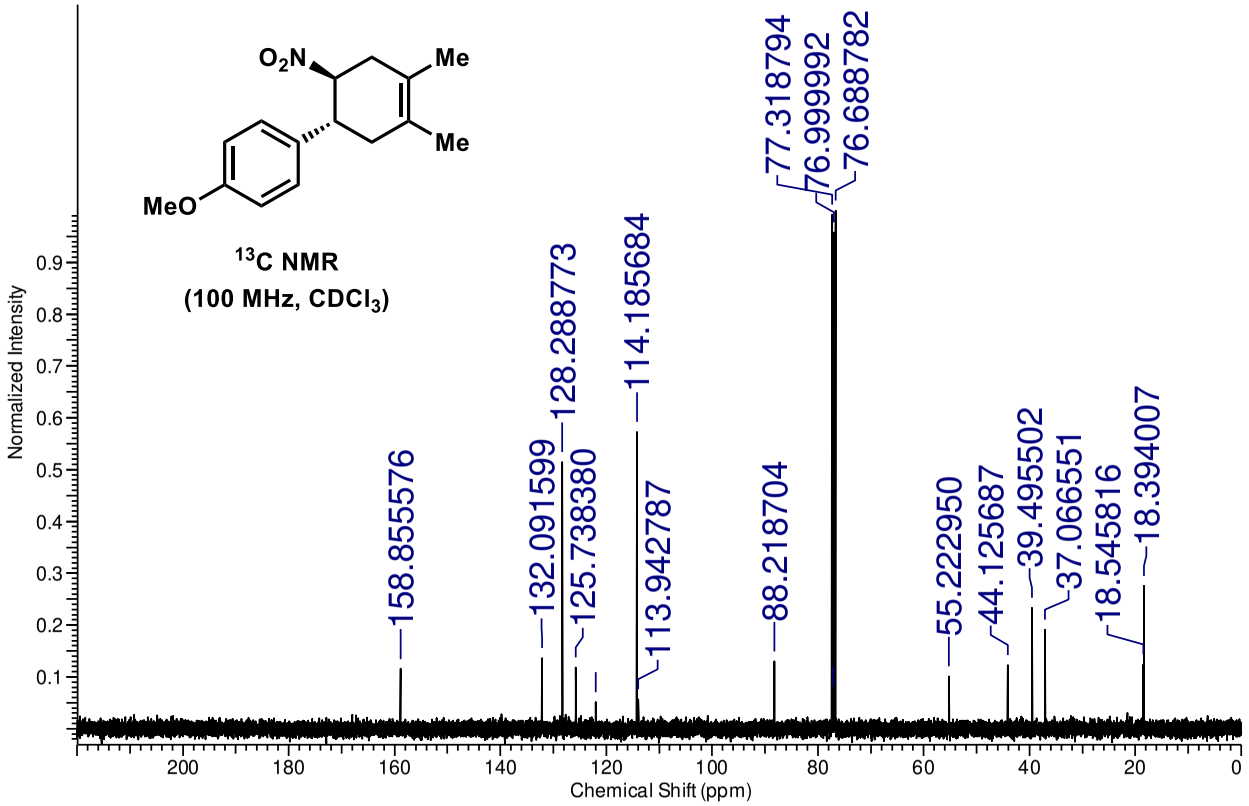
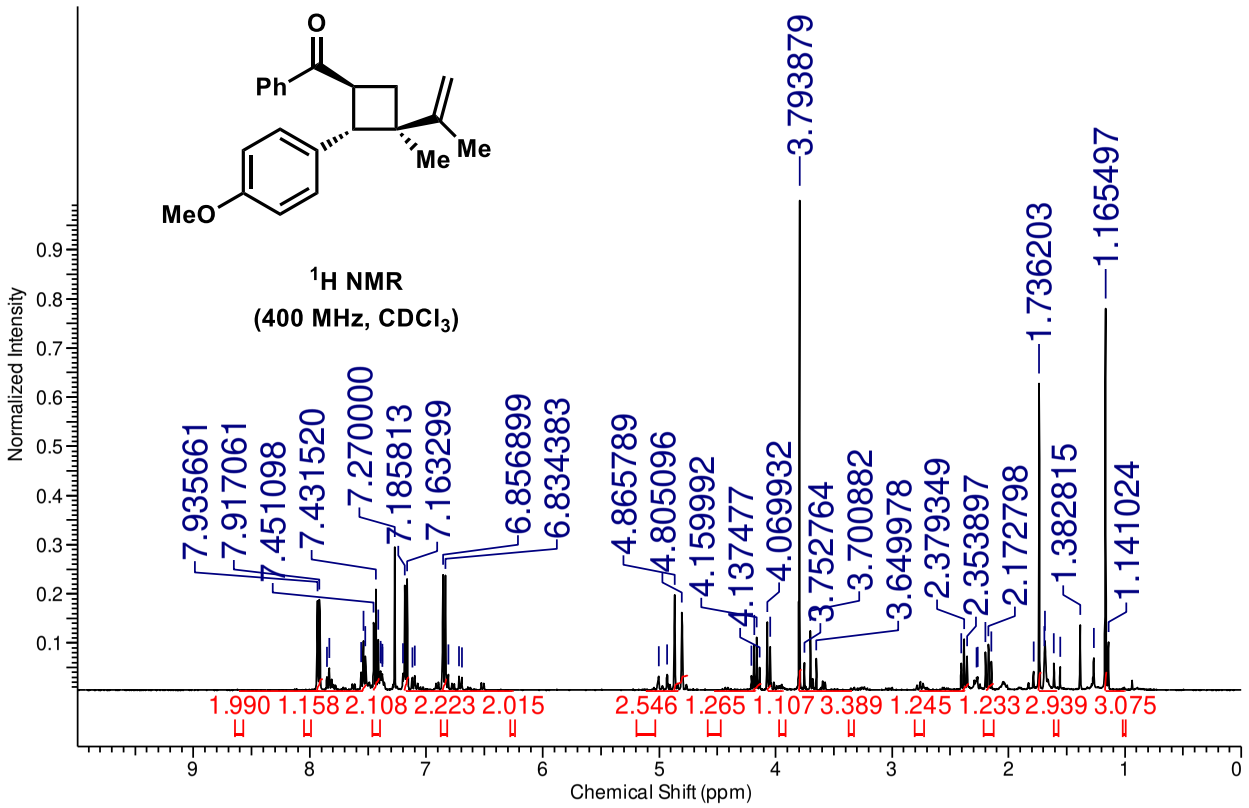
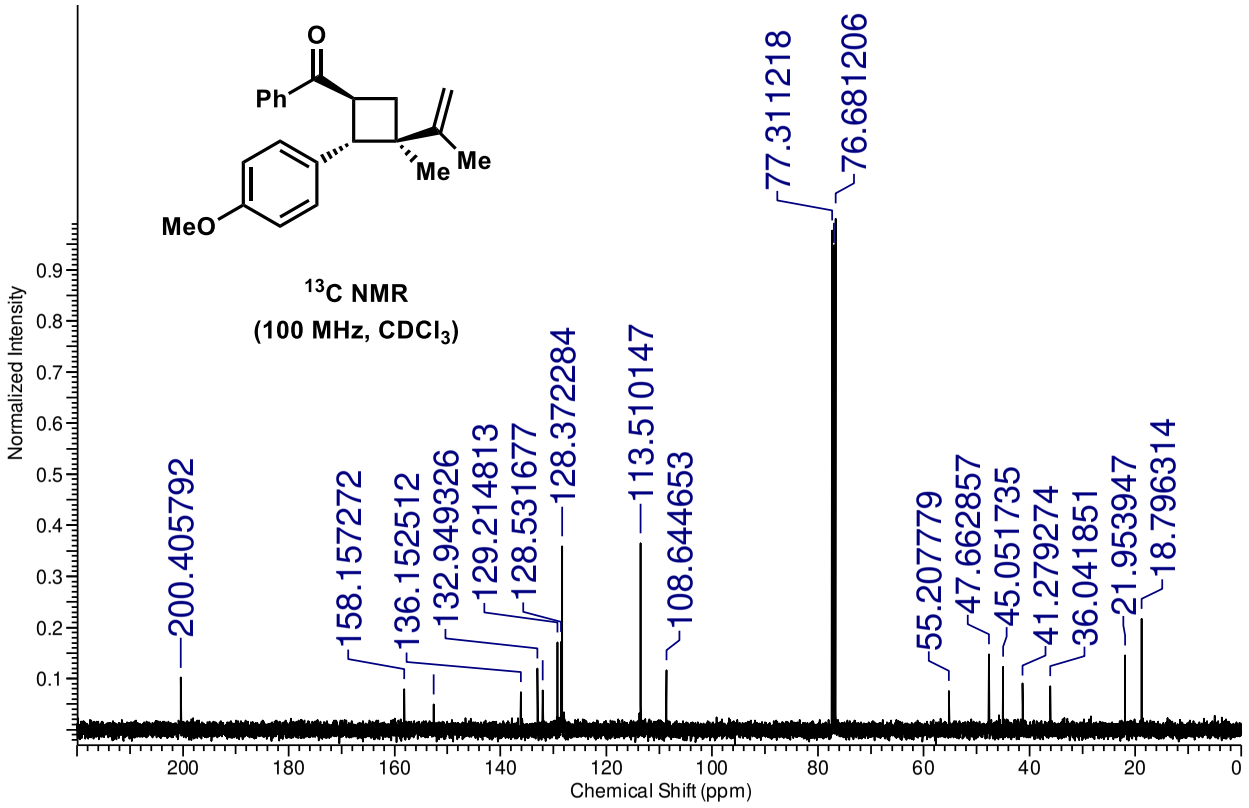


Figure A6.7. Unsuccessful substrates attempted in the reaction conditions.


O2N
Me
Me
MeO
1H NMR
(400 MHz, CDCl3)
Normalized Intensity
Chemical Shift (ppm)
7.154488
7.131973
6.857877
6.836341
4.930397
4.916692
4.902987
4.896135
4.876557
3.784090
3.374904
3.368052
3.349452
2.607436
2.330404
2.311804
1.704878
1.662785
2.095 2.073
1.375 2.991 1.173 1.323 1.199 2.110 3.120 3.121


O2N
Me
Me
MeO
13C NMR
(100 MHz, CDCl3)
Normalized Intensity
Chemical Shift (ppm)
158.855576
132.091599
128.288773
125.738380
114.185684
113.942787
88.218704
77.318794
76.999992
76.688782
55.222950
44.125687
39.495502
37.066551
18.545816
18.394007


O
Ph
Me
Me
MeO
^{1}H NMR
(400 MHz, CDCl$_3$)
Normalized Intensity
7.935661
7.917061
7.451098
7.431520
7.270000
7.185813
7.163299
6.856899
6.834383
4.865789
4.805096
4.159992
4.137477
4.069932
3.793879
3.752764
3.700882
3.649978
2.379349
2.353897
2.172798
1.736203
1.382815
1.165497
1.141024
1.990 1.158 2.108 2.223 2.015
2.546 1.265 1.107 3.389 1.245 1.233 2.939 3.075
Chemical Shift (ppm)


O
Ph
Me
Me
MeO
^{13}C NMR
(100 MHz, CDCl$_3$)
Normalized Intensity
200.405792
158.157272
136.152512
132.949326
129.214813
128.531677
128.372284
113.510147
108.644653
77.311218
76.681206
55.207779
47.662857
45.051735
41.279274
36.041851
21.953947
18.796314
Chemical Shift (ppm)

Appendix 7: Supporting information for chapter 9

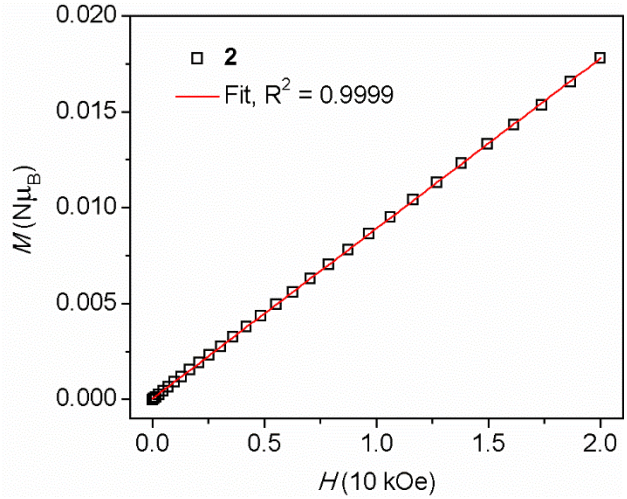


*Figure A7.1. Field dependence of magnetization for **9.2** collected at 100 K. The data are fit to a linear regression (y = 0.00887x + 4.51E-5) that does not include H = 0 Oe.*

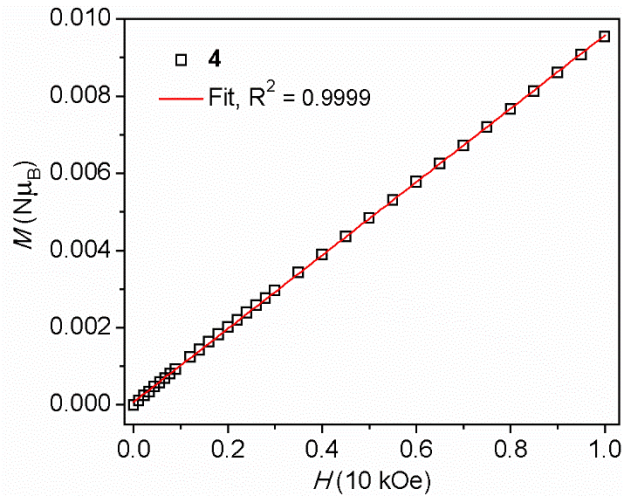


*Figure A7.2. Field dependence of magnetization for **9.4** collected at 100 K. The data are fit to a linear regression (y = 0.0095x + 7.54E-5) that does not include H = 0 Oe. The data point at 1 kOe is omitted due to a centering error.*

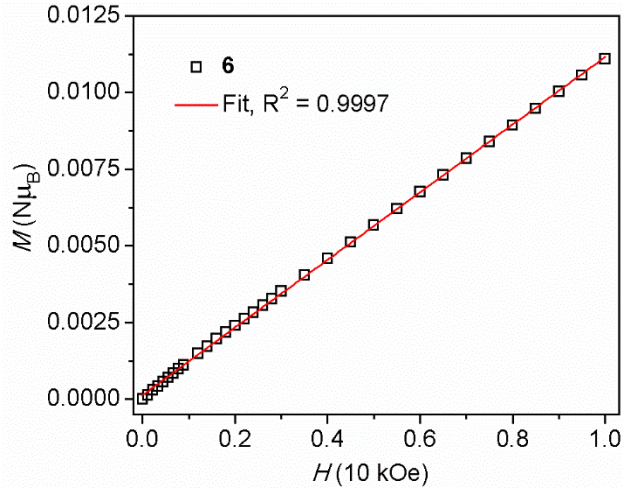


*Figure A7.3. Field dependence of magnetization for **9.6** collected at 100 K. The data are fit to a linear regression (y = 0.011x + 1.34E-4) that does not include H = 0 Oe.*

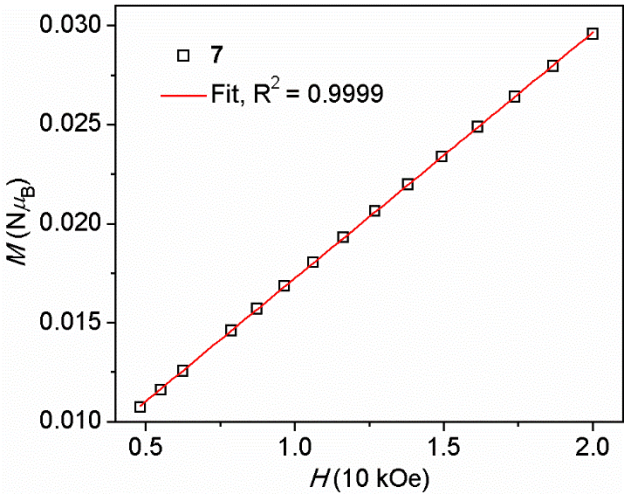


*Figure A7.4. Field dependence of magnetization for **9.7** collected at 100 K. The data are fit to a linear regression (y = 0.012x + 4.81E-3) that does not include H = 0 Oe. The data point at 7 kOe is omitted due to a centering issue.*

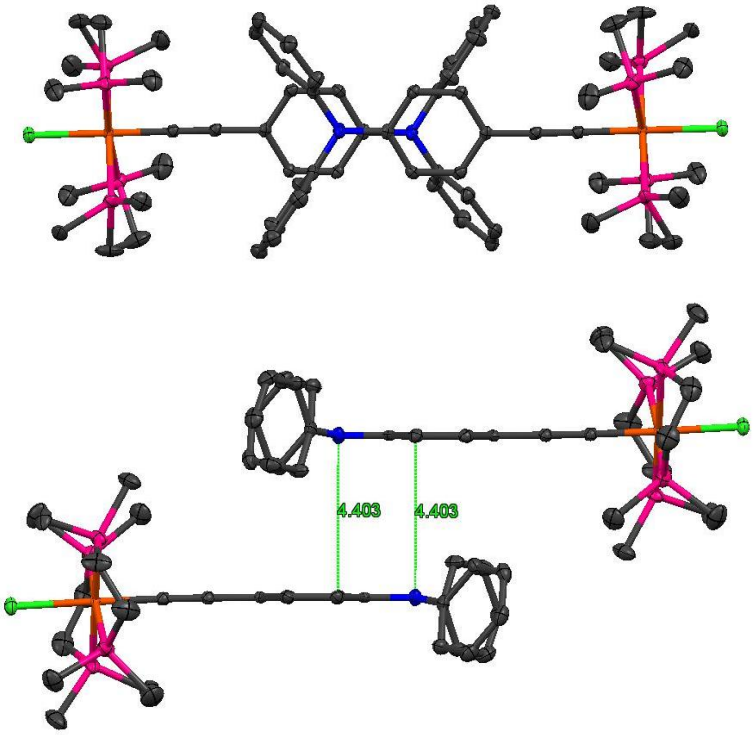


*Figure A7.5. Intermolecular contacts in the crystal structure of **9.2**. The distance between C and N atoms is 4.403(4) Å.*

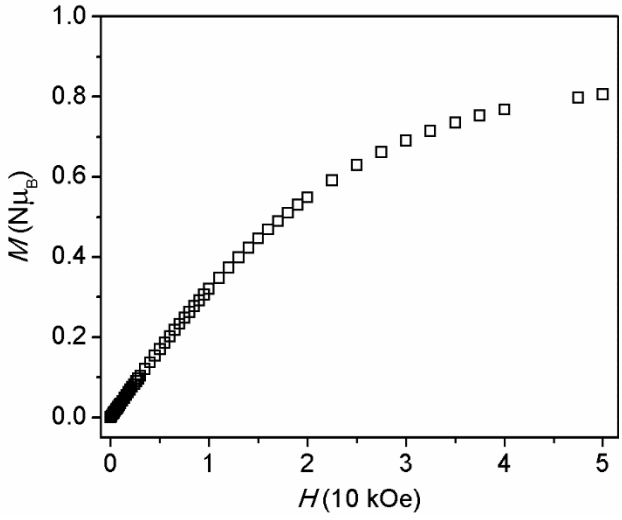


*Figure A7.6. Field dependence of magnetization for **9.2** collected at 1.8 K. The data points at 42.5 and 45 kOe are omitted because of a centering issue.*

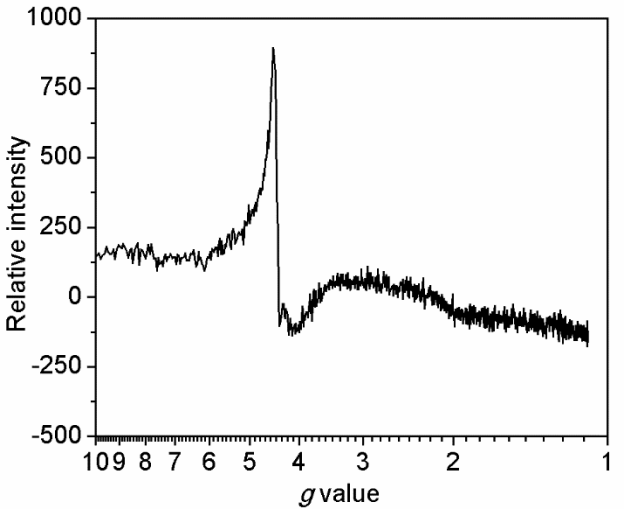


*Figure A7.7. EPR spectrum of **9.6** in a 1:1 mixture of CH_2Cl_2:$ClCH_2CH_2Cl$ measured at 100 K.*

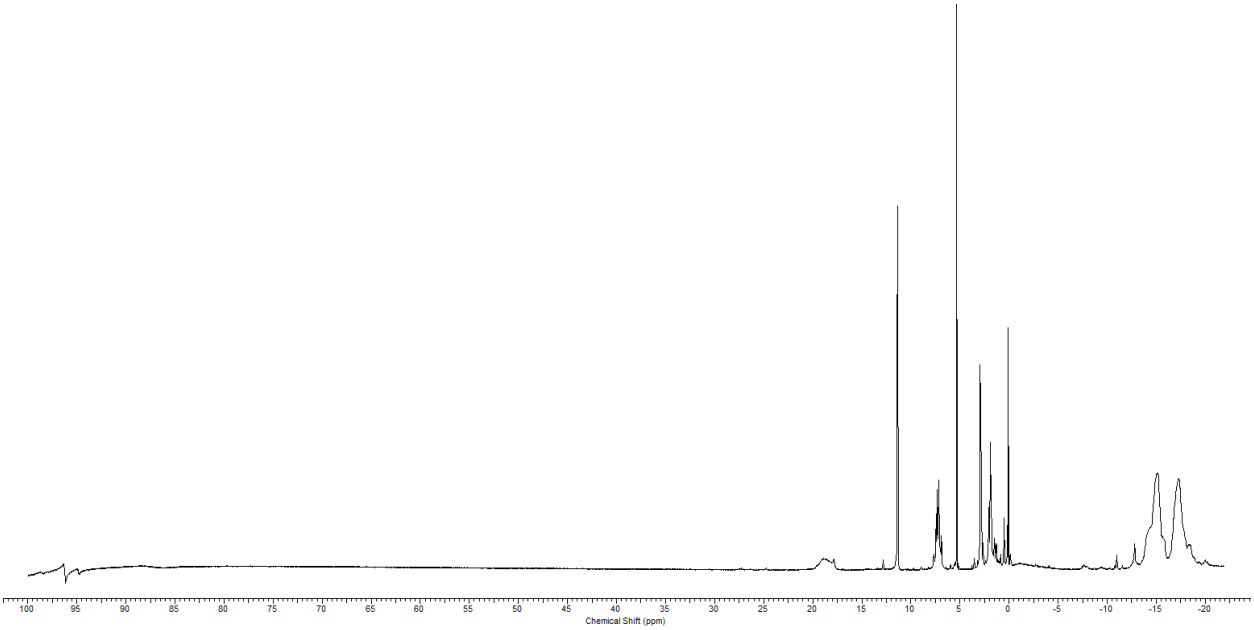


*Figure A7.8. ^1H NMR of **9.2** in CD_2Cl_2.*

*Table A7.1. Magnetic fits for **9.7** where four S = 1/2 spins were used.*

Fit #	J_{12} (cm^{-1})	J_{34} (cm^{-1})	g_1	g_2	g_3	g_4	TIP (cm^3/mol) x 10^6	Θ (cm^{-1})	f_{sum}
1	-1.77	-87.31	2.36	2.36	2.36	2*	-1925.8	0	0.047
2	279.52	-1728.85	2*	2*	2*	2*	796.4	0	0.096
3	131.40	-2235.96	1.91	1.91	1.91	2*	1430	0	0.065
4	-34.67	0.69	2.05*	2.05*	2.05*	2*	-1280	0	0.073
5	-75.13	53.01	2.05*	2.05*	2.05*	2*	-1051.9	-1.99	0.033
6	27.49	-43.65	1.91	1.91	1.91	2*	-710	-0.92	0.039

*indicates the value was held constant for the fit. The g_1, g_2 and g_3 values were restrained to be the same value.

*Table A7.2. Magnetic fits for **9.7** where 2 S=1/2 spins were used.*

Fit #	J_{12} (cm^{-1})	g_1	g_2	TIP (cm^3/mol) x 10^6	Θ (cm^{-1})	f_{sum}
1	-1.65	2.26	2.33	883.2	0	0.035
2	0	0.65	3.26	675.4	-2.53	0.025
3	0	2.35	2.35	674.2	-2.54	0.025
4	-1.65	2.29	2.29	881.5	0	0.035
5	286.54	2*	2*	791	0	0.096
6	138.83	2*	2*	1065	-2.13	0.022
7	-9.25	2.94	2.94	-1516	-10.27	0.175
8	-9.25	2.47	2.47	666	0	0.244

*indicates the value was held constant for the fit. Fits 3-8 were run where g_1=g_2.

Appendix 8: Supporting information for chapter 10

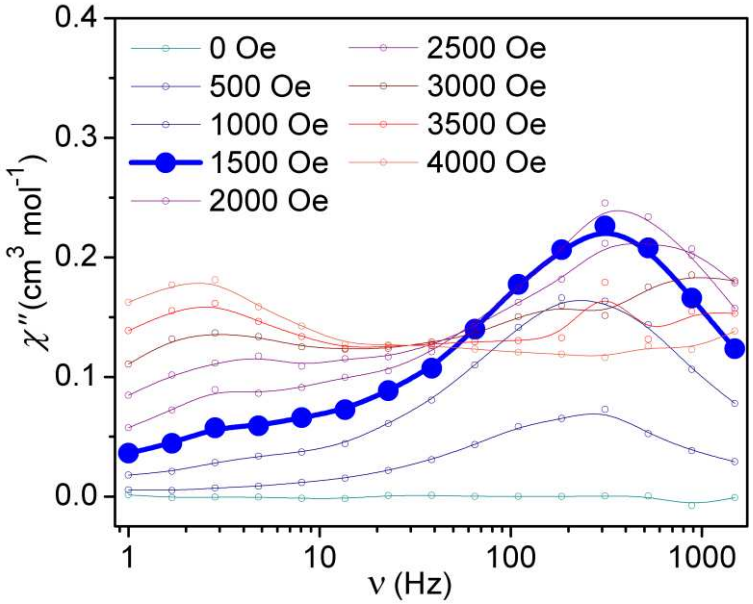


*Figure A8.1. Field and frequency dependence of the out-of-phase magnetic susceptibility data for **10.1** at 1.8 K.*

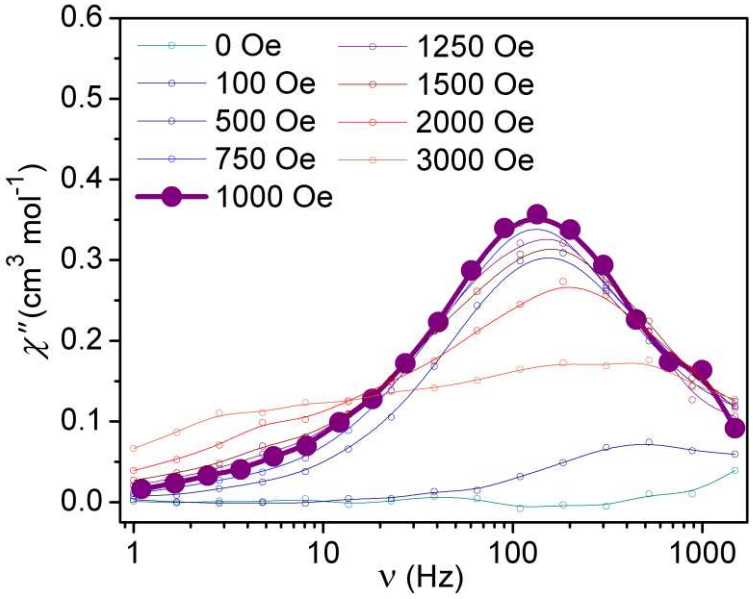


*Figure A8.2. Field and frequency dependence of the out-of-phase magnetic susceptibility data for **10.2b** at 1.8 K.*

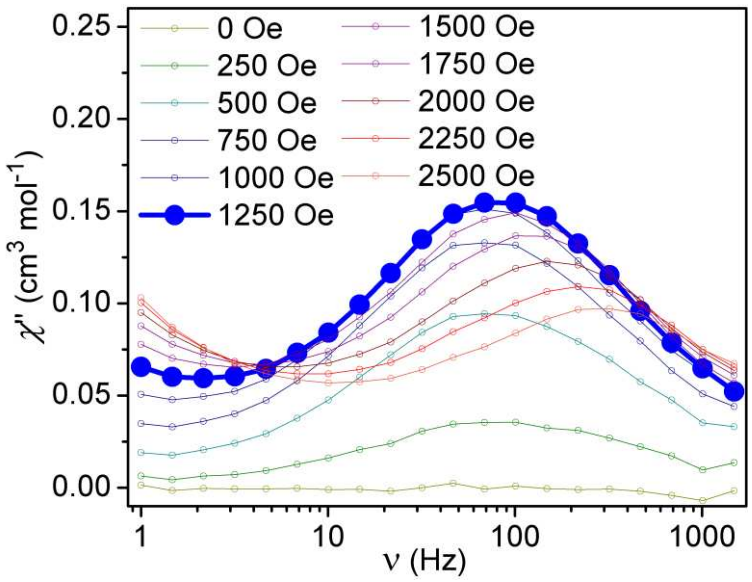


*Figure A8.3. Field and frequency dependence of the out-of-phase magnetic susceptibility data for **10.3** at 1.8 K.*

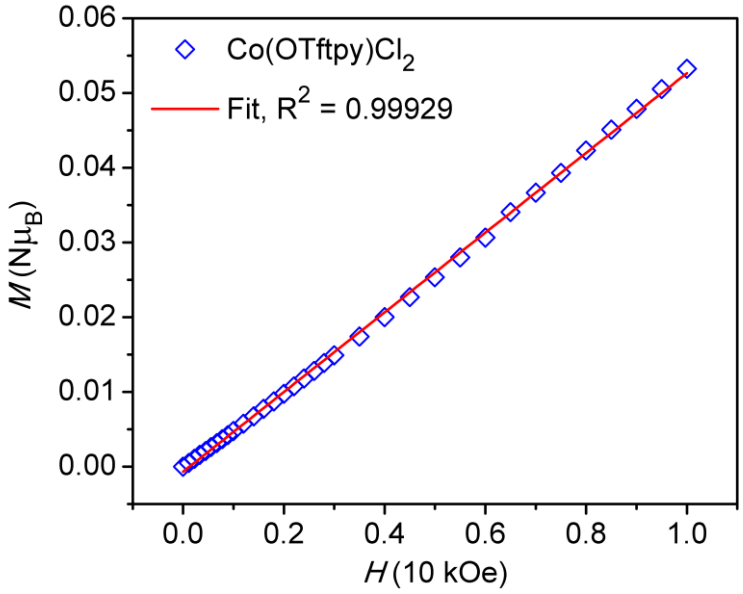


*Figure A8.4. Field dependence of magnetization for compound **10.1** collected at 100 K. The data are fit to a linear regression (y = 0.0533x – 6.70E-4) without the 0 kOe data point.*

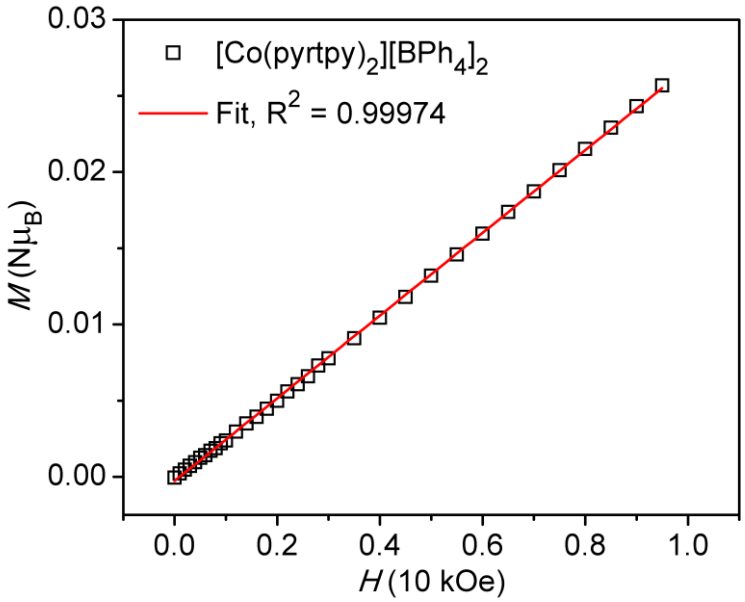


*Figure A8.5. Field dependence of magnetization for compound **10.2b** collected at 100 K. The data are fit to a linear regression (y = 0.0271x – 2.71E-4) without the 0 kOe data point.*

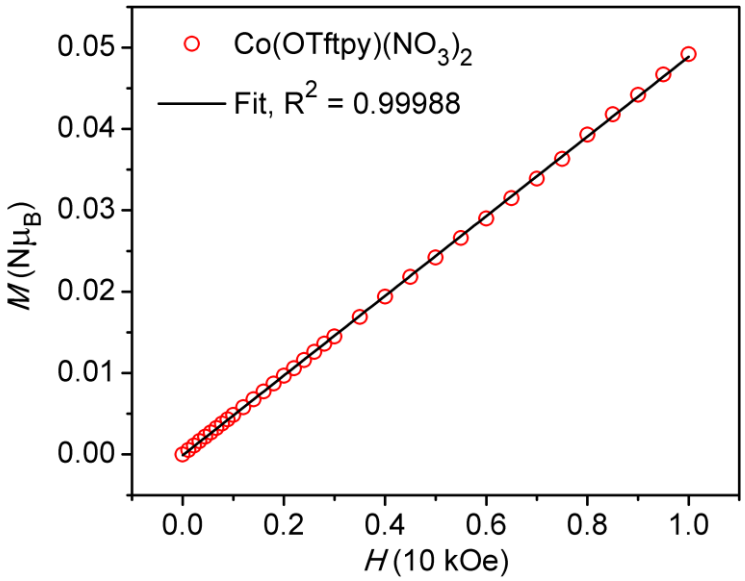


*Figure A8.6. Field dependence of magnetization for compound **10.3** collected at 100 K. The data are fit to a linear regression (y = 0.0490x – 1.04E-4), without the 0 kOe data point.*

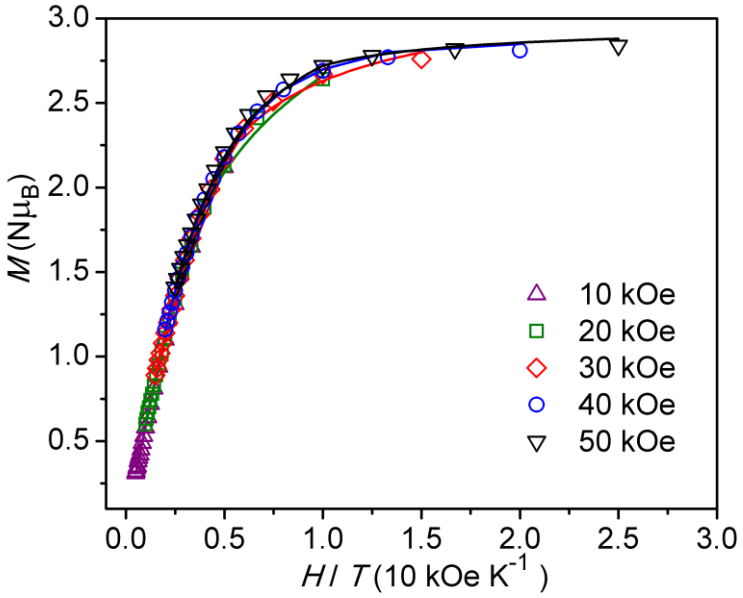


*Figure A8.7. Reduced magnetization collected on **10.1**. The lines represent fits obtained from ANISOFIT 2.0. The values associated with the fit to an anisotropic S = 3/2 ground spin state are as follows: g = 3.39 , D = -105 cm^{-1}, E = 31.6 cm^{-1}.*

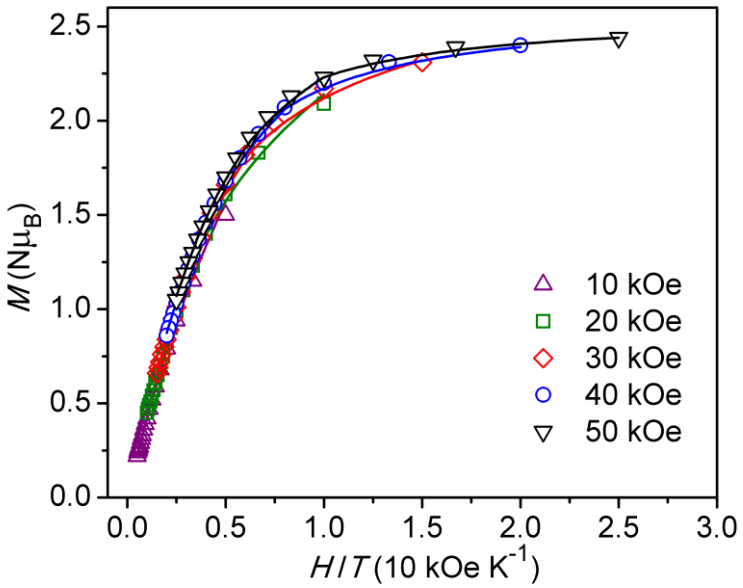


*Figure A8.8. Reduced magnetization collected on **10.3**. The lines represent fits obtained from ANISOFIT 2.0. The values associated with the fit to an anisotropic S = 3/2 ground spin state are as follows: g = 2.70, D = 43.6 cm^{-1}, E = 14.5 cm^{-1}.*

Appendix 9: Supporting information for chapter 11

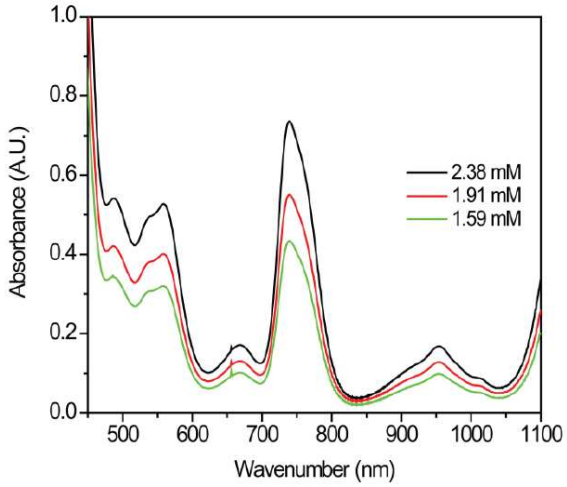


*Figure A9.1. UV-vis spectra of **11.1** in Et_2O.*

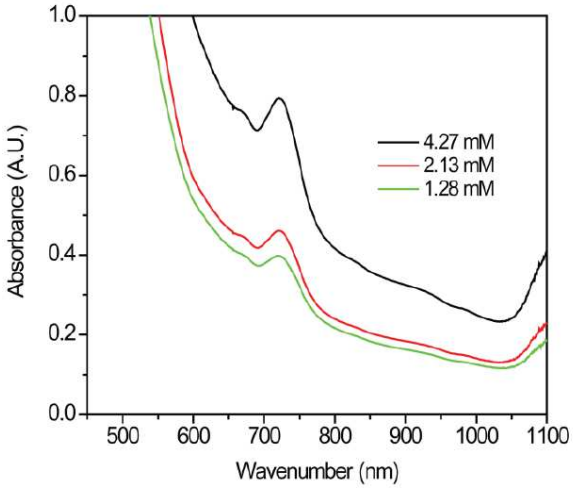


*Figure A9.2. UV-vis spectra of **11.2** in Et_2O.*

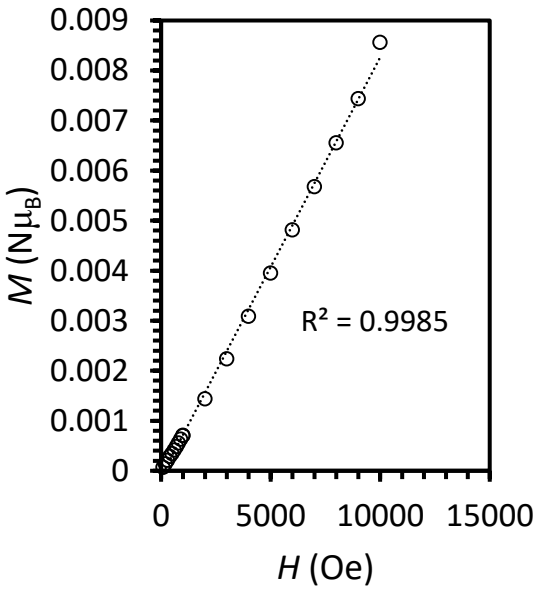


*Figure A9.3. M vs. H data at 100 K for **11.1**.*

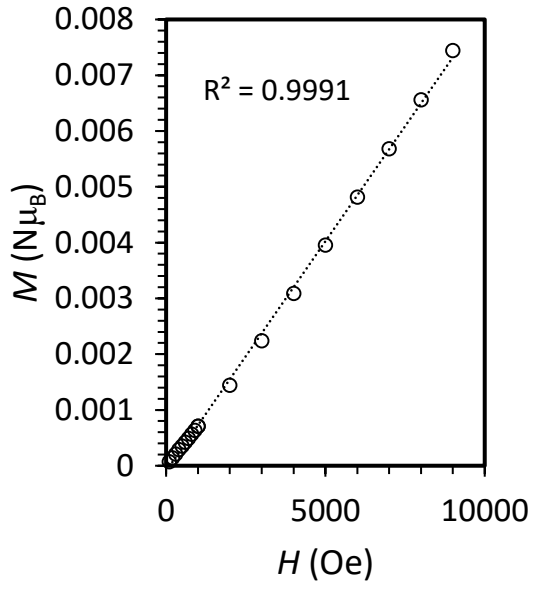


*Figure A9.4. M vs. H data at 100 K for **11.2**.*

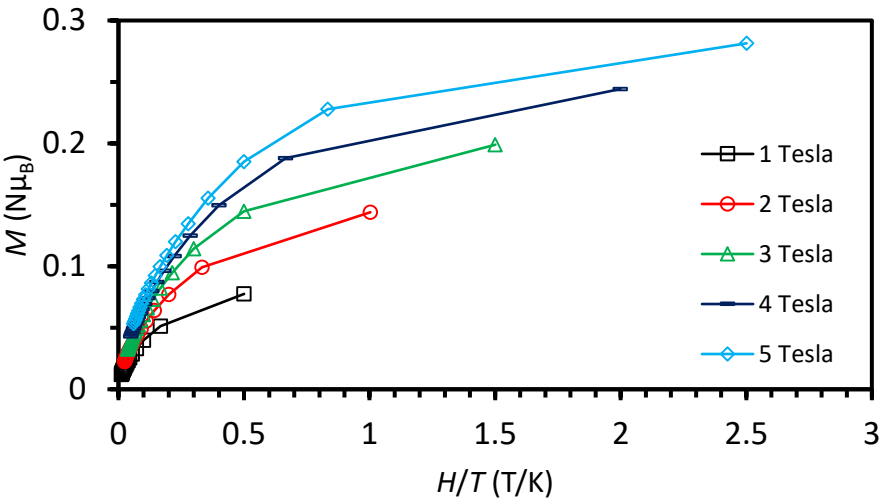


*Figure A9.5. M vs. H/T at lower temperatures for **11.1** at applied dc fields from 1-5 T at 1 T increments.*

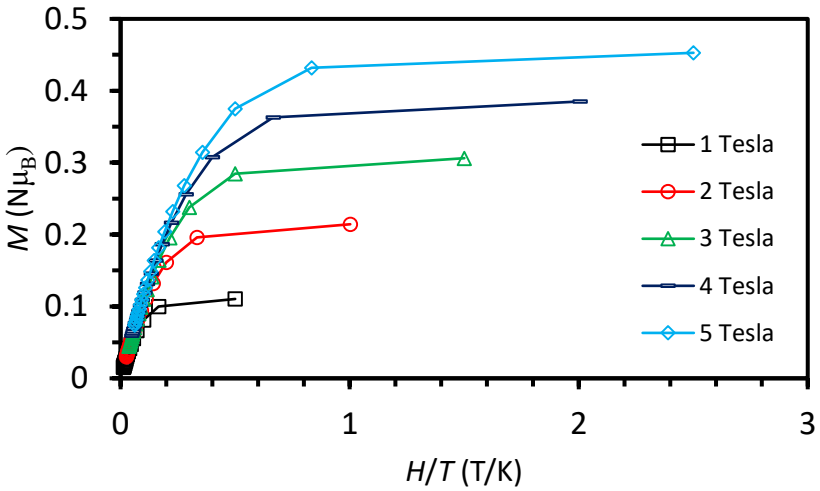


*Figure A9.6. M vs. H/T at lower temperatures for **11.2** at applied dc fields from 1-5 T at 1 T increments.*

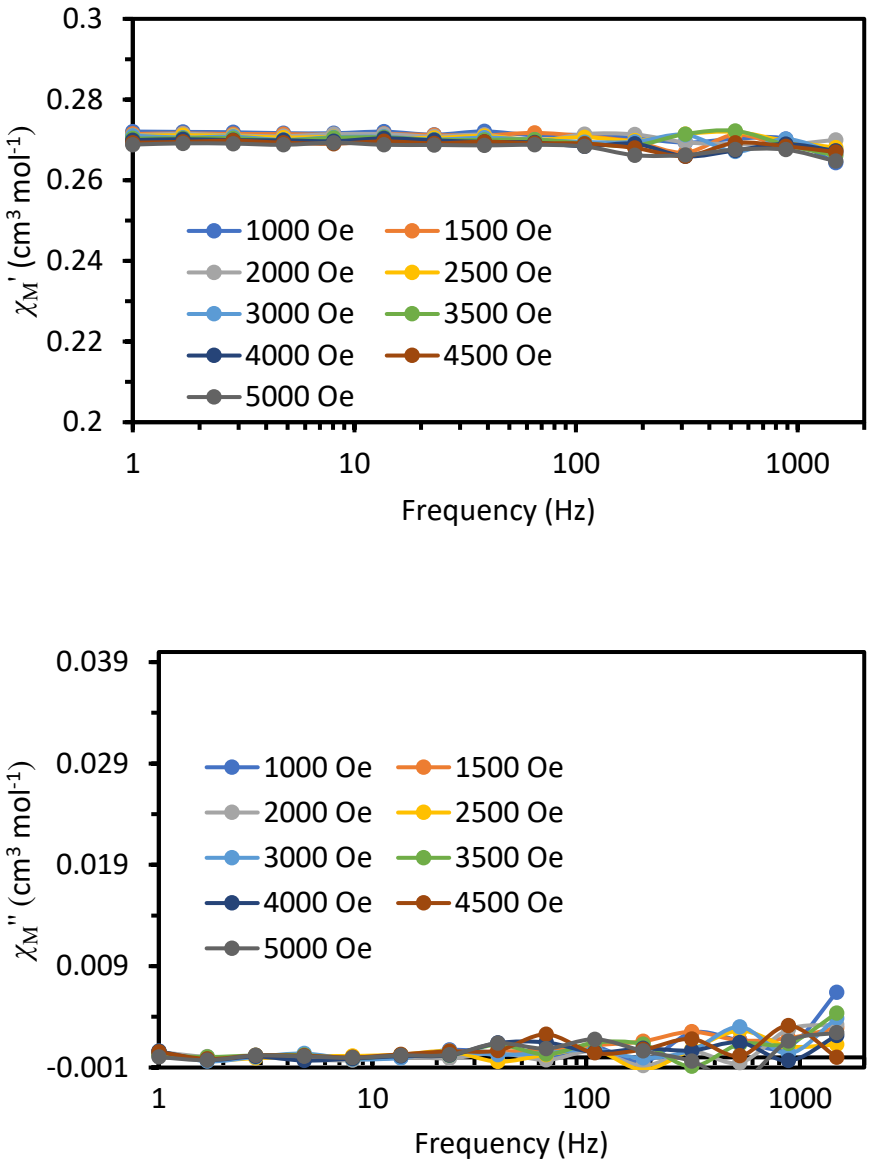


Figure A9.7. In-phase (top) and out-of-phase (bottom) ac magnetic susceptibility data for ***11.2*** *with applied dc fields from 1000 to 5000 Oe at a 4 Oe applied ac field sweeping frequency (1-1500 Hz) at 1.8 K.*

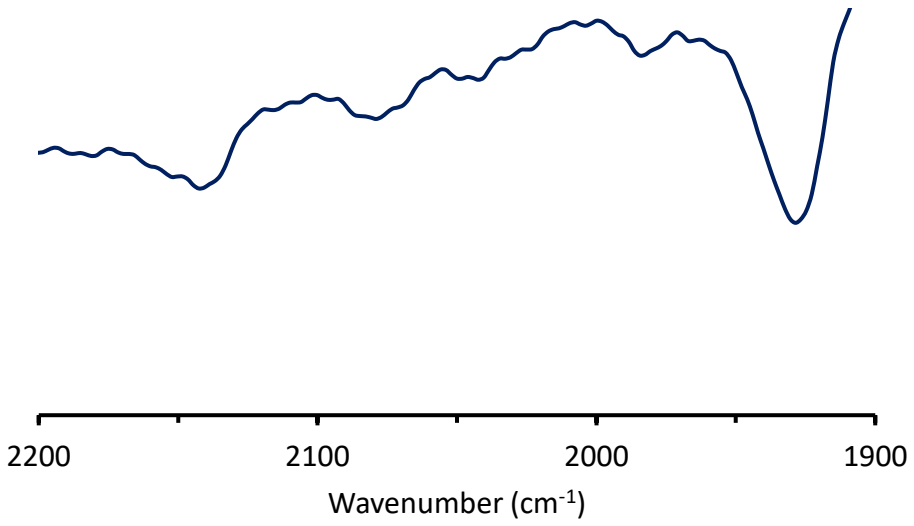


Figure A9.8. IR spectrum of the isolated filtrate from the reaction that produces **11.3**. The broad peak at 2143 cm^{-1} corresponds to diphenylbutadiyne.

Appendix 10: Supporting information for chapter 12

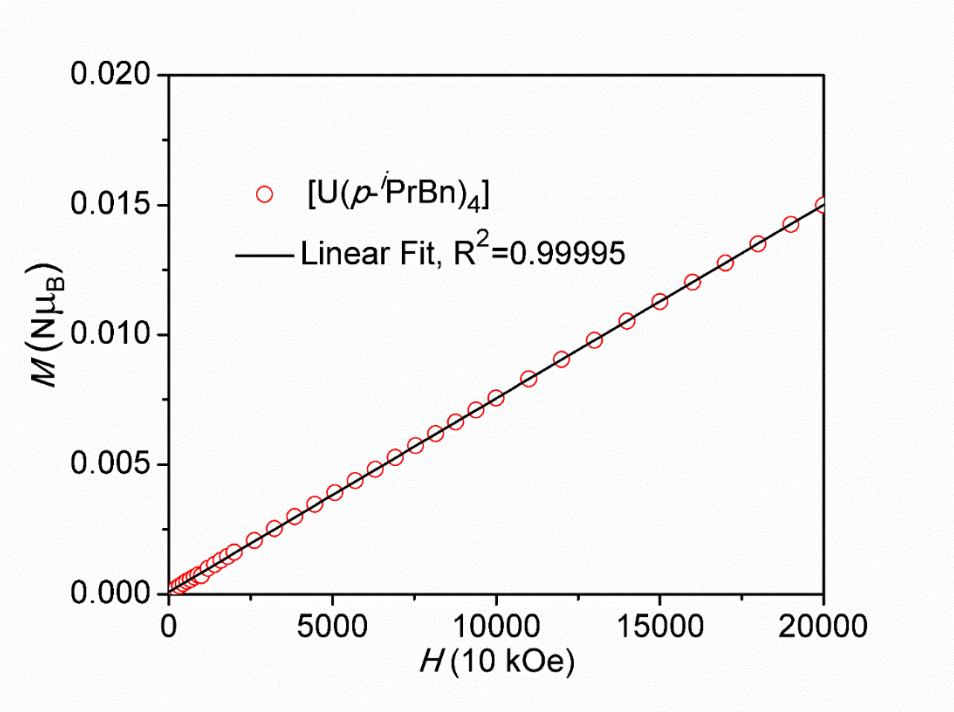


Figure A10.1. Field dependence of magnetization for [U(p-IPrBn)$_4$] collected at 100 K.

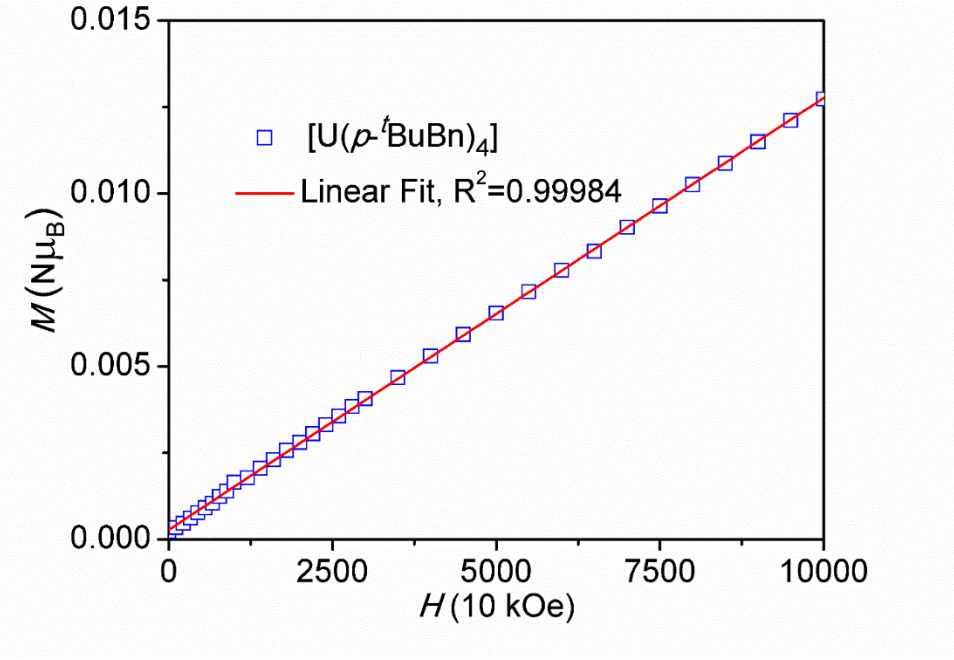


Figure A10.2. Field dependence of magnetization for [U(p-tBuBn)$_4$] collected at 100 K.

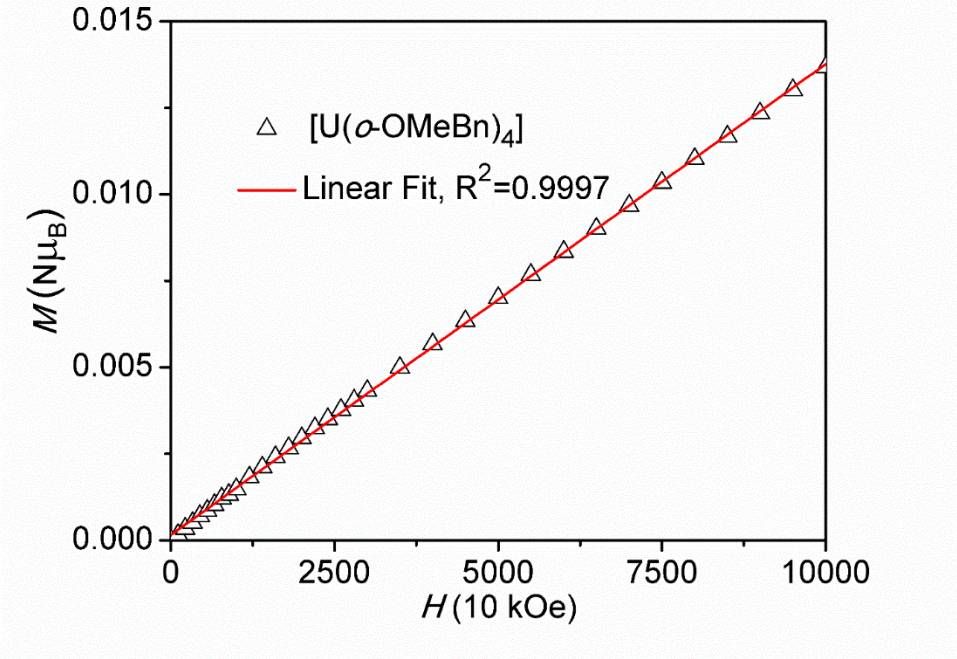


Figure A10.3. Field dependence of magnetization for [U(o-OMeBn)$_4$] collected at 100 K.

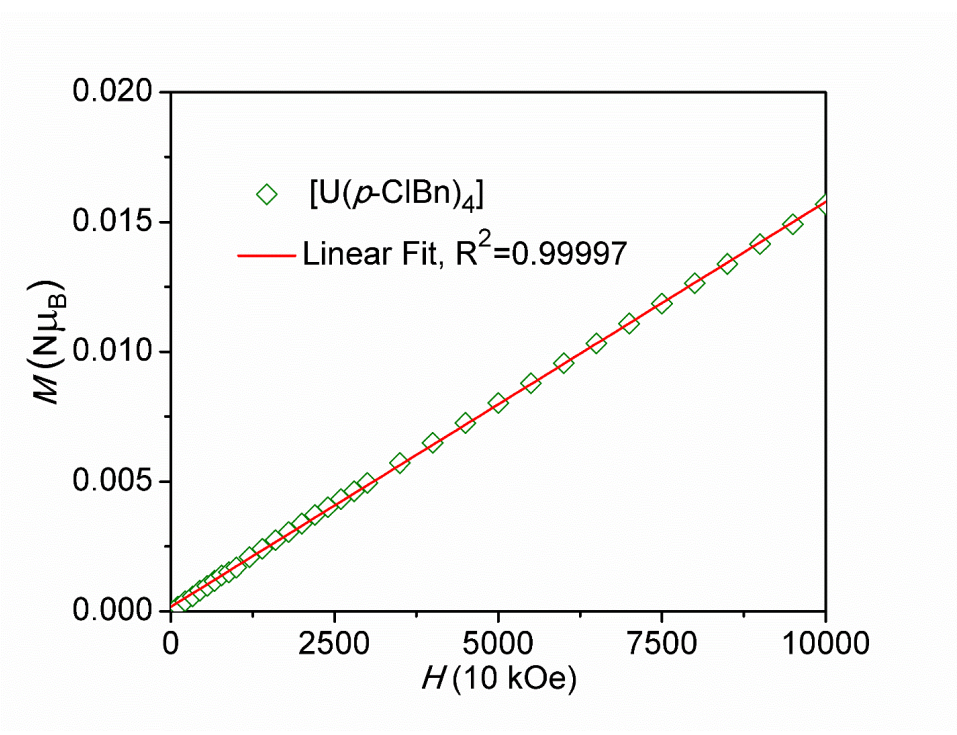


Figure A10.4. Field dependence of magnetization for [U(p-ClBn)$_4$] collected at 100 K.

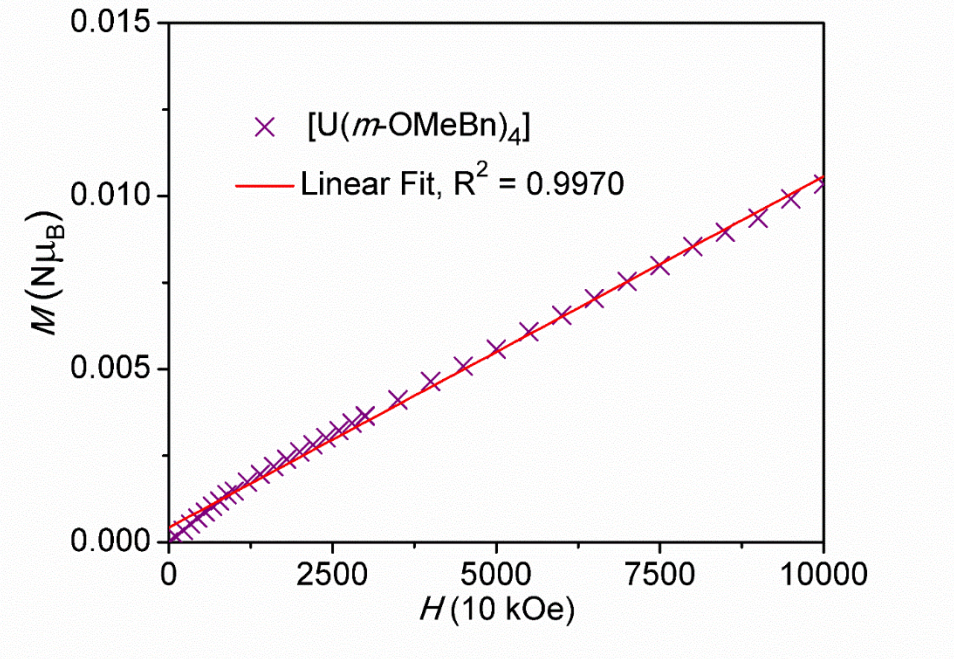


Figure A10.5. Field dependence of magnetization for [U(m-OMeBn)$_4$] collected at 100 K.

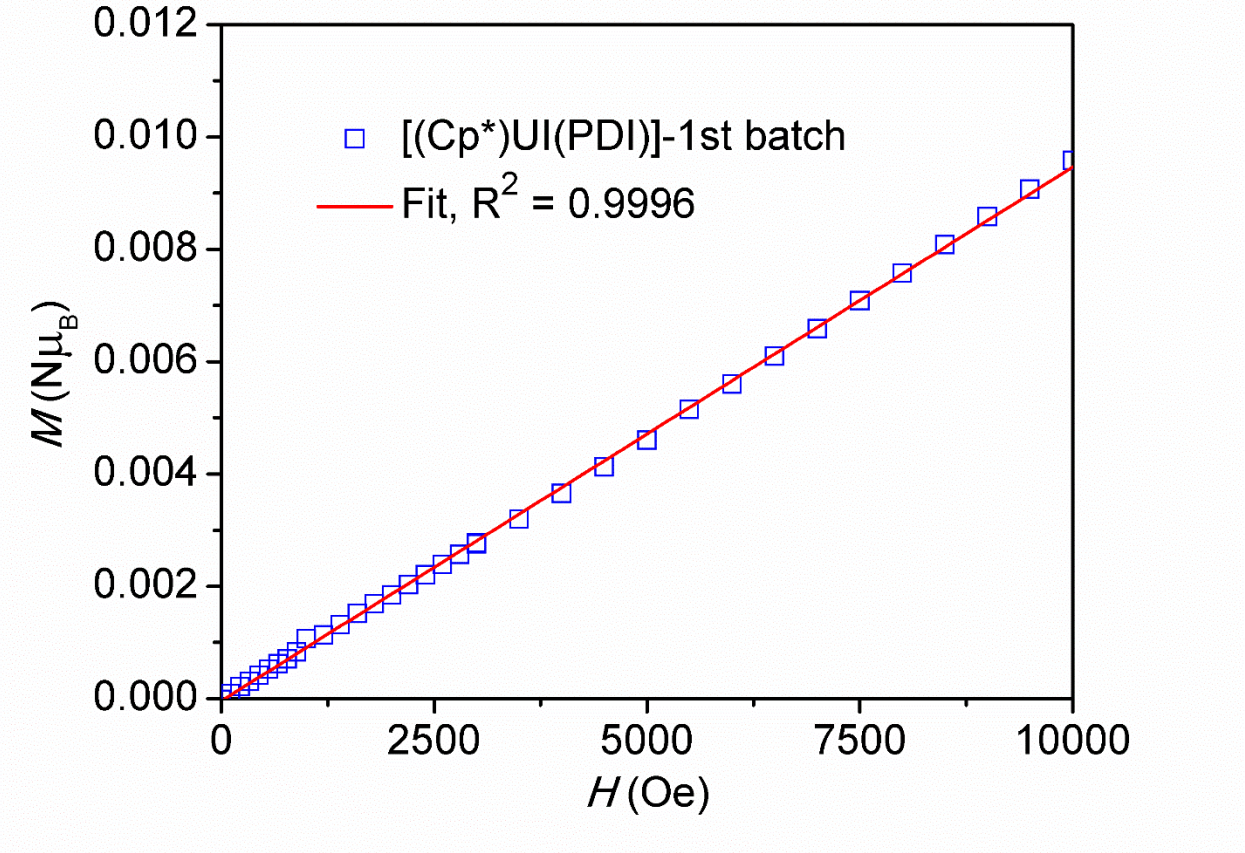


Figure A10.6. Field dependence of magnetization for compound [(^{Mes}PDI^{Me})U(Cp)I] collected at 100 K. The data are fit to a linear regression (y = 9.50E-7x – 4.09E-5) that does not include H = 0 Oe.*

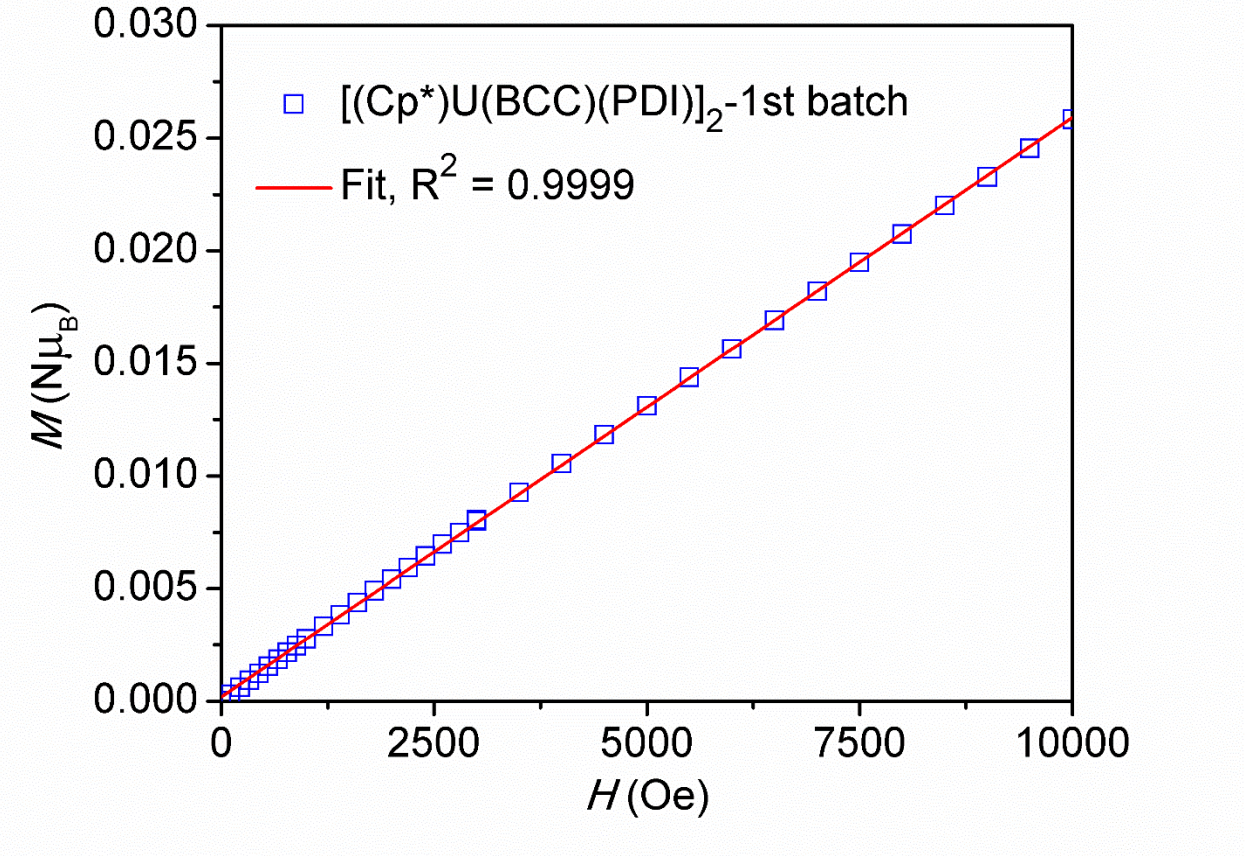


Figure A10.7. Field dependence of magnetization for compound [(^{Mes}PDI^{Me})U(Cp)(BCC)]$_2$ collected at 100 K. The data are fit to a linear regression (y = 2.57E-6x + 1.90×10^{-4}) that does not include H = 0 Oe.*

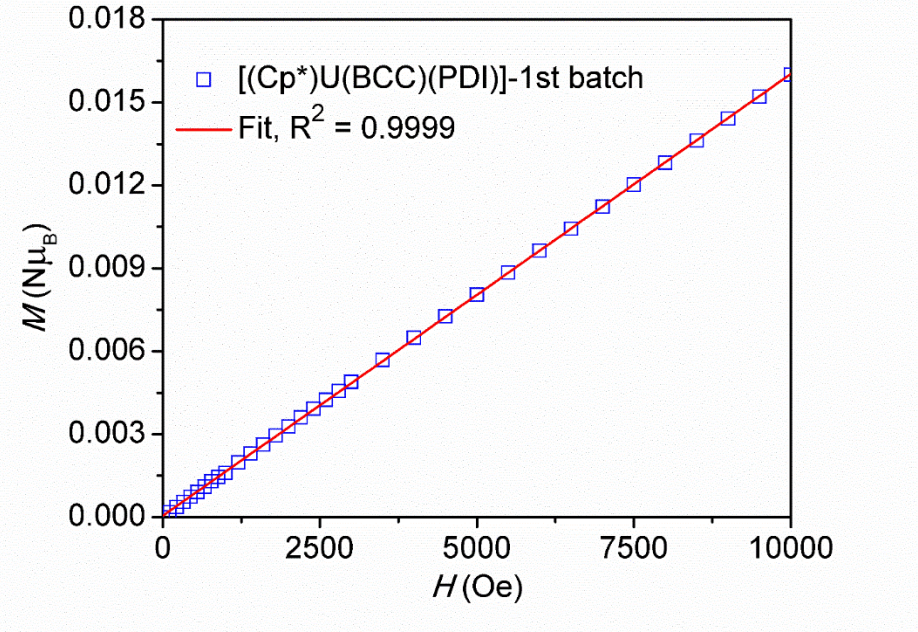


Figure A10.8. Field dependence of magnetization for compound [(^{Mes}PDI^{Me})U(Cp)(BCC)] collected at 100 K. The data are fit to a linear regression (y = 1.60E-6x + 5.15×10^{-5}) that does not include H = 0 Oe.*

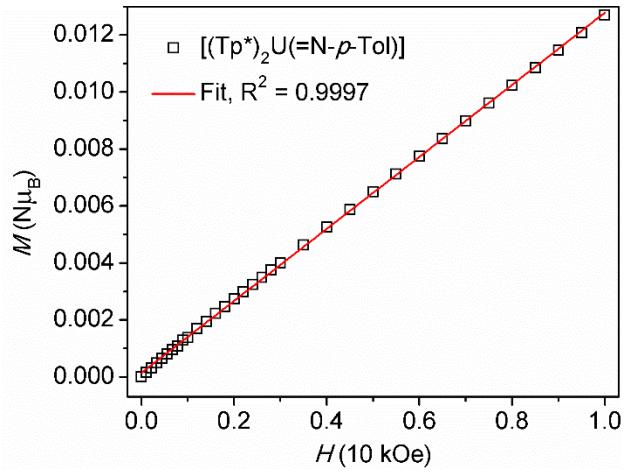


Figure A10.9. Field dependence of magnetization for compound [(Tp)$_2$U(=N-p-Tol)] collected at 100 K. The data are fit to a linear regression (y = 0.0126x - 1.47E-4) that does not include H = 0 Oe.*

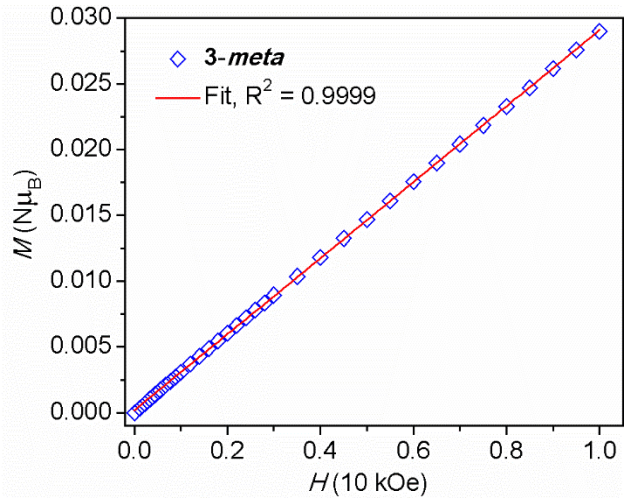


Figure A10.10. Field dependence of magnetization for compound [((Tp)$_2$U)$_2$(m-DIB)] collected at 100 K. The data are fit to a linear regression (y = 0.0289x - 1.73E-4) that does not include H = 0 Oe.*

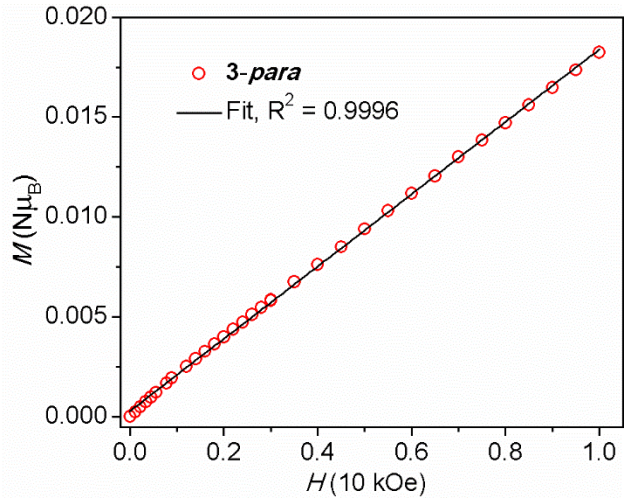


Figure A10.11. Field dependence of magnetization for compound [((Tp)$_2$U)$_2$(p-DIB)] collected at 100 K. The data are fit to a linear regression (y = 0.0181x – 2.93E-4) that does not include H = 0 Oe.*

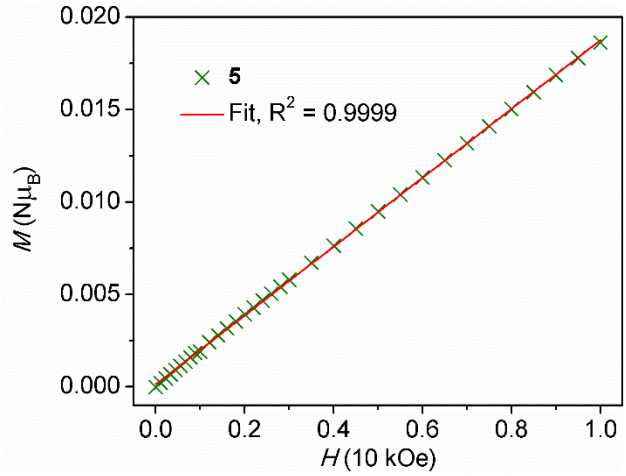


Figure A10.12. Field dependence of magnetization for compound [(Tp)$_2$U)]-insertion product collected at 100 K. The data are fit to a linear regression (y = 0.0151x – 8.94E-5) that does not include H = 0 Oe.*

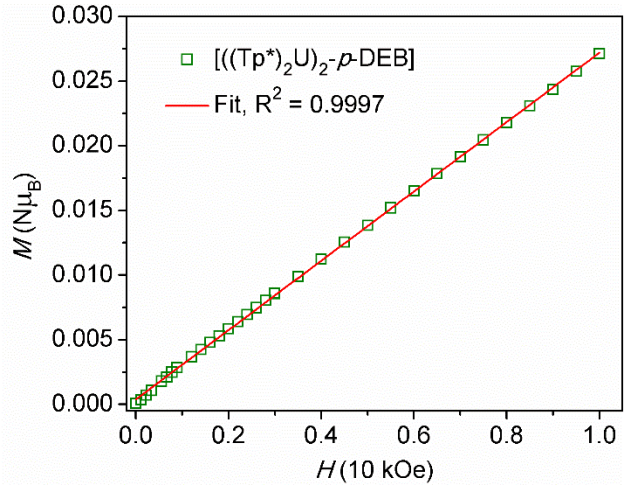


Figure A10.13. Field dependence of magnetization for compound [((Tp)$_2$U)$_2$-p-DEB] collected at 100 K. The data are fit to a linear regression (y = 0.0268x - 3.89E-5) that does not include H = 0 Oe.*

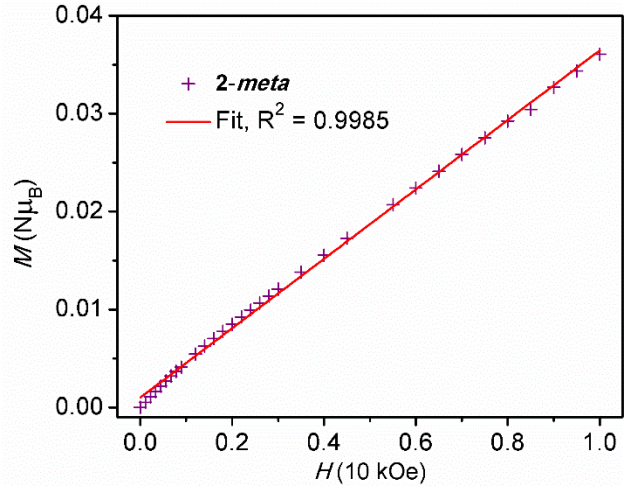


Figure A10.14. Field dependence of magnetization for compound [((Tp)$_2$U)$_2$-m-DEB] collected at 100 K. The data are fit to a linear regression (y = 0.0128x - 3.42E-5) that does not include H = 0 Oe.*

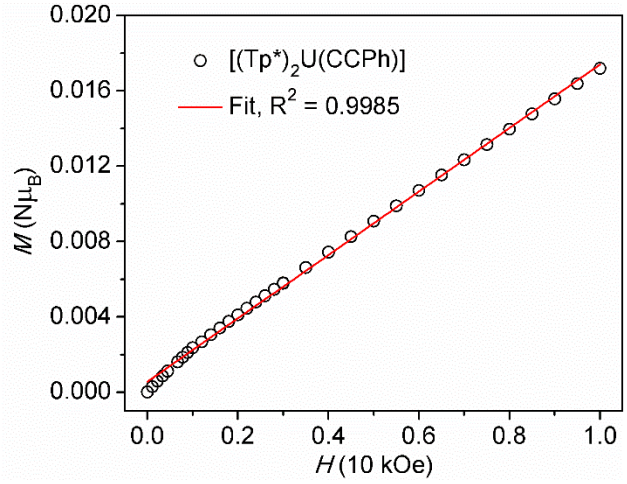


Figure A10.15. Field dependence of magnetization for compound [(Tp)$_2$U(CCPh)] collected at 100 K. The data are fit to a linear regression (y = 0.0168x – 5.60E-4) that does not include H = 0 Oe.*

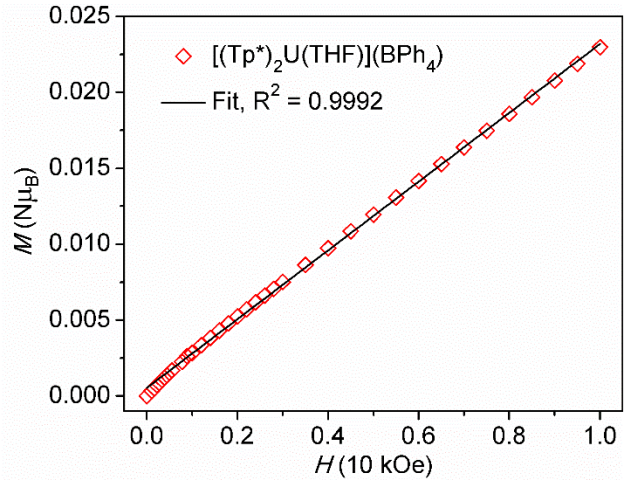


Figure A10.16. Field dependence of magnetization for compound [(Tp)$_2$U(THF)](BPh$_4$) collected at 100 K. The data are fit to a linear regression (y = 0.0227x – 5.37E-4) that does not include H = 0 Oe.*

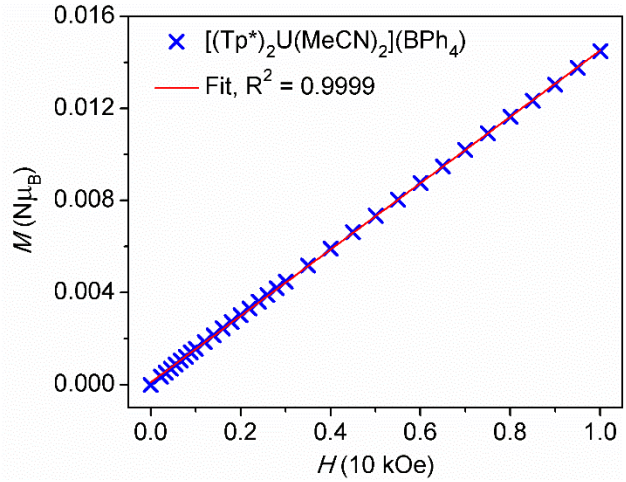


Figure A10.17. Field dependence of magnetization for compound [(Tp)$_2$U(MeCN)$_2$](BPh$_4$) collected at 100 K. The data are fit to a linear regression (y = 0.0144x – 1.10E-4) that does not include H = 0 Oe.*

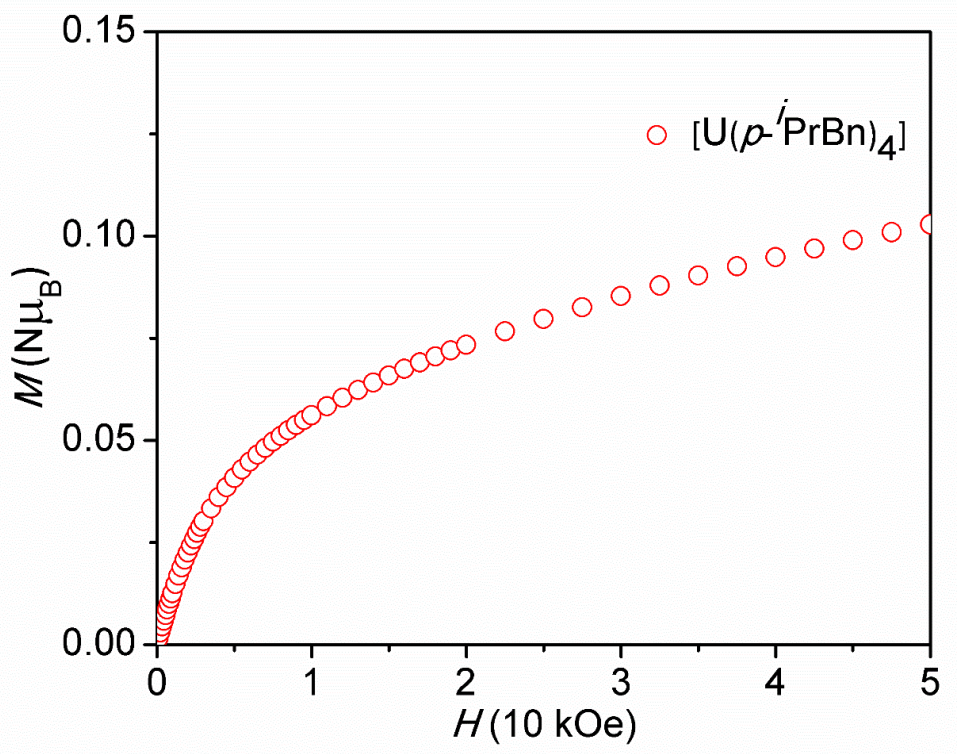


Figure A10.18. Field dependence of magnetization for [U(p-iPrBn)$_4$] collected at 1.8 K.

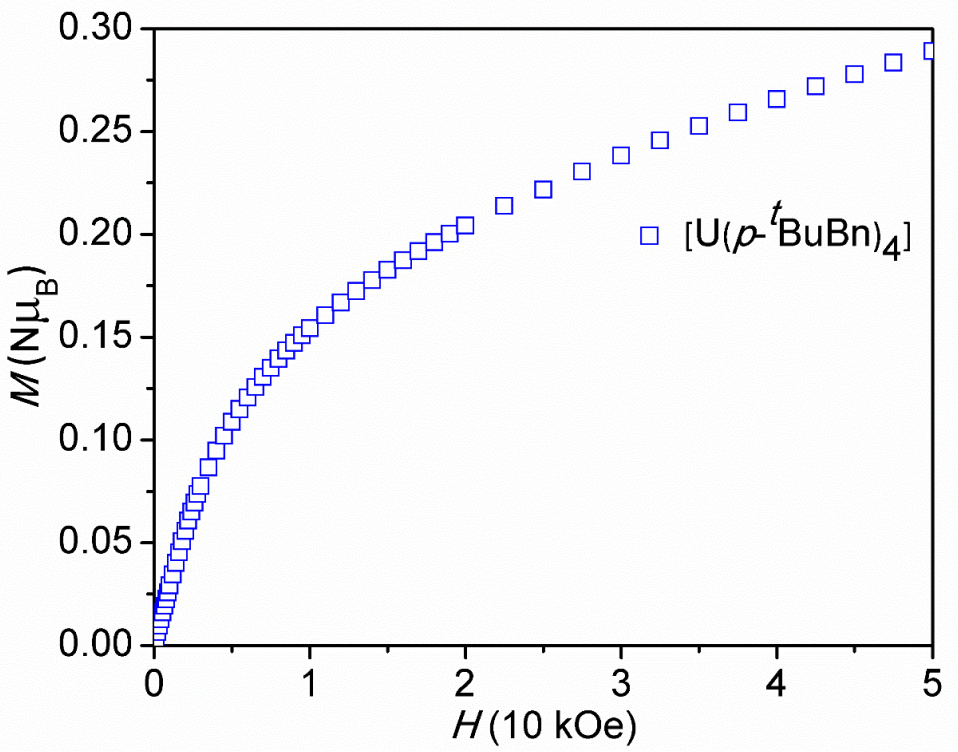


Figure A10.19. Field dependence of magnetization for [U(p-tBuBn)$_4$] collected at 1.8 K.

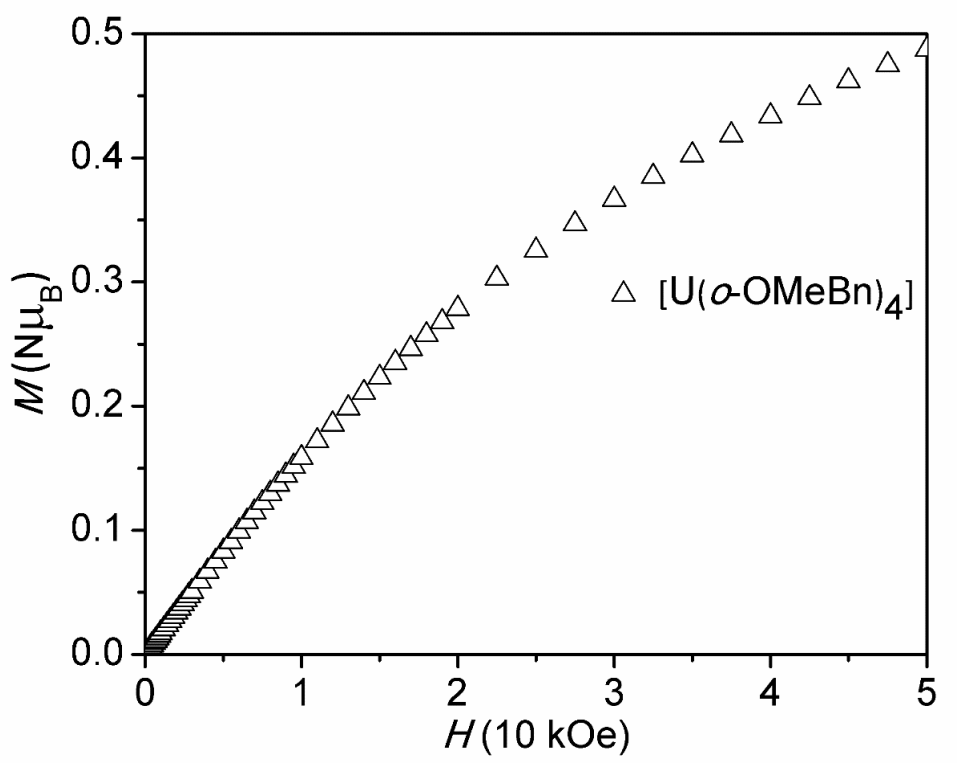


Figure A10.20. Field dependence of magnetization for [U(o-OMeBn)$_4$] collected at 1.8 K.

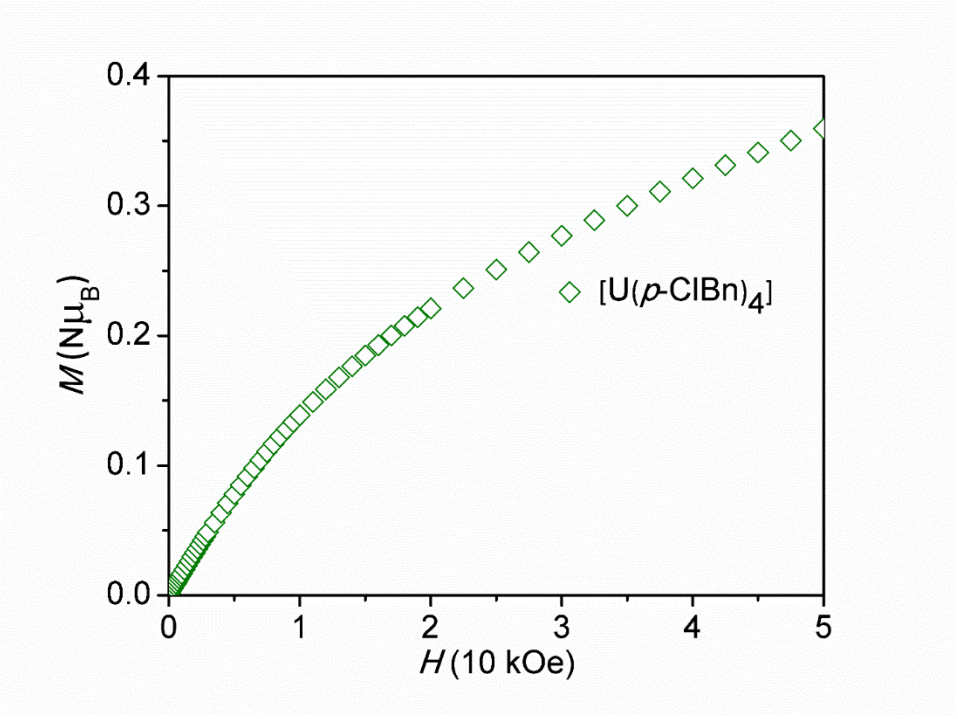


Figure A10.21. Field dependence of magnetization for [U(p-ClBn)$_4$] collected at 1.8 K.

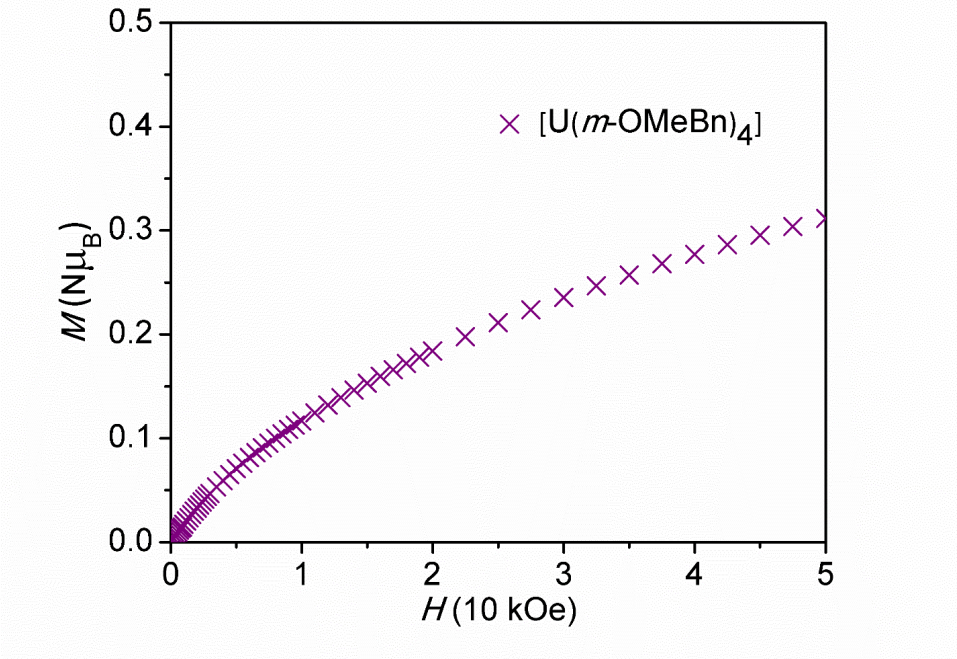


Figure A10.22. Field dependence of magnetization for [U(m-OMeBn)$_4$] collected at 1.8 K.

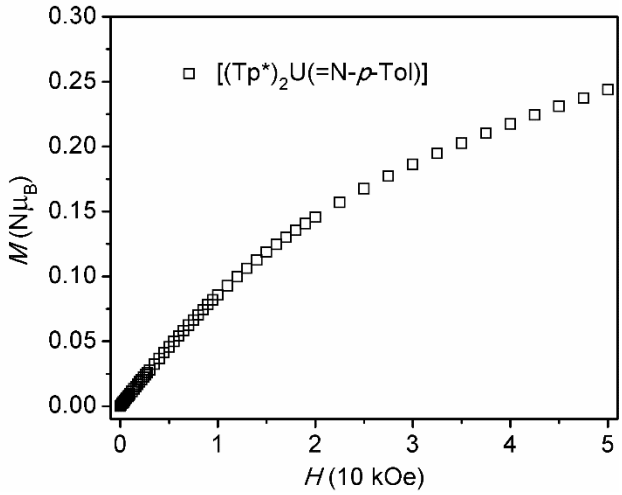


Figure A10.23. Field dependence of magnetization for compound [(Tp)$_2$U(=N-p-Tol)] collected at 1.8 K.*

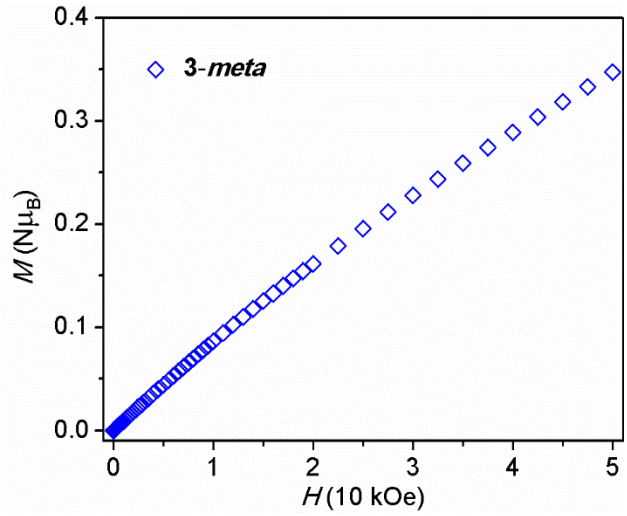


Figure A10.24. Field dependence of magnetization for compound [((Tp)$_2$U)$_2$(m-DIB)] collected at 1.8 K.*

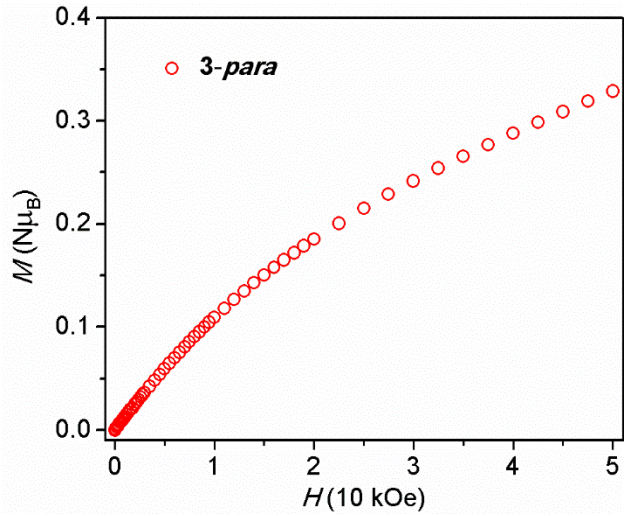


Figure A10.25. Field dependence of magnetization for compound [((Tp)$_2$U)$_2$(p-DIB)] collected at 1.8 K.*

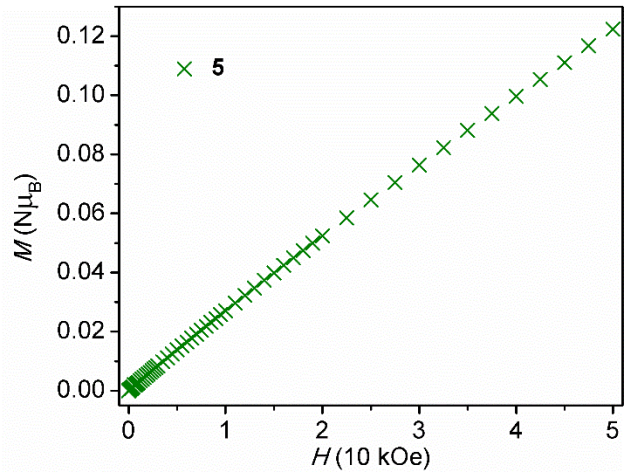


Figure A10.26. Field dependence of magnetization for compound [(Tp)$_2$U)]-insertion product collected at 1.8 K.*

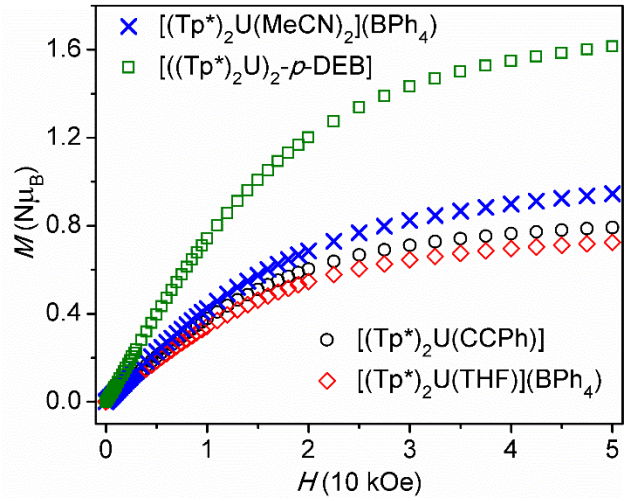


Figure A10.27. Field dependence of magnetization for compounds [((Tp)$_2$U)$_2$-p-DEB], [(Tp*)$_2$U(CCPh)], [(Tp*)$_2$U(THF)](BPh$_4$) and [(Tp*)$_2$U(MeCN)$_2$](BPh$_4$) collected at 1.8 K.*

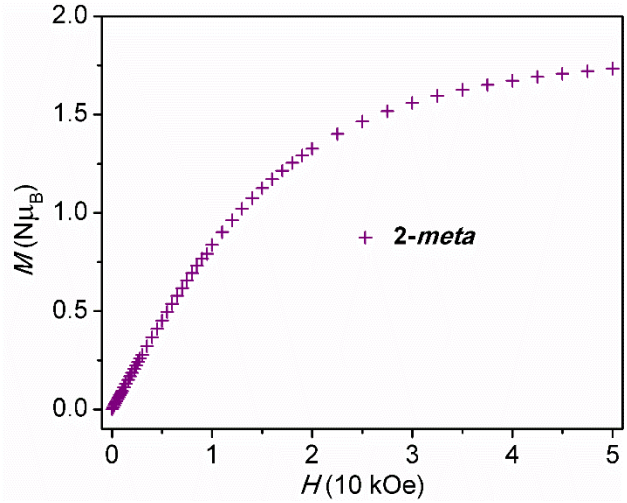


Figure A10.28. Field dependence of magnetization for compound [((Tp)$_2$U)$_2$-m-DEB] collected at 1.8 K.*

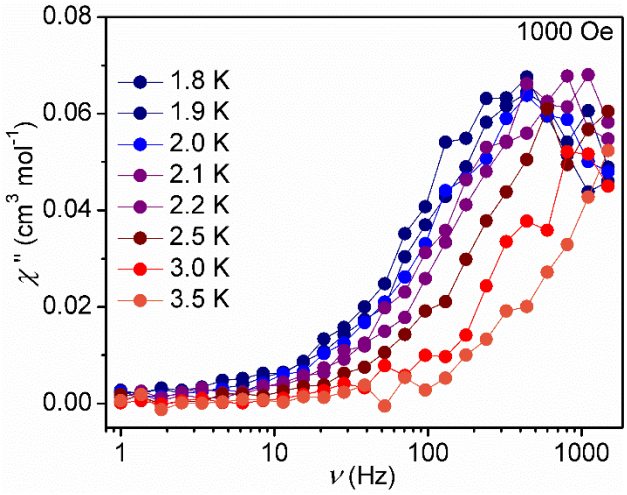


Figure A10.29. Temperature dependence of the out-of-phase magnetic susceptibility for [(Tp)$_2$U(CCPh)] collected with an applied ac field of 4 Oe and an applied dc field of 1000 Oe.*

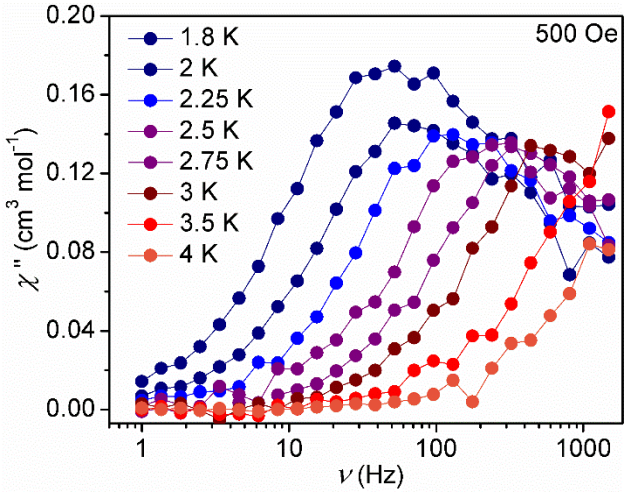


Figure A10.30. Temperature dependence of the out-of-phase magnetic susceptibility for [(Tp)$_2$U(THF)](BPh$_4$) collected with an applied ac field of 4 Oe and an applied dc field of 500 Oe.*

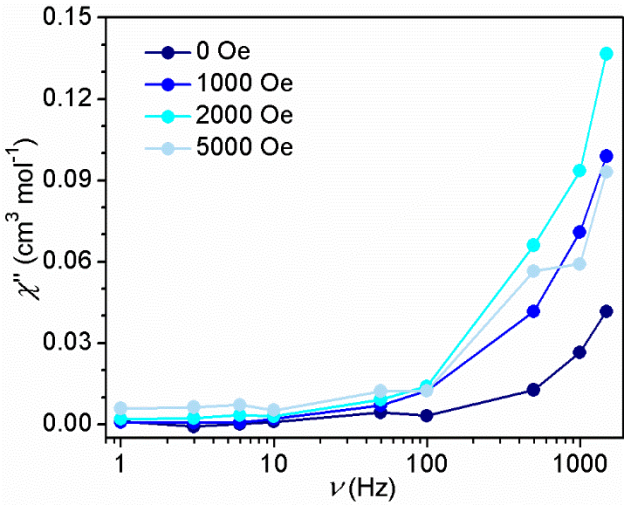


Figure A10.31. Field and frequency dependence of the out-of-phase magnetic susceptibility for compound [((Tp)$_2$U)$_2$-p-DEB] collected at 2 K (4 Oe ac field).*

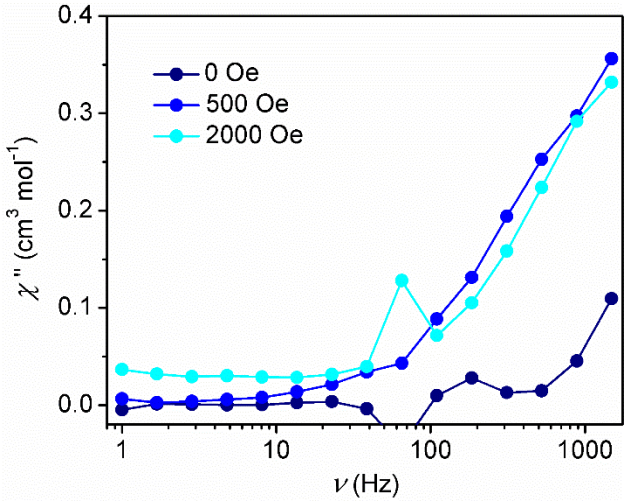


Figure A10.32. Field and frequency dependence of the out-of-phase magnetic susceptibility for compound [((Tp)$_2$U)$_2$-m-DEB] collected at 2 K (4 Oe ac field).*

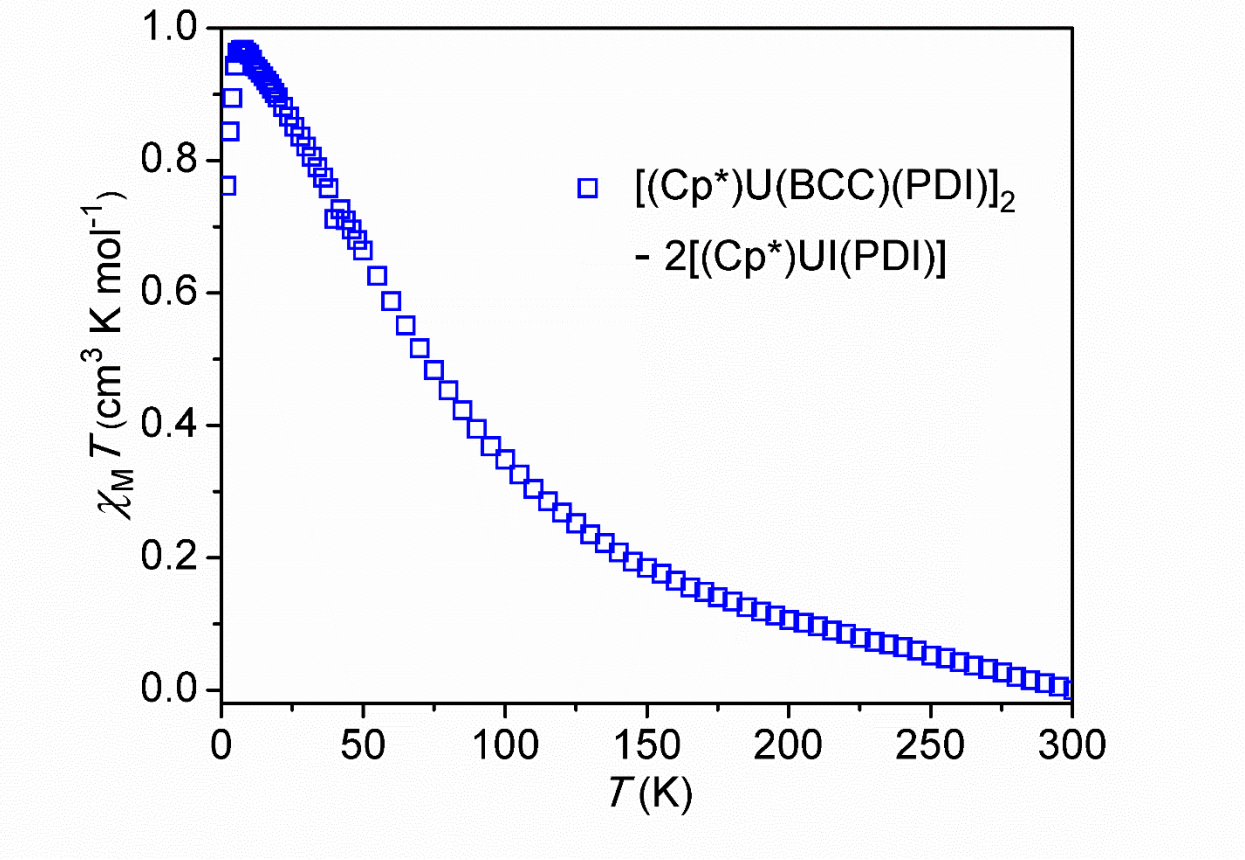


Figure A10.33. Temperature dependent magnetic susceptibility of [(^{Mes}PDI^{Me})U(Cp)(BCC)]$_2$ and two times the magnetic susceptibility of compound [(^{Mes}PDI^{Me})U(Cp*)I] both collected at 5000 Oe.*

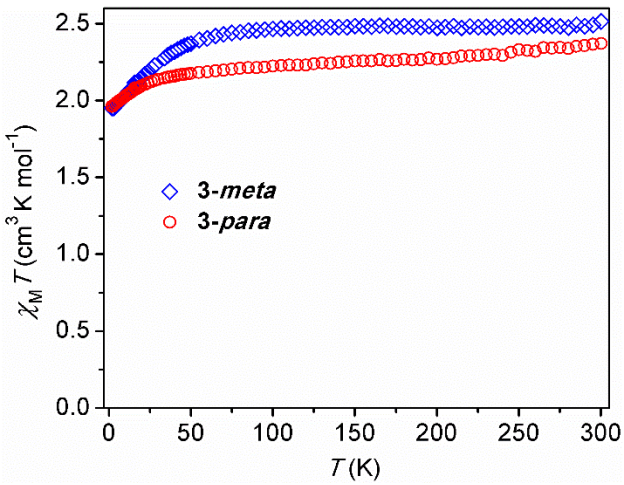


Figure A10.34. Temperature dependence of the magnetic susceptibility for compounds [((Tp)$_2$U)$_2$(p-DIB)] and [((Tp*)$_2$U)$_2$(m-DIB)], both collected at 1000 Oe, where the $\chi_M T$ data have been subtracted from the data obtained for [(Tp*)$_2$U(=N-p-Tol)].*

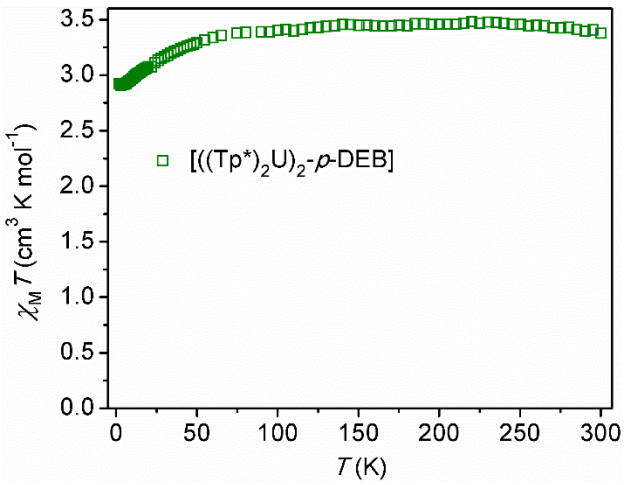


Figure A10.35. Temperature dependence of the magnetic susceptibility for compound [((Tp)$_2$U)$_2$-p-DEB] collected at 1000 Oe. The magnetic susceptibility values were subtracted according to the following equation:*

$$\chi_M T_{subtract} = \chi_M T_{raw} - 2(\chi_M T_{mono}) + 2(\chi_M T_{spin-only})$$

Where $\chi_M T_{mono}$ data are used from [(Tp*)$_2$U(CCPh)] and $\chi_M T_{spin\text{-}only}$ is 1.645 cm^{3}Kmol^{-1} given by the ground state term symbol for a U(III) ion ($^4I_{9/2}$). The downturn in susceptibility value could be attributed to antiferromagnetic coupling between the U centers; however, fits acquired using the program PHI[1] did not give any reasonable fit parameters and the computed *J* values were all small in magnitude (>|0.3| cm^{-1}). In addition, a small increase in $\chi_M T$ value is observed at very low temperatures (>10 K), making antiferromagnetic coupling less reasonable of a conclusion for [(Tp*)$_2$U)$_2$-*p*-DEB].

Table A10.1. Comparison of different magnetic and crystallographic properties of U(Tp) complexes.*

Complex	τ_0 (1 × 10^{-6} s)	U_{eff} (cm^{-1})	Closest U···U distance (Å)	Average U···B distance (Å)
[(Tp*)$_2$U(I)]	0.18	21.0	9.074(5)	3.478(8)
[(Tp*)$_2$U(bpy)](I)	0.14	18.2	9.455(4)	3.565(8)
[((Tp*)$_2$U)$_2$-*p*-DEB]	--	--	9.064(4)	3.646(3)
[(Tp*)$_2$U(CCPh)]	2.08	6.81	9.983(8)	3.626(8)
[(Tp*)$_2$U(THF)](BPh$_4$)	4.28	9.00	8.893(6)	3.575(6)
[(Tp*)$_2$U(MeCN)$_2$](BPh$_4$)	4.00	8.36	10.636(7)	3.652(8)